Second Coordination Sphere Engineering in Macrocyclic Ruthenium Water Oxidation Catalysts

Dissertation zur Erlangung

des naturwissenschaftlichen Doktorgrades

der Julius-Maximilians-Universität Würzburg

vorgelegt von

Niklas Noll

aus Bad Soden-Salmünster

Würzburg 2023

Eingereicht bei der Fakultät für Chemie und Pharmazie am:

_____09.01.2023_____

Gutachter der schriftlichen Arbeit:

1. Gutachter: Prof. Dr. Frank Würthner

2. Gutachter: Prof. Dr. Todd B. Marder

Prüfer des öffentlichen Promotionskolloquiums:

1. Prüfer: Prof. Dr. Frank Würthner

2. Prüfer: Prof. Dr. Todd B. Marder

3. Prüfer: Prof. Dr. Tobias Brixner

4. Prüfer: Prof. Dr. Roland Mitrić

5. Prüfer: Prof. Dr. Udo Radius

Datum des öffentlichen Promotionskolloquiums:

_____28.02.2023_____

Doktorurkunde ausgehändigt am:

_____

Abbreviations

2D	two-dimensional
3D	three-dimensional
AFM	atomic force microscopy
a.u.	arbitrary units
ax	axial
bda	2,2'-bipyridine-6,6'-dicarboxylate
bpaH$_2$	2,2'-bipyridine-6,6'-diylbis(hydrogen phosphonate)
bpb	1,4-bis(pyridin-3-yl)benzene
bpHc	6'-(hydroxyoxidophosphoryl)-2,2'-bipyridine-6-carboxylate
bpy	2,2'-bipyridine
bpyms	2,2'-bipyridine-5,5'-bis(methane sulfonate)
CAN	cerium ammonium nitrate
COF	covalent organic framework
COSMO	conductor-like screening model
COSY	correlation spectroscopy
CPE	controlled potential electrolysis
CV	cyclic voltammetry
d	doublet
DCM	dichloromethane
DCTB	*trans*-2-[3-(4-*tert*-butylphenyl)-2-methyl-2 propenylidene]malononitrile
DFT	density functional theory
DMF	*N,N*-dimethylformamide
DMSO	dimethyl sulfoxide
dmso	dimethyl sulfoxide as ligand
DOSY	diffusion-ordered spectroscopy
dppf	1,1'-bis(diphenylphosphino)ferrocene
DPV	differential pulse voltammetry
engl.	english
EPR	electron paramagnetic resonance
eq	equatorial
eq.	equation
equiv.	equivalent
ESI	electrospray ionization
FOWA	foot of the wave analysis

FTIR	fourier transform infrared spectroscopy
GC	gas chromatography
GPC	gel permeation chromatography
His	histidine
HMBC	heteronuclear multiple bond coherence
HOMO	highest occupied molecular orbital
HPLC	high-performance liquid chromatography
HR	high resolution
HSQC	heteronuclear single quantum coherence
I2M	interaction of two metal-oxyl species
isoq	isoquinoline
KIE	kinetic isotope effect
L	ligand
LUMO	lowest unoccupied molecular orbital
m	multiplet
MALDI TOF	matrix-assisted laser desorption/ionization time-of-flight
MeOH	methanol
min	minute
MLCT	metal-to-ligand charge-transfer
MOPAC	molecular orbital package
MS	mass spectrometry
n.d.	not determined
NHC	*N*-heterocyclic carbene
NHE	normal hydrogen electrode
NMR	nuclear magnetic resonance
NOE	nuclear Overhauser effect
NOESY	nuclear Overhauser effect spectroscopy
OEC	oxygen-evolving complex
OEG	oligo ethylene glycol
ORTEP	Oak Ridge thermal-ellipsoid plot
PBI	perylene bisimide
PCET	proton-coupled electron transfer
pda	1,10-phenanthroline-2,9-dicarboxylate
pdc	2,6-pyridinedicarboxylate
phs	phenanthroline-2-sulfonate
pic	4-picoline
PM6	parameterization method 6

ppm	parts per million
PS	photosensitizer
PSII	photosystem II
PTFE	polytetrafluoroethylene
ptz	phthalazine
py	pyridine
rds	rate-determining step
ref.	reference
rt	room temperature
s	singlet
SEA	sacrificial electron acceptor
SEM	scanning electron microscopy
t	triplet
tda	2,2′:6′,2″-terpyridine-6,6″-dicarboxylate
TFE	2,2,2-trifluoroethanol
TLC	thin layer chromatography
TOF	turnover frequency (deutsch: Wechselzahl)
TON	turnover number (deutsch: Umsatzzahl)
$tpaH_2$	2,2′:6′2″-terpyridine-6,6″-diylbis(hydrogen phosphonate)
tpc	2,2′:6′2″-terpyridine-6-carboxylate
tpy	2,2′:6′,2″-terpyridine
UV	ultraviolet
Vis	visible
VPO	vapor pressure osmometry
vs.	versus
WNA	water nucleophilic attack
WOC	water oxidation catalyst
WOK	Wasseroxidationskatalysator
XAS	X-ray absorption spectroscopy
XFEL	X-ray free electron laser

Variables and Constants

k_B	Boltzman constant
c	concentration
δ	chemical shift
d	distance
D	diffusion coefficient
Δ	energy splitting of d-orbitals
ε	extinction coefficient
E	potential
I	current
I	intensity
J	NMR coupling constant
λ	wavelength
n	amount of substance
η	overpotential
p	pressure
pH	potential of hydrogen
pK_a	potential of acidity constant
k	rate constant
μ	viscosity
R	ideal gas constant (8.314 J K^{-1} mol^{-1})
r	radius
r_H	hydrodynamic radius
θ	rotation angle
T	temperature
t	time
V	volume

Table of Contents

Chapter 1

Introduction and Aim of the Thesis

In 2015, 197 countries committed to the Paris Climate Agreement with the overarching goal of *"holding the increase in the global average temperature to well below 2 °C above pre-industrial levels and pursuing efforts to limit the temperature increase to 1.5 °C above pre-industrial levels"*.[1] According to recent studies, a temperature increase of nearly 3 °C by 2100 is projected, as anthropogenic greenhouse gas emissions have not yet peaked due to progressive global economic and population growth.[2, 3] As of 2022, the current energy crisis has resulted in high prices for finite fossil fuel reserves due to political tensions.[4] Combined with the potentially catastrophic consequences of global warming, our society has to increase its investments in the development of carbon-neutral and sustainable energy technologies.[5] Solar energy has the highest energy potential of all renewable energy sources (solar, wind, hydropower, etc.), as one hour of solar radiation would be sufficient to supply all of the world's energy consumption for an entire year.[6] Besides its great potential, the sun's diurnal fluctuations must be compensated by the development of appropriate large-scale energy storage solutions and technologies to ensure a secure energy supply.[7] In this context, decades of research have been invested in photovoltaic cells to convert solar power into electricity, which is directly stored in batteries.[8] Although battery technologies have advanced considerably in recent years, their low storage density and age-related deterioration make batteries less suitable for a complete substitution of fossil fuels.[9-11] In contrast, terrestrial plants have been using natural photosynthesis for more than 2.4 billion years to produce about 100 billion tons of dry biomass annually by utilizing photosynthetic organisms to capture sunlight and convert it into energy-rich biomolecules such as carbohydrates.[12-14] In this way, photosynthesis is responsible for the production of most of the fossil fuel reserves on earth.[15] The biomimetic mimicking of nature's ingenuity by converting solar energy into chemical energy and storing it in the chemical bonds of high-energy molecules, so-called 'solar fuels', has led to the promising concept of artificial photosynthesis.[16-19] Compared to other solar fuels,[20] hydrogen as an energy carrier has the advantage of a very high energy density and can therefore be utilized for long-term storage and transportation via transformation into methanol or ammonia as a carrier medium.[21, 22] In this context, it is most attractive if the necessary protons for the production of green hydrogen are obtained from the abundant resource H_2O by using the process of photochemical water splitting.[16, 17, 23] As direct water splitting by sunlight is not possible,[24] artificial photosynthetic systems require individual

components that perform the essential light-harvesting, charge separation and redox catalysis to generate hydrogen as a solar fuel similar to the natural blueprint (Figure 1).[18, 25]
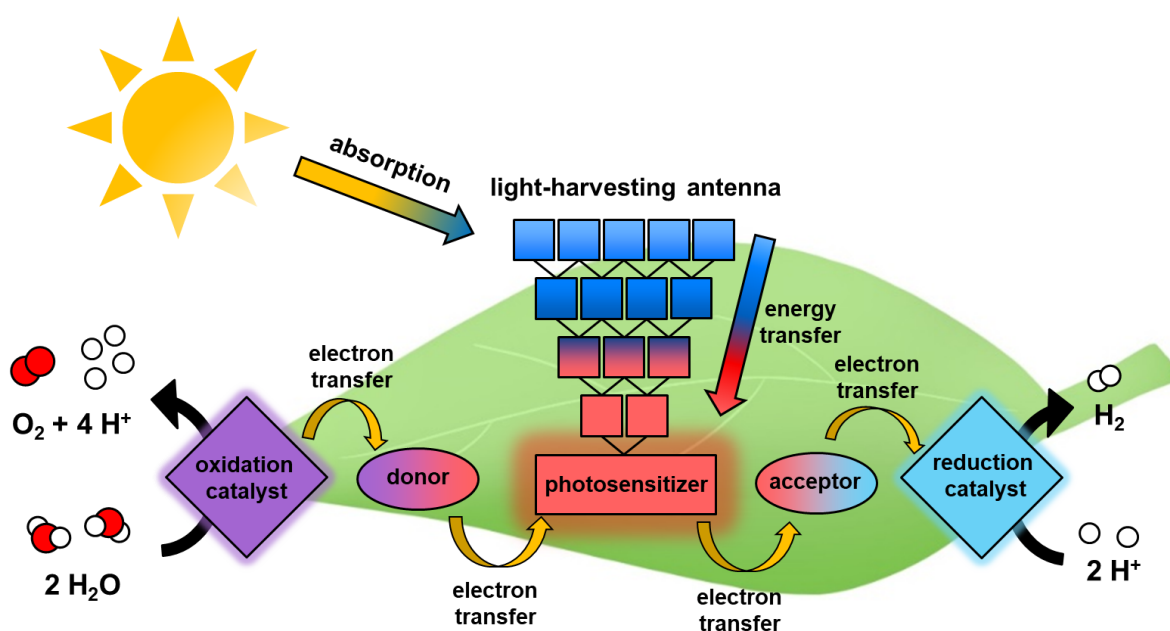

Figure 1. Schematic illustration of the individual key components of an artificial system for the photochemical water splitting. Adapted with permission from ref. [18]. Copyright 2013 The Royal Society of Chemistry.

The major challenge in the development of such an artificial photosynthetic device is the thermodynamically demanding water oxidation reaction, which requires the removal of four electrons and four protons, the presence of high-energetic intermediates, and finally the step of O_2 evolution.[26] Nature has overcome the energetic hurdles of water oxidation by evolving a distorted tetramanganese-calcium cluster (Mn_4CaO_5), commonly known as oxygen-evolving complex (OEC), which performs water splitting at a high catalytic rate and with low overpotential.[27-29] The active site of the OEC is embedded in a large and highly sophisticated protein domain that regulates the reactivity of the catalytic center by facilitating substrate preorganization in confined space.[30, 31] Attempts to construct functional mimics of the OEC active site have led to synthetic clusters with low catalytic performances and high overpotentials due to the lack of a supporting protein environment.[32, 33] Consequently, concepts from the emerging field of supramolecular catalysis have been applied to the design of molecular water oxidation catalysts (WOCs) working at low overpotential.[34-36] In recent years, several literature examples have emphasized conformational substrate orientation to the catalytically active metal site of ruthenium-based water oxidation catalysts by secondary, non-covalent interactions of the ligand framework, which led to activities comparable to the natural OEC.[34-36] As a next step, Würthner and co-workers demonstrated the enormous

potential of confined environments for water oxidation catalysis by implementing the catalytically active Ru(bda) (bda: 2,2'-bipyridine-6,6'-dicarboxylate) subunit into cyclic metallosupramolecular macrocycles.[37-39] Remarkably, these trinuclear WOCs displayed high catalytic activity and stability similar to their natural counterparts. According to theoretical calculations, the interaction with substrate H_2O molecules is promoted by the formation of a hydrogen-bonded network of preorganized water molecules inside the macrocyclic cavity through cooperative effects between the individual catalytic centers.[37, 38, 40]

The aim of the present thesis was to develop novel molecular design strategies for enhanced interactions with the intracavity H_2O environment by the sophisticated second coordination sphere engineering of macrocyclic Ru(bda) WOCs (Figure 2).
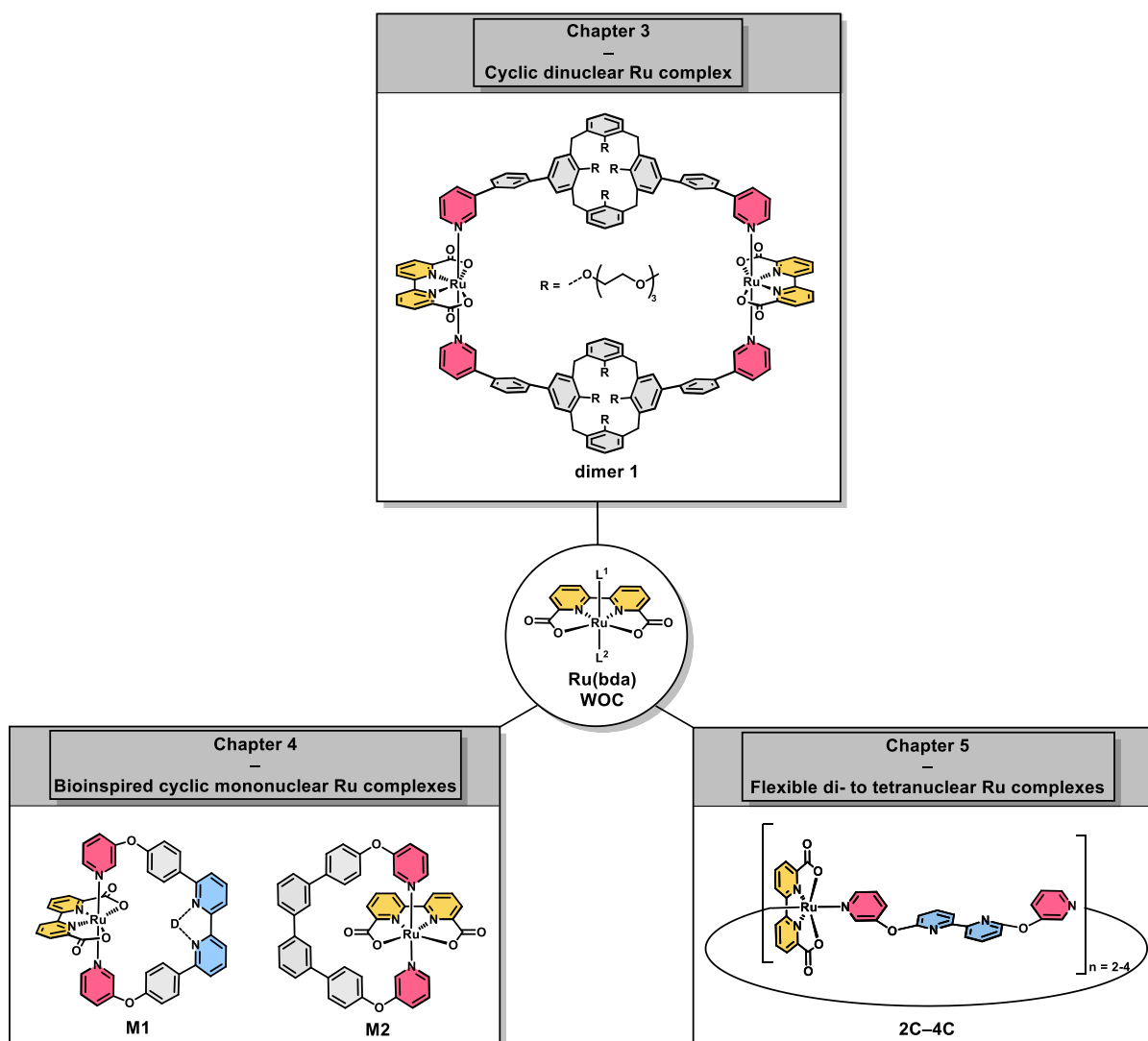

Figure 2. Chemical structures of novel mono- and multinuclear Ru(bda)-based water oxidation catalysts investigated in the present thesis.

Following our successful 'macrocycle approach', in the first section of the thesis a cyclic calix[4]arene scaffold functionalized with solubilizing tri(ethylene) glycol chains in **dimer 1** was applied for water oxidation catalysis. As a next step towards artificial enzyme mimics, two different approaches using either a rigid or a more flexible macrocyclic ligand framework were investigated. In a first approach, we envisioned to conceptually mimic the active site of natural enzymes by preorganizing substrate H_2O molecules via non-covalent interactions in the rigid pocket of mononuclear complex **M1**. While a more flexible ligand framework in Ru complexes of varying sizes **2C−4C** should promote tailored folding of the dynamic ligand backbone for enhanced interaction with H_2O and facilitate proton abstraction by the pendant base.

The first part of *Chapter 2* briefly reviews the role of non-covalent interactions from the surrounding protein environment on enzymatic reactions, using the metalloenzymes hydrogenases, cytochrome *c* oxidases and, especially, the oxygen-evolving complex in photosystem II (OEC-PSII) as examples. After an introduction to artificial water oxidation catalysis, the two literature-known mechanistic pathways and experimental techniques for studying water oxidation are presented. The final section introduces concepts for a fine-tuning of the first and second coordination sphere of homogeneous Ru-based WOCs, with a special emphasis on the Ru(bda) catalyst family.

Chapter 3 describes the synthesis and characterization of a calix[4]arene-based cyclic dinuclear Ru(bda) complex **dimer 1**, which is functionalized with solubilizing tri(ethylene) glycol chains. The influence of the second coordination sphere on the catalytic mechanism is investigated by chemical and photocatalytic water oxidation experiments as well as kinetic measurements.

In *Chapter 4*, a single Ru(bda) unit is embedded into the macrocyclic environment of complex **M1**, which is equipped with a bipyridine-functionalized ligand located opposite to the active site, to preorganize H_2O molecules similar as in enzymatic clefts. In-depth studies by pH-dependent NMR spectroscopy and single crystal X-ray analysis are performed to explain the different catalytic behaviour under chemical and photocatalytic conditions compared to the unfunctionalized reference **M2**.

In *Chapter 5*, a series of structurally more flexible di- to tetranuclear Ru(bda) complexes **2C–4C** bearing base-functionalized axial ligands for chemical and photocatalytic water oxidation catalysis are reported. Detailed single crystal X-ray analysis of the whole molecular series provided conformational insights to explain the observed differences in catalytic activity under acidic and neutral conditions.

Chapter 6 and *Chapter 7* summarize and conclude the results of the present thesis in English and German, respectively.

Chapter 8 provides details on the experimental methods and materials used in this thesis, as well as additional information on the synthesis and characterization of new compounds presented in *Chapter 3*, *Chapter 4* and *Chapter 5*.

Chapter 2

Literature Survey

The first section of this chapter will provide an overview of the role of secondary interactions from the outer coordination sphere on enzymatic reactions in nature. Following a general introduction, the role of non-covalent interactions will be discussed using the metalloenzymes hydrogenases, cytochrome *c* oxidases and the oxygen-evolving complex in photosystem II as examples. The second section will introduce molecular catalysts for artificial water oxidation catalysis. Furthermore, the two literature-known mechanisms for water oxidation, as well as experimental techniques to investigate the catalytic performance of molecular catalysts, will be addressed. The final section, which has two subsections, is focused on the development of Ru-based molecular water oxidation catalysts. In the first subsection, the development of artificial catalysts based on variations within the first coordination sphere up to the first report on Ru(bda) water oxidation catalysts will be presented. In addition, possible explanations for the high catalytic activity of the Ru(bda) catalyst family will be discussed. The second subsection will review the effects of secondary interactions on the catalytic performance of water oxidation catalysts, with a particular focus on non-covalent interactions, the influence of pendant functional groups and the design of confined environments.

2.1   Outer coordination sphere of natural metalloenzymes

2.1.1   Role of weak non-covalent interactions in metalloenzymes

Metalloenzymes are tailor-made, catalytically active metalloproteins that perform a wide range of complex and thermodynamically challenging biological processes with high selectivity.[41, 42] Prominent examples include water oxidation in photosystem II as part of oxygenic photosynthesis,[43] cytochrome *c* oxidases that catalyze the reverse reaction of oxygen reduction[44] and hydrogenases.[45] Apart from biological transformations, natural enzymes perform several other functions, including small molecule transportation and storage,[46] protein structure stabilization[47] and signal transduction.[48] Substrate activation and transformation proceed at the so-called active site of enzymes. The active site of metalloenzymes comprises a redox-active metal center as the catalytic site, with directly coordinated amino acid residues forming the primary coordination sphere.[41] These coordinating ligands play a crucial role in defining the available chemistry of the active site by controlling substrate binding or modulating the redox properties of the metal center.[41, 49, 50] The surrounding protein environment, which

is composed of individual peptide groups and amino acid side chains, is important for fine-tuning and regulating the reactivity of the active site.[51] Several transport channels are present in the outer coordination sphere, which regulate the delivery of substrates and products between the active site and the protein surface.[52, 53] Through non-covalent interactions such as hydrogen bonding, electrostatic interactions and hydrophobic interactions, the adjacent residues stabilize transition states and promote regio- and stereoselective substrate binding. Furthermore, regeneration of the outer coordination sphere after catalysis is facilitated by the reversible character of non-covalent bonds.[51]
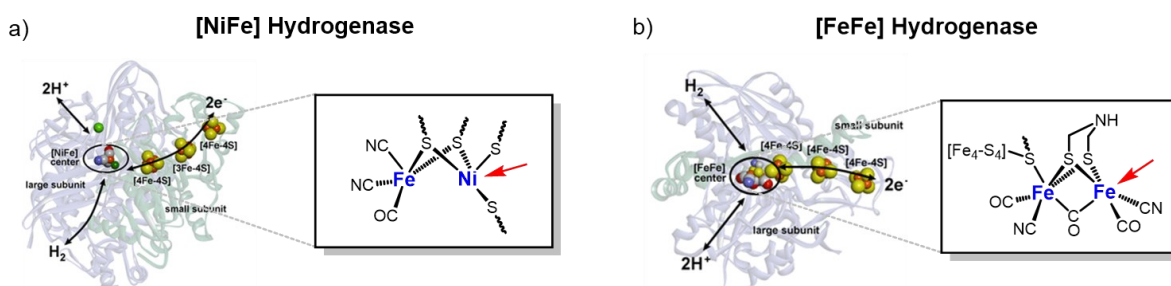

Figure 3. Three-dimensional structure of the small and large subunits of a) [NiFe] hydrogenase and b) [FeFe] hydrogenase with enlarged chemical structures of the respective active sites. The arrow indicates the open metal coordination site at the respective center. In both structures the electron transfer chain via [4Fe-4S] clusters and pathways for H_2 and H^+ transfer are schematically illustrated. Figures 3a) and 3b) are adapted with permission from ref. [45]. Copyright 2014 American Chemical Society.

Hydrogenases represent an important class of metalloenzymes, which catalyze the reversible oxidation of molecular hydrogen in archae, bacteria and some eukaryotes.[45, 54, 55] In nature, there are two main classes of hydrogenases, which can be distinguished into [NiFe]- and [FeFe]-hydrogenases on the basis of the metal ions in the active center (Figure 3).[45, 55] The [NiFe]-hydrogenase is more active in H_2 oxidation, while the [FeFe]-hydrogenases are more active in H_2 production, although there are some exceptions.[56] The binuclear active site of both hydrogenases contains inorganic CO and CN^- ligands coordinated to the respective Fe center. These ligands fine-tune the redox properties of the metal center and stabilize it via hydrogen bonding to the surrounding protein environment.[57, 58] Additionally, the binuclear [NiFe]-center is linked by a bridging sulfur residue, whereas [FeFe]-hydrogenases have an azadithiolate residue that serves as a bridging unit and is involved in proton transfer to and from the catalytic site. (Figure 3).[59] In general, hydrogenases are composed of two subunits. The respective active sites are located within the large subunit of hydrogenases, and three [4Fe-4S]-clusters, which mediate the electron transport chain, are part of the small subunit.[59, 60] To achieve fast H_2 activation rates, hydrogenases require efficient proton-coupled electron transfer (PCET) pathways, which are provided by the surrounding protein matrix via

hydrogen-bonding networks of polar amino acid residues, H_2O molecules and hydrophilic cofactors. Furthermore, three separate channels for H_2, electron and proton transport connect the active site with the protein surface.[59, 61]

A fascinating example of biological control in nature is the thermodynamically challenging interconversion between O_2 and H_2O as part of the biological processes of photosynthesis and respiration (eq. 1).[62] Cytochrome *c* oxidases catalyze the four-electron reduction of O_2 at a binuclear heme-copper active site within the inner membrane of mitochondria and many bacteria,[62-64] whereas the reversed reaction proceeds within the oxygen-evolving complex in PSII, which will be further discussed in the subsequent chapter 2.1.2.[27, 31]

$$O_2 + 4H^+ + 4e^- \underset{\text{photosynthesis}}{\overset{\text{respiration}}{\rightleftharpoons}} 2\,H_2O \qquad (1)$$
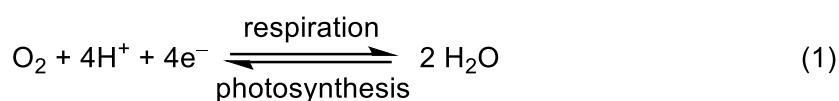
During oxygen reduction, heme-copper oxidases generate an electrochemical proton gradient across the inner membrane to transfer electrons from the positively charged P side to the active site and pump protons in the reverse direction from the negatively charged N side to the P side (Figure 4).[44, 65] Hydrophilic amino acids and H_2O molecules within the protein scaffold facilitate these PCETs, and a unique tyrosine residue near the active site assists the O–O bond breaking step by providing protons for H_2O formation.[44, 66] In addition, molecular simulations revealed that protonated H_2O clusters close to the active site serve as proton storage during the proton pumping process.[67]
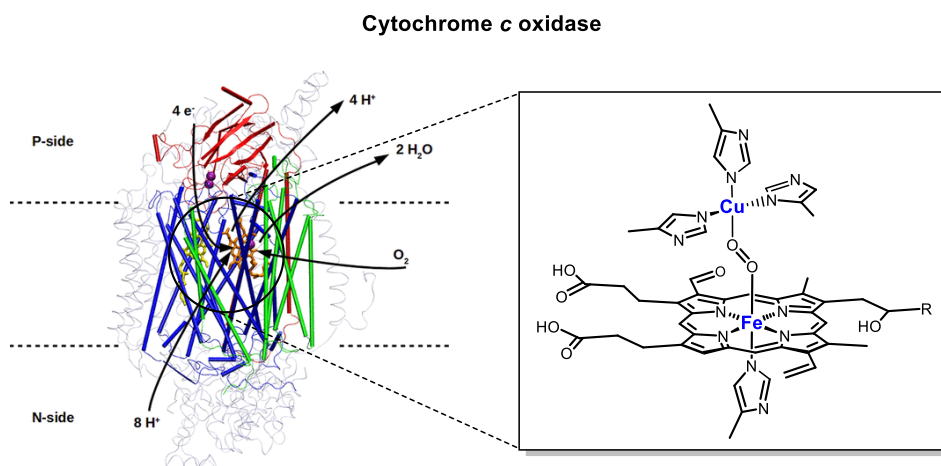

Figure 4. Structure of cytochrome *c* oxidase with three subunits (highlighted in blue, red and green). Lipid bilayer boundaries (dotted lines) between negatively charged N-side, active site and positively charged P-side and electron, proton, H_2O and O_2 pathways are marked. The enlarged chemical structure of the binuclear heme-copper active site is shown. Figure 4 is adapted with permission from ref. [44]. Copyright 2018 American Chemical Society.

2.1.2   Oxygen-evolving complex in photosystem II

Remarkably, the multi-subunit protein complex PS II is the only molecular machine within our natural environment that uses the oxidation of water to molecular oxygen as a proton and electron source to store solar energy in organic compounds (carbohydrates).[13, 14, 68] The catalytic core of PSII is located in the thylakoid membranes of cyanobacteria, algae and green plants and contains a tetramanganese-calcium cluster (Mn_4CaO_5), commonly known as the oxygen-evolving complex. This performs the complex four-electron and four-proton transfer demanding oxidation of water to molecular oxygen under mild temperature and pH conditions with a low overpotential (η = 0.30−0.35 V) and a high turnover frequency (TOF) of up to 100−400 s^{-1}.[27-29] The OEC achieves around 10^6 turnovers until replacement and is stable for approximately 30 min under light irradiation.[27, 69] A wide range of techniques are used to provide structural information on the molecular architecture of the OEC in order to fully understand the molecular mechanism of the water-splitting reaction.[14, 43] The first crystallographic data of PSII at 3.8 Å resolution was reported in 2001 by Zouni et al., showing the spatial distribution of most protein subunits.[70] In the following years, the structural resolution of PSII was gradually increased[71, 72] up to 1.9 Å in 2011, when Umena et al. revealed the geometric arrangement of the Mn_4CaO_5 cluster and its coordination environment.[31] The OEC is composed of a distorted Mn_3CaO_4 heterocubane cluster linked to a fourth Mn atom by a di-μ-oxo bridge with four water molecules bound to the cluster as terminal ligands. As shown in Figure 5a, the cluster is directly coordinated by a large number of hard Lewis basic and oxygen-rich ligands consisting of oxygen bridges and carboxylate protein side chains, as well as a single nitrogen ligand from the His332 imidazole side chain, which results in a saturated ligand environment for the Mn cluster.[31] In an aqueous environment, the abundant element manganese is able to access a plethora of oxidation states between Mn^0 and Mn^{VII}.[73] Furthermore, in the Mn^{III} and Mn^{IV} oxidation states, the manganese centers of the OEC act as hard Lewis acids, forming strong metal−oxo bonds with the hard donor O^{2-}.[74] In contrast, the role of the redox-inactive Ca^{2+} ion in the OEC of PSII has not yet been completely elucidated, as it is not only limited to its function as a structural cofactor for maintaining the distorted cubane structure,[28] since the removal of Ca^{2+} by any metal except Sr^{2+} inhibits oxygen generation.[75, 76] These findings suggest that the Ca^{2+} ion acts as Lewis acid during water oxidation by tuning the nucleophilic reactivity of bound H_2O molecules and modulating the redox properties of the Mn centers.[77-79] Additionally, it has been proposed that the Ca^{2+} ion facilitates PCETs during the water oxidation cycle of the OEC.[80] Several artificial Mn complexes that closely mimic the cubane-like structure of the OEC have been synthesized.[32, 81-83] In 2015, Zhang et al. accomplished for the first time the synthesis of an artificial Mn_3CaO_4 cubane cluster with a dangling Mn atom.[33, 84] The surrounding amino acid
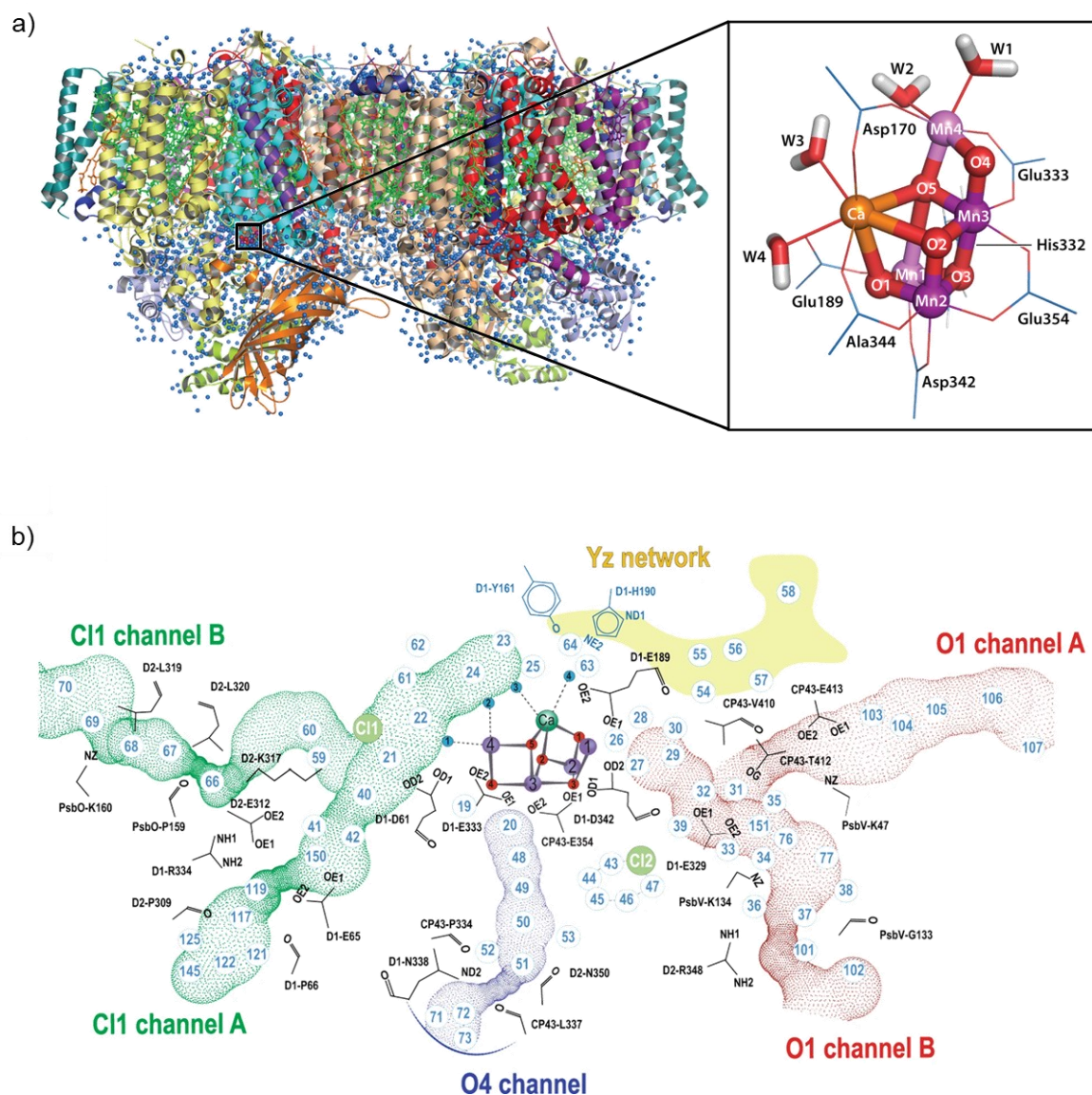
a)

b)

Figure 5. a) X-ray crystal structure of the Mn_4CaO_4 cluster and its ligand environment at a resolution of 1.9 Å, which is embedded in the photosystem II. b) Schematic overview of the water channels filled with long-range hydrogen-bonding networks of preorganized water molecules. These channels connect the OEC with the protein surface of PSII. Figure 5a) was adapted with permission from ref. [29]. Copyright 2017 Annual Reviews and Figure 5b) was reproduced with permission from ref. [88]. Copyright 2021 Nature Publishing Group.

residues are replaced by organic acetate and neutral ligands like pyridine. Although this artificial Mn_4CaO_4 cluster closely mimics the structural features of the native OEC, no oxygen formation could be detected. This might be attributed to the missing coordinated H_2O molecules at both Ca and dangling Mn atoms and to the absence of a sophisticated protein matrix, which preorganizes substrate H_2O molecules.[85] In the high-resolution X-ray structure of PSII, a huge number of H_2O molecules were present, which form long-range hydrogen-bonding networks along water-filled channels to connect the active site with the lumenal bulk

phase (Figure 5b).[31] These channels stabilize oxidized intermediates and ensure access of H_2O molecules to the OEC while simultaneously regulating proton and O_2 transport out of the active site.[86, 87] Recently, using an X-ray free electron laser (XFEL), Hussein et al. showed that substrate transport through separate channels is controlled by an interplay between OEC, amino acid side chains and the hydrogen-bonding networks along the channels (Figure 5b).[88] These findings emphasize the impact of the surrounding water network on the water oxidation process.[89]

Already in 1970, Kok et al. proposed the so-called S_n-state cycle (n = 0–4) to describe the complex four-step water oxidation mechanism of the OEC.[90, 91] Before oxygen release, the Mn cluster passes through five distinct redox states S_n, which vary in the number of stored oxidizing equivalents n (Figure 6). The S_n–state cycle is driven by four light-mediated absorption events by the P680 pigment assembly in PSII, which gets oxidized and forms the radical cation [P680]$^{.+}$ upon charge separation.[87, 92, 93] The generated hole at [P680]$^{.+}$ is balanced with the help of the redox active tyrosine residue Y_z, which acts as an electron shuttle and bridges the reaction center of PSII to the Mn cluster. In addition, Y_z slows down charge recombination and prevents non-productive quenching of [P680]* by spatial separation of the two linked reaction centers.[94] Starting at the most reduced state S_0 ($Mn^{III}_3Mn^{IV}$), the OEC gets sequentially oxidized by three concerted PCETs to the metastable S_3 oxidation state (Mn^{IV}_4). After generation of the final transient S_4 state, O−O bond formation takes place, followed by oxygen liberation.[87, 92, 93] Whilst X-ray crystallography can only determine the dark-stable S_1 state, studies with XFEL allowed the structural determination of S_0−S_3 states due to limited radiation damage and data acquisition under physiological conditions.[87, 88, 95, 96] Recently, Sun et al. proposed the presence of an equilibrium between an open and closed cubane form for the S_1−S_3 transition, which can be attributed to the unique distorted shape of the Mn cluster enabling structural rearrangement during the S_n−state cycle (Figure 6a).[97] In contrast, experimental data on the short-lived S_4 state is scarce, preventing a clear picture of the precise water oxidation mechanism until to date.

Currently, two major O−O bond formation pathways are discussed, which either occur inside or outside the distorted cubane unit of the Mn_4CaO_5 complex (Figure 6b).[96, 98] Using the X-ray data of the OEC in combination with theoretical calculations, Siegbahn et al.[99-101] proposed an internal oxo/oxyl radical coupling mechanism for oxygen formation, which was recently supported by Suga et al.[95] In this mechanism, the O−O bond is formed between a terminally bound oxyl radical and a nearby μ−oxo bridge in the transient S_4 state.[98] In contrast, the competing mechanistic pathway supported by Pecoraro[102] and Barber et al.[103] involves a nucleophilic attack of a Ca^{2+}-bound H_2O molecule or OH^- group on a terminal, electrophilic Mn^V−oxo or Mn^{IV}−oxyl radical at the dangling Mn4 atom of the Mn cluster. However, alternate coupling mechanisms are discussed in the literature, which, for example, propose the

presence of a tyrosyl radical[104, 105] or the involvement of a Mn^{VII}−dioxo intermediate during O−O bond formation.[106, 107] In recent years, our understanding of biological water oxidation has grown tremendously due to advancements in crystallography and time-resolved spectroscopy. Nevertheless, a complete elucidation of the critical O−O bond formation step will be necessary for the design of efficient artificial catalysts to produce solar fuels.
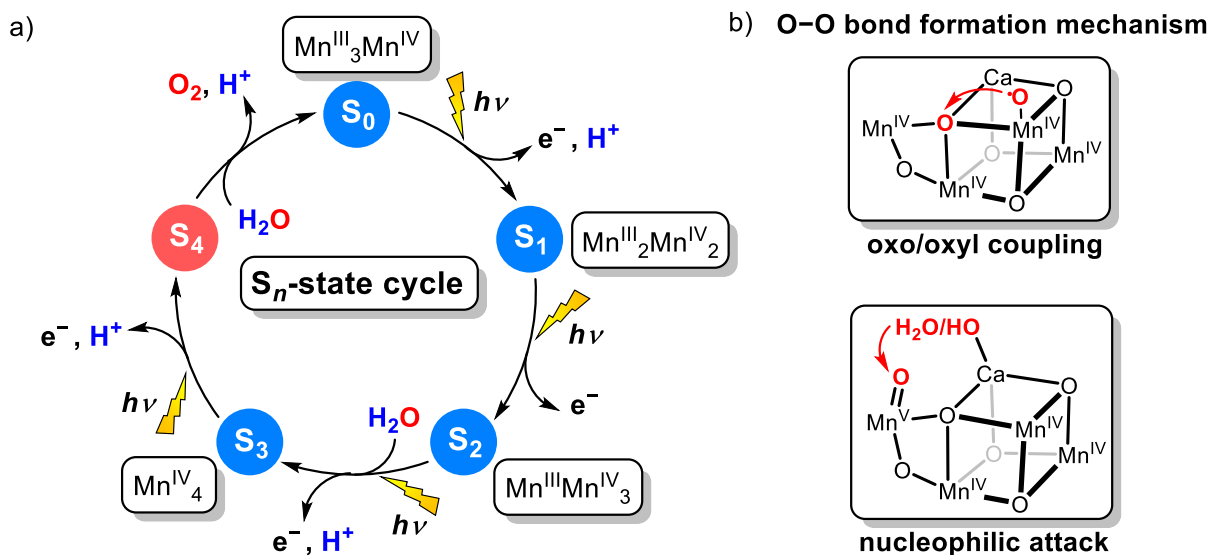

Figure 6. a) Scheme of the S_n-state cycle proposed by Kok et al. for catalytic water oxidation by the OEC-PSII. b) Proposed O−O bond formation mechanisms in the transient S_4 state of PSII. Figure 6 is adapted with permission from ref. [34]. Copyright 2017 Wiley-VCH.

2.2 Fundamental aspects of artificial water oxidation catalysis

2.2.1 Requirements for redox-active transition metal centers

Water oxidation is a kinetically and thermodynamically challenging reaction as it involves the removal of four electrons and four protons from two H_2O molecules, the rearrangement of multiple bonds, a large number of *in situ* formed oxidized intermediates and the final O−O bond formation (eq. 2).[108, 109]

$$2\,H_2O \longrightarrow O_2 + 4H^+ + 4e^- \quad \left| E^0(H_2O) = +1.23\ V\ at\ pH = 0 \right. \qquad (2)$$
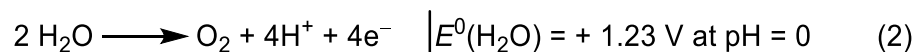
From a thermodynamic point of view, the oxidative half reaction represents the overall bottleneck in generating molecular H_2 from H_2O, since e.g., the thermal splitting of H_2O requires high temperatures above 2500 °C. In order to apply electrochemical water splitting, a standard redox potential of E^0 = +1.23 V (vs. a standard hydrogen electrode) at pH 0 and +0.81 V at pH 7, is also required. The Nernst equation states that this standard redox potential shifts thermodynamically with the pH (−59 mV per pH unit).[110] In practice, a higher potential is required to drive the reaction at a given rate due to the intrinsic overpotential of the investigated catalysts, which originates from catalytic intermediates.[111] To lower the activation barrier, molecular catalysts operating at low overpotential are necessary. In this regard, redox-active transition metal complexes are excellent candidates for catalytic studies due to their broad range of accessible oxidation states and the vacant d-orbitals in both spatial and energetic proximity, which enable them both to act as electron donor and/or electron acceptor in combination with other molecules.[108] Focusing on water oxidation, the stability and reactivity of metal-oxo intermediates are crucial for O_2 evolution. The reactivity of the high-valent M=O species is mainly determined by the metal and the surrounding ligand field.[112] As shown in Figure 7, coordination of an oxo ligand (O^{2-}) to an octahedral metal complex (O_h) causes configuration distortion under formation of a pseudo-octahedral environment with C_{4V} symmetry due to the short M=O bond. Due to partial delocalization to the O^{2-} ligand the d_{z^2} orbital is destabilized and the non-bonding d_{xz} and d_{yz} orbitals are degenerated to form one σ- and two π-bonds of M=O in the tetragonal ligand field (Figure 7).[113, 114] Based on this electronic structure, the choice of the transition metal center is dictated by the number of filled d-orbitals. The late transition metals such as Ni^{III} [d^7] and Cu^{III} [d^8] with oxidation states below +4 have filled e(d_{xz}, d_{yz}) orbitals and, thus, cannot accept the electrons from the oxygen ligand. Conversely, the early transition metals (Ti^{IV} [d^0], V^V [d^0]) possess no d-electrons at high oxidation states, hence, forming very stable M−O bonds. Therefore, transition metals in the groups 7−9 such as Mn^V [d^2], Mn^{IV} [d^4] and Ru^V [d^3] with suitable empty d-orbitals are mostly
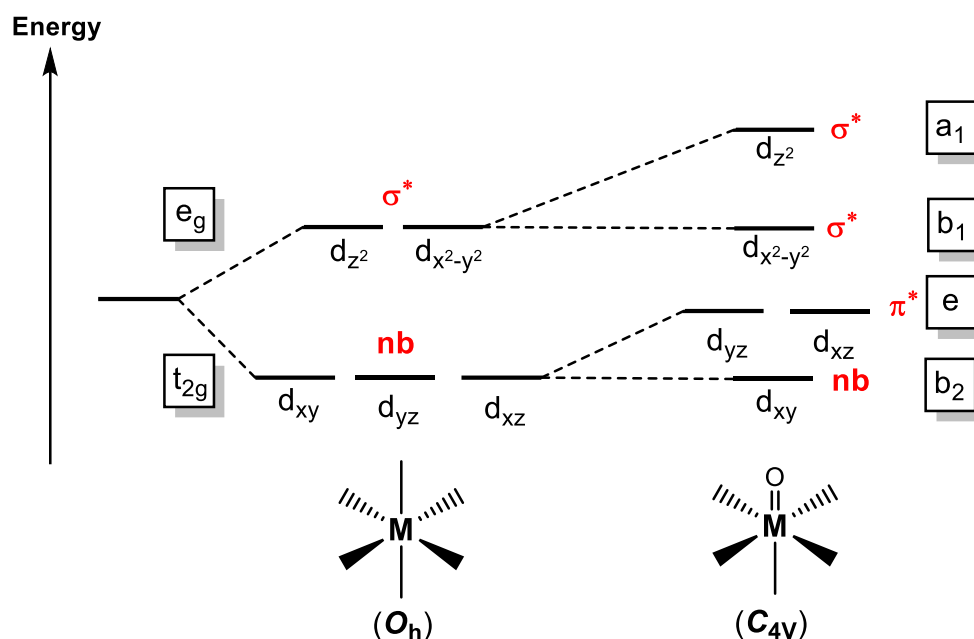
Figure 7. Qualitative energy-splitting diagrams of d-orbitals for an octahedral metal complex (O_h) and for a metal-oxo complex (M=O, C_{4V}) with tetragonal ligand field. Figure 7 is adapted with permission from ref. [113]. Copyright 2008 American Chemical Society.

used as WOCs for the formation of reactive metal-oxo bonds.[113] Compared to the first row of transition metals (Mn, Fe, Co and Cu), Ru- and Ir-based catalysts have a higher ligand field stabilisation energy that leads to the formation of more robust and very active WOCs.[115] As a consequence, WOCs based on first row transition metals are less stable under strongly oxidizing conditions and are susceptible to irreversible structural modifications and transformation into heterogeneous metal oxides as true catalytically active species.[116, 117] Furthermore, the redox chemistry of the metal ruthenium is extremely versatile, having accessible oxidation states in the range of +8 to −2. This is important for the process of water oxidation, which requires oxidation states up to +5 for oxygen release.[118] These high oxidation states are stabilised by the σ- and π-donating abilities of directly attached oxo groups, which partially remove electron density from the metal center.[119] Furthermore, the study of catalytic intermediates to evaluate the respective mechanistic pathway is facilitated for ruthenium complexes at low oxidation states due to their slow ligand exchange rates in H_2O that are nearly eight orders of magnitude slower compared to their earth-abundant Fe^{II} and Fe^{III} counterparts.[120, 121]

2.2.2   Mechanistic pathways for water oxidation

For the development of efficient catalysts for molecular water oxidation, a profound knowledge of the underlying mechanistic pathway is crucial. In recent years, a variety of analytical

methods including spectroelectrochemistry, stopped/flow UV/Vis spectroscopy, electrochemical methods, mass spectrometry or ^{18}O-isotope-labeling experiments, as well as complementary theoretical calculations, have facilitated the elucidation of reactive intermediates in the mechanism of homogenous catalysis, whereas such studies are difficult to apply to heterogeneous catalytic systems.[119, 122, 123] Similar to the natural OEC in PSII, two different mechanistic pathways for O_2 formation are known for artificial transition metal catalysts, namely the water nucleophilic attack (WNA) mechanism and intermolecular coupling of two metal-oxo species (I2M).[110, 124, 125] As can be seen in Scheme 1, three main reactive intermediates are involved in both mechanisms until O_2 release. Multiple concerted PCETs are fundamental components of both mechanisms, which ensure fast kinetics by reducing the reaction barriers for the multiple oxidative processes and provide access to less positively charged high-valent oxidation states via low energy pathways.[126, 127] The stepwise oxidation of the metal center reduces the pK_a of the H_2O bond at the vacant site, which leads to the formation of a high-valent metal-oxo species after several consecutive oxidation steps coupled to proton transfer reactions, while the oxo ligand acts as a strong σ-donor.[122] In the unimolecular WNA mechanism, a metal hydroperoxide intermediate is formed after nucleophilic attack of a second H_2O molecule at the electrophilic M=O species. The generated O−O bond is the result of the interaction between the highest occupied molecular σ-orbital (HOMO) of the substrate H_2O and the lowest occupied molecular π^*-orbital (LUMO) of the high-valent M=O moiety. Subsequent PCET facilitates O_2 release and the regeneration of the molecular catalyst. In this regard, each step of the WNA cycle exhibits a first-order dependency on both the catalyst and the oxidant.[110, 128] In contrast, the O−O bond in the competitive I2M pathway is formed by the bimolecular coupling of distinct LUMOs of two high-valent metal-oxyl radicals. The so formed peroxo intermediate can either be generated in an intramolecular fashion or is based on intercatalyst coupling, followed by O_2 formation.[124, 129] Catalysts following the bimolecular I2M pathway are more sensitive to varying molecular concentrations, which usually leads to enhanced catalytic performance at higher concentrations compared to systems following the unimolecular WNA mechanism.[124] However, the bimolecular reaction mechanism prevents application on heterogeneous surfaces due to restricted catalyst mobility, which results in a mechanistic switch to a usually less efficient WNA pathway after catalyst immobilization.[130, 131] Therefore, the development of molecular catalysts following a WNA mechanism would be beneficial for the engineering of solar fuel devices. Since subtle structural changes or steric constraints might alter the respective mechanistic pathway,[132-134] detailed mechanistic investigations, including kinetic isotope effect studies and complementary theoretical calculations, are required to obtain sound knowledge.
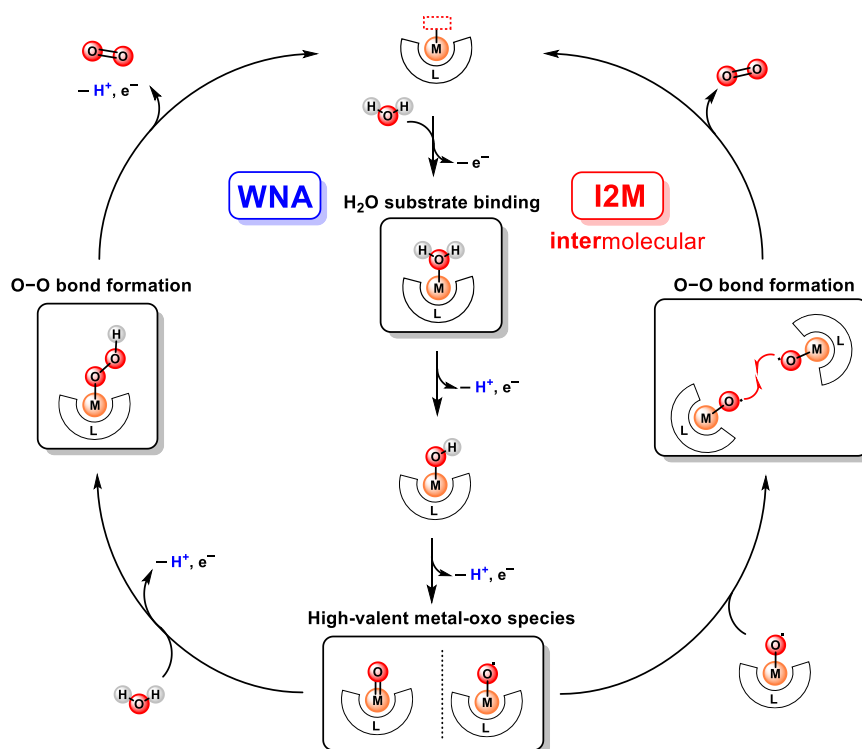
Scheme 1. Mechanistic scheme representing the two possible pathways for homogeneous water oxidation: single-site water nucleophilic attack (WNA) and bimolecular interaction of two metal-oxo species (I2M). The three most important intermediates are highlighted.

2.2.3   Techniques for studying water oxidation

To examine the water oxidation activity of potential molecular catalysts, several techniques can be applied. In the following section, three different methods, namely a) chemical, b) photochemical and c) electrochemical water oxidation will be discussed.

a) Chemical water oxidation

For fast screening and tuning of molecular WOCs, chemically induced experiments are preferred, which are carried out in the presence of sacrificial electron acceptors (SEA) in bulk solution to replace the reductive half reaction. Although such experiments do not perfectly mimic the conditions of an artificial photosynthetic cell, the received data can give preliminary information about the suitability of the catalyst in a potential device.[135] Most commonly, the strong one-electron acceptor cerium(IV) ammonium nitrate (CAN, $(NH_4)_2[Ce(NO_3)_6]$) is applied for the characterization of novel WOCs due to its good solubility and stability in aqueous acidic solution at pH 1 as well as organic solvents.[135, 136] As shown in equation (3), four equivalents of CAN are needed to oxidize a molecular catalyst and promote O_2 evolution.

$$2\ H_2O + 4\ Ce^{IV} \xrightarrow{\textbf{Catalyst}} O_2 + 4\ H^+ + 4\ Ce^{III} \tag{3}$$
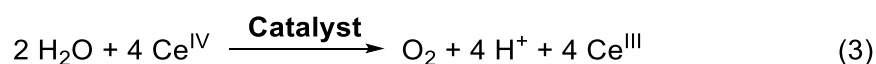
CAN is commercially available and acts as a non-oxo transfer agent compared to other known SEAs such as potassium peroxymonosulfate (Oxone, $KHSO_5$) or sodium periodate ($NaIO_4$), which are both strong two-electron oxidants that promote oxygen atom transfer during the catalytic cycle.[135, 137] Additionally, because photoelectrochemical cells are based on one-electron transfer events, the use of these two-electron acceptors does not reflect catalytic processes within those cells.[108] As another requirement, SEAs should display a higher oxidation potential than the investigated WOC. CAN has a reduction potential of 1.75 V vs. NHE (Normal hydrogen electrode) at pH 1 and stable adjacent oxidation states of +3 and +4.[138] In addition, CAN shows a strong absorption band in the UV region, which makes it suitable for mechanistic studies via spectroscopic techniques.[139] However, it requires strongly acidic conditions (pH 1) due to the formation of insoluble cerium oxide particles at pH above 3.0.[138] This not only limits the applicability of CAN to study WOCs under conditions relevant for artificial devices, but also requires WOCs that are stable under highly acidic conditions.[135] Thus, it is important to check the nature of molecular catalysts after several catalytic turnovers, since the usage of CAN may promote the degradation of WOCs into nanosized metal oxides, which then act as real catalysts.[119] In this regard, post-catalytic analysis of the molecular catalysts by high-resolution mass spectrometry, scanning electron microscopy (SEM) or X-ray absorption spectroscopy (XAS) are important techniques.[140-142]

The evolved O_2 can be measured in the gas phase with attached pressure sensors that monitor the pressure increase in tight reaction vessels during the catalytic cycles. Via the ideal gas law, the amount of evolved oxygen can be calculated based on the pressure difference. Gas chromatographic analysis of the head space after the catalytic reaction allows the determination of the composition of the generated gas mixture.[143, 144] A major advantage of this technique is the simultaneous execution of several experiments. Due to the limited sensitivity of the pressure sensors, this technique is not suitable for catalytic reactions that generate low amounts of O_2. In this regard, Clark electrodes can be applied, which measure the generated O_2 directly in the liquid phase based on electrocatalytic reduction on a platinum electrode.[145]

b) Photochemical water oxidation

Light-driven water oxidation experiments can be used to study novel WOCs under neutral conditions relevant for solar fuel devices.[122] The photocatalytic activity of WOCs is generally studied in a light-driven, three-component system comprising a WOC, a photosensitizer (PS) and a SEA.[146-148] As shown in Figure 8a, after light absorption by PS and concomitant generation of the excited state PS* [eq. (4)], photoinduced oxidative quenching of PS* by the SEA results in the generation of oxidant PS+ [eq. (5)]. After the transfer of four consecutive

oxidizing equivalents from PS$^+$ to the WOC, the oxidation of H_2O to O_2 can take place and the WOC and PS are restored to their initial states [eq. (6,7)]. To drive water oxidation thermodynamically at pH 7, a photosensitizer with an oxidation potential higher than 0.82 V is needed (Figure 8b).[149] Most commonly, photosensitizers based on the ruthenium tris(bipyridine) $[Ru(bpy)_3]^{2+}$ chromophore are employed as one-electron oxidants with high oxidation potentials (E^0 = 1.26 V *vs*. NHE for the parent $[Ru(bpy)_3]^{2+}$). Additionally, these complexes feature a good absorption in the visible range and are able to form long-lived triplet excited states (^{3}MLCT) required for an efficient electron transfer to the WOC.[135, 150] In addition, ring-substituted derivatives of $[Ru(bpy)_3]^{2+}$ enable a wide range of accessible oxidation potentials (1.10−1.79 V vs. NHE) to drive water oxidation.[108] Typically, sodium peroxodisulfate ($Na_2S_2O_8$) or chloropentaamminecobalt(III) chloride $[Co(NH_3)_5Cl_3]$ are used as SEAs to generate oxidant $[Ru(bpy)_3]^{3+}$ in aqueous media due to the fast degradation route of their
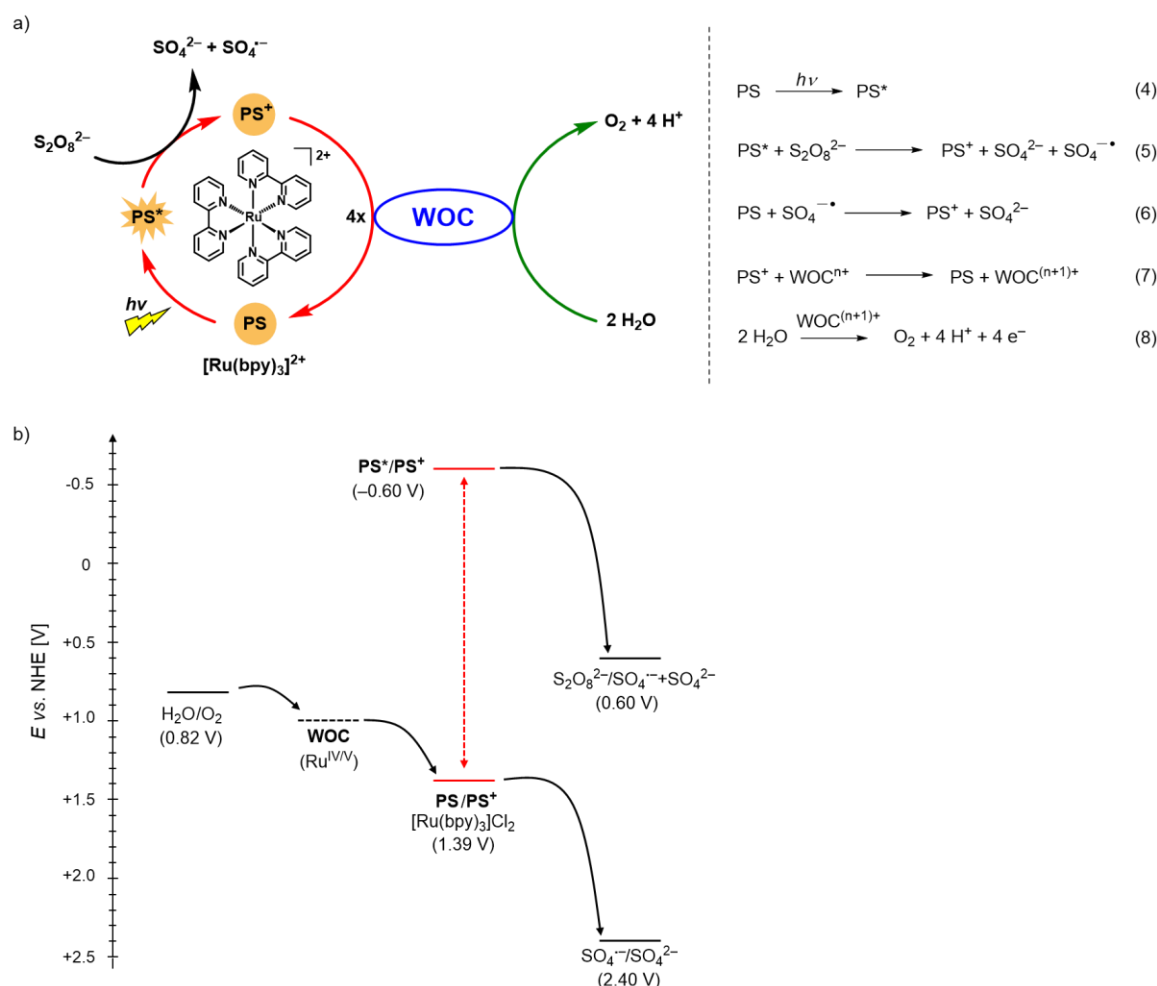
Figure 8. a) Catalytic cycle and b) energy scheme for photochemical water oxidation using $[Ru(bpy)_3]^{2+}$ as PS, $Na_2S_2O_8$ as SEA and a molecular WOC. The potential for water oxidation was calculated using the Nernst equation: E = 1.23−(0.059 x pH) V *vs*. NHE.[151] The oxidation potentials of PS and SEA are reported based on literature references.[135, 148, 152, 153]

reduced products, which limits competitive recombination processes with PS[+].[152] In addition, irreversible splitting of the persulfate ion into a sulfate ion and a sulfate radical anion leads to the generation of a second equivalent of PS[+] due to the high oxidation potential of $SO_4^{\bullet-}$ [eq. (6)]. In comparison, the cobalt complex $[Co(NH_3)_5Cl_3]$ undergoes ligand dissociation.[152] Photocatalytic experiments are usually performed with an excess of PS and SEA compared to the WOC concentration to prevent competing side processes such as the direct oxidation of the WOC by the strong oxidant $SO_4^{\bullet-}$ or the possible quenching of PS* by the molecular catalyst.[135, 148] Compared to chemical conditions, photochemical water oxidation catalysis is strongly influenced by the complex interplay of the numerous parameters involved, such as light intensity, reaction media, buffer concentration and concentrations of catalyst and sensitizer.[146, 148, 153] In addition, usually lower activities are observed under neutral conditions due to the limited stability of the PS in neutral or basic aqueous conditions.

In literature, two decomposition pathways for $[Ru(bpy)_3]^{3+}$ in the photocatalytic cycle are reported (Figure 9).[146, 154] The predominant dark decomposition pathway is considered to be the nucleophilic attack of a hydroxide anion at a bpy ligand of the PS (Figure 9a). In the presence of light, the excited sensitizer PS[+] may also react with another equivalent of SEA, resulting in the generation of a Ru dimer as a decomposition product (Figure 9b).[146, 154] Therefore, it is necessary to always prepare a fresh solution of the PS and the SEA prior to the experiments.

a) **Dark decomposition pathway:**
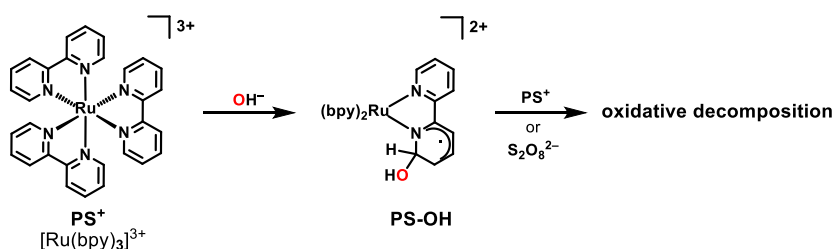
b) **Light-induced decomposition pathway:**
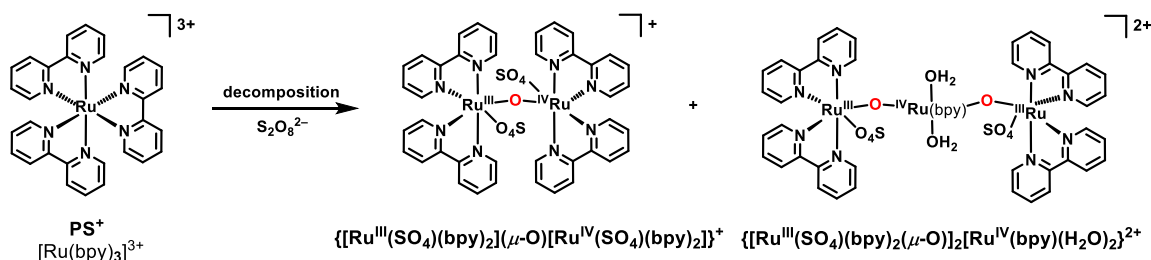
Figure 9. Major literature-known a) dark and b) light-induced decomposition pathways for oxidized photosensitizer $[Ru(bpy)_3]^{3+}$.[146, 154]

c) Electrochemical water oxidation

Complementary to the application of sacrificial oxidants, electrochemical experiments using cyclic voltammetry (CV) and bulk electrolysis can be employed to benchmark novel WOCs.[111, 155] Compared to experiments in the homogenous phase, where only a small amount of catalyst is active in the diffusion layer, heterogenization of molecular WOCs on a conducting surface is considered the next step toward an artificial device that offers the advantage of controlling the exact amount of catalyst.[108, 122] In recent years, the number of examples of such hybrid materials for electrochemical H_2O oxidation has significantly increased.[156-159]

An important thermodynamic parameter for electrochemical half reactions such as H_2O oxidation represents the overpotential (η), which can originate from a variety of different factors such as intrinsic activation barriers, ion mobility, cell geometry or other additional parameters.[111, 160] This kinetic phenomenon is defined as the difference between the applied potential (E^O) and the tabulated standard potential of H_2O oxidation ($E^o(H_2O)$[110] at the operating pH value (eq. 9) that is needed to drive the reaction.[161, 162]

$$\eta = E^o - E^o(H_2O) \qquad \left| E^0(H_2O) = +1.23 \text{ V at pH} = 0 \quad (9) \right.$$

In addition to a low overpotential, an ideal molecular catalyst should likewise possess a high current density through the electrode for O_2 evolution.[163] The catalytic efficiency of a catalyst can be determined using the so-called foot of the wave analysis (FOWA) from Savéant and coworkers[111], which is applicable to both heterogeneous and homogeneous catalytic reactions.[111, 155] Under the assumption of low catalyst degradation and absence of competing side reactions, the respective TOF is extracted from the initial period of the water oxidation curve.[111, 162] The stability of such hybrid materials over long time periods is another important parameter for the characterization of novel WOCs, which can be determined by controlled potential electrolysis (CPE) experiments at a constant current above the onset potential of the investigated WOC. If no catalyst degradation or detachment is observed, the current should remain constant throughout the experiment.[159] To exclude the presence of any side reactions during the electrochemical water oxidation, the Faraday efficiency gives information about the efficient charge transfer within the system through CPE experiments under inert conditions.[164] For systems with low Faraday efficiency, usually chemical by-products or heat are observed during the electrocatalytic experiments.[165]

2.3   Molecular engineering of Ru-based water oxidation catalysts

2.3.1   First coordination sphere of Ru-based water oxidation catalysts

In the initial research period on ruthenium-based molecular WOCs, researchers focused on a multinuclear complex design based on the pioneering work of Meyer and co-workers in 1982, when they discovered the first artificial water oxidation catalyst, the so-called 'blue dimer' (**1**).[166, 167] Structurally, this Ru polypyridyl complex is equipped with oxidatively robust aromatic polypyridine ligands as molecular building blocks that are stable towards hydrolysis and consist of two strongly interacting μ-oxo-bridged Ru^{III} centers (Figure 10).[114, 168] Comprehensive mechanistic studies revealed the importance of PCETs to facilitate the water nucleophilic attack at a high-valent $Ru^V=O$ state during the observed WNA pathway.[169-173] Oxidative cleavage of the μ-oxo-bridge during catalysis to form inactive monomers proved to be a major bottleneck of the catalyst design, which explains the very low catalytic performance of complex **1** in chemical water oxidation (TOF = 0.004 s^{-1}, TON = 13.2).[108, 174, 175] More than two decades later, Llobet and co-workers reported the successful replacement of the unstable Ru−O−Ru motif with a rigid polypyridine bridging ligand in the dinuclear Ru catalyst **2** (Figure 10).[176] Promoted by the through space interaction between the two preorganized Ru centers, complex **2** showed a three times faster O_2 evolution rate under chemical conditions (TOF(**2**) = 0.014 s^{-1}, TON(**2**) = 18.6) compared to the 'blue dimer'.[129, 177] Interestingly, ^{18}O-labelling experiments and theoretical calculations showed that the dinuclear complex **2** follows an intramolecular I2M pathway. Based on follow-up work by the same group, it was shown that small structural changes in the auxiliary ligand scaffold can alter the mechanistic pathway for O−O bond formation.[178, 179]

In 2005, Thummel and co-workers reported the first example of a mononuclear Ru WOC **3**, which was initially synthesized as a reference complex for a series of dinuclear Ru complexes (Figure 10).[180] Compared to previous examples, a combination of an equatorial *bis*-tridentate polypyridine ligand and monodentate axial *N*-heterocycles were used as molecular building blocks for complex **3** to create a large open catalytic site for H_2O binding in the equatorial sphere. Originally, it was assumed that the two non-coordinated nitrogen atoms of the equatorial ligand would act as an internal base to facilitate proton abstraction. Later experimental and theoretical studies under acidic conditions showed the formation of N−O bonds after oxygen atom transfer to the non-coordinated nitrogen atoms and, thus, the closure of the basic function.[181] Mechanistically, a mononuclear WNA pathway under the involvement of a seven-coordinated, electrophilic $[Ru^{IV}=O]^{2+}$ species during O−O bond formation was proposed for **3**. In the following years, the number of molecular WOCs increased significantly after this breakthrough due to the ease of synthetic preparation and facilitated mechanistic investigations.[112, 182] Another important class of mononuclear WOCs was
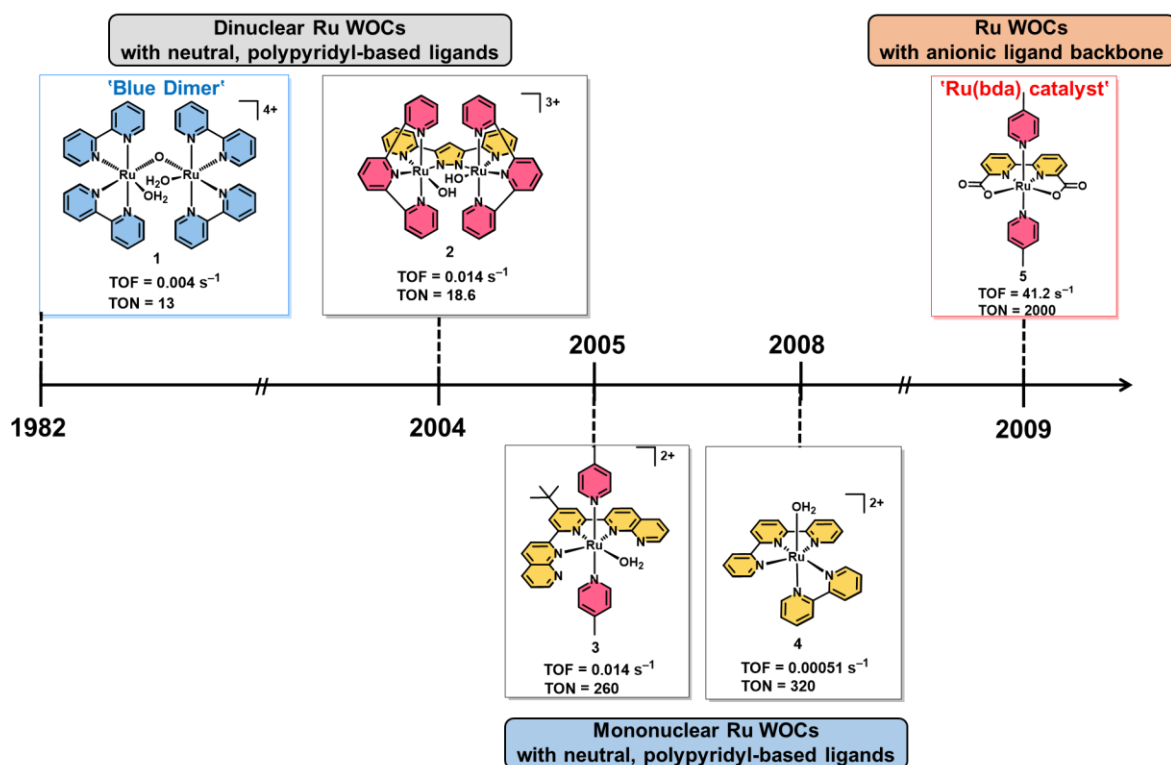
Figure 10. Important developments of Ru-based homogenous WOCs until the discovery of the [Ru(bda)L$_2$] (L = aromatic *N*-heterocycles) catalyst family in 2009. The catalytic performances of the selected catalysts are reported based on chemical water oxidation.

described in 2008 by the groups of Meyer,[139, 183] Sakai[184, 185] and Berlinguette.[186, 187] with complexes such as [Ru(tpy)(bpy)OH$_2$]$^{2+}$ **4** and various derivatives (Figure 10). In comparison to complex **3**, the H$_2$O molecule binds to the Ru site as an axial ligand, resulting in lower catalytic performance due to catalyst deactivation after ligand oxidation. This is caused by weakening of the Ru−N bond located *trans* to the H$_2$O ligand at higher oxidation states.[186, 188]

Development and properties of Ru(bda) catalyst family

The major drawback of the previously reported WOCs containing neutral polypyridine-based ligands is their high intrinsic overpotential, which prevents light-driven water oxidation in presence of mild photosensitizers as oxidants.[108] Inspired by the oxygen-rich ligand environment of the OEC in PSII and based on early work by Åkermark and co-workers, the introduction of negatively charged carboxylate ligands is an efficient strategy to reduce oxidation potentials.[189, 190] As a result, the Sun and Åkermark groups were the first to apply this strategy to a series of dinuclear Ru complexes that demonstrated impressive catalytic activities in chemical water oxidation.[191-193] In addition, the low onset potential of these dinuclear Ru complexes allowed light-driven water oxidation under neutral conditions in the presence of [Ru(bpy)$_3$]Cl$_2$ as photosensitizer.[191-193] Building on these positive results, Sun and

co-workers introduced the dianionic chelate ligand bda^{2-} (bda: 2,2'-bipyridine-6,6'-dicarboxylate) in the mononuclear complex [Ru(bda)(pic)$_2$] **5** (pic: 4-picoline) in 2009 (Figure 10).[194] This novel catalyst showed a remarkably high TOF of 41 s^{-1} and a TON of 2000 using CAN as oxidant.[195] In electrochemical studies, a TOF of 11 s^{-1} was observed for complex **5** at neutral and basic pH values at a low overpotential of 180 mV.[155] In addition, the low onset potential for water oxidation of **5** at 0.98 V under neutral conditions allowed light-driven water oxidation in presence of [Ru(bpy)$_3$]Cl$_2$. Interestingly, [Ru(bda)(pic)$_2$] only showed a moderate catalytic performance (TOF = 0.15 s^{-1}, TON = 100) at pH 7, which was attributed to oxidative degradation of the axial picoline ligand after several catalytic turnovers.[149] The notable catalytic performance can be attributed to the unique structural features of the [Ru(bda)L$_2$] (L = aromatic *N*-heterocycles) complex family. X-ray crystal structure analysis at the initial Ru^{II} state revealed a strongly distorted octahedral coordination geometry with a six-coordinated Ru complex for [Ru(bda)(pic)$_2$]. The complex exhibits a large O−Ru−O bite angle of ~123° in the equatorial sphere, which is much larger compared to an ideal rectangular arrangement (Figure 11), leading to the formation of a seventh coordination site for substrate H$_2$O binding that acts as a proton source to reach high-valent oxidation states.[194] To enter the catalytic cycle, an activation step from Ru^{II} to the Ru^{III} state under coordination of H$_2$O is required. This process is disfavoured due to nearly filled electronic shells at these low oxidation states with 18 and 17 valence electrons, respectively. Detailed studies by the groups of Llobet and Sun at these low oxidation states have proven the existence of a dynamic equilibrium between a bonding and an approaching mode of a metastable Ru^{III}(bda) species with a pseudo-octahedral geometry.[196] The labile carboxylate ligation and coordination flexibility of
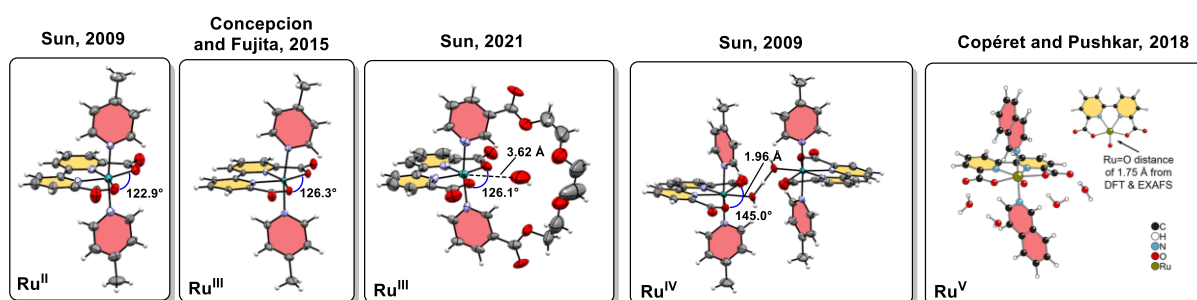
Figure 11. Single crystal X-ray structures of Ru(bda) intermediates with Ru centers in oxidation states II,[194] III[197, 198] and IV[194] and a DFT optimized structure of a [Ru^V=O(bda)(isoq)$_2$]$^+$ intermediate.[199] Organic solvent molecules and counterions are omitted for clarity. ORTEP diagram with thermal ellipsoids set as 50% probability. C, grey; H, white; O, red; N, purple; Ru, turquoise. Crystallographic data are adapted with permission from ref. [194]. Copyright 2009 American Chemical Society, ref. [197]. Copyright 2015 Royal Society of Chemistry and ref. [198]. Copyright 2021 Chinese Chemical Society. The DFT optimized structure is adapted with permission from ref. [199]. Copyright 2018 American Chemical Society.

the equatorial bda ligand facilitates PCETs to reach higher oxidation states, which represents a crucial element for the remarkable catalytic performance.[196, 200] So far, no structural model of a seven-coordinated Ru^{III}(bda)-H_2O species has been provided. Only the crystal structures of six-coordinated Ru^{III}(bda) complexes either with or without a substrate H_2O molecule approaching the Ru center were reported by the groups of Fujita and Sun, respectively (Figure 11).[197, 198] Mononuclear [Ru(bda)(pic)$_2$] dimerizes after reaching the Ru^{IV} state via PCETs, resulting in the formation of a seven-coordinated Ru^{IV} dimer intermediate linked by a [HOHOH]⁻ group. As shown in Figure 11, the respective crystal structure features two highly disordered Ru centers with a pentagonal bipyramidal configuration.[194] Compared to the X-ray structure at the initial Ru^{II} state, no significant structural changes are observed for complex **5** upon oxidation. The increased O−Ru−O bite angle of 145° at the Ru^{IV} state facilitates H_2O coordination and provides a low reorganization energy pathway for the rate-determining intermolecular interaction of the I2M mechanism.[194, 201] Theoretical studies suggested a hydrophobic, attractive interaction between the oxo groups of two high valent [Ru^V=O]⁺ intermediates as the driving force for the evidenced bimolecular pathway.[202] In addition, a distinct radical character of the high-valent oxo species was determined, which can be described by the following resonance structure: [Ru^V=O ↔ Ru^{IV}−O˙]⁺. Consequently, the formation of a preorganized dimer through a radical coupling mechanism is promoted, which explains the almost negligible intrinsic barrier for the intermolecular interaction in the absence of hydrogen bonds with surrounding H_2O molecules.[202, 203] Experimental evidence for the existence of such a high-valent [Ru^V=O]⁺ active species has recently been confirmed spectroscopically by Pushkar and co-workers (Figure 11).[199] The most interesting feature of Ru(bda) complexes is the vacant seventh coordination site for substrate H_2O, whereas a six-coordinated complex can only incorporate H_2O after ligand exchange. This can be illustrated by comparing the crystal field splitting of the d-orbitals for six- and seven-coordinated transition metal complexes with octahedral (O_h) and pentagonal bipyramidal (D_{5h}) geometry. As depicted in Figure 12, the addition of a seventh coordination site lowers the energy level of the d_{xz} and d_{yz} orbitals compared to the octahedral coordination sphere, which leads to the stabilization of electron-deficient higher oxidation states of the metal center by providing additional electron density through the coordination of one more Lewis base donor.[204] While low spin d_4 Ru^{IV} complexes with octahedral geometry are generally paramagnetic [$(t_{2g})^4(e_g)^0$], the corresponding pentagonal bipyramidal low spin d_4 Ru^{IV} complexes have a diamagnetic [$(e_1'')^4(e_2')^0(a_1')^0$] electronic configuration.[35, 128]
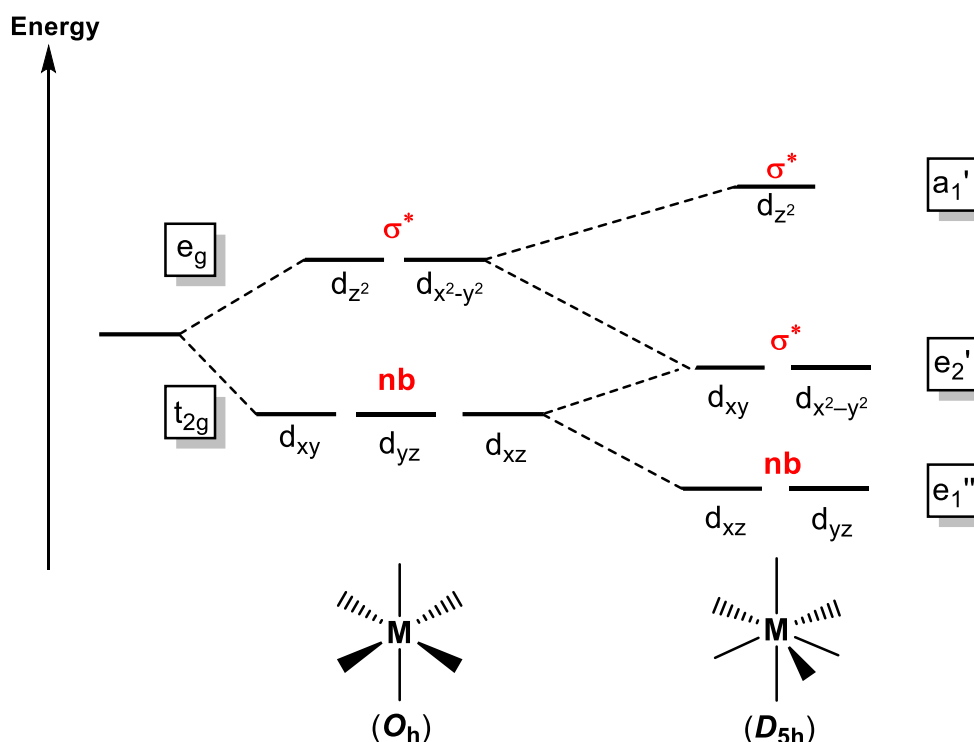
Figure 12. Qualitative crystal field splitting of d-orbitals for six- and seven-coordinated transition metal complexes with octahedral (O_h) and pentagonal bipyramidal (D_{5h}) geometry. Figure 12 is adapted with permission from ref. [35]. Copyright 2019 American Chemical Society.

Besides the effect of seven-fold coordination, the reactivity and stability of the high-valent Ru=O species are also dominated by the respective equatorial ligand environment. This can be elucidated using a selection of different equatorially modified six- and seven-coordinated Ru(bda) analogues (Figure 13). For the closely related seven-coordinated complex [Ru(pda)(pic)$_2$] **6** (pda: 1,10-phenanthroline-2,9-dicarboxylate) a mechanistic switch to a very inefficient mononuclear WNA mechanism with a decreased catalytic performance (TOF(**6**) = 0.1 s^{-1}, TON(**6**) = 210) was observed, which was attributed to additional reorganization before O−O bond formation.[132, 205] Although both complexes share the same coordination environment, it was concluded that the rigid pda ligand leads to a reduced adaptability at different oxidation states and the more hydrophobic pda backbone disfavours the formation of a prereactive dimer for the I2M mechanism compared to the more flexible bpy backbone of Ru(bda)WOCs.[128, 132, 205] To investigate the electronic effect of the bda ligand, the Sun group synthesized complex [Ru(tpc)(pic)$_2$] **7** (tpc: 2,2':6'2''-terpyridine-6-carboxylate), replacing one carboxylate group by a pyridine moiety. Although complex **7** shares a distorted octahedral coordination geometry with a comparable O−Ru−O angle of ~122.5°, a very inefficient WNA mechanism (TOF(**7**) = 0.17 s^{-1}, TON(**7**) = 360) was observed.[206] The single charged tpc$^-$ ligand exhibits a reduced electron-donating ability to the metal center, resulting in a 420 mV higher oxidation potential of the crucial Ru$^{IV/V}$ couple and, thus, lowering the

stabilization at higher oxidation states.[206] These results were supported by investigating complex [Ru(pdc)(pic)$_3$] **8** (pdc: 2,6-pyridinedicarboxylate), equipped with a tridentate pdc^{2-} ligand and having no free coordination site for H$_2$O embedded in the structure.[207] Interestingly, complex **8** also showed a poor catalytic performance (TOF(**8**) = 0.23 s^{-1}, TON(**8**) = 553), which undergoes ligand dissociation at the Ru^{III} state to form [Ru(pdc)(pic)$_2$(H$_2$O)]$^+$ as active species. The lower catalytic performance of the selected Ru(bda) analogues supports the importance of the electronic and structural features of the equatorial bda^{2-} ligand for water oxidation, which are summarized in Figure 13b.
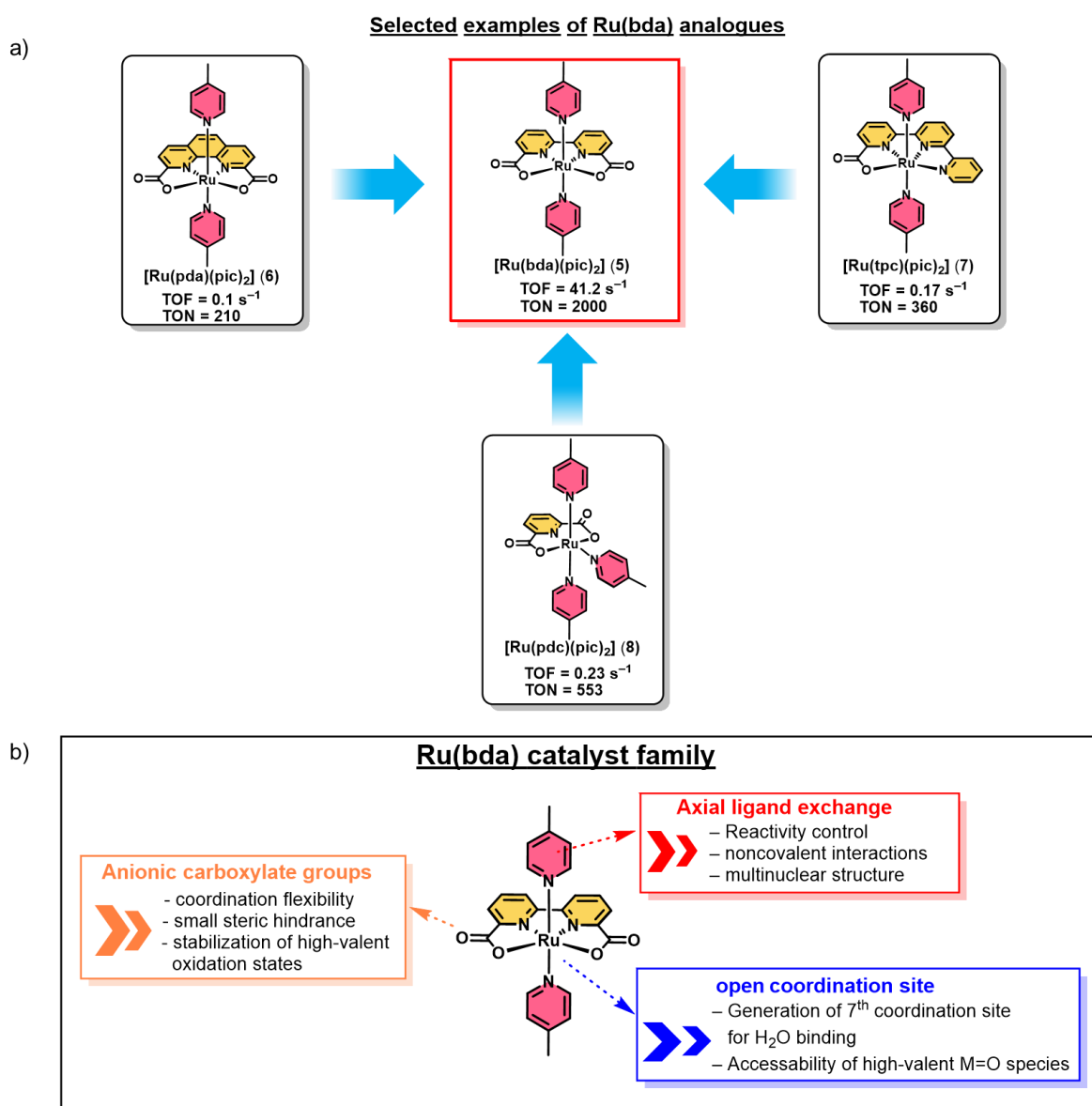
Figure 13. a) Overview over selected examples of equatorially modified Ru(bda) analogues with their catalytic performance under chemical water oxidation conditions. b) Structural features of the [Ru(bda)L$_2$] (L = aromatic *N*-heterocycles) catalyst family.

2.3.2   Secondary interactions within Ru-based water oxidation catalysts

According to the literature on the molecular engineering of the first coordination sphere of Ru-based WOCs, the supporting ligands primarily serve as spectators, only affecting the geometry of the metal ion and indirectly modulating the catalysis and the mechanistic pathway through electronic and steric effects.[208, 209] In recent years, the role of secondary, non-covalent interactions of the ligand scaffold around the active site has been emphasized to significantly enhance the catalytic performance through substrate preorganization and reduction of the kinetic barrier by promoting PCETs.[34, 36, 210, 211] Focusing on Ru(bda) catalysts, the easy manipulation of the axial ligands enabled the design and synthesis of a wide range of different mono- and multinuclear Ru WOCs within the following years. Intelligent second coordination sphere engineering resulted in high turnover frequencies comparable to or even higher than those of the oxygen-evolving complex in PSII.[128] In this section, the various types of secondary interactions and effects will be discussed using selected examples of Ru-based molecular WOCs.

1. Non-covalent interactions ($\pi-\pi$-, van-der-Waals and electrostatic interactions)

One of the first approaches to utilize non-covalent interactions in water oxidation catalysis focused on the use of hydrophobic $\pi-\pi$ stacking interactions to promote the rate-determining intercatalyst coupling of two metal-oxo/metal-oxyl species in the bimolecular I2M pathway (Figure 14a). In comparison to [Ru(bda)(pic)$_2$], the introduction of the more hydrophobic, highly polarizable isoquinoline (isoq) axial ligand resulted in an order of magnitude higher catalytic performance with a TOF of 303 s^{-1} and a TON of 8360 for complex **9**.[212] The stronger dimerization tendency of the π-extended isoq ligands combined with a lower steric bulk compared to 4-picoline accelerates the reaction rate of chemically driven water oxidation. Later, Ahlquist and co-workers discovered that the π-stacked configuration is mainly driven by a hydrophobic effect in aqueous media.[202, 213] Post-catalytic analysis revealed that the main limitation for the catalytic stability of [Ru(bda)(isoq)$_2$] is axial ligand dissociation.[212] Based on DFT calculations, a relationship between the HOMO level and the binding strength to the Ru center was demonstrated for a series of axial ligands, which showed that ligands with a high HOMO energy such as phthalazine (ptz) should lead to an increased longevity of Ru(bda) catalysts.[144] Indeed, the replacement of axial isoquinoline by phtalazine ligands led to an impressive increase in stability with a TON of 55400 for [Ru(bda)(ptz)$_2$] **10** under chemical conditions (Figure 14a).[144] Building on these results, further variations of the axial ligand sphere were achieved by the introduction of halogen substituents in the catalysts [Ru(bda)(6−X−isoq)$_2$] **11a−11c** (X = F, Cl, Br), which led to enhanced reaction rates due to additional van-der-Waals interactions (halogen-π and dipole-induced dipole interactions).
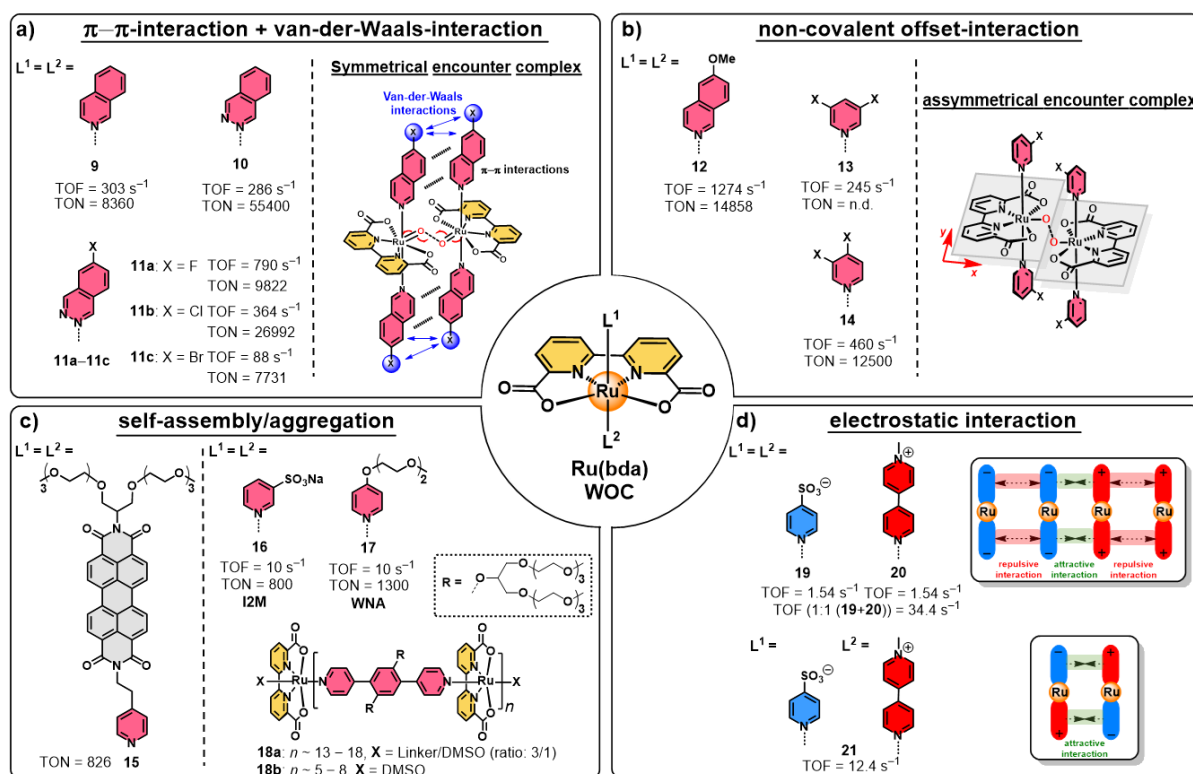
Figure 14. (a–d) Overview of different strategies to improve catalytic performance by applying non-covalent interactions. Selected examples of homogenous Ru(bda) WOCs are provided for a) $\pi-\pi$ and van-der-Waals interactions,[144, 212, 214] b) non-covalent offset-interactions,[215, 216] c) self-assembly/aggregation[217-219] and d) electrostatic interactions.[220] The given catalytic performances of the selected complexes are measured under chemical conditions.

These are offset for the larger halogen atoms (Cl, Br) due to obstructed $\pi-\pi$ overlap.[214, 221] Interestingly, incorporation of a methoxy group in the catalyst [Ru(bda)(6-MeO-isoq)₂] **12** resulted in an even higher TOF of 1274 s^{-1} under chemical conditions, which was explained by a slight off-set in the symmetrical bimolecular encounter complex in the I2M pathway based on theoretical calculations (Figure 14b).[214, 215] Recently, Sun and co-workers further supported this hypothesis by studying a broad range of mononuclear Ru(bda) catalysts with symmetrically and asymmetrically substituted pyridine ligands, resulting in a twofold increase in TOF for complex [Ru(bda)(3,4-Br-py)₂] **14** compared to its symmetrical analogue **13** (Figure 14b).[216] In addition, Ru(bda) complexes equipped with either imidazole,[195] pyrazole[222] or *N*-heterocyclic carbenes (NHCs)[133] as axial ligands have also been studied as WOCs but are not discussed within this literature survey.

Non-covalent interactions can likewise be utilized for the self-assembly of molecular WOCs into larger, aggregated supramolecular structures to increase the lifetime of catalysts or manipulate the O−O bond formation pathway (Figure 14c). In 2015, Würthner and co-workers successfully embedded a Ru-based WOC into supramolecular nanofibers via $\pi-\pi$-stacking

induced self-assembly of the axial PBI ligands of complex **15** (PBI: perylene bisimide) (Figure 14c).[217] In chemical water oxidation, the supramolecular fibers exhibited an increased TON of 826 compared to the mononuclear reference [Ru(bda)(pic)$_2$] **5** (TON = 632) that was attributed to suppressed axial ligand dissociation within the aggregated structure. In addition, a delay of the catalytic response of up to five minutes was observed for the aggregated structure, which was explained by shielded active sites within the supramolecular fibers that led to less efficient diffusion of H$_2$O and oxidant CAN.[217] Wu and co-workers demonstrated the control of the O−O bond formation pathway through different aggregation patterns of two self-assembled amphiphilic Ru complexes **16** and **17**, respectively (Figure 14c).[218] Both complexes form vesicular structures with a diameter of 100 nm only when a critical concentration is reached in pure water, while no particle formation was observed in the presence of acetonitrile. Interestingly, both complexes show different reaction kinetics for oxygen evolution using CAN as a sacrificial oxidant. A second-order dependency on the catalyst concentration was observed for complex **16** bearing sulfonated pyridine axial ligands, which promote a closely stacked aggregation mode of the Ru centers that facilitates the bimolecular I2M pathway. In strong contrast, complex **17** equipped with ethylene glycol chains adopts an alternate aggregation mode, which features large distances between the Ru centers, thus, resulting in a mechanistic switch to the mononuclear WNA mechanism. Surprisingly, both complexes exhibit the same catalytic activity of 10 s^{-1}, and only moderate differences in catalyst stability (TON(**16**) = 800; TON(**17**) = 1300) were observed, indicating that the different aggregation modes do not have a significant effect on the catalytic performance of these WOCs.[218] Building on these previous examples, Würthner and co-workers recently reported on linear oligomeric Ru complexes of different sizes equipped with ditopic OEG-modified 1,4-di(pyridine-4-yl)benzene linker units (OEG = oligo ethylene glycol) that self-assemble into aggregated superstructures in pure water (Figure 14c).[219] The size of the oligomers was controlled by varying the ratio between both precursors, which resulted in oligomeric structures with an average number of 17−18 for **18a** or 6−7 repeating units for **18b.** The different size distribution was confirmed by thorough ^{1}H-NMR end group analysis, DOSY NMR, AFM, VPO and elemental analysis. Both complexes were investigated at neutral pH under photocatalytic conditions, showing a high catalytic activity and stability with TOFs of 14.9 s^{-1} and TONs of more than 1000 per Ru center independent of the oligomer length. Interestingly, again a switch from second to first-order kinetics while maintaining the I2M pathway was evidenced for these supramolecular aggregates. The difference in kinetics was explained by the high local concentration of Ru centers within the aggregate, which favours intra-assembly oxygen evolution over the bimolecular diffusion-controlled process.[219] Several other studies have been published, focusing either on the formation of irregularly cross-linked Ru(bda) polymers[223] or on the generation of defined supramolecular polymers by vertical step-growth

polymerization on an ITO electrode.[224]In comparison to the reported strategies, the incorporation of charged axial ligands usually leads to a drop in catalytic performance due to coulombic repulsion, which hampers the formation of the crucial bimolecular encounter complex as part of the I2M pathway.[215, 225] In this context, the attractive force of electrostatic interactions between axial ligands of opposite charge can promote antiparallel intermolecular coupling as demonstrated by Ahlquist and co-workers.[220] To prove their conceptual approach, they synthesized the two symmetric complexes **19**, **20** with two either positively or negatively charged axial ligands and the asymmetric complex **21**, which is equipped with two differently charged axial ligands (Figure 14d). The use of attractive electrostatic interactions for asymmetric complex **21** and a 1:1 mixture of complexes **19**, **20** resulted in a substantial rate enhancement by more than one order of magnitude in the antiparallel intercatalyst coupling process (TOF(**21**) = 12.4 s^{-1}, TOF (1:1 (**19+20**)) = 34.4 s^{-1}).[220]

2. Influence of pendant functional groups (e.g., carboxylate, phosphonate, sulfonate and pyridyl derivatives)

The incorporation of pendant functional groups such as an auxiliary base or a nucleophile close to the active site represents an appealing strategy to promote the interaction of the catalytic center with substrate H_2O molecules and facilitate O−O bond formation. The implementation of carboxylate groups near the active site can improve the catalytic performance by acting as a proton donor or acceptor moiety due to their hemilability (Figure 15).[108, 190] In 2015, Meyer and co-workers reported the beneficial effect of this feature on water oxidation catalysis using complex [Ru(bda)(isoq)$_2$] **9** in the presence of CH_3CN (Figure 15a). The hemilability of the carboxylate moiety was confirmed by single crystal X-ray analysis.[226] In electrochemical water oxidation at pH 7.2, a significant rate enhancement was observed for the open-arm chelate **9b** in the presence of proton acceptors such as phosphate or hydroxide, which directly participated in the mechanistic water oxidation pathway.[226] In a similar approach, Llobet and co-workers synthesized complex [Ru(tda)(py)$_2$] **22** (tda = 2,2':6'2''-terpyridine-6,6''-dicarboxylate). The equatorial tda^{2-} ligand is equipped with an additional pyridine unit compared to the known bda^{2-} ligand, which results in an unbound, dangling carboxylate group close to the catalytic site (Figure 15a).[227] This intramolecular arrangement in complex **22** leads to impressive catalytic rates of 8000 s^{-1} at pH 7 and 50000 s^{-1} at pH 10 under electrochemical conditions, which are three orders of magnitude higher than the rate of [Ru(bda)(isoq)$_2$] **9** upon addition of an external base (TOF = 6 s^{-1}).[226] Based on DFT calculations, the pendant carboxylate group lowers the activation barrier of O−O bond formation by preorganizing incoming H_2O molecules and facilitating PCETs through intramolecular proton transfer (Figure 15a).[227] Later, Ahlquist and co-workers computationally proposed an alternative
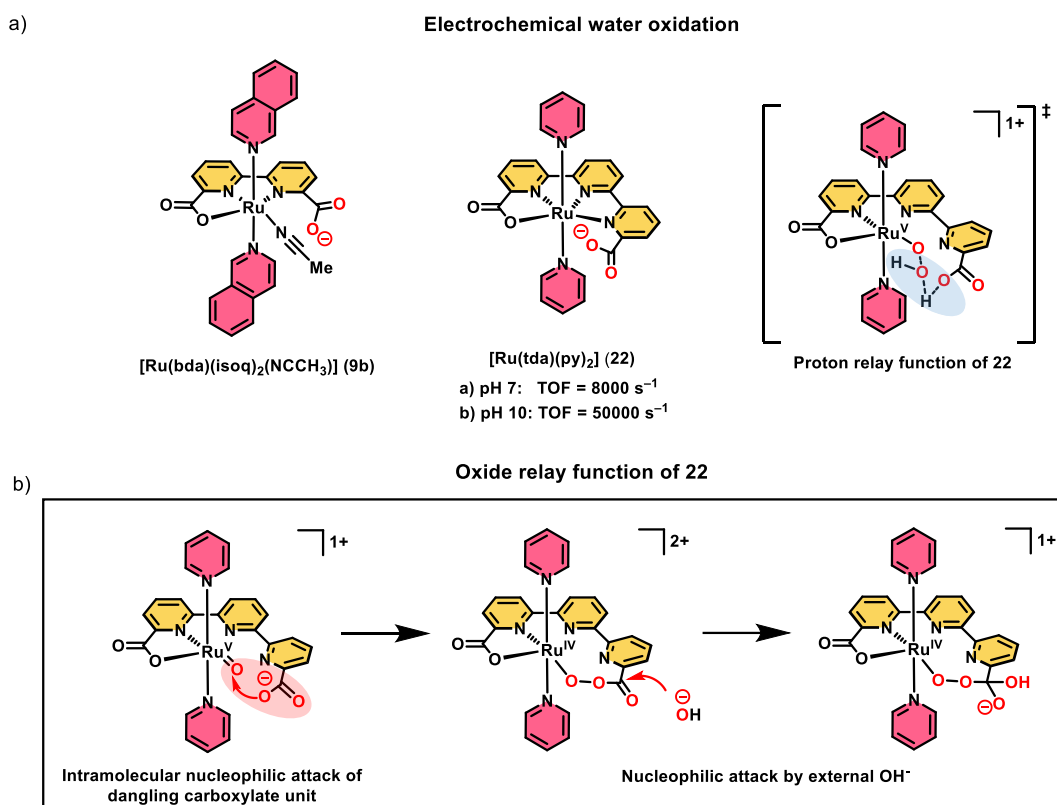
Figure 15. a) Catalysts [Ru(bda)(isoq)$_2$(NCCH$_3$)] **9a** and [Ru(tda)(py)$_2$] **22** containing hemilabile carboxylate groups. For complex **22**, the water nucleophilic attack transition state based on DFT calculations is schematically drawn.[227] b) The alternatively proposed oxide relay function of the dangling carboxylate unit of **22** based on DFT calculations by Ahlquist and co-workers.[228]

function of the carboxylate moiety as an oxide relay in the mechanism.[228] In contrast to the direct nucleophilic attack of a remote H$_2$O molecule,[227] the pendant oxide nucleophile of **22** reacts with Ru^V=O under formation of a percarboxylate intermediate, followed by nucleophilic attack of an incoming OH$^-$ ion and subsequent O$_2$ generation (Figure 15b). Unfortunately, no experimental evidence has yet been provided for either the proton relay (Llobet et al.)[227] or the oxide relay (Ahlquist et al.)[228] pathway. In general, catalysts with pendant, non-coordinated carboxylate groups mostly show promising catalytic rates under neutral to basic conditions due to the reduced basicity of carboxylates at low pH (pH < 2-3)[226]

In 2016, Concepcion and co-workers reported novel WOC [Ru(bpaH$_2$)(pic)$_2$] **23** (bpaH$_2$ = 2,2'-bipyridine-6,6'-diylbis(hydrogen phosphonate)) containing two negatively charged phosphonate moieties (Figure 16).[229] From an electronic perspective, phosphonate groups act as stronger σ-donors than carboxylates, which results in significantly lower oxidation potentials, thus, making higher oxidation states more accessible. In addition, deprotonation of phosphonic acid groups under acidic conditions allows charge balancing of the Ru center at higher oxidation states, and thus these groups can act as intramolecular proton acceptors to

facilitate PCETs. Interestingly, Ru(bda) analogue **23** demonstrated a significantly lower catalytic performance in chemical water oxidation (TOF(**23**) = 0.65 s^{-1}, TON(**23**) = 5) following a WNA pathway. This was explained by the lack of coordination lability of the novel bpaH$_2^{2-}$ ligand at low oxidation states, which hinders crucial H$_2$O coordination.[229, 230] As a consequence, they synthesized the hybrid WOC [Ru(bpHc)(pic)$_2$] **24** (bpHc = 6'-(hydroxyoxidophosphoryl)-2,2'-bipyridine-6-carboxylate) by replacing one phosphonate group by a carboxylate unit (Figure 16).[230] The combination of the coordination flexibility of the carboxylate moiety with the auxiliary base function of phosphonate groups significantly increased the catalytic rate under chemical conditions by two orders of magnitude (TOF(**24**) = 58 s^{-1}, TON(**24**) = 7.5) and also resulted in a 200 mV lower overpotential (330 mV at pH 1) compared to previous [Ru(bpaH$_2$)(pic)$_2$] **23**.[230] In 2020, the Llobet group expanded their studies by modifying the equatorial tda^{2-} ligand with two phosphonate groups, yielding complex [Ru(tpaH$_2$)(py)$_2$] **25** (tpaH$_2$ = 2,2':6'2''-terpyridine-6,6''-diylbis(hydrogen phosphonate)) (Figure 16).[210] Under electrochemical conditions, complex **25** achieved a high catalytic performance with a rate of 16000 s^{-1} following a WNA pathway at neutral pH. Based on theoretical calculations, the dangling phosphonate group acts as an intramolecular proton relay during O−O bond formation. Interestingly, the competing oxide relay pathway is energetically disfavoured for complex **25**.[210] Further investigations revealed that complex **25** undergoes oxidative degradation and forms complex [Ru(bpHc)(pic)$_2$] **24** after several calatytic turnovers, which was previously reported by Concepcion and co-workers.[231] The post-catalytically formed complex **24** showed good catalytic performance, but also suffered from oxidative degradation during electrocatalysis, which finally resulted in the formation of RuO$_2$ nanoparticles.[231] This work clearly shows that pyridyl carboxylate groups have higher

Chemically-driven water oxidation   **Electrochemical water oxidation**

[Ru(bpaH$_2$)(pic)$_2$] (23)   [Ru(bpHc)(pic)$_2$] (24)   [Ru(tpaH$_2$)(py)$_2$] (25)
TOF = 0.65 s^{-1} TOF = 58 s^{-1} pH 7: TOF = 16000 s^{-1}
TON = 5   TON = 7.5
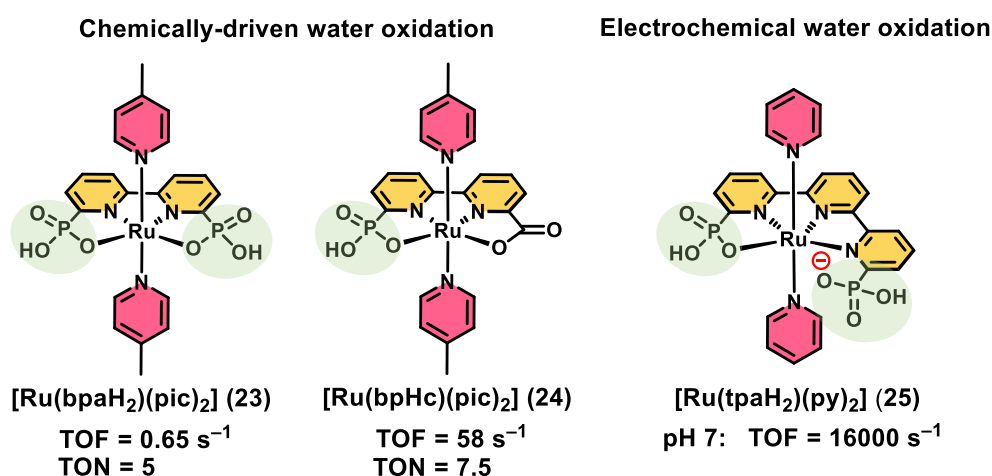
Figure 16. Structures of homogenous Ru WOCs **23−25** containing pendant phosphonate groups (highlighted in green) close to the catalytic center. The respective catalytic activities are given under chemical or electrochemical water oxidation conditions, respectively.

catalytic stability than their corresponding phosphonate derivatives. Due to their higher coordination labilty and lower geometrical strain, carboxylate units are more stable towards chemical transformations. Therefore, the development of novel and oxidatively robust molecular WOCs should focus on the incorporation of carboxylate rather than phosphonate groups.[211]

Compared to carboxylates, sulfonate groups provide an increased water solubility, especially at low pH, due to their presence as deprotonated conjugated base of sulfonic acid ($pK_a < 0$) and the formation of strong hydrogen bonds in acidic aqueous media.[179, 225, 232] Based on these arguments, Grotjahn and co-workers introduced a sulfonate moiety as a pendant base into the ligand sphere of [Ru(tpy)(phs)(OH$_2$)] **26** (tpy = 2,2':6',2''-terpyridine; phs = phenanthroline-2-sulfonate) (Figure 17).[232] Theoretical studies revealed that the sulfonate moiety supports PCET processes by acting as an intramolecular proton relay under acidic conditions, resulting in a very effective electrocatalyst with a rate of 1501 s^{-1} at pH 1.1. The catalyst was also studied using CAN, where it showed a much higher catalytic performance (TOF(**26**) = 0.88 s^{-1}, TON(**26**) = 7400) compared to its carboxylic analogue [Ru(tpy)(phc)(OH$_2$)] (phc = phenanthroline-2-carboxylate) (TOF = 0.15 s^{-1}, TON 700).[142, 232] Another interesting property of sulfonates is their high binding affinity to Lewis-acidic metal ions.[233] As shown by Masaoka and co-workers for complex [Ru(tpy)(bpyms)(OH$_2$)] **27** (bpyms = 2,2'-bipyridine-5,5'-bis(methane sulfonate)) functionalized with pendant SO$_3^-$ groups as binding site for Ce^{4+} ions in chemical water oxidation (Figure 17).[234] Via preorganization of Ce^{IV}-OH close to the active site, a two-fold acceleration of the reaction rate was observed for **27** compared to a non-sulfonated analogue.[234]

Chemically-driven water oxidation

[Ru(tpy)(phs)(OH$_2$)] (26)

TOF = 0.88 s^{-1}
TON = 7400

proposed O–O bond formation step
of [Ru(tpy)(bpyms)(OH$_2$)] (27)
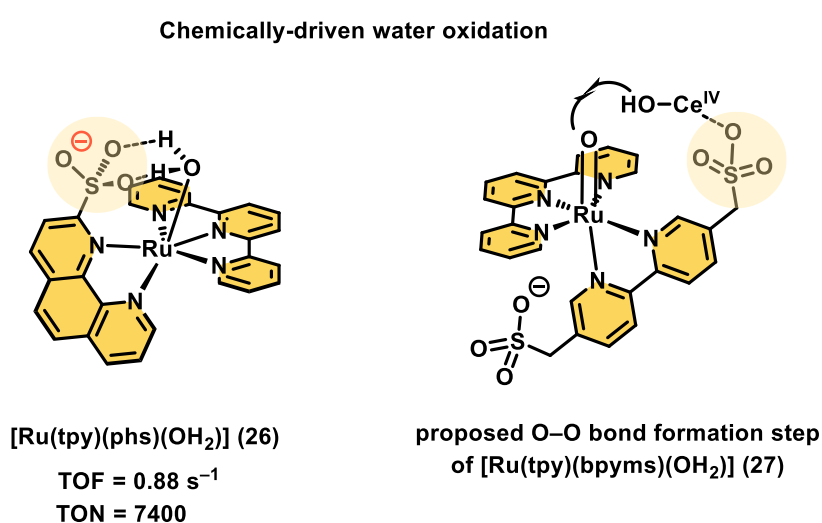
Figure 17. Homogeneous Ru water oxidation catalysts **26** and **27** containing pendant sulfonate groups (highlighted in orange).

Besides using anionic groups, pendant pyridyl groups can also reduce the activation barrier of water oxidation by acting as proton-accepting units. At pH 1, free pyridyl units can be protonated to preorganize H_2O molecules through hydrogen bonding interactions, as could be shown by Chen and co-workers.[235] Under chemical conditions, a slightly higher catalytic activity of complex **28a** compared to the non-coordinated reference **28b** was observed (Figure 18). In another report, Llobet and co-workers demonstrated this property for the mononuclear Ru complex **29** containing a rigid pentapyridine ligand backbone.[236] Interestingly, this complex acts as a precatalyst and isomerizes in the presence of CAN to form the chlorido-aqua Ru complex **act-29** with a dangling pyridine moiety as the active catalyst in solution after a prolonged time (Figure 18). Catalyst **act-29** outperforms the respective analogue without pendant base by more than an order of magnitude higher performance (TOF(**act-29**) = 0.71 s^{-1}, TON(**act-29**) = 168). Subsequent DFT calculations revealed that the decoordination of the pyridine unit is favourably affected by the release of structural strain.[236]
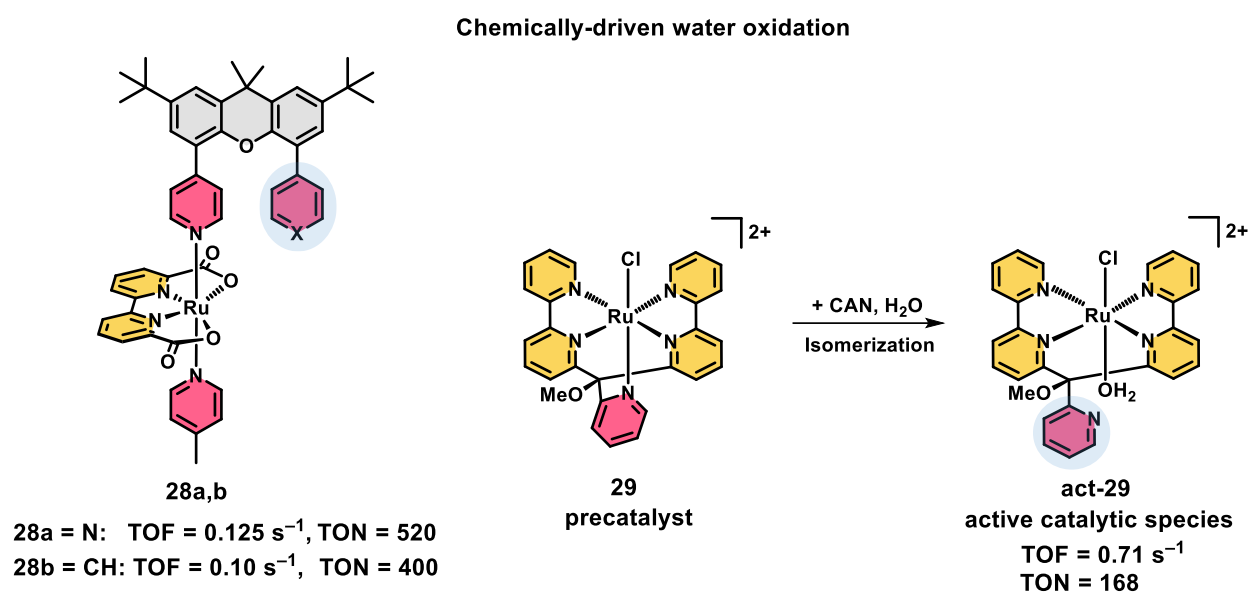
Figure 18. Overview of selected homogeneous Ru WOCs with pendant pyridyl groups (highlighted in blue) close to the active site and their water oxidation performance using CAN.

3. Design of confined environments

Reminiscent of enzymatic pockets, the formation of confined molecular environments around the active site is advantageous to improve catalytic selectivity and activity and to promote supramolecular substrate preorganization or inter-catalyst coupling.[237-239] One of the first approaches focused on the encapsulation of the well-known catalyst [Ru(bda)(pic)$_2$] **5** into the nanocages of mesoporous silica (SBA-16) (Figure 19a).[240] To ensure a high local catalyst concentration, up to seven catalytic units were trapped inside the pores of each nanocage by

a silylation reaction. In presence of CAN, a higher catalytic activity and stability of entrapped complex **5** (TOF(**5**·SBA-16) = 8.7 s^{-1}), TON(**5**·SBA-16) = 3300) was observed compared to the performance of the catalyst in homogeneous phase (TOF(**5**) = 4.5 s^{-1}), TON(**5**) = 1200). These results were explained by enhanced bimolecular catalyst interaction of **5** within the confined nanocage. Interestingly, encapsulation of varying amounts of structurally related complex [Ru(pda)(pic)$_2$] **6**, which follows the unimolecular WNA pathway, resulted in only a slightly improved catalytic performance.[240]

Using supramolecular hydrogen bonding interactions, Reek and co-workers demonstrated the encapsulation of sulfonated Ru(bda) WOCs **30** into Pt$_{12}$L$_{24}$ (L = bispyridyl building block) nanospheres, which are endohedrally functionalized with guanidinium groups (Figure 19c). In electrochemical water oxidation, spatial preorganization of the catalytic WOCs within confined space accelerates the diffusion-controlled bimolecular rate (TOF(**30**·Pt$_{12}$L$_{24}$) = 125 s^{-1}) by two orders of magnitude compared to the non-encapsulated system TOF(**30**) = 0.93 s^{-1}).[241] Remarkably, no rate enhancement was observed upon encapsulation of [Ru(pda)(pic)$_2$] **5** into Pt$_{12}$L$_{24}$ nanospheres and, furthermore, no increase in catalytic current was detected when catalyzing free sulfonated Ru(bda) WOC **30** in the presence of guanidinium-binding sites.[241]
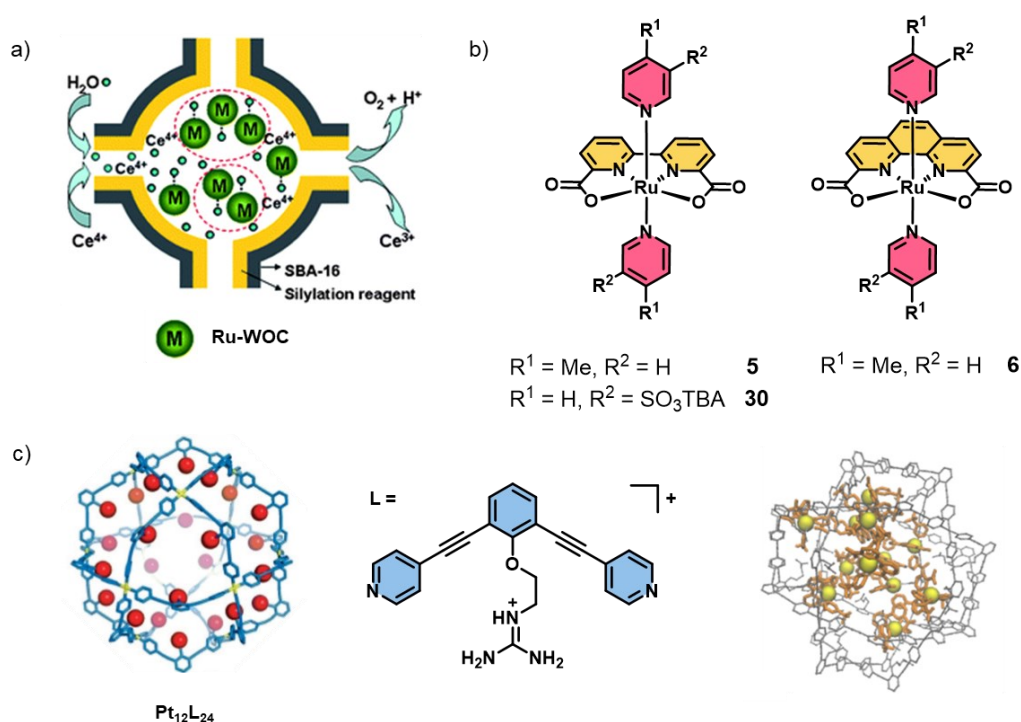
Figure 19. a) Ru WOCs encapsulated in mesoporous silica (SBA-16). b) Molecular structures of complexes **5**, **6** and **30** used in encapsulation studies. c) Self-assembled 3D structure of Pt$_{12}$L$_{24}$ nanosphere and formed host-guest complex upon encapsulation of sulfonated WOC **30**. Figure 19a) is reproduced with permission from ref. [240]. Copyright 2012 Royal Society of Chemistry and Figure 19c) is adapted with permission from ref. [241]. Copyright 2018 Wiley-VCH.

Recently, Würthner and co-workers introduced another supramolecular strategy to promote rate-determining cooperative catalyst interaction by synthesizing a Ru(bda)-based three-dimensional covalent organic framework (COF) as a heterogeneous catalyst for chemical and photocatalytic water oxidation (Figure 20a).[242] Here, the highly ordered crystalline network of the novel COF material led to preorganization of the incorporated catalytic Ru units, which facilitates rate-determining cooperative interaction in the I2M pathway (Figure 20b). The reported heterogeneous system belongs to the most active COF-based hydrogen or oxygen evolving catalysts to date. Moreover, the catalytic performance of the novel COF remained almost unaltered after several consecutive cycles under both acidic and neutral conditions, demonstrating the high stability and recyclability of the interpenetrated network.[242]

Interpenetrated 3D network of a
novel Ru(bda) COF
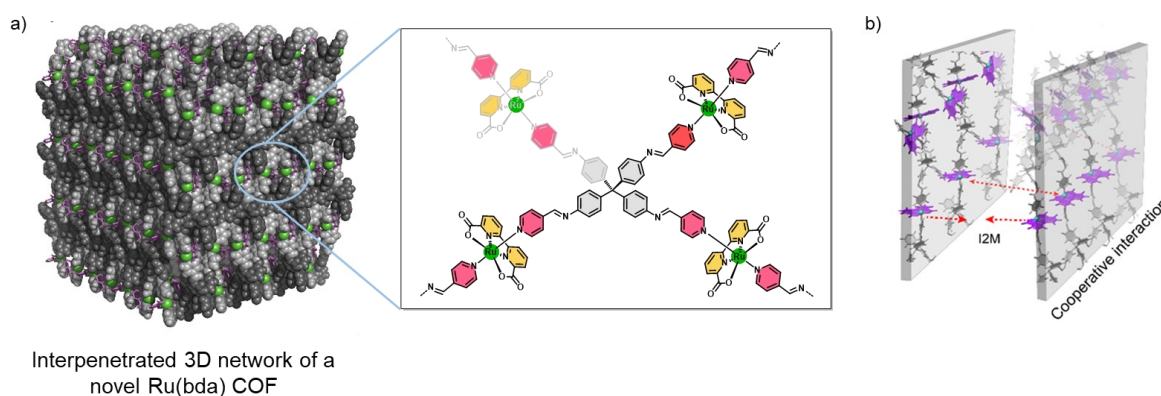
Figure 20. Interpenetrated 3D network of a Ru(bda) COF and representation of the covalent imine bonding framework. b) Schematic illustration of rate-determing cooperative interaction of metal centers at COF interface. Figure 20 is adapted with permission from ref. [242]. Copyright 2022 American Chemical Society.

Di- or trinuclear Ru complexes can be synthesized by introducing axial bridging ligands to bring single catalytic units into close proximity and promote intra-catalyst coupling (Figure 21). Sun and co-workers first made use of this supramolecular strategy by introducing flexible bidentate ligands to link two or more Ru(bda)(pic) units.[243, 244] The observed first-order kinetics for non-cyclic dimer **31** and trimer **32** indicated an intramolecular I2M pathway for both complexes with improved catalytic rates of 68 s^{-1} and 126 s^{-1} and increased TON values of 44400 and 86500 for di- and trinuclear WOCs **31** and **32** in chemical water oxidation, respectively (Figure 21).[243, 244] Nevertheless, these high catalytic rates were determined only after several minutes of oxygen evolution, indicating oxidative degradation of the benzylic units of the catalytic ligand scaffold under harsh oxidative conditions, as reported in the literature.[119] In an alternative approach, a rigid xanthene ligand was used as a spacer unit in dinuclear WOC **33**, resulting in a low TON of 900 (Figure 21). Compared to the previous flexible dinuclear WOC **31**, the steric
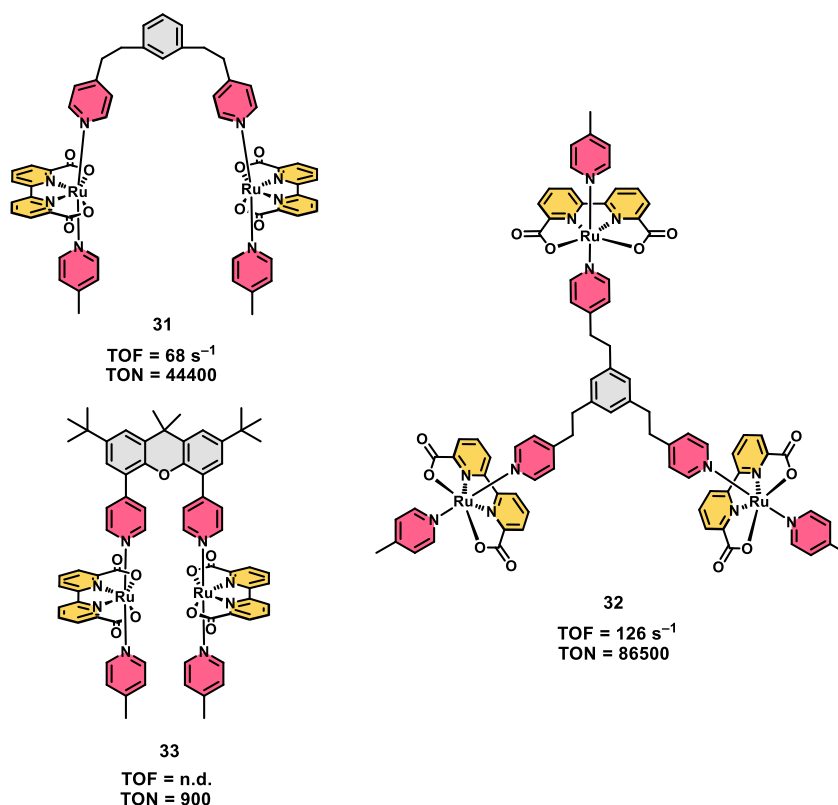
Figure 21. Molecular structures of non-cyclic di- and trinuclear Ru complexes **31−33** and respective catalytic performances under chemical conditions.

confinement of the Ru(bda) units hinders intramolecular communication between them, which results in a mechanistic switch to a less efficient unimolecular WNA mechanism.[134]

Compared to the reported non-cyclic complexes, implementation of Ru(bda) subunits into defined cyclic metallosupramolecular architectures leads to increased catalytic stability through the chelate effect of the preorganized ditopic bridging ligands.[34, 245] Würthner and co-workers reported the first example for this 'macrocycle approach' with a novel trinuclear Ru macrocycle [Ru(bda)(bpb)]$_3$ (**MC3**) (bpb = 1,4-bis(pyridyl-3- yl)benzene) (Figure 22a).[37] This multinuclear catalyst design is particularly appealing due to a significant increase in catalyst stability and high performances via the mononuclear WNA pathway under chemical (TOFs > 100 s^{-1}) and photocatalytic conditions (TOF = 11 s^{-1}). As evidenced by kinetic studies and ^{18}O labelling experiments, a mechanistic switch to a unimolecular WNA mechanism was observed because the rigidity of the metallosupramolecular assembly prevented the bimolecular I2M mechanism. According to molecular dynamics simulations, the excellent activity was attributed to the formation of a hydrogen-bonded network of preorganized water molecules inside the macrocyclic cavity through cooperative effects between the catalytic Ru centers, which facilitates proton-coupled oxidation steps and leads to reduced activation

a)

	TOF [s⁻¹]	TON
MC1	0.3	660
MC2	1.6	680
MC3	7.9	3590
MC4	3.8	1810

spacer = none

b)

c)

R =

OEG-MC2
TOF = 12 s⁻¹
TON = 200

OEG-MC3
TOF = 26 s⁻¹
TON = 2200

OEG-MC4
TOF = 42 s⁻¹
TON = 2870
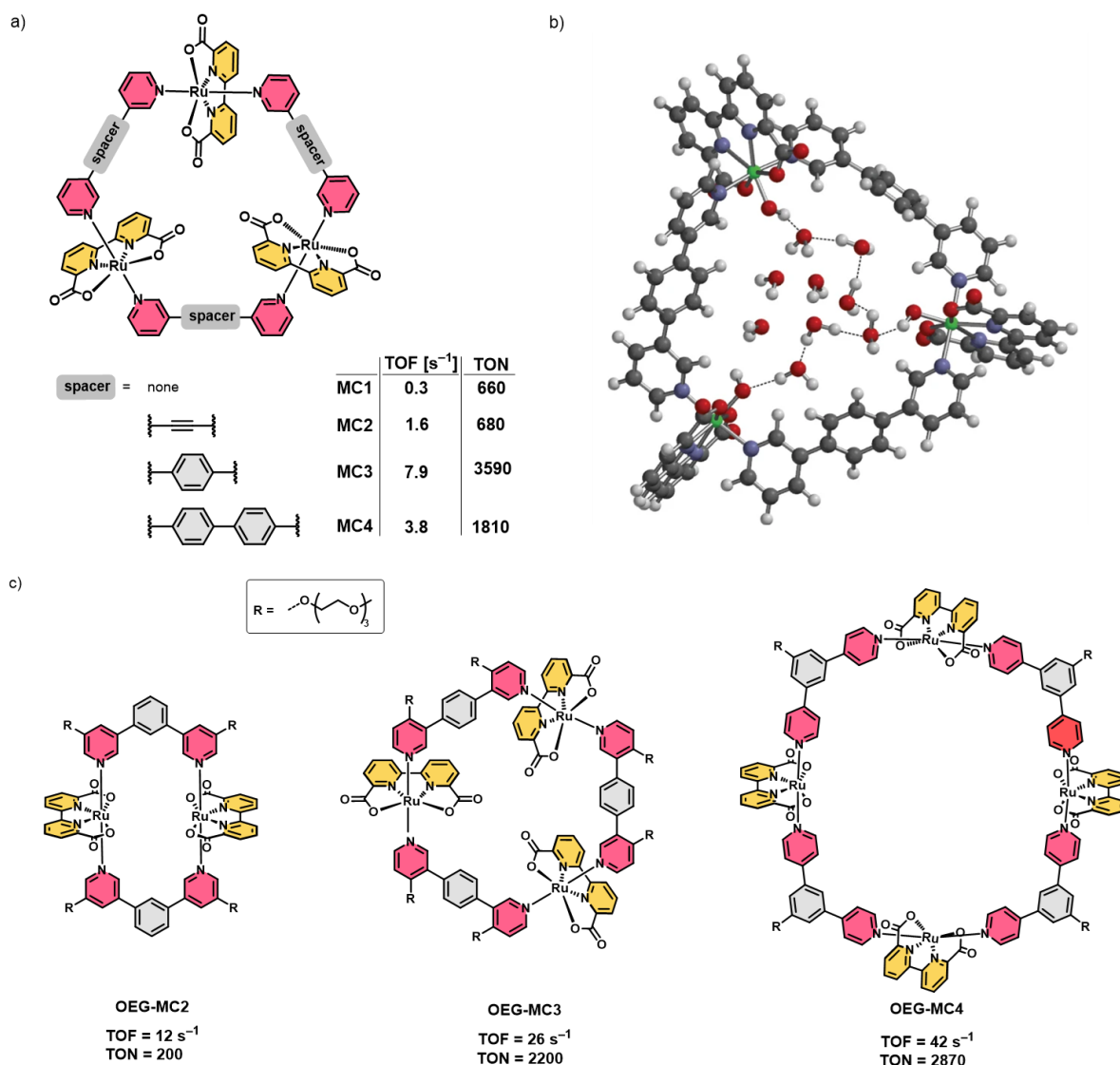
Figure 22. a) Metallosupramolecular macrocycles **MC1−MC4** with ditopic bridging ligands of varying lengths. b) DFT-optimized hydrogen-bonded network of up to ten preorganized H_2O molecules inside the cavity of **MC3** in Ru_3^{IV} state. c) Structures of macrocyclic di- to tetranuclear WOCs **OEG-MC2–OEG-MC4**. Figure 22b) is reproduced with permission from ref. [37]. Copyright 2016 Nature Publishing Group.

barriers (Figure 22b).[34, 37] Varying the length of the ditopic ligands resulted in the trinuclear macrocycles **MC1−MC4** having different cavity sizes (Figure 22a).[38] Subsequent studies under chemical conditions revealed a strong dependency of the catalytic performance on the ring size and, thus on the quality of the formed hydrogen-bonded water network. Remarkably, the first reported macrocycle **MC3** still shows the highest catalytic rate in the series of differently sized trinuclear macrocycles **MC1−MC4** in the presence of 80% CH_3CN (Figure 22a). Theoretical calculations showed that steric constraints imposed by the axial ligands prevent efficient cooperative effects between the individual centers in the smaller macrocycles, which results in limited access of substrate H_2O molecules to the individual Ru centers and restricted accessibility to the inner water network.[38, 40] To investigate the effect of

the number of Ru units on the catalytic performance of multinuclear macrocycles, a series of di- to tetranuclear Ru(bda) macrocycles **OEG-MC2−OEG-MC4** were recently published by the Würthner group (Figure 22c).[39] Under both chemical and photocatalytic conditions, continuously rising catalytic rates per Ru unit towards larger structures were observed, which was attributed to enhanced cooperative effects with an increasing number of Ru units, promoting the formation of hydrogen-bonded networks.[39]

Recently, Sun and co-workers reported on a series of pocket-shaped mononuclear Ru(bda) complexes equipped with flexible, aliphatic bridging ligands that operate via inefficient WNA pathways.[198, 246] The authors suggested that the formed hydrophobic environment affords thermodynamic stabilization of higher oxidation states and should be suited for kinetic acceleration of PCETs, but very low catalytic activities were observed.

Chapter 3

A Calix[4]arene-Based Cyclic Dinuclear Ruthenium Complex for Light-Driven Catalytic Water Oxidation
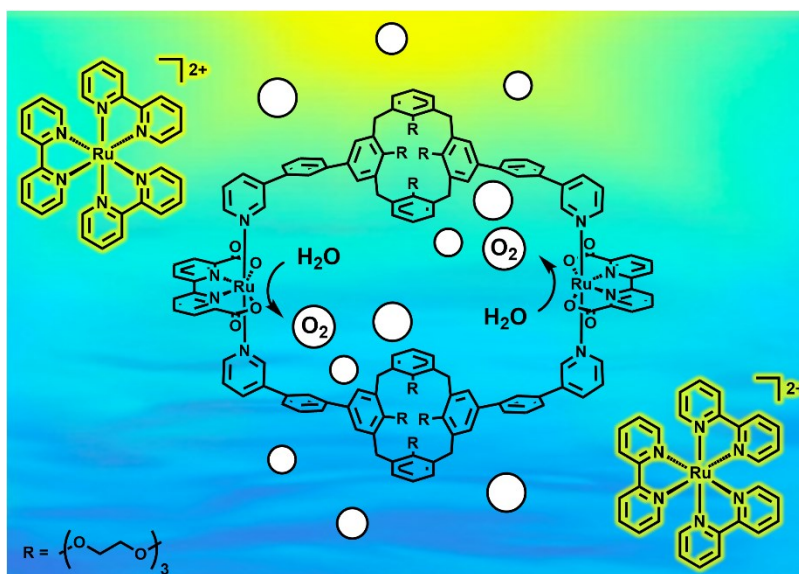
This chapter and the corresponding supporting information (*Chapter 8.1*) were published in:

N. Noll, F. Würthner, *Chem. Eur. J.* **2021**, *27*, 444−450.

(https://chemistry-europe.onlinelibrary.wiley.com/doi/full/10.1002/chem.202004486).

Adapted or reprinted with permission from reference[247]. Copyright 2020 The Authors. Published by Wiley-VCH Verlag GmbH & Co. KGaA, Weinheim.

Abstract: A cyclic dinuclear ruthenium(bda) (bda: 2,2'-bipyridine-6,6'-dicarboxylate) complex, equipped with oligo(ethylene glycol)-functionalized axial calix[4]arene ligands has been synthesized for homogenous catalytic water oxidation. This novel Ru(bda) macrocycle showed significantly increased catalytic activity in chemical and photocatalytic water oxidation compared to the archetype mononuclear reference [Ru(bda)(pic)$_2$]. Kinetic investigations, including kinetic isotope effect studies, disclosed a unimolecular water nucleophilic attack (WNA) mechanism of this novel dinuclear water oxidation catalyst (WOC) under the involvement of second coordination sphere. Photocatalytic water oxidation with this cyclic dinuclear Ru complex using [Ru(bpy)$_3$]Cl$_2$ as a standard photosensitizer revealed a turnover

frequency of 15.5 s^{-1} and a turnover number of 460. This so far highest photocatalytic performance reported for a Ru(bda) complex underlines the potential of this water-soluble WOC for artificial photosynthesis.

3.1 Introduction

Since the industrial revolution in the mid-18th century, the economic welfare and growth of our society has been significantly driven by the finite reservoir of fossil fuels, including coal, oil and natural gas.[248, 249] To satisfy the growing energy demands of the rapidly increasing world population, the transition to a clean, sustainable and carbon-neutral economy is inevitable.[15, 250, 251] In search of alternative energy carriers, a long-standing challenge has been the construction of artificial photosynthetic systems in which solar energy is stored in the chemical bonds of solar fuels originating from abundant resources like water or CO_2.[18, 122, 252, 253] In this regard, the thermodynamically demanding oxidation of water to molecular oxygen in a complex four-electron process is a critical bottleneck for the generation of carbon-neutral fuels like hydrogen.[26, 254] To enable water oxidation at low overpotentials, however, efficient catalysts are required.[35, 110] Accordingly, considerable efforts have been made in the last years to develop water oxidation catalysts (WOCs) based on earth-abundant transition metals (Mn, Fe, Co, Ir and Ru).[34, 109, 116, 255]

Ruthenium-based catalysts belong to the earliest and most studied molecular WOCs,[34, 35, 256] where especially the invention of the Ru(bda) system (bda: 2,2'-bipyridine-6,6'-dicarboxylate)[128, 133, 257] enabled catalytic activities that are comparable to those of the natural oxygen evolving cluster (OEC).[212] The highly versatile Ru(bda) fragment facilitated by axial ligand exchange the isolation of multinuclear Ru complexes including dimers[134, 243, 258] and trimers,[244] which showed increased catalytic activities compared to mononuclear complexes due to covalent linkage of the catalytic centers accelerating the underlying bimolecular I2M (interaction of two M-O units) mechanism.[201]

In recent years, many examples reported in the literature have emphasized the role of second coordination sphere effects,[35] that is $\pi-\pi$ interactions,[144, 202, 212, 214, 215, 221, 240] accessible pendant bases,[210, 226, 227, 230, 234] hydrogen bonding,[37, 38, 241, 259] and steric effects[37, 38, 40] on the overall water oxidation mechanism. In this regard, several supramolecular approaches have mainly focused on accelerating the underlying bimolecular I2M mechanism by self-assembly of two catalytic subunits through $\pi-\pi$ interactions,[144, 202, 212, 214, 215, 221, 240] whereas the integration of accessible pendant bases like carboxylates in the second coordination sphere leads to a mechanistic change to the water nucleophilic attack (WNA) pathway due to their ability to act as a intramolecular proton acceptor in the rate-determining step of oxygen bond formation.[210, 226, 227, 230, 234] Our group has shown that the incorporation of Ru(bda) units into

trimeric metallosupramolecular macrocycles leads to high catalytic activity in water splitting through the formation of a hydrogen-bonded water network inside the cavity, resulting in a lower activation barrier for water nucleophilic attack by involving the second coordination sphere.[37, 38] Kinetic studies indeed confirmed that these trinuclear Ru(bda) macrocycles function through a WNA mechanism.

Although several non-cyclic dinuclear Ru WOCs that exhibit variable catalytic activities involving the I2M mechanism have been reported in the literature,[134, 243, 244, 258] studies on catalytic water oxidation with cyclic dinuclear Ru complexes are barely known and only in a patent have the synthesis and X-ray crystal structure analysis of such cyclic complexes, but no catalytic activities, been reported.[260] Motivated by the fact that cyclic complexes are structurally by far more preorganized than the previously investigated non-cyclic dinuclear systems, and indeed the high catalytic activities of our previously reported trinuclear Ru(bda) macrocycles, we have now designed a cyclic dinuclear complex by employing an axial calix[4]arene ligand for catalytic water oxidation involving the second coordination sphere.

Due to the poor water solubility of unmodified calix[4]arenes,[261] the hydrophilic narrow lower rim of the ligand was functionalized with four triethylene glycol chains. In combination with two phenylpyridine units, substituted at the hydrophobic wider upper rim, the calix[4]arene ligand was conformationally fixed in its cone conformation.[262] A large variety of calix[*n*]arenes have been applied as ancillary ligands in metal-based catalysis,[263] whereas to date only one example of a calix[4]arene-based mononuclear Ru(bda) complex is reported for catalytic water oxidation with rather poor performance (turnover number (TON) = 762, turnover frequency (TOF) not reported)[264] and, to the best of our knowledge, cyclic dinuclear Ru complexes based on calix[*n*]arenes are so far unprecedented.

Herein, we report the synthesis of a novel cyclic dinuclear Ru(bda) complex **dimer 1** containing functionalized calix[4]arene axial ligands that exhibits high catalytic activities in both chemical and photocatalytic water oxidation. Our kinetic studies revealed that this macrocyclic WOC operates by a WNA mechanism. Under highly diluted conditions, this dinuclear Ru(bda) complex performed outstanding photocatalytic water oxidation with a TOF value of 15.5 s^{-1}, which makes **dimer 1** the most active homogenous Ru(bda) catalyst for light-driven water oxidation reported in literature to date.

3.2 Results and Discussion

3.2.1 Synthesis, electrochemical and spectroscopic studies of dimer 1

The dinuclear calix[4]arene-based cyclic Ru complex **dimer 1**, bearing eight tri(ethylene glycol) chains as water-solubilizing groups, was synthesized according to the route depicted in Scheme 2. The solubilizing groups were incorporated into the axial calix[4]arene-based

ligand **42** in five steps by literature adapted procedures,[265-267] starting from commercially available 4-*tert*-butylcalix[4]arene **34**. The target Ru complex **dimer 1** was then synthesized through a ligand exchange reaction of the precursor [Ru(bda)(dmso)$_2$] **43**[268] with the phenylpyridine-functionalized calix[4]arene ligand **42** in a chloroform/methanol mixture under a nitrogen atmosphere. Purification of the crude product by column chromatography afforded the desired dinuclear complex **dimer 1** in 50% isolated yield. The structures of **dimer 1** and all unknown precursors were elucidated by 1D and 2D NMR spectroscopy and high-resolution mass spectrometry. The purity of the compounds were confirmed by elemental analysis. Detailed synthetic procedures and characterization data of all new compounds are reported in *Chapter 8.1*. Semiempirical PM6 calculations (for details see *Chapter 8.1*) suggested that in the lowest energy, geometry-optimized structure (Figure A8.1.3) both Ru centers are directed into the interior of the cavity of the macrocycle. To further confirm the size of the dimeric structure, diffusion-ordered spectroscopy (DOSY) was performed, revealing a hydrodynamic radius of r = 13.8 Å (Figure A8.1.4).The obtained value matches very well with the calculated distance between the two Ru(bda) centers (d = 27.6 Å) of the geometry-optimized structure of **dimer 1** (Figure A8.1.3).
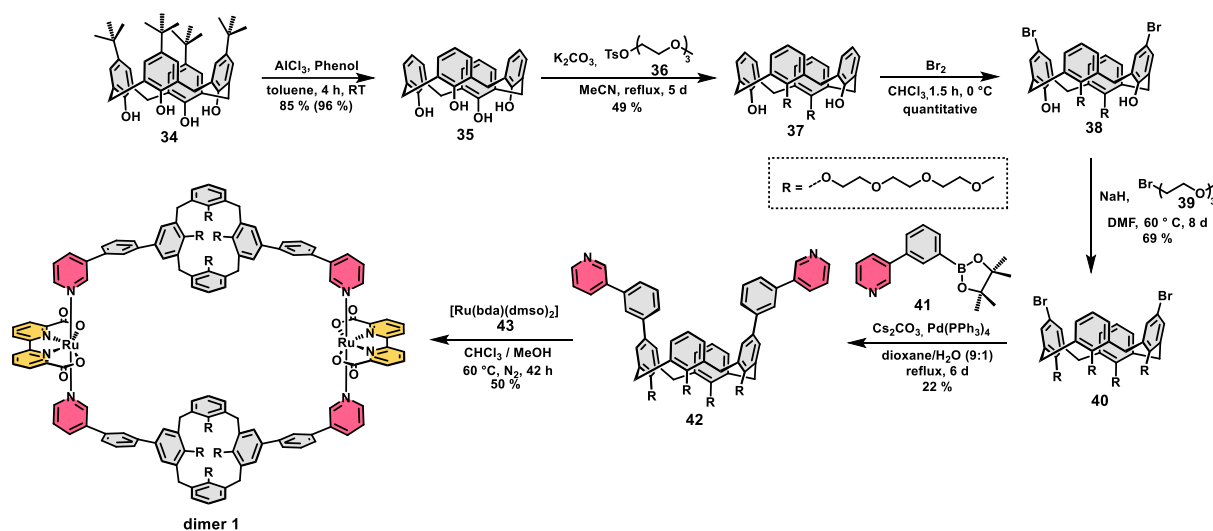
Scheme 2. Synthesis of the target dinuclear calix[4]arene Ru complex **dimer 1**. Boronic ester **41** was prepared in two steps starting from the respective pyridine boronic acid according to ref.[266].

Electrochemical studies of **dimer 1** were performed by cyclic voltammetry (CV) and differential pulse voltammetry (DPV) in aqueous solution under acidic (pH 1, triflic acid) and neutral conditions (pH 7, phosphate buffer) containing 40% 2,2,2-trifluorethanol (TFE) as a non-coordinating co-solvent for solubilization. The redox properties of **dimer 1** under the applied experimental conditions are summarized in Table A8.1.2 and compared with those of the mononuclear reference complex [Ru(bda)(pic)$_2$], and the voltammograms are displayed in

Figures A8.1.5−A8.1.8.[194, 212] In acidic aqueous solution (pH 1), **dimer 1** displayed two subsequent oxidation processes which can be assigned to the Ru_2^{II}/Ru_2^{III} and Ru_2^{III}/Ru_2^{IV} redox couples for each metal center in accordance to the redox processes reported for [Ru(bda)(pic)$_2$] (Figures A8.1.5 and A8.1.6).[212] Due to the overlap with the water oxidation current, the oxidation to Ru_2^V could not be observed as it has previously been described for other dinuclear non-cyclic Ru complexes.[134, 243] Under neutral conditions (pH 7), three two-electron oxidation events were observed for **dimer 1** which correspond to the oxidation potentials Ru_2^{II}/Ru_2^{III}, Ru_2^{III}/Ru_2^{IV} and Ru_2^{IV}/Ru_2^V for each metal center (Figure A8.1.7). Compared to the mononuclear complex [Ru(bda)(pic)$_2$], the incorporation of the axial calix[4]arene in **dimer 1** affected under both acidic and neutral conditions only the Ru_2^{II}/Ru_2^{III} redox potential, resulting in an approximately 50 mV higher oxidation potential for this dinuclear cyclic Ru(bda) complex.

The UV/Vis absorption spectra of **dimer 1** at the Ru_2^{II} state under both acidic and neutral conditions displayed a very strong absorption band at around 250 nm, which belongs to an electronic transition along the long molecular axis (^1L_a) for the axial calix[4]arene ligand (Figure A8.1.9).[269] The transition along the short molecular axis (^1L_b) of the calix[4]arene ligand is usually very weak and is presumably overlapping with the ligand centered $\pi-\pi^*$ transitions at around 300 nm.[270] The weak absorption bands in the visible region can be attributed to several metal-to-ligand charge transfer (MLCT) absorptions,[197, 271] where the band at around 360 nm is characteristic for the transition from the Ru d-orbital to the π^*-orbital of the axial ligand, while the less energetic bands at 450 and 500 nm can be explained by the transition from the Ru d-orbital to the π^*-orbital of the equatorial bda ligand.[38] Compared to the mononuclear [Ru(bda)(pic)$_2$], the high-energy MLCT band at 360 nm is bathochromically shifted for **dimer 1** indicating a less donating character of the axial calix[4]arene ligand.[271]

To investigate the spectral changes of **dimer 1** upon oxidation, spectroelectrochemistry in CH$_3$CN/H$_2$O 4:6 at pH 7 (phosphate buffer) was performed (Figure 23). Upon increasing the potential from 500 mV to approximately 800 mV, the MLCT bands at 350 nm and 450−500 nm are bleached with concomitant appearance of a new band at 700 nm which is characteristic for the Ru_2^{III} state.[38, 40] A further increase of the potential to approximately 960 mV results in a decrease of the transition at 700 nm and a broad absorption at around 520 nm arises for the formation of the Ru_2^{IV} state (Figure 23 and Figure A8.1.10).[40] No further spectral changes were observed upon increasing the potential because a strong catalytic current is associated with the formation of Ru^V and subsequent oxidation of water.[37, 38]
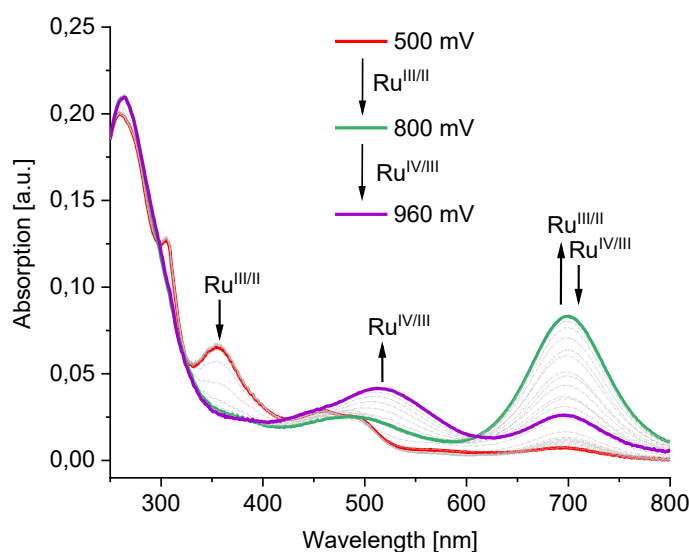
Figure 23. Spectroelectrochemistry of **dimer 1** in CH_3CN/H_2O (4:6; pH 7, phosphate buffer) at c = 2.4 · 10^{-4} M. The applied voltages for the generation of Ru_2^{II} (red), Ru_2^{III} (green) and Ru_2^{IV} (purple) are indicated.

3.2.2 Chemical water oxidation under acidic conditions

The catalytic performance of **dimer 1** was first investigated in the presence of cerium ammonium nitrate (CAN) as a sacrificial oxidant in aqueous acidic solutions (pH 1, triflic acid) with 40% acetonitrile as co-solvent due to its oxidative stability.[225, 272] A large excess of CAN was applied in these experiments to ensure a direct dependence of the overall catalytic rate on the catalyst concentration.[133] After the injection of the catalyst solution into the acidic CAN mixture, the subsequent pressure increase due to oxygen evolution was monitored by the attached pressure sensors. The gas composition at the end of each run was then analyzed by gas chromatography (GC; for experimental details and reaction conditions see *Chapter 8.1*). The catalytic performance of **dimer 1** was then screened in different acetonitrile/water ratios to determine the optimal experimental conditions (Figure A8.1.11a). The amount of acetonitrile used as co-solvent strongly correlates with the overall catalytic activity, which can be attributed to its competitive binding to the seventh coordination site of the ruthenium center compared with water.[217, 225] For **dimer 1** the highest catalytic activity was achieved in aqueous mixtures containing 40% acetonitrile, whereas higher acetonitrile content led to lower catalytic activity in the initial first two seconds of catalytic water oxidation (Figure A8.1.11b). Hence, all further catalytic experiments were performed in CH_3CN/H_2O 4:6 solvent mixtures and compared to the mononuclear complex [Ru(bda)(pic)$_2$][212] under the same conditions.

Concentration-dependent water oxidation experiments were conducted to determine the turnover number (TON) and the turnover frequency (TOF) for the dinuclear cyclic complex

dimer 1 and [Ru(bda)(pic)$_2$] as a mononuclear reference under identical experimental conditions (Figure 24b and Figure A8.1.12). The oxygen evolution for both catalysts was detected in the range of 25−200 µM of catalyst concentration (Figure 24a, Figures A8.1.12 and A8.1.13) and afterwards the initial rates of catalysis were evaluated within the first seconds of catalysis at different catalyst loadings. Notably, the analysis of the head space of each catalytic reaction by gas chromatography confirmed that oxygen was the only gaseous product detected during catalysis with **dimer 1** (Figure A8.1.14). As clearly shown in Figure 24b, a linear dependency on the catalyst concentration is observed for **dimer 1** which is indicative of a first-order reaction kinetic in the rate-determining step (RDS) of oxygen evolution according to a WNA mechanism.[37, 38, 259] In contrast, mononuclear complex [Ru(bda)(pic)$_2$] displayed a second order dependency on the catalyst concentration in accordance with the reported bimolecular I2M reaction mechanism (Figure 24b).[128, 194, 212] In case of a linear relationship, as found for **dimer 1**, the slope of the linear regression represents the averaged TOF value of the catalyst, whereas for a second order dependency TOF values for each catalyst concentration is calculated. Under optimized conditions, **dimer 1** displayed an averaged TOF of 19 ± 0.5 s^{-1} (~9.5 s^{-1} per Ru unit) while for the mononuclear [Ru(bda)(pic)$_2$] an averaged TOF could not be determined and thus concentration-dependent TOF values of 0.9−9 s^{-1} in the catalyst concentration range from 25−200 µM are shown (Figure 24b). These results clearly show that **dimer 1** is a more efficient WOC than the mononuclear reference with substantial benefit, in particular, at lower concentrations.
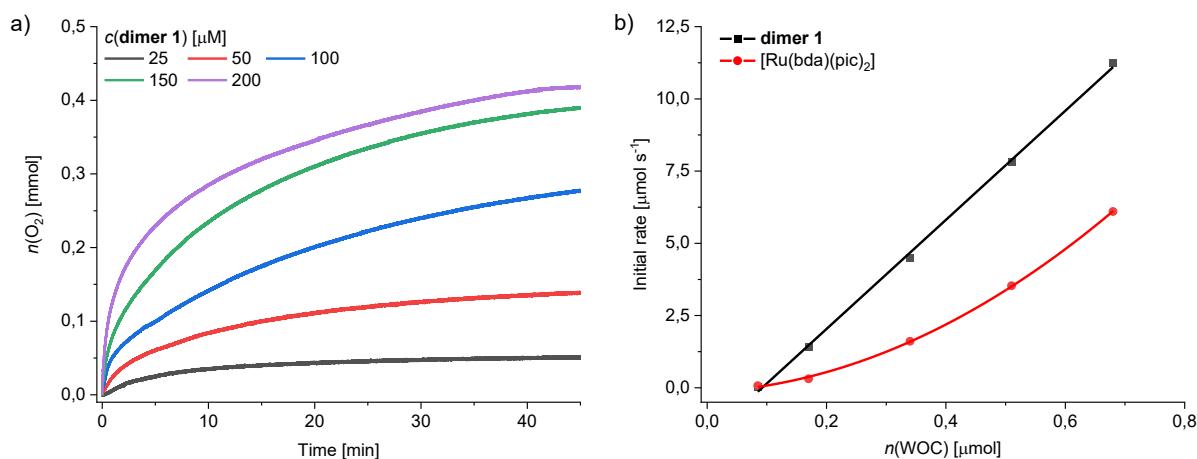
Figure 24. a) Oxygen evolution curves for **dimer 1** at various concentrations in CH$_3$CN/H$_2$O (4:6; pH 1, triflic acid), *c*(CAN) = 0.6 M. b) Concentration-dependent initial rates of **dimer 1** vs. [Ru(bda)(pic)$_2$] including linear regression for the determination of averaged TOF for **dimer 1**.

Post-catalytic analysis of the reaction mixture of **dimer 1** by HR ESI mass spectrometry indicated oxidative decomposition of the methylene bridges between the aryl units of the axial calix[4]arene ligands (Figure A8.1.15). Such oxidative decomposition of methylene groups has

been reported previously in literature.[119, 273, 274] Thus, we assume that axial ligand exchange of the Ru(bda) WOC,[212] combined with oxidative decomposition of the calix[4]arene ligand in **dimer 1** under acidic conditions, is the main catalyst deactivation pathway. These findings are in accordance with the somewhat lower stability of the cyclic **dimer 1** containing axial calix[4]arene ligands compared to [Ru(bda)(pic)$_2$] as TONs of 760 ± 60 (~380 per Ru unit) and 880 ± 20, respectively, were observed. To get some insights into the reaction kinetics of the underlying water oxidation mechanism of the new WOC **dimer 1**, further experiments in the presence of stoichiometric amounts of cerium ammonium nitrate (CAN) were carried out (for experimental details see *Chapter 8.1* and Figures A8.1.16 and A8.1.17). Thus, the characteristic decay of the CAN absorption band at 360 nm after addition of the catalyst was monitored by UV/Vis spectroscopy over time.[38, 139] To study the dependency of the catalytic reaction rate on both components, two different types of experiments were conducted. In a first experiment at a constant CAN concentration, the initial reaction rates at varying catalyst concentration (Figure A8.1.16) showed a linear dependency on the catalyst concentration which is in proper accordance with the results of the previous experiments using CAN in large excess (Figure 24). In a second experiment, the catalyst concentration was kept constant and only the oxidant concentration was varied (Figure A8.1.17). Under these conditions, **dimer 1** exhibited a linear dependency of the reaction rate on the CAN concentration. Accordingly, an oxidation process from Ru^{IV}−OH to Ru^{V}=O has to be involved in the rate-determining step (rds) of the oxygen evolution as it has been previously reported for the trinuclear macrocycle **MC3** by our group.[37]

To further explore the mechanism of catalytic water oxidation with **dimer 1**, kinetic isotope effect (KIE) of **dimer 1** and monomeric complex [Ru(bda)(pic)$_2$] were studied in a comparative manner by focusing on possible involvement of an element-hydrogen bond breaking in the RDS of the catalytic process.[131, 170, 172, 275] The WNA pathway is characterized by a primary kinetic isotope effect when a direct O−H/D bond cleavage takes place and shows a difference in the reaction rates of at least two (KIE ≥ 2).[131, 276] If the RDS involves a dimerization of two Ru=O units, the reaction shows a secondary isotope effect (KIE = 0.7−1.5).[276] Therefore, catalytic water oxidation experiments for both catalysts were conducted in aqueous mixtures (H$_2$O and D$_2$O, pH 1, triflic acid) with 40% acetonitrile in the presence of CAN as sacrificial oxidant and a Clark electrode for O$_2$ detection (Figures A8.1.18 and A8.1.19). The reaction rates in H$_2$O (k(H$_2$O)) and D$_2$O (k(D$_2$O)) for each catalyst were determined from the slope of a linear regression of the initial rates vs. the catalyst amount at different concentrations. For **dimer 1**, a KIE value of 1.8 was obtained due to a significantly reduced reaction rate in heavy water (k(D$_2$O) = 2.4 s^{-1}) compared to normal water (k(H$_2$O) = 4.2 s^{-1}). In contrast, the mononuclear complex [Ru(bda)(pic)$_2$] displayed an expected second order dependency on the catalyst amount (Figure A8.1.19b). The reaction rates were determined by plotting the initial

rates vs. the square of catalyst amount for linearization of the rate dependency (Figure A8.1.19c). The linear regression revealed a secondary isotope effect with a KIE of 0.9 for [Ru(bda)(pic)$_2$], providing evidence for no proton involvement in the RDS of oxygen evolution. The higher KIE value for **dimer 1** is strongly supportive for a primary isotope effect and a mechanistic change from the mostly observed I2M mechanism for Ru(bda) complexes[128] to the WNA mechanism involving a nucleophilic attack of water. As previously shown for a series of Ru(bda) macrocycles of different sizes,[38] small structural changes in the ring size can lead to significant changes of the proton coupling and thus in the KIE.[277] The slightly lower KIE value of 1.8 for **dimer 1** can be taken as an indication for a not fully concerted proton-coupled oxidation of Ru^{IV}−OH to Ru^{V}=O. Thus, we propose a stepwise oxidation process characterized by an initial oxidation to Ru^{V}−OH followed by subsequent deprotonation to Ru^{V}=O.[278-280]

3.2.3 Photocatalytic water oxidation under neutral conditions

To assess the suitability of the catalyst **dimer 1** for potential application in an artificial photosynthetic cell,[122] **dimer 1** was investigated under the conditions of photocatalytic water oxidation with the milder oxidant [Ru(bpy)$_3$]$^{3+}$, which is photogenerated *in situ* from the common photosensitizer (PS) [Ru(bpy)$_3$Cl$_2$], in the presence of Na$_2$S$_2$O$_8$ as sacrificial electron acceptor (Figures 25 and 26).[135, 146, 150] For the purpose of comparison, mononuclear [Ru(bda)(pic)$_2$] was also investigated under identical conditions. Irradiation was performed with a xenon lamp (I = 100 mW cm^{-2}, see Figure A8.1.20) and a Clark electrode was used to detect the generated oxygen. Photocatalytic water oxidation was studied in phosphate buffer at pH 7 containing
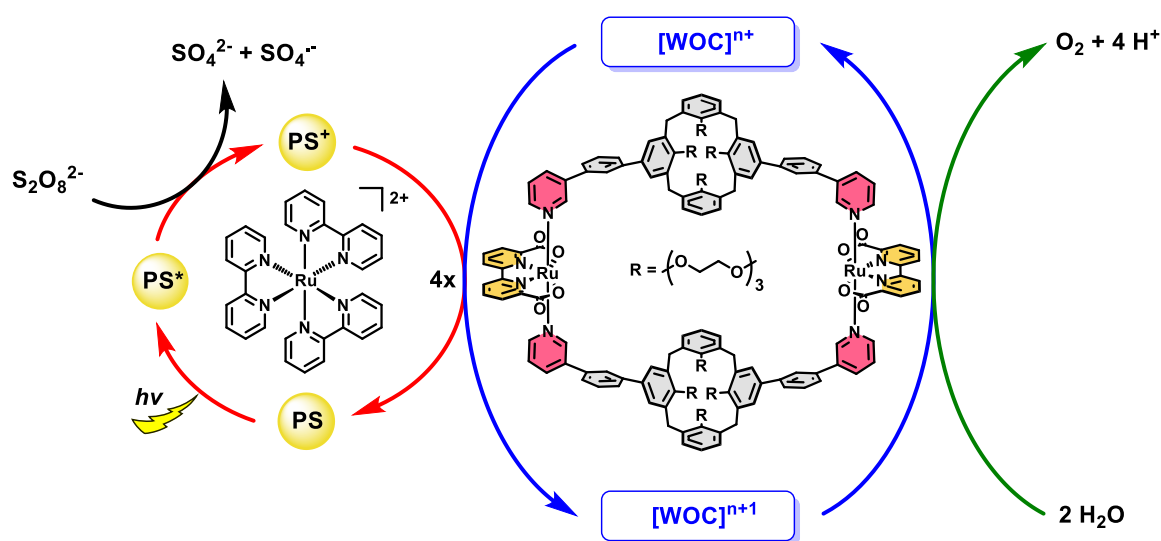
Figure 25. Schematic presentation of the photocatalytic water oxidation cycle in a three-component system containing Na$_2$S$_2$O$_8$ as sacrificial electron acceptor, [Ru(bpy)$_3$]$^{2+}$ as photosensitizer (PS) and **dimer 1** as WOC.

40% acetonitrile in accordance with the experiments performed for chemical water oxidation. The concentration of PS (c([Ru(bpy)$_3$Cl$_2$]) = 1.5 mM) and electron acceptor (c(Na$_2$S$_2$O$_8$) = 37 mM) were kept constant and only the concentration of the catalyst was varied for each experiment (for experimental details see *Chapter 8.1*). As depicted in Figure 26a, the oxygen evolution curves of **dimer 1** showed no gas evolution in the dark but after light exposure a linear part in each curve is observed, where the initial rates of catalysis between 55−70 s were determined. The initial rates are hereby limited by the oxidized photosensitizer (PS$^+$),[153] together with the general complexity of the water oxidation reaction under photocatalytic conditions.[146, 281, 282] The linear regression in the plot of the initial rates vs. the amount of catalyst revealed a first-order reaction rate for **dimer 1** (Figure 26b). The catalytic activity of the latter could be observed down to a nanomolar concentration regime (12−200 nM), where a remarkably high averaged TOF value of 15.5 ± 0.3 s^{-1} (~7.5 s^{-1} per Ru unit) and a TON of 460 ± 20 (~230 per Ru unit) was obtained. Further, the influence of acetonitrile on the overall catalysis was investigated by repeating the experiment for **dimer 1** in 1:1 CH$_3$CN/H$_2$O (pH 7) mixtures (Figure 26b and Figure A8.1.21) resulting in a decreased catalytic activity (TOF = 13.3 ± 0.3 s^{-1}, (~6.5 s^{-1} per Ru unit) and a slightly increased stability (TON = 540 ± 20; (~270 per Ru unit)). These findings are in accordance with the previously reported competitive binding ability of acetonitrile, leading to a decrease in catalytic activity.[153, 258] A catalytic sample of the dinuclear complex **dimer 1** was studied before and after catalysis by UV/Vis absorption spectroscopy (Figure A8.1.24), which showed a considerable degradation of the photosensitizer at the end of catalysis. For the mononuclear complex [Ru(bda)(pic)$_2$], a higher concentration regime (2.5−20 µM) had to be applied as no catalytic activities could be observed at lower concentrations in the nM regime. Even at higher concentration range (2.5−20 µM), a very low catalytic performance (TOF = 0.1−0.45 s^{-1}, TON = 30 ± 10) was observed for the mononuclear reference (Figure A8.1.22).

These studies reveal an outstanding performance of our novel dinuclear cyclic WOC **dimer 1** in photocatalytic water oxidation with a TOF of 15.5 s^{-1} which is indeed so far unprecedented for dinuclear homogenous ruthenium WOCs and even superior to our previously reported highly active trinuclear macrocyclic Ru catalysts[37, 40] (see Table A8.1.3 for comparison of TOF and TON values of selected mono-, di- and trinuclear Ru WOCs). Usually, significantly higher catalytic values are observed for chemical water oxidation compared with photocatalytic oxidation due to the lower stability and general complexity of the photocatalytic system,[146, 282] which is explained based on the limited stability of the photosensitizer.[148, 281, 283] In the case of **dimer 1**, however, the difference between the chemical and photocatalytic activities (TOF$_{Chem}$ = 19 ± 0.5 s^{-1}, TON$_{Chem}$ = 760 ± 60; TOF$_{Photo}$ = 15.5 ± 0.3 s^{-1}, TON$_{Photo}$ = 460 ± 20) are comparably small. We attribute this to the higher stability of the dinuclear complex under neutral (photocatalysis) compared to the strong acidic (chemical oxidation) conditions, as it is

evidenced by post-catalytic mass spectrometry studies (Figure A8.1.15). Further, the photocatalytic activity of **dimer 1** could be improved in aqueous mixtures with lower MeCN content (TOF$_{40\% MeCN}$ = 15.5 ± 0.3 s^{-1}; TOF$_{50\% MeCN}$ = 13.3 ± 0.3 s^{-1}) as the ability of acetonitrile to competitively bind to the seventh coordination site of the ruthenium center is reduced at higher co-solvent content.[217, 225] These results are also in line with a reduced solvation of the photosensitizer at lower amounts of organic co-solvent in CH$_3$CN/H$_2$O mixtures, which leads to a more efficient generation of photooxidant PS$^+$ by quenching with sodium persulfate (Na$_2$S$_2$O$_8$, see Figure 25).[284]
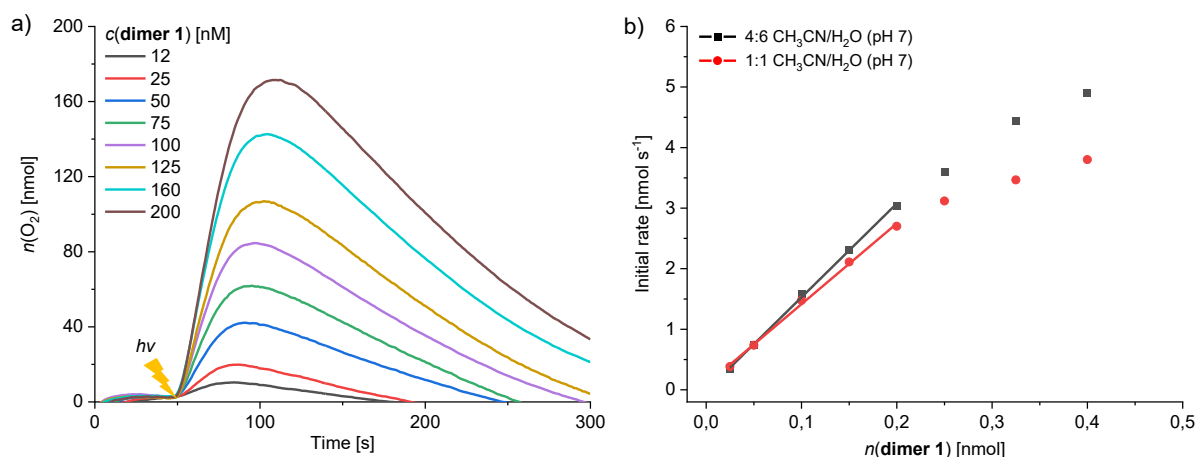
Figure 26. a) Concentration-dependent oxygen evolution curves of **dimer 1** in CH$_3$CN/H$_2$O (4:6; pH 7, phosphate buffer), c(PS) = 1.5 mM, c(Na$_2$S$_2$O$_8$) = 37 mM. The lighting symbol indicates the start of sample irradiation at t = 50 s. b) Initial rates for **dimer 1** at different acetonitrile contents with linear regression for the determination of averaged TOFs.

3.3 Conclusions

Here we have applied one of the most versatile and easily accessible supramolecular hosts, that is, calix[4]arene, as a scaffold for the assembly of a cyclic dinuclear Ru(bda) complex **dimer 1** for catalytic water oxidation. Due to the easy functionalization of the calix[4]arenes with four tri(ethylene glyol) chains at the narrow rim, sufficient water solubility is provided for catalytic water oxidation in the nanomolar concentration regime. Our detailed studies revealed a linear dependency of the reaction rate in catalytic water oxidation with the dinuclear Ru(bda) complex on the catalyst concentration. This was further supported by kinetic experiments and kinetic isotope effect studies, confirming that the catalytic rate depends linearly on the catalyst and oxidant concentration in chemical oxidation. Accordingly, the newly synthesized cyclic dinuclear complex **dimer 1** demonstrates another example of the influence of the second coordination sphere on the catalytic mechanism, where the cyclic ligand environment for Ru(bda) complexes leads to a mechanistic change from bimolecular I2M mechanism to

unimolecular WNA pathway.[34, 35, 37, 128, 210] The calix[4]arene-based cyclic WOC allowed the investigation of catalytic activity under highly diluted conditions;[37] this is highly beneficial for photocatalytic water oxidation in which **dimer 1** reached an unprecedently high catalytic activity for Ru(bda) WOCs with a TOF of 15.5 ± 0.3 s^{-1}.

Chapter 4

Enzyme-like Water Preorganization in a Synthetic Molecular Cleft for Homogenous Water Oxidation Catalysis
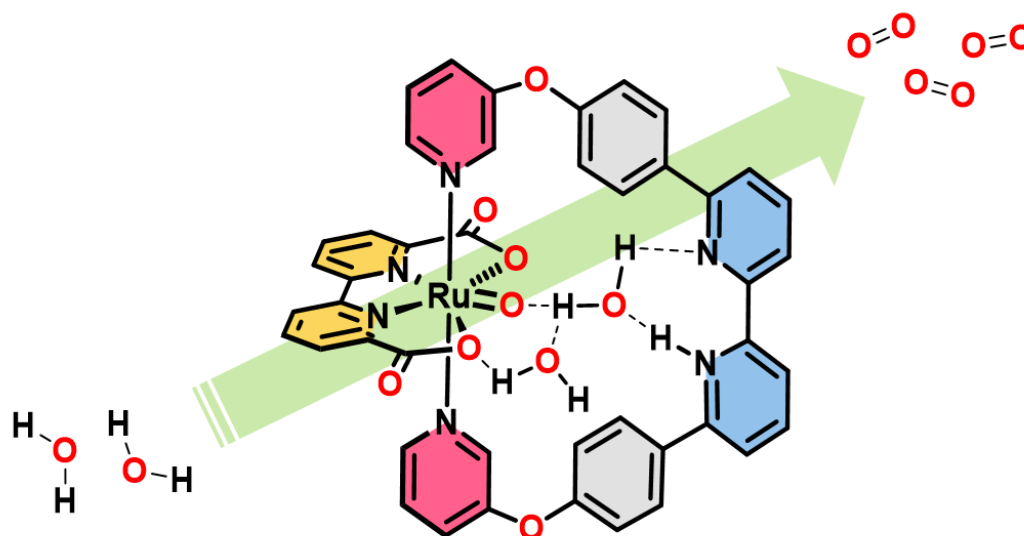
This chapter and the corresponding supporting information (*Chapter 8.2*) were published in:

N. Noll, A.-M. Krause, F. Beuerle, F. Würthner, *Nat. Catal.* **2022,** *5*, 867−877.

(https://www.nature.com/articles/s41929-022-00843-x).

Adapted or reprinted with permission from reference[285]. Copyright 2022, The Author(s), under exclusive licence to Springer Nature Limited.

Abstract: Inspired by the proficiency of natural enzymes, mimicking of nanoenvironments for precise substrate preorganization is a promising strategy in catalyst design. However, artificial examples of enzyme-like activation of H_2O molecules for the challenging oxidative water splitting reaction are hardly explored. Here, we introduce a mononuclear Ru(bda) complex (**M1**, bda: 2,2'-bipyridine-6,6'-dicarboxylate) equipped with a bipyridine-functionalized ligand to preorganize H_2O molecules in front of the metal center as in enzymatic clefts. The confined pocket of **M1** accelerates chemically driven water oxidation at pH 1 by facilitating a water nucleophilic attack pathway with a remarkable turnover frequency of 140 s^{-1} that is comparable

to the oxygen-evolving complex of photosystem II. Single crystal X-ray analysis of **M1** under catalytic conditions allowed the observation of a seventh H_2O ligand directly coordinated to a Ru^{III} center. Via a well-defined hydrogen-bonding network, another H_2O substrate is preorganized for the crucial O−O bond formation by nucleophilic attack.

4.1 Introduction

Enzymes as highly efficient natural catalysts have long inspired the field of supramolecular chemistry.[286, 287] Initiated by Emil Fischer's famous lock-and-key hypothesis in 1894,[288] the importance of a sophisticated design for catalytic pockets in artificial enzyme mimics was manifested early on.[237, 238, 289] At the active sites of hydrogenases,[45, 290] the cytochrome *c* oxidases[44, 67] or the oxygen-evolving complex of photosystem II (OEC-PSII),[27, 31, 95] the surrounding protein domains create a well-defined nanoenvironment, which facilitates substrate preorganization by applying weak non-covalent interactions such as hydrogen bonding or electrostatic interactions.[30] X-ray crystal structure analysis revealed extensive hydrogen-bonding water networks surrounding the active sites of these metalloproteins, which serve as channels for water diffusion and proton transfer to the surrounding bulk solvent.[27, 31, 44, 45, 67, 290] In OEC-PSII, the kinetically demanding four-electron oxidation of H_2O into molecular O_2 occurs on the millisecond timescale.[27, 31, 95] As a key component of PSII, a particular tyrosine-histidine pair acts as proton-coupled redox mediator between the OEC and the nearby light-harvesting chromophore assemblies and alters the hydrogen-bonding environment around the active site.[94]

Inspired by the natural archetype, numerous synthetic mimics of the natural OEC have been reported previously, but typically very low or no catalytic activity and high overpotentials are obtained as such synthetic clusters lack the protein environment.[32, 33] Consequently, there is a continuing need for molecular water oxidation catalysts (WOCs) working at low overpotential for sustainable fuel production.[108-110] After the introduction of the 'blue dimer' by Meyer and co-workers,[166] ruthenium-based catalysts, especially the Ru(bda) system (bda: 2,2'-bipyridine-6,6'-dicarboxylate),[128, 194] have been established as homogenous catalysts with activities comparable to the natural OEC.[37, 212] The performance of these artificial WOCs strongly depends on the mechanism for O−O bond formation, where two general pathways are distinguished: water nucleophilic attack (WNA) and interaction of two metal-oxyl species (I2M).[125] As a paramount factor to distinguish between these two pathways, second coordination sphere effects by a well-defined ligand framework have been widely applied.[34, 35] As an appealing strategy, the activation barrier for the WNA mechanism can be lowered by the presence of an additional base, which acts as a proton-accepting unit and leads to preorganization of incoming H_2O molecules. Intuitively, any intramolecular

arrangement should improve catalytic performance compared to the addition of an external base.[226, 227, 229, 291] Therefore, the molecular design of confined environments provides the next step towards synthetic enzyme mimics. For example, recent examples showcased a significant rate enhancement in the I2M pathway after inter-catalyst coupling by supramolecular encapsulation of Ru WOCs either within mesoporous silica[240] or a self-assembled Pt nanosphere.[241] Additionally, this concept was also applied to proton reduction catalysts encapsulated in supramolecular cages[292] or metallopolymers[293] which resulted in improved catalytic performance and lower overpotentials. In earlier work, we presented multinuclear macrocyclic assemblies, which showed high catalytic performance via the WNA pathway by benefiting from cooperative effects between the catalytic centers.[34, 37]

In classical transition metal catalysis, the supporting ligands act as spectators and only indirectly modulate catalysis by electronic and steric effects. To closer mimic biological systems, substrate preorganization to the catalytically active metal site by non-covalent interactions (hydrogen bonds, electrostatic interactions and so on) with a remote recognition unit was applied in different types of transition metal-catalyzed reactions such as hydrogenation,[294, 295] hydroformylation,[296, 297] C−H activation[298-301] and C−H oxidation reactions.[302, 303] For an enzyme-inspired approach, the formation of a confined environment around the active center allows for a more precise positioning of a recognition site for selective substrate preorganization. Until now, such a conceptual design strategy has only been reported for selected examples focusing on hydroformylation[304] and proton-reduction catalysis[292] but not for water oxidation catalysis.

Here, we introduce a molecular design strategy that incorporates one single catalytic Ru(bda) subunit into a well-defined macrocyclic nanostructure. Accordingly, we present the bioinspired cyclic mononuclear Ru(bda) catalyst **M1**, which is equipped with a proximal base in its ligand framework to facilitate preorganization of substrate water molecules via non-covalent interactions. As a reference, we also synthesized the unsubstituted complex **M2**. Detailed investigations by pH-dependent NMR experiments and H/D kinetic isotope effect (KIE) studies revealed a severe reliance of the mechanistic pathway and catalytic performance of **M1** on the relative spatial orientation of the axial ligand sphere. Under acidic conditions, **M1** reached a turnover frequency (TOF) of 140 s^{-1} per Ru unit via the WNA pathway. Single crystal X-ray analysis of **M1** at a predominant Ru^{III} oxidation state gave clear evidence for the formation of a confined space around the catalytic center. This allowed the observation of a seventh H_2O ligand directly coordinated to a Ru^{III} center after acidic catalytic water oxidation. The preorganization of additional hydrogen-bonded H_2O molecules in proximity prepares the system for the crucial water nucleophilic attack and could be additionally confirmed by Fourier transform infrared (FTIR) spectroscopy experiments.

4.2 Results and Discussion

4.2.1 Synthesis

Mononuclear Ru(bda) complexes **M1** and **M2**, as synthetic enzyme mimetics (Figure 27a,b), were synthesized in a two-step procedure (Figure 27c). The ditopic ligands **L1** and **L2** were obtained via twofold Suzuki-Miyaura reaction between the axial pyridine ligand **44** and central bipyridine (**BP1**) or biphenyl (**BP2**) units, respectively (for details see *Chapter 8.2*). Subsequentially, twofold ligand exchange at [Ru(bda)(dmso)$_2$] with the respective bidentate ligand gave **M1** or **M2** in 35−49% yield besides higher macrocycles as side products (for details see *Chapter 8.2*). The mononuclear assemblies were fully characterized by NMR spectroscopy, mass spectrometry, elemental analysis, and X-ray crystallography. The UV-Vis absorption and redox properties comply with previously reported Ru complexes (Table A8.2.1 and Figures A8.2.1−A8.2.3).[37]
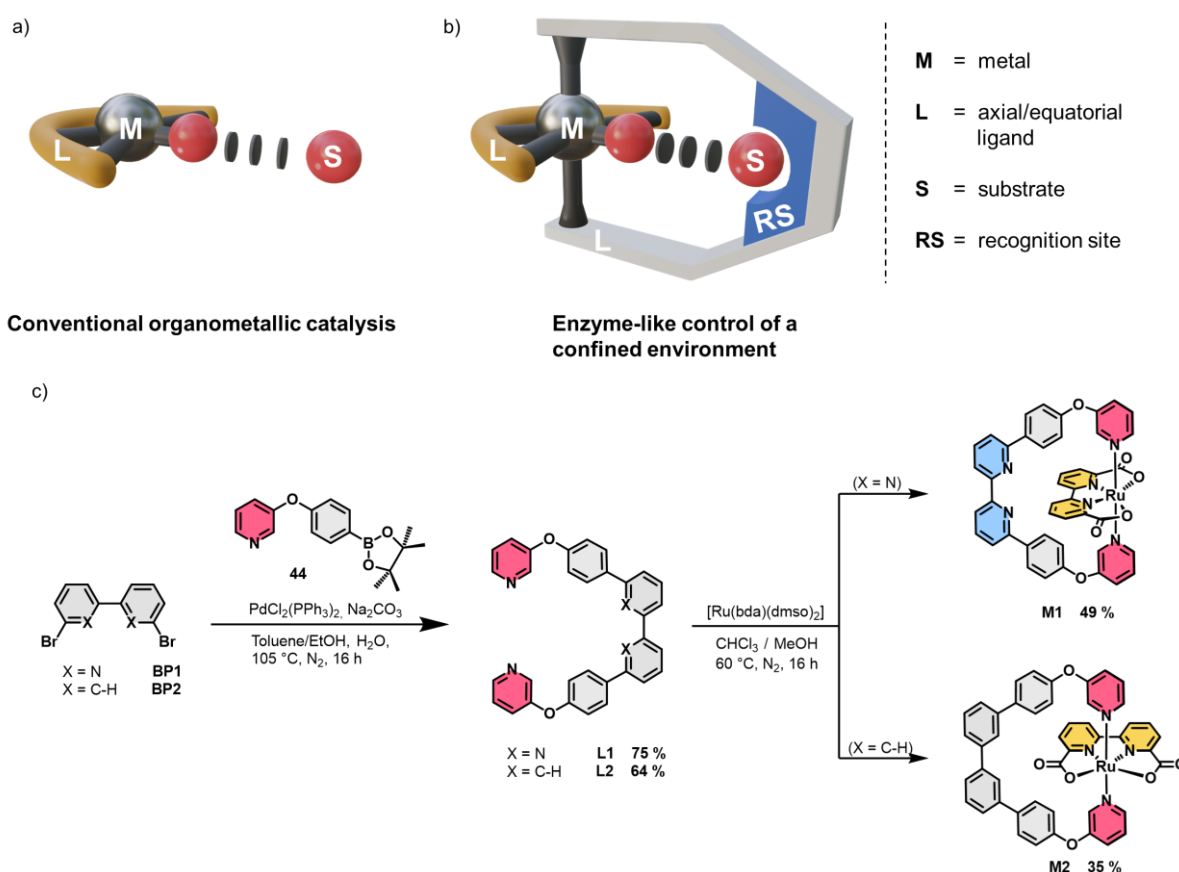
Figure 27. Enzyme-mimetic approach and synthesis of mononuclear Ru(bda) complexes **M1** and **M2**. a) Conventional organometallic catalysis. b) Enzyme-like control of a confined environment. Non-covalent interactions between the metal centers and the substrates are indicated by black discs. c) Synthesis of mononuclear Ru(bda) complexes **M1** and **M2**. Boronic ester **44** was prepared in two steps starting from commercially available 4-(pyridine-3-yloxy) aniline (see *Chapter 8.2*).

4.2.2 Catalytic water oxidation

Initially, we tested these Ru(bda) complexes in chemical water oxidation catalysis using cerium ammonium nitrate (CAN) as sacrificial oxidant[135] in an acidic aqueous solution (CH_3CN/H_2O 4:6, pH 1, triflic acid) (Figure 28a, Figures A8.2.6 and A8.2.7 and for experimental details see Chemical water oxidation in *Chapter 8.2*). The evolved O_2 was monitored by attached pressure sensors in combination with end-point analysis of the gas composition by gas chromatography (GC) of the headspace, which verified O_2 as the only gaseous product generated during catalysis (Figures A8.2.8 and A8.2.9). For the bipyridine-containing **M1**, the observed linear relationship between the amount of evolved O_2 and the concentration of the catalyst is indicative for the unimolecular WNA mechanism as previously reported for multinuclear macrocycles from our group.[37] Using linear regression, an exceptionally high average TOF value of 140 ± 5 s^{-1} was obtained. In stark contrast, for the unfunctionalized reference **M2**, the initial rates of O_2 evolution were of second order with respect to the catalyst concentration, which is in line with the bimolecular I2M mechanism.[128] Apparently, this switch in the reaction mechanism is accompanied by a significantly lower catalytic performance for **M2** as shown by lower TOF values in the range of 18–54 s^{-1} in the measured concentration range. In addition, these activities also correlate with the obtained turnover number (TON) values as **M1** (TON = 950 ± 50) exhibits an almost two times higher turnover compared to the unfunctionalized reference **M2** (TON = 500 ± 50). Post-catalytic analysis of the reaction mixtures by matrix-assisted laser desorption/ionization time-of-flight (MALDI TOF) mass spectrometry indicated axial ligand dissociation as main degradation pathway (Figures A8.2.10 and A8.2.11). In order to verify if this mechanistic change is pH-dependent, both complexes were also investigated at neutral conditions. Since the sacrificial oxidant CAN is only stable at low pH,[135] we applied photocatalytic water oxidation in 50 mM phosphate buffered CH_3CN/H_2O 4:6 mixtures at pH 7 (Figure 28b, Figures A8.2.12 and A8.2.13 and for experimental details see Photocatalytic water oxidation in *Chapter 8.2*). Surprisingly, both complexes showed a second-order dependency of the initial O_2 evolution rate on the WOC concentration. Apparently, the reaction kinetics for base-containing **M1** change when going from acidic to neutral conditions. Moreover, the performance is strongly reduced in comparison to reference **M2** as significantly higher concentrations are needed for substantial O_2 generation (c(**M1**) = 5–45 µM and c(**M2**) = 0.5–3 µM, Figures A8.2.14 and A8.2.15) and a more than one-order-of-magnitude lower catalytic activity is observed with TOFs of 0.4–3.2 s^{-1} and 0.05–0.1 s^{-1} for **M2** and **M1**, respectively. The generally lower TOFs for photocatalytic compared to chemical conditions are most likely attributed to the limited stability of the sacrificial oxidant $[Ru(bpy)_3]^{3+}$ under the applied conditions.[135, 146] MALDI TOF mass spectrometry after photocatalysis with either **M1** and **M2** confirmed that the Ru(bda) catalysts were still present, and that photosensitizer

degradation is the main deactivation pathway (Figures A8.2.16 and A8.2.17). The direct correlation between the measured TON (TON(**M1**) = 10 ± 1 and TON(**M2**) = 105 ± 10) and TOF values indicates a much higher stability of reference **M2** under the applied conditions.
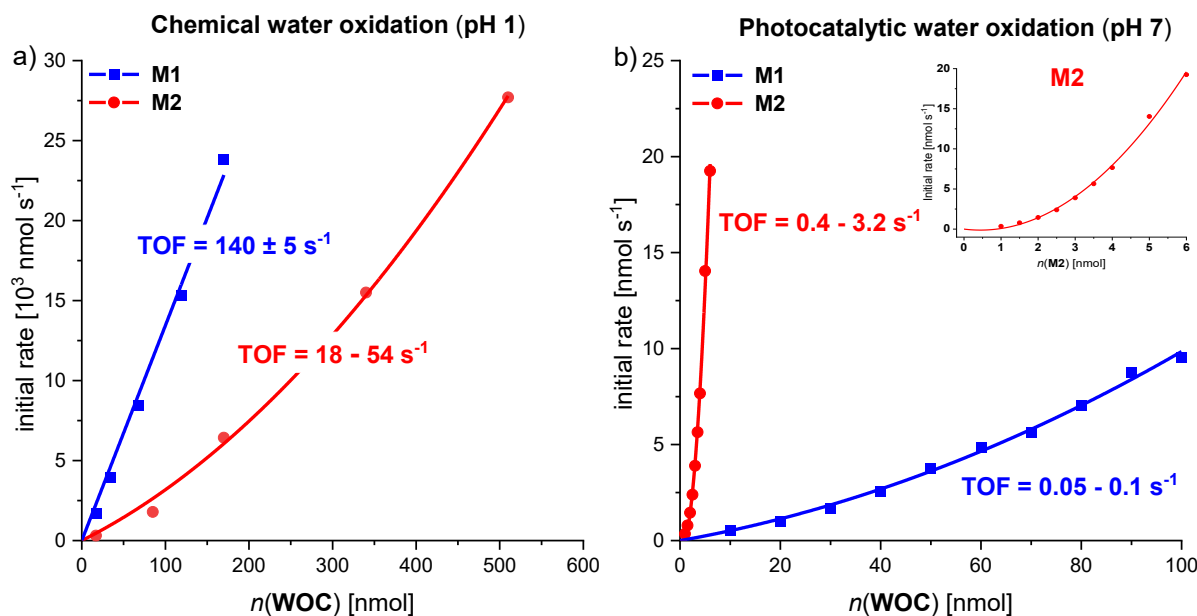
Figure 28. Chemical and photocatalytic water oxidation catalysis with **M1** and **M2**. a) Chemical water oxidation catalysis with **M1** and **M2**: Plots of initial rates of O_2 evolution against the WOC concentration with corresponding linear (**M1**, blue) and quadratic (**M2**, red) regression fits (average TOF for **M1** was determined by linear regression, whereas the range of individual TOF values is given for **M2**). Individual reaction rates were obtained by a linear fit of O_2 evolution curves for the first 2 s of catalysis for **M1** and **M2**. Experimental conditions: 4:6 CH_3CN/H_2O mixture using CAN as sacrificial oxidant (pH 1, triflic acid, c(CAN) = 0.6 M). b) Photocatalytic water oxidation catalysis with **M1** and **M2**: Plot of initial rates (obtained by linear fit of O_2 evolution curve between 50 and 60 s) of O_2 evolution against the WOC concentration and quadratic fit for second-order kinetics. The observed second-order dependency of **M2** is shown as inset. O_2 evolution experiments were performed at varying WOC concentrations in CH_3CN/H_2O 4:6 (pH 7, 50 mM phosphate buffer, c(PS) = 1.5 M, c(Na$_2$S$_2$O$_8$) = 37 mM; (PS = photosensitizer)).

For further insight, kinetic isotope effects (KIE) for water oxidation with **M1** and **M2** were studied under both chemical (pH 1) and photocatalytic (pH 7) conditions (for experimental details see Kinetic isotope experiments in *Chapter 8.2*). For chemical water oxidation, a linear dependency and a KIE of 1.6 was observed for **M1**, indicating a WNA mechanism (Figure A8.2.18). By contrast, a KIE of 1.0 with a second-order dependency indicated the bimolecular I2M mechanism for reference **M2** (Figure A8.2.19). Subsequently, KIEs for both **M1** and **M2** were investigated under photocatalytic conditions at pH 7 (Figures A8.2.20 and A8.2.21). In accordance with the previous results, both **M1** and **M2** showed the expected quadratic

dependency on the catalyst concentration and after linearization a KIE value of around 1.2 was obtained in both cases, with similar reaction rates $k(H_2O)$ and $k(D_2O)$. In summary, these results clearly indicate different reactions kinetics and a mechanistic switch for bipyridine-containing catalyst **M1** at either acidic or neutral conditions, which might be induced by different conformations for the bridging macrocycle.

4.2.3 pH-dependent NMR measurements

To probe for pH-dependent conformational changes in both **M1** and **M2** at the initial Ru^{II} state, ^{1}H NMR spectra were measured in aqueous 1:1 mixtures of D$_2$O (pD = 1.0 (0.1 M CF$_3$SO$_3$D) or pD = 7.0) and TFE-d$_3$ as a non-coordinating co-solvent for better solubility (Figure 29). All signals were assigned to the individual protons based on 1D and 2D NMR spectroscopy (Figures A8.2.22–A8.2.25). Both complexes show the anticipated planar symmetry as indicated by only one set of signals for all chemically non-equivalent protons. For **M1**, significant differences in the chemical shifts depending on the pD value were observed (Figures 29a,b). This was especially evident for the *ortho* protons of the axial pyridines. While the blue-labelled *ortho* proton resonates at 8.19 ppm at pD 1.0, this signal is significantly upfield shifted to 6.39 ppm at pD 7.0. Conversely, reverse shifting is observed for the red-labelled *ortho* proton next to the bridging ligand. Whereas the upfield-shifted protons are magnetically shielded due to proximity of the equatorial bda ligands,[198] the pronounced downfield shifts of the opposite *ortho* protons indicate positioning above the open Ru site. At pD 7.0, severe signal broadening was observed for both *ortho* protons. This was overcome by heating the sample to 333 K (Figure A8.2.24) and is attributed to the reduced structural flexibility of the ligand due to [C-H⋯N] hydrogen bonding interactions with the bda backbone. Further evidence for such stabilizing interactions is given by the pronounced downfield shift of the green-labelled bda proton compared to pD 1.0. By contrast, reference **M2** showed almost pH-independent chemical shifts for all aromatic protons. Again, a significant difference in the chemical shifts of the *ortho* protons of the axial pyridines was observed. This indicates a different chemical environment due to a slight rotation of the axial pyridine units. While the red-labelled proton (8.56 ppm) is oriented more towards the open site of the catalytic center and is thus strongly deshielded, the blue-labelled proton (5.83 ppm) is again affected by the magnetic shielding of the nearby equatorial bda ligand (Figures 29c,d). Further evidence for this conformation is provided by a nuclear Overhauser effect (NOE) cross signal (Figure A8.2.25d) between the bda unit (yellow proton) and the axial biphenyl unit (purple proton). However, the three sharp signals for the bda ligand without any splitting at room temperature suggests fast switching of the axial ligand **L2** between the two symmetrical side-on conformations on the NMR time scale. Based on these data, we conclude that the conformation of **M1** is strongly

affected by the proximal base in the ligand backbone. At pD 7.0, the bda unit is fixed inside the macrocyclic cavity by weak [C-H···N] interactions between the bda backbone and the free bipyridine base. Protonation of the proximal base[235] at pD 1.0 induces a ligand rotation due to electrostatic repulsion and now confines the active site in the cyclic cavity. ^{1}H NMR titration experiments from pD 1.0 to pD 7.0 for **M1** indicated the deprotonation followed by rotation of the bipyridine-containing ligand **L1** in the range of pD 1.0 to 4.0 (Figure A8.2.26). Therefore, the active Ru center is only fully confined in the macrocyclic cavity under highly acidic conditions at pD 1.0. For reference **M2**, weak [C-H···O] hydrogen bonding interactions between the axial and equatorial ligand spheres lead to a lateral orientation of the macrocyclic ligand over the whole pH range.
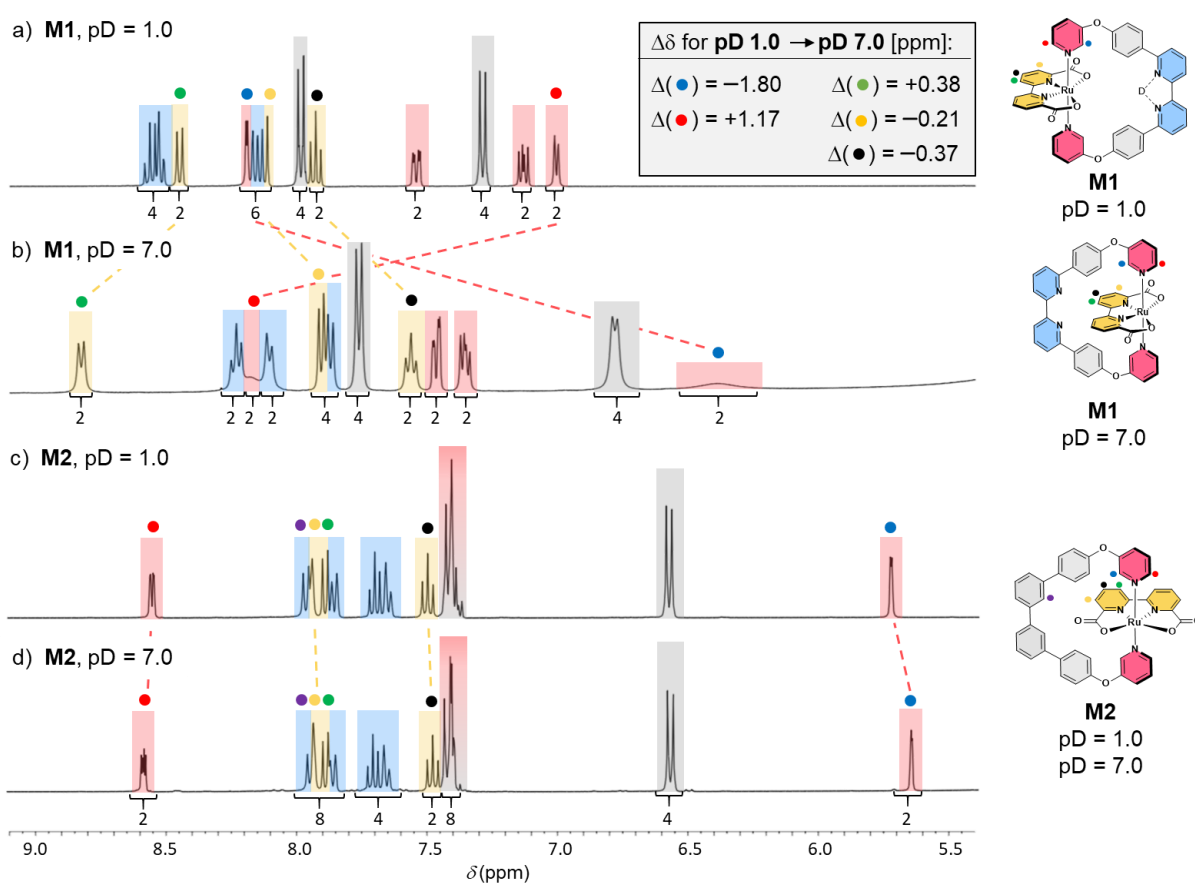
Figure 29. pD-dependent ^{1}H NMR experiments of **M1** and **M2**. (a−d) Aromatic region of the ^{1}H NMR spectra (1:1 TFE-d$_3$/D$_2$O, 400 MHz, ascorbic acid, room temperature) of complexes a) **M1** at pD = 1.0 (0.1 M CF$_3$SO$_3$D), b) **M1** at pD = 7.0, c) **M2** at pD = 1.0 (0.1 M CF$_3$SO$_3$D) and d) **M2** at pD = 7.0 with the proposed molecular structures of the respective complexes based on 2D NMR structural analysis shown on the right. Signals are colour coded in yellow (bda), red (axial pyridine), grey (biphenyl) or blue (bipyridine) as highlighted in the structures.

60

4.2.4 Single crystal X-ray analysis

To gain a deeper insight into these conformational features, we grew single crystals of both **M1** and **M2** in the initial Ru^{II} state at neutral conditions and even of **M1** after acidic catalytic water oxidation. The ORTEP representations for all three solid-state structures in Figure 30 (for crystallographic details see Single crystal X-ray analysis in *Chapter 8.2* and Tables A8.2.5 and A8.2.6) unequivocally confirm the cyclic nature of the mononuclear complexes **M1** and **M2**, but each features a different spatial orientation of the axial pyridine ligands. Remarkably, all three solid-state structures are in excellent agreement with the proposed predominant conformations derived from ^{1}H-NMR measurements for the macrocycles in solution. Under neutral conditions, both **M1** and **M2** exhibit a six-coordinated Ru atom with a distorted octahedral coordination geometry and two slightly different conformers are present in the unit cell of **M1**. The obtuse O−Ru−O angles of 121.8(1)°/122.7(1)° and 123.1(9)° for **M1** and **M2**, respectively, are comparable to the previously reported acyclic mononuclear complex [Ru(bda)(pic)$_2$] (pic = 4-picoline) (122.9(9)°).[194] Structurally, the bridging macrocycle of **M1** is fixed over the bda backbone by weak [C−H···N] hydrogen bonding interactions[305] between the axial and equatorial ligand framework (Figure 30b, 2.58(7) and 2.80(2) Å; Figure A8.2.28, 2.65(2) and 2.99(7) Å). This rigid conformation with torsional angles of 79.5° or 82.8° (55.8° and 82.5° for the second conformer in the unit cell) for the pyridine units relative to the open coordination site of the Ru center (Figures A8.2.27a,b) induces a slight deviation from an ideal linear orientation with a decreased N$_{ax}$−Ru−N$_{ax}$ bond angle of 171.4(2)°/173.2(1)°. By contrast, reference **M2** shows a substantially different conformation for the bridging ligand and a more linear orientation of the axial pyridine units with a larger N$_{ax}$−Ru−N$_{ax}$ bond angle of 175.5(4)°. Weak [C−H···O] hydrogen bonding interactions between the biphenyl backbone and one
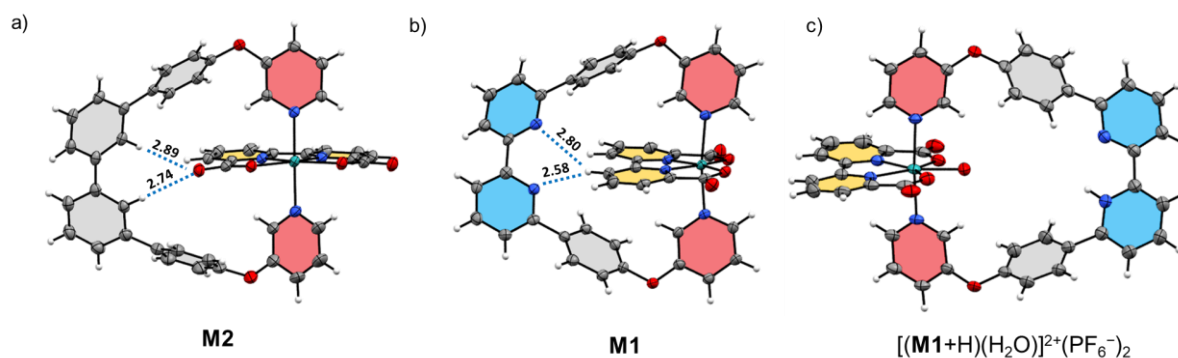
Figure 30. Single-crystal X-ray structures of **M1**, **M2** and [(**M1**+H)(H$_2$O)]$^{2+}$(PF$_6$$^-$)$_2$. a) **M2** ([Ru^{II}(bda)(**L2**)]), b) **M1** ([Ru^{II}(bda)(**L1**)]) and c) **M1** after acidic catalytic water oxidation ([Ru^{III}(bda)(**L1**+H)(H$_2$O)]$^{2+}$(PF$_6$$^-$)$_2$). For **M1**, only one of the two macocyclic complexes in the unit cell is shown. Organic solvent molecules and PF$_6$$^-$ counterions are omitted for clarity. ORTEP diagram with thermal ellipsoids set at 50% probability. C, grey; H, white; O, red; N, purple; Ru, turquoise.

carboxylate of the equatorial bda ligand (Figure 30a, 2.74(3) and 2.89(9) Å)[305] induce a lateral orientation of the macrocyclic ligand. This results in smaller torsional twist of the axial pyridine units relative to the open coordination site of the Ru center with 10.0° and 37.9°, respectively (Figure A8.2.27c and Table A8.2.4).

Searching for a structural model for **M1** after acidic catalytic water oxidation, we attempted to isolate catalytic intermediates directly from the reaction mixture after several catalytic turnovers by precipitation with NH_4PF_6. To our delight, orange needle-like single crystals suitable for X-ray analysis could be grown at room temperature during the precipitation process. To begin with, the Ru oxidation state of the isolated crystals was investigated by means of high resolution mass spectrometry (HRMS) measurements (Figure A8.2.31). Two species were observed by electrospray ionization time-of-flight (ESI-TOF) experiments and the major component was assigned to the $[Ru^{III}(bda)(\mathbf{L1})]^+(PF_6^-)$ intermediate. By contrast, the *m/z* ratio for the second signal with ~10% relative intensity fits exactly to $[Ru^{IV}(bda)(\mathbf{L1})(OH)]^+(PF_6^-)$, which is in accordance to the respective Ru^{IV} intermediate of complex **M1**. The assumed mixed Ru^{III}/Ru^{IV} oxidation state is further supported by a ^{1}H-NMR spectrum (Figure A8.2.32) that showed the expected equilibrium between one set of broad signals and another set of clearly resolved signals corresponding to the paramagnetic Ru^{III} and diamagnetic Ru^{IV} species, respectively (Figures A8.2.33 and A8.2.34).

Compared to the ^{1}H NMR spectra of **M1** at the initial Ru^{II} state, the higher oxidation of the Ru center induces a significant downfield shift of the equatorial bda signals.[194] Therefore, we conclude that these crystals of **M1** obtained after acidic catalytic water oxidation represent the catalytic resting state at the early transition from Ru^{III} to Ru^{IV} oxidation state. For the sake of clarity, we assume the Ru^{III} oxidation state for the following discussion, but it cannot be excluded that a minor fraction of the complexes is already oxidized to Ru^{IV} as evidenced by NMR and mass spectrometry measurements for the isolated crystals. An ORTEP representation for the crystal structure of $[Ru^{III}(bda)(\mathbf{L1}+H)(H_2O)]^{2+}(PF_6^-)_2$ is shown in Figure 30c. It is composed of a seven-coordinated $[Ru^{III}(bda)(\mathbf{L1}+H)]^{2+}$ cation with a directly seventh coordinated H_2O ligand in a highly distorted pentagonal bipyramidal configuration and a significant increase of the O−Ru−O bite angle from 121.8(1)° to 136.4(1)°. The additional H_2O ligand directly points towards the cavity defined by the macrocyclic bridge. To balance the overall charge, on average 2.4 PF_6^- counterions compensate for the positive charge at the Ru center, the protonated bipyridine moiety and the presumed partial protonation of a substrate H_2O molecule under the experimental acidic conditions.

Within the macrocyclic cavity, a well-defined hydrogen-bonding network preorganizes up to four H_2O molecules between the protonated bipyridine site, the Ru center and the carboxylates of the equatorial bda ligand (Figure 31). Intriguingly, three different occupancies give unprecedented insight into subtle equilibria at the coordination sphere for Ru(bda) at low
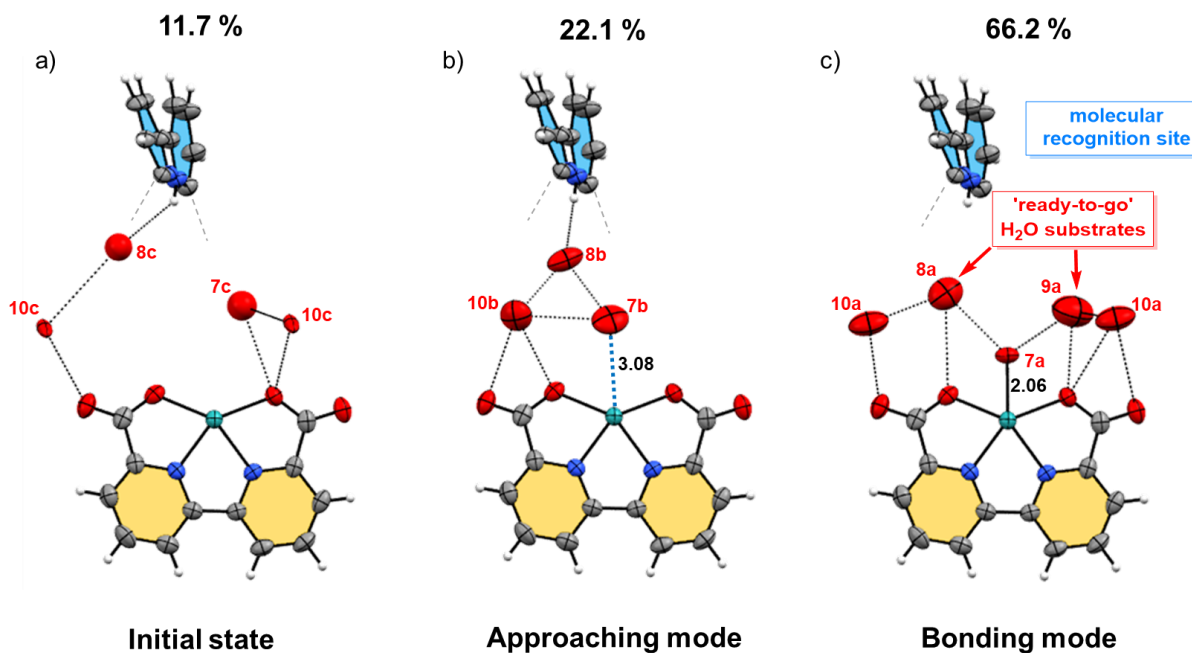
Figure 31. (a−c) Three different states for the hydrogen-bonding network of preorganized H_2O molecules inside the supramolecular cavity of $[(M1+H)(H_2O)]^{2+}(PF_6^-)_2$ obtained by single crystal X-ray analysis. The a) initial state (11.7% occupancy), b) approaching mode (22.1% occupancy) and c) bonding mode (66.2% occupancy) with additional H_2O substrates ready-to-go for O−O bond formation via nucleophilic attack.

oxidation states such as Ru^{II} and Ru^{III}.[128, 200] In a minor occupancy (11.7%, Figure 31a), three H_2O molecules are only loosely bound to the cavity. As a next step towards water oxidation, the first H_2O molecule approaches the Ru center (d_{Ru-O} = 3.08 Å)[198] while being stabilized by two other H_2O molecules between the bipyridinium unit und the bda ligand as directional binding sites (22.1%, Figure 31b). Finally, the main occupancy (66.2%, Figure 31c) shows direct structural evidence for a seventh coordinated H_2O ligand in a distorted $Ru^{III}(bda)−H_2O$ complex, which represents one of the key intermediates in the overall catalytic cycle. The short Ru−O distance of 2.06 Å indicates a strong affinity of the incoming H_2O ligand to the Ru center and is in perfect agreement with recent quantum-chemical calculations on $[Ru^{III}−OH_2]$ complexes in either approaching (d = 2.51 Å) or bonding mode (d = 2.07 Å).[196] This $Ru^{III}(bda)−H_2O$ complex is again further stabilized by several preorganized water molecules within the cavity and a second 'ready-to-go' H_2O molecule, thus highly facilitating the subsequent nucleophilic attack at the catalytically active $Ru^V=O$ oxidation state during the WNA pathway. Further experimental evidence for the proposed H_2O preorganization was obtained by an additional broad absorption at around 3620 cm^{-1} in the FTIR spectrum of isolated crystals $[(M1+H)(H_2O)]^{2+}(PF_6^-)_2$ (Figure A8.2.35). We attribute this band, which was not observed for similarly prepared samples of **M2**, to O−H stretching vibrations for H_2O molecules that strongly interact with the oxidized Ru center, as it was recently shown for a

hydrogen-evolving catalyst.[306] Intriguingly, a similar absorption was also observed for a solution of **M1** only at pH 1, but not under neutral conditions (Figure A8.2.36). We therefore conclude that a defined water network within the cavity of **M1** under acidic conditions is not only formed and conserved in crystalline solids but also persists in solution phase. Reinvestigation of isolated crystals [(**M1**+H)(H$_2$O)]$^{2+}$(PF$_6^-$)$_2$ in chemical water oxidation resulted in virtually the same activity as for freshly prepared **M1** (Figure A8.2.37), once again demonstrating the high stability and activity of **M1**. Apparently, the crystal structure shown in Figure 31 represents an active intermediate or resting state during the WOC cycle.

These results clearly highlight and justify our molecular design strategy towards a sophisticated second coordination sphere. Supramolecular preorganization of water molecules in a well-defined pocket around the catalytic Ru center resulted in high-performance molecular water oxidation catalysis and stabilized higher Ru^{III} or Ru^{IV} oxidation states. A Ru^{III} complex with a seventh coordinated H$_2$O ligand was isolated, which is typically rather short-lived due to violation of the 18-electron rule.[307] From this work, unprecedented structural insight into early catalytic intermediates for the WNA pathway was obtained.

4.2.5 Proposed mechanisms for water oxidation with M1 and M2

After compiling all analytical data, we propose the following mechanistic picture for water oxidation with cyclic mononuclear Ru complexes (Figure 32). For reference **M2** containing the unfunctionalized biphenyl unit, water oxidation always follows the bimolecular I2M mechanism independent of the applied experimental conditions. In accordance with the literature,[128, 194, 212] we propose a symmetrical bimolecular encounter complex for the rate-determining step of the I2M pathway for **M2**. The assumed lateral orientation of the macrocyclic ligand stabilizes this assembly by $\pi-\pi$ interactions and facilitates the O−O bond formation via radical combination of two Ru^V=O intermediates (Figure 32c). By contrast, the analogous bimolecular complex for **M1** at neutral conditions is sterically hindered by the presumed edge-to-edge orientation of the axial pyridine ligands, thus hampering the bimolecular approach, and significantly lowering the catalytic activity of **M1** in the I2M mechanism at pH 7 (Figure 32d). However, at pH 1, protonation of the proximal base in the ligand backbone induces a rotation of the macrocycle, which confines the active site in the cyclic cavity and impedes any bimolecular interactions at the active Ru site. This structural switch obviously endowes **M1** with an advantage compared to other mono- and dinuclear WOCs reported in the literature that also involve a mechanistic switch from bimolecular I2M to monomolecular WNA mechanism.[132-134] For instance, a series of pocket-shaped Ru(bda) complexes equipped with flexible, aliphatic bridging ligands and structural similarity to **M1** and **M2** operate via a quite inefficent WNA mechanism.[198, 246] However, for **M1** an X-ray structure for the predominant

Ru[III] resting state revealed that the well-defined macrocyclic pocket stabilizes the bound Ru[III]−OH$_2$ center and preorganizes additional water molecules in close proximity. Thus, the kinetic barrier for the nucleophilic attack of a second H$_2$O molecule is strongly reduced, resulting in a mechanistic switch to the unimolecular WNA mechanism for **M1** under acidic conditions (Figure 32b). Further evidence for this transition is provided by a change from secondary (1.2) to primary (1.6) KIE for **M1** under neutral and acidic conditions, respectively. Presumably, the enzyme-like nanoenvironment in the macrocyclic pocket for the active conformation of **M1** leads to a very product-like transition state. This explains the observed slightly lower KIE of 1.6 at pH 1.[276] Furthermore, this mechanistic switch and significantly enhanced catalytic performance of **M1** under acidic conditions are well reflected by a pronounced reduction of the overpotential from 440 to 290 mV when going from pH 7 to 1. In contrast, the overpotential for **M2** is much less affected by a change in pH (Table A8.2.2 and Figures A8.2.4 and A8.2.5).
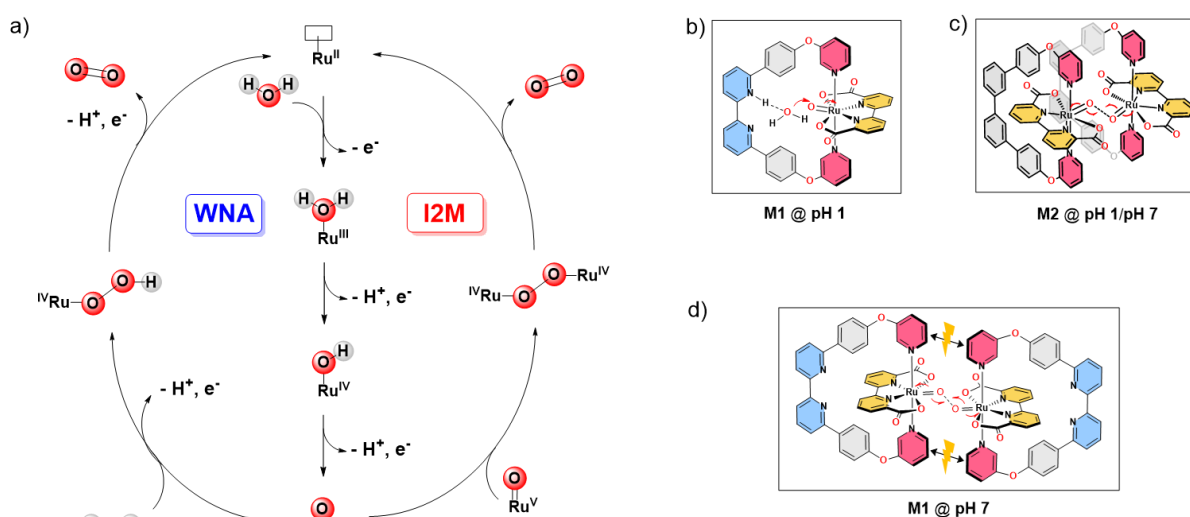
Figure 32. Mechanisms for water oxidation catalysis and proposed key intermediates for **M1** and **M2**. a) Mechanistic picture for the water nucleophilic attack (WNA) and bimolecular radical-radical coupling (I2M) pathways of catalytic water oxidation. (b−d) Graphical representation of the proposed key intermediates at the Ru[V] state of the water oxidation cycle for b) **M1** at pH 1, c) **M2** at pH 1 and 7 and d) **M1** at pH 7.

4.3 Conclusions

In an enzyme-mimetic approach, we have synthesized the Ru(bda) catalyst **M1** whose catalytic activity is controlled by a bipyridine ligand located opposite to the metal center in a macrocyclic architecture. In chemical water oxidation at pH 1, an impressive TOF of 140 ± 5 s^{-1} is achieved, which is far superior to the unsubstituted control compound **M2** (TOF = 18–54 s^{-1}) and even comparable to the natural archetype OEC-PSII. Detailed kinetic investigations disclosed a mechanistic switch from the bimolecular I2M mechanism for **M2** to the usually much less effective unimolecular WNA pathway for the base-containing **M1**. In this regard, single-crystal X-ray analysis for the Ru^{III} resting state of **M1** after catalytic water oxidation revealed the preorganization of several H$_2$O molecules within the rigid pocket around the active Ru center. Direct structural evidence for a seventh H$_2$O ligand directly coordinated to a catalytically active Ru^{III} species is observed, while further H$_2$O molecules are fixed as 'ready-to-go' substrates in proximity via hydrogen bonding to the protonated bipyridine site and carboxylates of the bda backbone. This well-defined H$_2$O network significantly reduces the kinetic barrier for this crucial and extremely effective nucleophilic attack and provides unprecedented insight into the initial states of O−O bond formation in the WNA mechanism. However, under the neutral conditions for photocatalytic water oxidation weak [C−H⋯N] interactions between the bda backbone and the free bipyridine base induce a ligand rotation, which breaks the catalytic pocket and restricts any activity to an inferior and sterically hindered I2M mechanism. This study establishes a molecular design approach for water oxidation catalysis that conceptually mimics active sites in natural enzymes where water channels are preorganized in molecular clefts. Whilst we demonstrated here the design of a catalytic pocket by preorganizing the substrate water molecules from a ligand located opposite to the metal center for accelerated O$_2$ evolution, we envision in a broader sense that our conceptual design will inspire many other kinds of catalytic transformations and might be efficiently implemented in solar fuel devices.

Chapter 5

Folding-Induced Promotion of Proton-Coupled Electron Transfers via Proximal Base for Light-Driven Water Oxidation
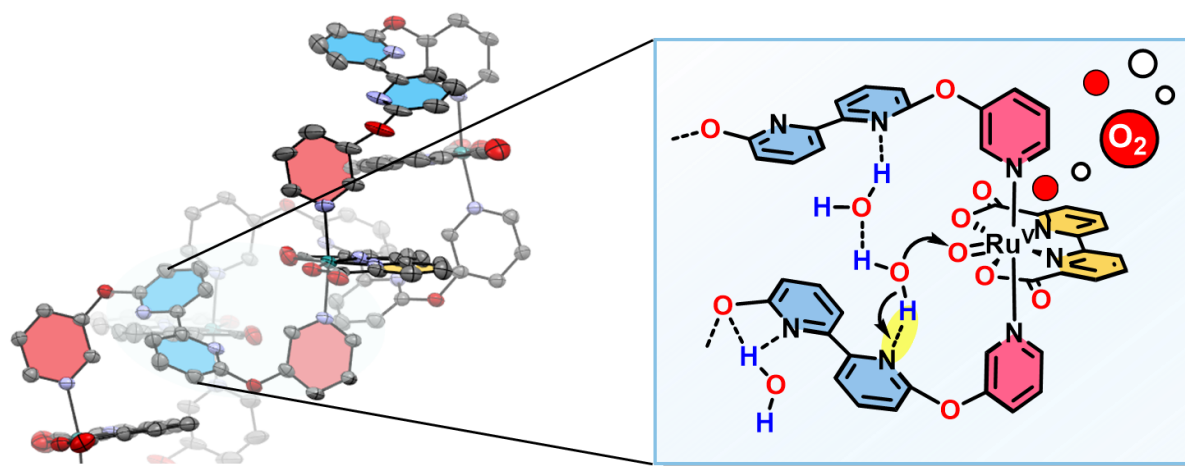
This chapter and the corresponding supporting information (*Chapter 8.3*) were published in:[i]
N. Noll, T. Groß, K. Shoyama, F. Beuerle, F. Würthner, *Angew. Chem. Int. Ed.* **2023**, *62*, e202217745. (https://onlinelibrary.wiley.com/doi/full/10.1002/anie.202217745).

Abstract: Proton-coupled electron transfer (PCET) processes play a key role in biocatalytic energy conversion and storage, for example, photosynthesis or nitrogen fixation. Here, we report a series of bipyridine-containing di- to tetranuclear Ru(bda) macrocycles **2C−4C** (bda: 2,2'-bipyridine-6,6'-dicarboxylate) to promote O−O bond formation. In photocatalytic water oxidation under neutral conditions, all complexes **2C−4C** prevail in a folded conformation that support the water nucleophilic attack (WNA) pathway with remarkable turnover frequencies of up to 15.5 s^{-1}, per Ru unit respectively. Single crystal X-ray analysis revealed an increased tendency for intramolecular π−π stacking and preorganization of the proximal bases close to

---

[i] Part of the results have been described in: T. Groß, Bachelor Thesis, Universität Würzburg, **2020**.

the active centers for the larger macrocycles. H/D kinetic isotope effect studies and electrochemical data demonstrate the key role of the proximal bipyridines as proton acceptors in lowering the activation barrier for the crucial nucleophilic attack of H_2O in the WNA mechanism.

5.1 Introduction

The molecular and biological properties of proteins are generally controlled by the three-dimensional shape and conformation.[51, 68] To facilitate the high structural order of specific protein domains, sophisticated biological processes such as protein folding benefit from secondary, non-covalent interactions, e.g., hydrogen bonding, electrostatic interactions or hydrophobic effects.[30] The folded, native structure is essential for the protein functionality, e.g., specific substrate recognition, as misfolding can lead to inactive or even toxic assemblies.[309] Two prominent biological systems showcasing a highly sophisticated folded protein environment are the oxygen-evolving complex of photosystem II (OEC-PSII),[27, 31, 98] Nature's photosynthetic workhorse to accomplish the fourfold process of water oxidation, and the cytochrome *c* oxidases, which catalyze the reverse reaction.[44, 62] Inspired by these natural archetypes, related principles have been applied in the development of artificial metal complexes to promote ligand-substrate interactions via supramolecular approaches.[35, 36, 237, 289] For instance, reminiscent of natural [FeFe] hydrogenases, the incorporation of pendant amines into the ligand framework promoted intramolecular hydride transfer to accelerate proton reduction catalysis.[291, 310] Similar concepts have also been applied in ruthenium-based water oxidation catalysis with several reports on the incorporation of proximal functionalities such as phosphonate or carboxylate groups. Under oxidative conditions, the auxiliary base acts as proton-accepting unit to deprotonate incoming H_2O molecules and, thus, significantly reduces the activation barrier for the water nucleophilic attack (WNA) pathway by facilitating PCETs.[227, 229, 311, 312] In recent years, our group has likewise demonstrated the enormous potential of implementing Ru(bda) (bda: 2,2'-bipyridine-6,6'-dicarboxylate) catalysts into cyclic metallosupramolecular architectures, which led to a significant increase in both catalyst stability and performance via promotion of the WNA mechanism through cooperative effects between the catalytic centers.[37, 38, 40] Very recently, we have presented a high-performing water oxidation catalyst (WOC) by the incorporation of a single Ru(bda) subunit into a well-defined macrocyclic nanostructure equipped with a bipyridine-functionalized ligand.[285] Under acidic conditions, an enzyme-mimetic molecular cleft is formed. In this catalytic pocket, a well-defined water network is stabilized by hydrogen bonds to the protonated bpy (bipyridine) site, which cannot facilitate proton abstraction but rather serves as hydrogen bond acceptor for H_2O preorganization. Under neutral conditions however, deprotonation of the bipyridinium site

induces outward rotation of the free base, which breaks the catalytic pocket and significantly lowers the catalytic activity. Inspired by these exciting findings, we envisioned that the combination of both a preorganized H_2O network and a proximal Brønsted base might further boost the catalytic performance of enzyme-mimicking WOCs. Building on previously studied rigid macrocycles,[37, 38, 40] we expected that for more flexible, oxygen-bridged macrocyclic frameworks of varying size, the interaction with and activation of the intracavity H_2O environment can be optimized by tailored folding of the dynamic backbone. In particular, catalysis at pH 7 was envisaged to enable proton abstraction by pendant bpy units. Until now, synthetic foldamers[313] have found broad application in the fields of nanotechnology or biomedicine[314, 315] while their catalytic functions have only been reported for selected examples focusing on C−C bond formation and cleavage reactions[316-318] but not for water oxidation catalysis.

Here, we introduce a novel series of structurally more flexible bpy-functionalized di- to tetranuclear Ru(bda) catalysts **2C−4C**. Our detailed studies revealed a tremendous increase in catalytic performance under neutral photocatalytic conditions with turnover frequencies (TOFs) of 5.5 s^{-1}, 14 s^{-1} and 15.5 s^{-1} per Ru unit for complexes **2C−4C**, respectively, which even outperform the previously reported benchmark macrocycle **MC3** with a TOF$_{Ru}$ of 3.7 s^{-1}.[37, 40] Conformational insights by single-crystal X-ray analysis for the whole series showcased how the tendency for intramolecular folding, driven by $\pi-\pi$ stacking of the bpy units, increased from **2C** to **4C** and orientated the proton-accepting groups towards the active centers. This folding-induced preorganization of both reactive Ru centers and pendant bpy bases in the larger macrocycles increases the catalytic performance from dimer **2C** to tetramer **4C** by facilitating PCETs in the WNA pathway, which was experimentally confirmed by H/D kinetic isotope effect (KIE) studies and electrochemical measurements.

5.2 Results and Discussion

5.2.1 Synthesis of multinuclear Ru(bda) complexes 2C−4C

Multinuclear Ru(bda) macrocycles **2C–4C** were synthesized in a two-step procedure (Scheme 3). First, *m*-hydroxypyridine (**45**) was attached to the bpy linker **BP1** via twofold nucleophilic aromatic substitution reaction to give ditopic ligand **46** with modestly flexible diaryl ether linkages. Subsequently, a mixture of multinuclear complexes **2C−4C** were synthesized via twofold ligand exchange reaction at the Ru precursor [Ru(bda)(dmso)$_2$][194] with bidentate ligand **46**. The separation of the macrocycles of different size was achieved by size-exclusion chromatography to yield pure dimer **2C** and trimer **3C** in 39% and 15% yield, respectively. Further purification of crude tetramer **4C** by gel permeation chromatography (GPC) to remove open- and closed-chain side products of higher nuclearity afforded pure **4C** in 3% yield.

Detailed synthetic procedures and characterization data for all new compounds are provided in *Chapter 8.3*.
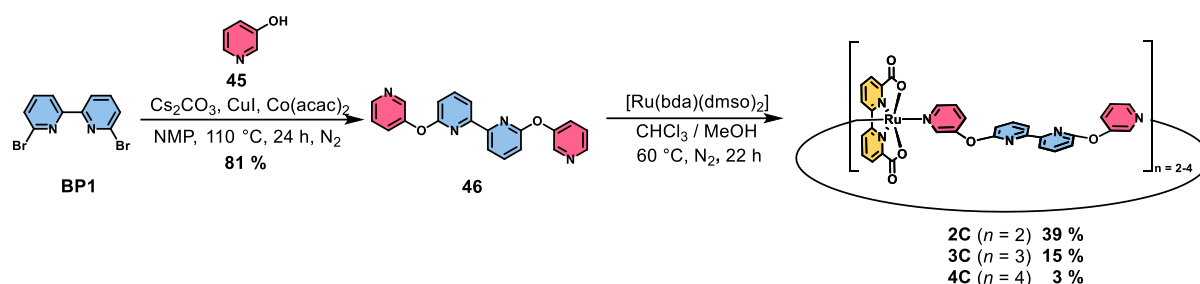
Scheme 3. Two-step procedure for the synthesis of multinuclear Ru(bda) complexes **2C**−**4C**.

5.2.2 Single crystal X-ray analysis

Single crystals suitable for X-ray diffraction of all complexes **2C**−**4C** in the initial Ru^{II} state were grown either by slow evaporation or vapour diffusion (for crystallographic details see *Chapter 8.3*). The three solid-state structures shown in Figure 33 unequivocally confirm the cyclic nature of the multinuclear complexes. Solid-state packing and macrocycle conformations are strongly affected by the *trans*-oriented bpy units in the axial ligand backbone. All complexes exhibit distorted octahedrally coordinated Ru centers with obtuse O−Ru−O angles in the range of 121-123° (Table A8.3.1), which is in good accordance with the previously reported macrocyclic Ru complex **MC4** (123.0(2)°) from our group.[38] The conformation of dimer **2C** is dominated by intramolecular π−π interactions (d = 3.7–4.2 Å),[319] which induce a rigid parallel stacking of the two reversely oriented Ru(bda) units between the two bipy moieties (Figure 33a). After incorporation of another molecular unit in trimer **3C**, the closely folded structure opens up into a less symmetric conformation (Figure 33b). π−π−Stacking (d = 3.6–3.8 Å) between two of the three bpy units in trimer **3C** results in three crystallographically distinct Ru sites, with one Ru(bda) unit being directly aligned towards the π−π−interacting bpy units (cutout 1 in Figure 33b). For the largest macrocycle **4C**, a more ordered conformation is again observed that is dictated by π−π interactions between the axial and equatorial ligand spheres (Figure 33c). This arrangement leads to similar distances between the four reversely oriented Ru(bda) units and positions the basic bpy units near the reactive Ru sites. In summary, these solid-state X-ray structures demonstrate the ordering effect of intramolecular π−π interactions within these series of semi-rigid macrocycles. Whereas a rather parallel stacking between the bpy and bda units rigidifies the structure of dimer **2C**, the incorporation of additional molecular units within the larger and more flexible complexes **3C** and **4C** allows for preorganization of the proximal base near the active centers.
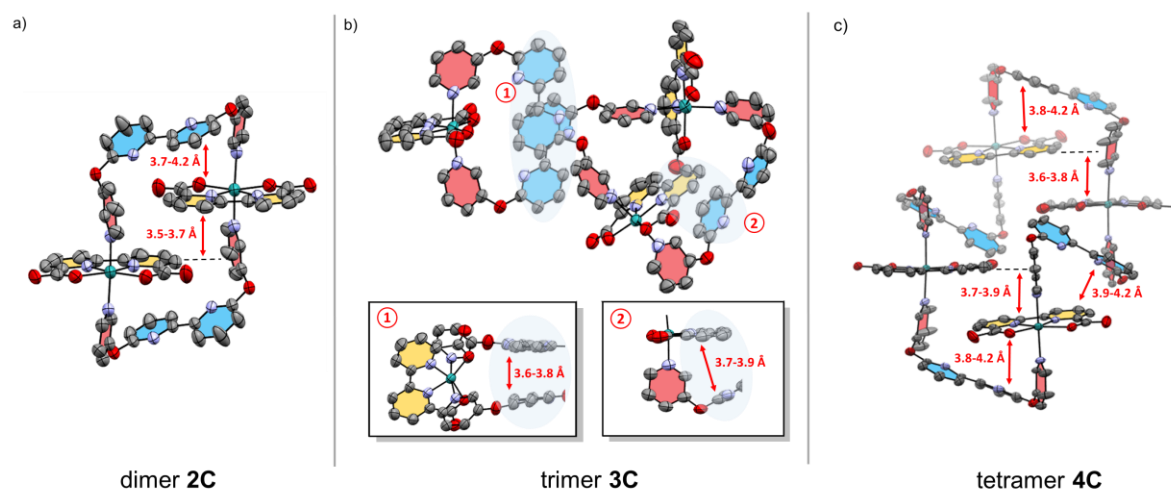
Figure 33. (a-c) Single crystal X-ray structures for **2C−4C** under neutral conditions. The respective distances between intramolecular π−π interactions are highlighted. For **2C** only one of the two macrocyclic complexes in the unit cell is shown; organic solvent molecules and hydrogen atoms of the respective complexes are omitted for clarity. ORTEP diagram with thermal ellipsoids set at 50% probability; C, grey; O, red; N, purple; Ru, turquoise.

5.2.3 Structural characterization via NMR measurements

To determine whether these conformational nuances of **2C−4C** in the solid state are maintained in aqueous solution, we measured ^{1}H NMR spectra of the three complexes in aqueous mixtures of 1:1 D$_2$O/TFE-d_3 (pD = 7.0) (Figure 34). All proton signals were assigned based on 2D NMR spectroscopy (Figures A8.3.8−A8.3.10). For all three macrocycles, only one set of signals was observed for all chemically non-equivalent protons. This indicates either a highly symmetrical structure or dynamic relaxation between more folded conformers that is fast on the NMR time scale. With increasing size of the cyclic complexes, distinct chemical shift changes are observed especially for the *ortho* protons of the axial pyridine units. While the red-labelled *ortho* protons have a moderate upfield shift when going from dimer **2C** (8.41 ppm) to trimer **3C** (8.23 ppm), the reverse effect is observed for the blue-labelled opposite *ortho* protons (6.85 ppm (**2C**); 7.33 ppm (**3C**); Figures 34a,b). These opposing chemical shift changes were attributed to a partially restricted rotation of the Ru(bda) units, which exposes the red- and blue-labelled protons either to enhanced magnetic shielding from the adjacent equatorial bda ligands (upfield shift)[198] or to the open Ru site (downfield shift). Further evidence for this conformational rotation in trimer **3C** is given by nuclear Overhauser effect (NOE) cross signals between the bda unit (green proton) and both red- and blue-labelled protons (Figure A8.3.9), which indicates a rather flexible character of the axial pyridine units and, thus, every Ru unit can rotate more freely. By contrast, only one NOE cross signal was observed for **2C** between the green-labelled proton of the bda unit and the blue-labelled *ortho* proton (Figure A8.3.8), which suggest a much more rigid conformation for the smallest

71

macrocycle. For the larger **4C**, very similar ^{1}H NMR data with only minor upfield shifts compared to **3C** and equal NOE cross signals between the bda unit and both red- and blue-labelled *ortho* protons were obtained (Figure 34c and Figure A8.3.10). Since only three sharp signals without any splitting at room temperature were observed for the bda units in the larger complexes **3C** and **4C**, fast switching of these axial ligands between different conformers on the NMR time scale is suggested. To check the possibility for freezing out the predominant conformers and to get deeper insight into structural peculiarities, VT-NMR experiments were performed for both **3C** and **4C** from 190–295 K in CD$_2$Cl$_2$/CD$_3$OD 1:1 (Figures A8.3.11 and A8.3.12). Unfortunately, no defined signal splitting due to symmetry breaking but only severe signal broadening was observed in the accessible temperature range. These results suggest still highly dynamic conformations and, thus, did not allow any structural assignment at lower temperatures. For dimer **2C**, similar experiments could not be performed due to the poor solubility of the complex in organic media. To probe for the effect of protonation of the bpy units,[285] we compared ^{1}H NMR spectra for **2C**−**4C** at pD 7.0 and 1.0 (1:1 TFE-d_3/D$_2$O, 0.1 M CF$_3$SO$_3$D) (Figures A8.3.13−A8.3.15 and Tables A8.3.3−A8.3.5). For all three macrocyles, the respective blue-labelled protons show a moderate downfield shift at pD 1.0, whereas the signals of the red-labelled protons only changed negligible for the larger complexes **3C** and **4C**. In addition, most of the signals for the respective axial bpy units showed minor downfield shifts under acidic conditions. These results indicate a more dynamic rotation of the Ru(bda) units due to protonation of the bpy units under acidic conditions.[285, 320] Due to repulsive interactions between the charged bipyridinium units, the folded structures open up, which diminishes any close intramolecular interactions between the axial and equatorial ligand sphere. This is also evidenced by the absence of NOE cross signals between the green-labelled protons of the bda units and the purple-labelled protons protons of the axial bpy units (Figures A8.3.16−A8.3.18). More proof for this lack of stabilizing intramolecular folding in the protonated macrocycles is given by moderate upfield shifts for the green-labelled protons of the bda units in the larger complexes **3C** and **4C** (Figures A8.4.14, A8.4.15 and Tables A8.4.4, A8.3.5).

To probe the effect of pH change on size and conformation of **2C**−**4C** in solution, diffusion-ordered spectroscopy (DOSY) measurements were performed in aqueous mixtures of D$_2$O/TFE-d_3 1:1 at pD = 1.0 (0.1 M CF$_3$SO$_3$D) or pD = 7.0 (Figures A8.3.19−A8.3.24). Notably, varying diffusion coefficients for **2C**−**4C** were obtained by DOSY NMR and the hydrodynamic radii were calculated via the Stokes-Einstein equation. Under neutral conditions, a continuous increase of the hydrodynamic radii was observed with increasing complex size for **2C**−**4C** (r_H(**2C**) = 11.6 Å; r_H(**3C**) = 11.9 Å; r_H(**4C**) = 15.6 Å) (Figures A8.3.20, A8.3.22, A8.3.24). The obtained values are in good accordance with space-filling models obtained from the solid-state structures of **2C**−**4C**. Under acidic conditions, only slightly larger hydrodynamic radii were

observed for **2C** and **3C**, while a larger difference of 1.1 Å between the hydrodynamic radii at pH 1 and pH 7 was observed for tetranuclear complex **4C** (d(r_H(pH 1, **2C**)–r_H(pH 7, **2C**) = 0.2 Å; d(r_H(pH 1, **3C**)–r_H(pH 7, **3C**) = 0.1 Å; d(r_H(pH 1, **4C**)–r_H(pH 7, **4C**) = 1.1 Å) (Figures A8.3.19, A8.3.21, A8.3.23). In summary, these results provide further evidence for the strong intramolecular folding of complexes **2C−4C** under neutral conditions, while a continuous trend towards larger unfolded complex sizes was observed under acidic conditions.
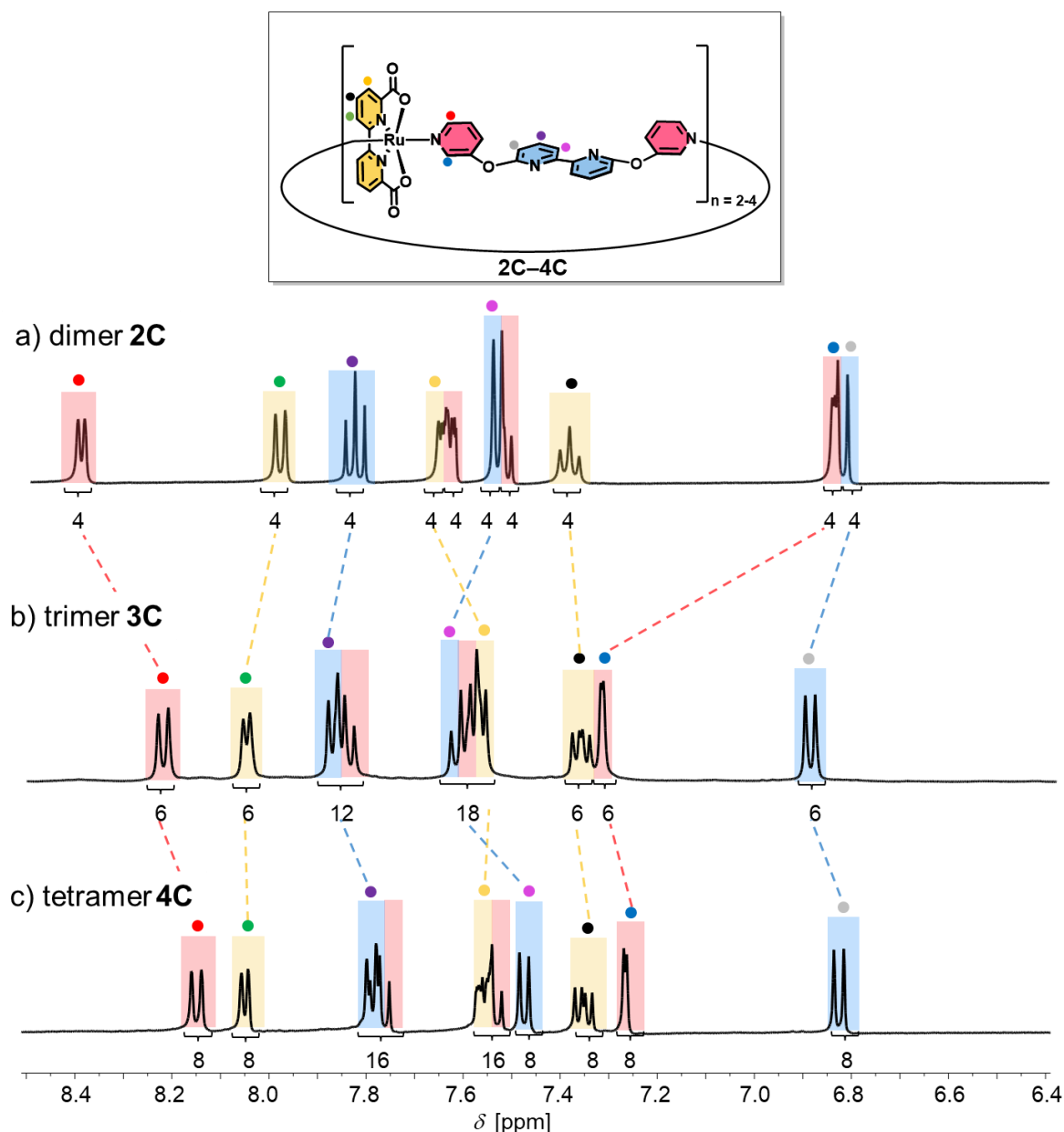
Figure 34. (a−c) Aromatic region of the ^{1}H NMR spectra (1:1 TFE-d_3/D$_2$O, 400 MHz, ascorbic acid, rt) of complexes **2C−4C** at pD 7.0. The colours of the signals correspond to bda (yellow), axial pyridine fragment (red) and bipyridine unit (blue) of the ligand backbone as highlighted in the structure.

5.2.4 Catalytic water oxidation

Towards artificial photosynthesis, the catalytic properties of complexes **2C−4C** were investigated under photochemical conditions in a three-component system in 50 mM phosphate buffered CH_3CN/H_2O 4:6 mixtures at pH 7 with $[Ru(bpy)_3Cl_2]$ as photosensitizer and $Na_2S_2O_8$ as sacrificial electron acceptor (Figure 35a and Figure A8.3.25; for detailed experimental conditions see *Chapter 8.3*).[135, 146, 148, 153, 321-324] Irradiation was performed with a xenon lamp (I = 100 mW cm^{-1}) and a Clark electrode was used for O_2 detection. All complexes displayed a first-order dependency of the evolution of O_2 on the WOC concentration, which is typical for catalysts following the WNA pathway as previously shown for multinuclear macrocycles from our group.[37-40] As shown in Figure 35a, the catalytic activity of **2C−4C** strongly correlates with the size of the macrocycle. Apparently, the activity per Ru unit is almost three times higher for trimer **3C** (TOF$_{Ru}$(**3C**) = 14 ± 0.2 s^{-1}, Figure A8.3.28) compared to dinuclear counterpart **2C** (TOF$_{Ru}$(**2C**)= 5.5 ± 0.1 s^{-1}, Figure A8.3.27). For the largest macrocyle **4C**, only a moderate increase in catalytic performance (TOF$_{Ru}$(**4C**) = 15.5 ± 0.4 s^{-1}, Figure A8.3.28) was observed. These activities also correlate with the turnover numbers (TON) per Ru center, as the larger macrocycles **3C** and **4C** (TON(**3C**)$_{Ru}$ = 550 ± 50; TON(**4C**)$_{Ru}$ = 600 ± 50) exhibit significantly higher turnover compared to dimer **2C** (TON$_{Ru}$(**2C**) = 200 ± 20). The catalytic performance of these macrocyclic Rub(bda) complexes is among the most active homogenous WOCs reported to date (see table A8.3.6 for a comparison with recent literature examples). While the smallest macrocyle **2C** has already a catalytic activity comparable to our previously reported tri- and tetranuclear macrocycles **MC3** (TOF$_{Ru}$ = 3.7 s^{-1})[37, 40] and **OEG-MC4** (TOF$_{Ru}$ = 5.8 s^{-1}),[39] the larger analogs significantly outperform most of the literature benchmarks.

To probe if this trend in activity is maintained after protonation of the bpy units, all three Ru(bda) complexes were investigated in chemical water oxidation under acidic conditions (CH_3CN/H_2O 4:6, pH 1, triflic acid) using cerium ammonium nitrate as sacrificial oxidant[135] (for experimental details see *Chapter 8.3*). Surprisingly, a similar activity for each Ru center with a TOF/Ru of ≈50 s^{-1} was observed for the whole series **2C−4C** via linear regression of the first-order kinetics of O_2 evolution (Figure 35b and Figures A8.3.30–A8.3.32). This activity is even comparable to our previously reported macrocycle **MC3** with a TOF$_{Ru}$ of 45 s^{-1} under identical conditions.[37, 40] The same trend is reflected in the TON of the respective complexes, which gave very similar values for the whole series (TON(**2C**)$_{Ru}$ = 500 ± 100; TON(**3C**)$_{Ru}$ = 500 ± 100;TON(**4C**)$_{Ru}$ = 450 ± 100). Analysis of the reaction mixtures of **2C−4C** by MALDI-TOF mass spectrometry revealed high stabilities of the complexes after catalysis, as indicated by identical fragmentation patterns before and after catalysis, which was attributed to decomposition of the complexes by ionization during mass spectrometry (Figures A8.3.34−A8.3.42). Accordingly,

the macrocyclic nature of **2C**−**4C** confers higher stability through the chelate effect of the ditopic ligand **46**.[37, 38] For further insight into the mechanistic pathway, kinetic isotope effect (KIE) studies were performed for **2C**−**4C** under previously described photocatalytic conditions in 50 mM phosphate buffered aqueous solutions (H_2O and D_2O, pH 7) containing 40% acetonitrile.[276] For all three multinuclear complexes, linear kinetics were observed with a significantly higher reaction rate in H_2O compared to D_2O. The highest KIEs of 1.9 and 2.4 were observed for tri- and tetranuclear complexes **3C** and **4C**, respectively. In contrast, dinuclear complex **2C** exhibits a significantly lower KIE of 1.4 (Figures A8.3.43–A8.3.45). Therefore, a competing intramolecular I2M pathway under these conditions cannot completely be ruled out for the compact conformation of rigid **2C**. In accordance with previous results,[38] these findings indicate a stronger degree of proton coupling in the rate-determining Ru^{IV}−OH to Ru^V=O oxidation within the mechanistic pathway of the larger macrocycles **3C** and **4C** at pH 7. Under these conditions, the proximal bpy groups serve as proton acceptor in close proximity to the reactive Ru sites compared to its protonated state at pH 1.
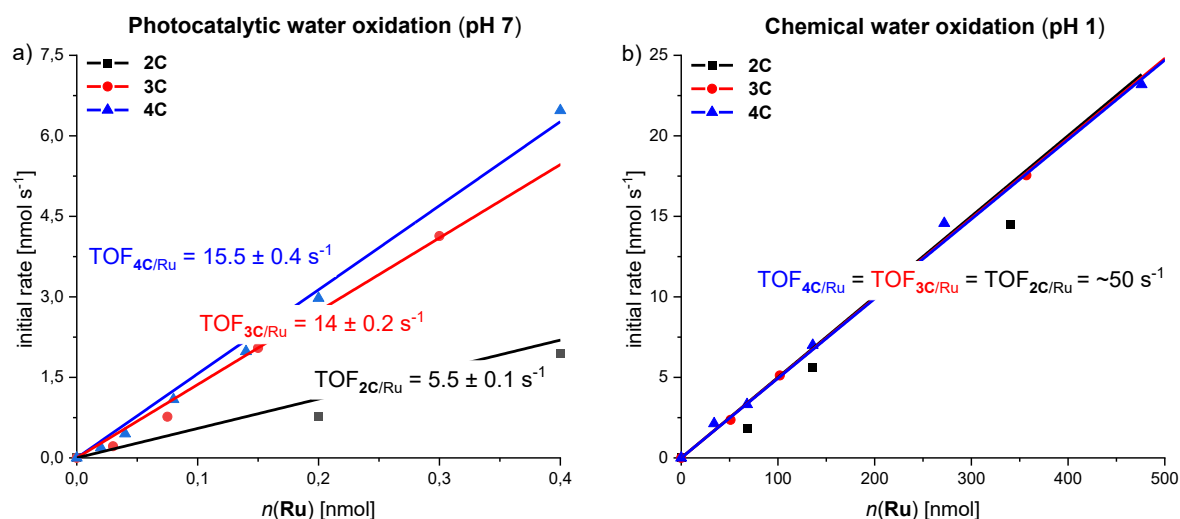
Figure 35. a) Photochemical water oxidation catalysis with **2C**−**4C**: Plot of initial rates (obtained by linear fit of O_2 evolution curve after light exposure between 50−60 s) of O_2 evolution against the WOC concentration and linear fit for first order kinetics. O_2 evolution experiments were performed at varying WOC concentrations in CH_3CN/H_2O 4:6 (pH 7, 50 mM phosphate buffer, c(PS) = 1.5 mM, c($Na_2S_2O_8$) = 37 mM). b) Chemical water oxidation experiments with **2C**−**4C** as WOCs in 4:6 CH_3CN/H_2O mixture using CAN as sacrificial oxidant (pH 1, triflic acid, c(CAN) = 0.6 M). Plots of initial rates of O_2 evolution against the WOC concentration with corresponding linear regression fit. Individual reaction rates were obtained by a linear fit of O_2 evolution curves for the first 2 s of catalysis for **2C**−**4C**, respectively.

5.2.5 Discussion

Comparative studies on photocatalytic (pH 7) and chemical (pH 1) water oxidation for a series of base-functionalized di- to tetranuclear Ru(bda) macrocyles **2C−4C** revealed a significant increase in activity induced by basic bpy moieties in the semi-flexible ligand framework. Under photocatalytic conditions, an unprecedented boost in catalytic performance was observed with TOF_{Ru} values of 5.5 s^{-1}, 14 s^{-1}, and 15.5 s^{-1} for **2C–4C**, respectively. Under chemical conditions however, each Ru unit of macrocycles **2C−4C** with varying size exhibited an average TOF of ≈50 s^{-1} with no apparent size effects. In comparison to our previously reported trinuclear macrocycle **MC3**, very similar activities are obtained under acidic conditions (TOF_{Ru} (**MC3**) = 45 s^{-1}).[37, 40] At pH 7 however, the base-containing complexes **2C−4C** clearly outperform **MC3** (TOF_{Ru}(**MC3**) = 3.7 s^{-1}). Interestingly, H/D KIE studies under neutral conditions revealed a direct correlation between the catalytic activity and the degree of proton coupling in the rate-determining nucleophilic attack of an H_2O molecule in the WNA pathway. Additional support for these findings was obtained by cyclic voltammetry (CV) and differential pulse voltammetry (DPV). Measurements for **2C−4C** were performed in phosphate-buffered aqueous solutions at pH 7 containing 40% 2,2,2- trifluorethanol (TFE) as a non-coordinating co-solvent for better solubilization and the redox properties are summarized in Table A8.3.7. Under neutral conditions, three subsequent oxidation processes were observed for all three compounds **2C−4C**, which can be assigned to the Ru^{II}/Ru^{III}, Ru^{III}/Ru^{IV} and Ru^{IV}/Ru^{V} redox couples, respectively (Figures A8.3.46−A8.3.48). At pH 7, the typically rate-determining Ru^{IV}/Ru^{V} oxidations for **3C** and **4C** are cathodically shifted by 30−40 mV with regard to dimer **2C** and a gradual enhancement of the catalytic current density is observed (Figure 36). This thermodynamically more favourable oxidation to Ru^{V} for the larger macrocycles is presumably induced by a stronger contribution of the proximal proton acceptor unit in the rate-determining step of O−O bond formation for the larger complexes, as it was recently shown for a Ru-based catalyst.[236] In addition, Pourbaix diagrams for **2C** and **3C** display the involvement of proton-coupled electron transfer (PCET) processes for the Ru^{III}/Ru^{IV} and Ru^{IV}/Ru^{V} redox couples, while the oxidation from Ru^{II} to Ru^{III} is independent of the pH value (Figure A8.3.49). For the Ru^{III}/Ru^{IV} oxidation event, slopes in the range of −57 to −74 mV per pH unit are found for these complexes indicating 2e$^-$/2H$^+$ or 3e$^-$/3H$^+$ processes, respectively, in accordance with the Nernstian ideal of 59 mV/pH for a general ne$^-$/nH$^+$ process.[187]

Based on the combined analytical and kinetic data, we propose the following mechanistic picture for the excellent water oxidation catalysis with **2C−4C**. As shown previously, a hydrogen-bonded H_2O network can either be stabilized by cooperative effects within the cavities of macrocyclic Ru(bda) assemblies of different size by utilizing the carboxy groups of the bda ligands as directional bonding sites or via hydrogen bonding interactions to a
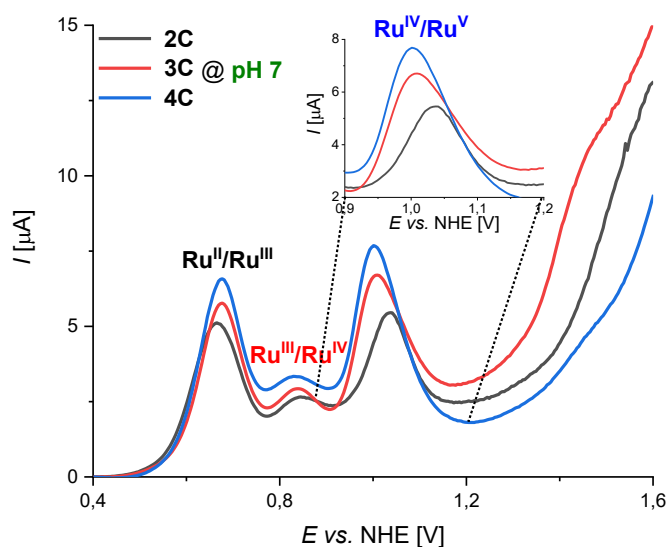
Figure 36. Differential pulse voltammograms of macrocycles **2C−4C** at pH 7 in TFE/H_2O 4:6 (phosphate buffer with I = 0.1 M, c(WOC) = 2.5·10^{-4} M). The inset shows the amplified region between 0.9−1.2 V at pH 7.

protonated bpy site located opposite to the active site within a synthetic molecular molecular cleft.[39, 40, 285, 325] In this work, we demonstrate the powerful effect of an auxiliary base in the ligand sphere on the catalytic performance of more flexible macrocycles of varying size. Single crystal X-ray analysis of the multinuclear series **2C−4C** showed that within the larger complexes **3C** and **4C**, intramolecular $\pi-\pi$ interactions of the *trans*-oriented bpy units put the proximal base in close proximity to the active sites**.** Detailed ^{1}H-NMR experiments gave further support that these solid-state conformations of **2C−4C** are to some extent preserved in solution. Therefore, we conclude that the free bpy moieties act as proton-accepting units at pH 7 and facilitate PCETs by deprotonating incoming H_2O molecules at the rds of O−O bond formation, which promotes the subsequent hydroperoxide formation (Figure 37). The observed boost in catalytic performance for the larger and more folded macrocycles can be presumably attributed to a stronger preorganization of the proton-accepting unit near the active site, since the proton transfer efficiency strongly depends on the donor-acceptor distance and the right structural orientation.[126, 277, 278, 311] At pH 1, the now *cis*-oriented bipyridinium cations[285, 320] can no longer accept any protons and a constant TOF of ≈50 s^{-1} without any size effect is observed for the whole series **2C−4C**. Here, the non-folded conformations of the macrocycles are reminiscent of **MC3**, with the protonated bases preorganizing several water molecules and presumably stabilizing a hydrogen-bonding network.
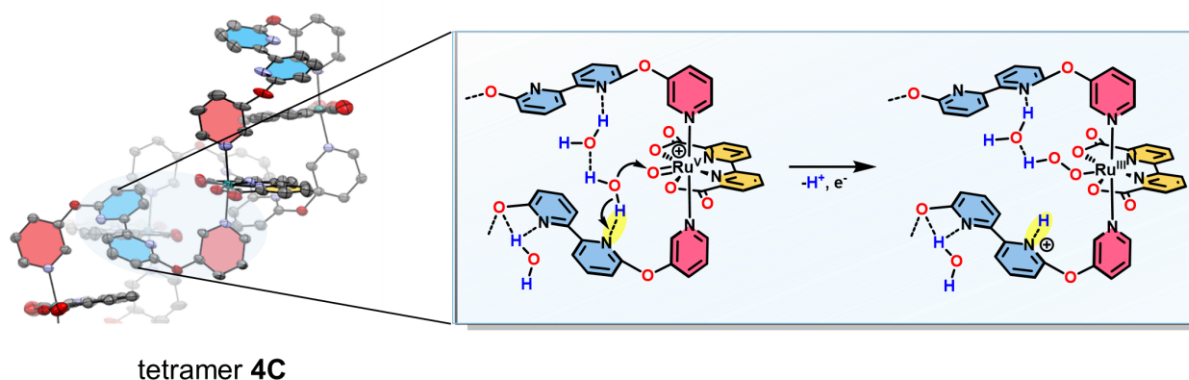
tetramer **4C**

Figure 37. Cutout from the single-crystal X-ray structure of tetramer **4C** showcasing the effect of proton abstraction of the pendant base (highlighted in yellow) within the rate-determining step of O−O bond formation in the WNA pathway.

5.3 Conclusions

In this work, we have integrated a base-functionalized ligand as proton acceptor within the flexible architecture of a series of di- to tetranuclear Ru macrocycles **2C**−**4C**. Single crystal X-ray analysis of complexes **2C**−**4C** revealed that the conformations of the differently sized complexes are dominated by intramolecular π−π interactions from the bpy unit in the axial ligand sphere. For the larger tri- and tetranuclear macrocycles, this leads to an increased tendency of intramolecular folding and a more pronounced orientation of the active centers towards the auxiliary base. In photocatalytic water oxidation at pH 7, a remarkable increase in TOF per Ru center to 5.5 s^{-1}, 14 s^{-1} and 15.5 s^{-1} was observed for **2C**−**4C**, respectively, while following the WNA pathway. Under chemical conditions at pH 1 however, the activity per Ru unit remained constant with a value of ≈50 s^{-1} for the whole series. Our detailed kinetic studies and electrochemical measurements under neutral conditions revealed an increasing H/D kinetic isotope effect and a cathodic shift of the rate-determining Ru^{IV}/Ru^{V} oxidation in the series **2C**−**4C**. This is most likely explained by the more flexible proximal base facilitating proton abstraction with increased tendency of intramolecular folding in the rate-determining Ru^{IV}−OH to Ru^{V}=O oxidation in the WNA pathway. Under acidic conditions, transformation of the bpy units to the respective *cis*-conjugated acids opens up the folded structures and shuts down the proton relay function. In summary, this study highlights the importance of second coordination sphere engineering for efficient molecular water oxidation catalysis and showcases the importance of a proximal base as an auxiliary ligand to enhance the crucial substrate-catalyst interaction.

Chapter 6

Summary and Conclusion

About 2.4 billion years ago, nature has fundamentally revolutionized life on earth by inventing the multi-subunit protein complex photosystem II, the only molecular machine in nature that catalyzes the thermodynamically demanding photosynthetic splitting of water into oxygen and reducing equivalents.[13, 326] Nature chose a distorted Mn_4CaO_5 cluster as catalyst, better known as oxygen-evolving complex (OEC), thus recognizing the need for transition metals to achieve high-performance catalysts.[27, 28] The curiosity has always driven mankind to mimic nature's achievements, but the performance of natural enzymes such as the oxygen-evolving complex in photosystem II remain commonly unmatched.[287, 327] An important role in fine-tuning and regulating the activity of natural enzymes is attributed to the surrounding protein domain, which facilitates substrate preorganization within well-defined nanoenvironments (*Chapter 2.1*).[30, 41] In light of growing energy demands and the depletion of fossil fuels, the unparalleled efficiency of natural photosynthesis inspires chemists to artificially mimic its natural counterpart to generate hydrogen as a 'solar fuel' through the light-driven splitting of H_2O (*Chapter 2.2*).[16-19] As a result, significant efforts have been devoted in recent decades to develop molecular water oxidation catalysts based on earth-abundant transition metals and the discovery of the Ru(bda) (bda: 2,2'-bipyridine-6,6'-dicarboxylate) catalyst family enabled activities comparable to the natural OEC.[128, 212] Similar to the natural archetypes, the design of homogeneous catalysts that interplay judiciously with the second coordination sphere of the outer ligand framework proved to be a promising concept for catalyst design.[34-36] To promote catalysis in confined space, Würthner and co-workers introduced cyclic metallosupramolecular macrocyles as powerful water oxidation catalysts (WOCs).[37] According to theoretical calculations, an ordered hydrogen-bonding network of H_2O molecules inside the macrocyclic cavity reduces the activation barrier of the water nucleophilic attack (WNA) by facilitating cooperative proton abstraction during catalysis (*Chapter 2.3*).[38] In this present thesis, novel supramolecular design approaches for enzyme-like activation of substrate H_2O molecules for the challenging oxidative water splitting reaction were established via tailor-made engineering of the secondary ligand environment of macrocyclic Ru(bda) catalysts.

In the first approach pursued in this thesis, two Ru(bda) catalytic subunits were incorporated into the cyclic dinuclear environment of **dimer 1** containing functionalized calix[4]arene axial ligands, to investigate the effect of second coordination sphere on the catalytic mechanism (*Chapter 3*). The narrow lower rim of the calix[4]arene ligand was modified with four

oligo(ethylene glycol) side chains to provide sufficient water solubility for catalytic water oxidation experiments. The novel complex was characterized by NMR spectroscopy, mass spectrometry, elemental analysis and diffusion-ordered spectroscopy (DOSY). Moreover, the geometry-optimized structure of **dimer 1** indicated an alignment of both Ru centers into the interior of the macrocyclic cavity. The catalytic performance of **dimer 1** was evaluated by chemical water oxidation using cerium ammonium nitrate (CAN) at pH 1 and by photocatalytic water oxidation experiments applying a three-component system with $[Ru(bpy)_3]^{3+}$ (bpy: bipyridine) as an oxidant at pH 7 (Figure 38).
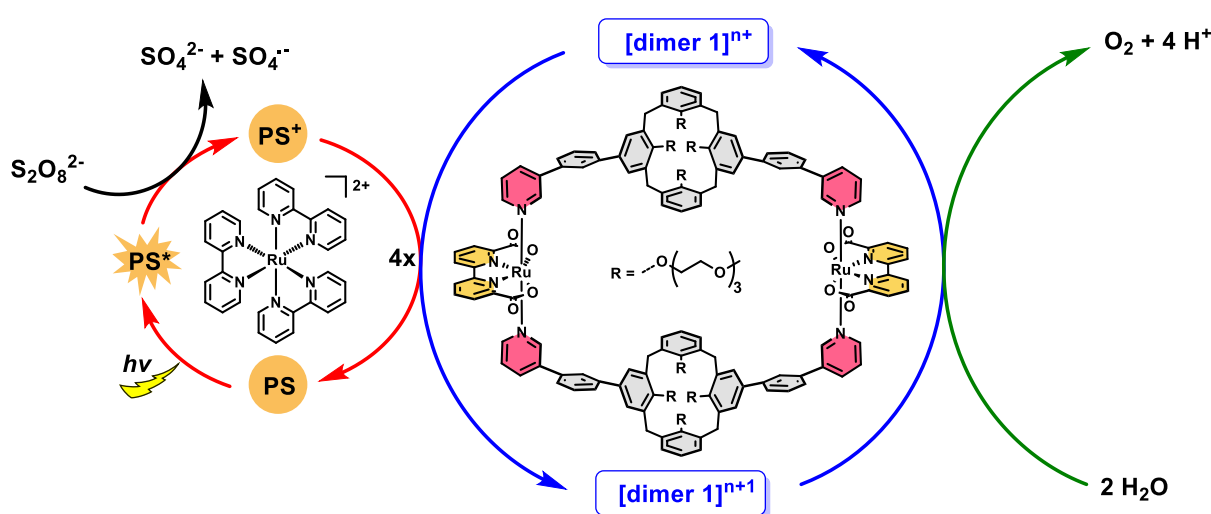
Figure 38. Schematic presentation of the photocatalytic water oxidation cycle with **dimer 1** as WOC, $[Ru(bpy)_3]^{2+}$ as photosensitizer (PS) and $Na_2S_2O_8$ as sacrificial electron acceptor.

Under photocatalytic conditions, usually much lower catalytic values are observed due to the limited stability of the applied photosensitizer and the higher complexity of the multi-component system.[146, 148] Interestingly, almost comparable catalytic rates were determined under chemical (TOF(**dimer 1**) = 19 s^{-1}; TOF$_{Ru}$(**dimer 1**) = 9.5 s^{-1}) and photocatalytic (TOF(**dimer 1**) = 15.5 s^{-1}; TOF$_{Ru}$(**dimer 1**) = 7.75 s^{-1}) conditions for this dinuclear complex. Post-catalytic mass spectrometry analysis of the reaction mixture revealed that the main catalyst deactivation pathway at pH 1 was oxidative decomposition of the methylene units as part of the axial calix[4]arene ligand. In this regard, the cyclic dinuclear environment of **dimer 1** provides a much higher catalyst stability under neutral conditions and, thus, enables catalytic water oxidation studies under highly diluted conditions. Additionally, kinetic studies, such as kinetic isotope effect (KIE) investigations, revealed a mechanistic switch from a bimolecular I2M (interaction of two metal-oxyl species) mechanism, which is usually observed for Ru(bda) complexes,[128] to a unimolecular WNA pathway for **dimer 1**.

In the following *Chapter 4*, a novel enzyme-inspired approach was introduced by embedding

the catalytic Ru(bda) framework in the confined environment of cyclic mononuclear complex **M1** (X = N). The axial ligand is equipped with a recognition site to promote the preorganization of H_2O molecules in front of the active site (Figure 39a). As a reference, the unfunctionalized complex **M2** (X = CH) was synthesized (Figure 39a). As shown in Figures 39b and c, different reaction kinetics were observed for base-functionalized WOC **M1** at either acidic (linear dependency) or neutral (quadratic dependency) conditions. In contrast, reference **M2** showed the expected second-order dependency under both conditions, which is indicative of the bimolecular I2M mechanism. Subsequent pH-dependent KIE studies confirmed the observed mechanistic switch for **M1** from a very inefficient bimolecular I2M mechanism at pH 7 to a very effective unimolecular WNA mechanism at pH 1 (Figure 39b,c). This results in an exceptionally high average TOF value of 140 s^{-1} for **M1** under chemical water oxidation conditions, which is far superior to the reference **M2** (TOF = 18−54 s^{-1}) and to the previously reported macrocycle **MC3** (TOF_{Ru} = 45 s^{-1}).[37, 40]
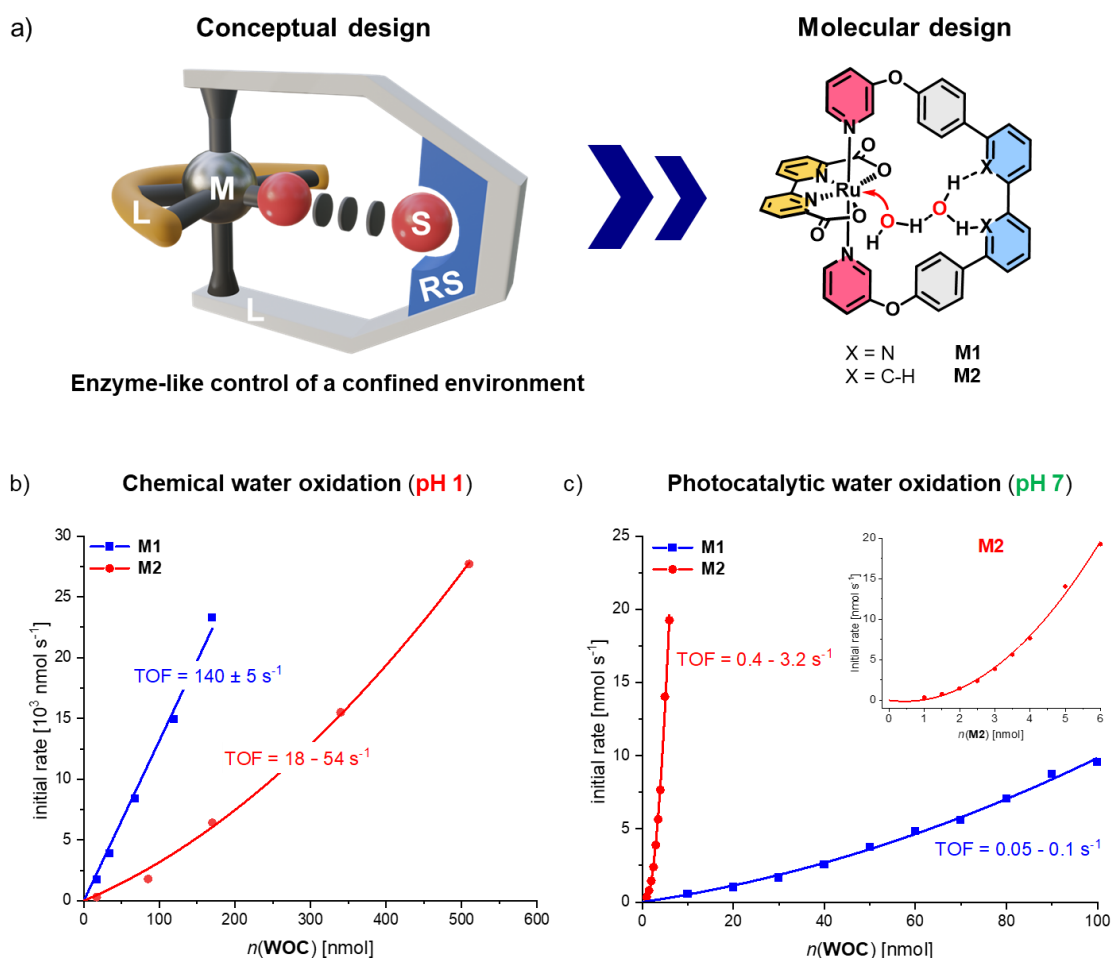
Figure 39. a) Conceptual design for an enzyme-like control of a confined environment (M = metal site, L = axial/equatorial ligand, S = substrate, RS = recognition site) and molecular design of cyclic mononuclear Ru(bda) complexes **M1** (X = N) and **M2** (X = CH). b) Chemical and c) photocatalytic water oxidation catalysis with **M1** and **M2**. For details on experimental conditions see *chapter 4*.
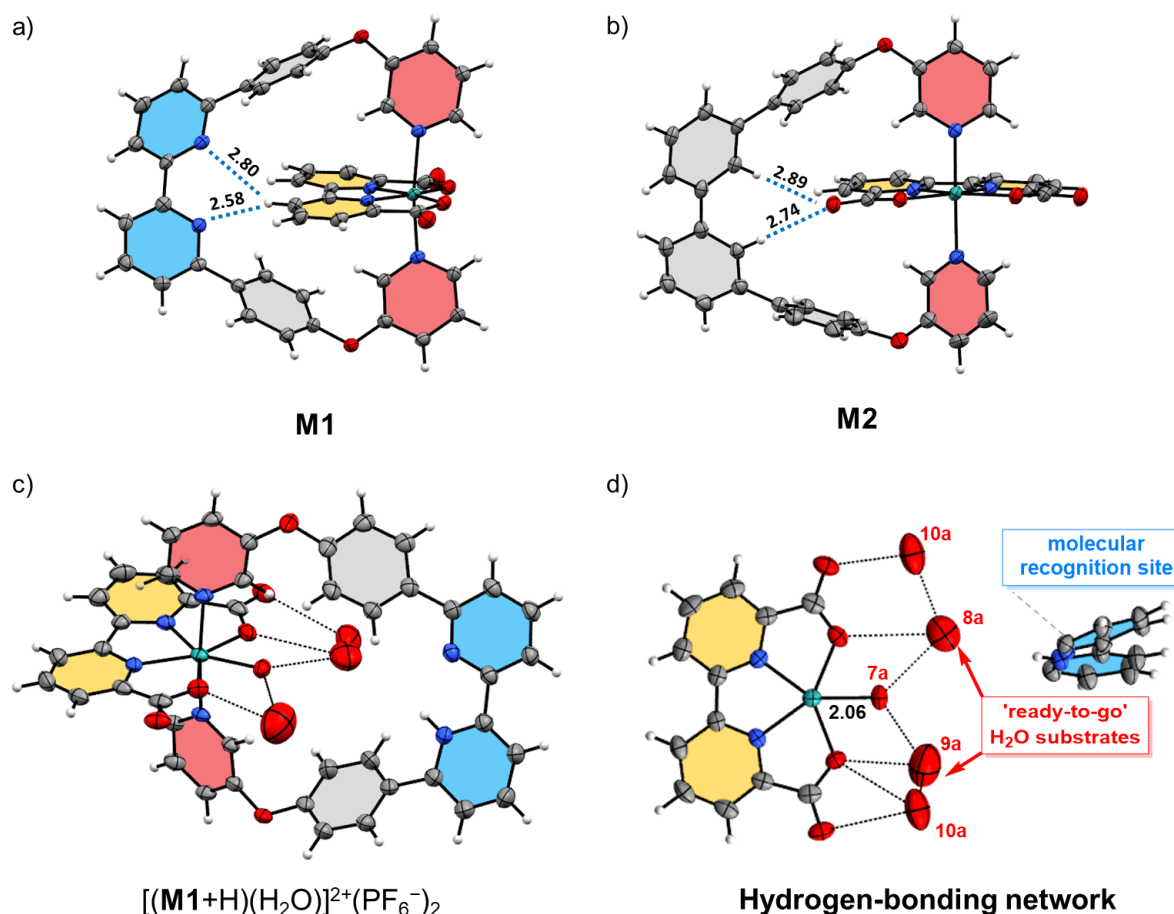
Figure 40. Single crystal X-ray structures of a) **M1**, b) **M2** and c) [(**M1**+H)(H$_2$O)]$^{2+}$(PF$_6^-$)$_2$. In d) the main occupancy (66.2%) within the supramolecular cavity of [(**M1**+H)(H$_2$O)]$^{2+}$(PF$_6^-$)$_2$ is displayed, showing a hydrogen-bonding network with preorganized H$_2$O substrates for O−O bond formation via nucleophilic attack. Organic solvent molecules and PF$_6^-$ counterions are omitted for clarity. ORTEP diagram with thermal ellipsoids set at 50% probability. C, grey; H, white; O, red; N, purple; Ru, turquoise.

Detailed single crystal X-ray analysis of both complexes in the Ru^{II} state under neutral conditions and of complex **M1** at a predominant Ru^{III} state after acidic catalytic water oxidation provided unparalleled structural insights into the conformational orientation of the axial ligands depending on the pH value (Figure 40). At pH 7, weak hydrogen bonding interactions between the axial and equatorial ligand spheres stabilize the conformations of **M1** and **M2**, respectively, which either lead to a fixation of the axial ligand over the bda framework for **M1** (Figure 40a) or to a lateral orientation of the macrocyclic ligand in the case of **M2** (Figure 40b). In contrast, protonation of the bipyridine moiety of **M1** at pH 1 breaks the weak hydrogen bonding interactions and causes a ligand rotation (Figure 40c). Consequently, a confined enzyme-like binding pocket is created in which several hydrogen-bonded H$_2$O molecules are preorganized in front of the seven-coordinated Ru^{III}−OH$_2$ center in [(**M1**+H)(H$_2$O)]$^{2+}$(PF$_6^-$)$_2$ (Figure 40d). In addition, this intracavity water network gave unprecedented structural insight into the O−O

bond formation pathway, as a second H_2O molecule is preorganized close to the active site for the subsequent crucial water nucleophilic attack. These results demonstrate the efficacy of an enzyme-like pocket design by using the protonated bipyridine unit as hydrogen bond acceptor site to preorganize H_2O molecules in front of the active site to accelerate the WNA pathway.

In *Chapter 5*, the oxygen-bridged ligand framework of **2C−4C** was modified by removing the phenyl moieties to increase structural flexibility and promote the tailored folding of macrocyclic Ru WOCs of different size (Figure 41a). In this way, it was expected that the basic function is in close proximity to the respective Ru centers to facilitate proton-coupled electron transfers (PCETs) at pH 7 and promote O−O bond formation (Figure 41d). Single crystal X-ray analysis of complexes **2C−4C** under neutral conditions showed an increased tendency for intramolecular folding for the larger tri- and tetranuclear Ru complexes due to intramolecular $\pi-\pi$ interactions from the axial bipyridine unit (Figure 41b,c). Under chemical reaction conditions, a constant TOF per Ru center of ≈ 50 s^{-1} was measured for the whole complex series. In contrast, an unprecedented boost in catalytic activity per Ru center of 5.5 s^{-1}, 14 s^{-1} and 15.5 s^{-1} for **2C−4C** following a WNA pathway was measured under photocatalytic conditions. Detailed kinetic studies revealed an increased H/D kinetic isotope effect toward larger complex sizes at pH 7, while no change in the mechanistic pathway was observed at pH 1. Based on electrochemical studies, a cathodic shift of the rate-determining Ru^{IV}/Ru^{V} oxidation for **2C−4C** was determined. This shift can be explained by a more pronounced contribution of the proximal proton-accepting unit at the rate-determining step of the mechanistic pathway for the larger macrocycles, which is in accordance with the accelerated rate under photocatalytic conditions for **2C−4C**. At pH 1, the favoured *cis*-orientation of the bipyridinium cations prevent the folded state and, thus, turns off the proton relay function of the basic unit.
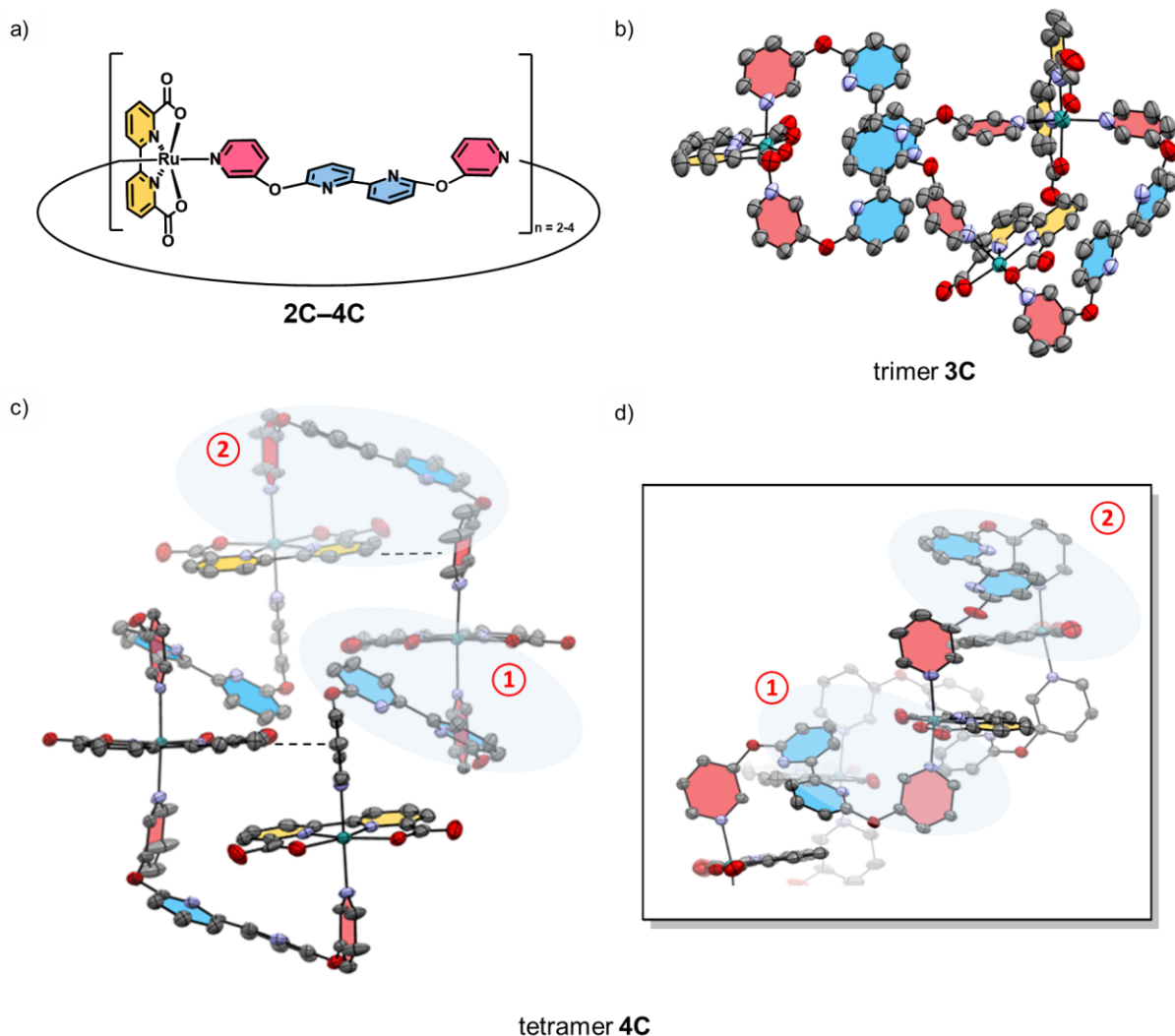
Figure 41. a) Chemical structures of multinuclear Ru(bda) complexes **2C−4C**. Single crystal X-ray structures of b) trimer **3C**, c) tetramer **4C** and d) cutout from the single crystal X-ray structure of **4C** to showcase the close proximity of the pendant base to the Ru center. Organic solvent molecules are omitted for clarity. ORTEP diagram with thermal ellipsoids set at 50% probability. C, grey; H, white; O, red; N, purple; Ru, turquoise.

In summary, a series of novel bioinspired macrocyclic water oxidation catalysts were developed within the scope of this thesis that promote the challenging oxidative water splitting reaction through enzyme-like activation of H_2O molecules. To mimic the catalytic binding pocket of natural enzymes, the catalytic Ru(bda) moieties were embedded in well-defined macrocyclic nanostructures, that are equipped with proton-accepting units to preorganize H_2O molecules in front of the active site. As a particular highlight of this thesis, *Chapter 4* described a mononuclear Ru(bda) complex with an increased catalytic activity at pH 1. For this complex enhanced catalyst-substrate interaction occurred through a preorganized water network within the enzyme-mimetic molecular cleft. In contrast, for the flexible molecular ligand framework described in *Chapter 5* the catalytically more active folded conformations are formed under

neutral conditions, which resulted in an enhanced interaction of the catalytic Ru center with intracavity H_2O molecules. In addition, the folded conformation facilitates proton abstraction by the proximal proton-accepting unit in the rate-determining step of O−O bond formation of the WNA mechanism, which led to accelerated O_2 evolution rates. In conclusion, this thesis highlighted the importance of the secondary coordination sphere on the water network toward the promotion of water oxidation into molecular oxygen by the WNA mechanism. These insights into accelerated mechanistic pathways for proton-coupled electron transfer steps will contribute to a more rational design of efficient molecular catalysts for water oxidation or might be an inspiration for many other kinds of catalytic transformations.

Chapter 7

Zusammenfassung und Fazit

Vor etwa 2.4 Milliarden Jahren hat die Natur das Leben auf der Erde mit der Entwicklung des mehrgliedrigen Proteinkomplexes Photosystem II grundlegend revolutioniert. Dieser stellt die einzige molekulare Maschine in der Natur dar, die die thermodynamisch anspruchsvolle photosynthetische Spaltung von Wasser in Sauerstoff und reduzierende Äquivalente katalysieren kann.[13, 326] Als Katalyator hat die Natur hierfür ein verzerrtes Mn_4CaO_5-Cluster ausgewählt, welcher besser bekannt ist als Sauerstoff-produzierender Komplex (OEC, engl.: oxygen-evolving complex). Damit wird die Notwendigkeit von Übergangsmetallen als leistungsfähige Katalysatoren belegt.[27, 28] Die Wissbegierde hat die Menschheit schon immer dazu angetrieben, die Errungenschaften der Natur zu imitieren. Dennoch bleiben die Leistungen natürlicher Enzyme wie die des OEC in Photosystem II häufig unerreicht.[287, 327] Eine wichtige Rolle bei der Feinabstimmung und Regulierung der Aktivität natürlicher Enzyme nimmt die umliegende Proteindomäne ein, die die Vororganisation der Substrate in einer genau definierten Nanoumgebung ermöglicht (*Kapitel 2.1*).[30, 41] Angesichts des wachsenden Energiebedarfs und der Erschöpfung von fossilen Brennstoffen werden Chemiker von der unvergleichlichen Effizienz der natürlichen Photosynthese zu deren künstlichen Nachahmung inspiriert, damit Wasserstoff als "solarer Brennstoff" durch die lichtgetriebene Spaltung von H_2O erzeugt werden kann (*Kapitel 2.2*).[16-19] Infolgedessen wurden in den letzten Jahrzehnten erhebliche Anstrengungen in die Entwicklung molekularer Wasseroxidationskatalysatoren (WOKs) auf der Basis von Übergangsmetallen unternommen, wobei mit der Entdeckung der Katalysatorfamilie Ru(bda) (bda: 2,2'-Bipyridin-6,6'-dicarboxylat) Aktivitäten vergleichbar mit der des natürlichen OEC realisiert wurden.[128, 212] Als vielversprechendes Konzept für die Entwicklung von Katalysatoren erwies sich die Konstruktion homogener Katalysatoren, die, ähnlich zu den natürlichen Vorbildern, gezielt mit der zweiten Koordinationssphäre eines äußeren Liganden interagieren.[34-36] Zur Förderung der Katalyse in begrenzter Umgebung entwickelten Würthner und Mitarbeiter zyklische metallosupramolekulare Makrozyklen als leistungsfähige WOKs.[37] Auf Basis theoretischer Berechnungen wurde festgestellt, dass ein geordnetes Wassernetzwerk innerhalb des makrozyklischen Hohlraums die Aktivierungsbarriere des nukleophilen Angriffs von Wasser (WNA, engl.: water nucleophilic attack) verringert, indem es die kooperative Protonenabstraktion während der Katalyse erleichtert (*Kapitel 2.3*).[38] In der hier vorliegenden Arbeit wurden neuartige supramolekulare Konzepte zur enzymartigen Aktivierung von Wassermolekülen entwickelt. Hierbei sollte durch

eine maßgeschneiderte Konstruktion der sekundären Ligandenumgebung von makrozyklischen Ru(bda)-Katalysatoren die anspruchsvolle oxidative Wasserspaltungs-reaktion begünstigt werden.

Um die Auswirkungen der zweiten Koordinationssphäre auf den katalytischen Mechanismus zu untersuchen, wurden in *Kapitel 3* zwei katalytische Ru(bda)-Fragmente in die zyklische zweikernige Umgebung von **dimer 1** eingefügt, welches über funktionalisierte axiale Calix[4]arene-Liganden verfügt. Der schmale untere Rand des Calix[4]arene-Liganden wurde mit vier Oligo(ethylenglykol)-Seitenketten modifiziert, um eine ausreichende Wasserlöslichkeit für katalytische Wasseroxidationsexperimente zu gewährleisten. Zu Beginn wurde der neue Komplex mithilfe von NMR-Spektroskopie, Massenspektrometrie, Elementaranalyse und diffusionsgeordneter Spektroskopie (DOSY, engl.: diffusion-ordered spectroscopy) vollständig charakterisiert. Ferner wies die geometrisch-optimierte Struktur von **dimer 1** darauf hin, dass die beiden Ru-Zentren in das Innere des makrozyklischen Hohlraums ausgerichtet sind. Die katalytische Aktivität von **dimer 1** wurde durch chemische Wasseroxidationsexperimente unter Verwendung von Cer(IV)-ammoniumnitrat (CAN) bei pH 1 und durch photokatalytische Wasseroxidationsexperimente unter Verwendung eines Dreikomponentensystems mit $[Ru(bpy)_3]^{3+}$ (bpy: Bipyridin) als Oxidationsmittel bei pH 7 untersucht (Abbildung 1).
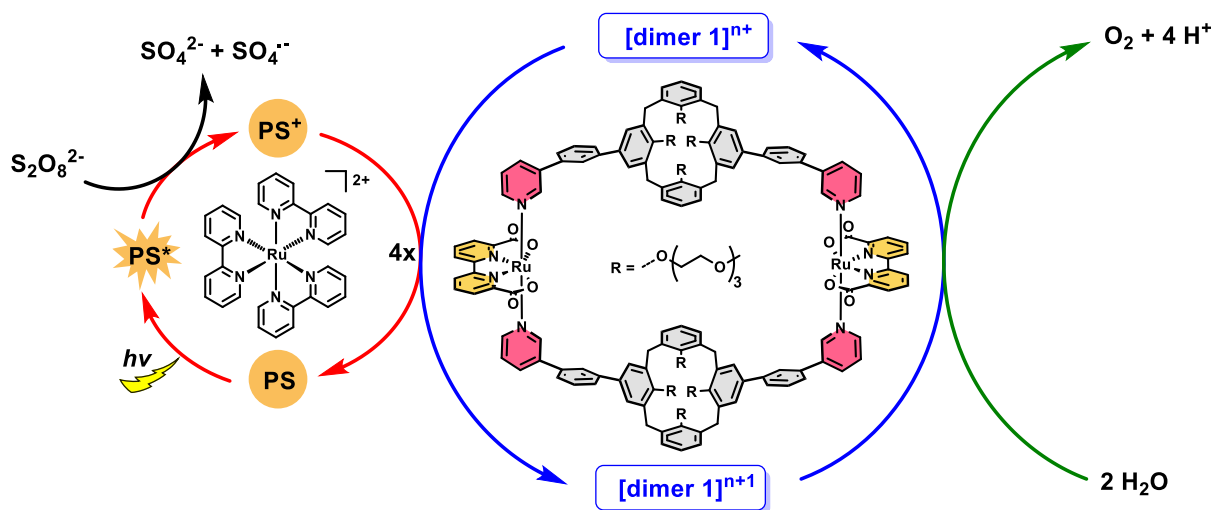
Abbildung 1. Schema der photokatalytischen Wasseroxidation mit **dimer 1** als Wasseroxidationskatalysator, $[Ru(bpy)_3]^{2+}$ als Photosensibilisator (PS) und $Na_2S_2O_8$ als Elektronenakzeptor.

Im Allgemeinen werden unter photokatalytischen Bedingungen deutlich niedrigere katalytische Raten (TOF: Umsatzfrequenz, engl.: turnover frequency) aufgrund der begrenzten Stabilität des verwendeten Photosensibilisators sowie der höheren Komplexität des

Mehrkomponentensystems beobachtet.[146, 148] Interessanterweise wurden für diesen zweikernigen Komplex unter chemischen (TOF(**dimer 1**) = 19 s^{-1}; TOF$_{Ru}$(**dimer 1**) = 9.5 s^{-1}) und photokatalytischen (TOF(**dimer 1**) = 15.5 s^{-1}; TOF$_{Ru}$(**dimer 1**) = 7.75 s^{-1}) Bedingungen nahezu vergleichbare katalytische Raten bestimmt. Anhand von postkatalytischen massenspektrometrischen Untersuchungen des Reaktionsgemischs konnte die oxidative Zersetzung der Methyleneinheiten als Teil des axialen Calix[4]arene-Liganden als Hauptdeaktivierungsweg des Katalysators bei pH 1 nachgewiesen werden. In dieser Hinsicht ergibt sich durch die zyklische zweikernige Umgebung von **dimer 1** eine viel höhere Katalysatorstabilität unter neutralen Bedingungen und ermöglicht somit katalytische Wasseroxidationsstudien unter stark verdünnten Bedingungen. Darüberhinaus wurde anhand von kinetischen Studien ein Wechsel des Wasseroxidationsmechanismus vom bimolekularen I2M (Wechselwirkung zweier Metalloxid-Einheiten, engl.: interaction of two metal-oxyl species) Mechanismus, der üblicherweise für Ru(bda)-Komplexe beobachtet wird,[128] zu einem unimolekularen WNA Mechanismus für **dimer 1** festgestellt.

Im folgenden *Kapitel 4* wurde ein neuartiger, von Enzymen inspirierter Ansatz vorgestellt, bei dem das katalytische Ru(bda)-Fragment in die begrenzte Umgebung des zyklischen einkernigen Komplexes **M1** (X = N) eingegliedert wurde. Der axiale Ligand ist mit einer Erkennungsstelle ausgestattet, um die Präorganisation von Wassermolekülen vor dem aktiven Zentrum zu begünstigen (Abbildung 2a). Als Referenz wurde der nicht funktionalisierte Komplex **M2** (X = CH) synthetisiert (Abbildung 2a). Wie in Abbildung 2b und c dargestellt, wurden für den basenfunktionalisierten WOK **M1** unter sauren (lineare Abhängigkeit) sowie neutralen (quadratische Abhängigkeit) Bedingungen unterschiedliche Reaktionskinetiken beobachtet. Im Gegensatz dazu zeigte die Referenz **M2** unter beiden Bedingungen die erwartete Abhängigkeit zweiter Ordnung, welches auf den bimolekularen I2M Mechanismus hinweist. Nachfolgende pH-abhängige Studien zum kinetischen Isotopeneffekt (KIE, engl.: kinetic isotope effect) bestätigten den beobachteten mechanistischen Wechsel für Komplex **M1** von einem sehr ineffizienten bimolekularen I2M Mechanismus bei pH 7 zu einem sehr effektiven unimolekularen WNA Mechanismus bei pH 1 (Abbildung 2b,c). Daraus ergibt sich ein außergewöhnlich hoher durchschnittlicher TOF-Wert von 140 s^{-1} für **M1** unter chemischen Oxidationsbedingungen, der deutlich verbessert ist im Vergleich zum Referenzmolekül **M2** (TOF = 18−54 s^{-1}) und dem zuvor berichteten Makrozyklus **MC3** (TOF$_{Ru}$ = 45 s^{-1}).[37, 40]

a) **Konzeptioneller Entwurf**   **Molekularer Entwurf**

**Enzymartige Bindungstasche zur
Präorganisation von Wassermolekülen**

X = N   **M1**
X = C-H **M2**

b) **Chemische Wasseroxidation (pH 1)**   c) **Photokatalytische Wasseroxidation (pH 7)**
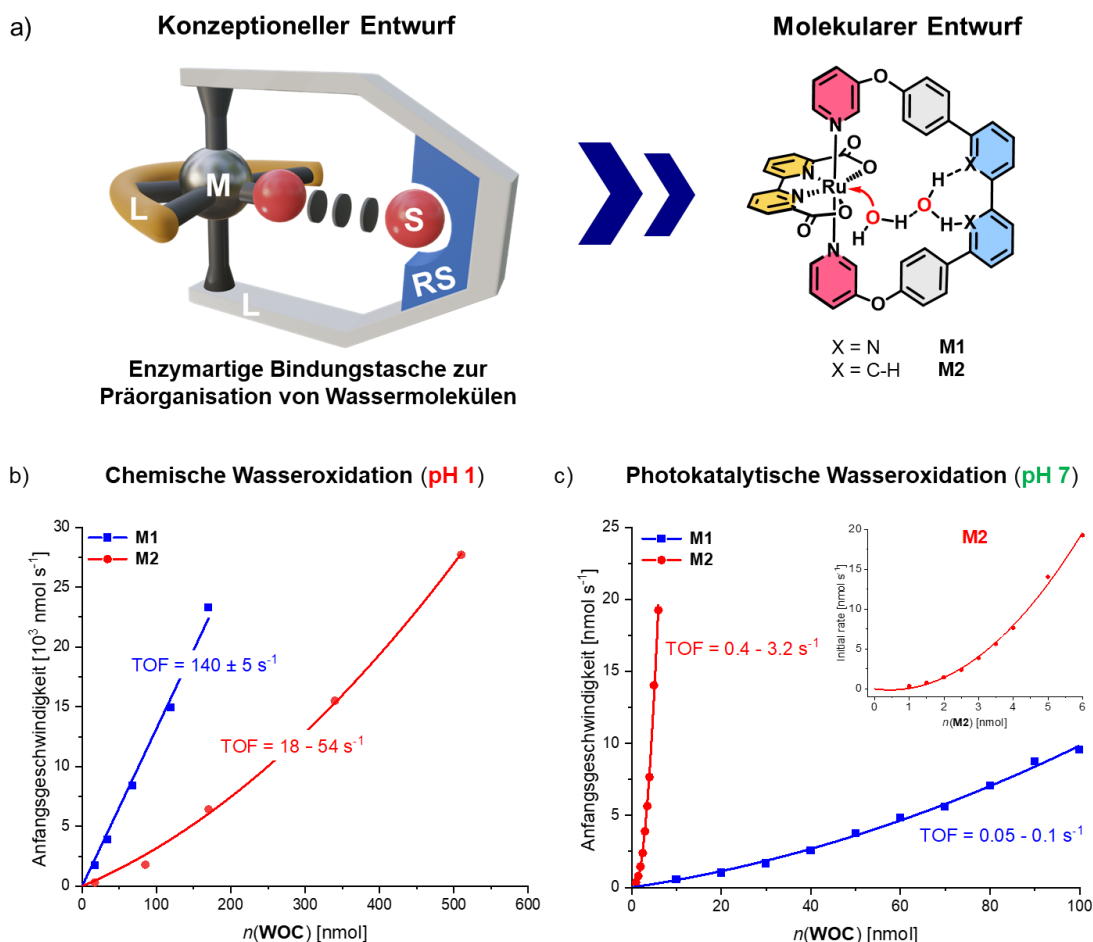
Abbildung 2. a) Konzeptioneller Entwurf für eine enzymartige Bindungstasche zur Präorganisation von Wassermolekülen (M = Metall, L = axialer/äquatorialer Ligand, S = Substrat, RS = Erkennungsstelle) und auf diesem Konzept basierende zyklische mononukleare Ru(bda)-Komplexe **M1** (X = N) und **M2** (X = CH). b) Chemische und c) photokatalytische Wasseroxidationskatalyse mit **M1** und **M2**. Für Einzelheiten zu den Versuchsbedingungen siehe *Kapitel 4*.

Detaillierte Röntgen-Einkristallstrukturanalysen von beiden Komplexen im Ru^{II}-Zustand unter neutralen Bedingungen und von Komplex **M1** in einem vorherrschenden Ru^{III}-Zustand nach saurer katalytischer Wasseroxidation gewährten beispiellose strukturelle Einblicke in die konformative Ausrichtung der axialen Liganden in Abhängigkeit vom pH-Wert (Abbildung 3). Bei pH 7 stabilisieren schwache Wasserstoffbrückenbindungen zwischen den axialen und äquatorialen Liganden die jeweiligen Konformationen von **M1** bzw. **M2**. Dies führt entweder zu einer Fixierung des axialen Liganden über dem bda-Gerüst für **M1** (Abbildung 3a) oder zu einer lateralen Ausrichtung des makrozyklischen Liganden wie im Fall von **M2** (Abbildung 3b). Im Gegensatz dazu hebt die Protonierung der Bipyridineinheit von **M1** die schwachen Wasserstoffbrückenbindungen bei pH 1 auf und führt zu einer Drehung des Liganden (Abbildung 3c). Infolgedessen entsteht eine enzymartige Bindungstasche, in der mehrere Wassermoleküle durch Wasserstoffbrückenbindungen vor dem siebenfach koordinierten

Ru^{III}−OH$_2$ Zentrum in [(**M1**+H)(H$_2$O)]$^{2+}$(PF$_6^-$)$_2$ präorganisiert sind (Abbildung 3d). Darüber hinaus ermöglichte dieses intrakavitäre Wassernetzwerk einen bemerkenswerten strukturellen Einblick in die Entstehung der O−O-Bindung, da hier ein zweites Wassermolekül in der Nähe des aktiven Zentrums für den entscheidenden nukleophilen Angriff von Wasser präorganisiert wird. Diese Ergebnisse zeigen die Wirksamkeit eines enzymartigen Bindungstaschendesigns, indem die protonierte Bipyridineinheit als eine akzeptierende Stelle für Wasserstoffbrückenbindungen genutzt wird, um Wassermoleküle vor dem aktiven Zentrum zu positionieren und damit den WNA Mechanismus zu beschleunigen.
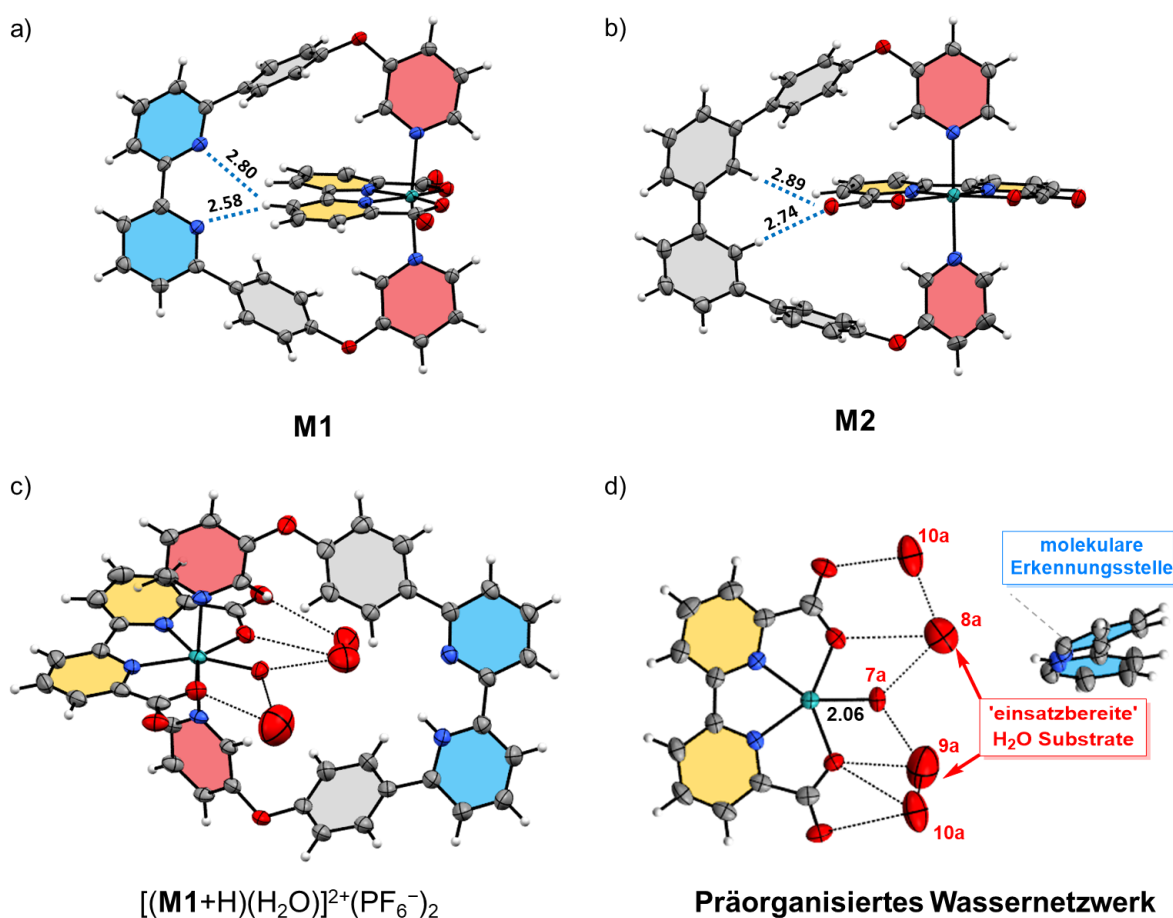
Abbildung 3. Röntgen-Einkristallstrukturanalyse von a) **M1**, b) **M2** und c) [(**M1**+H)(H$_2$O)]$^{2+}$(PF$_6^-$)$_2$. In d) wird die Hauptbesetzung (66.2%) innerhalb der supramolekularen Kavität von [(**M1**+H)(H$_2$O)]$^{2+}$(PF$_6^-$)$_2$ veranschaulicht, worin ein Netzwerk aus Wassermolekülen für den nukleophilen Angriff zur Bildung der O−O-Bindung präorganisiert sind. Organische Lösungsmittelmoleküle und PF$_6^-$ Gegenionen sind aus Gründen der Übersichtlichkeit ausgeblendet. Röntgen-Einkristalle gezeigt als thermische Ellipsoide mit 50 %-iger Wahrscheinlichkeit. C, grau; H, weiß; O, rot; N, violett; Ru, türkis.

Zur Erhöhung der strukturellen Flexibiliät sowie zur Förderung der maßgeschneiderten Faltung von makrozyklischen Ru-WOKs unterschiedlicher Größe wurde in *Kapitel 5* das sauerstoffverbrückte Ligandengerüst von **2C−4C** mittels Entfernung der Phenyleinheiten

modifiziert (Abbildung 4a). Dadurch sollte eine unmittelbare Nähe der basischen Einheit zum jeweiligen Ru-Zentrum erreicht werden, um protonengekoppelte Elektronentransferprozesse (PCETs, engl.: proton-coupled electron transfers) bei pH 7 zu erleichtern und die Bildung der O−O-Bindung zu begünstigen (Abbildung 4). Anhand von Röntgen-Einkristallstrukturanalysen der Komplexe **2C−4C** unter neutralen Bedingungen wurde eine erhöhte Tendenz zur intramolekularen Faltung für die größeren drei- und vierkernigen Ru-Komplexe aufgrund intramolekularer $\pi-\pi$-Wechselwirkungen zwischen den axialen Bipyridineinheiten nachgewiesen (Abbildung 4b,c). Unter den Bedingungen der chemischen Wasseroxidation konnte eine konstante TOF pro Ru-Zentrum von ≈50 s^{-1} für die gesamte Komplexreihe gemessen werden. Dagegen wurde unter photokatalytischen Bedingungen ein bemerkenswerter Anstieg der katalytischen Aktivität pro Ru-Zentrum in der Serie **2C−4C** von 5.5 s^{-1}, 14 s^{-1} zu 15.5 s^{-1} festgestellt, welche alle dem WNA Mechanismus unterliegen. Detaillierte kinetische Studien ergaben einen Anstieg des kinetischen H/D Isotopeneffekts in Richtung der größeren Makrozyklen bei pH 7. Dagegen wurde bei pH 1 keine Änderung des Mechanismus beobachtet. Auf der Grundlage elektrochemischer Studien wurde eine kathodische Verschiebung der geschwindigkeitsbestimmenden Ru^{IV}/Ru^{V}-Oxidation für **2C−4C** festgestellt. Diese Verschiebung lässt sich durch einen ausgeprägteren Beitrag der nahen, protonenaufnehmenden Einheit im geschwindigkeitsbestimmenden Schritt des Mechanismus für die größeren Makrozyklen erklären, die mit der gesteigerten katalytischen Rate unter photokatalytischen Bedingungen für **2C−4C** übereinstimmen. Bei pH 1 verhindert hingegen die bevorzugte *cis*-Orientierung der Bipyridiniumkationen den gefalteten Zustand und schaltet damit die Protonenrelais-Funktion der basischen Struktureinheit aus.
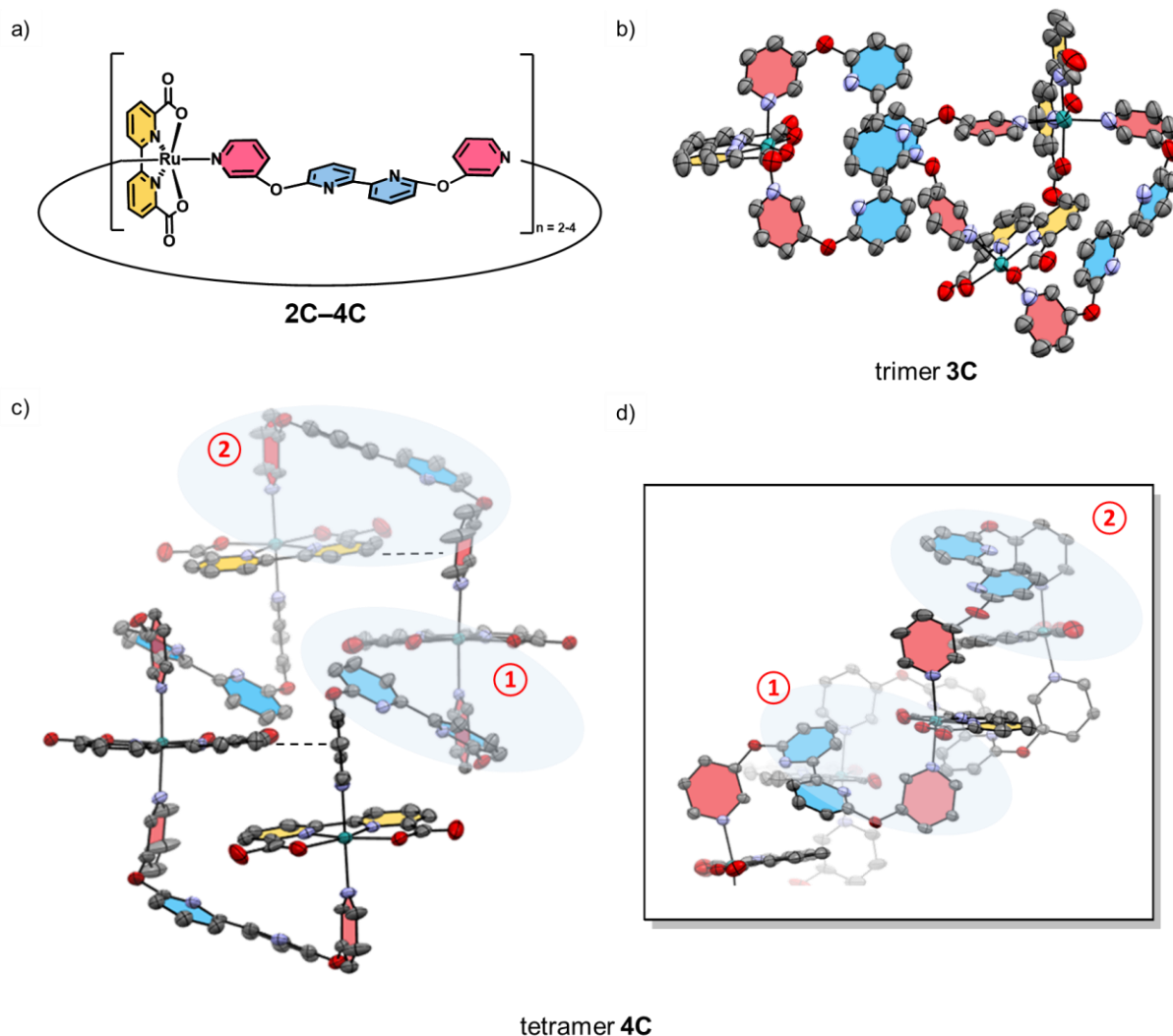
Abbildung 4. a) Chemische Strukturen der multinuklearen Ru(bda)-Komplexe **2C−4C**. Röntgen-Einkristallstrukturen von b) Trimer **3C**, c) Tetramer **4C** und ein d) Ausschnitt aus der Röntgen-Einkristallstruktur von **4C** um die unmittelbare Nähe der Base zum Ru-Zentrum darzustellen. Organische Lösungsmittelmoleküle sind aus Gründen der Übersichtlichkeit ausgeblendet. Röntgen-Einkristalle gezeigt als thermische Ellipsoide mit 50 %-iger Wahrscheinlichkeit. C, grau; H, weiß; O, rot; N, violett; Ru, türkis.

Zusammenfassend wurden im Rahmen dieser Dissertation neuartige, bioinspirierte makrozyklische Wasseroxidationskatalysatoren entwickelt, die die anspruchsvolle oxidative Wasserspaltungsreaktion durch enzymartige Aktivierung von Wassermolekülen begünstigen. Um die Bindungstasche natürlicher Enzyme zu imitieren, wurden die katalytischen Ru(bda)-Einheiten in definierte makrozyklische Nanostrukturen eingebettet, welche über protonenakzeptierende Einheiten zur Präorganisation von Wassermolekülen vor dem katalytisch aktiven Zentrum verfügen. Als besonderes Highlight dieser Arbeit wurde in *Kapitel 4* ein einkerniger Ru(bda)-Komplex mit einer erhöhten katalytischen Aktivität bei pH 1 vorgestellt. Für diesen Komplex wurde eine verstärkte Katalysator-Substrat-Wechselwirkung

aufgrund eines präorganisierten Wassernetzwerks innerhalb der enzymartigen Bindungstasche festgestellt. Dagegen wurde bei dem in *Kapitel 5* beschriebenem flexibleren molekularen Ligandengerüst die katalytisch aktiveren, gefalteten Konformationen unter neutralen Bedingungen gebildet, woraus eine verstärkte Wechselwirkung des katalytischen Ru-Zentrums mit intrakavitären Wassermolekülen resultierte. Ebenso begünstigt die gefaltete Konformation die Protonenabstraktion durch die nahegelegene protonenakzeptierende Einheit innerhalb des geschwindigkeitsbestimmenden Schritts der O−O-Bindungsbildung des WNA Mechanismus, woraus eine beschleunigte Sauerstoffentwicklung hervorgeht. In der vorliegenden Dissertation wurde der Einfluss der sekundären Koordinationssphäre auf das Wassernetzwerk zur Förderung der Oxidation von Wasser zu molekularen Sauerstoff nach dem WNA Mechanismus demonstriert. Die im Rahmen dieser Arbeit gewonnen Erkenntnisse zur Beschleunigung von protongekoppelten Elektronentransferprozessen als Teil des mechanistischen Reaktionsweges können einen Beitrag zur Entwicklung von effizienten molekularen Katalysatoren für die Wasseroxidation leisten oder als Inspiration für viele andere Arten von katalytischen Umwandlungen dienen.

Chapter 8

Appendix

8.1 Supporting Information for *Chapter 3*

Materials and methods

General

All reagents and solvents were purchased from commercial sources and used without further purification, unless otherwise stated. The starting material 4-*tert*-butylcalix[4]arene (**34**) was purchased from Alfa Aesar. 2,2'-Bipyridine-6,6'-dicarboxylic acid,[328] [RuCl$_2$(dmso)$_4$],[329, 330] [Ru(bda)(dmso)$_2$],[268] 3-(3-bromo-phenyl) pyridine,[267] 3-(3-(4,4,5,5-tetramethyl-1,3,2-dioxa-borolan-2-yl)phenyl)pyridine[267] (**41**) and tri(ethylene glycol) monomethyl ether tosylate[266] (**36**) were synthesized according to literature known procedures. Anhydrous toluene, acetonitrile and DMF were prepared using a Pure Solv MD-5 solvent purification system (Innovative Technology). All experiments in aqueous solutions were performed either in phosphate buffer pH 7 (Honeywell) or deionized water obtained from a Purelab Classic water purification system (ELGA). The purification of the crude compounds were performed, where specified, by column chromatography using silica gel (60M, 0.04−0.063 mm, Macherey-Nagel).

^{1}H NMR and proton decoupled ^{13}C NMR spectra were recorded at 600 Mhz, 400 MHz and 100 MHz, respectively, using a Bruker Avance III HD 400 or Bruker Avance III HD 600 spectrometer at 298 K. Chemical shifts (δ) are stated in parts per million (ppm) relative to the residual undeuterated solvent signal[331] and coupling constants (*J*) in Hz. The following abbreviations were applied to describe signal multiplicities: s = singlet, d = doublet, t = triplet and m = multiplet. For a correct assignment of 1D NMR spectra of new compounds 2D NMR spectra (COSY, NOESY, HSQC and HMBC) were recorded. High resolution electrospray ionization (HR-ESI) mass spectra were measured using a ESI micrOTOF focus or a ESI micrOTOF-Q III mass spectrometer (Bruker Daltonics). Elemental analysis was performed using a Vario MICRO cube (Elementar Analysensysteme). Melting points were determined

using a BX41 optical microscope (Olympus) connected with a temperature controller TP94 (Linkam Scientific Instruments Ltd.) and are uncorrected.

Electrochemistry

Cyclic voltammetry (CV) and differential pulse voltammetry (DPV) measurements were performed at a BAS Cell Stand C3 (BAS Epsilon) with a standard three-electrode configuration (working electrode: glassy carbon, counter electrode: Pt wire, reference electrode: Ag/AgCl (3 M KCl). CV and DPV were recorded at a scan rate of 100 mV s^{-1} and 20 mV s^{-1}. The experiments were carried out in a 4:6 solvent mixture of 2,2,2-trifluorethanol/water either at pH 1 (triflic acid) or at pH 7 (phosphate buffer). The Ag/AgCl (3 M KCl) potential values were added up to +0.21 V to obtain NHE potentials.[332]

Spectroelectrochemistry

Spectroelectrochemistry in reflexion mode was performed in an Agilent Cary 5000 spectrometer in combination with a home-built sample compartment consisting of a cylindrical PTFE cell with a sapphire window and an adjustable three-in-one electrode (6 mm platinum disc working electrode, 1 mm platinum counter and pseudo reference electrode) with a layer thickness of ~100 µM. The experiments were carried out at a sample concentration of c = 0.24 mM in 4:6 acetonitrile/water (pH 7, phosphate buffer). The potential was referenced to the first oxidation event as it was determined by differential pulse voltammetry (DPV) against a Ag/AgCl reference electrode (3 M KCl).

UV/Vis absorption and emission spectroscopy

UV/Vis absorption spectra were recorded at a Jasco V-670 spectrometer at 25 °C in 1 cm quartz cuvettes with spectroscopic grade solvents. The chemical water oxidation catalysis in the presence of stoichiometric amounts of cerium ammonium nitrate (CAN) was investigated by monitoring the decay of the CAN absorption at 360 nm at a) fixed catalyst concentration and varying CAN concentration (c(cat.) = 1.2 µM, c(CAN) = 1.0−3.0 mM) and b) fixed CAN concentration and varying catalyst concentration (c(cat.) = 0.3−1.2 µM, c(CAN) = 2.0 mM). The studies were performed in 4:6 acetonitrile/water (pH 1, acid: nitric acid) as followed: 1.99 mL of a freshly prepared cerium ammonium nitrate solution were mixed with 10 µL of the catalyst solution. Afterwards the cuvette was shaken and placed inside the spectrometer. After equilibration of the solution for 30 s the CAN absorption decay at 360 nm (ε_{360} = 680 M^{-1} cm^{-1}) was recorded for 600 s.

Chemical water oxidation

Chemical water oxidation measurements were performed at 20 °C in reaction vessels (V = 20.6 mL) connected to SSCDANN030PAAA5 pressure sensors (Honeywell, absolute pressure, 0 to 30 psi). For each measurement, 1.0 g (1.82 mmol) CAN was dissolved in 3.0 mL of 4:6 acetonitrile/water mixture (pH 1, triflic acid) and the catalyst solution (400 μL in the same solvent mixture) was injected through a septum using a Hamilton syringe. At the end of the gas evolution, 500 μL of the gas head space was injected using a gas tight Hamilton syringe into a gas chromatograph GC-2010 Plus (Shimadzu, thermal conductivity detector at 30 mA, argon as carrier gas) to determine the gas composition. The turnover number (TON) was calculated based on the total amount of oxygen evolved during catalysis divided by the amount of injected catalyst. The amount of evolved oxygen was determined by the pressure increase in the reaction vessel using the ideal gas law: $\Delta p \times V = \Delta n \times R \times T$ (T = 293.15 K, V = 20.6 mL, R = 8.314 J K^{-1} mol^{-1}). In concentration-dependent measurements a TON was calculated for each concentration and the highest TON is reported. The turnover frequency (TOF) was calculated by investigating the initial rate of catalysis for each concentration (linear regression of the oxygen evolution curve during the first two seconds of reaction). The TOF was then determined from the slope of a linear regression of the initial rates vs. the catalyst amount.

Photocatalytic water oxidation

Photocatalytic water oxidation experiments were performed using a Oxygraph Plus Clark-electrode system (Hansatech Instruments Ltd.) for oxygen detection. The samples were irradiated using a 150 W xenon lamp (Newport) equipped with a 400 nm cutoff filter. Irradiation was calibrated to 100 mW cm^{-1} using a PM 200 optical power meter with a S121C sensor (Thorlabs) in combination with a CCS 200/M wide range spectrometer (Thorlabs). For each measurement, a stock solution of [Ru(bpy)$_3$]Cl$_2$ used as photosensitizer (PS) and the sacrificial electron acceptor (Na$_2$S$_2$O$_8$) in an aqueous mixture (pH 7, phosphate buffer) with acetonitrile as organic co-solvent was prepared in the dark (c(Na$_2$S$_2$O$_8$) = 37 mM, c([Ru(bpy)$_3$]Cl$_2$) = 1.5 mM). An aliquot of this solution was transferred to the transparent reaction chamber and then mixed with the catalyst at varying concentrations while kept in the dark. Irradiation was started at 50 s to allow thermal equilibration of the sample in the temperature-controlled chamber at 20 °C. The TON was calculated based on the maximum amount of evolved oxygen during catalysis divided by the amount of used catalyst. In concentration-dependent experiments a TON was calculated for each concentration and the highest TON is reported. The turnover frequency (TOF) was calculated by determining the initial rate of catalysis for each concentration (linear regression of the oxygen evolution curve during the first five to ten seconds of reaction direct after the initial induction period (~1 s). The TOF was then determined from the slope of a linear regression of the initial rates vs. the catalyst amount.

Kinetic Isotope Effect

The experiments were performed using a Oxygraph Plus Clark-electrode system (Hansatech Instruments Ltd.) for oxygen detection at a constant temperature of 20 °C. The kinetic isotope effect was studied in 2.0 mL of a 4:6 acetonitrile/water (H_2O or D_2O (99.9% purity), pH 1, acid: triflic acid) mixture in the presence of CAN (c = 0.525 M) as sacrificial oxidant. For each measurement, 1.5 mL of a freshly prepared CAN solution (c = 0.7 M, 4:6 acetonitrile/water (H_2O or D_2O, pH 1)) was transferred to the transparent reaction chamber and after the baseline was constant (~40 s), 0.5 mL of the catalyst solution at varying concentrations was added. The reaction rates in H_2O ($k(H_2O)$) and D_2O ($k(D_2O)$) were calculated by determining the initial rate of catalysis for each concentration (linear regression of the oxygen evolution curve during the first five to ten seconds of reaction). The reaction rates were then determined from the slope of a linear regression of the initial rates vs. the catalyst amount.

Catalyst stability test under conditions of chemical water oxidation

The following procedure was applied to test the stability of the catalyst after water oxidation catalysis: 10.0 mg (3.0 µmol) of dinuclear complex **dimer 1** was dissolved in 1.0 mL of 4:6 acetonitrile/water mixture (pH 1, triflic acid). After addition of 500 mg (960 µmol) CAN, vigorous oxygen evolution occurred (~40 catalytic cycles). Subsequent addition of 250 mg of ammonium hexafluorophosphate lead to a brown precipitation, which was filtered off, washed with water and dried under high vacuum. Afterwards, the sample was taken up in 1:1 CH_2Cl_2/CH_3OH and ascorbic acid was added for reduction. The so prepared sample was then analyzed by HR-ESI mass spectrometry.

Theoretical calculations

Structure optimization was performed by the semiempirical PM6 method[333] including D3H4 correction (10.1021/ct200751e) by employing the MOPAC2016 program package[334] version 18.346L. Solvation was treated implicitly using the COSMO model for water.[335] The tri(ethylene glycol) chains of the axial calix[4]arene ligands were replaced by methoxy groups for simplification of the calculations.

Experimental Procedures

General information

For the correct assignment of the newly synthesized calix[4]arene-based structures, the generic name "calix[n]arene" was retained and the positions of the substituents in derivatives, particularly in their nomenclature, are specified by numbers that are indicated in the general structure shown in Figure A8.1.1.[336]
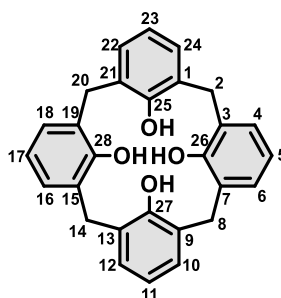
Figure A8.1.1. Structure and numbering of calix[4]arene derivatives in this work exemplarily shown for 25,26,27,28-tetrahydroxycalix[4]arene.[336]

25,26,27,28-Tetrahydroxycalix[4]arene (35)
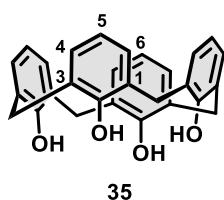
4-tert-Butylcalix[4]arene **34** (5.19 g, 8.00 mmol, 1.0 equiv.) was suspended in dry toluene (50 mL) and $AlCl_3$ (5.87 g, 44.0 mmol, 5.5 equiv.) and phenole (3.76 g, 40.0 mmol, 5.0 equiv.) were added and stirred at room temperature for 4 hours. The mixture was poured into 0.2 M HCl solution and extracted with ethyl acetate (3 x 50 mL). The combined organic phases were dried over anhydrous Na_2SO_4 and the solvent was removed under reduced pressure. Subsequent precipitation from methanol and filtration yielded **35** as a colorless powder (2.89 g, 6.81 mmol, 85%). **m.p.** 315 °C. **^{1}H NMR** (400 MHz, $CDCl_3$, rt): δ [ppm] = 10.2 (s, 4H, Ar-O*H*), 7.05 (d, $^3J_{H-H}$ = 7.6 Hz, 8H, *H-4,6*), 6.74 (t, $^3J_{H-H}$ = 7.6 Hz, 4H, *H5*), 4.26 (br s, 4H, Ar-*CH₂*-Ar), 3.54 (br s, 4H, Ar-*CH₂*-Ar). Analytical data are in accordance with the literature.[265]

25,27-Bis(2-(2-(2-methoxyethoxy)ethoxy)ethoxy))-26,28-dihydroxy-calix[4]arene (37)
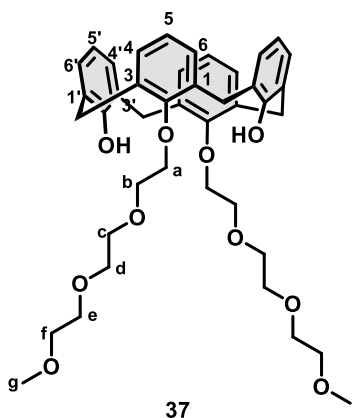
A suspension of calix[4]arene **35** (1.20 g, 2.83 mmol, 1.0 equiv.), tri(ethylene glycol) monomethyl ether tosylate **36** (1.89 g, 5.94 mmol, 2.1 equiv.) and K_2CO_3 (781 mg, 5.65 mmol, 2.0 equiv.) in CH_3CN (24 mL) was heated under reflux (82 °C) for 5 days. After being cooled down to room temperature, the solvent was removed under reduced pressure and the residue was treated with 10% aqueous HCl (40 mL) and dichloromethane (80 mL). The organic phase was washed with water and brine, dried over anhydrous Na_2SO_4 and the solvent was removed under reduced pressure. The residue was purified by column chromatography (SiO_2, dichloromethane/ ethyl acetate 9:1 to 1:1 to pure ethyl acetate) to yield **37** as a colorless solid (989 mg, 1.38 mmol, 49%). **m.p.** 69 °C. **^{1}H NMR** (400 MHz, $CDCl_3$, rt): δ [ppm] = 7.77 (s, 2H, Ar-O*H*), 7.05 (d, $^3J_{H-H}$ = 7.5 Hz, 4H, *H4 & H6*), 6.87 (d, $^3J_{H-H}$ = 7.6 Hz, 4H, *H4' & H6'*), 6.72 (t, $^3J_{H-H}$ = 7.9 Hz, 2H, *H5'*), 6.64 (t, $^3J_{H-H}$ = 7.5 Hz, 2H, *H5*), 4.42 – 4.39 (m, 4H, Ar-*CH_2*-Ar), 4.18 (dd, $^3J_{H-H}$ = 5.6, 4.0 Hz, 4H, *Ha*), 3.99 (dd, $^3J_{H-H}$ = 5.6, 4.0 Hz, 4H, *Hb*), 3.85 (dd, $^3J_{H-H}$ = 5.7, 3.9 Hz, 4H, *Hc*), 3.73 (dd, $^3J_{H-H}$ = 5.7, 3.9 Hz, 4H, *Hd*), 3.64 – 3.61 (m, 4H, *He*), 3.48 – 3.45 (m, 4H, *Hf*), 3.37 – 3.34 (m, 4H', Ar-*CH_2*-Ar), 3.34 (s, 6H, *Hg*). **^{13}C NMR** (100 MHz, $CDCl_3$, rt) δ [ppm] = 153.4, 152.0, 133.5, 129.0, 128.5, 128.2, 125.4, 119.0, 75.5, 72.0, 71.2, 70.9, 70.7, 70.1, 59.1, 31.3. **HRMS** (ESI-TOF, pos. mode, MeCN/$CHCl_3$ 1:1): *m/z* calcd for $C_{42}H_{52}O_{10}+Na^+$: 739.3453 [*M*+Na]$^+$; found: 739.3452. **elemental analysis** calcd (%) for $C_{42}H_{52}O_{10}$: C 70.37, H 7.31; found: C 70.07 H 7.49.

5,17-Dibromo-25,27-bis(2-(2-(2-methoxyethoxy)ethoxy)ethoxy))-26,28-dihydroxy-calix[4]arene (38)
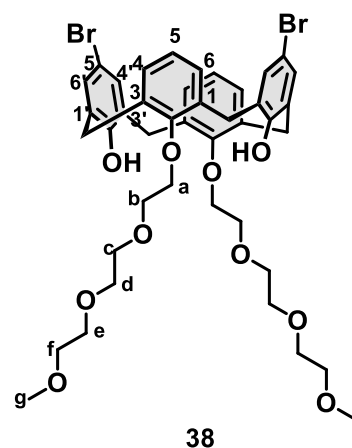
Calix[4]arene derivative **37** (870 mg, 1.21 mmol, 1.0 equiv.) was dissolved in $CHCl_3$ (50 mL) and a solution of Br_2 (148 µL, 2.67 mmol, 2.2 equiv.) in $CHCl_3$ (35 mL) was added dropwise over 1.5 hours at 0 °C. After stirring for additional 15 min the reaction was quenched with 5% $NaHSO_3$ solution (50 mL). The organic phase was separated and washed with water (50 mL) and brine (50 mL) and the combined organic phases were dried over anhydrous Na_2SO_4. The solvent was evaporated under reduced pressure to give product **38** (1.06 g, 1.21 mmol, quant.) as a colorless solid. **m.p.** 130 °C. **^{1}H NMR** (400 MHz, $CDCl_3$, rt):

δ [ppm] = 7.88 (s, 2H, Ar-O*H*), 7.16 (s, 4H, *H4' & H6'*), 6.89 (d, $^3J_{H-H}$ = 7.5 Hz, 4H, *H4 & H6*), 6.80 – 6.76 (m, 2H, *H5*), 4.37 (d, $^2J_{H-H}$ = 13.1 Hz, 4H, Ar-*CH₂*-Ar), 4.17 - 4.14 (m, 4H, *Ha*), 3.97 - 3.94 (m, 4H, *Hb*), 3.83 – 3.80 (m, 4H, *Hc*), 3.72 – 3-69 (m, 4H, *Hd*), 3.62 - 3.59 (m, 4H, *He*), 3.47 - 3.44 (m, 4H, *Hf*), 3.34 (s, 6H, *Hg*), 3.29 (d, $^2J_{H-H}$ = 13.2 Hz, 4H, Ar-*CH₂*-Ar). **¹³C NMR** (100 MHz, CDCl₃, rt) *δ* [ppm] = 152.6, 152.0, 132.8, 130.9, 130.2, 129.4, 125.6, 110.4, 75.6, 72.0, 71.2, 70.9, 70.8, 70.1, 59.2, 31.1. **HRMS** (ESI-TOF, pos. mode, MeCN/CHCl₃ 1:1): *m/z* calcd for $C_{42}H_{50}Br_2O_{10}+Na^+$: 895.1663 [*M*+Na]⁺; found: 895.1669. **elemental analysis** calcd (%) for $C_{42}H_{50}Br_2O_{10}$: C 57.68, H 5.76; found: C 57.24, H 5.96.

5,17-Dibromo-25,26,27,28-tetrakis(2-(2-(2-methoxyethoxy)ethoxy)ethoxy))-calix[4]arene (40)

40
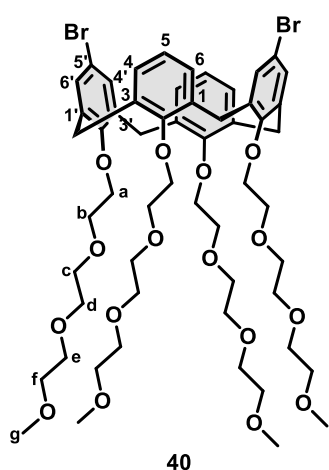
To a solution of calix[4]arene derivative **38** (1.20 g, 1.37 mmol, 1.0 equiv.) in dry DMF (45 mL) was added NaH (164 mg, 6.86 mmol, 5.0 equiv.) and the mixture was stirred at room temperature for 30 min. Subsequently diethyleneglycol-2-bromoethyl methyl ether **39** (1.21 mL, 6.86 mmol, 5.0 equiv.) was added and stirred at 60 °C for 8 days. After cooling to room temperature, water (20 mL) was added and the solvent was removed under reduced pressure. The residue was diluted with dichloromethane (20 mL) and the organic phase was washed with water (30 mL) and brine (30 mL). The combined organic phases were dried over anhydrous Na₂SO₄ and the solvent was removed under reduced pressure. The residue was purified by column chromatography (SiO₂, ethyl acetate to ethyl acetate/methanol 100:1) to yield **40** (1.11 g, 951 μmol, 69%) as a brown oil. **¹H NMR** (400 MHz, CDCl₃, rt): *δ* [ppm] = 6.79 (s, 4H, *H4' & H6'*), 6.57 (s, 6H, *H4, H5, H6*), 4.42 (d, $^2J_{H-H}$ = 13.4 Hz, 4H, Ar-*CH₂*-Ar), 4.11 − 4.05 (m, 8H, *Ha*), 3.83 - 3.80 (m, 8H, *Hb*), 3.61 − 3.56 (m, 24H, *Hc, Hd, He*), 3.51 − 3.48 (m, 8H, *Hf*), 3.34 (d, 12H, *Hg*), 3.07 (d, $^2J_{H-H}$ = 13.5 Hz, 4H, Ar-*CH₂*-Ar). **¹³C NMR** (100 MHz, CDCl₃, rt) *δ* [ppm] = 156.0, 155.8, 137.5, 134.2, 130.9, 128.5, 122.9, 115.0, 73.2, 72.1, 70.8, 70.8, 70.7, 70.7, 70.6, 70.5, 70.5, 70.5, 59.2, 30.9. **HRMS** (ESI-TOF, pos. mode, MeCN/CHCl₃ 1:1): *m/z* calcd for $C_{56}H_{78}Br_2O_{16}+Na^+$: 1187.3549 [*M*+Na]⁺; found: 1187.3549. **elemental analysis** calcd (%) for $C_{56}H_{78}Br_2O_{16}$: C 57.63, H 6.74; found: C 57.81, H 6.86.

5,17-Bis(3,1-(phenylene)pyridine)-25,26,27,28-tetrakis(2-(2-(2-methoxyethoxy)ethoxy)ethoxy))-calix[4]arene (42)
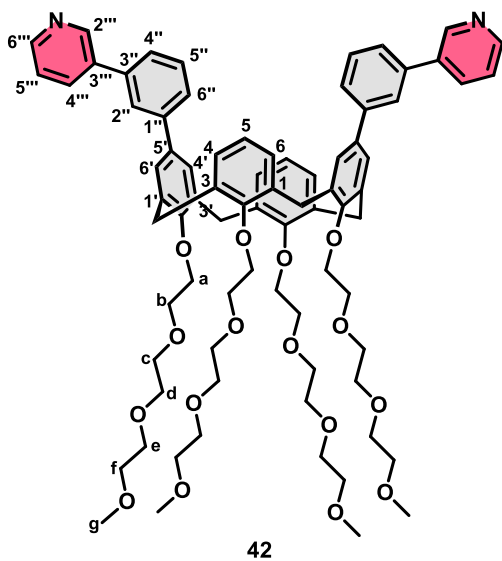
42

A mixture of precursor **40** (291 mg, 250 µmol, 1.0 equiv.), 3-(3-(4,4,5,5-tetramethyl-1,3,2-dioxaborolan2-yl)phenyl)pyridine **41** (147 mg, 525 µmol, 2.1 equiv.) and Cs_2CO_3 (244 mg, 750 µmol, 3.0 equiv.) in dioxane (1.8 mL) and water (0.2 mL) was degassed under nitrogen by three consecutive freeze-pump-thaw cycles. Subsequently, $Pd(PPh_3)_4$ (115 mg, 100 µmol, 0.4 equiv.) was added and the resulting mixture was heated under reflux for 6 days under nitrogen. After cooling down to room temperature, the solvent was removed under reduced pressure and the residue was diluted with dichloromethane (20 mL). The organic phase was separated and the aqueous phase extracted with dichloromethane (3 x 25 mL). The combined organic phases were dried over anhydrous Na_2SO_4 and concentrated under reduced pressure. The residue was purified by flash chromatography (SiO_2, ethyl acetate to ethylacetate/methanol 9:1) to yield calix[4]arene derivative **42** (71.9 mg, 54.7 µmol, 22%) as a yellow oil. **^{1}H NMR** (400 MHz, $CDCl_3$, rt): δ [ppm] = 8.71 (d, $^4J_{H-H}$ = 1.7 Hz, 2H, *H2'''*), 8.55 (dd, $^3J_{H-H}$ = 4.8 Hz, $^4J_{H-H}$ = 1.6 Hz, 2H, *H6'''*), 7.74 (ddd, $^3J_{H-H}$ = 7.9 Hz, $^4J_{H-H}$ = 2.2 Hz, $^4J_{H-H}$ = 1.7 Hz, 2H, *H4'''*), 7.36 (s, 2H, *H2''*), 7.33 − 7.28 (m, 4H, *H4'' & H5'''*), 7.20 − 7.04 (m, 4H, *H5'' & H6''*), 6.94 (s, 4H, *H4' & H6'*), 6.67 (d, $^3J_{H-H}$ = 7.3 Hz, 4H, *H4 & H6*), 6.59 (dd, $^3J_{H-H}$ = 8.2, 6.6 Hz, 2H, *H5*), 4.56 (d, $^2J_{H-H}$ = 13.3 Hz, 4H, Ar-*CH$_2$*-Ar), 4.20 − 4.16 (m, 4H, *Ha*), 3.93 − 3-90 (m, 4H, *Hb*), 3.68 − 3.60 (m, 24H, *Hc, Hd, He*), 3.54 − 3.50 (m, 8H, *Hf*), 3.36 (s, 6H, *Hg*), 3.34 (s, 6H, *Hg*), 3.22 (d, $^2J_{H-H}$ = 13.5 Hz, 4H, Ar-*CH$_2$*-Ar). **^{13}C NMR** (100 MHz, $CDCl_3$, rt) δ [ppm] = 156.6, 156.3, 148.5, 148.4, 142.0, 137.7, 136.5, 135.7, 134.9, 134.7, 134.3, 129.2, 128.5, 127.1, 126.5, 125.4, 125.0, 123.6, 122.6, 73.3, 73.2, 72.1, 72.1, 70.8, 70.8, 70.7, 70.7, 70.6, 59.2, 59.2, 31.2. **HRMS** (ESI-TOF, pos. mode, MeCN/CHCl$_3$ 1:1): *m/z* calcd for $C_{78}H_{94}N_2O_{16}$+Na$^+$: 1337.6496 [*M*+Na]$^+$; found: 1337.6479. **elemental analysis** calcd (%) for $C_{78}H_{94}N_2O_{16}$ · H_2O: C 70.25, H 7.26, N 2.10; found: C 69.93, H 7.35, N 2.00.

[Ru(bda)(5,17-bis(3,1-(phenylene)pyridine)-25,26,27,28-tetrakis(2-(2-(2-methoxyethoxy)ethoxy) ethoxy))-calix[4]arene]₂ (dimer 1)

dimer 1

R =
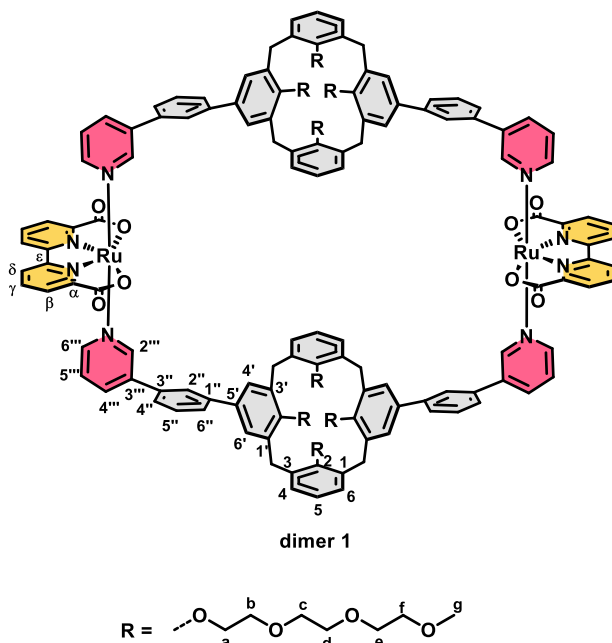
[Ru(bda)(dmso)₂] **43** (36.0 mg, 72.0 µmol, 1.0 equiv.) and calix[4]arene ligand **42** (113 mg, 86.4 µmol, 1.2 equiv.) were dissolved in a degassed mixture of chloroform (6 mL) and methanol (6 mL) and stirred for 42 hours at 60 °C under nitrogen. After cooling to room temperature, the solvent was removed under reduced pressure. The residue was purified by column chromatography (SiO₂, dichloromethane/methanol 10:0.1 to 10:2) and subsequent precipitation with *n*-hexane to yield **dimer 1** (119 mg, 35.8 µmol, 50%) as a dark red solid. **m.p.** 175 °C. **¹H NMR**

(400 MHz, CD₂Cl₂/CD₃OD (1:1), rt): δ [ppm] = 9.34 (d, ³J_{H-H} = 7.3 Hz, 4H, *Hδ*), 8.19 (t, ³J_{H-H} = 7.7 Hz, 4H, *Hγ*), 8.12 (d, ³J_{H-H} = 7.6 Hz, 4H, *Hβ*), 8.02 (br s, 4H, *H2'''*), 7.85 (br s, 4H, *H6'''*), 7.49 (d, ³J_{H-H} = 8.2 Hz, 4H, *H5'''*), 7.26 – 7.22 (m, 4H, *H4'''*), 7.10 (d, ³J_{H-H} = 7.5 Hz, 8H, *H4,6*), 6.87 (t, ³J_{H-H} = 7.4 Hz, 4H, *H5*), 6.60 (s, 4H, *H2''*), 6.31 (d, ³J_{H-H} = 7.6 Hz, 4H, *H4''*), 6.22 (s, 8H, *H4' & H6'*), 6.17 (d, ³J_{H-H} = 7.9 Hz, 4H, *H6''*), 5.91 (t, ³J_{H-H} = 7.7 Hz, 4H, *H5''*), 4.49 (m, 8H, Ar-*CH₂*-Ar), 4.32 – 4.29 (m, 8H, *Ha*), 3.96 – 3.90 (m, 16H, *Ha & Hb*), 3.80 – 3.75 (m, 8H, *Hb*), 3.64 – 3.61 (m, 8H, *Hc*), 3.60 – 3.50 (m, 40H, *Hd & He*), 3.46 – 3.42 (m, 16H, *Hf*), 3.28 (s, 12H, *Hg*), 3.24 (s, 12H, *Hk*), 3.13 (d, ²J_{H-H} = 13.5 Hz, 8H, Ar-*CH₂*-Ar). **¹³C NMR** (100 MHz, CD₂Cl₂/CD₃OD (1:1), rt): δ [ppm] = 174.5, 160.8, 158.8, 157.5, 155.4, 151.3, 150.1, 142.5, 137.9, 137.5, 134.7, 134.7, 134.6, 134.4, 133.3, 129.6, 128.9, 127.0, 126.9, 126.8, 126.6, 125.4, 124.7, 123.8, 122.7, 74.6, 73.2, 72.4, 72.4, 71.5, 71.1, 71.1, 71.0, 70.9, 58.9, 58.9, 31.4. **UV/Vis** (CH₃CN/H₂O 4:6 (pH 1)): λ_{max} (ε) = 255 (128560), 301 (64350), 349 (22855), 459 (7770), 496 nm (7224 M⁻¹ cm⁻¹); (CH₃CN/H₂O 4:6 (pH 7)): λ_{max} (ε) = 255 (129830), 305 (55340), 354 (25470), 459 (9718), 496 nm (8260 M⁻¹ cm⁻¹). **HRMS** (ESI-TOF, pos. mode, MeOH/CH₂Cl₂ 1:1): *m/z* calcd for $C_{180}H_{200}N_8O_4Ru_2+Na^{2+}$: 1670.0954 [*M*+Na]²⁺; found: 1670.0917. **elemental analysis** calcd (%) for $C_{180}H_{200}N_8O_4Ru_2 \cdot H_2O$: C 64.81, H 6.10, N 3.36; found: C 64.51, H 6.09, N 3.49.

Theoretical calculations
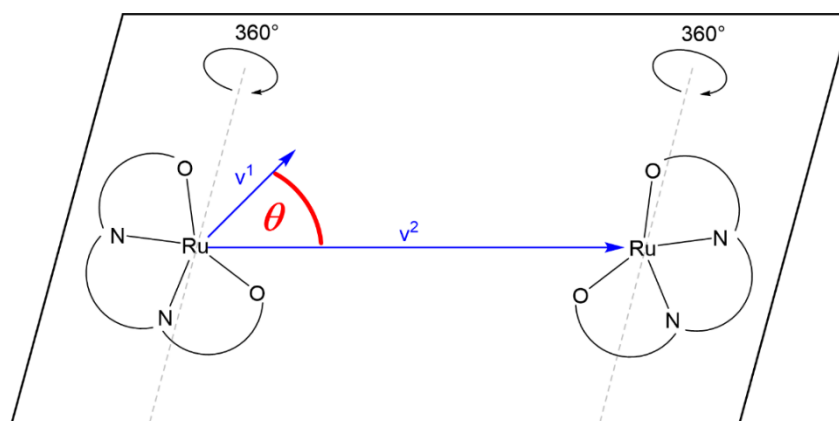
Figure A8.1.2. Definition of the rotation angle θ used to assess the rotation of the Ru(bda) unit around the axial coordinative bonds within the dinuclear structure of dimer 1. Although the definition of the angle θ is only shown for one of the Ru(bda) units for the sake of clarity, it was defined for the other Ru(bda) unit in an analogue way and rotation was carried out symmetrically using the same value of θ for both Ru centers in every step.

Table A8.1.1. Relative Energies of optimized structures of **dimer 1**.[a]

Rotation angle θ [°]	Relative optimized structure energy [kJ mol^{-1}]
0	0.0
30	7.8
60	13.9
90	34.8
120	35.1
150	21.1
180	13.3
210	10.7
240	9.6
270	27.2
300	38.3
330	2.3

[a] Optimized structures were generated by unconstrained optimization of **dimer 1** at Ru$_2^{II}$ oxidation state on the semiempirical PM6-D3H4/COSMO level of theory (see Materials and methods for details). Initial structures were prepared according to the given rotation angles θ.
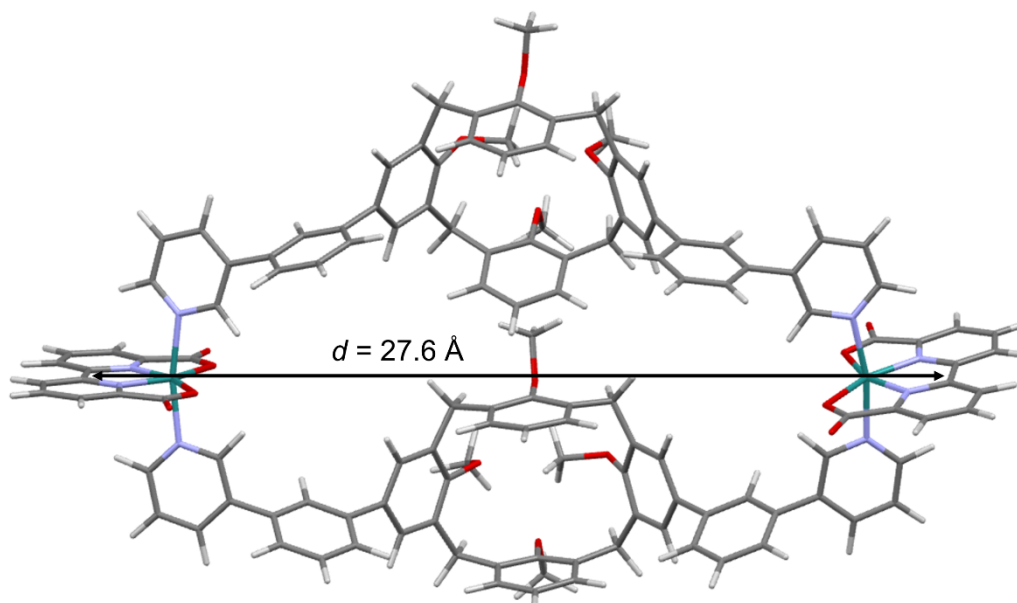
Figure A8.1.3. Lowest energy, geometry-optimized structure of **dimer 1** with $\theta = 0°$ in the Ru_2^{II} oxidation state with both Ru centers oriented inversely to each other into the cavity made by the axial calix[4]arene ligands. The structure was calculated on the semiempirical PM6-D3H4/COSMO level of theory (see "Materials and methods" for details). The tri(ethylene glycol) chains of the axial calix[4]arene ligands were replaced by methoxy groups for simplification of the calculations.

DOSY NMR spectroscopy
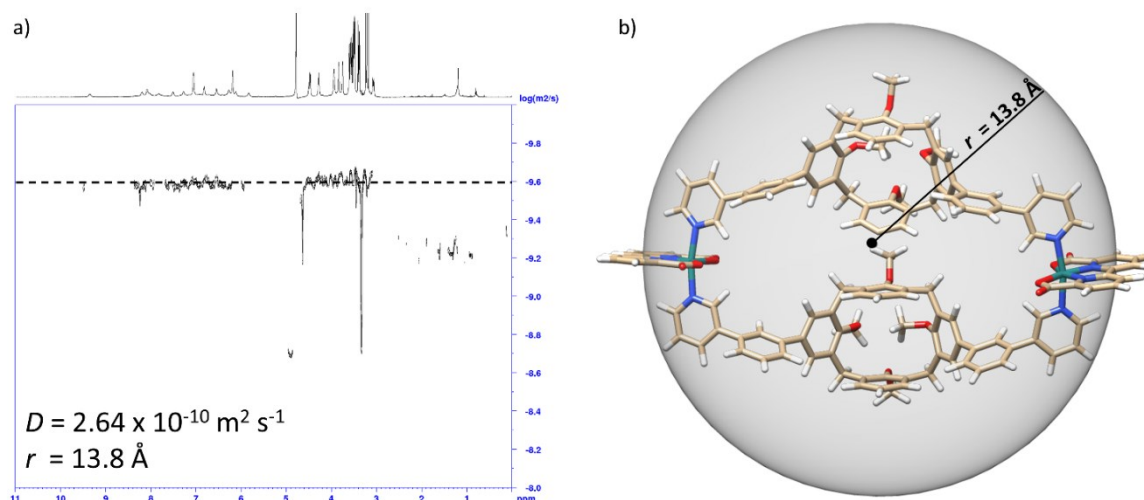
Figure A8.1.4. a) 2D plot of DOSY NMR spectra (600 MHz, CD$_3$OD) of dimer 1 (c = 3·10^{-3} M, 298 K). b) Illustration of the energy-minimized structure of **dimer 1** obtained from semiempirical PM6 calculations (PM6-D3H4/COSMO level of theory) and hydrodynamic radius as obtained from the Stokes-Einstein equation by using a literature reported viscosity(μ) for the solvent CD$_3$OD.[337]

Electrochemistry

Table A8.1.2. Redox properties of **dimer 1** and reference **[Ru(bda)(pic)$_2$]** under acidic (pH 1, triflic acid) and neutral aqueous conditions (pH 7, phosphate buffer) with 40% 2,2,2-trifluorethanol (TFE) as organic co-solvent.[a]

Catalyst	E vs. NHE [V]		
	Ru$_2^{III}$/Ru$_2^{II}$	Ru$_2^{IV}$/Ru$_2^{III}$	Ru$_2^V$/Ru$_2^{IV}$
dimer 1 (pH 1)	+0.72	+1.16	-[b]
[Ru(bda)(pic)$_2$] (pH 1)	+0.67	+1.16	-[b]
dimer 1 (pH 7)	+0.66	+0.82	+1.03
[Ru(bda)(pic)$_2$] (pH 7)	+0.61	+0.81	+1.01

[a] CV and DPV measurements under acidic and neutral conditions were performed at c = 2.5·10^{-4} M.

[b] No Ru^V oxidation potential was observed due to overlap with water oxidation current.
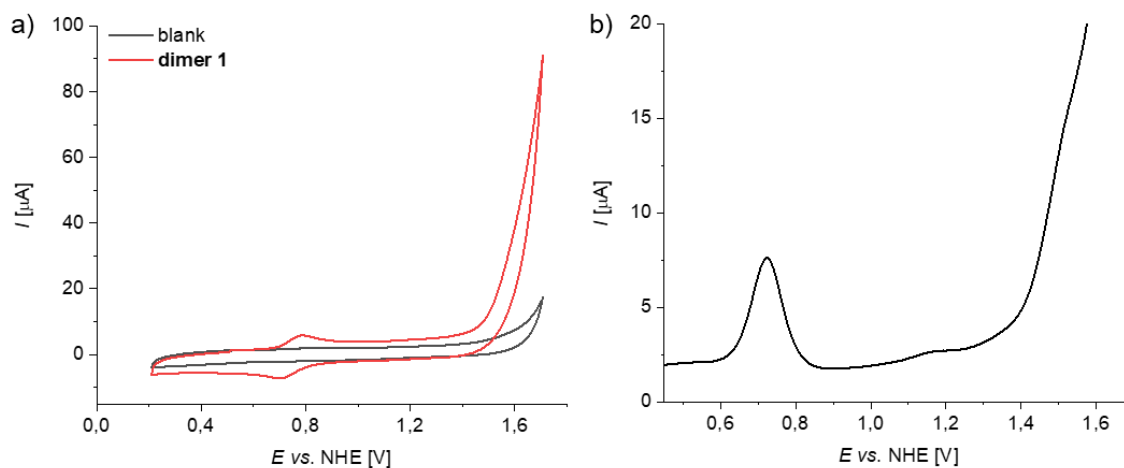
Figure A8.1.5. a) CV and b) DPV of **dimer 1** in TFE/H$_2$O 4:6 (pH 1, triflic acid), c = 2.5·10^{-4} M.
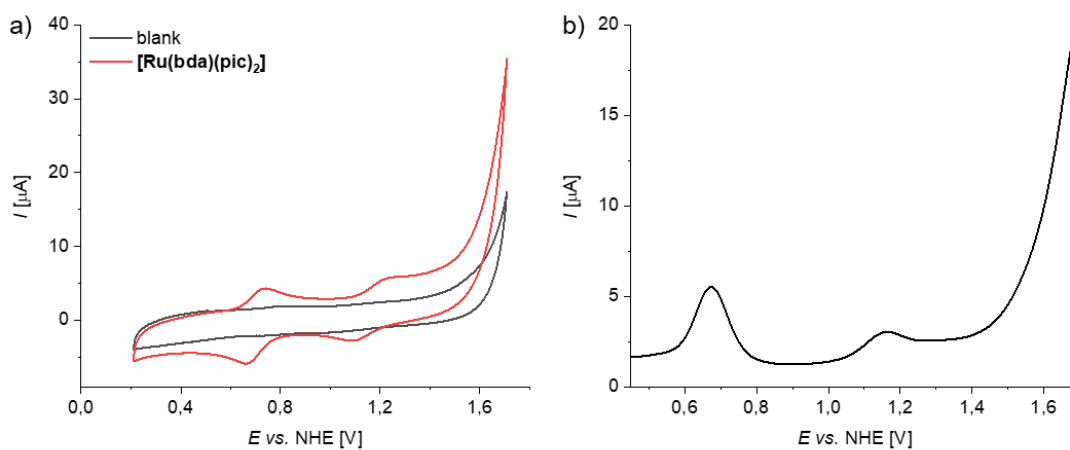
Figure A8.1.6. a) CV and b) DPV of **[Ru(bda)(pic)$_2$]** in TFE//H$_2$O 4:6 (pH 1, triflic acid), c = 2.5·10^{-4} M.
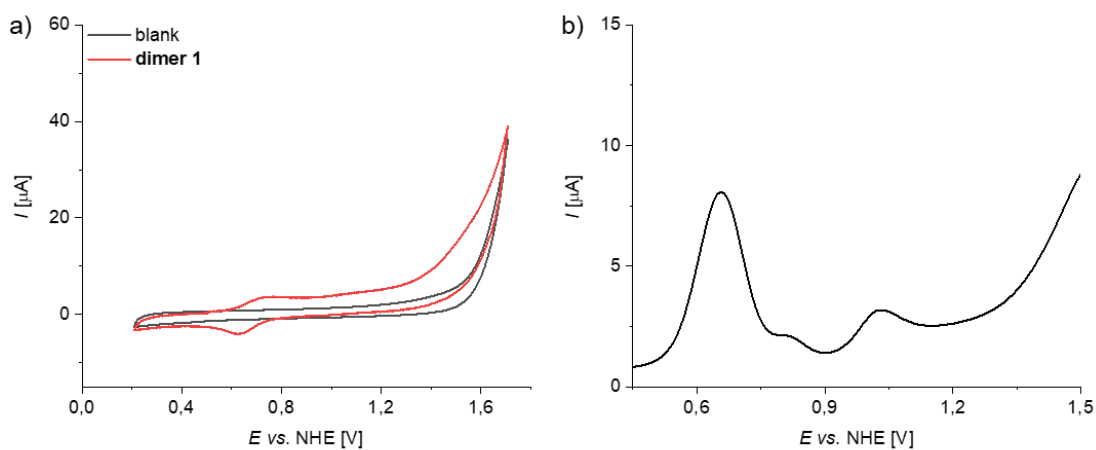
Figure A8.1.7. a) CV and b) DPV of **dimer 1** in TFE/H$_2$O 4:6 (pH 7, phosphate buffer), c = 2.5·10^{-4} M.
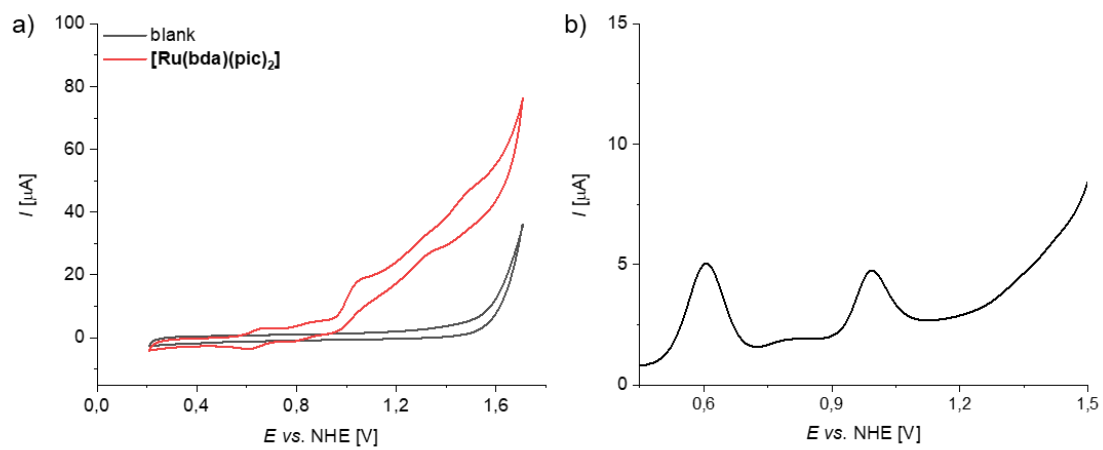
Figure A8.1.8. a) CV and b) DPV of **[Ru(bda)(pic)₂]** in TFE/H₂O 4:6 (pH 7, phosphate buffer), c = 2.5·10⁻⁴ M.

UV/Vis absorption spectroscopy and spectroelectrochemistry
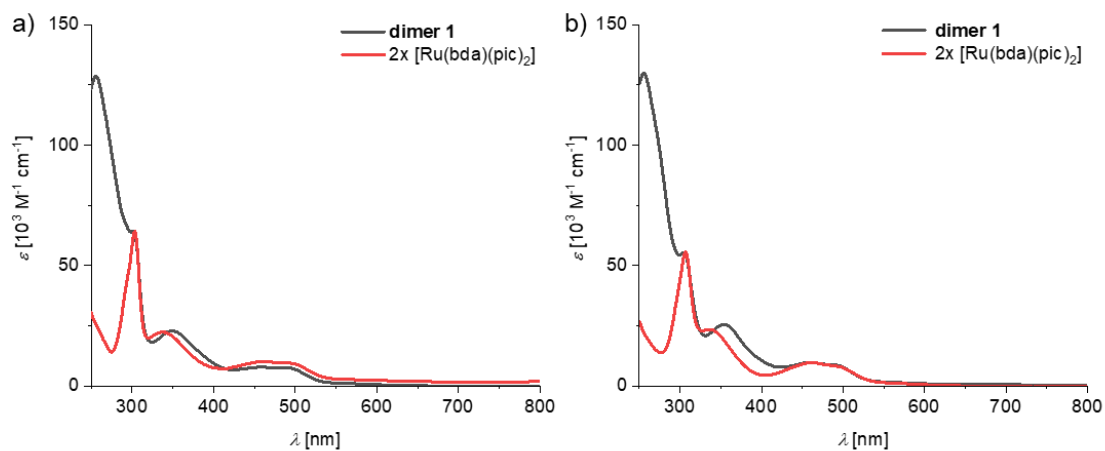
Figure A8.1.9. UV/Vis absorption spectra of **dimer 1** and the mononuclear reference compound **[Ru(bda)(pic)₂]** at the Ru_2^{II} state in CH_3CN/H_2O 4:6 at a) pH 1 and b) pH 7, $c = 10^{-5}$ M.
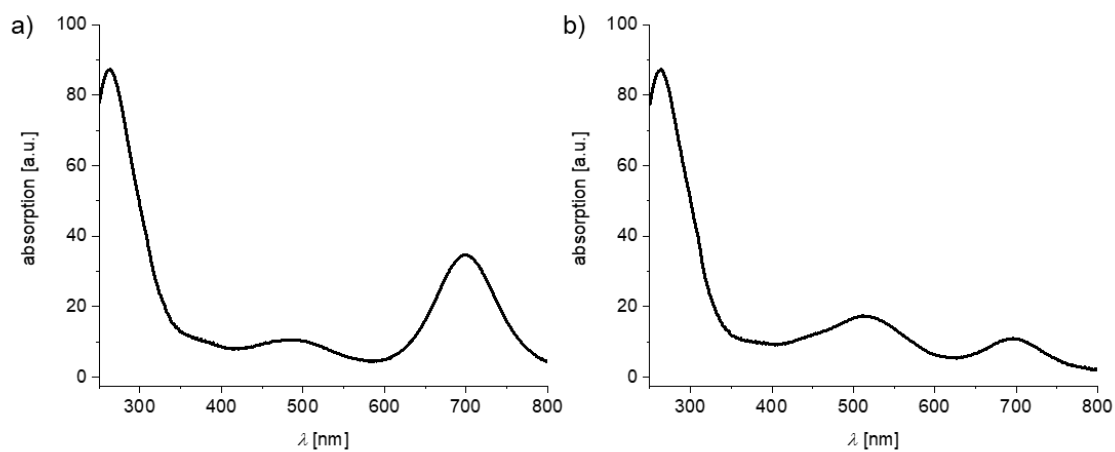
Figure A8.1.10. UV/Vis absorption spectra of **dimer 1** at the a) Ru_2^{III} and b) Ru_2^{IV} states in CH_3CN/H_2O 4:6 (pH 7, phosphate buffer) at $c = 2.4 \cdot 10^{-4}$ M. The oxidation states were obtained with spectroelectrochemistry by application of an increasing voltage from 500 mV to 960 mV.

Chemical water oxidation
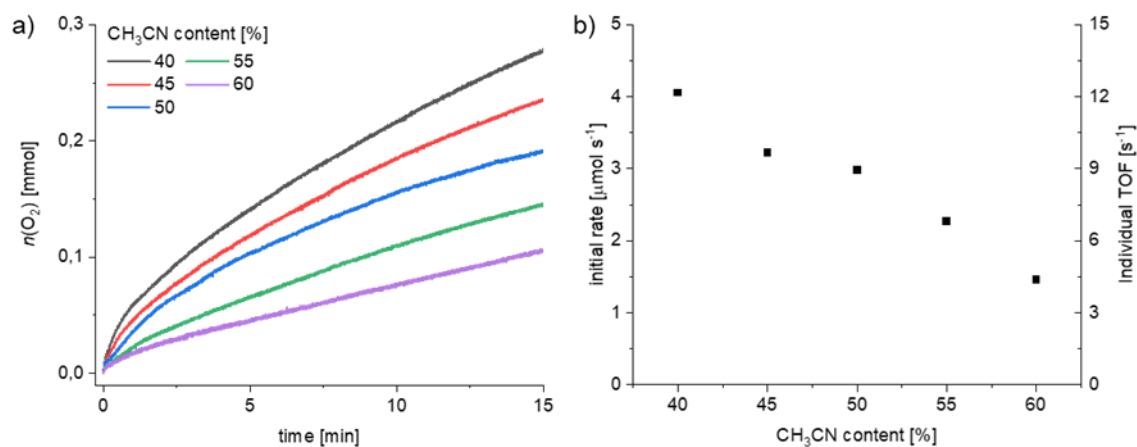
Figure A8.1.11. a) Oxygen evolution over time using **dimer 1** as catalyst (c(**dimer 1**) = 100 µM) with varying CH_3CN/H_2O (pH1, triflic acid) mixtures. b) Plot of the individual reaction rates in the first 2 s of water oxidation with **dimer 1** vs. CH_3CN content.
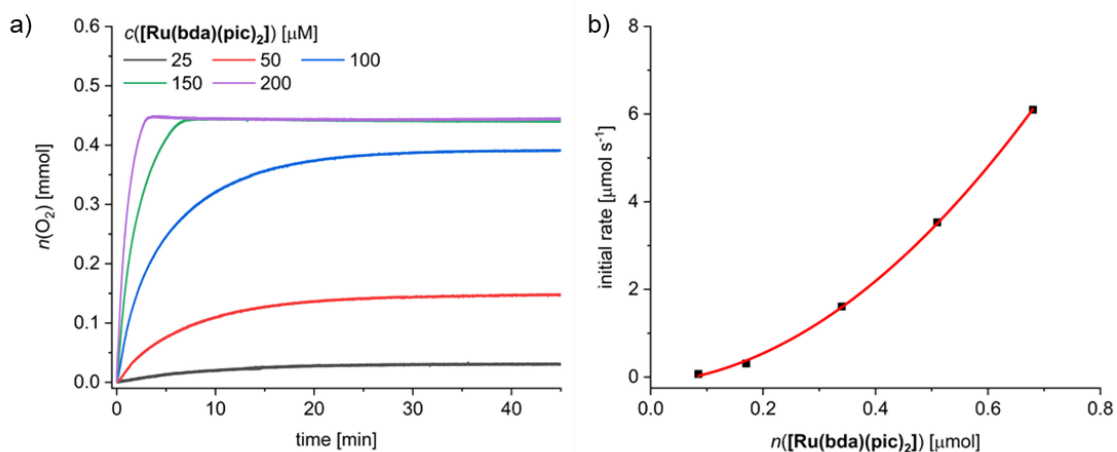
Figure A8.1.12. a) Oxygen evolution curves of **[Ru(bda)(pic)$_2$]** at variable concentrations in CH_3CN/H_2O 4:6 (pH1, triflic acid), c(CAN) = 0.6 M. b) Concentration-dependent initial rates of **[Ru(bda)(pic)$_2$]** vs. catalyst content.
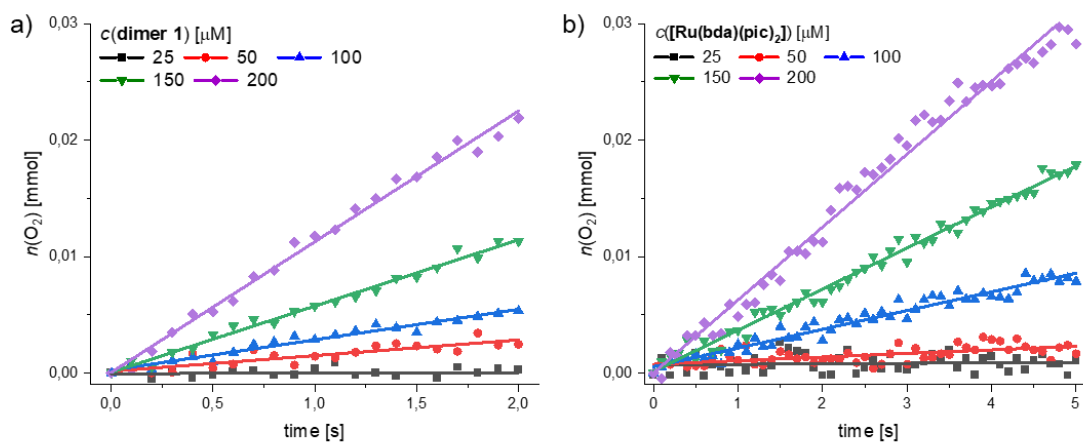
Figure A8.1.13. Comparison of the linear regression for a) **dimer 1** in the first 2 s and b) **[Ru(bda)(pic)$_2$]** in the first 5s of catalysis at variable concentrations in CH$_3$CN/H$_2$O 4:6 (pH 1, triflic acid), c(CAN) = 0.6 M.
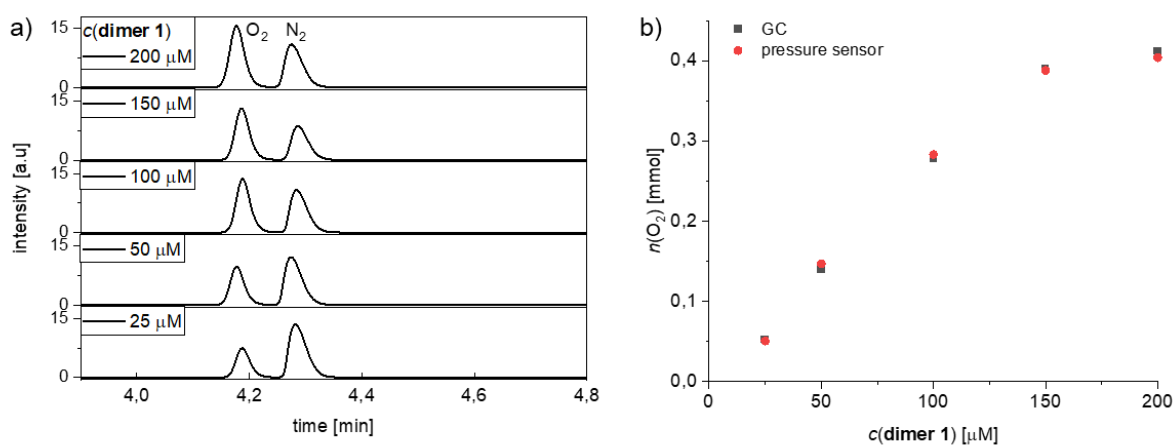
Figure A8.1.14. a) GC chromatogram of the reaction headspace after the water oxidation experiments with **dimer 1** as catalyst. b) Comparison of the amount of evolved oxygen determined by GC or with pressure sensors.

Stability tests under the conditions of chemical water oxidation
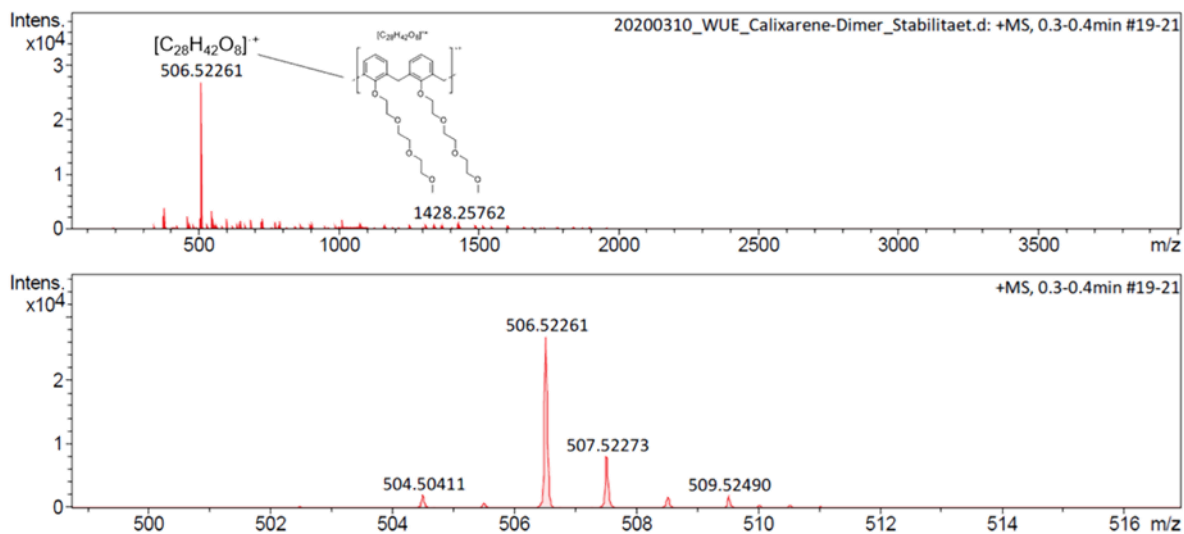
Figure A8.1.15. HR ESI mass spectrum (CH$_2$Cl$_2$/CH$_3$OH 1:1, positive mode) of **dimer 1** after water oxidation catalysis (~40 catalytic cycles) with cerium ammonium nitrate (CAN) as oxidant in 4:6 CH$_3$CN/H$_2$O (pH 1, triflic acid). Before the measurement, the sample was reduced with ascorbic acid.

CAN consumption – Variation of Catalyst concentration
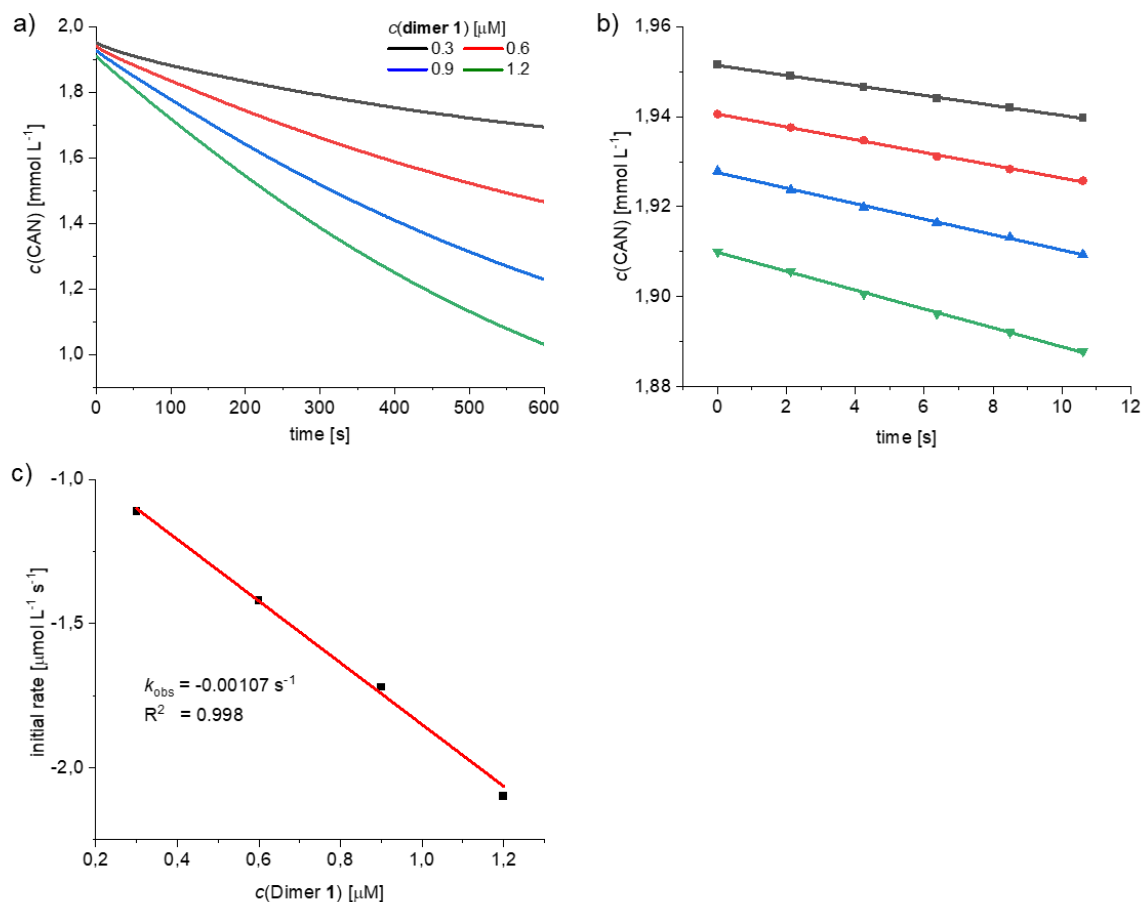
Figure A8.1.16. CAN absorbance decay at 360 nm depending on different **dimer 1** concentrations a) over 600 s and b) between 0 and 11 s in 2.0 mL in 4:6 CH_3CN/H_2O (pH 1, acid: HNO_3) at 25 °C. c(cat.) = 0.3−1.2 µM, c(CAN) = 2.0 mM. c) Plot of the initial rates vs. the concentration of the catalyst **dimer 1** with linear regression to determine the rate dependency of the water oxidation on the catalyst concentration.

CAN consumption – Variation of CAN concentration
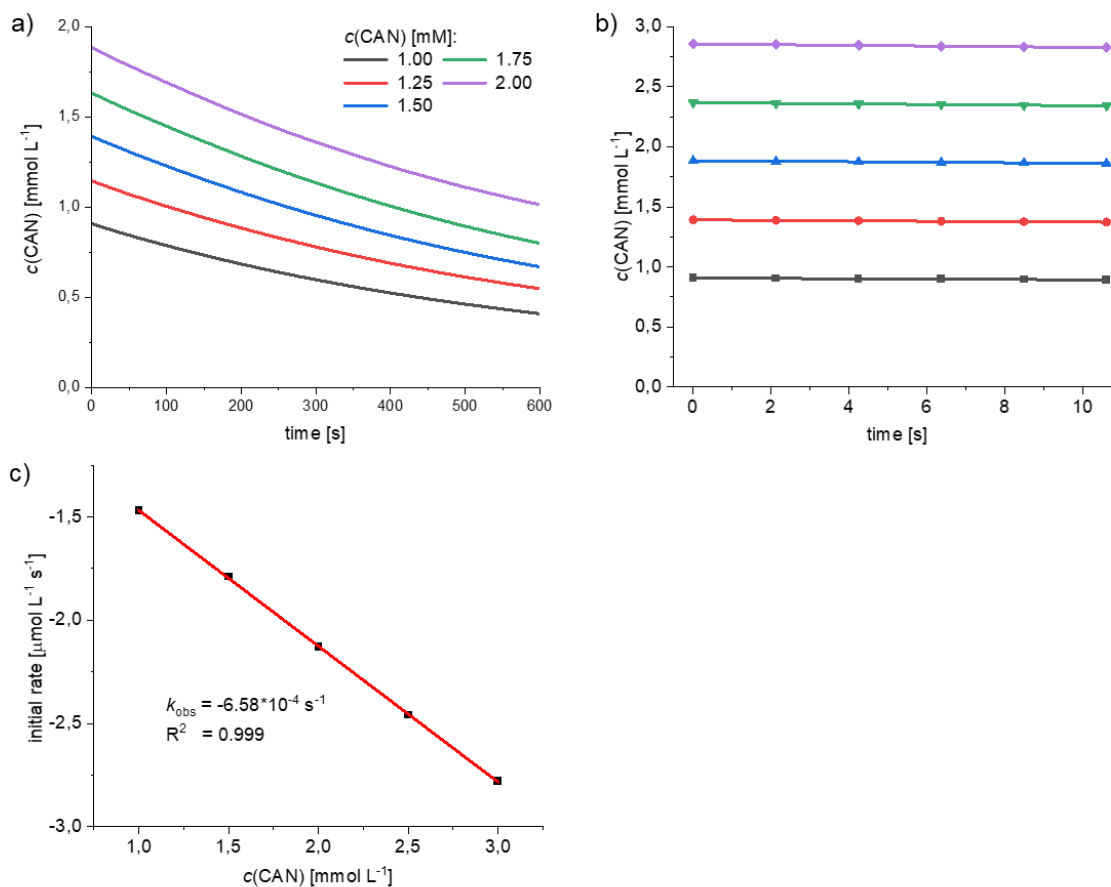
Figure A8.1.17. CAN absorbance decay at 360 nm depending on different CAN concentrations with **dimer 1** a) over 600 s and b) between 0 and 11 s in 4:6 MeCN/H$_2$O (pH 1, acid: HNO$_3$) at 25 °C. c(cat.) = 1.2 µM, c(CAN) = 1.0−3.0 mM. c) Plot of the initial rates vs. the CAN concentration with linear regression to determine the rate dependency of the water oxidation on the oxidant concentration.

Kinetic Isotope Effect
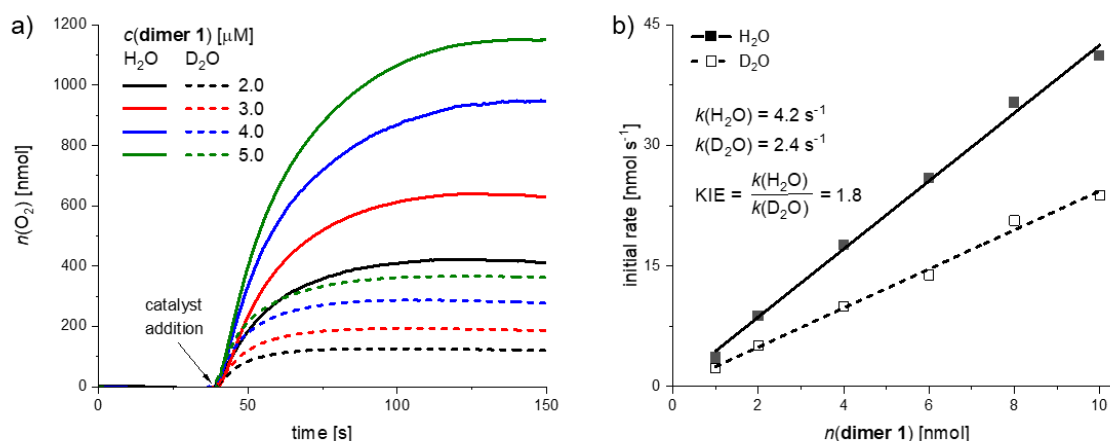
Figure A8.1.18. a) Concentration-dependent experiments with **dimer 1** as WOC in CH_3CN/H_2O or D_2O 4:6 (pH 1, triflic acid), c(CAN) = 0.525 M. b) Plot of the initial rates vs. the catalyst amount with linear regression for the determination of the reaction rates of $k(H_2O)$ and $k(D_2O)$.
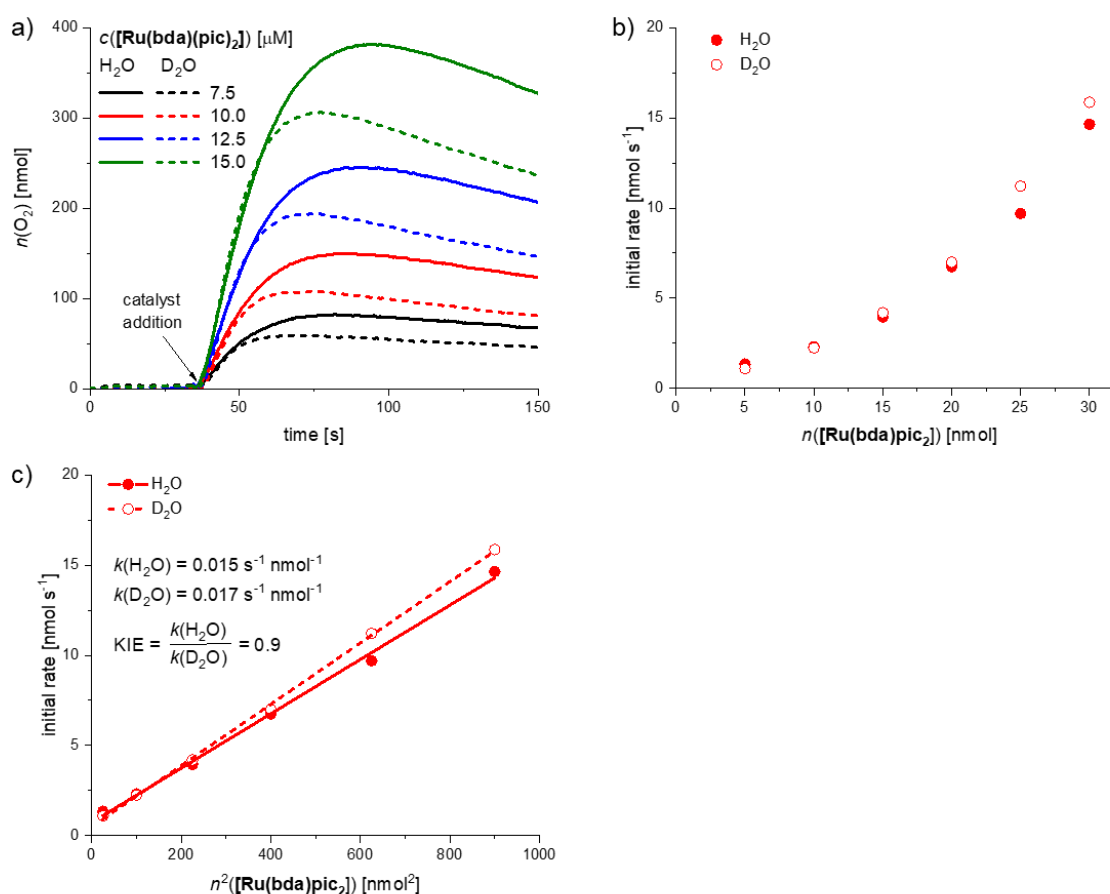
Figure A8.1.19. a) Concentration-dependent experiments with **[Ru(bda)(pic)$_2$]** as WOC in CH_3CN/H_2O or D_2O 4:6 (pH 1, triflic acid), c(CAN) = 0.525 M. b) Plot of the initial rates vs. the catalyst amount. c) The individual reaction rates $k(H_2O)$ and $k(D_2O)$ were obtained by plotting the initial rates vs. the square of concentration of catalyst **[Ru(bda)(pic)$_2$]**.

Photocatalytic water oxidation
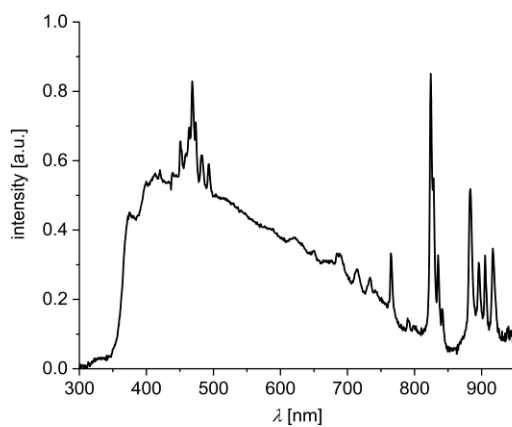
Figure A8.1.20. Emission spectrum of the xenon lamp used for photocatalytic water oxidation experiments.
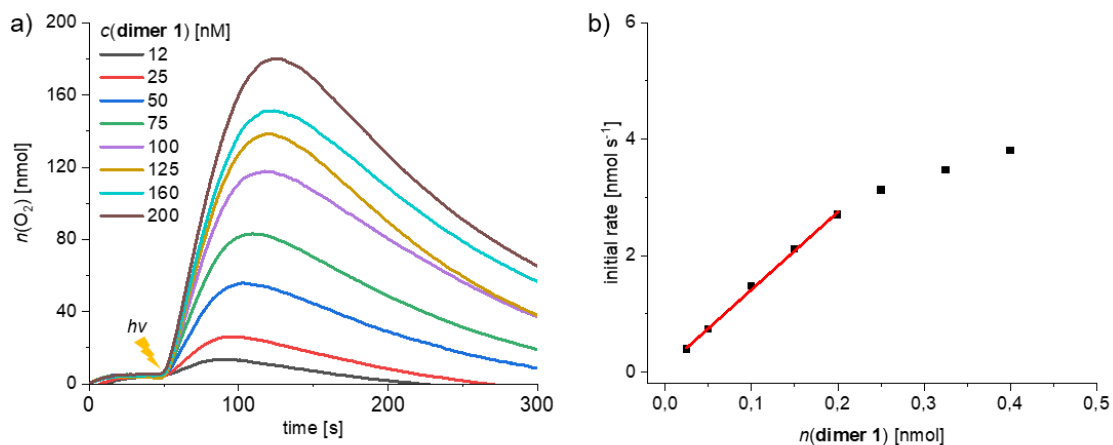
Figure A8.1.21. a) Concentration-dependent experiments with **dimer 1** as WOC in CH_3CN/H_2O 1:1 (pH 7, phosphate buffer). b) Plot of the initial rates vs. the catalyst amount with linear regression for the determination of the TOF.
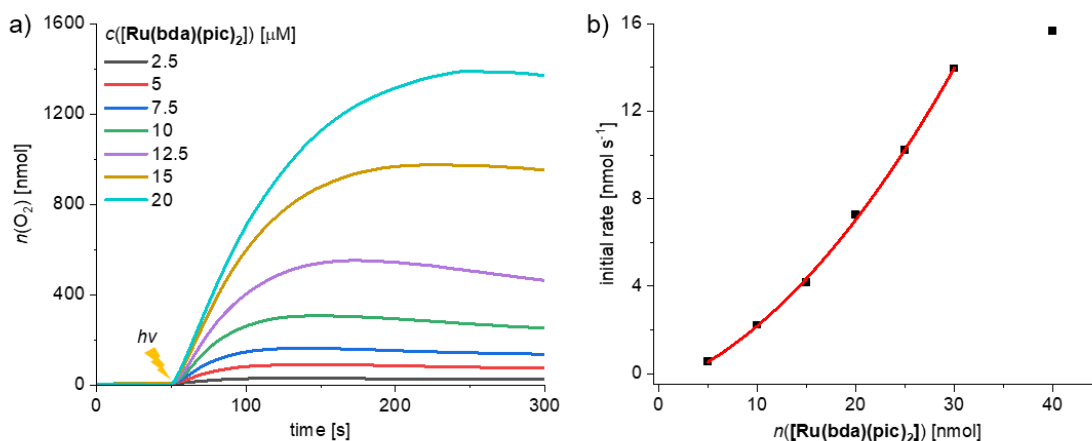
Figure A8.1.22. a) Concentration-dependent experiments with **[Ru(bda)(pic)$_2$]** as WOC in CH$_3$CN/H$_2$O 4:6 (pH 7, phosphate buffer). b) Plot of the initial rates vs. the catalyst amount with exponential regression.
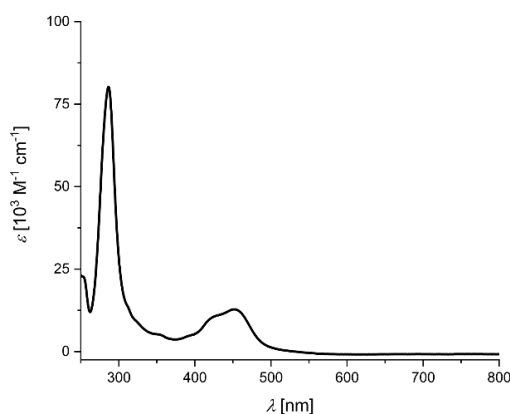
Figure A8.1.23. UV/Vis absorption spectrum of photosensitizer **Ru(bpy)$_3$Cl$_2$** in CH$_3$CN/H$_2$O 4:6 at pH 7, c = 10^{-5} M.
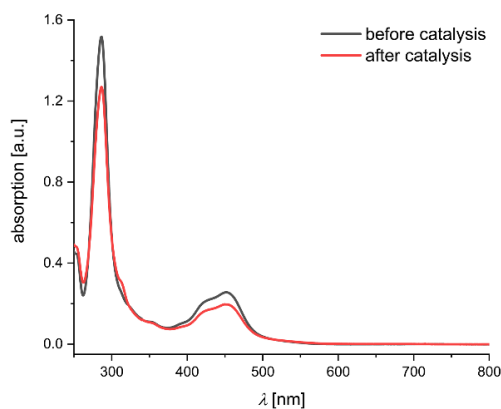
Figure A8.1.24. UV/Vis absorption spectra of the catalytic mixture before and after irradiation in CH$_3$CN/H$_2$O 4:6 (pH 7, phosphate buffer), c(PS) = 1.5 mM, c(Na$_2$S$_2$O$_8$) = 37 mM, c(**dimer 1**) = 200 nM.

Table A8.1.3. Catalytic activities of selected mono, di- and trinuclear Ru WOCs in chemical and photocatalytic water oxidation.

Catalyst	Chemical water oxidation (CAN)		Photocatalytic water oxidation (PS/SEA)	
	TOF_{max} [s^{-1}]	TON	TOF_{max} [s^{-1}]	TON
dimer 1[a]	19	820	15.5	460
5[b] [149, 195]	41	2000	0.35	10
9[c] [212, 338]	303	8360	0.24	140
47[d] [243, 258]	n.d.	20800	n.d.	640
33[e] [134]	n.d.	900	n.d.	n.d.
48[f] [179, 339]	0.068	211	11	5300
32[g] [244]	126	86498	n.d.	n.d.
MC3[h] [37, 40]	136	5300	11	430

Experimental conditions: [a] <u>Chemical WO:</u> 40:60 MeCN/H_2O (pH 1, triflic acid), c(CAN) = 0.6 M, c(**dimer 1**) = 50−300 µM; <u>Photocatalytic WO:</u> 40:60 MeCN/H_2O (pH 7, phosphate buffer), c(([Ru(bpy)$_3$]$^{2+}$) = 1.5 mM, c(Na$_2$S$_2$O$_8$) = 37 mM, c(**dimer 1**) = 12−200 nM. [b] <u>Chemical WO:</u> H_2O (pH 1, triflic acid), c(CAN) = 0.4 mM, c(**5**) = 12−216 µM;[195] <u>Photocatalytic WO:</u> H_2O (pH 7.2, phosphate buffer), c([Ru(bpy)$_3$]$^{2+}$) = 1 mM, c(Na$_2$S$_2$O$_8$) = 10 mM, c(**5**) = 9.5 µM;[149] [c] <u>Chemical WO:</u> H_2O (pH 1, triflic acid), c(CAN) = 0.5 mM, c(**9**) = 114-216 µM;[212] <u>Photocatalytic WO:</u> H_2O (pH 1, perchlorid acid), c([Ru(5-CF$_3$-bpy)$_3$]$^{2+}$) = 0.2 mM, c(Na$_2$S$_2$O$_8$) = 1 mM, c(**9**) = 20 µM;[338] [d] <u>Chemical WO:</u> H_2O (pH 1, triflic acid), c(CAN) = 5 mM, c(**47**) = 50 nM;[243] <u>Photocatalytic WO:</u> 6:4 MeCN/H_2O (pH 6.8, phosphate buffer), c([Ru(bpy)$_3$]$^{2+}$) = 1 mM, c(Na$_2$S$_2$O$_8$) = 45 mM, c(**47**) = 2 µM.[258] [e] <u>Chemical WO:</u> 1:9 CF$_3$CH$_2$OH/H_2O (pH 1, triflic acid), c(CAN) = 0.5 M, c(**33**) = 59 µM;[134] <u>Photocatalytic WO:</u> n.d. [f] <u>Chemical WO:</u> H_2O (pH 1, triflic acid), c(CAN) = 0.1 M, c(**48**) = 0.1−1 mM;[179] <u>Photocatalytic WO:</u> H_2O (pH 7, phopshate buffer), c([Ru(4,4'-COOEt-bpy)$_2$bpy]$^{2+}$) = 0.2 mM, c(Na$_2$S$_2$O$_8$) = 20 mM, c(**32**) = 0.2 µM;[339] [g] <u>Chemical WO:</u> H_2O (pH 1, triflic acid), c(CAN) = 50 mM, c(**32**) = 33 nM;[244] <u>Photocatalytic WO:</u> n.d. [h] <u>Chemical WO:</u> 1:1 MeCN/H_2O (pH 1, triflic acid), c(CAN) = 0.6 M, c(**MC3**) = 6−94 µM;[37] <u>Photocatalytic WO:</u> 1:1 MeCN/H_2O (pH 7, phosphate buffer), c(([Ru(bpy)$_3$]$^{2+}$) = 1.5 mM, c(Na$_2$S$_2$O$_8$) = 37 mM, c(**MC3**) = 60−880 nM.[40]
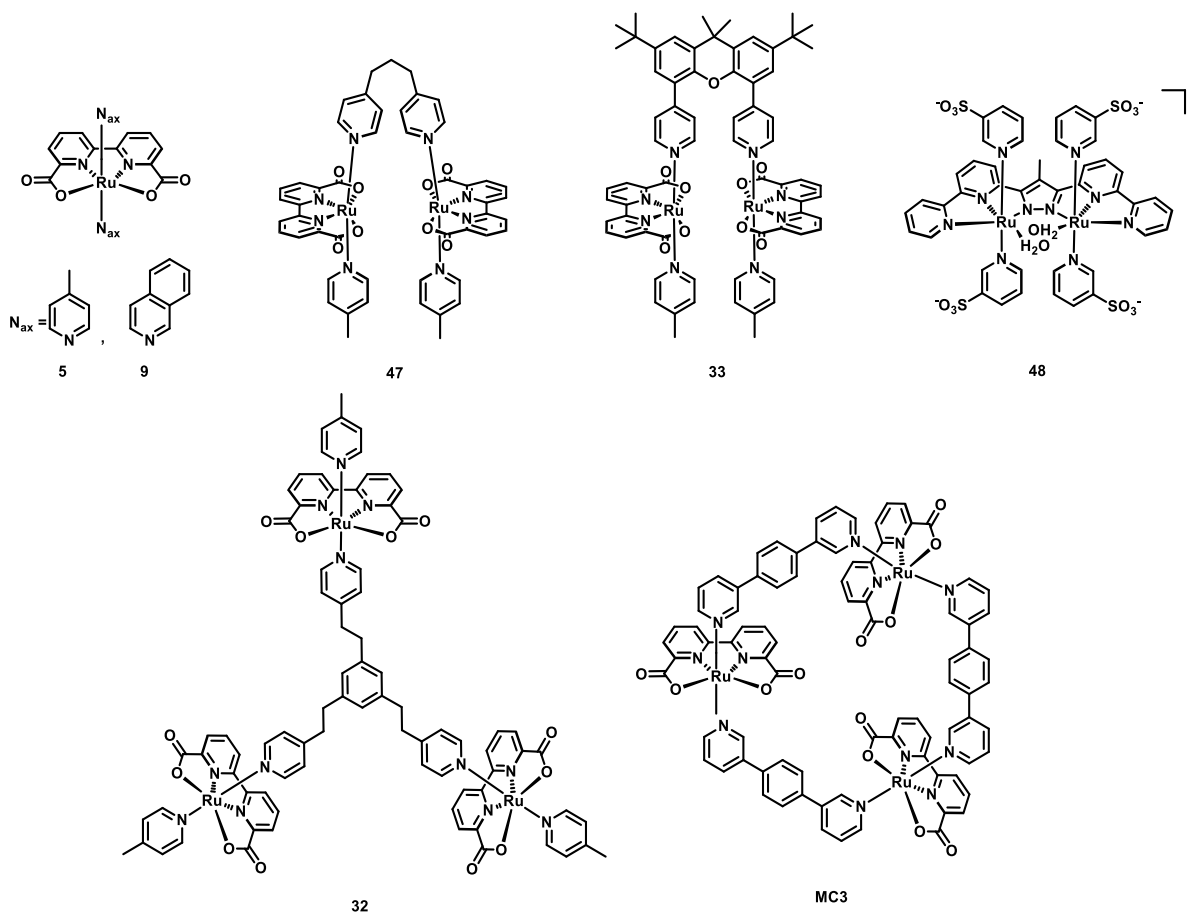
Figure A8.1.25. Chemical structures of selected mono- and multinuclear Ru WOCs.

NMR spectra
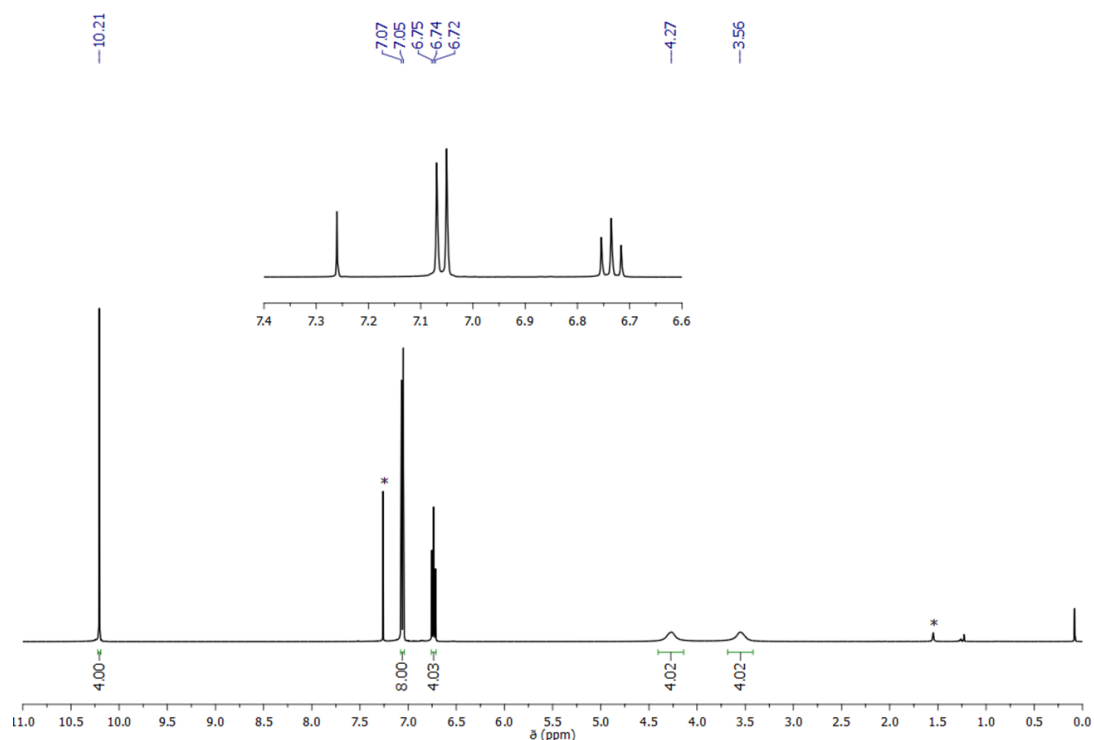
Figure A8.1.26. ^{1}H NMR spectrum (400 MHz, CDCl$_3$) of 25,26,27,28-tetrahydroxycalix[4]arene (**35**) (* residual solvent).
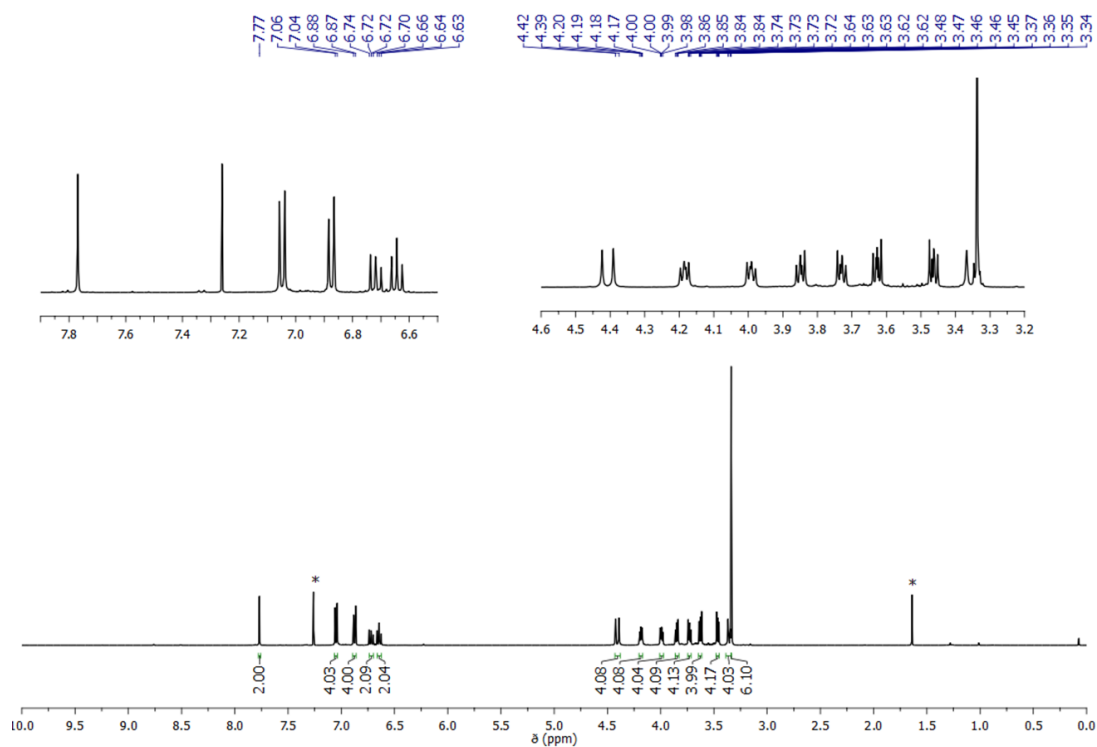
Figure A8.1.27. ^{1}H NMR spectrum (400 MHz, CDCl$_3$) of 25,27-bis(2-(2-(2-methoxyethoxy) ethoxy)ethoxy))-26,28-dihydroxycalix[4]arene (**37**) (* residual solvent).
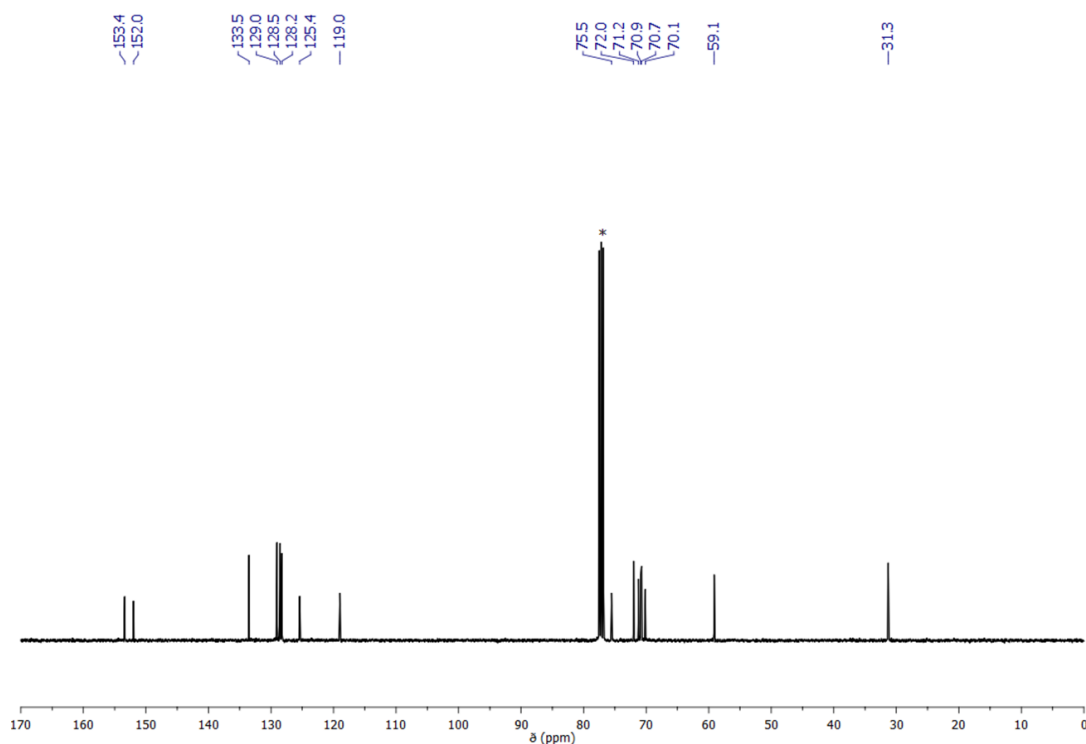
Figure A8.1.28. ^{13}C NMR spectrum (100 MHz, CDCl$_3$) of 25,27-bis(2-(2-(2-methoxyethoxy) ethoxy)ethoxy))-26,28-dihydroxycalix[4]arene (**37**) (* residual solvent).
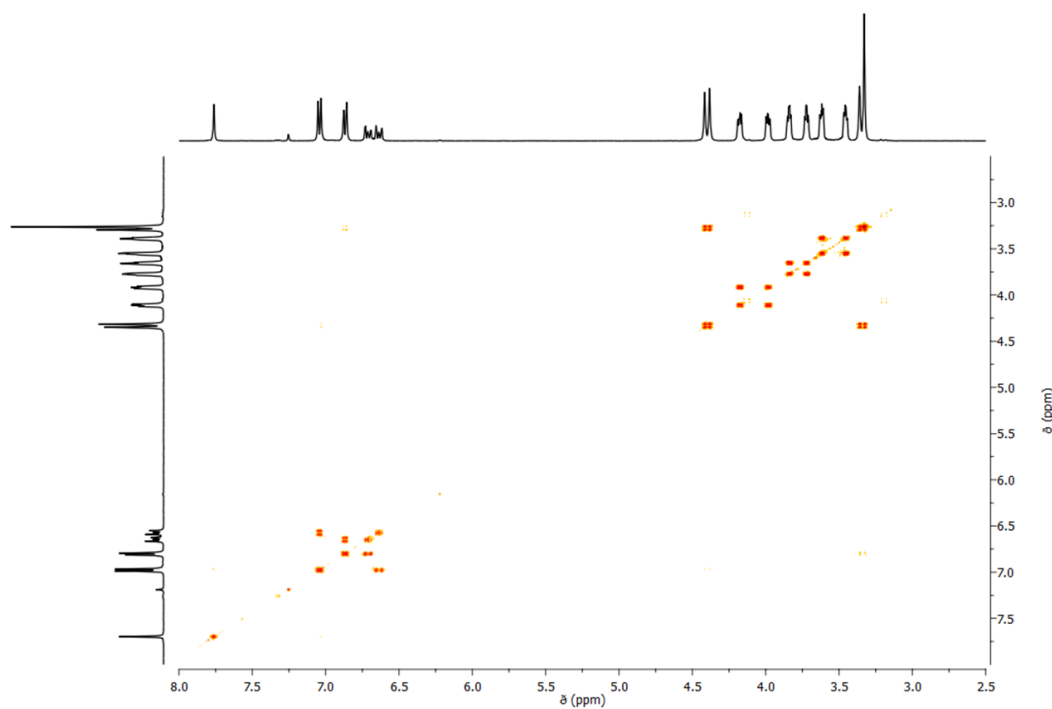
Figure A8.1.29. ^1H-^1H COSY NMR spectrum (400 MHz, CDCl$_3$) of 25,27-bis(2-(2-(2-methoxyethoxy)ethoxy)ethoxy))-26,28-dihydroxycalix[4]arene (**37**) (* residual solvent).
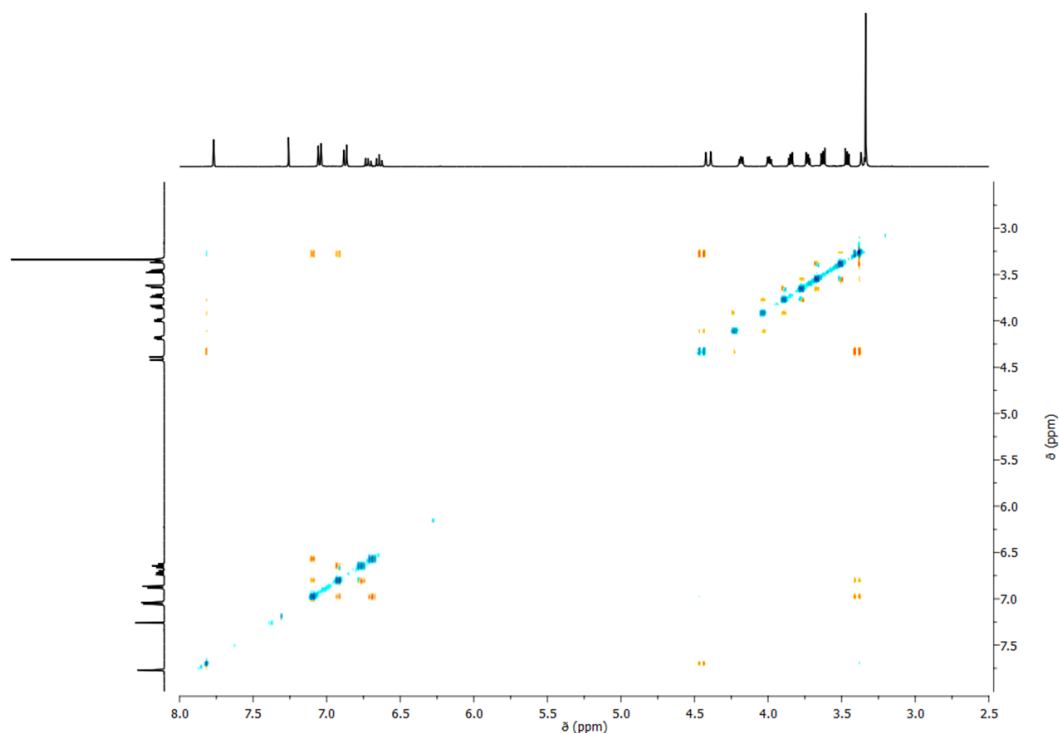
Figure A8.1.30. ^{1}H-^{1}H NOESY NMR spectrum (400 MHz, CDCl$_3$) of 25,27-bis(2-(2-(2-methoxyethoxy)ethoxy)ethoxy))-26,28-dihydroxycalix[4]arene (**37**) (* residual solvent).
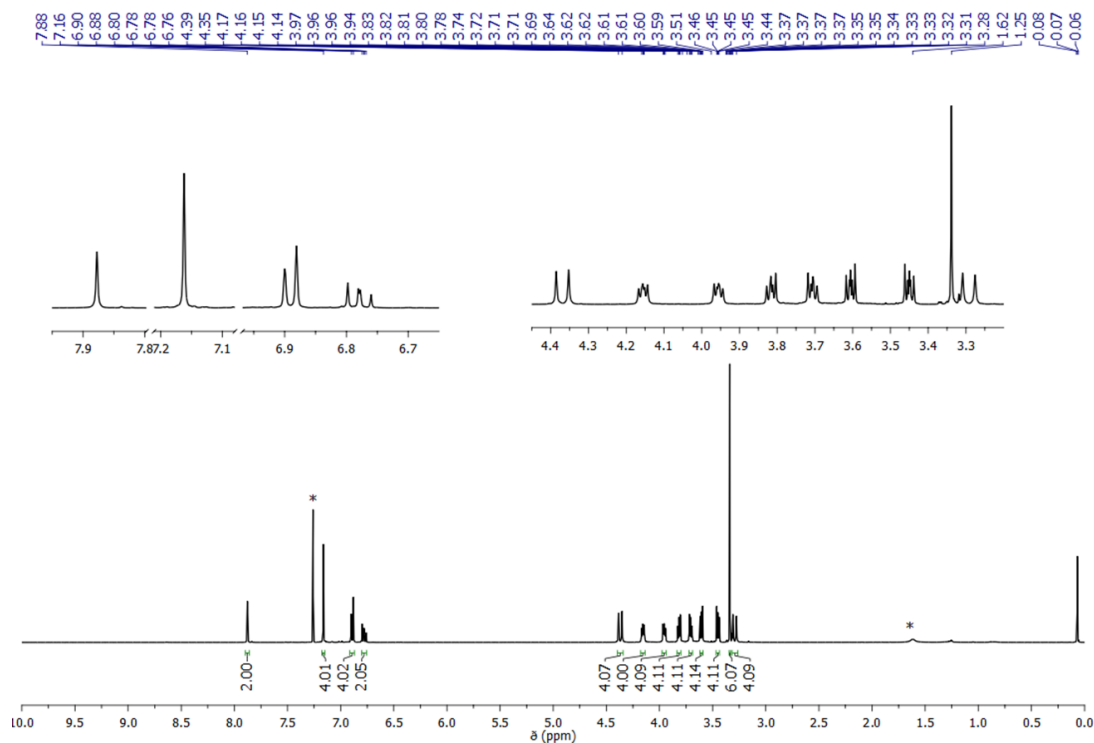
Figure A8.1.31. ^{1}H NMR spectrum (400 MHz, CDCl$_3$) of 5,17-dibromo-25,27-bis(2-(2-(2-methoxyethoxy)ethoxy)ethoxy))-26,28-dihydroxy-calix[4]arene (**38**) (* residual solvent).
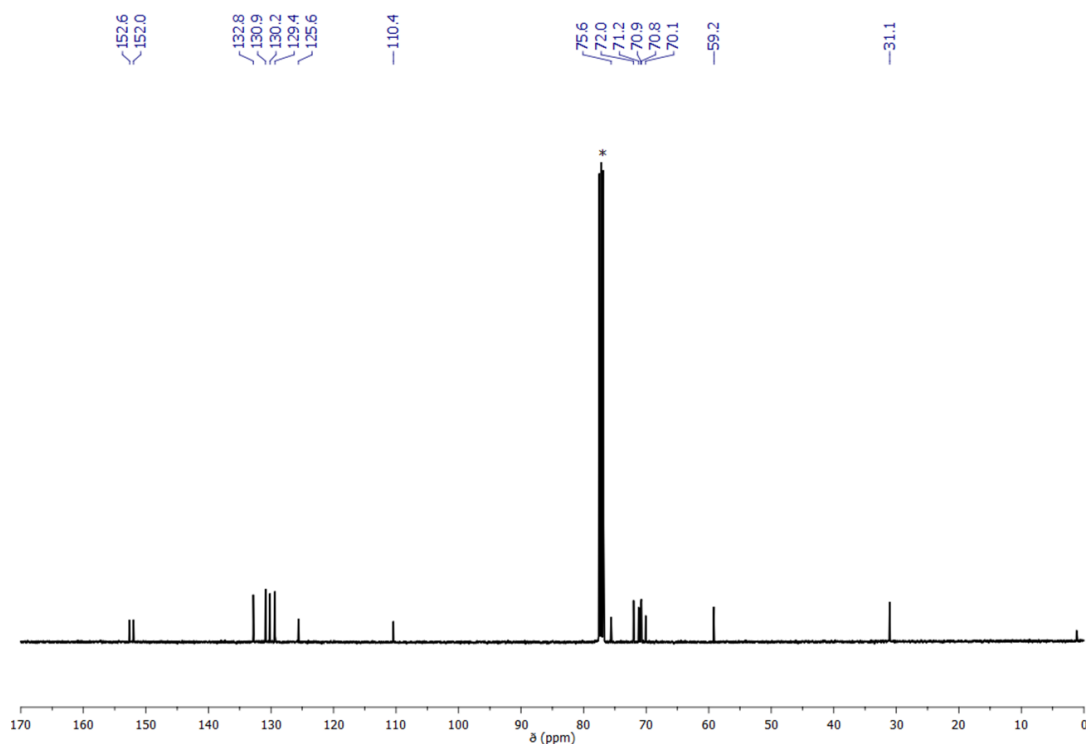
Figure A8.1.32. ^{13}C NMR spectrum (100 MHz, CDCl$_3$) of 5,17-dibromo-25,27-bis(2-(2-(2-methoxyethoxy)ethoxy)ethoxy))-26,28-dihydroxy-calix[4]arene (**38**) (* residual solvent).
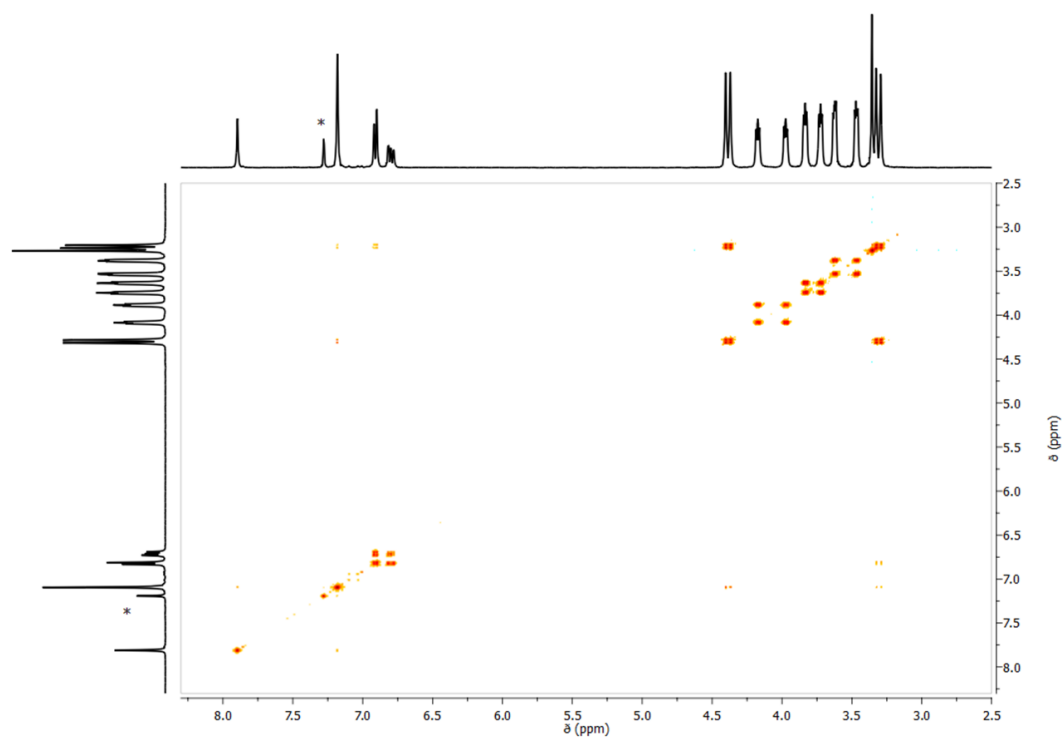
Figure A8.1.33. ^{1}H-^{1}H COSY NMR spectrum (400 MHz, CDCl$_3$) of 5,17-dibromo-25,27-bis(2-(2-(2-methoxyethoxy)ethoxy)ethoxy))-26,28-dihydroxy-calix[4]arene (**38**) (* residual solvent).
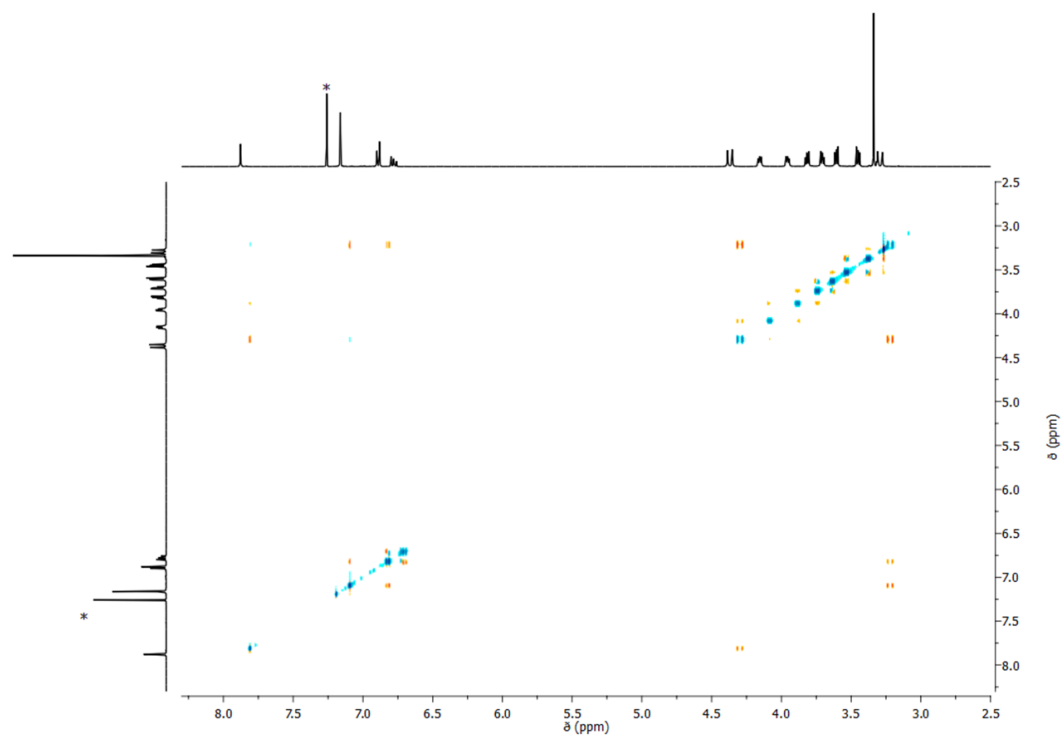
Figure A8.1.34. ^{1}H-^{1}H NOESY NMR spectrum (400 MHz, CDCl$_3$) of 5,17-dibromo-25,27-bis(2-(2-(2-methoxyethoxy)ethoxy)ethoxy))-26,28-dihydroxy-calix[4]arene (**38**) (* residual solvent).
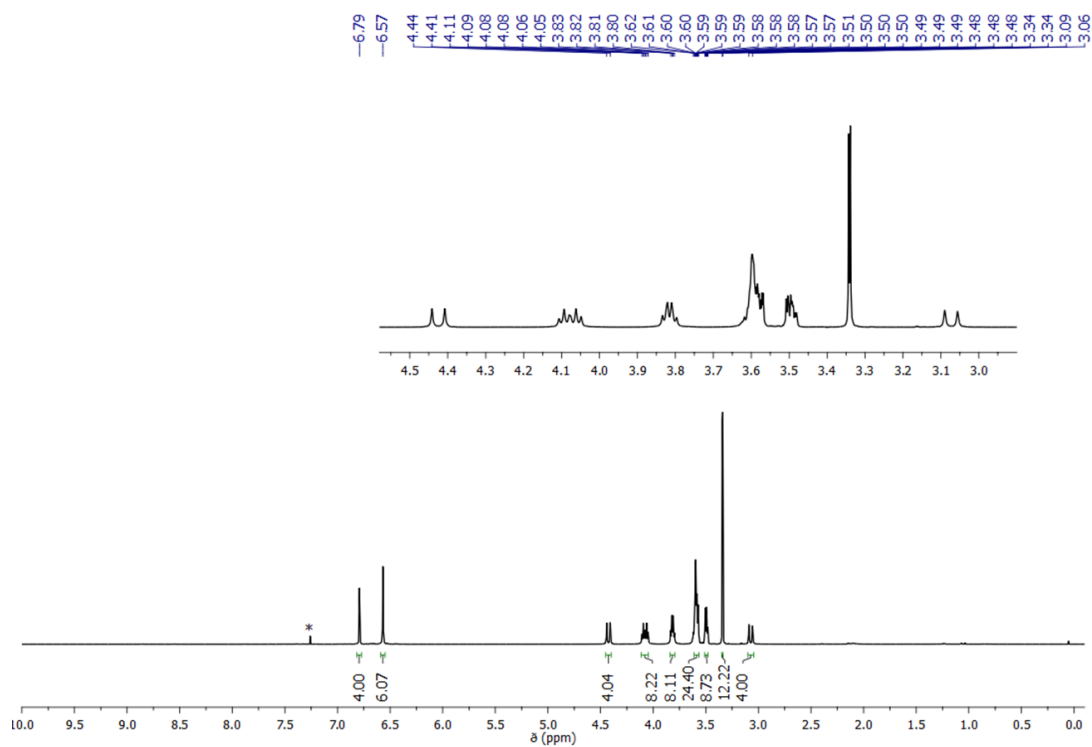
Figure A8.1.35. ^{1}H NMR spectrum (400 MHz, CDCl$_3$) of 5,17-dibromo-25,26,27,28-tetrakis(2-(2-(2-methoxyethoxy)ethoxy)ethoxy))-calix[4]arene (**40**) (* residual solvent).
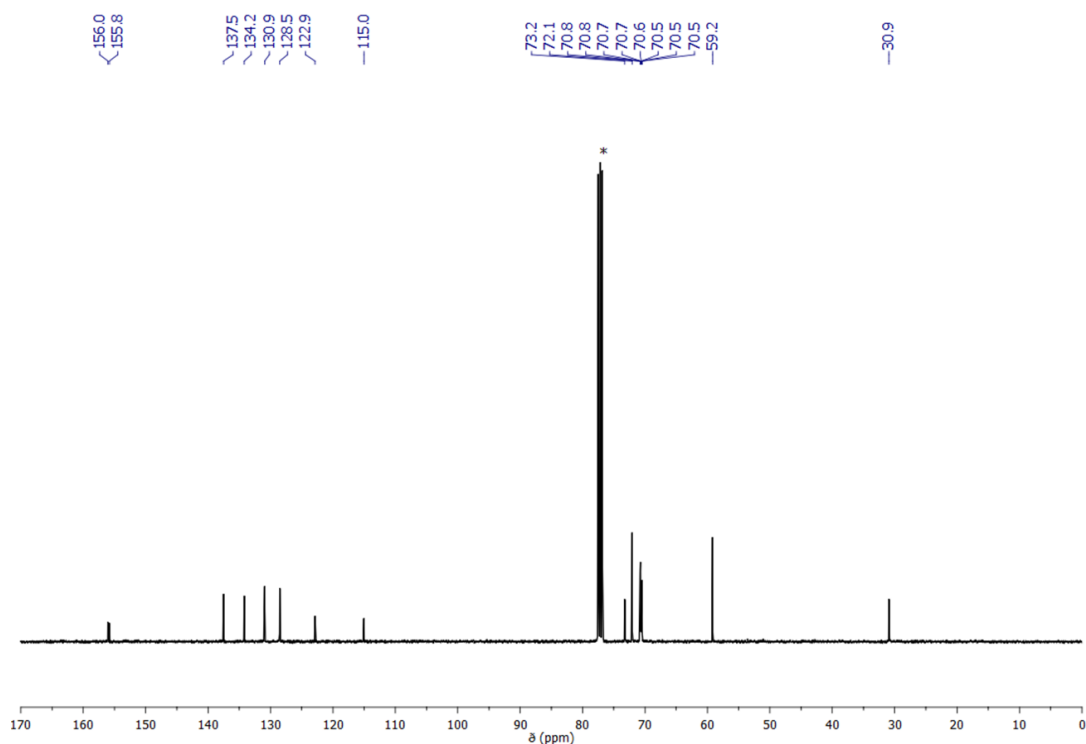
Figure A8.1.36. ^{13}C NMR spectrum (100 MHz, CDCl$_3$) of 5,17-dibromo-25,26,27,28-tetrakis(2-(2-(2-methoxyethoxy)ethoxy)ethoxy))-calix[4]arene (**40**) (* residual solvent).
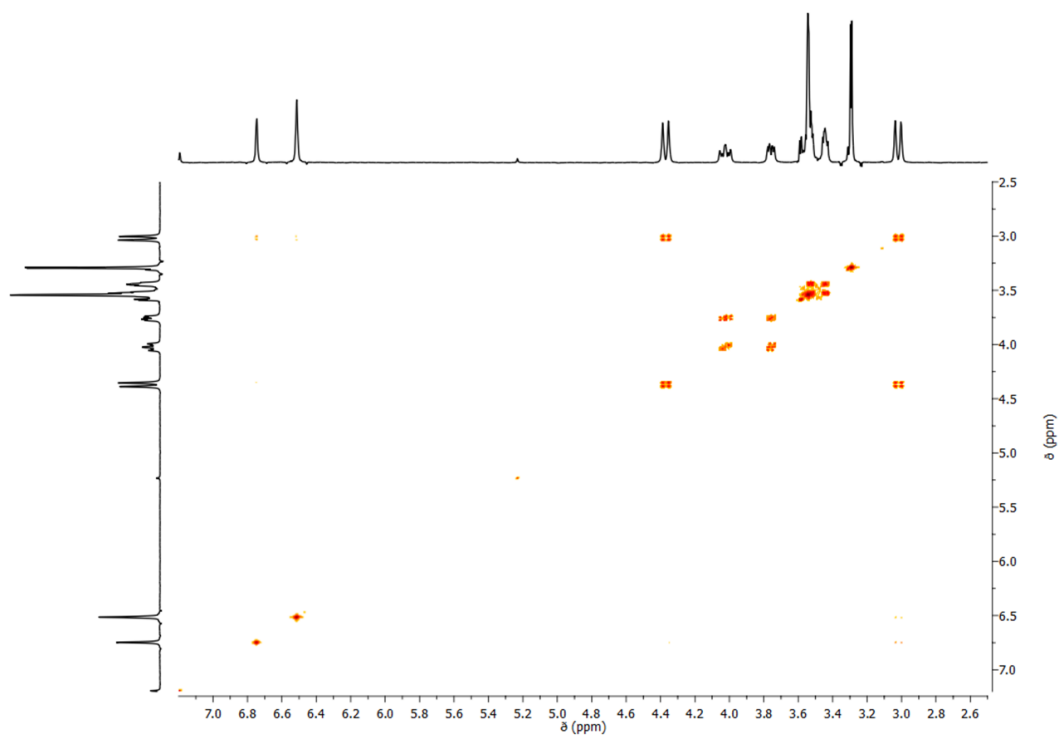
Figure A8.1.37. ^{1}H-^{1}H COSY NMR spectrum (400 MHz, CDCl$_3$) of 5,17-dibromo-25,26,27,28-tetrakis(2-(2-(2-methoxyethoxy)ethoxy)ethoxy))-calix[4]arene (**40**) (* residual solvent).
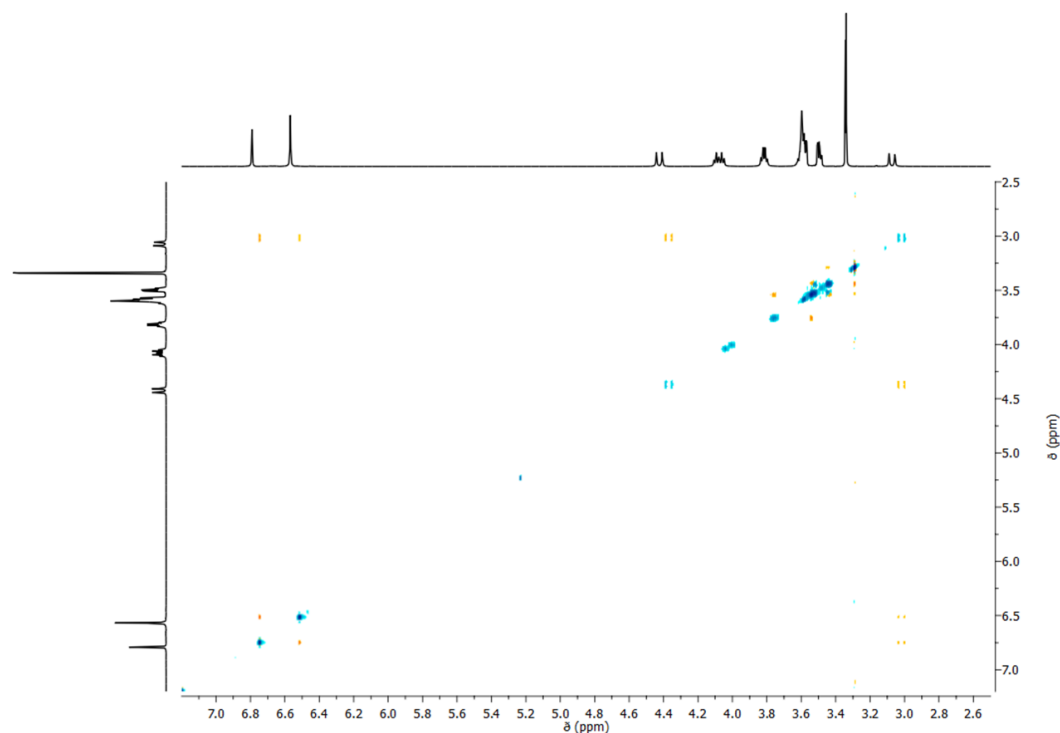
Figure A8.1.38. ^{1}H-^{1}H NOESY NMR spectrum (400 MHz, CDCl$_3$) of 5,17-dibromo-25,26,27,28-tetrakis(2-(2-(2-methoxyethoxy)ethoxy)ethoxy))-calix[4]arene (**40**) (* residual solvent).
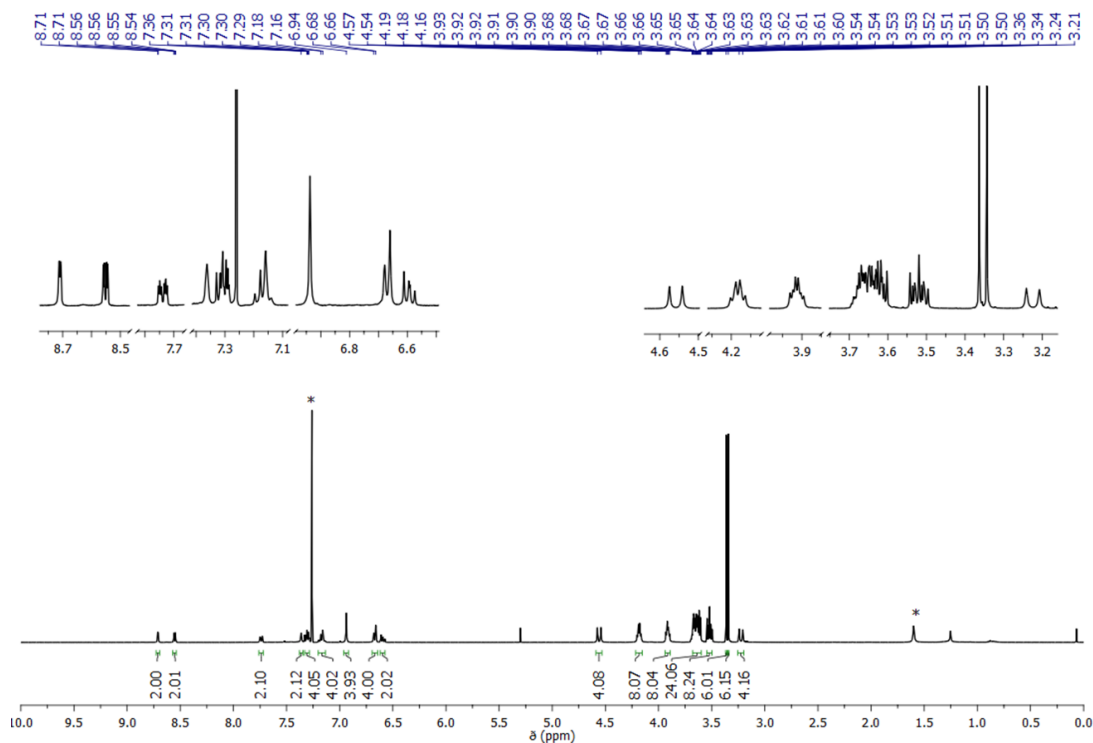
Figure A8.1.39. ^{1}H NMR spectrum (400 MHz, CDCl$_3$) of 5,17-bis(3,1-(phenylene)pyridine)-25,26,27,28-tetrakis(2-(2-(2-methoxyethoxy)ethoxy)ethoxy))-calix[4]arene (**42**) (* residual solvent).
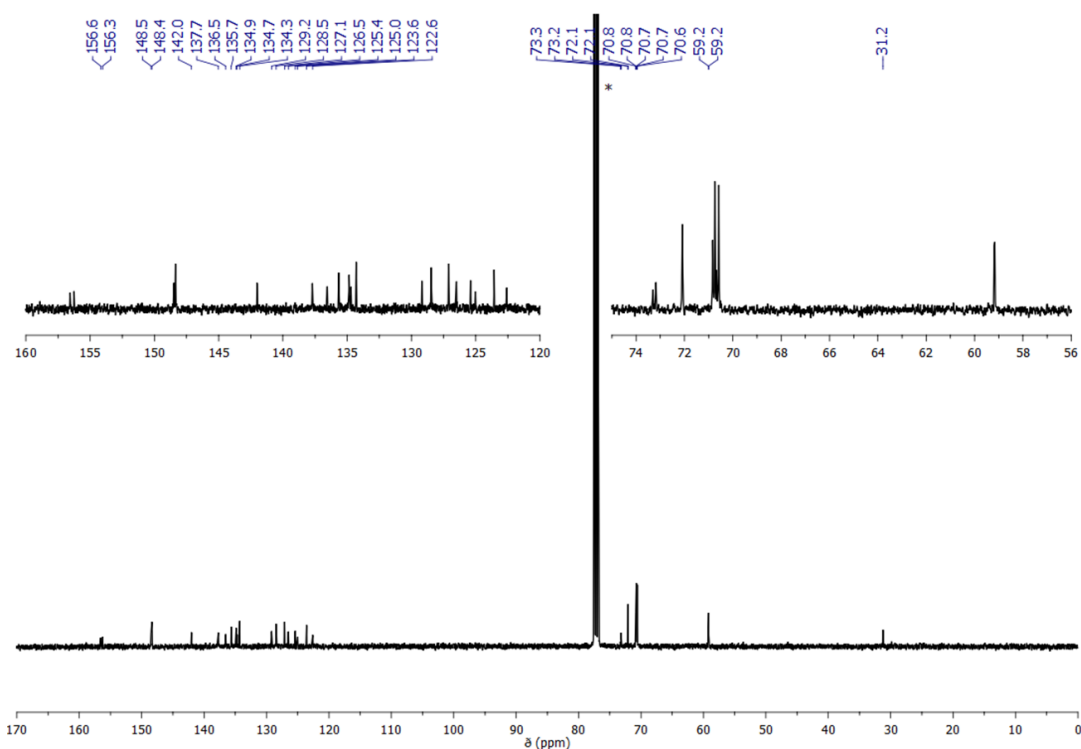
Figure A8.1.40. ¹³C NMR spectrum (100 MHz, CDCl₃) of 5,17-bis(3,1-(phenylene)pyridine)-25,26,27,28-tetrakis(2-(2-(2-methoxyethoxy)ethoxy)ethoxy))-calix[4]arene (**42**) (* residual solvent).
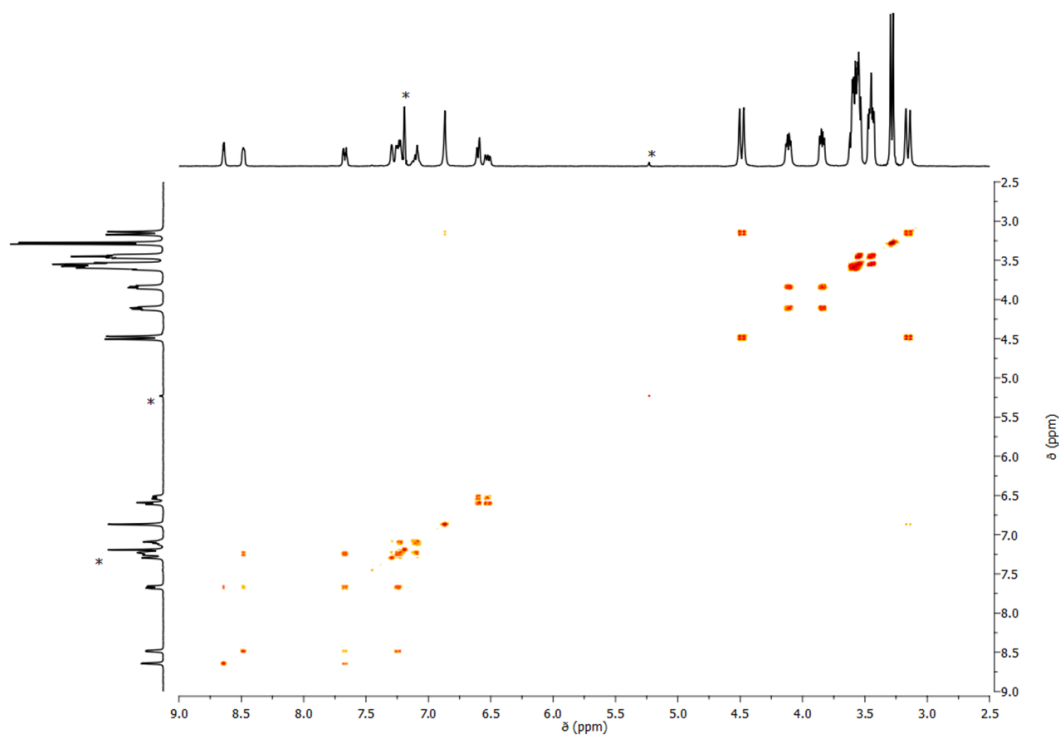
Figure A8.1.41. ¹H-¹H COSY NMR spectrum (400 MHz, CDCl₃) of 5,17-bis(3,1-(phenylene)pyridine)-25,26,27,28-tetrakis(2-(2-(2-methoxyethoxy)ethoxy)ethoxy))-calix[4]arene (**42**) (* residual solvent).
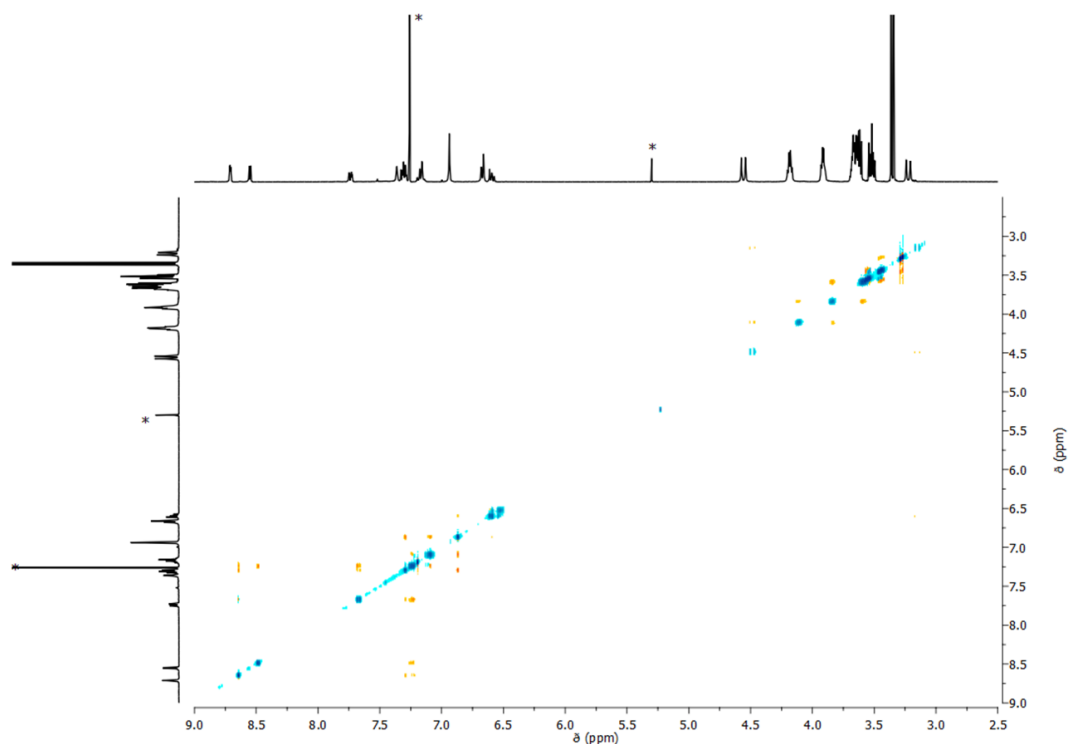
Figure A8.1.42. ^{1}H-^{1}H NOESY NMR spectrum (400 MHz, CDCl$_3$) of 5,17-bis(3,1-(phenylene)pyridine)-25,26,27,28-tetrakis(2-(2-(2-methoxyethoxy)ethoxy)ethoxy))-calix[4]arene (**42**) (* residual solvent).
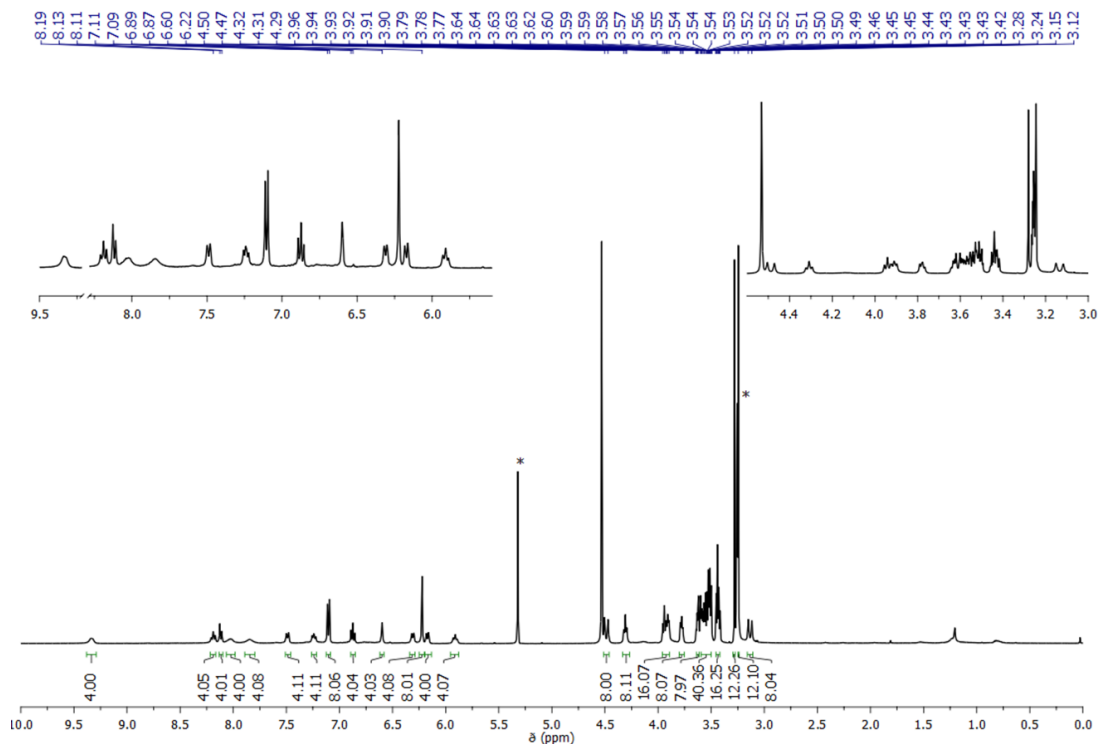
Figure A8.1.43. ^{1}H NMR spectrum (400 MHz, CD$_2$Cl$_2$/CD$_3$OD (1/1)) of [Ru(bda)(5,17-bis(3,1-(phenylene)pyridine)-25,26,27,28-tetrakis(2-(2-(2-methoxyethoxy)ethoxy)ethoxy))-calix[4]arene]$_2$ (**dimer 1**) (* residual solvent).

128
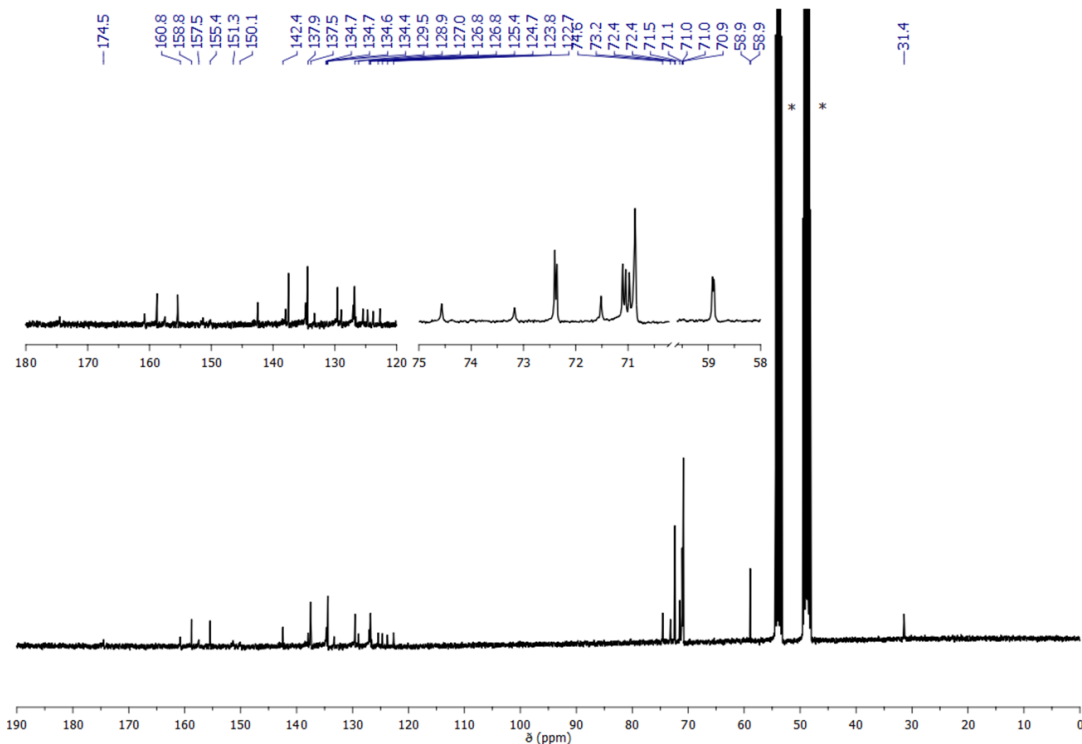
Figure A8.1.44. ^{13}C NMR spectrum (100 MHz, CD_2Cl_2/CD_3OD (1/1)) of [Ru(bda)(5,17-bis(3,1-(phenylene)pyridine)-25,26,27,28-tetrakis(2-(2-(2-methoxyethoxy)ethoxy)ethoxy))-calix[4]arene]$_2$ (**dimer 1**) (* residual solvent).
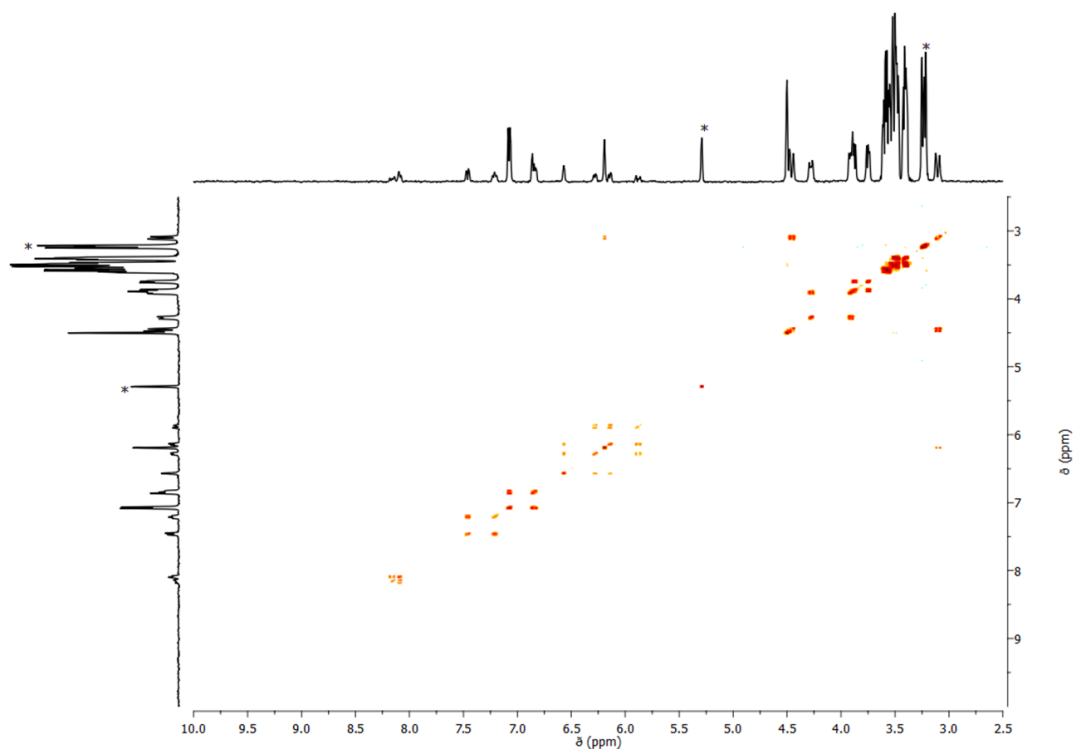
Figure A8.1.45. ^1H-^1H COSY NMR spectrum (400 MHz, CD_2Cl_2/CD_3OD (1/1)) of [Ru(bda)(5,17-bis(3,1-(phenylene)pyridine)-25,26,27,28-tetrakis(2-(2-(2-methoxyethoxy)ethoxy)ethoxy))-calix[4]arene]$_2$ (**dimer 1**) (* residual solvent).
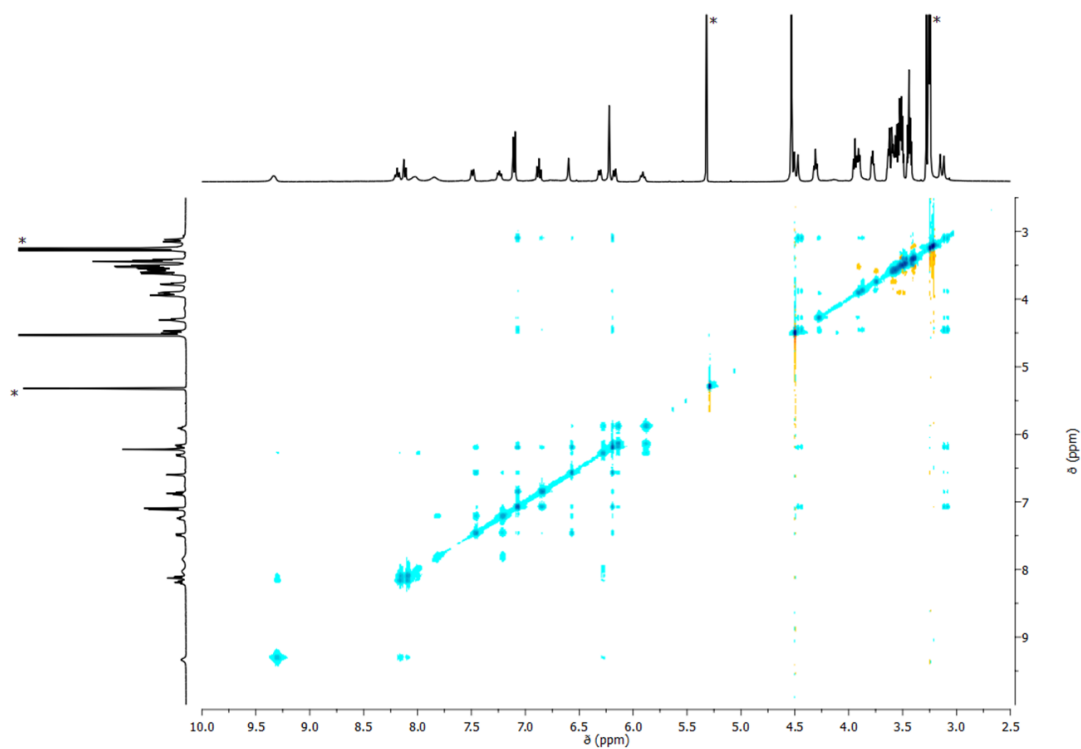
Figure A8.1.46. ^{1}H-^{1}H NOESY NMR spectrum (400 MHz, CD$_2$Cl$_2$/CD$_3$OD (1/1)) of [Ru(bda)(5,17-bis(3,1-(phenylene)pyridine)-25,26,27,28-tetrakis(2-(2-(2-methoxyethoxy)ethoxy)ethoxy))-calix[4]arene]$_2$ (**dimer 1**) (* residual solvent).
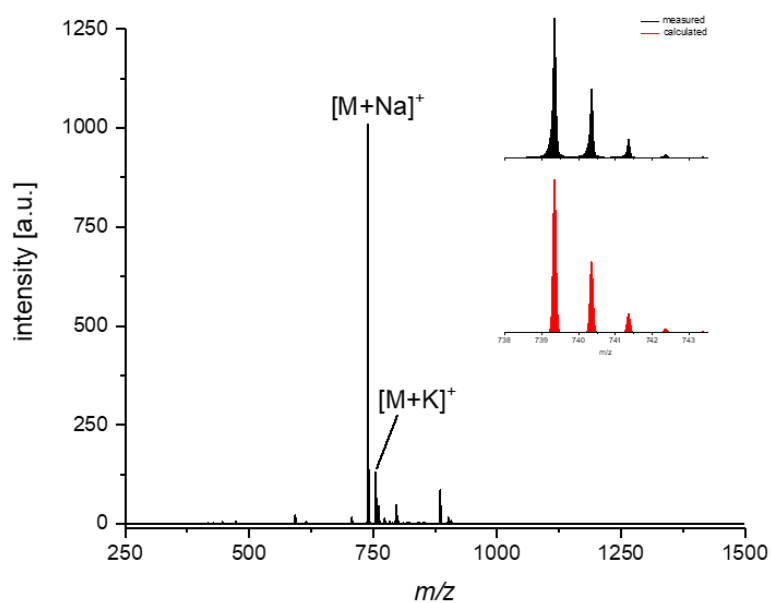
HR mass spectra

Figure A8.1.47. HRMS (ESI-TOF, pos mode) mass spectrum (CH$_3$CN/CHCl$_3$ 1:1, positive mode) of 25,27-bis(2-(2-(2-methoxyethoxy)ethoxy)ethoxy))-26,28-dihydroxycalix[4]arene (**37**) with the inset showing the measured and calculated isotopic distribution of [*M*+Na]$^+$.
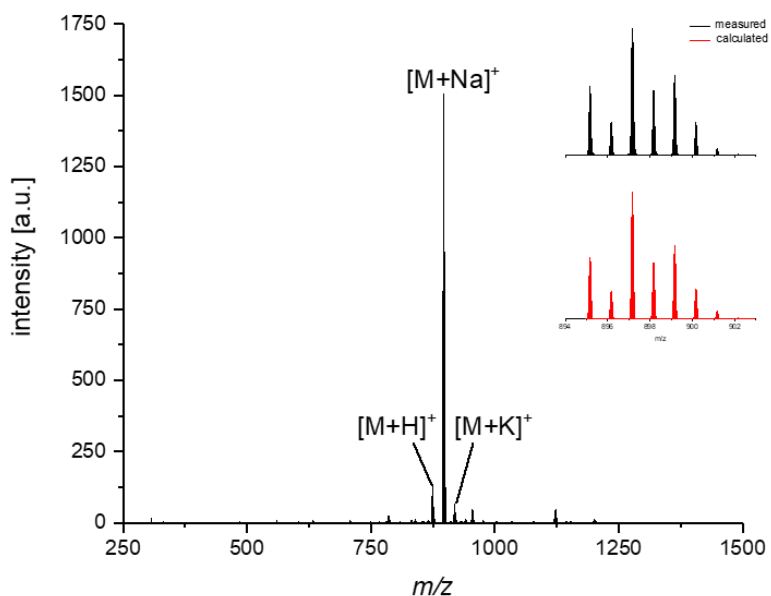
Figure A8.1.48. HRMS (ESI-TOF, pos mode) mass spectrum (CH$_3$CN/CHCl$_3$ 1:1, positive mode) of 5,17-dibromo-25,27-bis(2-(2-(2-methoxyethoxy)ethoxy)ethoxy))-26,28-dihydroxy-calix[4] arene (**38**) with the inset showing the measured and calculated isotopic distribution of [*M*+Na]$^+$.
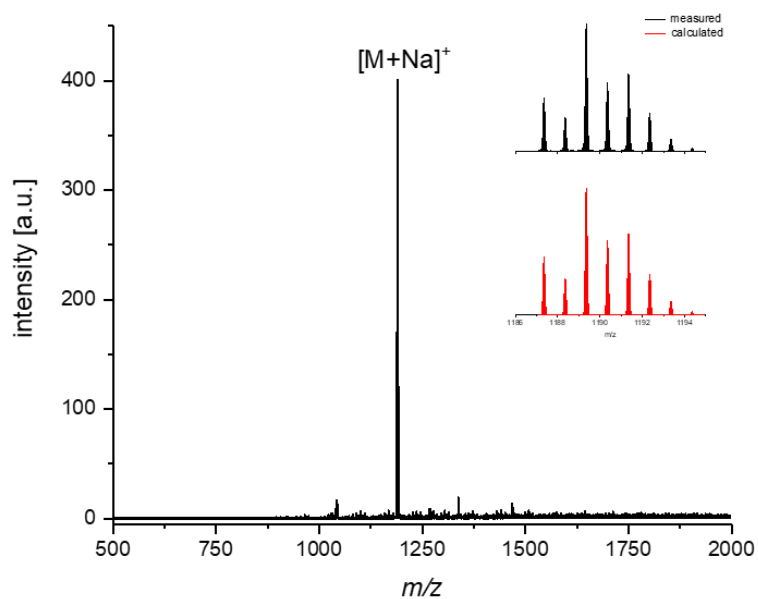
Figure A8.1.49. HRMS (ESI-TOF, pos mode) mass spectrum (CH₃CN/CHCl₃ 1:1, positive mode) of 5,17-dibromo-25,26,27,28-tetrakis(2-(2-(2-methoxyethoxy)ethoxy) ethoxy))-calix[4]arene (**40**) with the inset showing the measured and calculated isotopic distribution of [*M*+Na]⁺.
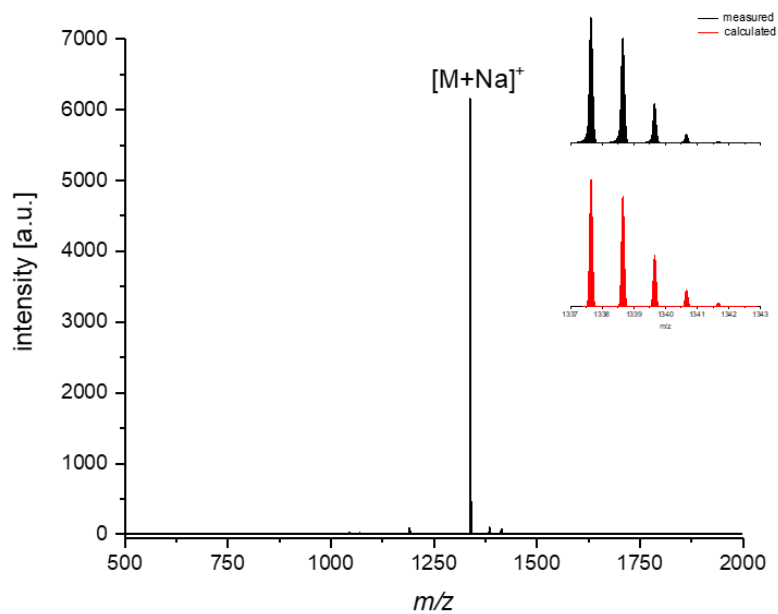
Figure A8.1.50. HRMS (ESI-TOF, pos mode) mass spectrum (CH₃CN/CHCl₃ 1:1, positive mode) of 5,17-bis(3,1-(phenylene)pyridine)-25,26,27,28-tetrakis(2-(2-(2-methoxyethoxy)   ethoxy)   ethoxy))-calix[4]arene (**42**) with the inset showing the measured and calculated isotopic distribution of [*M*+Na]⁺.
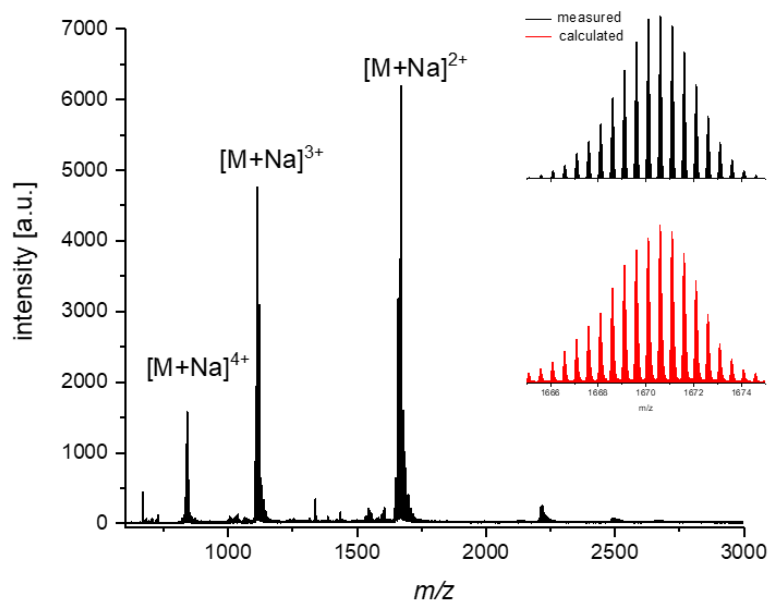
Figure A8.1.51. HRMS (ESI-TOF, pos mode) mass spectrum (CH_3OH/CH_2Cl_2 1:1, positive mode) of [Ru(bda)(5,17-bis(3,1-(phenylene)pyridine)-25,26,27,28-tetrakis(2-(2-(2-methoxyethoxy)ethoxy) ethoxy))-calix[4]arene]$_2$ (**dimer 1**) with the inset showing the measured and calculated isotopic distribution of [M+Na]$^{2+}$.

8.2 Supporting Information for *Chapter 4*

Please note: This Supporting Information has been published in reference[285]. For the sake of unity of this thesis, several editorial changes have been made, which, however, do not affect the contents of the thesis. Adapted or reprinted with permission from reference: N. Noll, A.-M. Krause, F. Beuerle, F. Würthner, *Nat. Catal.* **2022,** *5*, 867−877. Copyright 2022, The Author(s), under exclusive licence to Springer Nature Limited.

Materials and methods

Chemicals & Materials

2,2'-Bipyridine-6,6'-dicarboxylic acid,[328] [RuCl$_2$(dmso)$_4$],[329, 330] [Ru(bda)(dmso)$_2$],[268] 3-(4-bromophenoxy)pyridine[340] and 3-(4-(4,4,5,5-tetramethyl-1,3,2-dioxaborolan-2-yl)phenoxy) pyridine[340] were synthesized according to literature known procedures. Photosensitizer [Ru(bpy)$_3$Cl$_2$] was purchased from Sigma-Aldrich with 99.95% purity. Additional reagents and solvents were purchased from commercial sources and used without further purification, unless otherwise stated. Chemical water oxidation experiments were performed in deionized water obtained from a Purelab Classic water purification system (ELGA). For light-induced water oxidation experiments and UV/Vis studies, 50 mM phosphate buffer at pH 7 was used. Column chromatography was performed on silica gel (60M, 0.04−0.063 mm, Macherey-Nagel) with freshly distilled solvents. For further purifications, size exclusion chromatography with BioBeads particles (S-X1, Bio-Rad) suspended in a 9:1 DCM/MeOH mixtures were used.

Molecular characterization

^{1}H NMR and proton decoupled ^{13}C NMR spectra were recorded at 400 MHz and 100 MHz, respectively, using a Bruker Avance III HD 400 at 298 K. Chemical shifts (δ) are stated in parts per million (ppm) relative to the residual undeuterated solvent signal[331] and coupling constants (*J*) are given in Hz. The following abbrevations were applied to describe signal multiplicities: s = singlet, d = doublet, t = triplet and m = multiplet. For a correct assignment of 1D NMR spectra of new compounds, 2D NMR spectra (COSY, NOESY, HSQC and HMBC) were recorded. High resolution electrospray ionization (HR-ESI) mass spectra were measured using a ESI micrOTOF focus or a ESI micrOTOF-Q III mass spectrometer (Bruker Daltonics). MALDI TOF measurements were carried out on a Bruker Daltonics UltrafleXtreme mass spectrometer with DCTB (*trans*-2-[3-(4-tert-butylphenyl)-2-methyl-2-propenylidene]malononitrile) as matrix. Elemental analysis was performed using a Vario MICRO cube (Elementar Analysensysteme). The pH value of a respective aqueous solution was measured using a pH meter FG2/EL2 (Mettler Toledo), which was calibrated before each measurement. Melting points were

determined using a BX41 optical microscope (Olympus) connected with a temperature controller TP94 (Linkam Scientific Instruments Ltd.) and are uncorrected.

Preparation of aqueous solutions for NMR experiments and water oxidation catalysis

For preparation of pD 1.0 triflic acid (CF_3SO_3D) solution, a sample of deuterated neat triflic acid (1 g, 0.00663 mol) was diluted with 66.2 mL D_2O. For preparation of pH 1.0 triflic acid (CF_3SO_3H) solution, small amounts of neat triflic acid CF_3SO_3H were added to 1.0 mL deionized water and the respective pH value was detected by a pH meter FG2/EL2 (Mettler Toledo) until a pH of 1.0 was reached. A 50 mM phosphate buffer solution was prepared by dissolving NaH_2PO_4 (3.71 g, 30.9 mmol) and Na_2HPO_4 (2.7 g, 19.1 mmol) in deionized water or deuterated water (1000 mL).

Single crystal X-ray analysis

Single crystals of **M1** or **M2** were obtained by slow diffusion of diethyl ether in either a $CHCl_3$/MeOH (1:1) or DCM/MeOH (1:1) solution of the complexes **M1** and **M2**, respectively. These were stored in a refrigerator at 5 °C. Single crystals for complex $[(\mathbf{M1}+H)(H_2O)]^{2+}(PF_6^-)_2$ were obtained following a recent literature report for the crystallization of Ru(bda) complexes after chemical water oxidation conditions:[194] complex **M1** (10 mg, 12 µmol) was dissolved in 4 mL CH_3CN/H_2O 4:6 (pH 1, triflic acid) and cerium ammonium nitrate (400 mg, 720 µmol; ~60 eqiv.) was added stepwise. After vigorous oxygen evolution, subsequent addition of excess NH_4PF_6 led to slow precipitation and crystal formation after storing the mixture for several days in a refrigerator at 5 °C. Single crystal X-ray diffraction data were collected at 100 K on a Bruker D8 Quest Kappa Diffractometer with a PhotonII CPAD area detector and multi-layered mirror monochromated Cu Kα radiation (λ = 1.54178 Å). The structures were solved using direct methods, expanded with Fourier techniques and refined with the SHELX software package.[341] All non-hydrogen atoms were refined anisotropically. Hydrogen atoms were assigned to geometrically idealized positions and were included in calculation of structure factors. For all crystal structures, residual electron density for solvent molecules could not be modelled satisfactorily. Therefore, the PLATON squeeze routine was applied to remove the respective electron density.[342, 343] The remaining structure could then be refined nicely.

Chemical water oxidation

The measurements were performed with a standardized procedure as described in our previous publications.[37, 38, 40, 247] Water oxidation experiments under chemical conditions were carried out under ambient conditions in reaction vessels (V = 20.6 mL) connected to pressure sensors (Honeywell, SSCDANN030PAAA5, absolute pressure, 0 to 30 psi). For every experiment, CAN (1.0 g, 1.82 mmol) was dissolved in acetonitrile/water 4:6 mixture (3.0 mL,

pH 1, triflic acid) and the catalyst solution (400 μL stock solution) was then injected through a septum using a Hamilton syringe. Via gas chromatography (Shimadzu GC-2010 Plus, thermal conductivity detector at 30 mA, argon as carrier gas), the gas composition of the head space after each catalytic experiment (500 μL) was determined. The catalytic stability is defined by the respective turnover number (TON), which was calculated by dividing the total amount of generated oxygen by the amount of used catalyst. The amount of generated oxygen was determined by applying the ideal gas law: $\Delta p \times V = \Delta n \times R \times T$ (T = 293.15 K, V = 20.6 mL, R = 8.314 J K^{-1} mol^{-1}). For each concentration, a TON was calculated and the highest TON is given. The catalytic activity of molecular catalysts was determined by the turnover frequency (TOF). Therefore, the initial rate of catalysis for each concentration was calculated by linear regression of the first two seconds of catalysis. In case of a linear dependency between the respective initial rates and the catalyst concentration, the slope of the linear regression represents the averaged TOF. A range of the observed TOF values, calculated for each concentration, is given when a quadratic dependency is observed.

Photocatalytic water oxidation

The measurements were performed in an Oxygraph Plus Clark-electrode system with a transparent reaction chamber (Hansatech Instruments Ltd.) at 20 °C following a standardized procedure as described in our previous publications.[37, 40, 247] A Clark electrode was used for oxygen detection. The samples were irradiated using a 150 W xenon lamp (Newport) equipped with a 400 nm cutoff filter. All the experiments were carried out under a light intensity of 100 mW cm^{-1}. This was calibrated using CCS 200/M wide range spectrometer (Thorlabs) in combination with a PM 200 optical power meter equipped with an S121C sensor (Thorlabs), which was installed in a modified oxygen chamber (Hansatech Instruments Ltd.). Before the experiments, a stock solution of photosensitizer (PS) [Ru(bpy)$_3$]Cl$_2$ (c([Ru(bpy)$_3$]Cl$_2$) = 1.5 mM) and Na$_2$S$_2$O$_8$ (c(Na$_2$S$_2$O$_8$) = 37 mM) as the sacrificial electron acceptor (SEA) in CH$_3$CN/H$_2$O 4:6 mixtures (pH 7, 50 mM phosphate buffer) was prepared in the dark. At a constant temperature of 20 °C, the reaction chamber was filled with an aliquot of this solution (1.5 mL), mixed with catalyst solution at various concentrations (total volume: 2 mL) and kept in the dark for additional 50 s prior to irradiation. For each concentration, a TON was calculated (maximum amount of evolved oxygen during catalysis divided by the amount of used catalyst) and the highest TON is reported. After an initial induction period of ~1 s, the TOF for each concentration was determined based on the initial rate of catalysis. Therefore, the oxygen evolution curve was plotted against the reaction time and the initial rate was extracted by linear regression analysis of the oxygen amount versus the time for the first five to ten seconds of catalysis. The averaged TOF was then determined from the slope of a linear regression of the initial rates of

each concentration versus the respective catalyst amount. In case of a quadratic dependency, a range of the observed TOF values, calculated for each concentration, is given.

Kinetic Isotope Experiments

Based on standardized procedures described in our previous publications,[37, 38, 40, 247] the experiments were performed using a Oxygraph Plus Clark-electrode system (Hansatech Instruments Ltd.) for oxygen detection at a constant temperature of 20 °C. If the relative reactions rates for non-deuterated and deuterated solvent differ by approximately a factor of two, the reaction is characterized by a primary deuterium kinetic isotope effect (KIE) and a direct O−H/D bond cleavage is involved in the rate-determining step of the WNA pathway.[276] By contrast, for the bimolecular I2M mechanism no direct hydrogen substitution takes place and thus a secondary kinetic isotope effect (KIE = 0.7−1.5) is observed.[276] The experiments under conditions of chemical water oxidation were performed in 2.0 mL of a 4:6 acetonitrile/water (H_2O or D_2O (99.9% purity), pH 1, acid: triflic acid) mixture in the presence of CAN (c = 0.525 M) as sacrificial electron acceptor. For each measurement, 1.5 mL of a freshly prepared CAN solution (c = 0.7 M, 4:6 acetonitrile/water (H_2O or D_2O, pH 1)) was transferred to the transparent reaction chamber and after the baseline was constant (~40 s), 0.5 mL of the catalyst solution at varying concentrations was added. The experiments under photocatalytic conditions were performed in accordance with the procedures described for photocatalytic water oxidation. Therefore, a stock solution of PS (c([Ru(bpy)$_3$]Cl$_2$) = 1.5 mM) and SEA (c(Na$_2$S$_2$O$_8$) = 37 mM) in 4:6 acetonitrile/water (H_2O or D_2O (99.9% purity); pH 7, 50 mM phosphate buffer) was prepared in the dark. An aliquot of this solution (1.5 mL) was then mixed with a varying amount of catalyst concentration (total volume: 2 mL) in the dark. Irradiation was started at 50 s to allow thermal equilibration of the sample at a constant temperature of 20 °C. The reaction rates in H_2O ($k(H_2O)$) and D_2O ($k(D_2O)$) were calculated by determining the initial rate of catalysis for each concentration (linear regression of the oxygen evolution curve during the first five to ten seconds of reaction).
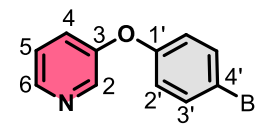
Stability test

To investigate the stability of the respective catalyst after chemical water oxidation, each complex (10.0 mg, 3.0 µmol) was dissolved in a mixture of CH$_3$CN/H$_2$O 4:6 (1.0 mL, pH 1, triflic acid). After addition of sacrificial oxidant CAN (500 mg, 960 µmol), intensive oxygen evolution occurred (~40 catalytic cycles). Then, ammonium hexafluorophosphate (250 mg) was added and a brown precipitate was formed. This was filtered off, washed with water and dried under reduced pressure. The sample was redissolved, reduced with ascorbic acid and analyzed using MALDI TOF mass spectrometry (positive, *trans*-2-[3-(4-tert-butylphenyl)-2-methyl-2-propenylidene] malononitrile (DCTB), CH$_2$Cl$_2$/CH$_3$OH 1:1).
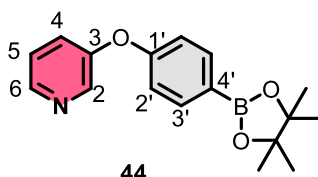
Experimental procedures

Synthesis of molecular precursor 44

3-(4-bromophenoxy)pyridine

4-(pyridin-3-yloxy)aniline (8.72 g, 46.8 mmol, 1.0 equiv.) was dissolved in 48% aqueous HBr (60 mL) and a solution of $NaNO_2$ (6.78 g, 98.3 mmol, 2.1 equiv.) in H_2O (48 mL) was added dropwise over 10 min at 0 °C. After stirring for additional 2 hours at room temperature, CuBr (10.1 g, 70.2 mmol, 1.5 equiv.) was added slowly at 0 °C and the mixture was stirred at room temperature for 2 hours and at 140 °C for 24 hours. After cooling to room temperature, the crude product was carefully neutralized with saturated $NaHCO_3$ solution at 0 °C and extracted with ethyl acetate (3 x 50 mL). The combined organic phases were dried over anhydrous Na_2SO_4 and concentrated under reduced pressure. The residue was purified by flash chromatography (SiO_2, cyclohexane/ethyl acetate 60:10) to yield 3-(4-bromophenoxy)pyridine (6.60 g, 26.4 mmol, 56%, Lit[340]: not reported) as a yellow oil. **^{1}H NMR** (400 MHz, CDCl$_3$, rt): δ [ppm] = 8.40 (dd, $^3J_{H-H}$ = 5.1 Hz, $^4J_{H-H}$ = 2.6 Hz, 2H, *H2 & H6*), 7.50−7.45 (m, 2H, *H4 & H5*), 7.32−7.28 (m, 2H, *H3'*), 6.93−6.89 (m, 2H, *H2'*). Analytic data are in accordance with the literature.[340]

3-(4-(4,4,5,5-tetramethyl-1,3,2-dioxaborolan-2-yl)phenoxy)pyridine (44)

44

A mixture of 3-(4-bromophenoxy)pyridine (1.05 g, 4.20 mmol, 1.0 equiv.), bis(pinacolato)diboron (2.35 g, 9.24 mmol, 2.2 equiv.) and KOAc (1.24 g, 12.6 mmol, 3.0 equiv.) in dry dioxane (5.3 mL) and dry DMF (0.7 mL) was degassed under nitrogen for 45 min. Subsequently, Pd(dppf)Cl$_2$ (92.2 mg, 126 µmol, 0.03 equiv.) was added and the mixture was stirred for 62 hours at 95 °C. After cooling down to room temperature, the crude mixture was filtrated over Celite and concentrated under reduced pressure. The residue was purified by flash chromatography (SiO_2, dichloromethane to dichloromethane / ethyl acetate 90:10) to yield compound **44** (766 mg, 2.58 mmol, 61%, Lit.[340]: not reported) as a pale white oil. **^{1}H NMR** (400 MHz, CDCl$_3$, rt): δ [ppm] = 8.44−8.42 (m, 1H, *H2*), 8.39 (dd, $^3J_{H-H}$ = 4.5 Hz, $^4J_{H-H}$ = 1.6 Hz, 1H, *H6*), 7.83−7.79 (m, 2H, *H3'*), 7.33−7.27 (m, 2H, *H4 & H5*), 7.02−6.98 (m, 2H, *H2'*), 1.35 (s, 12H). Analytic data are in accordance with the literature.[340]

Synthesis of bidentate ligands L1 & L2

6,6'-bis(4-(pyridin-3-yloxy)phenyl)-2,2'-bipyridine (L1)
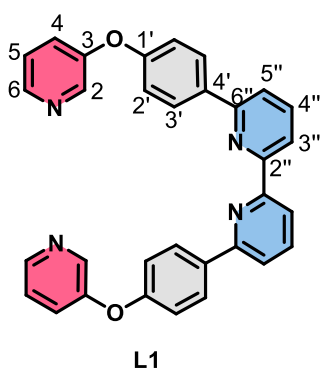
A mixture of 6,6'-dibromo-2,2'-bipyridine (**BP1**) (251 mg, 800 µmol, 1.0 equiv.), 3-(4-(4,4,5,5-tetramethyl-1,3,2-dioxaborolan-2-yl)phenoxy) pyridine (**44**) (523 mg, 1.76 mmol, 2.2 equiv.) and 2 M Na_2CO_3 aqueous solution (3.2 mL, 6.4 mmol, 8.0 equiv.) in toluene (6.4 mL) and ethanol (1.6 mL) was degassed under nitrogen by three consecutive freeze-pump-thaw cycles. Subsequently, $PdCl_2(PPh_3)_2$ (56.1 mg, 80 µmol, 0.1 equiv.) was added and the resulting mixture was heated at 110 °C for 18 hours. After cooling down to room temperature, the solvent was removed under reduced pressure and the residue was diluted with dichloromethane (15 mL). The organic phase was separated, and the aqueous phase extracted with dichloromethane (3×25 mL). The combined organic phases were dried over anhydrous Na_2SO_4 and concentrated under reduced pressure. The residue was purified by flash chromatography (SiO_2, cyclohexane/ethyl acetate 80:20 to 50:50) to yield ligand **L1** (297 mg, 600 µmol, 75%) as a white solid. **m.p.** 182 °C. **^{1}H NMR** (400 MHz, $CDCl_3$, rt): δ [ppm] = 8.57 (dd, $^3J_{H-H}$ = 7.8 Hz, $^4J_{H-H}$ = 0.9 Hz, 2H, *H3''*), 8.49 (dd, $^4J_{H-H}$ = 2.8 Hz, $^5J_{H-H}$ = 0.5 Hz, 2H, *H2*), 8.41 (dd, $^3J_{H-H}$ = 4.6 Hz, $^4J_{H-H}$ = 1.4 Hz, 2H, *H6*), 8.21−8.17 (m, 4H, *H3'*), 7.92 (t, $^3J_{H-H}$ = 7.8 Hz, 2H, *H4''*), 7.76 (dd, $^3J_{H-H}$ = 7.9 Hz, $^4J_{H-H}$ = 0.9 Hz, 2H, *H5''*), 7.38 (ddd, $^3J_{H-H}$ = 8.4 Hz, $^4J_{H-H}$ = 2.8 Hz, 1.5 Hz, 2H, *H4*), 7.31 (ddd, $^3J_{H-H}$ = 8.4 Hz, 4.6 Hz, $^5J_{H-H}$ = 0.7 Hz, 2H, *H5*), 7.19−7.15 (m, 4H, *H2'*). **^{13}C NMR** (100 MHz, $CDCl_3$, rt) δ [ppm] = 157.5, 156.0, 155.6, 153.8, 144.8, 141.8, 137.9, 135.5, 128.9, 125.9, 124.3, 120.1, 119.5, 119.1. **HRMS** (ESI-TOF, pos. mode, MeCN/$CHCl_3$ 1:1): *m/z* calcd for $C_{32}H_{22}N_4O_2$+H^+: 495.1815 [*M*+H]$^+$; found: 495.1802. **elemental analysis** calcd. (%) for $C_{32}H_{22}N_4O_2$: C 77.72, H 4.48, N 11.33; found: C 77.54, H 4.63, N 11.38.

4,4'''-bis(pyridin-3-yloxy)-1,1':3',1'':3'',1'''-quaterphenyl (L2)
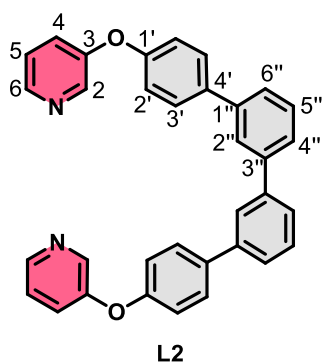
A mixture of 3,3'-dibromo-1,1'-biphenyl (**BP2**) (156 mg, 500 µmol, 1.0 equiv.), 3-(4-(4,4,5,5-tetramethyl-1,3,2-dioxaborolan-2-yl)phenoxy) pyridine (**44**) (327 mg, 1.10 mmol, 2.2 equiv.) and 2 M Na_2CO_3 aqueous solution (2.0 mL, 4.00 mmol, 8.0 equiv.) in toluene (4.0 mL) and ethanol (1.0 mL) was degassed under nitrogen by three consecutive freeze-pump-thaw cycles. Subsequently, $PdCl_2(PPh_3)_2$ (35.1 mg, 50 µmol, 0.1 equiv.) was added and the resulting mixture was heated at 110 °C for 18 hours. After cooling down to room temperature, the solvent was removed under reduced pressure and the residue was diluted with dichloromethane (10 mL). The organic phase was separated, and the aqueous phase extracted with dichloromethane (3×25 mL). The combined organic phases were dried over anhydrous Na_2SO_4 and concentrated under reduced pressure. The residue was purified by flash chromatography (SiO_2, cyclohexane to cyclohexane/ethyl acetate 80:20) to yield ligand **L2** (157 mg, 320 µmol, 64%) as a white gel. **^{1}H NMR** (400 MHz, $CDCl_3$, rt): δ [ppm] = 8.46 (d, $^4J_{H-H}$ = 2.6 Hz, 2H, *H2*), 8.40 (d, $^4J_{H-H}$ = 3.9 Hz, 2H, *H6*), 7.83 (t, $^4J_{H-H}$ = 1.7 Hz, 2H, *H2''*), 7.68−7.62 (m, 6H, *H3'* & *H6''*), 7.60−7.52 (m, 4H, *H4''* & *H5''*), 7.41 (ddd, $^3J_{H-H}$ = 8.4 Hz, $^4J_{H-H}$ = 2.7 Hz, 1.4 Hz, 2H, *H4*), 7.34 (dd, $^3J_{H-H}$ = 8.4 Hz, 4.7 Hz, 2H, *H5*), 7.15−7.10 (m, 4H, *H2'*). **^{13}C NMR** (100 MHz, $CDCl_3$, rt) δ [ppm] = 155.9, 154.3, 143.7, 141.9, 141.0, 140.6, 137.5, 129.5, 129.1, 126.4, 126.4, 126.3, 126.2, 124.6, 119.5. **HRMS** (ESI-TOF, pos. mode, MeCN/CHCl₃ 1:1): *m/z* calcd for $C_{34}H_{24}N_2O_2$+Na$^+$: 515.1730 [*M*+Na]$^+$; found: 515.1730. **elemental analysis** calcd. (%) for $C_{34}H_{24}N_2O_2$: C 82.91, H 4.91, N 5.69; found: C 82.51, H 4.80, N 5.79.

Synthesis of mononuclear Ru complexes M1 & M2

[Ru(bda)(6,6'-bis(4-(pyridin-3-yloxy)phenyl)-2,2'-bipyridine)] (M1)
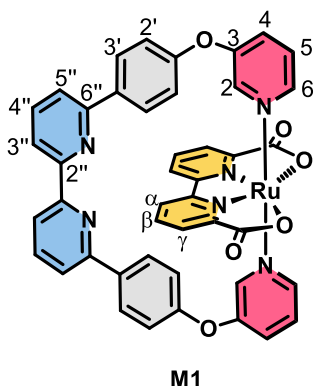
[Ru(bda)(dmso)$_2$] (165 mg, 330 µmol, 1.1 equiv.) and ligand **L1** (148 mg, 300 µmol, 1.0 equiv.) were dissolved in a degassed mixture of chloroform (50 mL) and methanol (50 mL) and stirred for 14 hours at 65 °C under nitrogen. After cooling to room temperature, the solvent was removed under reduced pressure. The residue was purified by column chromatography (SiO$_2$, dichloromethane/methanol 10:0.5 to 10:3) and isolated as the first fraction to yield complex **M1** (123 mg, 147 µmol, 49%) as a dark red solid. **m.p.** >300 °C. **^{1}H NMR** (400 MHz, CD$_2$Cl$_2$/CD$_3$OD (1:1) + ascorbic acid, rt): δ [ppm] = 8.84 (dd, $^3J_{\text{H-H}}$ = 8.1 Hz, $^4J_{\text{H-H}}$ = 1.0 Hz, 2H, *Hα*), 8.65 (dd, $^3J_{\text{H-H}}$ = 5.3 Hz, $^4J_{\text{H-H}}$ = 1.3 Hz, 2H, *H6*), 8.12 (t, $^3J_{\text{H-H}}$ = 7.8 Hz, 2H, *H4''*), 7.97 (dd, $^3J_{\text{H-H}}$ = 7.8 Hz, $^4J_{\text{H-H}}$ = 0.8 Hz, 2H, *H5''*), 7.79−7.77 (m, 4H, *Hγ* & *H6''*), 7.69−7.64 (m, 4H, *H3'*), 7.43−7.32 (m, 6H, *Hβ* & *H4* & *H5*), 6.61−6.55 (m, 4H, *H2'*), 5.59 (d, $^4J_{\text{H-H}}$ = 2.5 Hz, 2H, *H2*). **^{13}C NMR** (100 MHz, CD$_2$Cl$_2$/CD$_3$OD (1:1) + ascorbic acid, rt) δ [ppm] **=** 174.4, 159.8, 159.5, 159.1, 156.8, 156.4, 154.3, 150.1, 139.8, 138.9, 136.1, 132.2, 130.9, 127.8, 126.2, 121.9, 121.7, 121.7. **UV/Vis** (CH$_3$CN/H$_2$O 4:6 (pH 1)): λ$_{\text{max}}$ (ε) = 254 (42283), 302 (39153), 345 (18765), 454 (4954), 482 nm (4766 M^{-1} cm^{-1}); (CH$_3$CN/H$_2$O 4:6 (pH 7)): λ$_{\text{max}}$ (ε) = 253 (39909), 304 (31047), 366 (8854), 458 (4003), 482 nm (3537 M^{-1} cm^{-1}). **HRMS** (ESI-TOF, pos. mode, MeOH/CH$_2$Cl$_2$ 1:1): *m/z* calcd for C$_{44}$H$_{28}$N$_6$O$_6$Ru$^+$: 838.1108 [*M*]$^+$; found: 838.1112. **elemental analysis** calcd. (%) for C$_{44}$H$_{28}$N$_6$O$_6$Ru: C 63.08, H 3.37, N 10.03; found: C 62.79, H 3.50, N 10.00.

[Ru(bda)(4,4'''-bis(pyridin-3-yloxy)-1,1':3',1'':3'',1'''-quaterphenyl)] (M2)
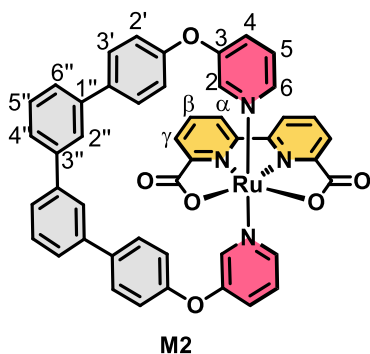
[Ru(bda)(dmso)$_2$] (165 mg, 330 µmol, 1.1 equiv.) and ligand **L2** (148 mg, 300 µmol, 1.0 equiv.) were dissolved in a degassed mixture of chloroform (50 mL) and methanol (50 mL) and stirred for 14 hours at 65 °C under nitrogen. After cooling to room temperature, the solvent was removed under reduced pressure. The residue was purified by column chromatography (SiO$_2$, dichloromethane/ methanol 10:0.3 to 10:3) and isolated as the first fraction to yield complex **M2** (87.8 mg, 105 µmol, 35%) as a red solid. **m.p.** >300 °C. **^{1}H NMR** (400 MHz, CD$_2$Cl$_2$/CD$_3$OD (1:1) + ascorbic acid, rt): δ [ppm] = 8.29 (dd, $^3J_{H-H}$ = 8.5 Hz, $^4J_{H-H}$ = 5.4 Hz, 2H, *H6*), 8.05 (m, 2H, H*2''*), 7.99 (dd, $^3J_{H-H}$ = 8.1 Hz, $^4J_{H-H}$ = 0.9 Hz, 2H, *Hα*), 7.91 (dd, $^3J_{H-H}$ = 7.7 Hz, $^4J_{H-H}$ = 0.9 Hz, 2H, *Hγ*), 7.84 (dt, $^3J_{H-H}$ = 7.0 Hz, $^4J_{H-H}$ = 1.8 Hz, 2H, *H6''*), 7.69−7.63 (m, 4H, *H4''* & *H5''*), 7.58 (t, $^3J_{H-H}$ = 7.9 Hz, 2H, *Hβ*), 7.50−7.47 (m, 4H, *H3'*), 7.42 (ddd, $^3J_{H-H}$ = 8.5 Hz, $^4J_{H-H}$ = 2.6 Hz, 1.1 Hz, 2H, *H4*), 7.27 (dd, $^3J_{H-H}$ = 8.5 Hz, 5.6 Hz, 2H, *H5*), 6.75−6.70 (m, 4H, *H2'*), 6.24 (d, $^4J_{H-H}$ = 2.0 Hz, 2H, *H2*). **^{13}C NMR** (100 MHz, CD$_2$Cl$_2$/CD$_3$OD (1:1) + ascorbic acid, rt) δ [ppm] = 173.9, 160.2, 157.8, 156.5, 154.1, 149.2, 142.6, 142.5, 140.1, 137.3, 132.3, 131.0, 130.5, 130.3, 127.4, 126.9, 126.3, 126.1, 125.9, 124.4, 121.2. **UV/Vis** (CH$_3$CN/H$_2$O 4:6 (pH 1)): λ$_{max}$ (ε) = 253 (66036), 303 (27017), 356 (10670), 460 (4123), 492 nm (4052 M^{-1} cm^{-1}); (CH$_3$CN/H$_2$O 4:6 (pH 7)): λ$_{max}$ (ε) = 254 (63988), 306 (24275), 358 (9988), 458 (4003), 492 nm (3454 M^{-1} cm^{-1}). **HRMS** (ESI-TOF, pos. mode, MeOH/CH$_2$Cl$_2$ 1:1): *m/z* calcd for C$_{46}$H$_{30}$N$_4$O$_6$Ru$^+$: 836.1209 [*M*]$^+$; found: 836.1233. **elemental analysis** calcd. (%) for C$_{46}$H$_{30}$N$_4$O$_6$Ru: C 66.10, H 3.62, N 6.70; found: C 65.63, H 3.69, N 6.73.

Optical and Electronic Properties
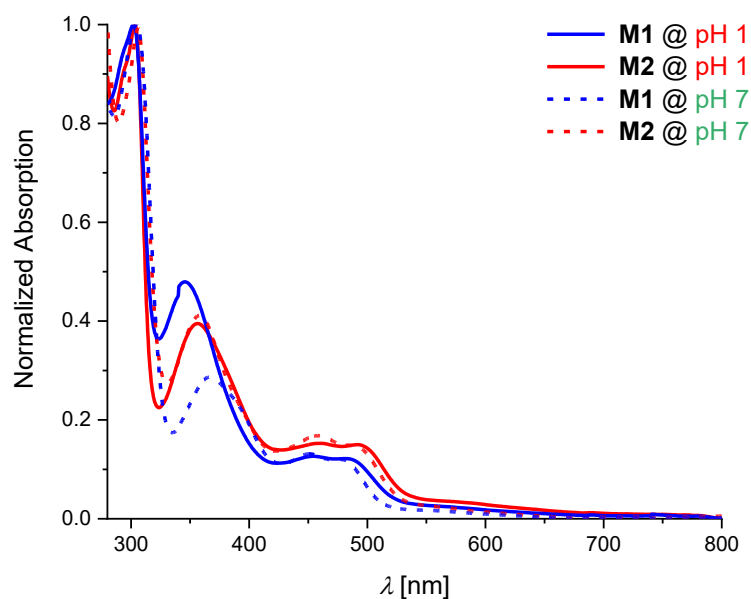
Figure A8.2.1. Normalized UV/Vis absorption spectra of **M1** (blue) and **M2** (red) at the Ru^{II} state in CH$_3$CN/H$_2$O 4:6 at pH 1 (solid line) and pH 7 (dotted line), c = 10^{-5} M.

Table A8.2.1. Redox properties of complexes **M1** and **M2** under acidic (pH 1, triflic acid) or neutral aqueous conditions (pH 7) with 40% 2,2,2-trifluorethanol (TFE) as organic co-solvent. The measurements were performed in 0.1 M ionic strength phosphate buffered aqueous mixtures at different pH.[a]

Catalyst	E vs. NHE [V]		
	Ru$_2^{III}$/Ru$_2^{II}$	Ru$_2^{IV}$/Ru$_2^{III}$	Ru$_2^{V}$/Ru$_2^{IV}$
M1 @ pH 1	+0.71	+1.14	+1.33
M2 @ pH 1	+0.76	+1.12	+1.33
M1 @ pH 7	+0.67	+0.83	+1.03
M2 @ pH 7	+0.69	+0.84	+0.99

[a] CV and DPV measurements under acidic or neutral conditions were performed at c = 2.5·10^{-4} M.
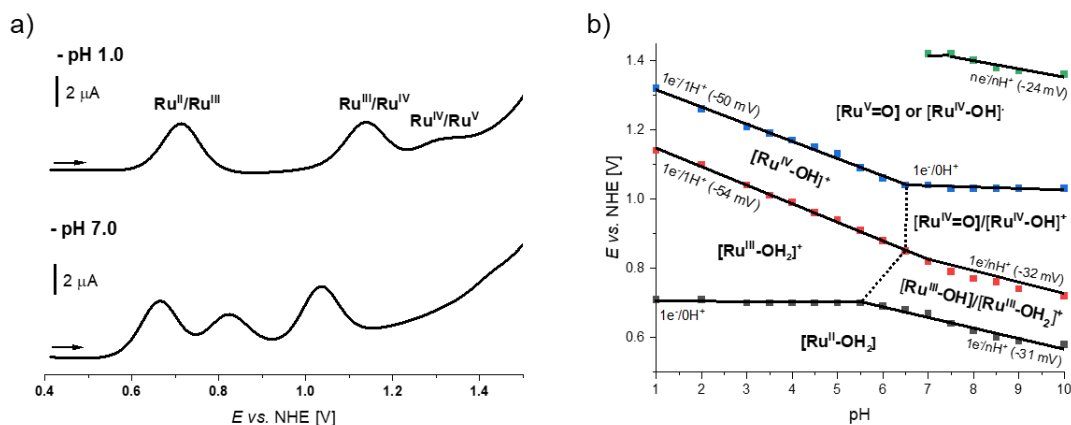
Figure A8.2.2. a) Differential pulse voltammogram of **M1** at pH 1 and pH 7. b) Pourbaix diagram of **M1**. DPV measurements were performed in TFE/H$_2$O 4:6 (phosphate buffer at different pH values with I = 0.1 M, c(**M1**) = 2.5·10^{-4} M).
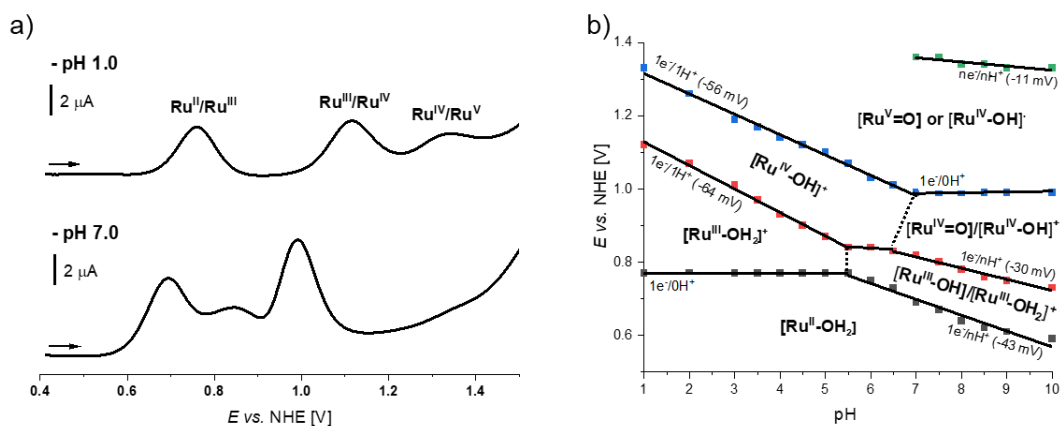
Figure A8.2.3. a) Differential pulse voltammogram of **M2** at pH 1 and pH 7. b) Pourbaix diagram of **M2**. DPV measurements were performed in TFE/H$_2$O 4:6 (phosphate buffer at different pH values with I = 0.1 M, c(**M2**) = 2.5·10^{-4} M).

Table A8.2.2. Comparison of measured overpotentials η of complexes **M1** and **M2** under acidic (pH 1, triflic acid) or neutral aqueous conditions (pH 7, 50 mM phosphate buffer) with 40% 2,2,2-trifluorethanol (TFE) as organic co-solvent.

Catalyst	Crossing point [mV]	Overpotential η [mV]
M1 @ pH 1	1460	290
M2 @ pH 1	1470	300
M1 @ pH 7	1260	440
M2 @ pH 7	1160	340
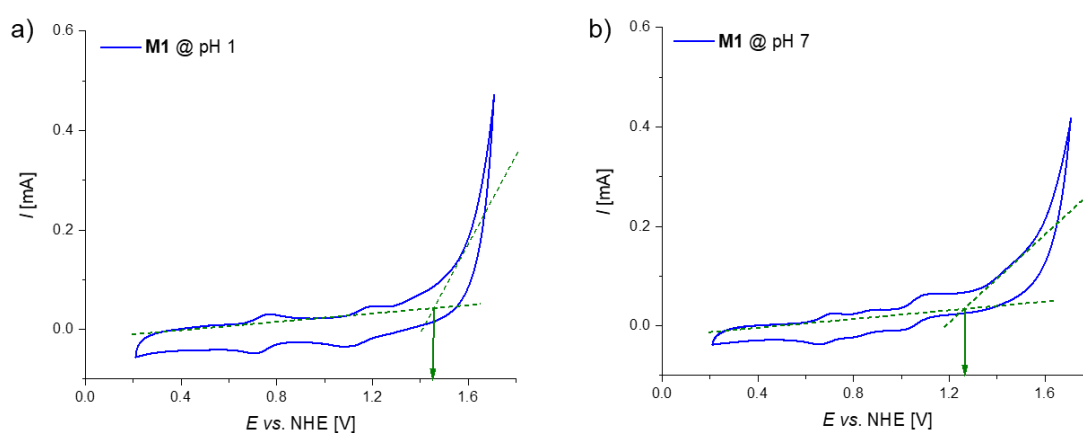
Figure A8.2.4. a,b) CV (scan rate: 100 mV s^{-1}) of **M1** in TFE/H$_2$O 4:6 at (a) pH 1 (triflic acid) and (b) pH 7, 50 mM phosphate buffer; c(**M1**) = 2.5·10^{-4} M). The onset potential was determined as the crossing point between the baseline and the slope of the catalytic water oxidation at the beginning of the process.
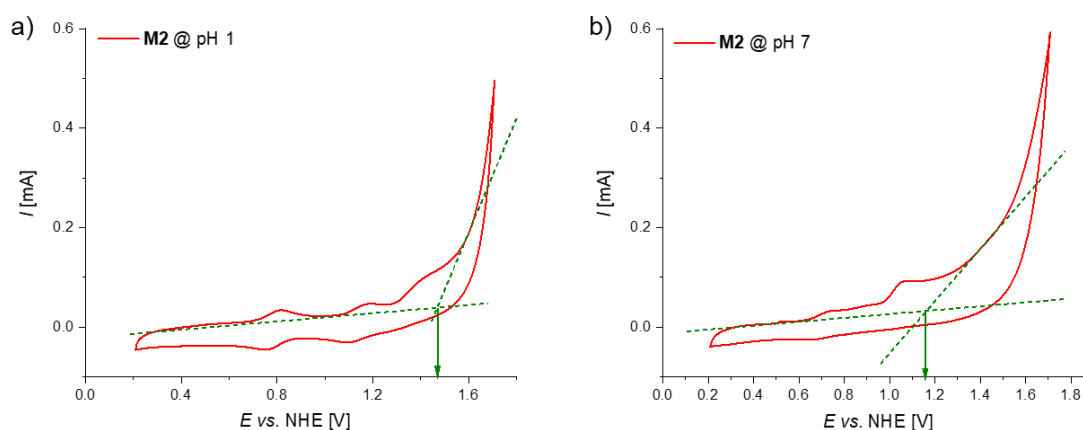
Figure A8.2.5. a,b) CV (scan rate: 100 mV s^{-1}) of **M2** in TFE/H$_2$O 4:6 at (a) pH 1 (triflic acid) and (b) pH 7, 50 mM phosphate buffer; c(**M2**) = 2.5·10^{-4} M). The onset potential was determined as the crossing point between the baseline and the slope of the catalytic water oxidation at the beginning of the process.

Chemical water oxidation
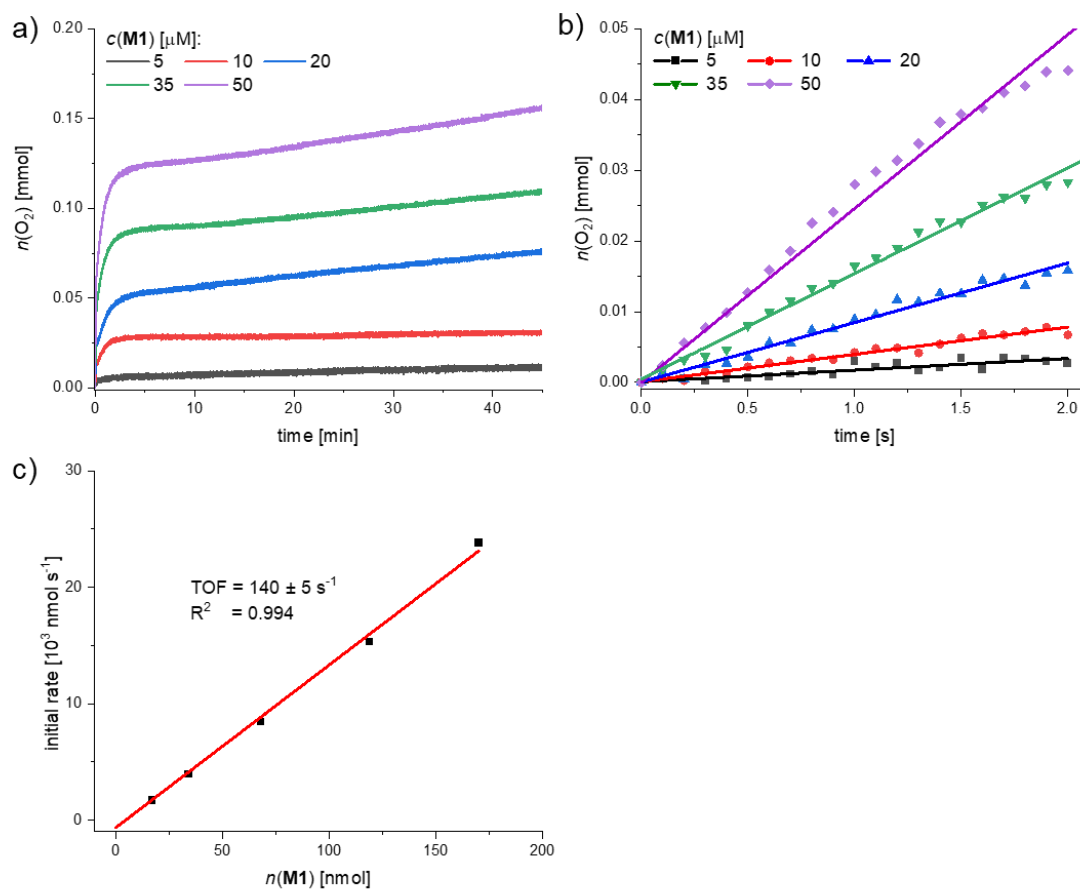
Figure A8.2.6. a) Oxygen evolution curves of **M1** at variable concentrations in CH_3CN/H_2O 4:6 (pH 1, triflic acid), c(CAN) = 0.6 M. b) linear regression of oxygen evolution for **M1** in the first 2 s of catalysis. c) plot of the initial rate vs. the catalyst amount with linear regression for the determination of the TOF.
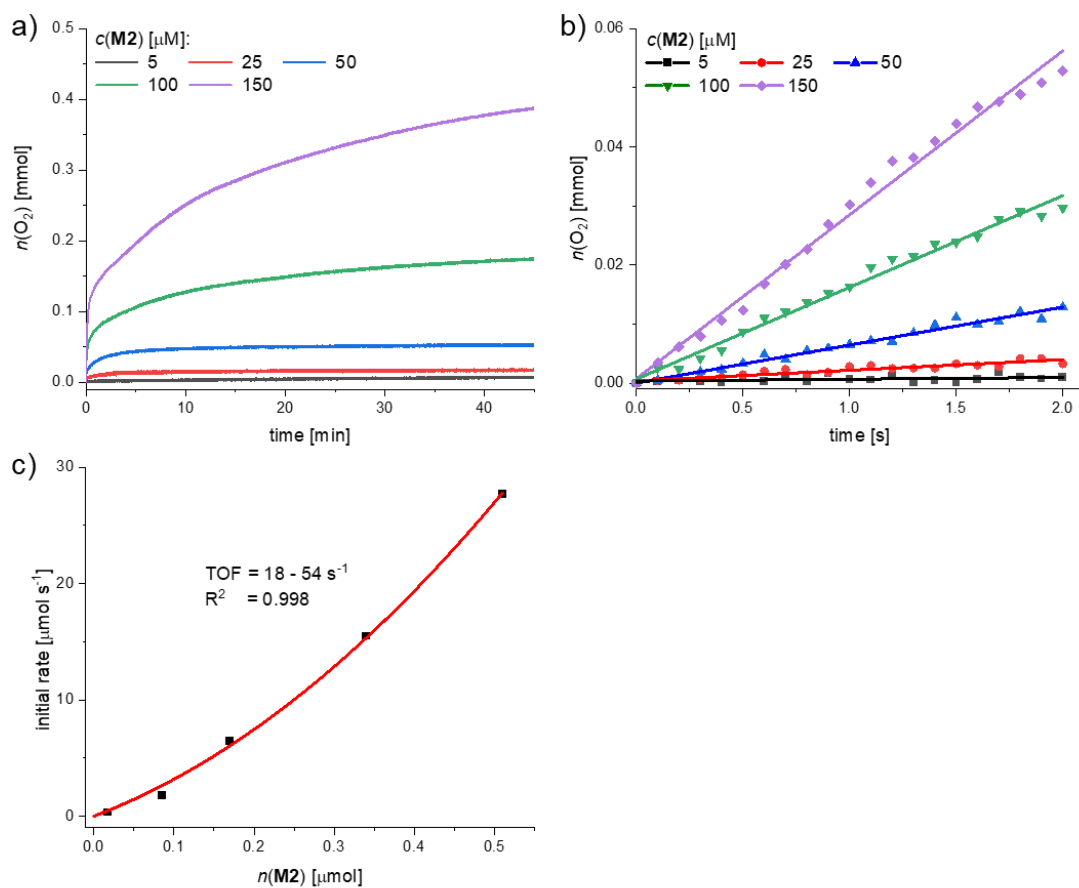
Figure A8.2.7. a) Oxygen evolution curves of **M2** at variable concentrations in CH_3CN/H_2O 4:6 (pH 1, triflic acid), c(CAN) = 0.6 M. b) linear regression of oxygen evolution for **M2** in the first 2 s of catalysis. c) plot of the initial rate vs. the catalyst amount with quadratic regression.
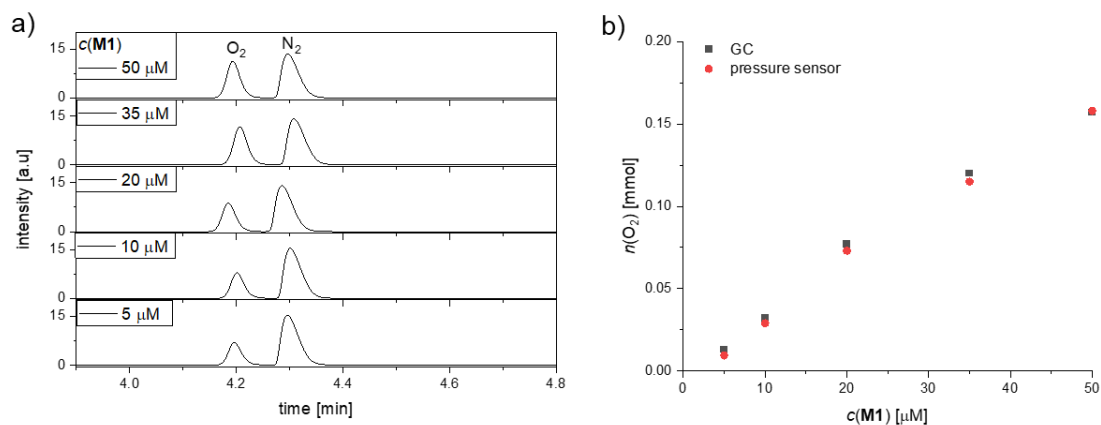
Figure A8.2.8. a) Gas chromatogram of the reaction headspace after the water oxidation experiments with **M1** as catalyst. b) Comparison of the amount of evolved oxygen determined by GC or with pressure sensors.
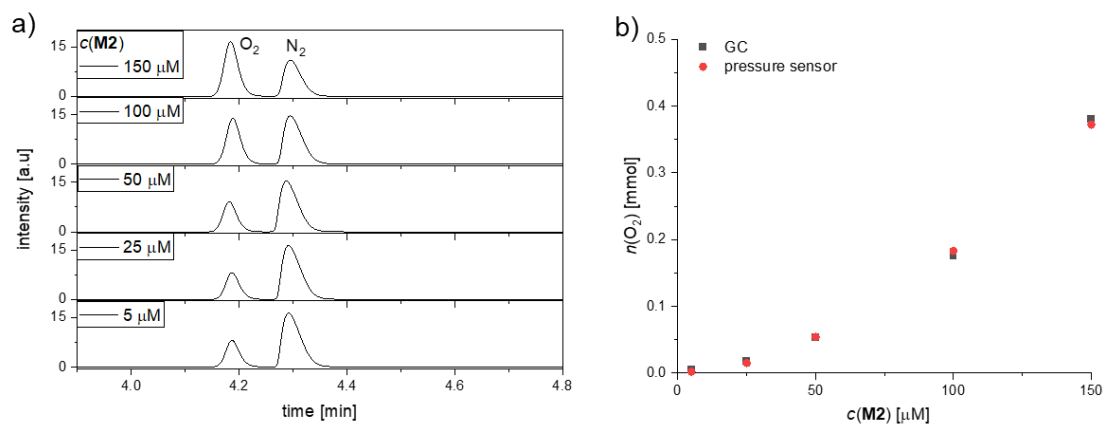
Figure A8.2.9. a) Gas chromatogram of the reaction headspace after the water oxidation experiments with **M2** as catalyst. b) Comparison of the amount of evolved oxygen determined by GC or with pressure sensors.

Stability tests after chemical water oxidation experiments
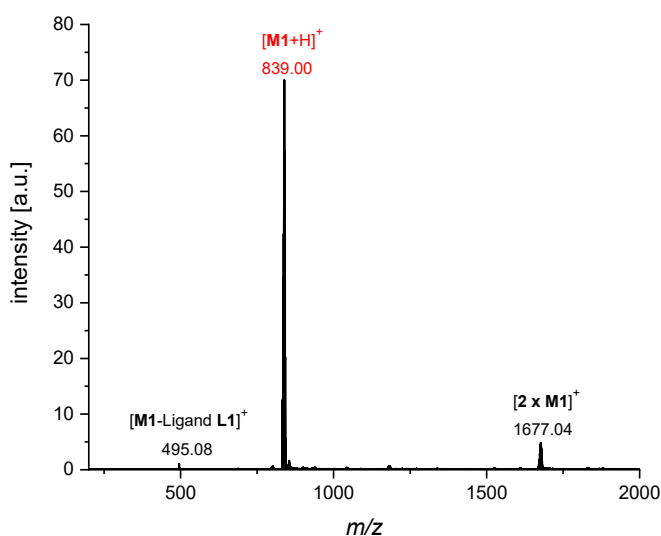
Figure A8.2.10. HR MALDI-TOF mass spectrum (CH_2Cl_2/CH_3OH 1:1, positive mode) of **M1** after water oxidation catalysis (~40 catalytic cycles) with cerium ammonium nitrate (CAN) as oxidant in 4:6 CH_3CN/H_2O (pH 1, triflic acid). Before the measurement, the sample was reduced with ascorbic acid.
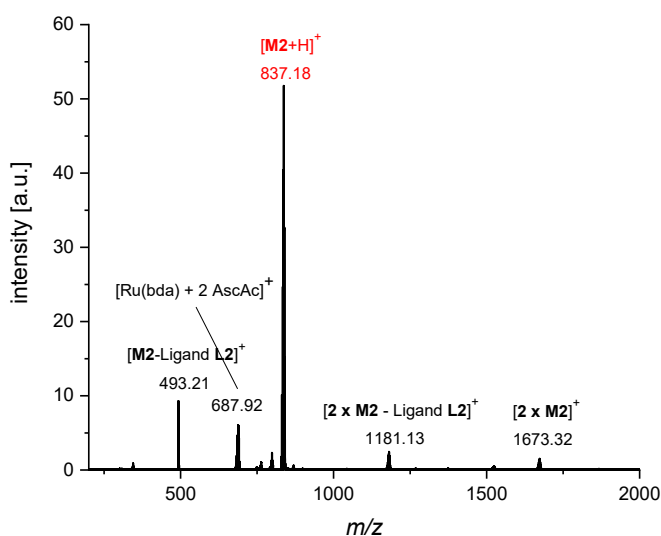
Figure A8.2.11. HR MALDI-TOF mass spectrum (CH_2Cl_2/CH_3OH 1:1, positive mode) of **M2** after water oxidation catalysis (~40 catalytic cycles) with cerium ammonium nitrate (CAN) as oxidant in 4:6 CH_3CN/H_2O (pH 1, triflic acid). Before the measurement, the sample was reduced with ascorbic acid.

Photocatalytic water oxidation
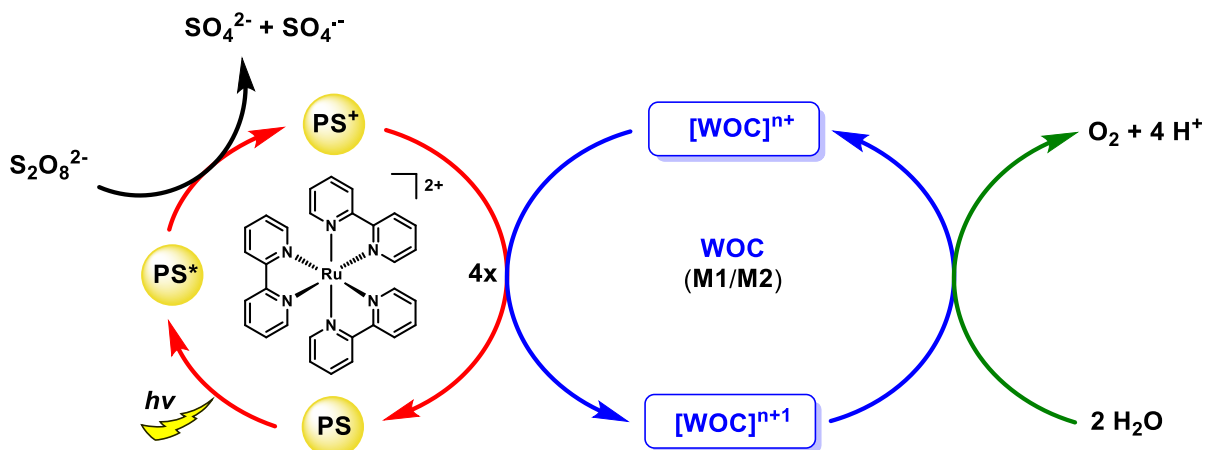
Figure A8.2.12. Schematic presentation of the photocatalytic water oxidation cycle in a three-component system containing $Na_2S_2O_8$ as sacrificial electron acceptor (SEA), $[Ru(bpy)_3]^{2+}$ as photosensitizer (PS) and complexes **M1** or **M2** as water oxidation catalyst (WOC).
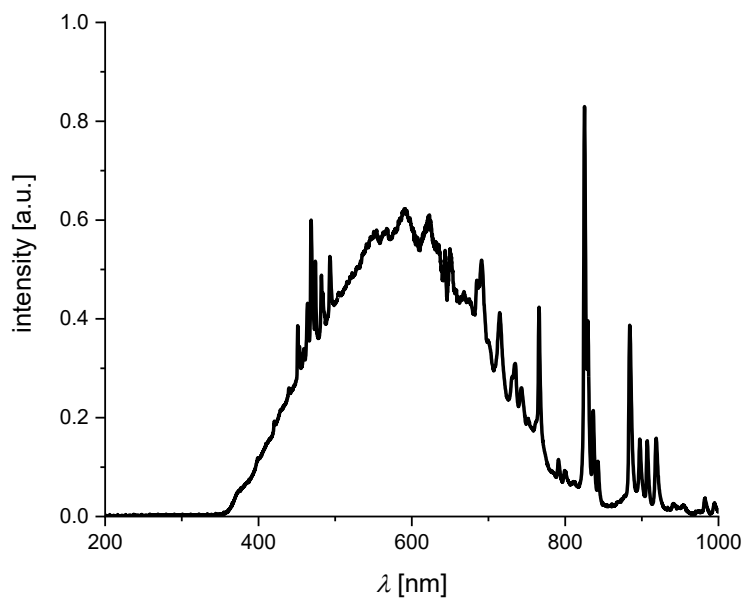
Figure A8.2.13. Emission spectrum of the xenon lamp used for photocatalytic water oxidation experiments.
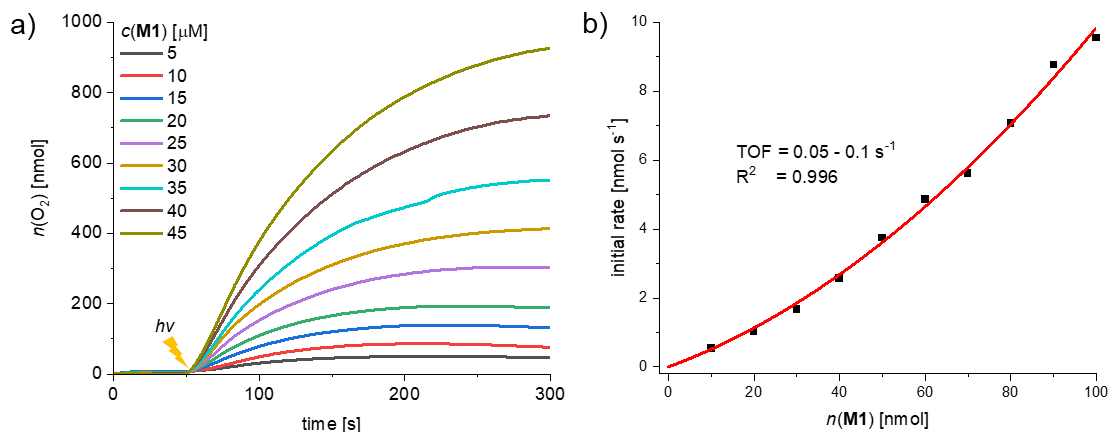
Figure A8.2.14. a) Concentration-dependent experiments with **M1** as WOC in CH_3CN/H_2O 4:6 (pH 7, 50 mM phosphate buffer), c(PS) = 1.5 M, c($Na_2S_2O_8$) = 37 mM. The lighting symbol indicates the start of sample irradiation at t = 50 s. b) plot of the initial rates vs. the catalyst amount with quadratic regression.
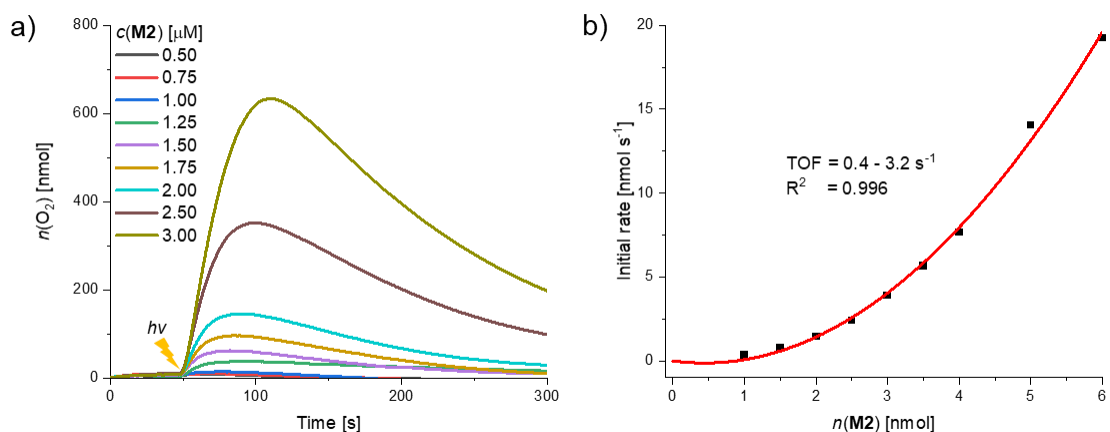
Figure A8.2.15. a) Concentration-dependent experiments with **M2** as WOC in CH_3CN/H_2O 4:6 (pH 7, 50 mM phosphate buffer), c(PS) = 1.5 M, c($Na_2S_2O_8$) = 37 mM. The lighting symbol indicates the start of sample irradiation at t = 50 s. b) plot of the initial rates vs. the catalyst amount with quadratic regression.

Stability tests after photocatalytic water oxidation experiments
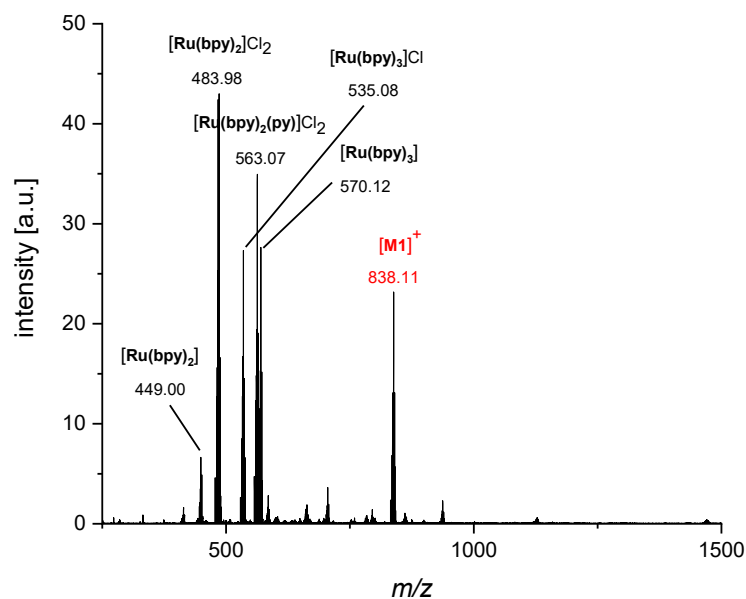
Figure A8.2.16. HR MALDI-TOF mass spectrum (CH$_3$CN/H$_2$O 4:6 (pH 7, 50 mM phosphate buffer, positive mode) of **M1** after photocatalytic water oxidation catalysis containing Na$_2$S$_2$O$_8$ as sacrificial electron acceptor (SEA) and [Ru(bpy)$_3$]$^{2+}$ as photosensitizer (PS).
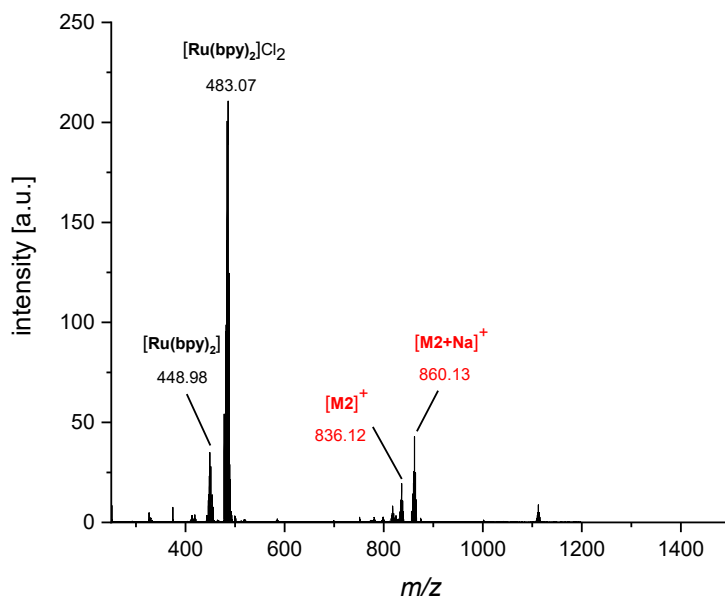
Figure A8.2.17. HR MALDI-TOF mass spectrum (CH$_3$CN/H$_2$O 4:6 (pH 7, 50 mM phosphate buffer, positive mode) of **M2** after photocatalytic water oxidation catalysis containing Na$_2$S$_2$O$_8$ as sacrificial electron acceptor (SEA) and [Ru(bpy)$_3$]$^{2+}$ as photosensitizer (PS).

Kinetic Isotope Effect under Conditions of Chemical Water Oxidation
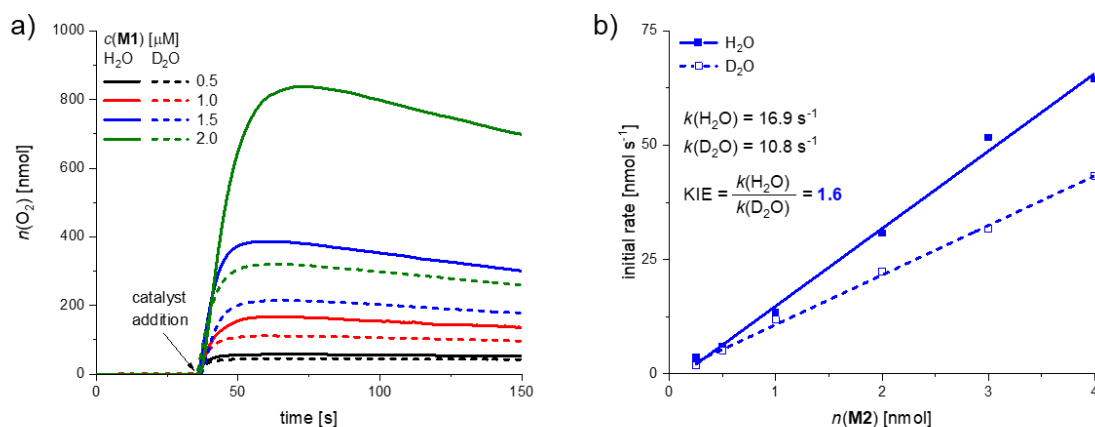
Figure A8.2.18. a) Concentration-dependent experiments for **M1** as WOC in CH_3CN/H_2O or D_2O 4:6 (pH 1, triflic acid), c(CAN) = 0.525 M. b) plot of the initial rates vs. the catalyst amount with linear regression for the determination of the individual reaction rates $k(H_2O)$ and $k(D_2O)$.
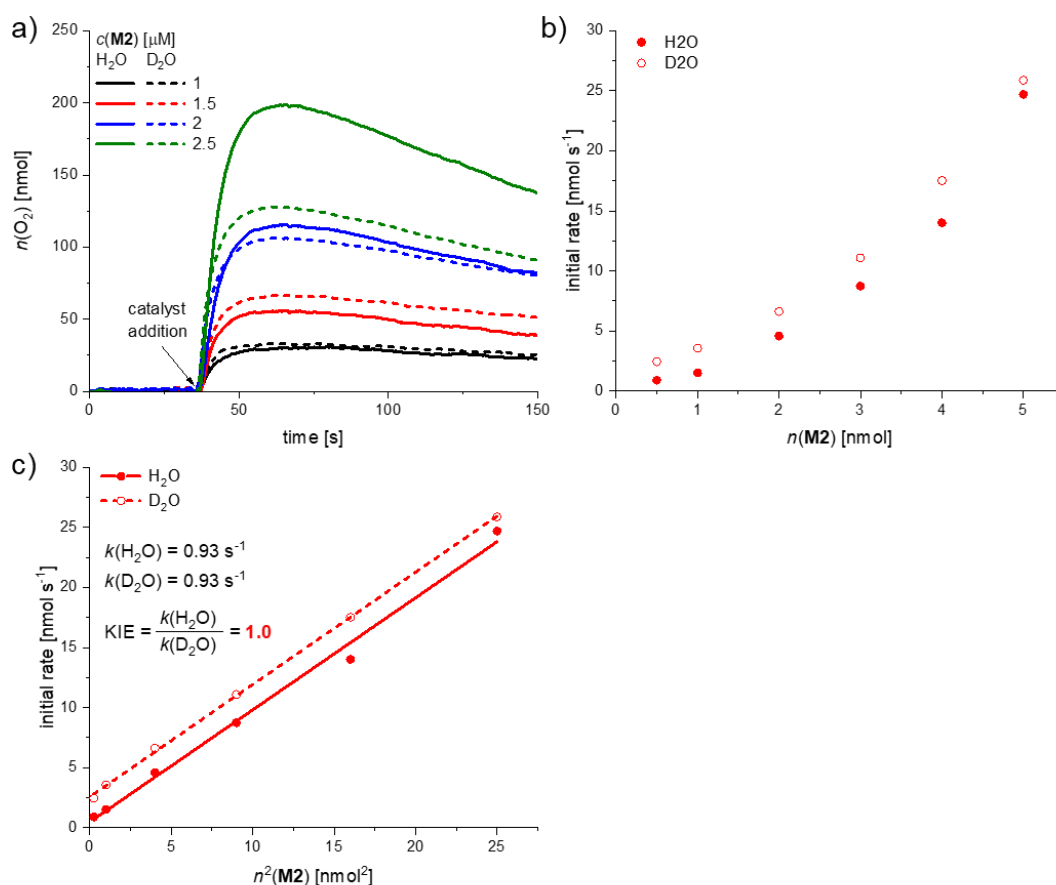
Figure A8.2.19. a) Concentration-dependent experiments for **M2** as WOC in CH_3CN/H_2O or D_2O 4:6 (pH 1, triflic acid), c(CAN) = 0.525 M. b) plot of the initial rates vs. the catalyst amount. c) the individual reaction rates $k(H_2O)$ and $k(D_2O)$ were obtained by plotting the initial rates vs. the square of catalyst concentration for **M2**.

Kinetic Isotope Effect under Conditions of Photocatalytic Water Oxidation
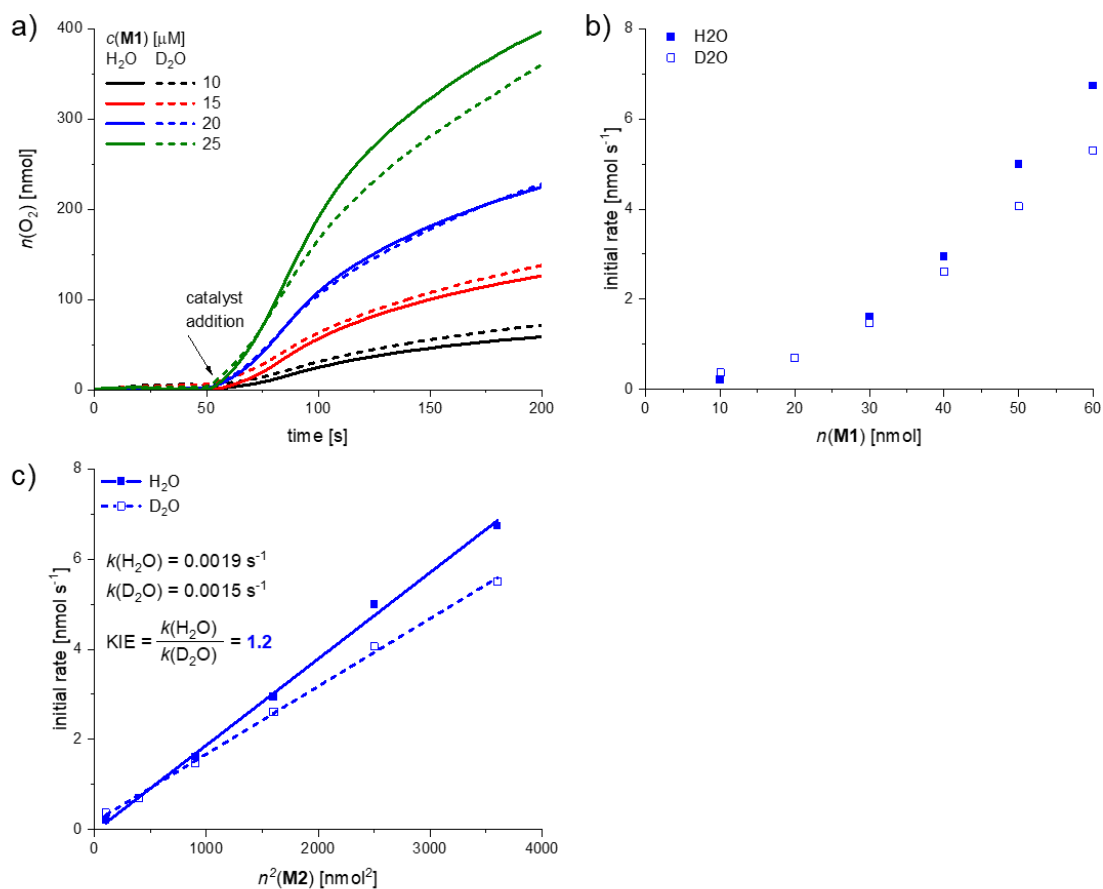
Figure A8.2.20. a) Concentration-dependent experiments for **M1** as WOC in CH_3CN/H_2O or D_2O 4:6 (pH 7, 50 mM phosphate buffer) c(PS) = 1.5 M, $c(Na_2S_2O_8)$ = 37 mM. b) plot of the initial rates vs. the catalyst amount. c) the individual reaction rates $k(H_2O)$ and $k(D_2O)$ were obtained by plotting the initial rates vs. the square of catalyst concentration for **M1**.
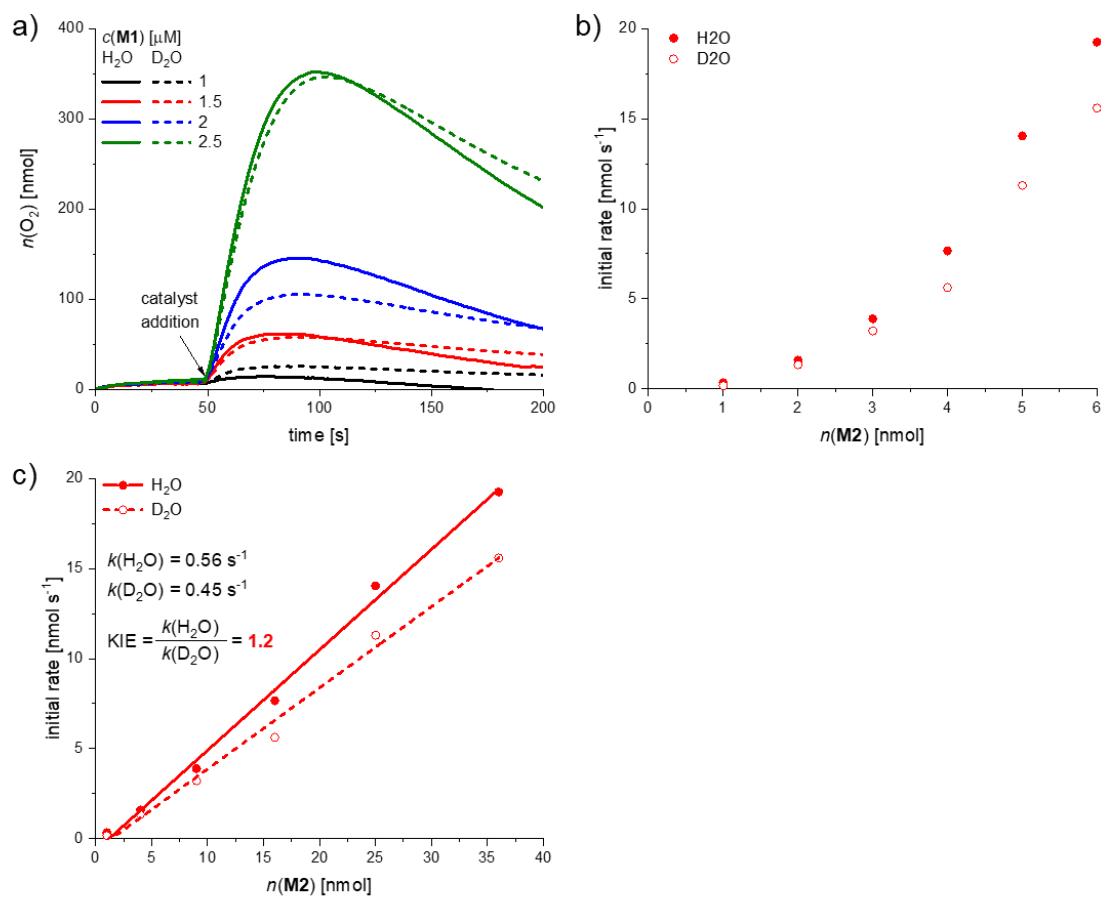
Figure A8.2.21. a) Concentration-dependent experiments for **M2** as WOC in CH_3CN/H_2O or D_2O 4:6 (pH 7, 50 mM phosphate buffer), c(PS) = 1.5 M, $c(Na_2S_2O_8)$ = 37 mM. b) plot of the initial rates vs. the catalyst amount. c) the individual reaction rates $k(H_2O)$ and $k(D_2O)$ were obtained by plotting the initial rates vs. the square of catalyst concentration for **M2**.

pH–dependent NMR structural analysis

Table A8.2.3. Chemical shifts δ (ppm) and assignment of significant ¹H-NMR signals (400 MHz) of complexes **M1** and **M2** in TFE-d_3/D₂O 1:1 (pD 1.0, 0.1 M CF₃SO₃D or pD 7.0).

	🔴	🔵	🟡	🟢	⚫
M1 (pD = 1.0)	7.00	8.19	8.12	8.45	7.93
M1 (pD = 7.0)	8.17	6.39	7.91	8.83	7.56
M2 (pD = 1.0)	8.56	5.83	7.97	7.92	7.54
M2 (pD = 7.0)	8.59	5.75	7.96	7.92	7.52
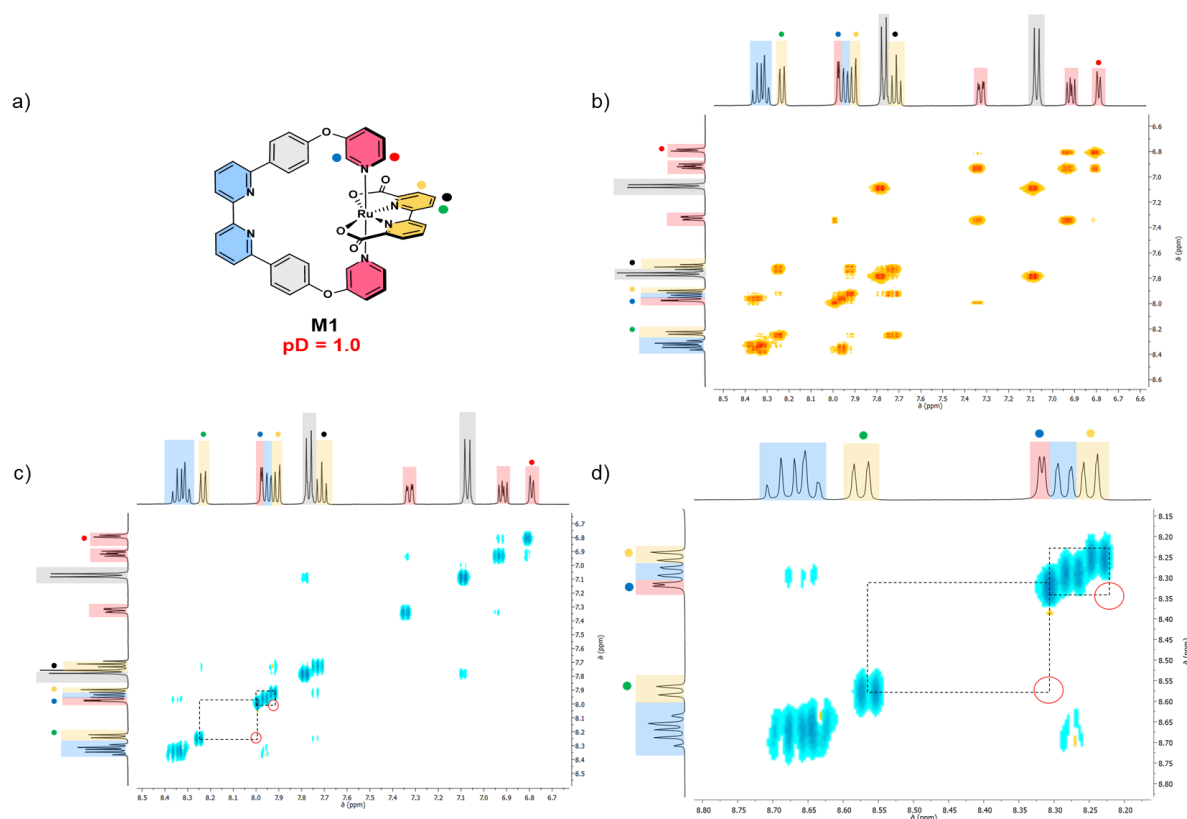
Figure A8.2.22. (a–d) Molecular structure of **M1** based on 2D-NMR structural analysis at pD 1.0 (a). ¹H-¹H COSY NMR spectrum (b) and ¹H-¹H NOESY NMR spectrum (c) with inset of ¹H-¹H NOESY NMR spectrum (d) for structural assignment of NMR signal in TFE-d_3/D₂O 1:1 (pD 1, 0.1 M CF₃SO₃D; 400 MHz; yellow: positive signals / cyan: negative signals). For better assignment, significant ¹H-NMR signals of **M1** are marked in the respective color based on the molecular structure drawn in (a).
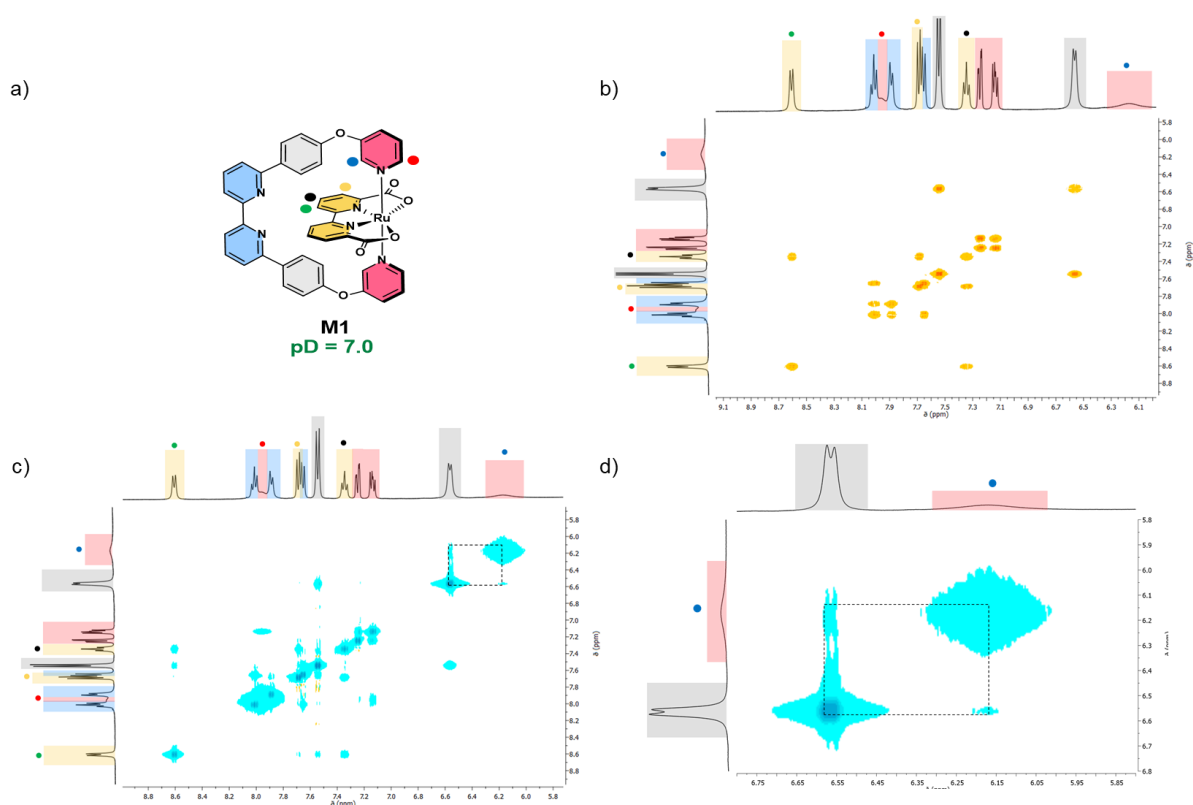
Figure A8.2.23. (a–d) Molecular structure of **M1** based on 2D-NMR structural analysis at pD 7.0 (a). ^{1}H-^{1}H COSY NMR spectrum (b) and ^{1}H-^{1}H NOESY NMR spectrum (c) with inset of ^{1}H-^{1}H NOESY NMR spectrum (d) for structural assignment of NMR signal in TFE-d_3/D$_2$O 1:1 (pD 7; 400 MHz; yellow: positive signals / cyan: negative signals). For better assignment, significant ^{1}H-NMR signals of **M1** are marked in the respective color based on the molecular structure drawn in (a).
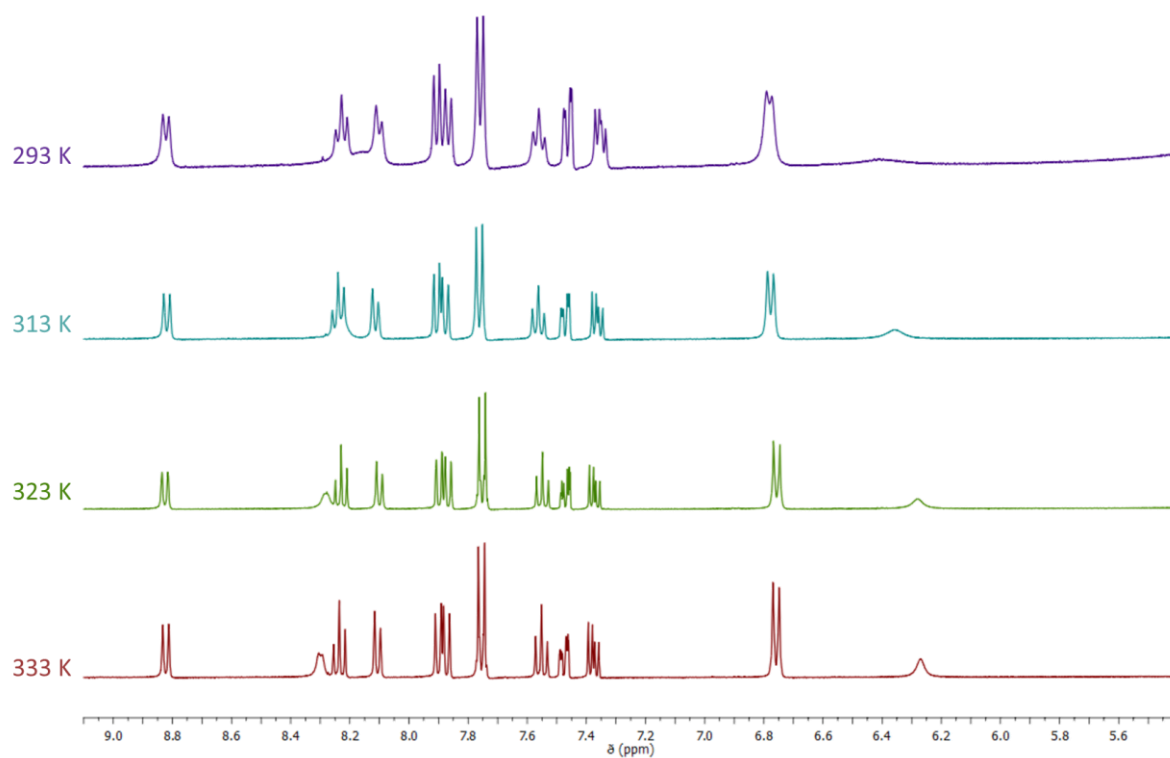
Figure A8.2.24. Aromatic region of temperature-dependent ^{1}H NMR spectra of **M1** under neutral conditions in TFE-d_3/D$_2$O 1:1 (pD 7.0, 400 MHz) from 293 K to 333 K.
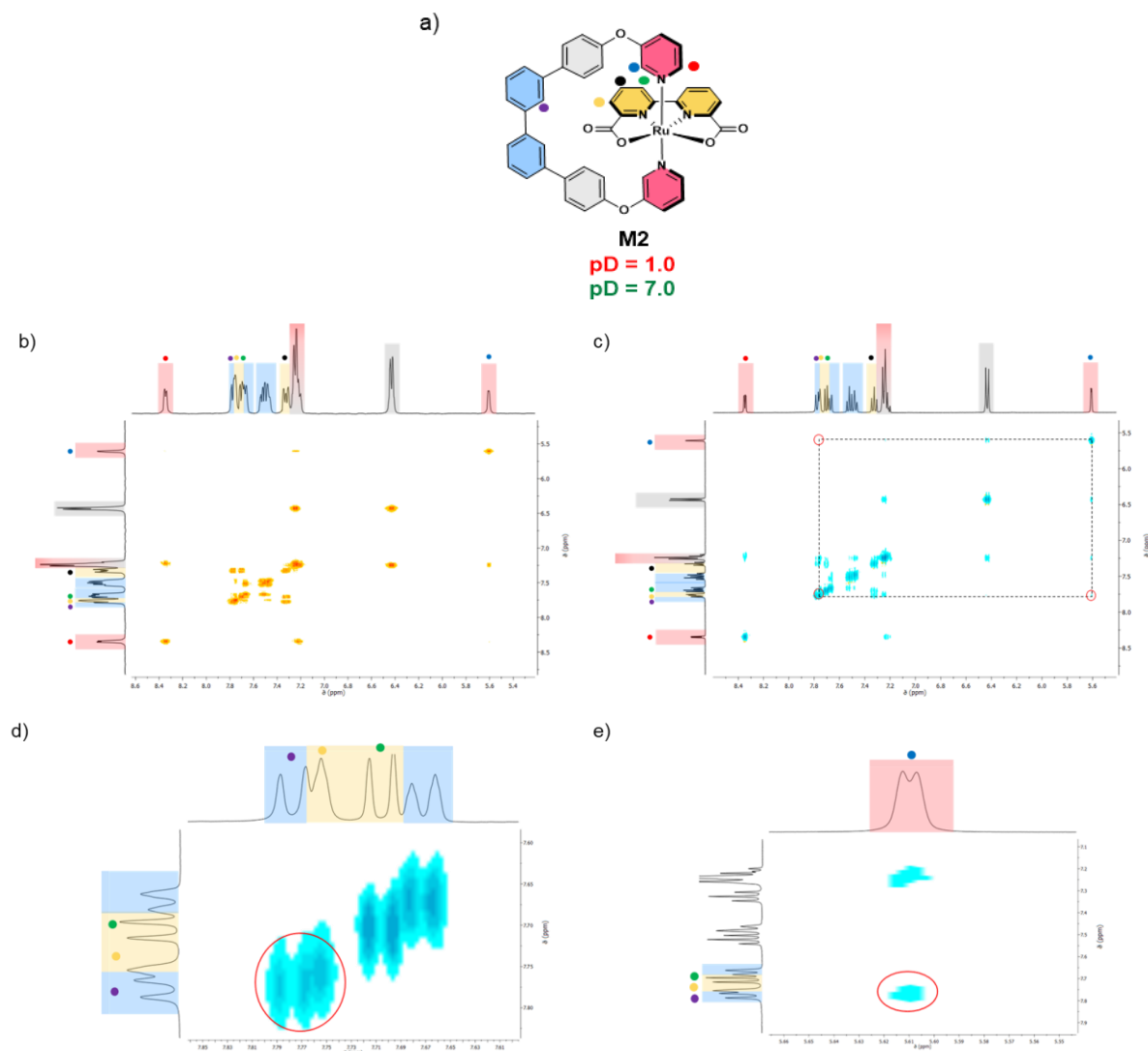
Figure A8.2.25. (a–e) Molecular structure of **M2** based on 2D-NMR structural analysis at pD 1.0 & pD 7.0 (a). ^{1}H-^{1}H COSY NMR spectrum (b) and ^{1}H-^{1}H NOESY NMR spectrum (c) with inset of ^{1}H-^{1}H-NOESY NMR spectrum (d,e) for structural assignment of NMR signal in TFE-d_3/D$_2$O 1:1 (pD 1, 0.1 M CF$_3$SO$_3$D; pD 7, 400 MHz; yellow: positive signals / cyan: negative signals). For better assignment, significant ^{1}H-NMR signals of **M2** are marked in the respective color based on the molecular structure drawn in (a).
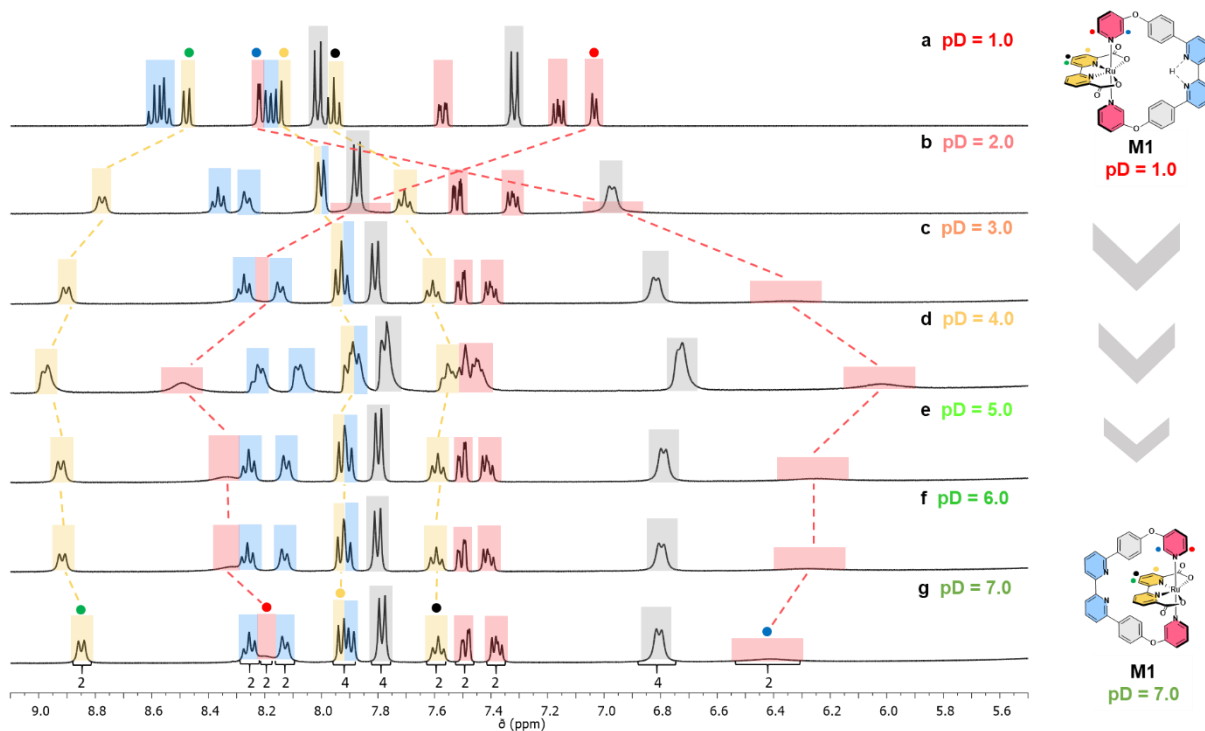
Figure A8.2.26. (a–g) Aromatic region of pD-dependent ^{1}H NMR titration experiments of **M1** in TFE-d_3/D$_2$O 1:1 (pD 7.0, 400 MHz, ascorbic acid, room temperature) from pD 1.0 (a) to pD 7.0 (g) with the proposed molecular structure of the complex based on the observed chemical shift changes and 2D-NMR structural analysis shown on the right (signals are color-coded in yellow (bda), red (axial pyridine), grey (biphenyl) or blue (bipyiridine) as highlighted in the structure). The different pD values of the solution were adjusted by addition of 0.1 M CF$_3$SO$_3$D and measured using a pH meter.

Single crystal X-ray analysis

$$[Ru^{II}(bda)(\textbf{L1})]\ (\textbf{M1})$$

a)

b)

c) $[Ru^{II}(bda)(\textbf{L2})]\ (\textbf{M2})$

d) $[Ru^{III}(bda)(\textbf{L1}+H)(H_2O)]^{2+}(PF_6^-)_2$
       $[(\textbf{M1}+H)(H_2O)]^{2+}(PF_6^-)_2$
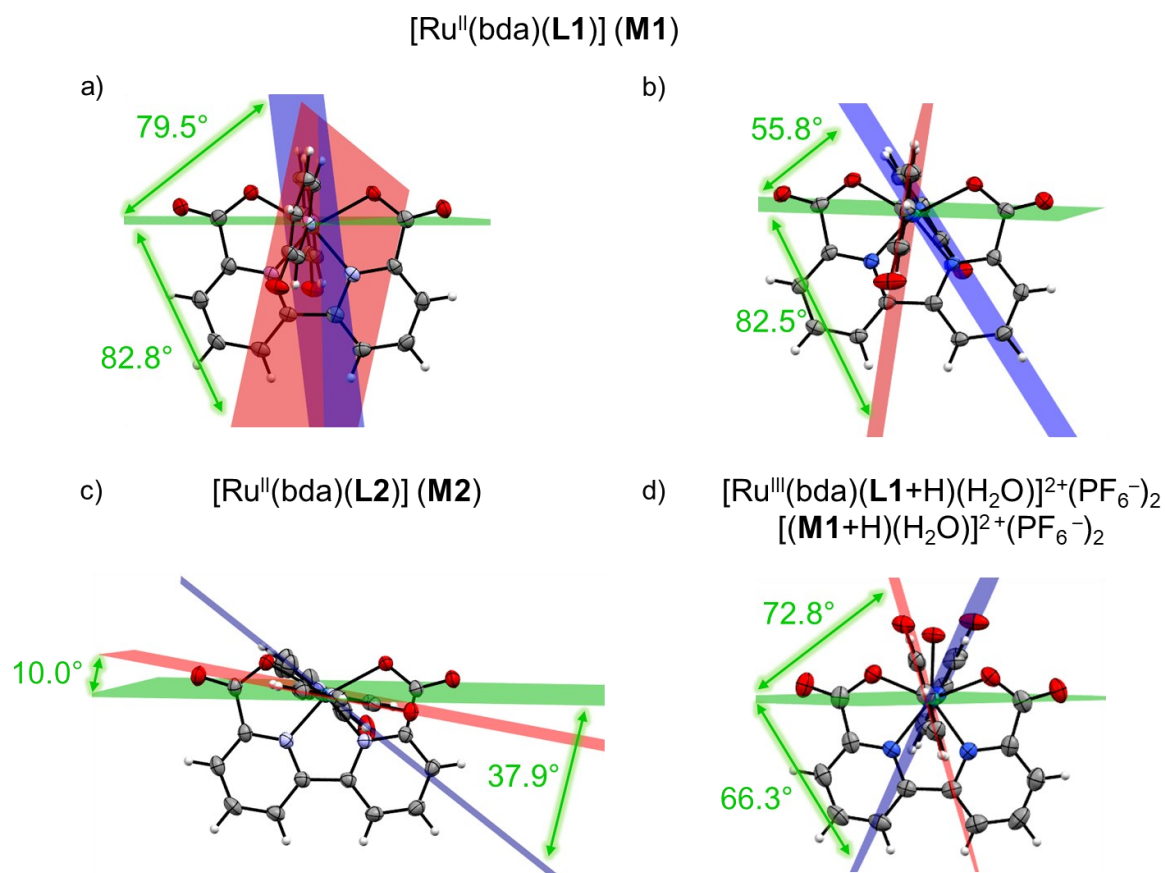
Figure A8.2.27. Comparison of the X-ray crystal structures of $[Ru^{II}(bda)(\textbf{L1})]$ (**M1**) (a,b), $[Ru^{II}(bda)(\textbf{L2})]$ (**M2**) (c) and $[Ru^{III}(bda)(\textbf{L1}+H)(H_2O)]^{2+}(PF_6^-)_2$ $[(\textbf{M1}+H)(H_2O)]^{2+}(PF_6^-)_2$ (d) regarding the torsion angles of the axial pyridyl rings relative to the respective Ru center (plane generated by the atoms $py(N_{ax})-C(=O)-Ru-C(=O)-py(N_{ax})$). From the axial ligands only the coordinating pyridine moiety is shown for the sake of clarity. ORTEP diagram with thermal ellipsoids set at 50% probability. C, grey; H, white; O, red; N, purple; Ru, turquoise.

Table A8.2.4. Comparison of selected bond lengths and angles for compounds [Ru^{II}(bda)(**L1**)] (**M1**), [Ru^{II}(bda)(**L2**)] (**M2**) and [Ru^{III}(bda)(**L1**+H)(H$_2$O)]$^{2+}$(PF$_6^-$)$_2$ [(**M1**+H)(H$_2$O)]$^{2+}$(PF$_6^-$)$_2$ in the solid state.

	[Ru^{II}(bda)(**L1**)] (**M1**)[a]	[Ru^{II}(bda)(**L2**)] (**M2**)	[Ru^{III}(bda)(**L1**+H)(H$_2$O)]$^{2+}$(PF$_6^-$)$_2$ (**M1**+H)(H$_2$O)]$^{2+}$(PF$_6^-$)$_2$
O-Ru-O [°]	121.8(1) / 122.7(1)	123.1(9)	136.4(1)
N$_{ax}$-Ru-N$_{ax}$ [°]	171.4(1) / 173.2(1)	175.5(4)	175.8(1)
d (Ru-N$_{ax}$) [Å]	2.081(3) / 2.079(3) 2.087(3) / 2.104(3)	2.112(1) 2.120(2)	2.096(3) 2.101(3)
d (Ru-O$_{eq}$) [Å]	2.178(3) / 2.179(4) 2.192(3) / 2.193(3)	2.198(2) 2.201(2)	2.043(2) 2.051(2)
d (Ru-N$_{eq}$) [Å]	1.926(3) / 1.932(4) 1.942(4) / 1.945(3)	1.945(2) 1.933(2)	2.066(3) 2.073(3)
Torsion py$_{ax}$-Ru-py$_{ax}$ relative to area of the Ru center[b] [°]	79.5 / 55.8 82.8 / 82.5	10.0 37.9	66.3 72.9

[a] Crystallographic data are given for both asymmetric conformers of the macrocycle within the unit cell.

[b] The plane of the respective Ru center is generated by the atoms py(N$_{ax}$)−C(=O)−Ru−C(=O)−py(N$_{ax}$).

Table A8.2.5. B alerts for refinement of crystal structure of [(**M1**+H)(H$_2$O)]$^{2+}$(PF$_6^-$)$_2$.

Type	Alert
B	**PLAT250_ALERT_2_B** **Problem**: Large U3/U1 Ratio for Average U(I,j) Tensor 5.4 **Response**: Due to threefold disorder, the position of one PF$_6^-$ counterion could not be refined perfectly
B	**PLAT430_ALERT_2_B** **Problem**: Short Inter D…A Contact O1 ..O10C 2.78 Ang. **Response**: Hydrogen-bonding network between water molecules in the catalytic pocket and carboxylates of the bda backbone
B	**PLAT430_ALERT_2_B** **Problem**: Short Inter D…A Contact O1 ..O9A 2.82 Ang. **Response**: Hydrogen-bonding network between water molecules in the catalytic pocket and carboxylates of the bda backbone
B	**PLAT430_ALERT_2_B** **Problem**: Short Inter D…A Contact O2 ..O10B 2.79 Ang. **Response**: Hydrogen-bonding network between water molecules in the catalytic pocket and carboxylates of the bda backbone

X-ray refinement details

M1 ([Ru^{II}(bda)(**L1**)]) at pH 7: The refinement showed residual electron density that could be attributed to solvent molecules and that could not be modeled satisfactorily. Therefore, the SQUEEZE routine of PLATON was used. The remaining structure could be refined nicely.

Each unit cell contains four (two different) macrocyclic Ru(bda) complexes and four (two different) MeOH solvent molecules.

Furthermore, two solvent-containing voids (440 Å^3, 127 electrons) occupying 21.6% of the unit cell volume was obtained by the SQUEEZE routine. Therefore, the presence of approximately **seven unresolved MeOH** molecules (285 Å^3, 65%, 126 electrons) per void is assumed.

M2 ([Ru^{II}(bda)(**L2**)]) at pH 7: The refinement showed residual electron density that could be attributed to solvent molecules and that could not be modeled satisfactorily. Therefore, the SQUEEZE routine of PLATON was used. The remaining structure could be refined nicely.

Each unit cell contains two macrocyclic Ru(bda) complexes and two MeOH solvent molecules.

Furthermore, two solvent-containing voids (213 Å^3, 56 electrons) occupying 20.8% of the unit cell volume was obtained by the SQUEEZE routine. Therefore, the presence of approximately **three unresolved MeOH** molecules (122 Å^3, 57%, 54 electrons) per void is assumed.

M1 ([Ru^{III}(bda)(**L1**-H)(H$_2$O)]$^{2+}$(PF$_6^-$)$_2$) at pH 1 after several catalytic cycles: The refinement showed residual electron density that could be attributed to solvent molecules and that could not be modeled satisfactorily. Therefore, the SQUEEZE routine of PLATON was used. The remaining structure could be refined nicely.

Each unit cell contains two macrocyclic Ru(bda) complexes and four (two different) MeCN solvent molecules. To compensate for the two positive charges in each macrocycle (Ru^{III} and protonated bipyridinium site) and the presumed partial protonation of substrate H$_2$O ligands, on average 4.68 PF$_6^-$ counterions are located at five positions (three different) in each unit cell. One PF$_6^-$ ion is twofold disordered (51.08%) and one PF$_6^-$ ion is threefold disordered (20.50, 41,69 and 21.61%). In the macroscopic cavity, three different states for a hydrogen-bonded water network (66.16, 22.15 and 11.69%) are observed (see manuscript for further details).

Furthermore, two solvent-containing voids (154 Å^3, 40 electrons) occupying 11.2% of the unit cell volume was obtained by the SQUEEZE routine. Therefore, the presence of approximately **two unresolved MeCN** molecules (106 Å^3, 69%, 44 electrons) per void is assumed.
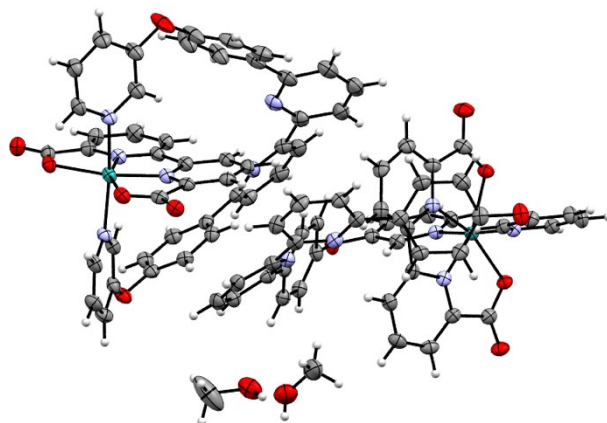
Figure A8.2.28. ORTEP diagram (thermal ellipsoids set at 50% probability; C, grey; H, white; O, red; N, purple; Ru, turquoise) for **M1** at pH 7.
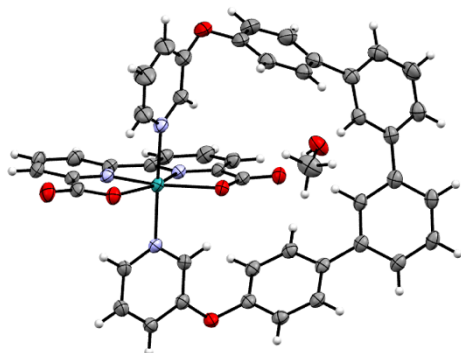
Figure A8.2.29. ORTEP diagram (thermal ellipsoids set at 50% probability C, grey; H, white; O, red; N, purple; Ru, turquoise) for X-ray structure of **M2** at pH 7.
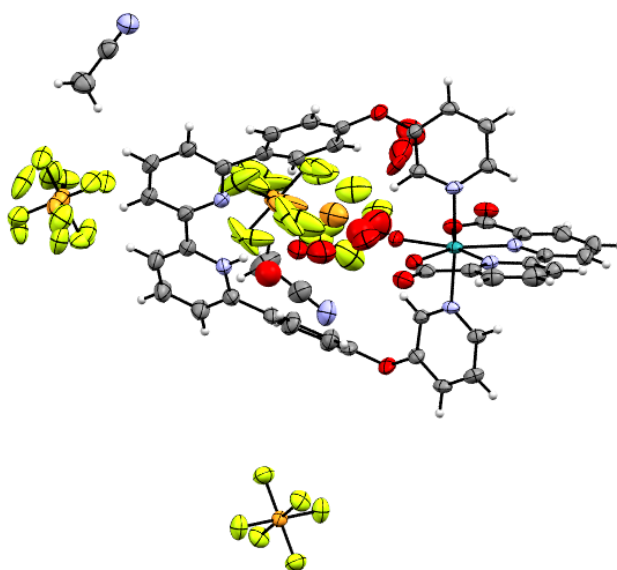
FigureA8.2.30. ORTEP diagram (thermal ellipsoids set at 50% probability; C, grey; H, white; O, red; N, purple; Ru, turquoise) for X-ray structure of **M1** at pH 1 in Ru^{III} state.

Table A8.2.6. Crystal data and structure refinement for compounds **M1**, **M2** and [(**M1**+H)(H$_2$O)]$^{2+}$(PF$_6^-$)$_2$.

Compound	M1	M2	[(M1+H)(H$_2$O)]$^{2+}$(PF$_6^-$)$_2$
CCDC Number	2157734	2157733	2157735
Empirical formula	C$_{45}$H$_{32}$N$_6$O$_7$Ru	C$_{47}$H$_{34}$N$_4$O$_7$Ru	C$_{48}$H$_{35}$F$_{14.03}$N$_8$O$_{9.39}$P$_{2.34}$Ru
M / g mol^{-1}	869.83	867.85	1314.02
Temperature / K	100(2)	100(2)	100(2)
Wavelength / Å	1.54178	1.54178	1.54178
Crystal system, space group	Triclinic, $P\bar{1}$	Triclinic, $P\bar{1}$	Triclinic, $P\bar{1}$
Unit cell dimensions:			
a / Å	15.5892(9)	8.3529(4)	7.9829(8)
b / Å	17.1283(9)	11.8211(6)	19.3522(19)
c / Å	17.5982(10)	21.6382(10)	19.3834(19)
α / °	82.280(3)	75.733(2)	68.434(5)
β / °	69.500(3)	79.869(2)	80.363(5)
γ / °	68.135(3)	89.902(2)	83.725(5)
Volume V / Å^3	4084.8(4)	2036.44(17)	2741.8(5)
Z	4	2	2
Calculated density ρ_{cal} / g cm^{-3}	1.414	1.415	1.592
Absorption coefficient / mm^{-1}	3.578	3.591	3.949
F(000)	1776	888	1319
Crystal size / mm^3	0.192 x 0.075 x 0.016	0.194 x 0.165 x 0.036	0.084 x 0.054 x 0.018
Measurement range of Θ / °	2.681 to 73.167	3.862 to 72.382	2.458 to 72.899
Limiting indices	-19<=h<=19, -21<=k<=21, -21<=l<=21	-9<=h<=10, -14<=k<=14, -26<=l<=26	-9<=h<=9, -23<=k<=19, -24<=l<=23
Reflections collected / unique	60329 / 16140 [R(int) = 0.0765]	38631 / 8028 [R(int) = 0.0376]	55512 / 10802 [R(int) = 0.0593]
Completeness / %	99.7	99.8	99.7
Absorption correction	Semi-empirical from equivalents	Semi-empirical from equivalents	Semi-empirical from equivalents
Max. & Min. transmission	0.7536 and 0.5943	0.7536 and 0.4854	0.7536 and 0.6577
Refinement method	Full-matrix least-squares on F^2	Full-matrix least-squares on F^2	Full-matrix least-squares on F^2
Data / restraints / parameters	16140 / 3 / 1067	8028 / 0 / 534	10802 / 589 / 1001
Goodness of fit for F^2	1.039	1.040	1.094
Final R indices [$I > 2\sigma(I)$]	R$_1$ = 0.0533, wR$_2$ = 0.1252	R$_1$ = 0.0289, wR$_2$ = 0.0690	R$_1$ = 0.0477, wR$_2$ = 0.1154
R indices (all data)	R$_1$ = 0.0690, wR$_2$ = 0.1335	R$_1$ = 0.0304, wR$_2$ = 0.0700	R$_1$ = 0.0526, wR$_2$ = 0.1228
Largest diff. peak and hole	1.488 and -0.565 e·Å^3	0.682 and -0.489 e·Å^3	0.760 and -0.543 e·Å^3

Characterization and properties of the oxidized Ru intermediate
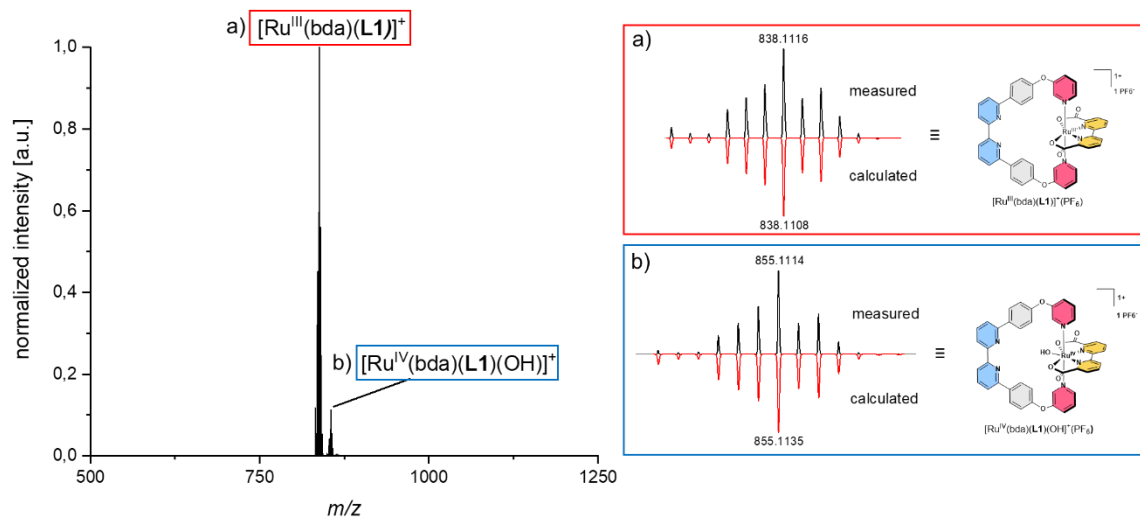
Figure A8.2.31. HR mass spectrum (ESI-TOF, CH₃CN/CH₃OH 5:1, positive mode) of the dissolved orange crystal of the oxidized complex **M1** with the insets showing the measured and calculated isotopic distributions for (a) [Ru^{III}(bda)(**L1**)]$^+$(PF₆) and (b) [Ru^{IV}(bda)(**L1**)(OH)]$^+$(PF₆$^-$) and their respective structures.
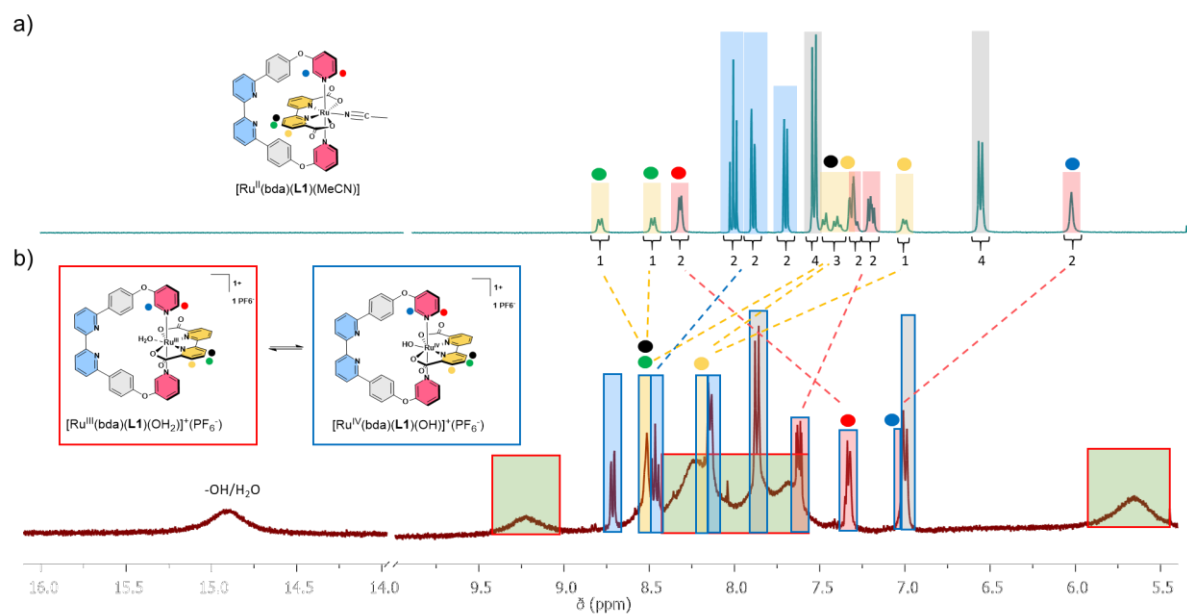
Figure A8.2.32. Aromatic region of the ^{1}H NMR spectra (CD$_3$CN/CD$_3$OD (5:1), 400 MHz, room temperature) of **M1** at (a) Ru^{II} and (b) mixed Ru^{III}/Ru^{IV} oxidation state. The proposed molecular structure of the complex at the respective oxidation state based on 2D-NMR structural analysis is shown on the right. Colours of the signals correspond to bda (yellow), axial pyridine fragment (red) and bipyridine unit (blue) of the axial ligand as highlighted in the structure. The broad signals of the paramagnetic Ru^{III} species of complex **M1** are marked in green and could not be further structurally assigned. The broad signal at ~15 ppm corresponds to the respective OH/H$_2$O group coordinated to the Ru^{III} and Ru^{IV} oxidation states.

167
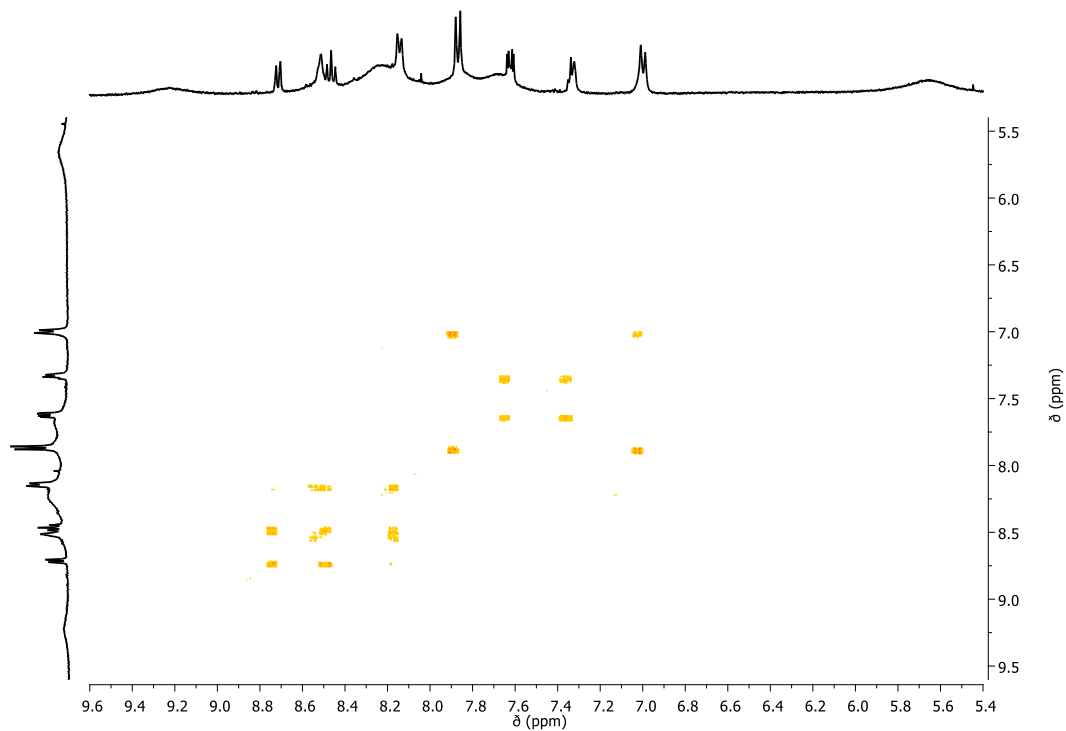
Figure A8.2.33. ^{1}H-^{1}H COSY NMR spectrum (400 MHz, CD$_3$CN/CD$_3$OD (5:1)) of **M1** at a mixed Ru^{III}/Ru^{IV} oxidation state (yellow: positive signals).
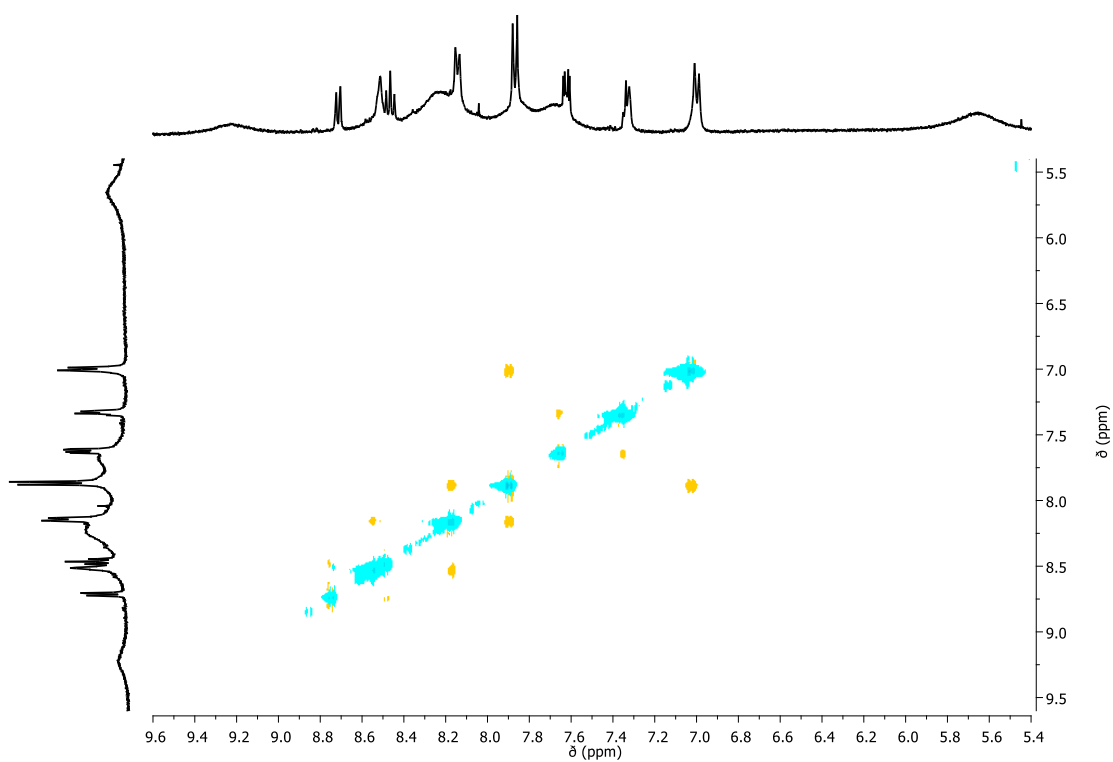
Figure A8.2.34. ^{1}H-^{1}H NOESY NMR spectrum (400 MHz, CD$_3$CN/CD$_3$OD (5:1)) of **M1** at a mixed Ru^{III}/Ru^{IV} oxidation state (yellow: positive signals / cyan: negative signals).
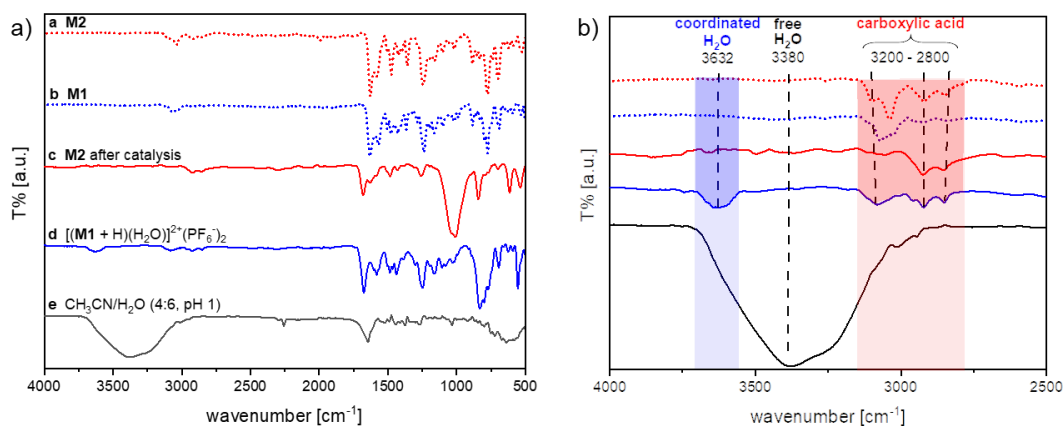
Figure A8.2.35. (a,b) Solid state FTIR spectra of **M2, M1,** precipitate of **M2** after catalysis, crystal [(**M1**+H)(H$_2$O)]$^{2+}$(PF$_6^-$)$_2$ and the solvent mixture CH$_3$CN/H$_2$O (4:6, pH 1) as reference with (b) insets showing the v(OH) stretching vibrations of carboxylic acid (highlighted in red) and of presumably coordinated H$_2$O molecules (highlighted in blue) to the catalytic center in [(**M1**+H)(H$_2$O)]$^{2+}$(PF$_6^-$)$_2$ exclusively.
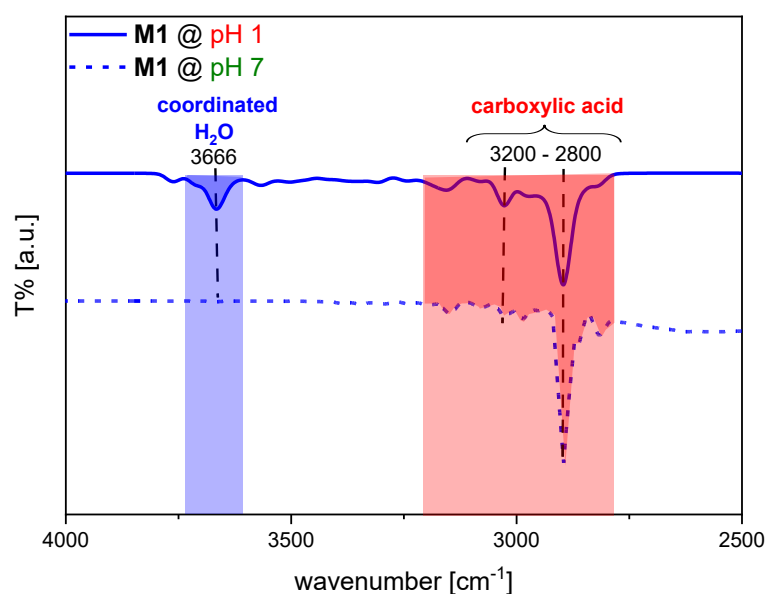
Figure A8.2.36. FTIR spectra of **M1** in acidic aqueous solution (CH$_3$CN/H$_2$O 4:6 (pH 1, triflic acid) and in neutral aqueous solution (CH$_3$CN/H$_2$O 4:6 (pH 7) showing the v(OH) stretching vibrations of carboxylic acid (highlighted in red) and of presumably coordinated H$_2$O molecules (highlighted in blue).
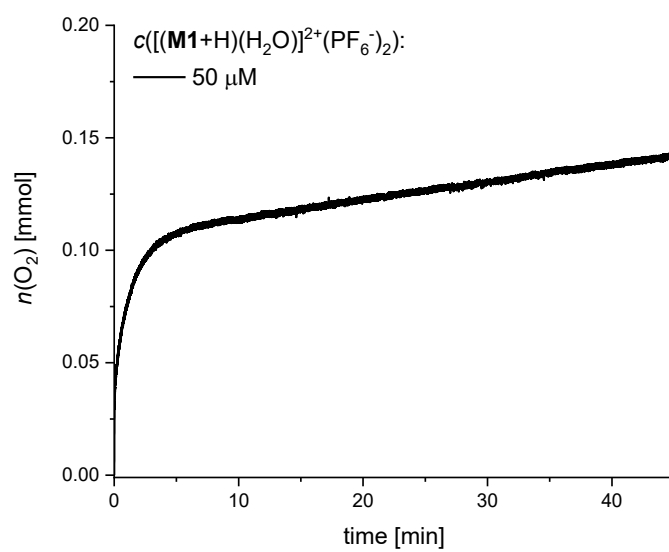
Figure A8.2.37. Oxygen evolution curve for a second chemical water oxidation experiment with crystals [(**M1**+H)(H$_2$O)]$^{2+}$(PF$_6$$^-$)$_2$ isolated after the first chemical water oxidation experiment (c = 50 mM, CH$_3$CN/H$_2$O 4:6, pH 1, triflic acid, c(CAN) = 0.6 M).

NMR spectra

Figure A8.2.38. ^{1}H NMR spectrum (400 MHz, CDCl$_3$, rt) of 3-(4-bromophenoxy)pyridine (* residual solvent).

Figure A8.2.39. ^{1}H NMR spectrum (400 MHz, CDCl$_3$, rt) of 3-(4-(4,4,5,5-tetramethyl-1,3,2-dioxaborolan-2-yl)phenoxy)pyridine (**44**) (* residual solvent).

Figure A8.2.40. ^{1}H NMR spectrum (400 MHz, CDCl$_3$, rt) of ligand **L1** (* residual solvent).

Figure A8.2.41. ^{13}C NMR spectrum (100 MHz, CDCl$_3$, rt) of ligand **L1** (* residual solvent).

Figure A8.2.42. ^{1}H NMR spectrum (400 MHz, CDCl$_3$, rt) of ligand **L2** (* residual solvent).

Figure A8.2.43. ^{13}C NMR spectrum (100 MHz, CDCl$_3$, rt) of ligand **L2** (* residual solvent).

Figure A8.2.44. ^{1}H NMR spectrum (400 MHz, CD$_2$Cl$_2$/CD$_3$OD (1:1), rt) of complex **M1** (* residual solvent; $^{+}$ ascorbic acid).

174

Figure A8.2.45. ^{13}C NMR spectrum (100 MHz, CD$_2$Cl$_2$/CD$_3$OD (1:1), rt) of complex **M1** (* residual solvent; + ascorbic acid).

Figure A8.2.46. ^{1}H-^{1}H COSY NMR spectrum (400 MHz, CD$_2$Cl$_2$/CD$_3$OD (1:1), rt) of complex **M1** (* residual solvent; + ascorbic acid; red: positive signals).

Figure A8.2.47. ^{1}H-^{1}H NOESY NMR spectrum (400 MHz, CD$_2$Cl$_2$/CD$_3$OD (1:1), rt) of complex **M1** (* residual solvent; $^+$ ascorbic acid; red: positive signals / cyan: negative signals).

Figure A8.2.48. ^{1}H NMR spectrum (400 MHz, CD$_2$Cl$_2$/CD$_3$OD (1:1), rt) of complex **M2** (* residual solvent; $^+$ ascorbic acid).

Figure A8.2.49. ^{13}C NMR spectrum (100 MHz, CD_2Cl_2/CD_3OD (1:1), rt) of complex **M2** (* residual solvent; + ascorbic acid).

Figure A8.2.50. ^{1}H-^{1}H COSY NMR spectrum (400 MHz, CD_2Cl_2/CD_3OD (1:1), rt) of complex **M2** (* residual solvent; + ascorbic acid; red: positive signals).

Figure A8.2.51. ^{1}H-^{1}H NOESY NMR spectrum (400 MHz, CD$_2$Cl$_2$/CD$_3$OD (1:1)) of complex **M2** (* residual solvent; $^+$ ascorbic acid; red: positive signals / cyan: negative signals).

HR mass spectra

Figure A8.2.52. HR mass spectrum (ESI-TOF, CH$_3$CN/CHCl$_3$ 1:1, positive mode) of ligand **L1** with the inset showing the measured and calculated isotopic distribution for [**L1**+H]$^+$.

Figure A8.2.53. HR mass spectrum (ESI-TOF, CH$_3$CN/CHCl$_3$ 1:1, positive mode) of ligand **L2** with the inset showing the measured and calculated isotopic distribution for [**L2**+Na]$^+$.

Figure A8.2.54. HR mass spectrum (ESI-TOF, CH₃OH/CH₂Cl₂ 1:1, positive mode) for complex **M1** with the inset showing the measured and calculated isotopic distribution for [**M1**]⁺.

Figure A8.2.55. HR mass spectrum (ESI-TOF, CH₃OH/CH₂Cl₂ 1:1, positive mode) for complex **M2** with the inset showing the measured and calculated isotopic distribution for [**M2**]⁺.

8.3 Supporting Information for *Chapter 5*

Materials and methods

General

All chemicals and solvents were purchased from commercial suppliers and used as received. 2,2'-Bipyridine-6,6'-dicarboxylic acid (**bda**),[328] [RuCl$_2$(dmso)$_4$],[329, 330] and [Ru(bda)(dmso)$_2$][268, 344] were synthesized according to literature known procedures. Reactions with air or moisture sensitive reagents were carried out under a nitrogen atmosphere using standard Schlenk techniques. Crude isolated compounds were further purified by column chromatography on silica gel (60M, 0.04−0.063 mm, Macherey-Nagel) with freshly distilled solvents. For experiments under aqueous conditions, 50 mM phosphate buffer solutions at pH 7 were used. The respective solution was prepared by dissolving NaH$_2$PO$_4$ (3.71 g, 30.9 mmol) and Na$_2$HPO$_4$ (2.7 g, 19.1 mmol) in deionized water or deuterated water (1000 mL).

Chromatography

For analytic thin-layer chromatography (TLC), pre-coated sheets with silica gel 60 layer (0.20 mm) with fluorescent indicator UV$_{254}$ (Alugram Xtra SIL G/UV$_{254}$, Macherey-Nagel) were used. Crude isolated compounds were purified by column chromatography on silica gel (60M, 0.04−0.063 mm, Macherey-Nagel) with freshly distilled solvents. For further purification, size exclusion chromatography with Bio-Beads particles (S-X1 Support (1% crosslinkage, 40−80 μM bead size, 600−14000 MW exclusion range) or SX-3 Support (3% crosslinkage, 40−80 μM bead size, ≤2000 MW limit), Bio-Rad) suspended in a 9:1 DCM/MeOH mixtures (HPLC grade) were used. Recycling gel permeation chromatography (GPC) was performed on a LC-5060 system of Japan Analytical Industries (three columns from Agilent, PLgel, 10 μm, 100 Å; 10 μm, 100 Å; 10 μm, 500 Å) using a mixture of 9:1 CHCl$_3$/MeOH (HPLC grade).

NMR spectroscopy

^{1}H NMR and proton decoupled ^{13}C NMR spectra were recorded on a Bruker Avance III HD 400 spectrometer at 298 K. Chemical shifts (δ) are reported in parts per million (ppm) relative to tetramethylsilane and referenced internally to the residual solvent signal.[331] The respective

coupling constants (*J*) are given in Hertz (Hz). To describe signal multiplicities, the following abbreviations were applied: s = singlet, d = doublet, t = triplet and m = multiplet. In addition, 2D NMR spectra (COSY, NOESY, HSQC and HMBC) were recorded to allow a correct assignment of 1D NMR spectra of novel compounds.

DOSY NMR

DOSY (Diffusion-ordered spectroscopy) spectra were carried out in aqueous mixtures of 1:1 D_2O/TFE-d_3 (pD = 1.0 (0.1 M CF_3SO_3D) or pD = 7.0) on a Bruker Avance III HD 600 spectrometer at 295 K. The hydrodynamic radius of the differently sized complexes **2C−4C** were calculated assuming a spherical shape in solution according to the Stokes-Einstein equation (A1).

$$D = \frac{k_B\, T}{6\,\pi\,\mu\,r_H} \qquad (A1)$$

Here, *D* is the calculated diffusion coefficient based on DOSY experiments, k_B is the Boltzman constant ($1.38 * 10^{-23}$ m^2 kg s^{-2} K^{-1}), *T* is the temperature, μ is the solution viscosity and r_H is the hydrodynamic radius. For the viscosity (μ) of the 1:1 D_2O/TFE-d_3 mixture a literature reported value ($\eta = 1.78*10^{-3}$ m^2 s^{-1}) of the undeuterated 1:1 solvent mixture was used.[345]

Mass spectrometry

High resolution electrospray ionization (HR-ESI) mass spectra were measured on an ESI micrOTOF focus or an ESI micrOTOF-Q III mass spectrometer (Bruker Daltonics). MALDI TOF (Matrix-assisted laser desorption/ionisation time-of-flight) mass spectrometry measurements were acquired on a Bruker Daltonics UltrafleXtreme mass spectrometer using DCTB (*trans*-2-[3-(4-tert-butylphenyl)-2-methyl-2-propenylidene] malononitrile) as matrix. All mass spectra were reported in positive reflector mode.

Melting points

Melting points were measured with an BX41 optical microscope (Olympus) connected to a temperature controller TP94 (Linkam Scientific Instruments Ltd.) and are uncorrected.

Elemental analysis

Elemental analysis was performed with a Vario MICRO cube (Elementar Analysensysteme).

UV/Vis absorption and emission spectroscopy

Spectroscopic measurements were recorded on a Jasco V-670 spectrometer under ambient conditions (298 K) in 1 cm quartz cuvettes using spectroscopic grade solvents.

Electrochemistry

Cyclic and differential pulse voltammetry (CV and DPV) experiments were performed on a BAS Cell Stand C3 (BAS Epsilon) using a glassy carbon disc as working electrode, a Pt wire as counter electrode and Ag/AgCl (3 M KCl) as reference electrode. The measurements were conducted at a scan rate of 100 mV s^{-1} and 20 mV s^{-1} at 298 K. All experiments were measured in homogenous phase in 4:6 mixtures of 2,2,2-trifluorethanol/H_2O (pH 7, 50 mM phosphate buffer). All measured potential are reported vs. normal hydrogen electrode (NHE) by addition of +0.21 V.[332] The respective Pourbaix diagrams were created based on multiple DPV measurements in phosphate buffered aqueous solution at different pH values (I = 0.1 M) in presence of 40% TFE.

Single crystal X-ray analysis

Single crystals of dimer **2C** and tetramer **4C** were grown by slow crystallization in a TFE-d_3/D_2O solution (1:1) of the respective compound used for NMR experiments and stored under ambient conditions. Single crystals of trimer **3C** were obtained by slow diffusion of diethyl ether either in a DCM/MeOH/TFE (1:1:1) solution of the complex stored in the fridge. Single crystal X-ray diffraction data for **2C−4C** were collected at the P11 beamline at DESY. The diffraction data were collected by a single 360° ϕ scan at 100 K. The diffraction data were indexed, integrated, and scaled using the XDS program package.[346] For **2C**, in order to compensate low completeness due to single-axis measurement two data sets were merged using the XPREP program from Bruker.[347] The structures were solved using SHELXT,[348] expanded with Fourier techniques and refined using the SHELX software package.[349] Hydrogen atoms were assigned at idealized positions and were included in the calculation of structure factors. All non-hydrogen atoms in the main residue were refined anisotropically. Heavily disordered solvent molecules that cannot be modelled satisfactorily were treated by the SQUEEZE[343] routine implemented in the program package PLATON.[342] Other disordered solvent molecules and disordered parts in the main residue were modelled with constraints and restraints using standard SHELX commands EADP, FLAT, SAME, RIGU, DELU, DFIX, DANG, and ISOR. The diffraction data for **4C** was analyzed as twins using HKLF5 data generated by the TwinRotMat function implemented in PLATON.[342] Crystallographic data for the structures reported in this Article have been deposited at the Cambridge Crystallographic Data Centre under deposition numbers CCDC 2214081 (**2C**), 2214083 (**3C**) and 2214082 (**4C**) Copies of these data can be

obtained free of charge from the Cambridge Crystallographic Data Centre via www.ccdc.cam.ac.uk/structures/.

Photocatalytic water oxidation

Photocatalytic water oxidation experiments were conducted after a standardized procedure following our previous publications.[37, 38, 40, 247] An Oxygraph Plus Clark-electrode system with a transparent and temperature-controlled reaction chamber (Hansatech Instruments Ltd.) was used for oxygen detection. For sample irradiation, a complete plug and play light source system including a 150 W Xenon arc lamp equipped with a cutoff filter (400 nm, Thorlabs) and an arc lamp power supply (Newport) was used. Prior to measurement, the power of the sun simulation was calibrated to an intensity of 100 mW cm^{-1} applying a collinear light path with collimated light. The calibration was performed with a PM 200 optical power meter equipped with a S121C sensor (Thorlabs), which was installed in a modified oxygen chamber (Hansatech Instruments Ltd.) combined with a CCS 200/M wide range spectrometer (Thorlabs). All experiments were conducted under the same operation conditions (V = 2 mL, T = 20 °C, stirring speed = 100 rpm). Following a standard procedure, a stock solution of photosensitizer (PS) [Ru(bpy)$_3$]Cl$_2$ and Na$_2$S$_2$O$_8$ as sacrificial electron acceptor (SEA) in 4:6 CH$_3$CN/H$_2$O mixture (pH 7, 50 mM phosphate buffer) was prepared in the dark (c(Na$_2$S$_2$O$_8$) = 37 mM, c([Ru(bpy)$_3$]Cl$_2$) = 1.5 mM) before each experiment. Then, an aliquot of this solution (1.5 mL) was transferred to the reaction chamber and mixed with varying amount of catalyst concentration (0.5 mL) in the dark. Irradiation of the sample was started after the baseline was constant (~50 s). For data evaluation, a blank measurement in absence of catalyst was subtracted from each measurement of concentration-dependent experiments. To benchmark the novel catalysts, the respective turnover frequency (TOF) and turnover number (TON) were determined. The TON, which is defined as total amount of evolved oxygen divided by the amount of used catalyst, is calculated for each concentration and the highest TON is reported. The TOF for each concentration can be determined by linear regression fit of the first 5−10 s of catalysis from the plot of evolved oxygen vs. reaction time. The extracted value represents the initial rate of catalysis for the respective concentration. The averaged, reported TOF was then determined from the slope of a linear regression of the initial rates of each concentration vs. the respective catalyst amount.

Chemical water oxidation

In accordance to previous publications,[37, 38, 40, 247] chemical water oxidation experiments were carried out in Schlenk reaction vessels (V = 20.6 mL) connected to pressure transducers (Honeywell, SSCDANN030PAAA5, absolute pressure, 0 to 30 psi) at 20 °C and a constant stirring speed (1000 rpm). For each concentration-dependent measurement, cerium

ammonium nitrate (CAN, 1.0 g, 1.82 mmol) was dissolved in 4:6 CH_3CN/H_2O mixture (3.0 mL, pH 1, triflic acid) and then a stock solution of the catalyst (400 µL) was injected through a septum. To determine the turnover number (TON), the total amount of evolved oxygen was divided by the amount of injected catalyst. The total amount of evolved oxygen during catalysis was calculated by applying the ideal gas law (A2):

$$\Delta p \times V = \Delta n \times R \times T \tag{A2}$$

with T = 293.15 K, V = 20.6 mL, R = 8.314 J K^{-1} mol^{-1}.

Based on the measured pressure increase in the reaction vessel, the pressure increase (Δp) can be converted into the amount of generated oxygen (Δn). A TON was calculated for each concentration and the highest TON is reported. From the same concentration-dependent measurements, a TOF was calculated for each concentration from the obtained initial rates by linear regression of the oxygen evolution curve during the first two seconds of catalysis. The reported TOF was then determined from the slope of a linear regression of the initial rates against the catalyst amount.

Catalyst stability test

To test the stability of the catalyst after water oxidation catalysis, each compound (10.0 mg, 3.0 µmol) was dissolved in 4:6 CH_3CN/H_2O mixture (1.0 mL, pH 1, triflic acid). After addition of CAN (500 mg, 960 µmol), vigorous oxygen evolution occurred (~40 catalytic cycles). Subsequently, ammonium hexafluorophosphate (ca. 250 mg) was added and a precipitate was formed. After filtration and several washing with H_2O, the sample was dried under high vacuum. The oxidized catalyst was further investigated by MALDI TOF mass spectrometry (positive, DCTB, CH_2Cl_2/CH_3OH 1:1) in presence of ascorbic acid.

Kinetic Isotope Experiments

Using our standardized procedures,[37, 38, 247] the experiments were performed using a Oxygraph Plus Clark-electrode system (Hansatech Instruments Ltd.) for oxygen detection (T = 20 °C, stirring speed = 100 rpm).

Kinetic Isotopic effect under conditions of photocatalytic water oxidation: Experiments were performed in accordance with the procedures described for photocatalytic water oxidation. A stock solution of PS (c([Ru(bpy)$_3$]Cl$_2$) = 1.5 mM) and SEA (c(Na$_2$S$_2$O$_8$) = 37 mM) in 4:6 CH_3CN/H_2O (H_2O or D_2O (99.9% purity); pH 7, 50 mM phosphate buffer) was prepared in the dark. An aliquot of this solution (1.5 mL) was mixed with catalyst solution at varying concentrations (0.5 mL) in the dark. Irradiation was started at 50 s to allow thermal equilibration of the sample at a constant temperature of 20 °C.

To evaluate the catalytic rates in H_2O ($k(H_2O)$) and D_2O ($k(D_2O)$), the initial rate of catalysis for each concentration was determined by linear regression of the evolved oxygen curve during the first five to ten seconds of catalysis.

Experimental Procedures

6,6'-bis(pyridin-3-yloxy)-2,2'-bipyridine (**46**)
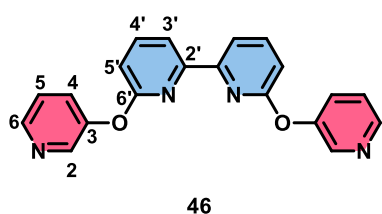
A mixture of 6,6-dibromo-2,2'-bipyridine (**BP1**) (314 mg, 1.00 mmol, 1.0 equiv.), 3-hydroxypyridine (**45**) (285 mg, 300 mmol, 3.0 equiv.), Cs_2CO_3 (977 mg, 3.00 mmol, 3.0 equiv.), CuI (57.1 mg, 300 µmol, 0.3 equiv.) and Co(acac)$_2$ (77.2 mg, 300 µmol, 0.3 equiv.) were suspended in *N*-methyl-2-pyrrolidon (3 mL) under nitrogen and the resulting mixture was stirred for 20 hours at 110 °C. After cooling down to room temperature, water (50 mL) was added, and the aqueous phase was extracted with ethyl acetate (4 x 50 mL). After removing the solvent under reduced pressure, the crude product was suspended in water and filtrated. The filtrate was further purified by flash chromatography (SiO_2, ethyl acetate/methanol 99:1 to 90:10) to yield ligand **46** as a light-brown solid (277 mg, 810 µmol, 81%). **m.p.** 112 °C. **^{1}H NMR** (400 MHz, CDCl$_3$): δ [ppm] = 8.61 (m, 2H, *H2*), 8.49 (m, 2H, *H6*), 7.77−7.70 (m, 4H, *H4'* & *H5'*), 7.58 (ddd, $^3J_{H-H}$ = 8.3 Hz, $^4J_{H-H}$ = 2.7 Hz, 1.4 Hz, 2H, *H4*), 7.38 (dd, $^3J_{H-H}$ = 8.3 Hz, $^4J_{H-H}$ = 4.7 Hz, 2H, *H5*), 6.95 (dd, $^3J_{H-H}$ = 7.5 Hz, $^4J_{H-H}$ = 1.4 Hz, 2H, *H3'*). **^{13}C NMR** (100 MHz, CDCl$_3$) δ [ppm] = 162.1, 153.1, 150.6, 145.7, 143.9, 140.8, 129.0, 124.0, 116.2, 112.0. **HRMS** (ESI-TOF, pos. mode, MeCN/CHCl$_3$ (1:1)): *m/z* calcd for $C_{20}H_{14}N_4O_2$+H$^+$: 343.1195 [*M*+H]$^+$; found: 343.1197. **Elemental analysis** calcd. (%) for $C_{20}H_{14}N_4O_2$: C 70.17, H 4.12, N 16.37; found: C 69.93, H 4.15, N 16.26.

Synthesis of [Ru(bda)(6,6'-bis(pyridin-3-yloxy)-2,2'-bipyridine)]$_n$ (n = 2−4), (dimer **2C**, trimer **3C** and tetramer **4C**)
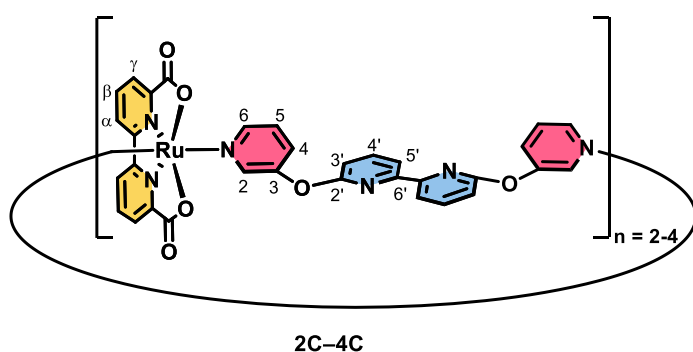
[Ru(bda)(dmso)$_2$] (165 mg, 330 µmol, 1.1 equiv.) and ligand **46** (103 mg, 300 µmol, 1.0 equiv.) were dissolved in a degassed mixture of chloroform (50 mL) and methanol (50 mL) and stirred under nitrogen at 60 °C for 22 hours. After cooling to room temperature, the solvent was removed under reduced pressure. The residue was purified by size-exclusion chromatography (Bio-Beads S-X1, dichloromethane/methanol 9:1) and three fractions were isolated. The last fraction corresponded to dimer **2C**. As second red fraction, trimer **3C** was collected. Tetramer **4C** was isolated as first broad fraction and was further purified by subsequent recycling gel permeation chromatography (GPC, chloroform/methanol 9:1) to yield pure **4C**.

187

Dimer **2C** (n=2): **Yield**: 81.0 mg, 59.1 µmol (39%) of a red powder. **m.p.** >300 °C. **^{1}H NMR** (400 MHz, DMSO−d_6): δ [ppm] = 9.27 (s, 4H, *H2*), 8.79 (dd, $^3J_{\text{H-H}}$ = 6.6 Hz, $^4J_{\text{H-H}}$ = 2.6 Hz, 4H, *H3'*), 8.57 (d, $^3J_{\text{H-H}}$ = 7.6 Hz, 4H, *Hα*), 8.26 (t, $^3J_{\text{H-H}}$ = 7.8 Hz, 4H, *Hβ*), 7.98−7.91 (m, 8H, *H4'* & *H5'*), 7.61 (ddd, $^3J_{\text{H-H}}$ = 8.4 Hz, $^4J_{\text{H-H}}$ = 2.6 Hz, $^5J_{\text{H-H}}$ = 1.1 Hz, 4H, *H6*), 7.17 (dd, $^3J_{\text{H-H}}$ = 8.4 Hz, $^4J_{\text{H-H}}$ = 5.6 Hz, 4H, *H5*), 7.10 (dd, $^3J_{\text{H-H}}$ = 8.0 Hz, $^5J_{\text{H-H}}$ = 0.5 Hz, 4H, *Hγ*), 6.59 (d, $^3J_{\text{H-H}}$ = 5.4Hz, 4H, *H4*). **^{13}C NMR** (100 MHz, DMSO−d_6) δ [ppm] = 172.0, 159.8, 159.3, 156.2, 152.4, 149.0, 148.5, 145.1, 142.7, 131.4, 127.91, 126.1, 125.0, 124.8, 119.5, 111.8. **UV/Vis** (CH_3CN/H_2O 4:6 (pH 7, 50 mM phosphate buffer)): λ_{max} (ε) = 255 (44095), 305 (73722), 347 (24564), 458 (8768), 491 nm (7577 M^{-1} cm^{-1}). **HRMS** (ESI-TOF, pos. mode, MeCN/CHCl$_3$ (1:1)): *m/z* calcd for $C_{64}H_{40}N_{12}O_{12}Ru_2$+$Na^+$: 1395.0898 [*M+Na*]$^+$; found: 1395.0889. **Elemental analysis** calcd. (%) for $C_{64}H_{40}N_{12}O_{12}Ru_2 \cdot 2H_2O$: C 54.62, H 3.15, N 11.94; found: C 54.17, H 3.21, N 11.67.

Trimer **3C** (n=3): **Yield**: 29.8 mg, 14.5 µmol (15%) of a dark red solid. **m.p.** >300 °C. **^{1}H NMR** (400 MHz, CD$_2$Cl$_2$/CD$_3$OD (1:1)): δ [ppm] = 8.58 (dd, $^3J_{\text{H-H}}$ = 8.1 Hz, $^4J_{\text{H-H}}$ = 1.0 Hz, 6H, *Hα*), 7.94 (dd, $^3J_{\text{H-H}}$ = 7.7 Hz, $^4J_{\text{H-H}}$ = 1.0 Hz, 6H, *Hγ*), 7.88−7.83 (m, 6H, *H4'*), 7.75−7.68 (m, 24H, *Hβ* & *H2* & *H6* & *H5'*), 7.53 (ddd, $^3J_{\text{H-H}}$ = 8.5 Hz, $^4J_{\text{H-H}}$ = 2.5 Hz, 1.2 Hz, 6H, *H4*), 7.17−7.12 (m, 6H, *H5*), 6.76 (dd, $^3J_{\text{H-H}}$ = 8.1 Hz, $^4J_{\text{H-H}}$ = 0.7 Hz, 6H, *H3'*). **^{13}C NMR** (100 MHz, CD$_2$Cl$_2$/CD$_3$OD (1:1)) δ [ppm] = 174.6, 161.3, 160.4, 157.5, 153.2, 152.1, 148.5, 145.8, 142.7, 132.8, 129.4, 126.7, 126.0, 126.0, 118.3, 113.2. **UV/Vis** (CH_3CN/H_2O 4:6 (pH 7, 50 mM phosphate buffer)): λ_{max} (ε) = 255 (58372), 306 (96419), 349 (31993), 456 (12670), 491 nm (10595 M^{-1} cm^{-1}). **HRMS** (ESI-TOF, pos. mode, CH$_3$OH/CH$_2$Cl$_2$ (1:1)): *m/z* calcd for $C_{96}H_{60}N_{18}O_{18}Ru_3$+$H^{2+}$: 1030.0805 [*M*+H]$^{2+}$; found: 1030.0845. **Elemental analysis** calcd. (%) for $C_{96}H_{60}N_{18}O_{18}Ru_3 \cdot 3H_2O$: C 54.62, H 3.15, N 11.94; found: C 54.18, H 3.29, N 11.67.

Tetramer **4C** (n=4): **Yield**: 5.40 mg, 2.00 µmol (3%) of a dark red solid. **m.p.** >300 °C. **^{1}H NMR** (400 MHz, CD$_2$Cl$_2$/CD$_3$OD (1:1)): δ [ppm] = 8.42 (d, $^3J_{\text{H-H}}$ = 8.1 Hz, 8H, *Hα*), 7.87−7.80 (m, 16H, *Hγ* & *H4'*), 7.73 (d, $^3J_{\text{H-H}}$ = 4.9 Hz, 8H, *H6*), 7.65 (t, $^3J_{\text{H-H}}$ = 7.9 Hz, 8H, *Hβ*), 7.60 (d, $^4J_{\text{H-H}}$ = 2.4 Hz, 8H, *H2*), 7.55−7.52 (m, 8H, *H5'*), 7.47 (ddd, $^3J_{\text{H-H}}$ = 8.5 Hz, $^4J_{\text{H-H}}$ =2.4 Hz, 1.0 Hz, 8H, *H4*), 7.18 (dd, $^3J_{\text{H-H}}$ = 8.4 Hz, 5.6 Hz, 8H, *H5*), 6.78 (dd, $^3J_{\text{H-H}}$ = 8.1 Hz, $^4J_{\text{H-H}}$ = 0.5 Hz, 8H, *H3'*). **^{13}C NMR** (100 MHz, CD$_2$Cl$_2$/CD$_3$OD (1:1)) δ [ppm] = 174.5, 161.8, 160.4, 157.4, 153.3, 152.1, 148.8, 146.0, 142.6, 132.7, 130.0, 126.7, 126.0, 125.9, 118.0, 113.2. **UV/Vis** (CH_3CN/H_2O 4:6 (pH 7, 50 mM phosphate buffer)): λ_{max} (ε) = 255 (65385), 305 (114341), 353 (36989), 457 (15627), 491 nm (13207 M^{-1} cm^{-1}). **HRMS** (ESI-TOF, pos. mode, CH$_3$OH/CH$_2$Cl$_2$ (1:1)): *m/z* calcd for $C_{128}H_{80}N_{24}O_{24}Ru_4^{2+}$: 1371.6005 [*M*]$^{2+}$; found: 1370.5998. **Elemental analysis** calcd. (%) for $C_{128}H_{80}N_{24}O_{24}Ru_4 \cdot 4H_2O$: C 54.62, H 3.15, N 11.94; found: C 54.53, H 3.04, N 11.69.

UV/Vis absorption spectroscopy
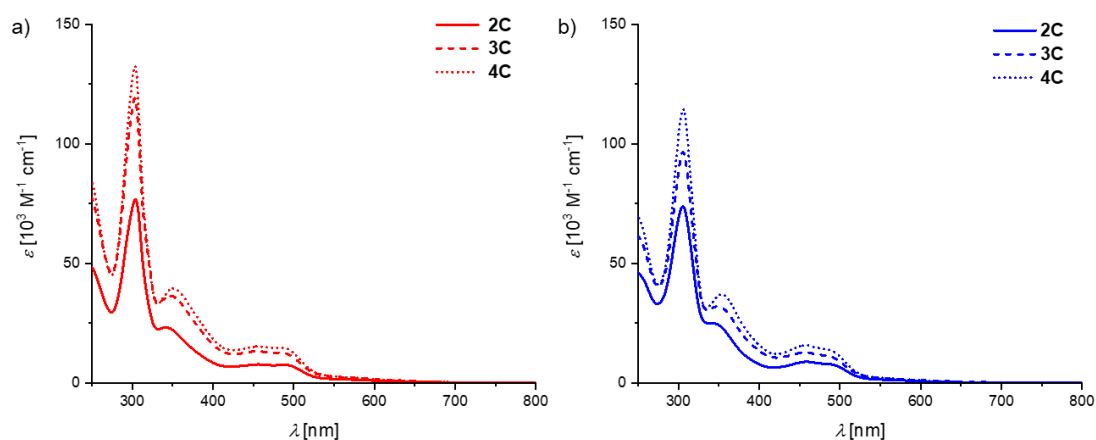
Figure A8.3.1. UV/Vis absorption spectra of Ru complexes **2C−4C** (c(WOC) = 10^{-5} M) at the Ru^{II} state in CH_3CN/H_2O 4:6 at a) pH 1 (red) and b) pH 7 (blue).

Single crystal X-ray analysis

Table A8.3.1. Comparison of selected bond lengths and angles for compounds **2C−4C** in the solid state.

	2C[a]	**3C**[b]			**4C**	
	Ru	Ru1	Ru2	Ru3	Ru1_1/ Ru1_2	Ru2_1/ Ru2_2
O−Ru−O [°]	121.7(2)/ 122.7(2)	121.8(8)	121.9(2)	121.1(1)	122.5(3)	122.0(2)
N_{ax}−Ru−N_{ax} [°]	171.3(2)/ 172.4(2)	170.8(7)	175.0(2)	169.9(6)	170.8(2)	171.3(2)
d (Ru−N_{ax}) [Å]	2.072(6)/ 2.064(5) 2.089(6)/ 2.067(5)	2.074(2) 2.087(2)	2.050(2) 2.104(2)	2.066(2) 2.074(2)	2.079(6) 2.087(6)	2.074(6) 2.077(6)
Torsion py_{ax}−Ru−py_{ax} [°]	30.6/27.9	45.4	27.8	15.1	13.7(9)	27.9(9)

[a] Crystallographic data are given for both asymmetric conformers of the macrocycle within the unit cell.

[b] Crystallographic data are given for the main Ru2(bda) unit of the macrocycle within the unit cell.

Contents in an asymmetric unit

2C: Each asymmetric unit contains half of two crystallographic isomers of dinuclear Ru(bda) complexes, four TFE solvent molecules and half ascorbic acid molecule.

3C: Each asymmetric unit contains one macrocyclic Ru(bda) complex with a disordered Ru2(bda) unit. In addition, each asymmetric unit contains 0.43 DCM solvent molecules and 0.84 TFE solvent molecules.

4C: Each asymmetric unit contains half of two similar but crystallographically independent tetranuclear Ru(bda) complexes and eight TFE solvent molecules.
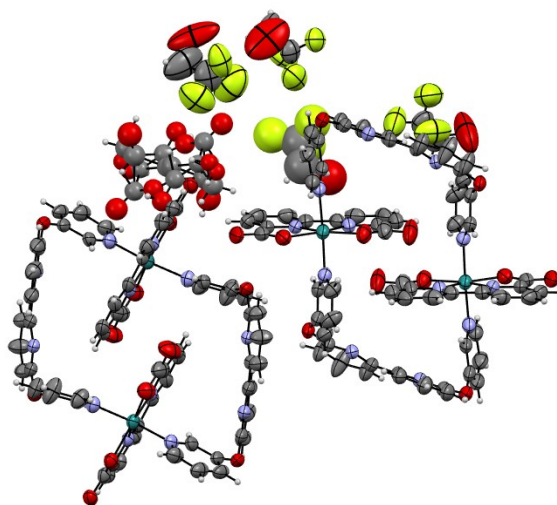
Figure A8.3.2. ORTEP diagram (thermal ellipsoids set at 50% probability; C, grey; H, white, O, red, N, purple; Ru, turquoise) for dimer **2C**.
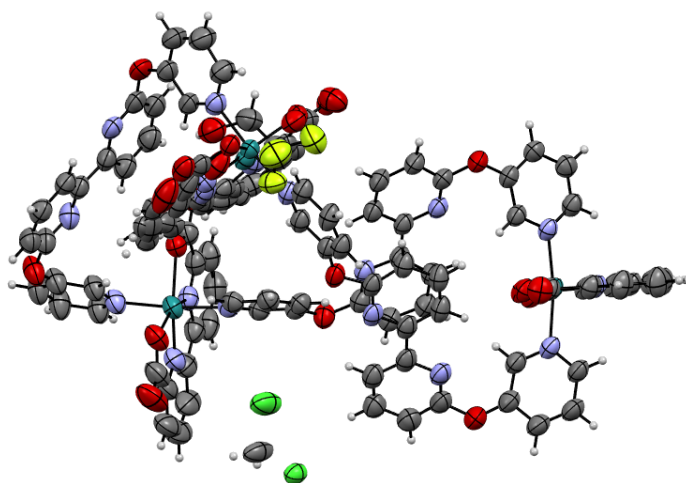
Figure A8.3.3. ORTEP diagram (thermal ellipsoids set at 50% probability; C, grey; H, white, O, red, N, purple; Ru, turquoise) for trimer **3C**.
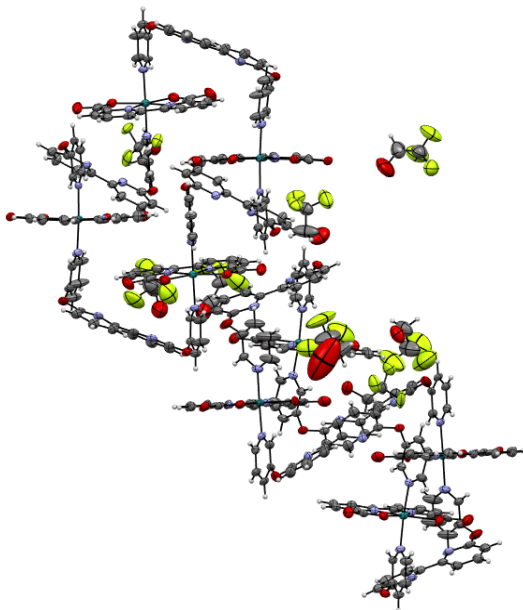
Figure A8.3.4. ORTEP diagram (thermal ellipsoids set at 50% probability; C, grey; H, white, O, red, N, purple; Ru, turquoise) for tetramer **4C**.
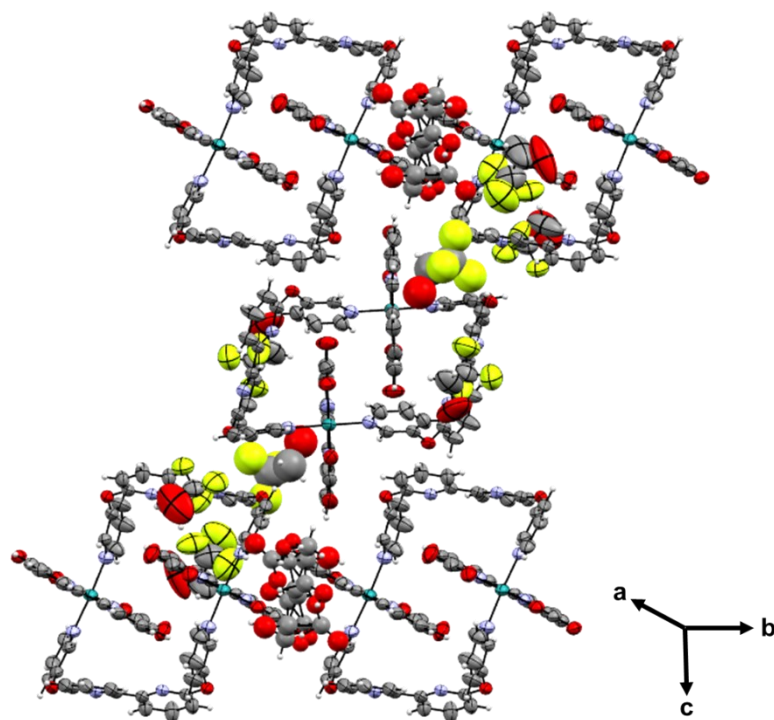
Figure A8.3.5. Crystal packing of **2C** viewed along the cell axis *a* with TFE solvent and ascorbic acid molecules in the crystal lattice.
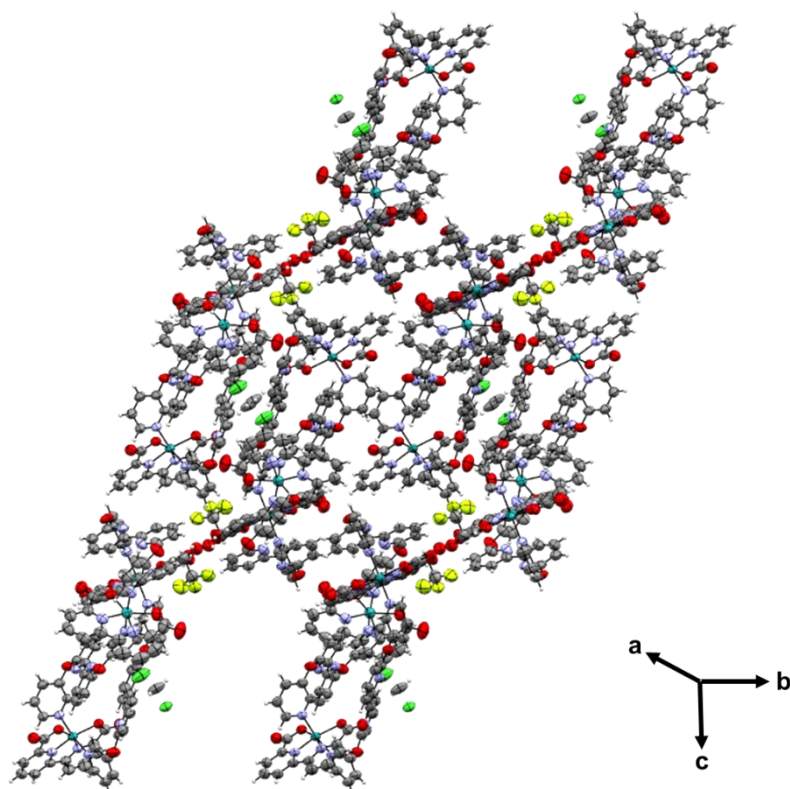
Figure A8.3.6. Crystal packing of **3C** viewed along the cell axis *a* with TFE and DCM solvent molecules in the crystal lattice.
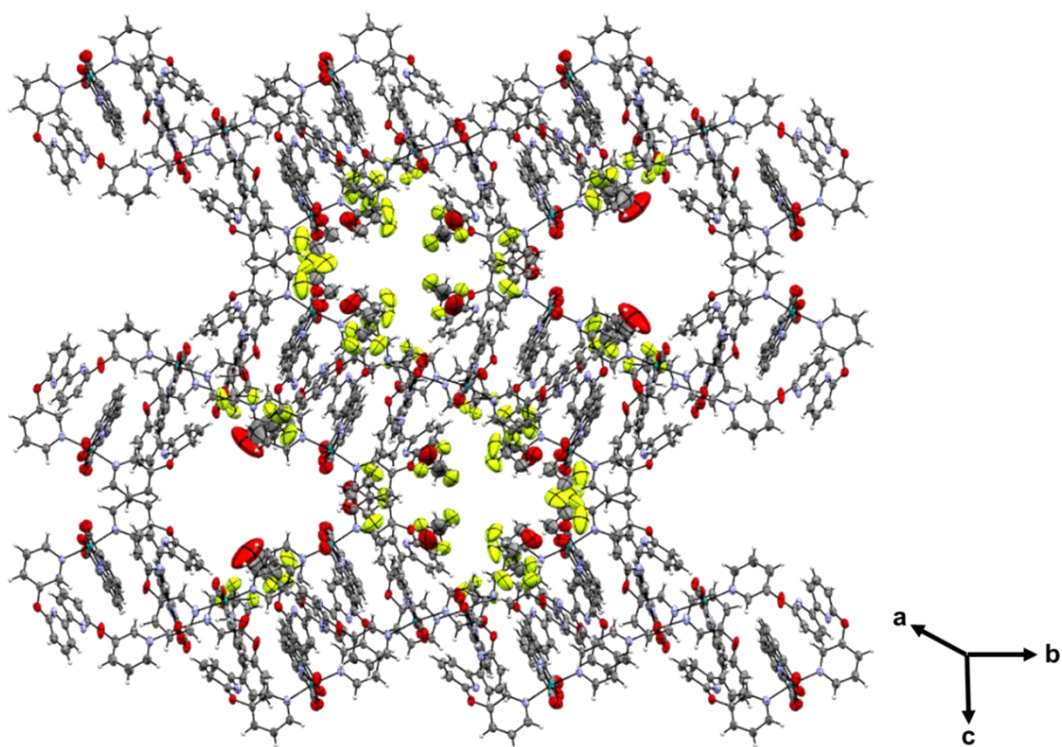
Figure A8.3.7. Crystal packing of 4**C** viewed along the cell axis *a* with TFE solvent molecules in the crystal lattice.

Table A8.3.2. Crystal data and structure refinement for compounds **2C–4C**.

Compound	2C	3C	4C
CCDC Number	2214081	2214083	2214082
Empirical formula	$C_{75}H_{52}F_{12}N_{12}O_{19}Ru_2$	$C_{98.11}H_{63.38}Cl_{0.86}F_{2.52}N_{18}O_{18.84}Ru_3$	$C_{144}H_{96}F_{24}N_{24}O_{32}Ru_4$
M / g mol^{-1}	1855.43	2177.36	3534.73
Temperature / K	100(2)	100(2)	100(2)
Wavelength / Å	0.61991	0.61992	0.61991
Crystal system, space group	Triclinic, $P\bar{1}$	Monoclinic, C2/c	Monoclinic, P2/c
Unit cell dimensions:			
a / Å	12.602(3)	44.496(8)	18.882(5)
b / Å	14.511(2)	15.520(5)	32.122(4)
c / Å	24.251(3)	35.529(6)	31.482(4)
α / °	102.832(6)	90	90
β / °	100.374(10)	108.633(6)	92.142(9)
γ / °	102.512(8)	90	90
Volume V / Å^3	4098.2(13)	23249(9)	19081(6)
Z	2	8	4
Calculated density ρ_{cal} / g cm^{-3}	1.504	1.244	1.230
Absorption coefficient / mm^{-1}	0.326	0.327	0.276
$F(000)$	1868	8784.4	7104
Crystal size / mm^3	$0.050 \times 0.020 \times 0.020$	$0.100 \times 0.100 \times 0.100$	$0.200 \times 0.200 \times 0.200$
Measurement range of Θ / °	0.774 to 28.172	0.842 to 27.672	0.553 to 26.282
Limiting indices	–17<=h<=17, -21<=k<=21, -33<=l<=34	-61<=h<=62, -20<=k<=20, -47<=l<=46	-25<=h<=24, -45<=k<=45, -40<=l<=40
Reflections collected / unique	140045	197369	320182
Independent reflections	23359 [R(int) = 0.0705]	31284 [R(int) = 0.0334]	52811 [R(int) = 0.0314]
Completeness / %	99.1	98.2	98.9
Absorption correction	none	None	none
Refinement method	Full-matrix least-squares on F^2	Full-matrix least-squares on F^2	Full-matrix least-squares on F^2
Data / restraints / parameters	23359 / 302 / 1036	31284 / 423 / 1472	52811 / 720 / 2053
Goodness of fit for F^2	1.019	1.074	1.108
Final R indices [$I > 2\sigma(I)$]	$R_1 = 0.1040$, $wR_2 = 0.3202$	$R_1 = 0.0451$, $wR_2 = 0.1423$	$R_1 = 0.1190$, $wR_2 = 0.3680$
R indices (all data)	$R_1 = 0.1266$, $wR_2 = 0.3412$	$R_1 = 0.0485$, $wR_2 = 0.1458$	$R_1 = 0.1216$, $wR_2 = 0.3696$
Extinction cooeficient	n/a	n/a	n/a
Largest diff. peak and hole	1.444 and –1.032 e·Å^{-3}	0.767 and –1.262 e·Å^{-3}	3.345 and –3.307 e·Å^{-3}

NMR experiments @ pD 7

a)

2C @ pD 7

b)

c)
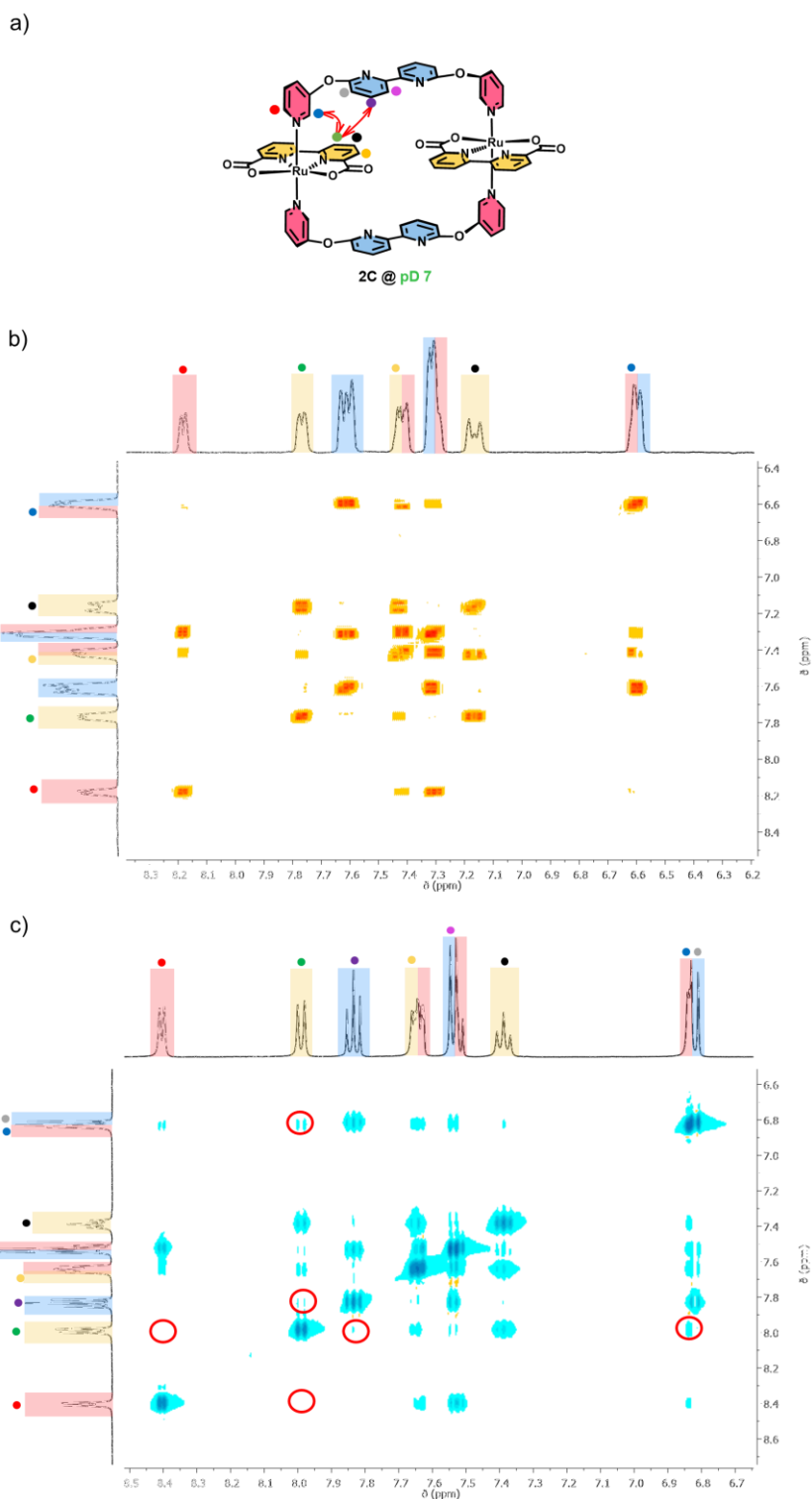
Figure A8.3.8. a) Molecular structure of **2C** with specific protons marked in colour. b) ^{1}H-^{1}H COSY NMR spectra (red) and c) ^{1}H-^{1}H NOESY NMR spectra (cyan: negative signal/red: positive signal) spectra of **2C** in TFE-d_3/D$_2$O 1:1 (pD 7, 400 MHz). The red double-headed arrows in figure a) indicate close spatial proximity between the protons according to the cross peaks marked with red circles in the NOESY spectra of **2C**.
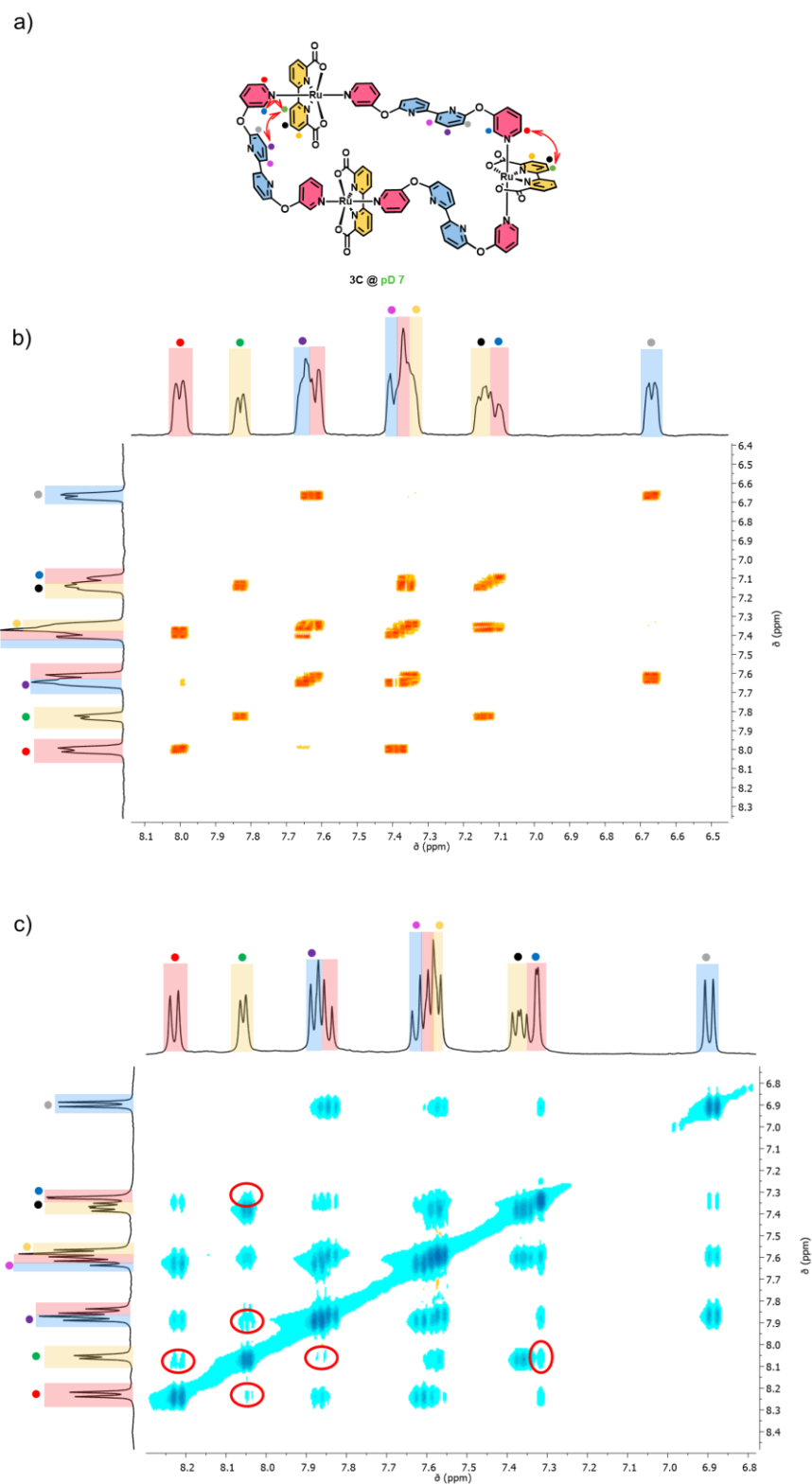
Figure A8.3.9. a) Molecular structure of **3C** with specific protons marked in colour. b) ^{1}H-^{1}H COSY NMR spectra (red) and c) ^{1}H-^{1}H NOESY NMR spectra (cyan: negative signal/red: positive signal) spectra of **3C** in TFE-d_3/D$_2$O 1:1 (pD 7, 400 MHz). The red double-headed arrows in figure a) indicate close spatial proximity between the protons according to the cross peaks marked with red circles in the NOESY spectra of **3C**.
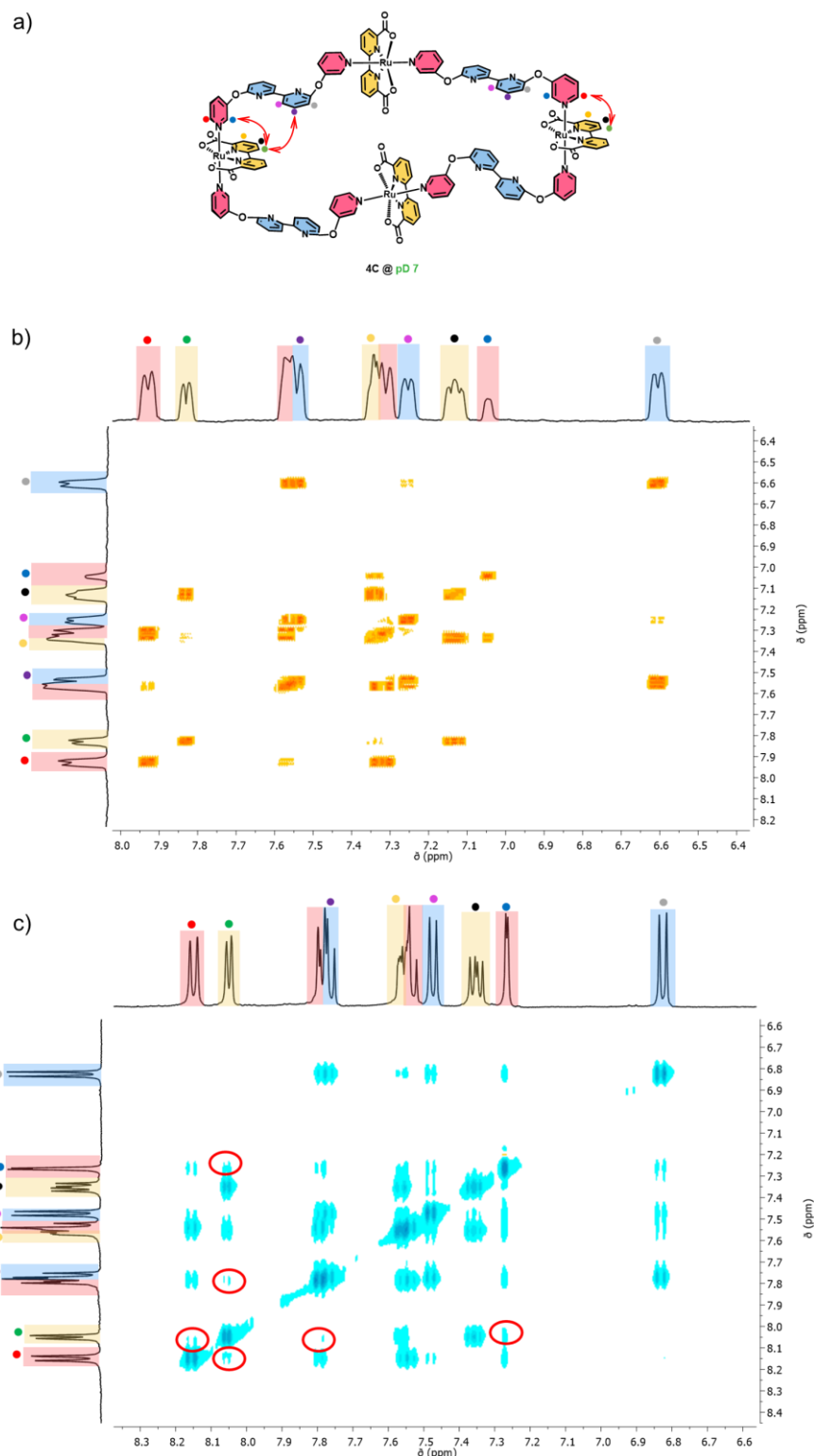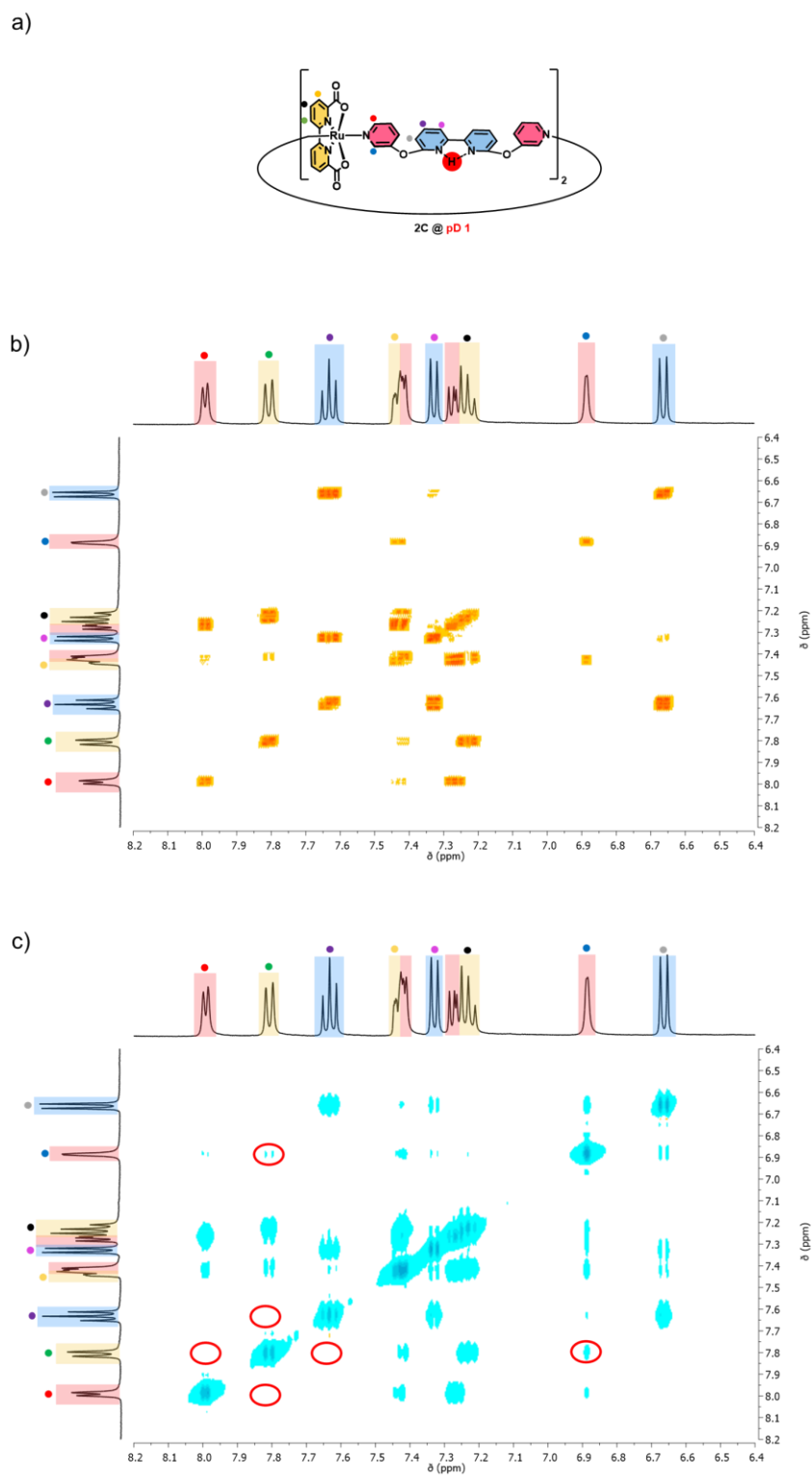
Figure A8.3.10. a) Molecular structure of **4C** with specific protons marked in colour. b) ^{1}H-^{1}H COSY NMR spectra (red) and c) ^{1}H-^{1}H NOESY NMR spectra (cyan: negative signal/red: positive signal) spectra of **4C** in TFE-d_3/D$_2$O 1:1 (pD 7, 400 MHz). The red double-headed arrows in figure a) indicate close spatial proximity between the protons according to the cross peaks marked with red circles in the NOESY spectra of **4C**.

VT–NMR experiments
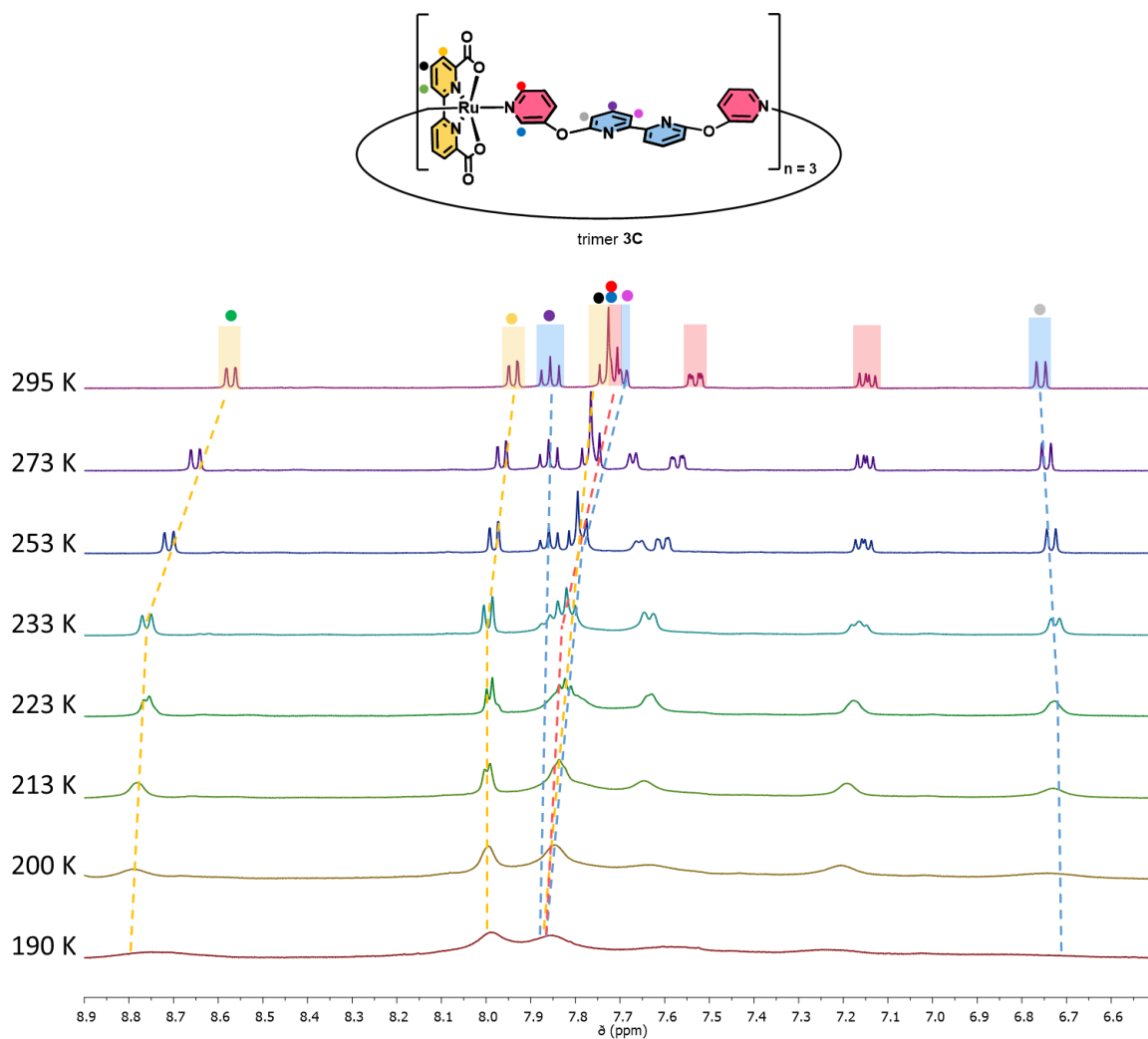
Figure A8.3.11. Aromatic region of temperature-dependent ^{1}H NMR spectra of **3C** in CD_2Cl_2/CD_3OD 1:1 (400 MHz) from 295 K to 190 K.
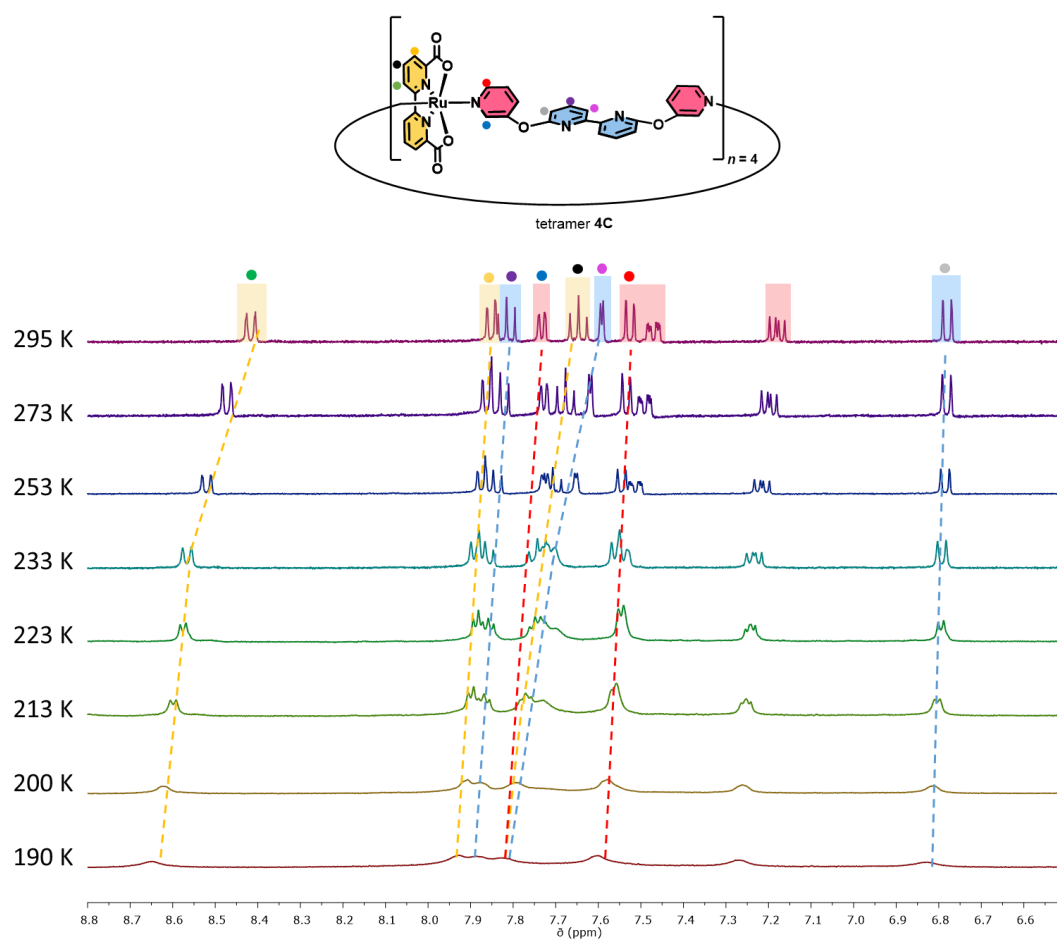
Figure A8.3.12. Aromatic region of temperature-dependent ^{1}H NMR spectra of **4C** in CD$_2$Cl$_2$/CD$_3$OD 1:1 (400 MHz) from 295 K to 190 K.

NMR experiments @ pD 1
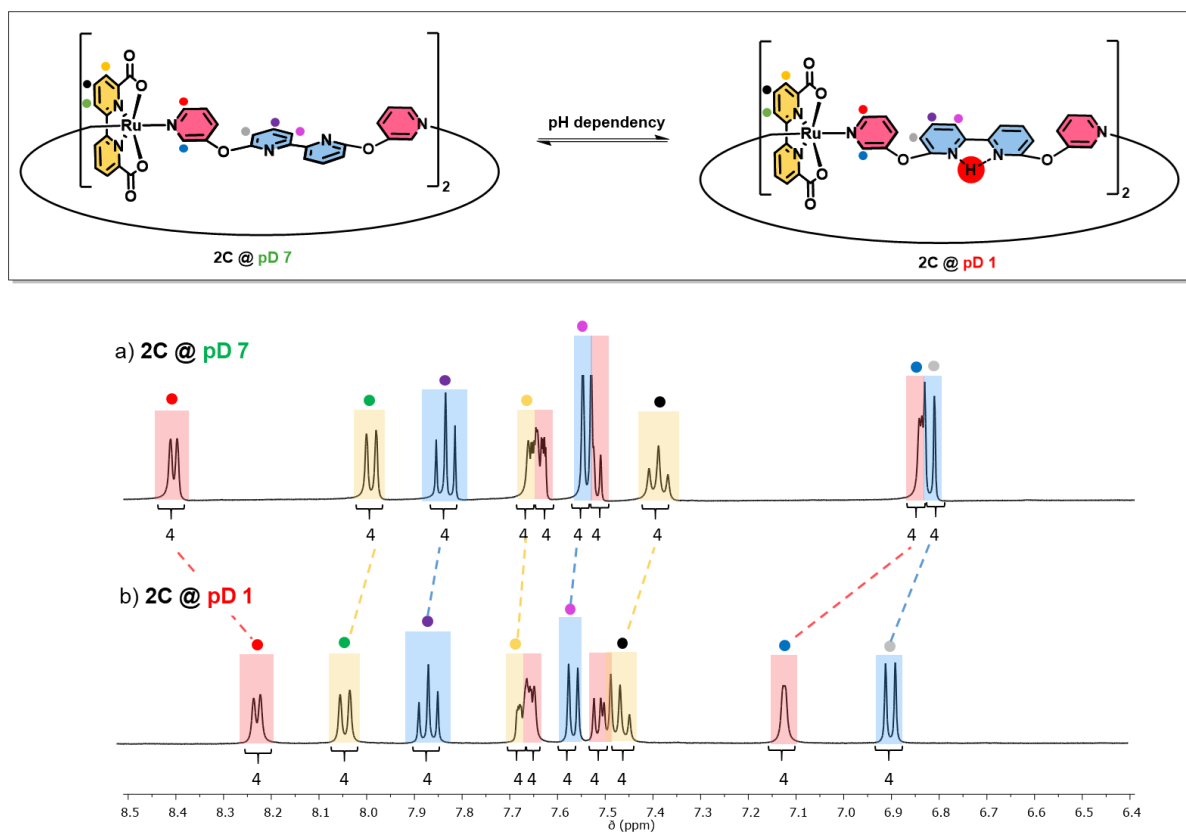
Figure A8.3.13. Comparison of the aromatic region of the ^{1}H NMR spectra of complex **2C** in 1:1 TFE-d_3/D$_2$O ((a) pD 7 and (b) pD 1, 0.1 M CF$_3$SO$_3$D, 400 MHz, ascorbic acid, rt). Colours of the signals correspond to bda (yellow), axial pyridine fragment (red) and bipyridine unit (blue) of the axial ligand as highlighted in the structure.

Table A8.3.3. Chemical shifts δ (ppm), chemical shift changes $\Delta\delta$ (ppm) and assignment of significant ^{1}H-NMR signals (400 MHz) of complex **2C** in TFE-d_3/D$_2$O 1:1 (pD 7 or pD 1, 0.1 M CF$_3$SO$_3$D).

2C	axial pyridine		equatorial bda ligand			axial bpy unit		
	🔴	🔵	🟢	🟡	⚫	🟣	🩷	⚪
pD 7	8.41	6.85	7.99	7.65	7.39	7.83	7.54	6.82
pD 1	8.21	7.11	8.03	7.65	7.44	7.86	7.55	6.89
$\Delta\delta$	-0.20	+0.26	+0.04	0	+0.05	+0.03	+0.01	+0.07
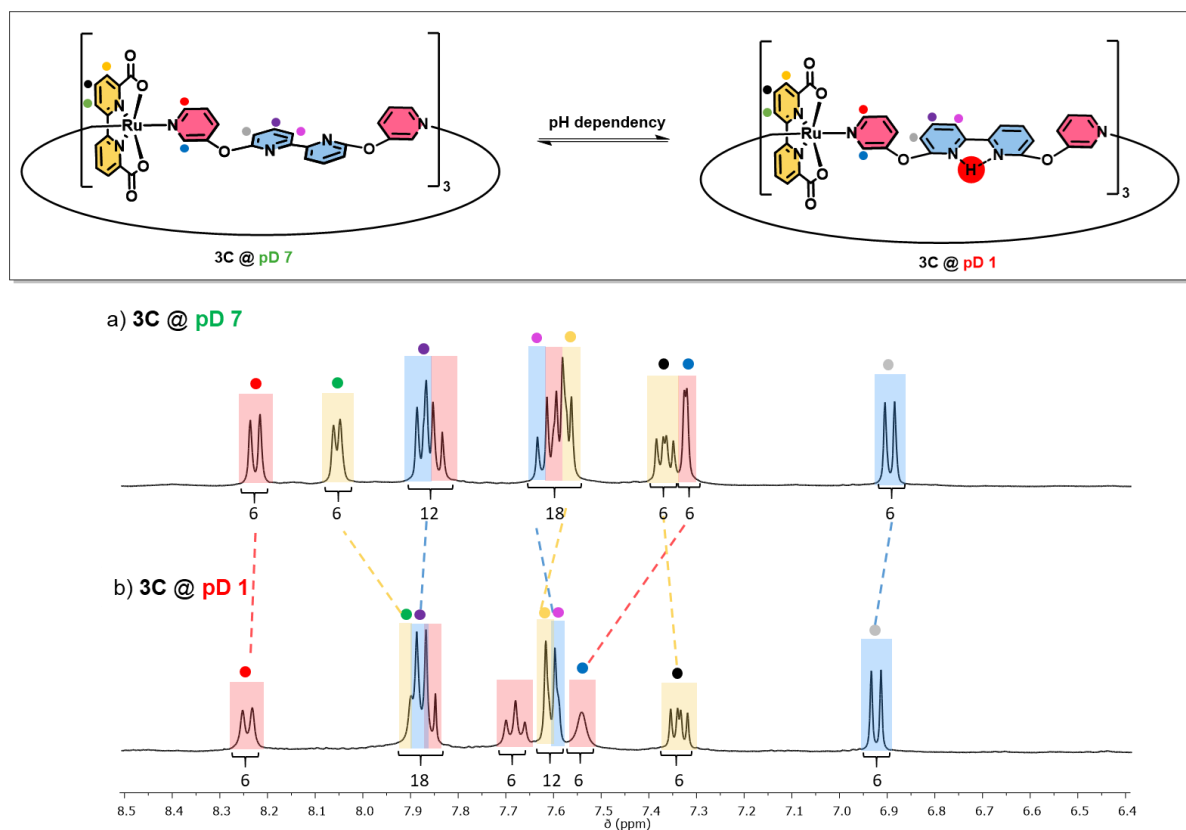
Figure A8.3.14. Comparison of the aromatic region of the ^{1}H NMR spectra of complex **3C** in 1:1 TFE-d_3/D$_2$O ((a) pD 7 and (b) pD 1, 0.1 M CF$_3$SO$_3$D, 400 MHz, ascorbic acid, rt). Colours of the signals correspond to bda (yellow), axial pyridine fragment (red) and bipyridine unit (blue) of the axial ligand as highlighted in the structure.

Table A8.3.4. Chemical shifts δ (ppm), chemical shift changes Δδ (ppm) and assignment of significant ^{1}H-NMR signals (400 MHz) of complex **3C** in TFE-d_3/D$_2$O 1:1 (pD 7 or pD 1, 0.1 M CF$_3$SO$_3$D).

	axial pyridine		equatorial bda ligand			axial bpy unit		
3C	🔴	🔵	🟢	🟡	⚫	🟣	🩷	⚪
pD 7	8.23	7.33	8.06	7.57	7.37	7.88	7.63	6.90
pD 1	8.25	7.54	7.90	7.62	7.34	7.89	7.60	6.93
Δδ	+0.02	+0.21	-0.16	+0.05	-0.03	+0.01	-0.03	+0.03
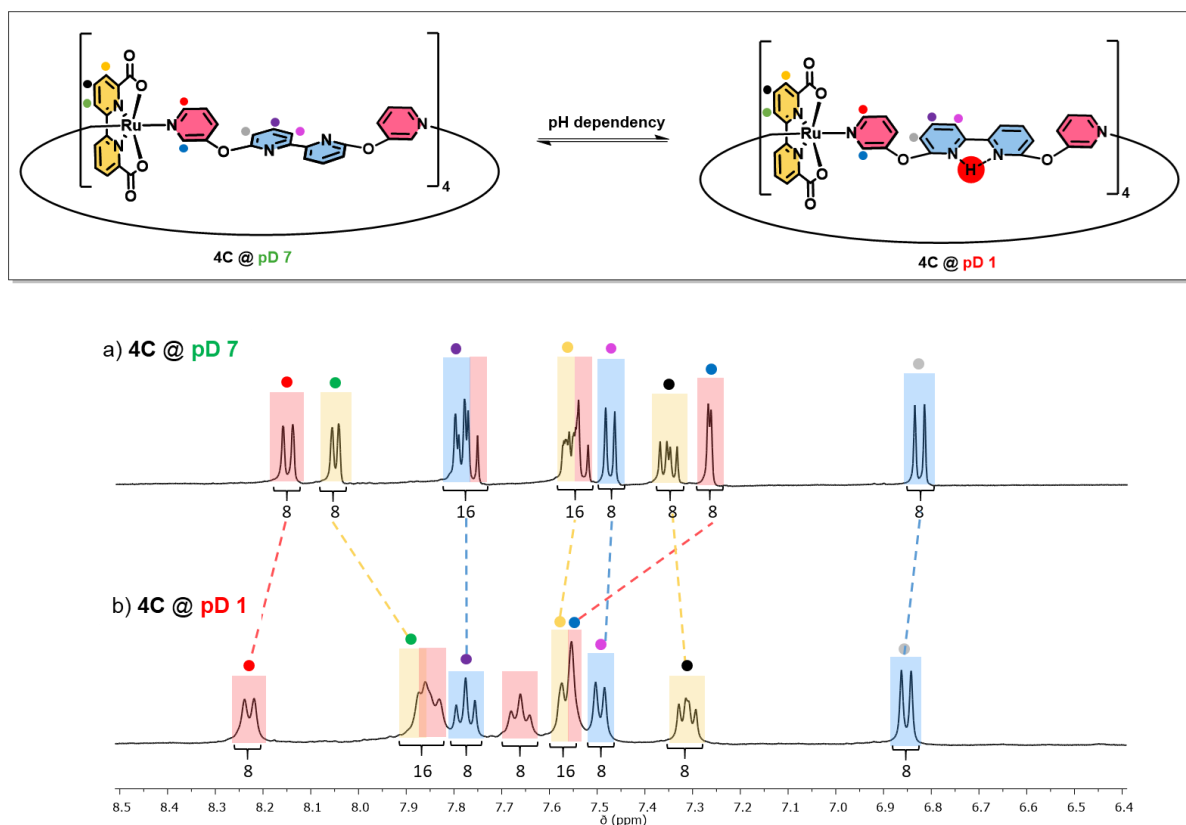
Figure A8.3.15. Comparison of the aromatic region of the ^{1}H NMR spectra of complex **4C** in 1:1 TFE-d_3/D$_2$O ((a) pD 7 and (b) pD 1, 0.1 M CF$_3$SO$_3$D, 400 MHz, ascorbic acid, rt). Colours of the signals correspond to bda (yellow), axial pyridine fragment (red) and bipyridine unit (blue) of the axial ligand as highlighted in the structure.

Table A8.3.5. Chemical shifts δ (ppm), chemical shift changes Δδ (ppm) and assignment of significant ^{1}H-NMR signals (400 MHz) of complex **4C** in TFE-d_3/D$_2$O 1:1 (pD 7 or pD 1, 0.1 M CF$_3$SO$_3$D).

	axial pyridine		equatorial bda ligand			axial bpy unit		
4C	🔴	🔵	🟢	🟡	⚫	🟣	🩷	⚪
pD 7	8.15	7.27	8.05	7.57	7.35	7.78	7.47	6.83
pD 1	8.23	7.55	7.87	7.57	7.31	7.77	7.49	6.85
Δδ	+0.08	+0.28	-0.18	0	-0.04	-0.01	+0.02	+0.02

Figure A8.3.16. a) Molecular repeating unit of **2C** with specific protons marked in colour. b) ^{1}H-^{1}H COSY NMR spectra (red) and c) ^{1}H-^{1}H NOESY NMR spectra (cyan: negative signal/red: positive signal) spectra of **2C** in TFE-d_3/D$_2$O 1:1 (pD 1, 0.1 M CF$_3$SO$_3$D, 400 MHz).

a)

3C @ pD 1

b)

c)
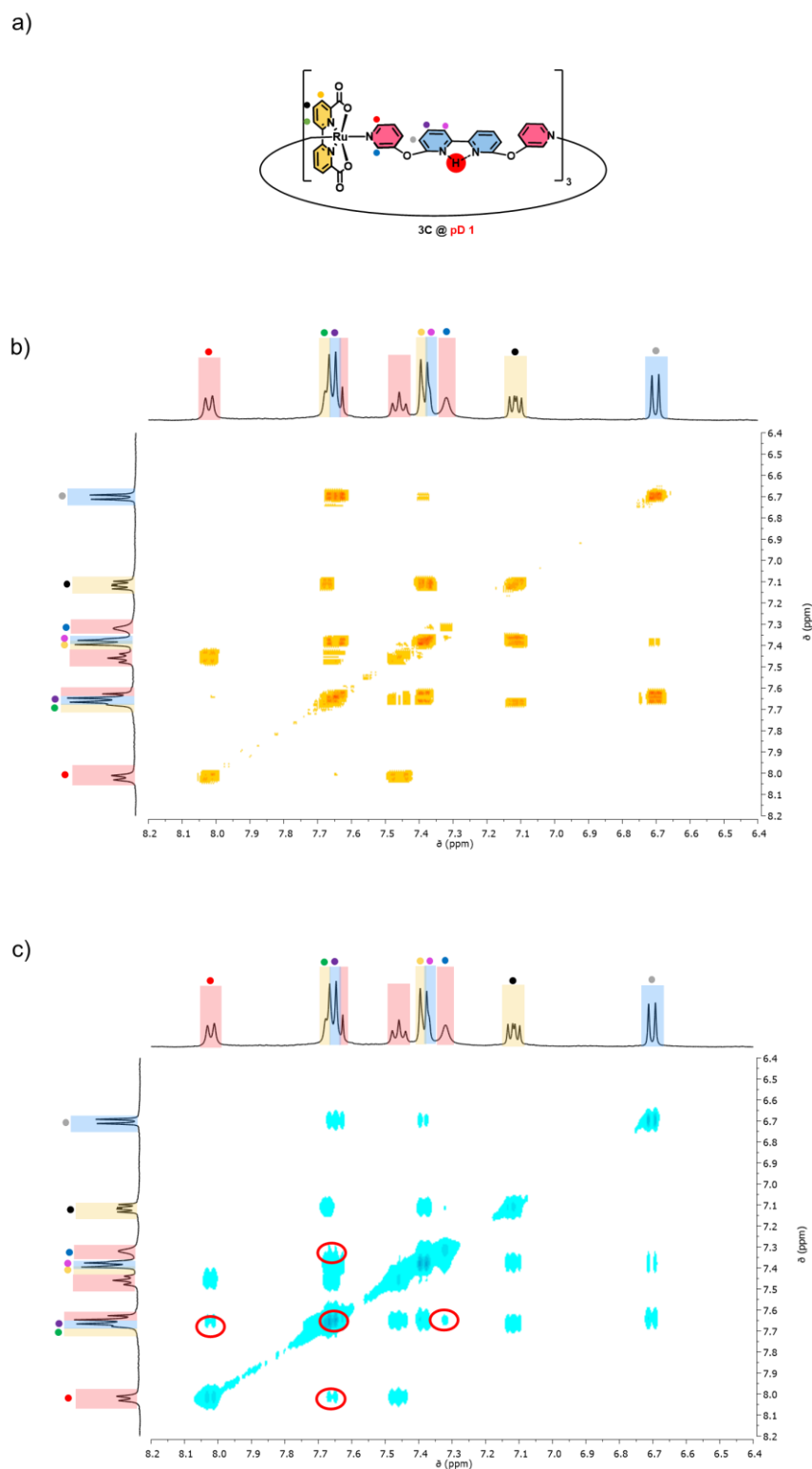
Figure A8.3.17. a) Molecular repeating unit of **3C** with specific protons marked in colour. b) ^{1}H-^{1}H COSY NMR spectra (red) and c) ^{1}H-^{1}H NOESY NMR spectra (cyan: negative signal/red: positive signal) spectra of **3C** in TFE-d_3/D$_2$O 1:1 (pD 1, 0.1 M CF$_3$SO$_3$D, 400 MHz).

a)

b)

c)
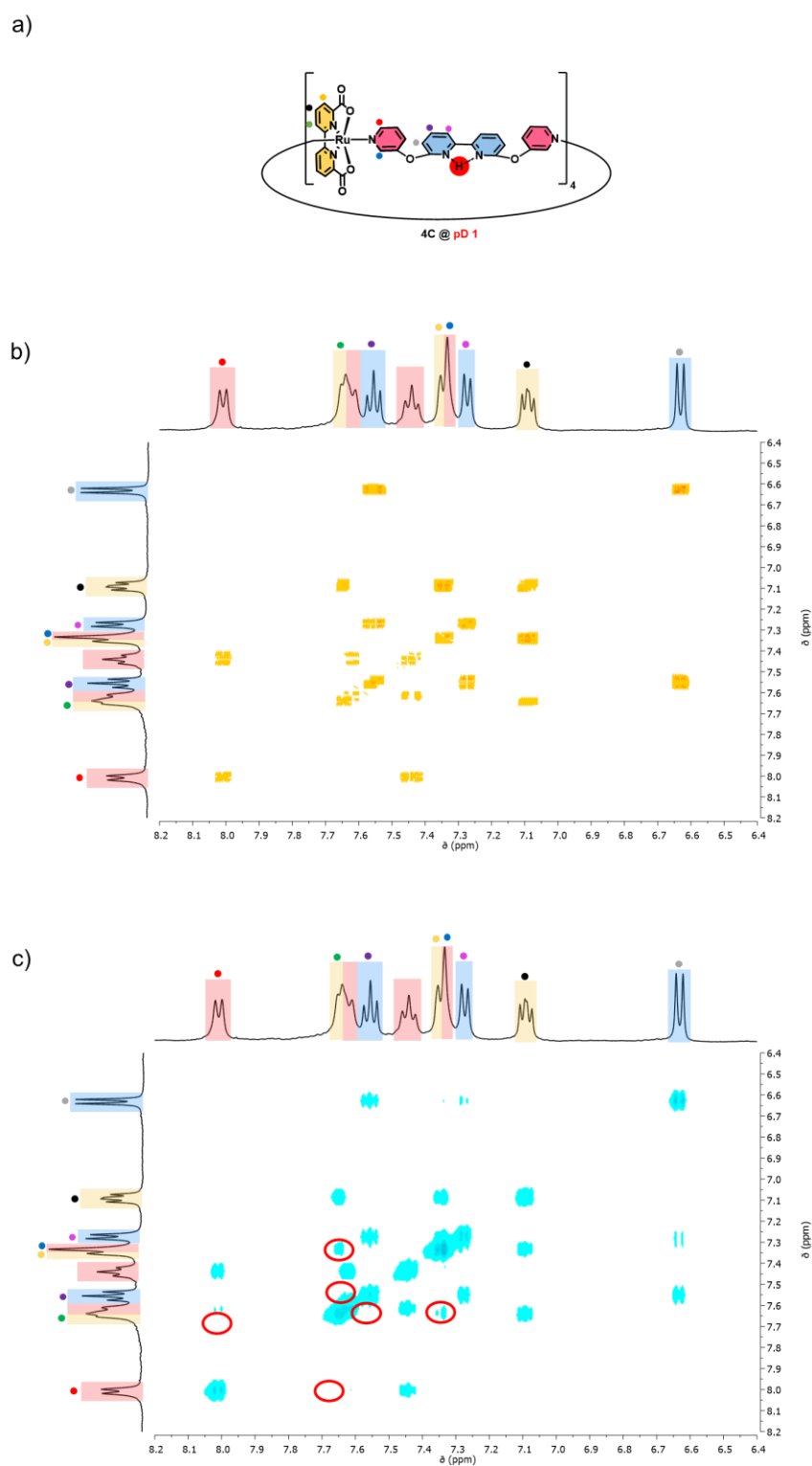
Figure A8.3.18. a) Molecular repeating unit of **4C** with specific protons marked in colour. b) ^{1}H-^{1}H COSY NMR spectra (red) and c) ^{1}H-^{1}H NOESY NMR spectra (cyan: negative signal/red: positive signal) spectra of **4C** in TFE-d_3/D$_2$O 1:1 (pD 1, 0.1 M CF$_3$SO$_3$D, 400 MHz).

DOSY NMR experiments
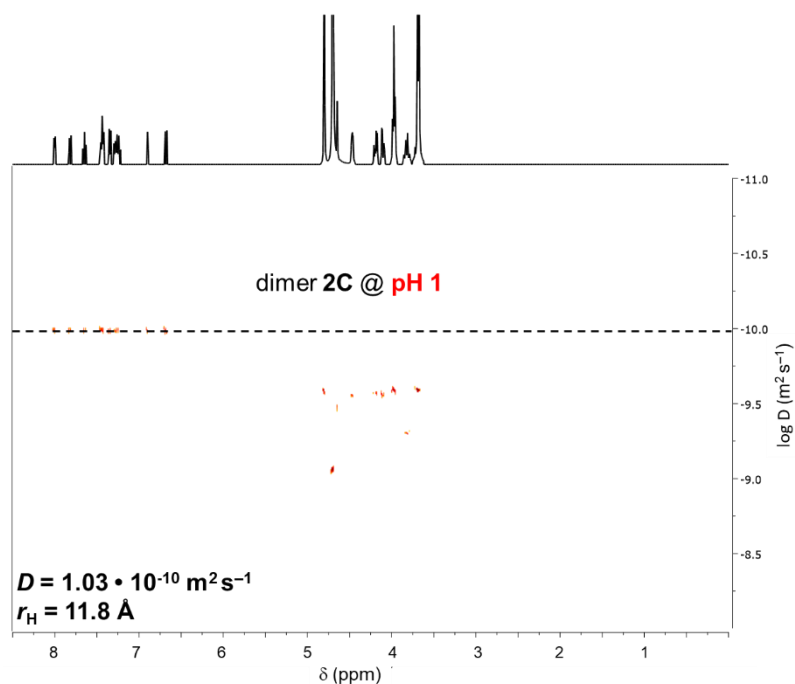
Figure A8.3.19. DOSY NMR spectra (600 MHz, TFE-d3/D2O 1:1, pD 1, 0.1 M CF3SO3D, 295 K) of dimer **2C.**
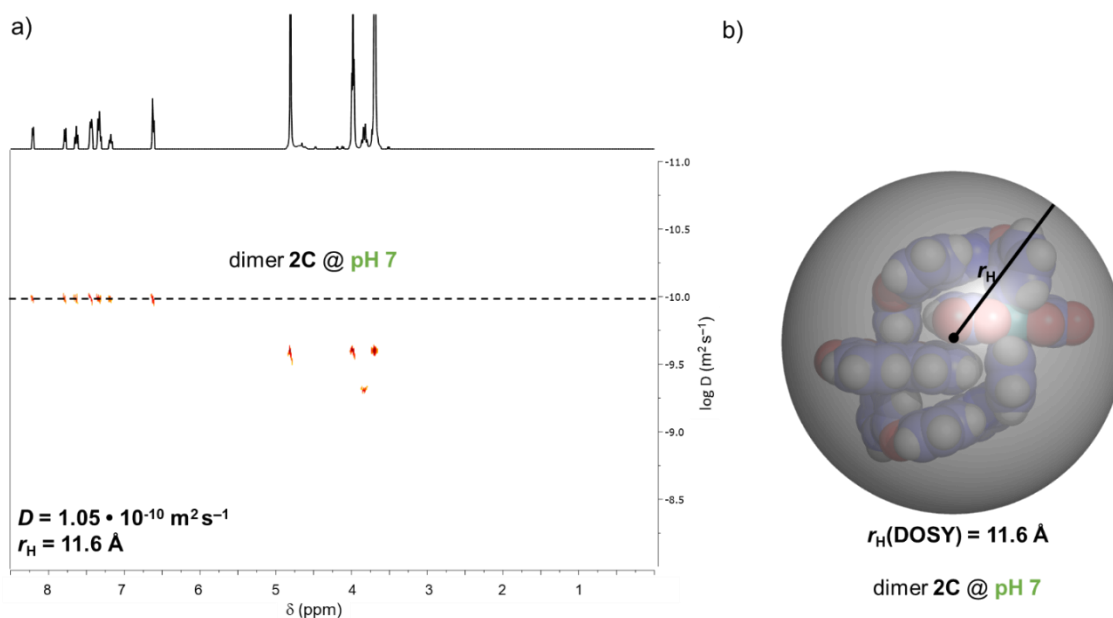
Figure A8.3.20. a) DOSY NMR spectra (600 MHz, TFE-d3/D2O 1:1, pD 7, 295 K) of dimer **2C.** b) Solvodynamic diameters are indicated as transparent spheres in the space-filling models of solid state structure of **2C.** The image b) has been prepared with PyMOL[350]).
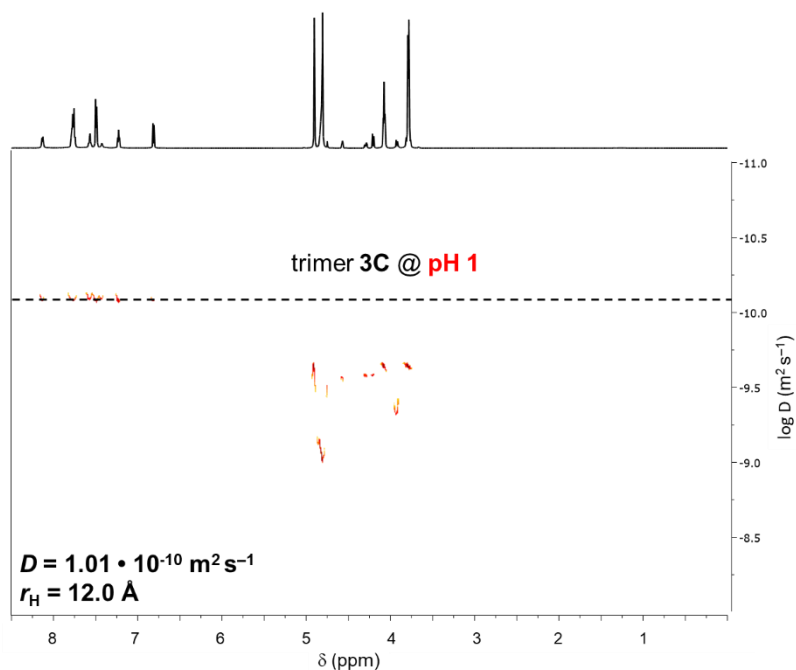
Figure A8.3.21. DOSY NMR spectra (600 MHz, TFE-d₃/D₂O 1:1, pD 1, 0.1 M CF₃SO₃D, 295 K) of trimer **3C.**
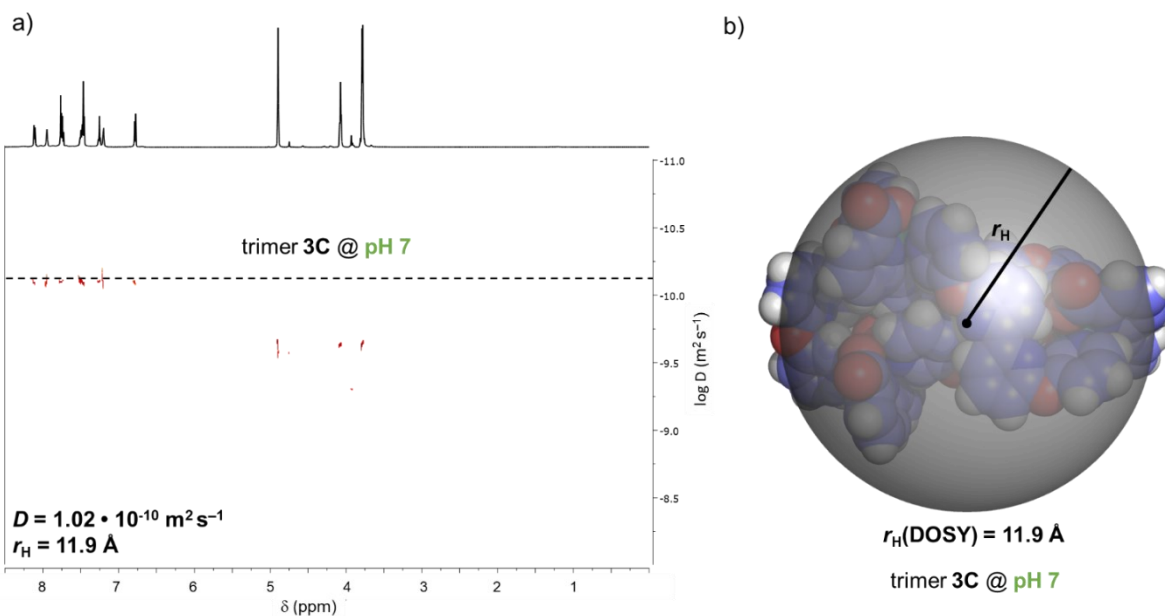
Figure A8.3.22. a) DOSY NMR spectra (600 MHz, TFE-d₃/D₂O 1:1, pD 7, 295 K) of trimer **3C**. b) Solvodynamic diameters are indicated as transparent spheres in the space-filling models of solid state structure of **3C.** The image b) has been prepared with PyMOL[350]).
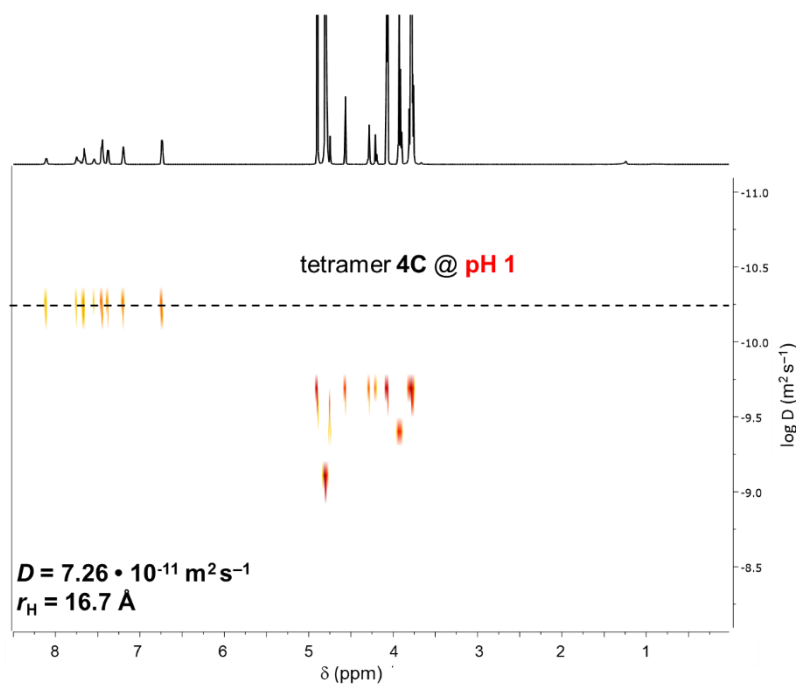
Figure A8.3.23. DOSY NMR spectra (600 MHz, TFE-d$_3$/D$_2$O 1:1, pD 1, 0.1 M CF$_3$SO$_3$D, 295 K) of tetramer **4C.**
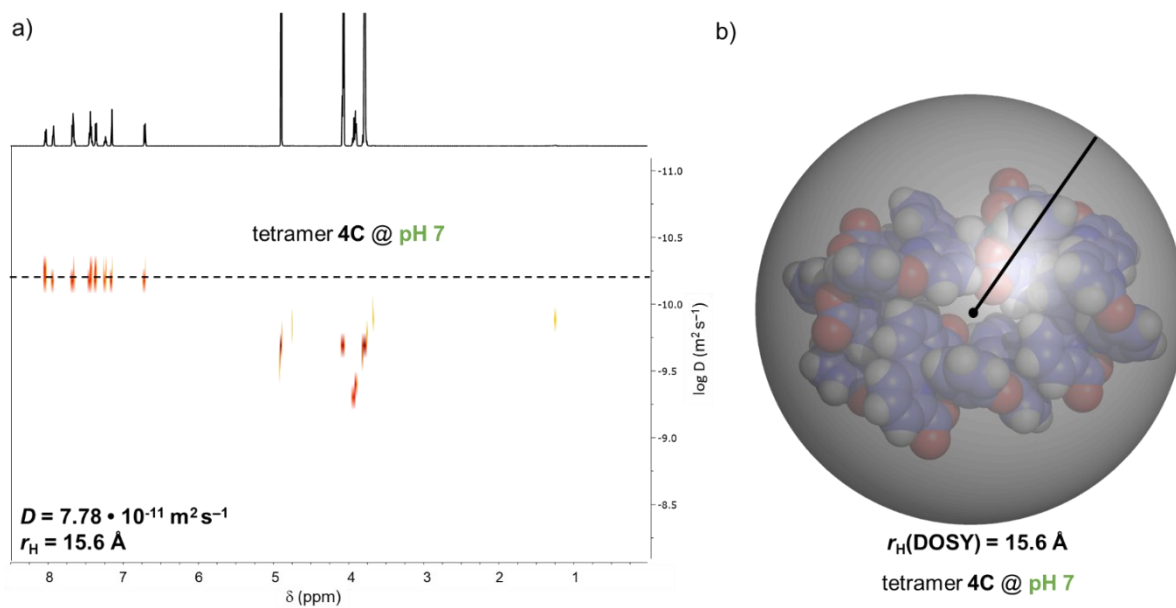
Figure A8.3.24. a) DOSY NMR spectra (600 MHz, TFE-d$_3$/D$_2$O 1:1, pD 7, 295 K) of tetramer **4C.** b) Solvodynamic diameters are indicated as transparent spheres in the space-filling models of solid state structure of **4C.** The image b) has been prepared with PyMOL[350]).

Photocatalytic water oxidation
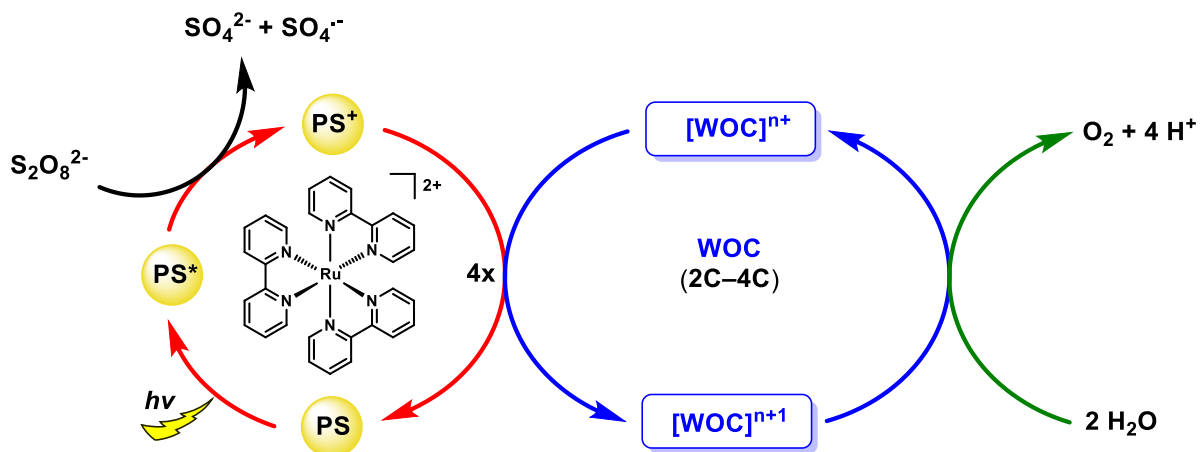
Figure A8.3.25. Schematic presentation of the photocatalytic water oxidation cycle in a three-component system containing $Na_2S_2O_8$ as sacrificial electron acceptor (SEA), $[Ru(bpy)_3]^{2+}$ as photosensitizer (PS) and complexes **2C**, **3C** or **4C** as water oxidation catalyst (WOC).
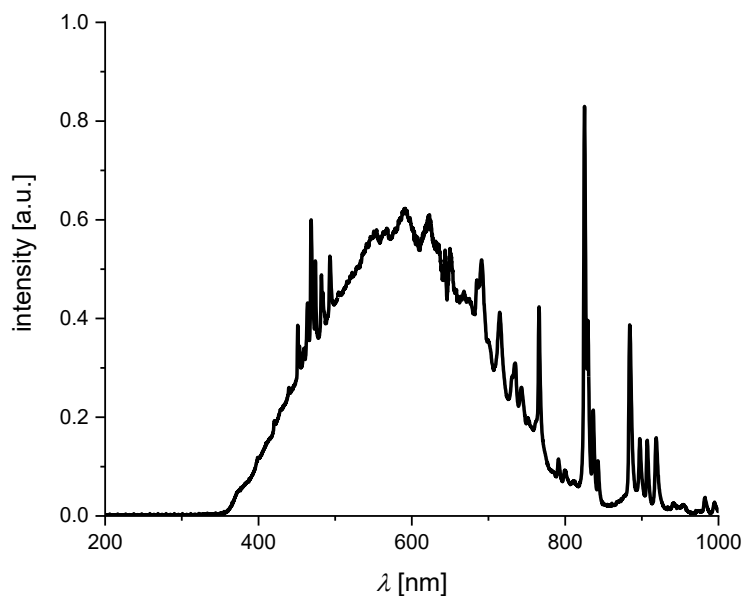
Figure A8.3.26. Emission spectrum of the xenon lamp used for photocatalytic water oxidation experiments.
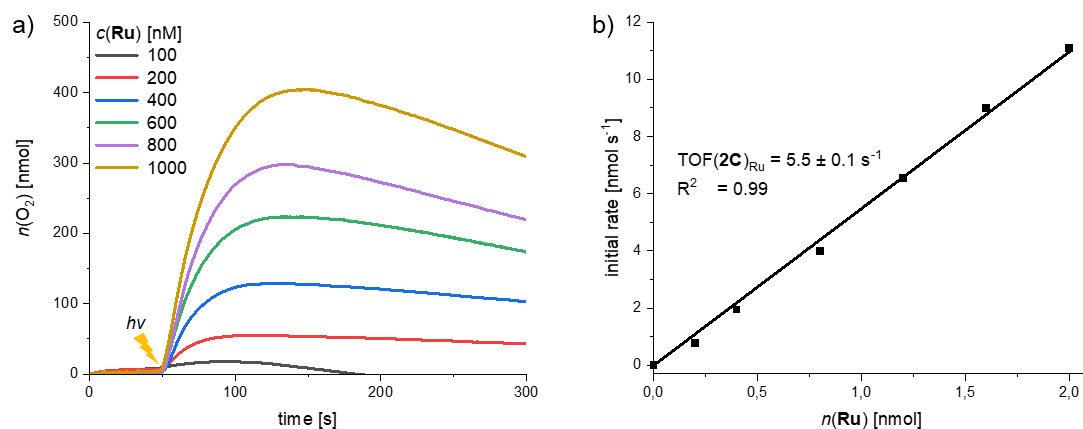
Figure A8.3.27. a) Concentration-dependent experiments with **2C** as WOC in CH_3CN/H_2O 4:6 (pH 7, 50 mM phosphate buffer), c(PS) = 1.5 mM, c($Na_2S_2O_8$) = 37 mM. The lighting symbol indicates the start of sample irradiation at t = 50 s. b) plot of the initial rates vs. the catalyst amount **per Ru unit** with linear regression for the determination of the TOF.
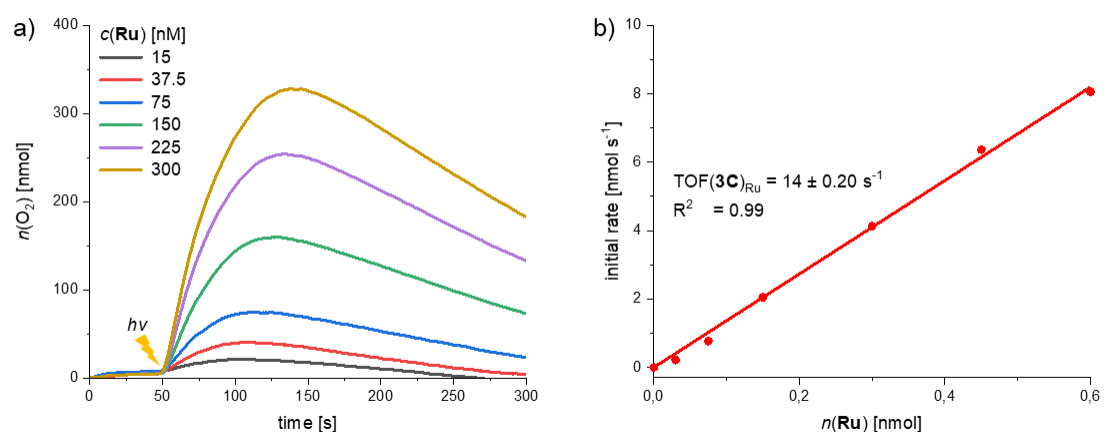
Figure A8.3.28. a) Concentration-dependent experiments with **3C** as WOC in CH_3CN/H_2O 4:6 (pH 7, 50 mM phosphate buffer), c(PS) = 1.5 mM, c($Na_2S_2O_8$) = 37 mM. The lighting symbol indicates the start of sample irradiation at t = 50 s. b) plot of the initial rates vs. the catalyst amount **per Ru unit** with linear regression for the determination of the TOF.
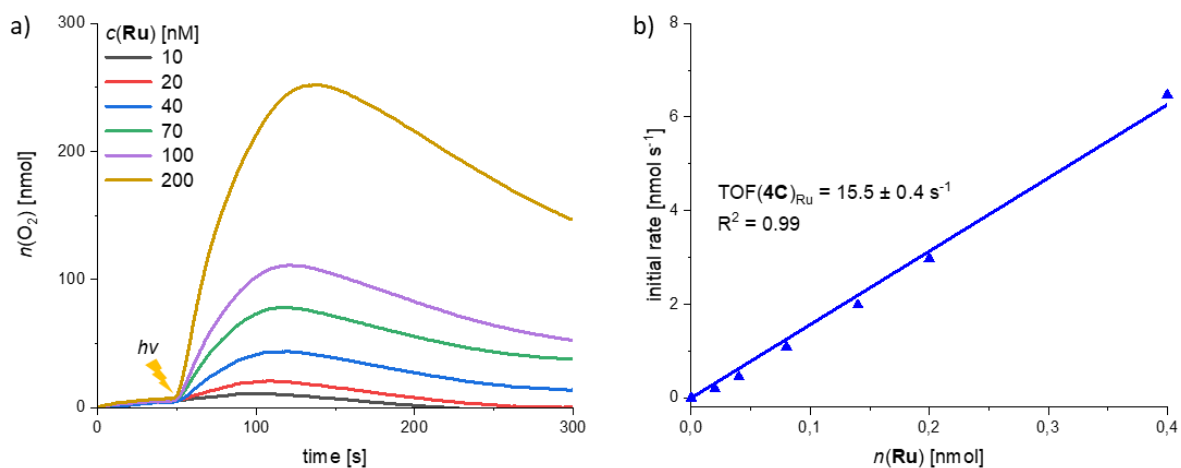
Figure A8.3.29. a) Concentration-dependent experiments with **4C** as WOC in CH_3CN/H_2O 4:6 (pH 7, 50 mM phosphate buffer), $c(PS)$ = 1.5 mM, $c(Na_2S_2O_8)$ = 37 mM. The lighting symbol indicates the start of sample irradiation at t = 50 s. b) plot of the initial rates vs. the catalyst amount **per Ru unit** with linear regression for the determination of the TOF.

Chemical water oxidation
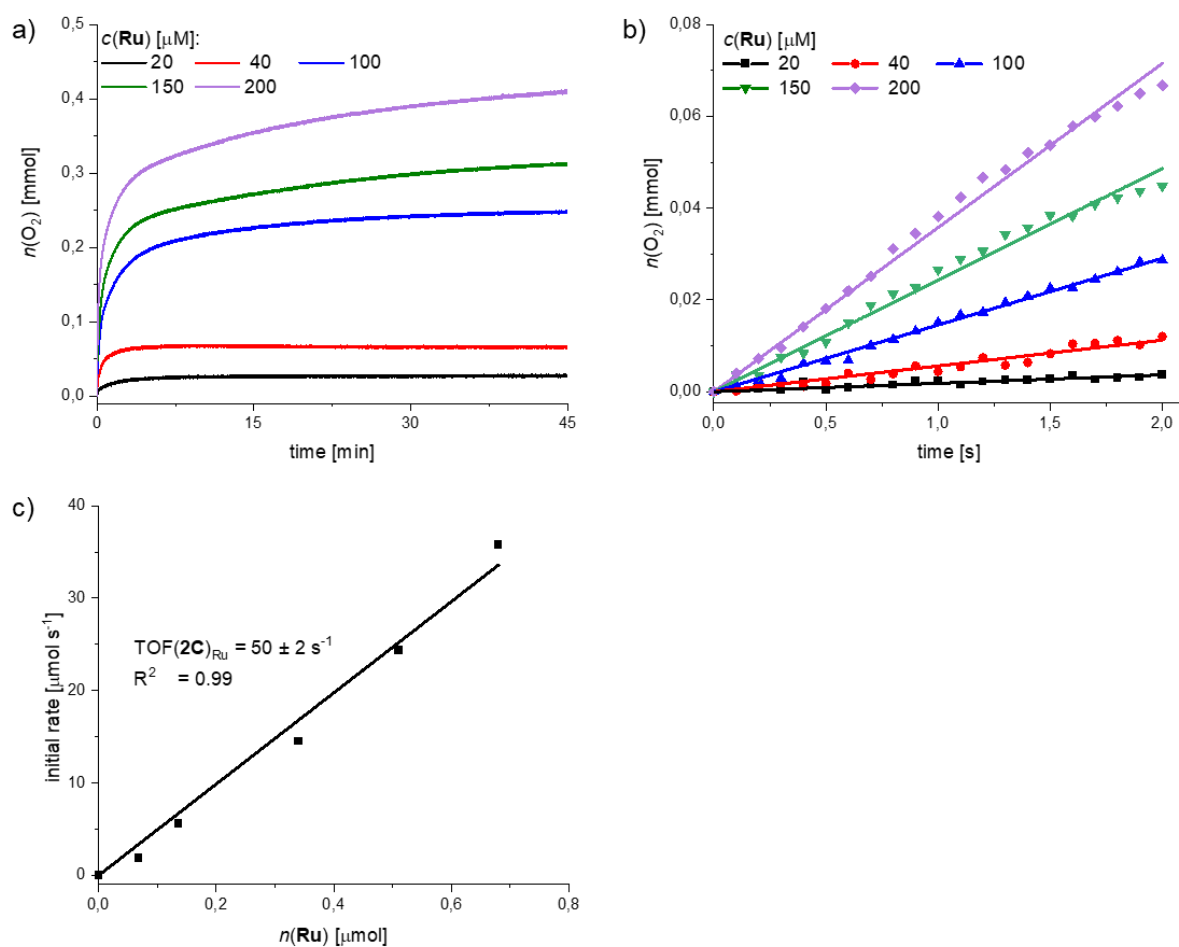
Figure A8.3.30. a) Oxygen evolution curves of **2C/Ru unit** at variable concentrations in CH_3CN/H_2O 4:6 (pH 1, triflic acid), c(CAN) = 0.6 M. b) linear regression of oxygen evolution for **2C/Ru unit** in the first 2 s of catalysis. c) plot of the initial rate vs. the catalyst amount with linear regression for the determination of the TOF_{Ru}.
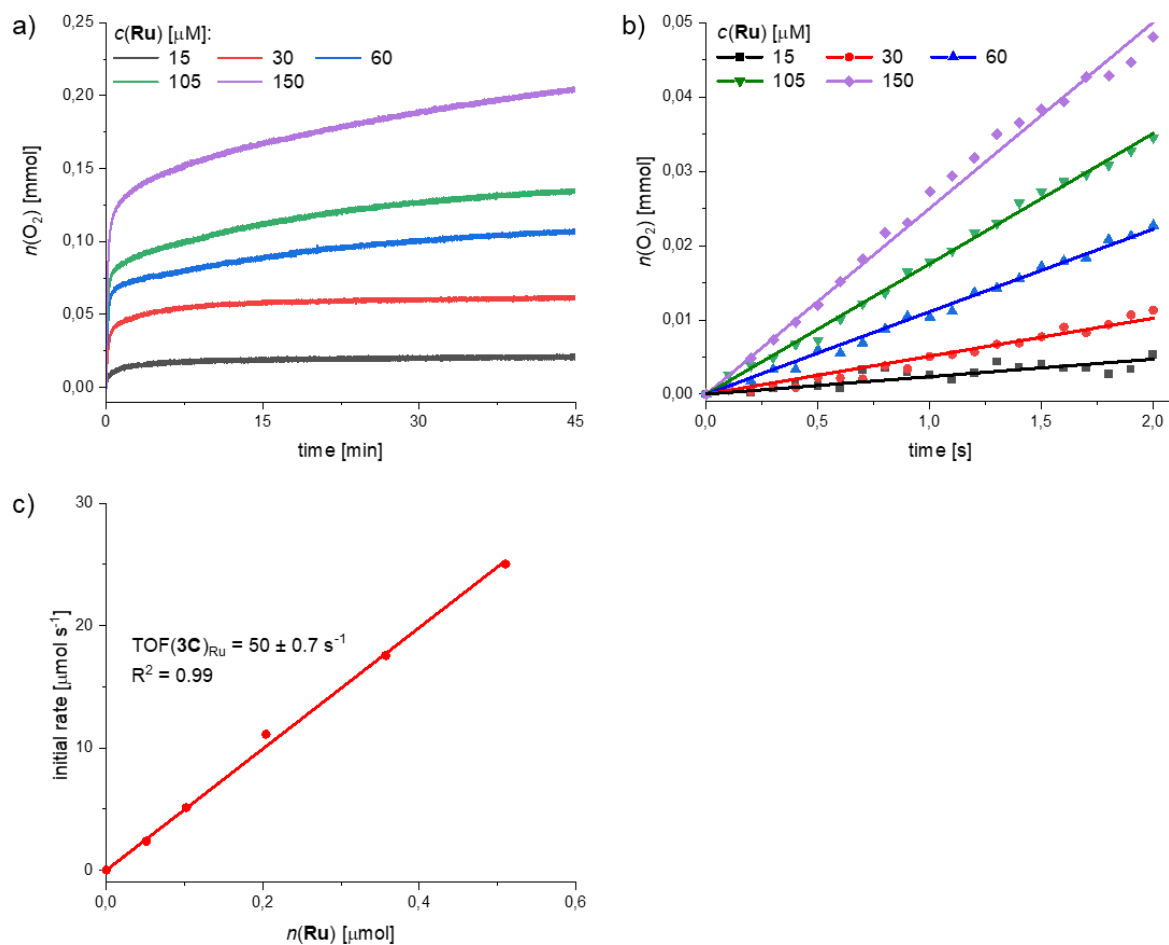
Figure A8.3.31. a) Oxygen evolution curves of **3C/Ru unit** at variable concentrations in CH_3CN/H_2O 4:6 (pH 1, triflic acid), c(CAN) = 0.6 M. b) linear regression of oxygen evolution for **3C/Ru unit** in the first 2 s of catalysis. c) plot of the initial rate vs. the catalyst amount with linear regression for the determination of the TOF_{Ru}.
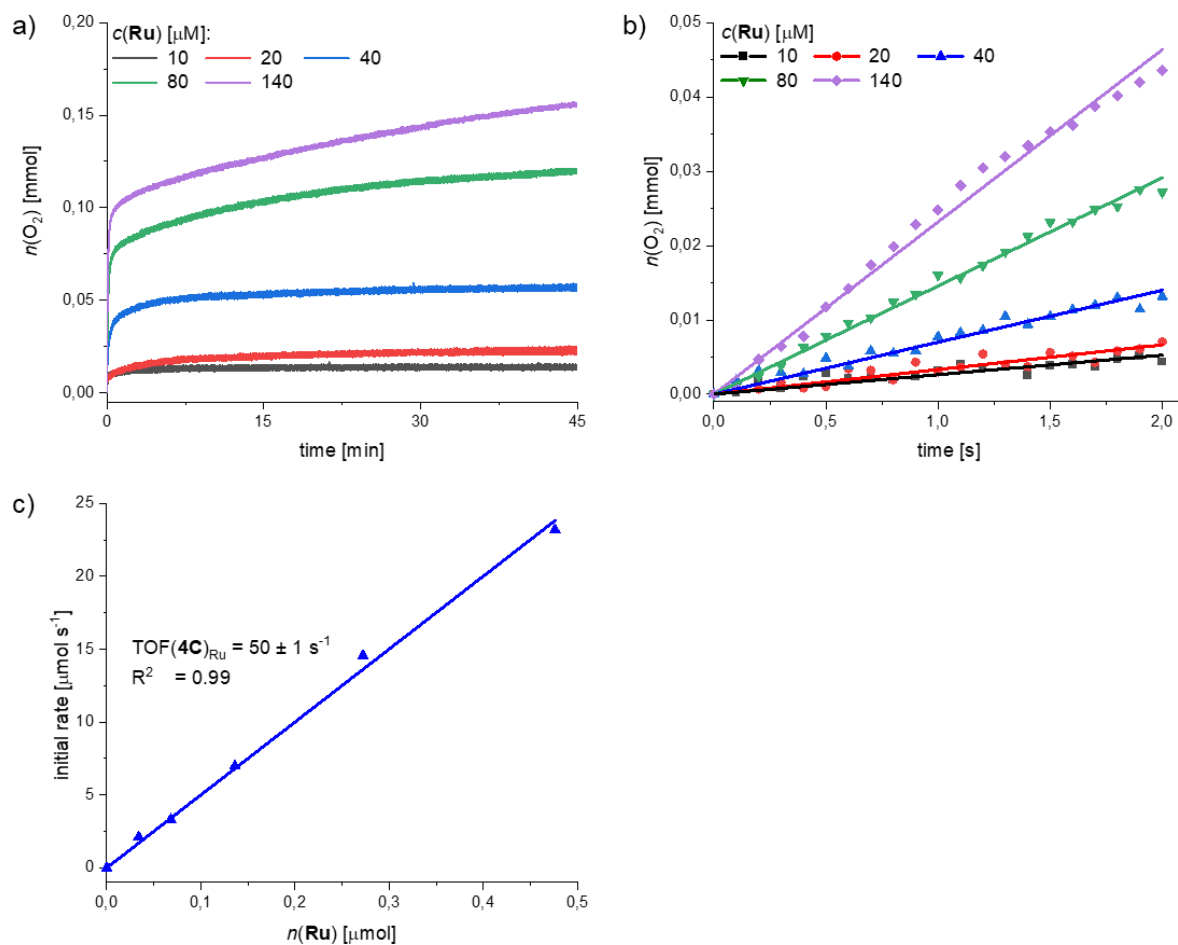
Figure A8.3.32. a) Oxygen evolution curves of **4C/Ru unit** at variable concentrations in CH_3CN/H_2O 4:6 (pH 1, triflic acid), $c(CAN) = 0.6$ M. b) linear regression of oxygen evolution for **4C/Ru unit** in the first 2 s of catalysis. c) plot of the initial rate vs. the catalyst amount with linear regression for the determination of the TOF_{Ru}.

Table A8.3.6. Catalytic activities and reported water oxidation mechanism for selected Ru WOCs in chemical and photocatalytic water oxidation.

Catalyst	Chemical water oxidation (CAN)			Photocatalytic water oxidation (PS/SEA)			Water Oxidation Mechanism
	TOF_{max} [s^{-1}]	TOF_{max}/ Ru [s^{-1}]	TON	TOF_{max} [s^{-1}]	TOF_{max}/ Ru [s^{-1}]	TON	
2C[a]	99	49.5	1200	11	5.5	400	WNA
3C[b]	149	49.5	1400	42	14	1500	WNA
4C[c]	200	50	1600	62	15.5	2200	WNA
5[d] [149, 195]	41	41	2000	0.35	0.35	10	I2M
9[e] [212, 338]	303	303	8360	0.24	0.24	140	I2M
22[f] [282]	inactive	/	inactive	50	50	1050	WNA
47[g] [243, 258]	n.d.	n.d	20800	n.d.	n.d.	640	I2M (Intra)
48[h] [179, 339]	0.068	0.034	211	11	5.5	5300	WNA
dimer 1[i] [285]	19	9.5	820	15.5	7.8	460	WNA
OEG-MC2[j] [39]	12	6	200	1.1	0.6	36	WNA
OEG-MC3[k] [39]	26	8.7	2200	10	3.3	400	WNA
MC3[l] [37, 40]	136	45	5300	11	3.7	430	WNA
OEG-MC4[m] [39]	42	10.5	2870	23	5.8	500	WNA

Experimental conditions:

[**a**] Chemical WO: 40:60 MeCN/H_2O (pH 1, triflic acid), c(CAN) = 0.6 M, c(**2C**) = 10−100 µM; Photocatalytic WO: 40:60 MeCN/H_2O (pH 7, 50 mM phosphate buffer), c(([Ru(bpy)$_3$]$^{2+}$) = 1.5 mM, c(Na$_2$S$_2$O$_8$) = 37 mM, c(**2C**) = 50−500 nM.

[**b**] Chemical WO: 40:60 MeCN/H_2O (pH 1, triflic acid), c(CAN) = 0.6 M, c(**3C**) = 5−50 µM; Photocatalytic WO: 40:60 MeCN/H_2O (pH 7, 50 mM phosphate buffer), c(([Ru(bpy)$_3$]$^{2+}$) = 1.5 mM, c(Na$_2$S$_2$O$_8$) = 37 mM, c(**3C**) = 5−100 nM.

[**c**] Chemical WO: 40:60 MeCN/H_2O (pH 1, triflic acid), c(CAN) = 0.6 M, c(**4C**) = 2.5−35 µM; Photocatalytic WO: 40:60 MeCN/H_2O (pH 7, 50 mM phosphate buffer), c(([Ru(bpy)$_3$]$^{2+}$) = 1.5 mM, c(Na$_2$S$_2$O$_8$) = 37 mM, c(**4C**) = 2.5−50 nM.

[**d**] Chemical WO: H_2O (pH 1, triflic acid), c(CAN) = 0.4 mM, c(**5**) = 12−216 µM;[195] Photocatalytic WO: H_2O (pH 7.2, phosphate buffer), c([Ru(bpy)$_3$]$^{2+}$) = 1 mM, c(Na$_2$S$_2$O$_8$) = 10 mM, c(**5**) = 9.5 µM.[149]

[**e**] Chemical WO: H_2O (pH 1, triflic acid), c(CAN) = 0.5 mM, c(**9**) = 114−216 µM;[212] Photocatalytic WO: H_2O (pH 1, perchlorid acid), c([Ru(5-CF$_3$-bpy)$_3$]$^{2+}$) = 0.2 mM, c(Na$_2$S$_2$O$_8$) = 1 mM, c(**9**) = 20 µM.[338]

[**f**] Chemical WO: inactive. Photocatalytic WO: H_2O (pH 7, phosphate buffer), c([Ru(4,4'-COOEt-bpy)$_2$bpy]$^{2+}$) = 0.2 mM, c(Na$_2$S$_2$O$_8$) = 10 mM, c(**22**) = 1−16 µM.[282]

[g] <u>Chemical WO:</u> H_2O (pH 1, triflic acid), c(CAN) = 5 mM, c(**47**) = 50 nM;[243] <u>Photocatalytic WO:</u> 6:4 MeCN/H_2O (pH 6.8, phosphate buffer), c([Ru(bpy)$_3$]$^{2+}$) = 1 mM, c(Na$_2$S$_2$O$_8$) = 45 mM, c(**47**) = 2 µM.[258]

[h] <u>Chemical WO:</u> H_2O (pH 1, triflic acid), c(CAN) = 0.1 M, c(**48**) = 0.1−1 mM;[179] <u>Photocatalytic WO:</u> H_2O (pH 7, phosphate buffer), c([Ru(4,4'-COOEt-bpy)$_2$bpy]$^{2+}$) = 0.2 mM, c(Na$_2$S$_2$O$_8$) = 20 mM, c(**48**) = 0.2 µM.[339]

[i] <u>Chemical WO:</u> 40:60 MeCN/H_2O (pH 1, triflic acid), c(CAN) = 0.6 M, c(**dimer 1**) = 50−300 µM; <u>Photocatalytic WO:</u> 40:60 MeCN/H_2O (pH 7, phosphate buffer), c(([Ru(bpy)$_3$]$^{2+}$) = 1.5 mM, c(Na$_2$S$_2$O$_8$) = 37 mM, c(**dimer 1**) = 12−200 nM.[247]

[j] <u>Chemical WO:</u> 1:1 MeCN/H_2O (pH 1, triflic acid), c(CAN) = 0.6 M, c(**OEG-MC2**) = 96−494 µM; <u>Photocatalytic WO:</u> 1:1 MeCN/H_2O (pH 7, 50 mM phosphate buffer), c(([Ru(bpy)$_3$]$^{2+}$) = 1.5 mM, c(Na$_2$S$_2$O$_8$) = 37 mM, c(**OEG-MC2**) = 0.05−5.8 µM.[39]

[k] <u>Chemical WO:</u> 1:1 MeCN/H_2O (pH 1, triflic acid), c(CAN) = 0.6 M, c(**OEG-MC3**) = 50−250 µM; <u>Photocatalytic WO:</u> 1:1 MeCN/H_2O (pH 7, 50 mM phosphate buffer), c(([Ru(bpy)$_3$]$^{2+}$) = 1.5 mM, c(Na$_2$S$_2$O$_8$) = 37 mM, c(**OEG-MC3**) = 60−2050 nM.[39]

[l] <u>Chemical WO:</u> 1:1 MeCN/H_2O (pH 1, triflic acid), c(CAN) = 0.6 M, c(**MC3**) = 6−94 µM;[37] <u>Photocatalytic WO:</u> 1:1 MeCN/H_2O (pH 7, phosphate buffer), c(([Ru(bpy)$_3$]$^{2+}$) = 1.5 mM, c(Na$_2$S$_2$O$_8$) = 37 mM, c(**MC3**) = 60−880 nM.[40]

[m] <u>Chemical WO:</u> 1:1 MeCN/H_2O (pH 1, triflic acid), c(CAN) = 0.6 M, c(**OEG-MC4**) = 10−60 µM; <u>Photocatalytic WO:</u> 1:1 MeCN/H_2O (pH 7, 50 mM phosphate buffer), c(([Ru(bpy)$_3$]$^{2+}$) = 1.5 mM, c(Na$_2$S$_2$O$_8$) = 37 mM, c(**OEG-MC4**) = 6−600 nM.[39]

5   9   **22**   **47**

48   **dimer 1**

OEG-MC2   **OEG-MC3 (R = OEG)**   **OEG-MC4**
                                    MC3 (R = H)
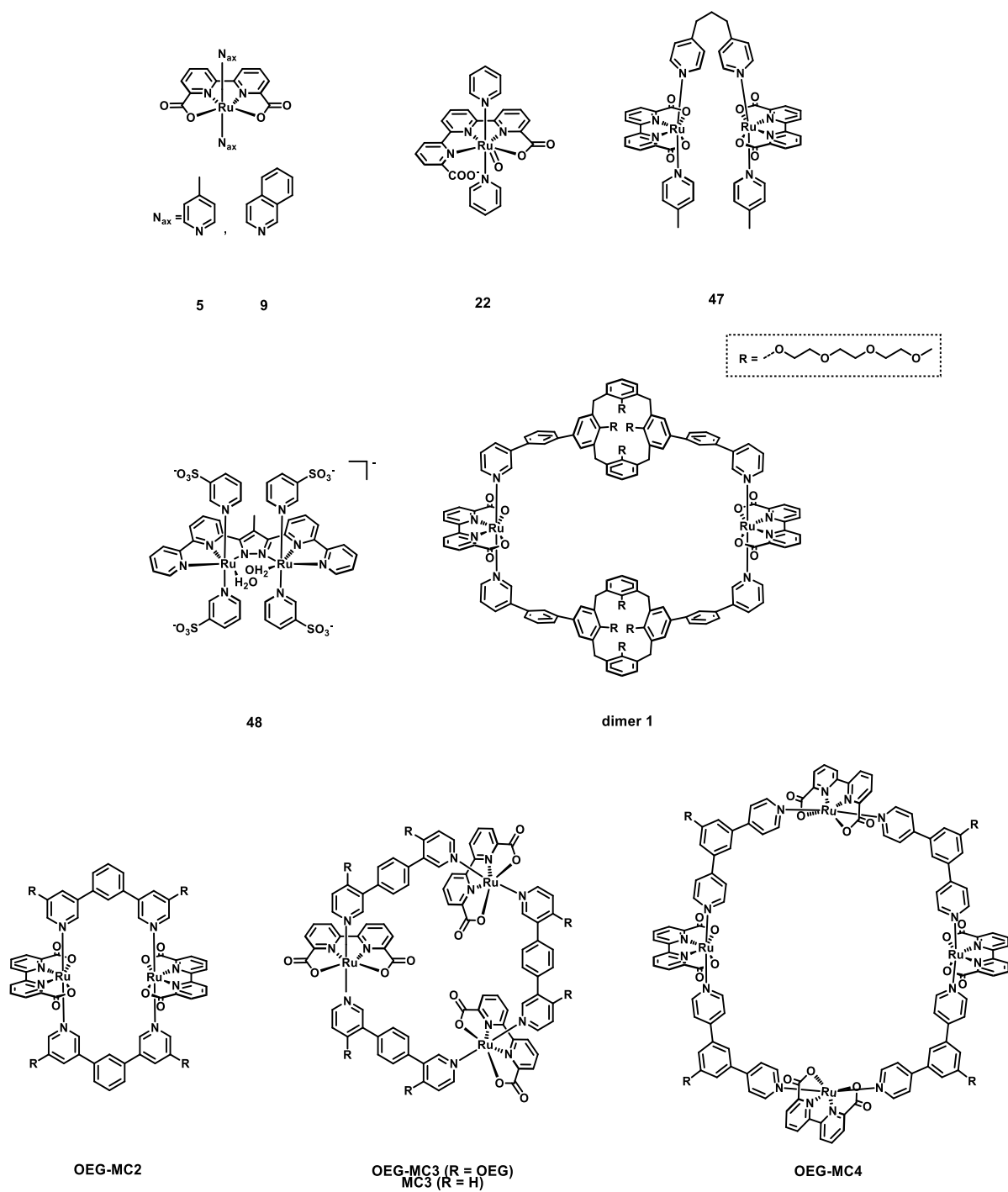
Figure A8.3.33. Chemical structures of selected mono- and multinuclear Ru WOCs.
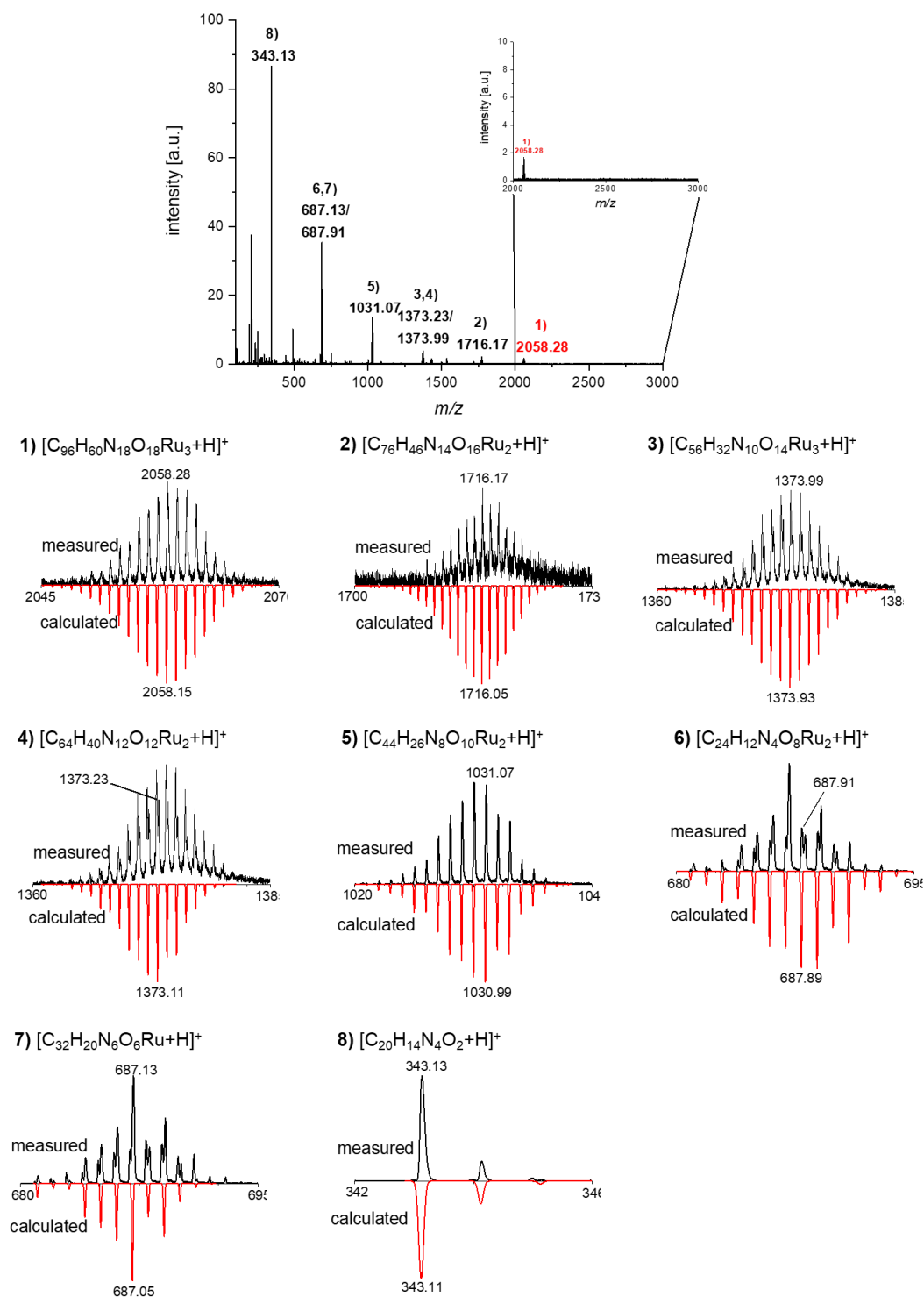
Stability tests before chemical water oxidation
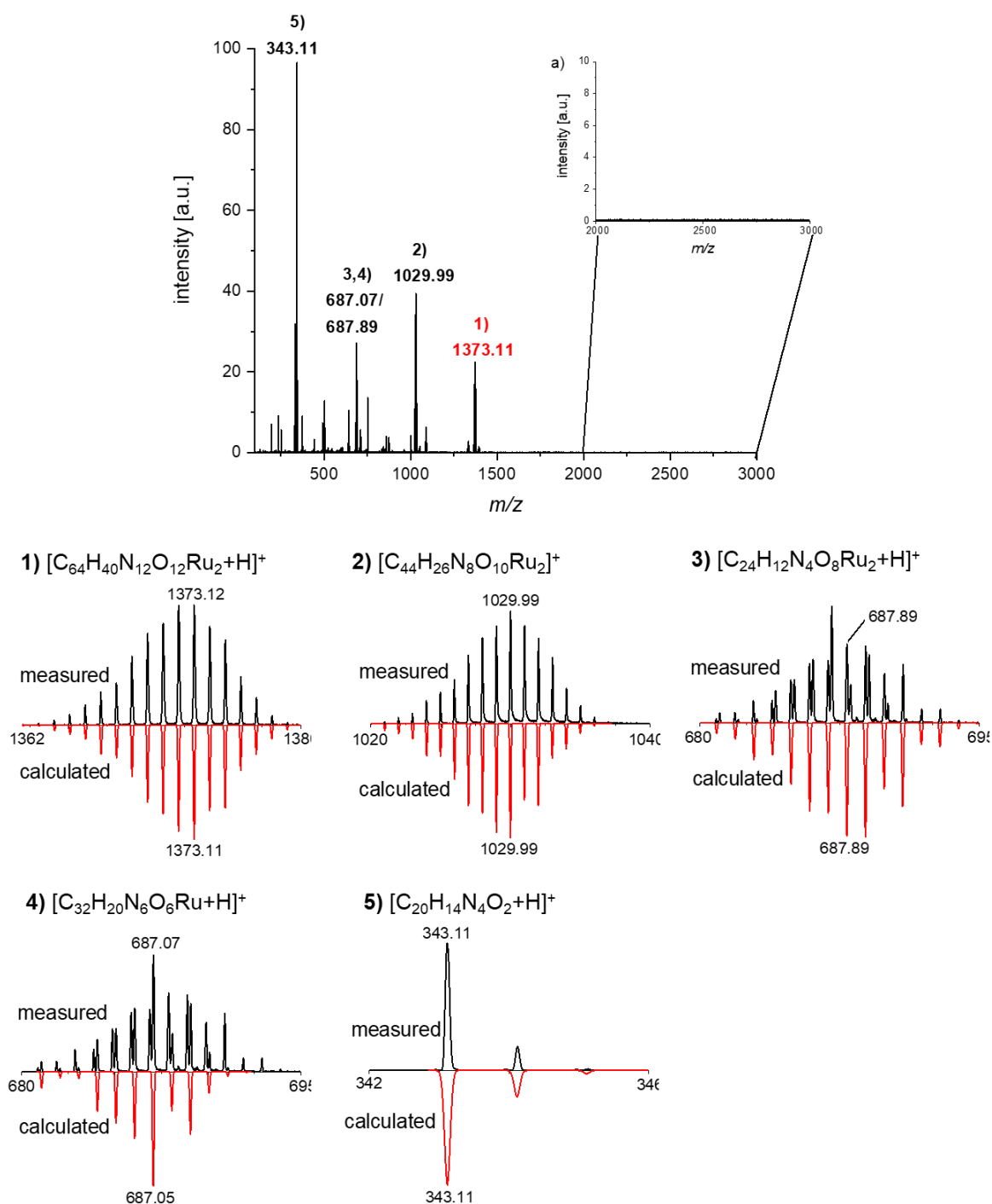
Figure A8.3.34. HR MALDI mass spectrum (CH_2Cl_2/CH_3OH 1:1, positive mode, DCTB) of **2C** before water oxidation catalysis The inset a) shows the amplified region between 2000−3000 m/z and insets 1−5) show the measured and calculated isotopic distribution of the most prominent fragmentation peaks.

217
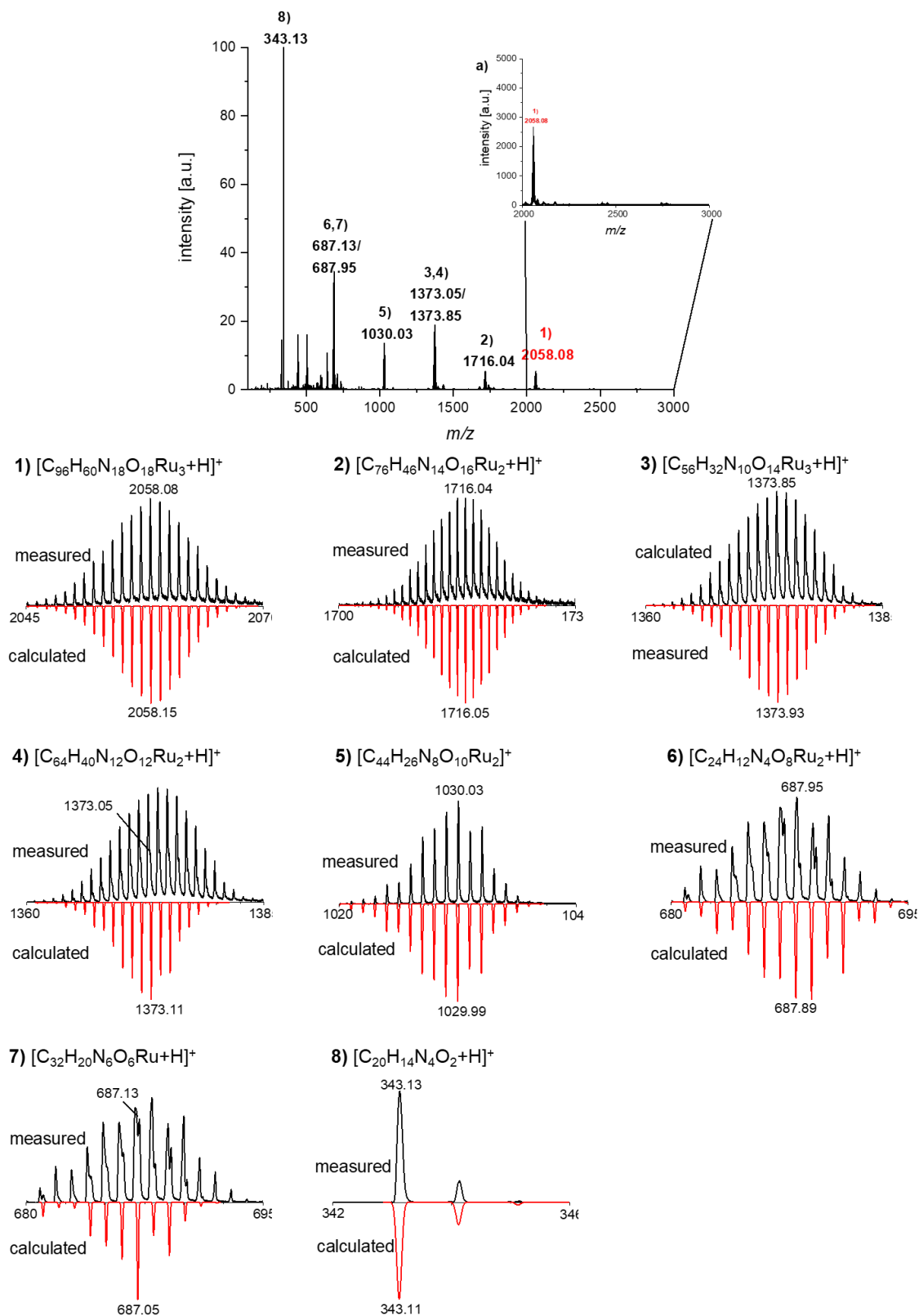
Figure A8.3.35. HR MALDI mass spectrum (CH$_2$Cl$_2$/CH$_3$OH 1:1, positive mode, DCTB) of **3C** before water oxidation catalysis The inset a) shows the amplified region between 2000−3000 m/z and insets 1−8) show the measured and calculated isotopic distribution of the most prominent fragmentation peaks.
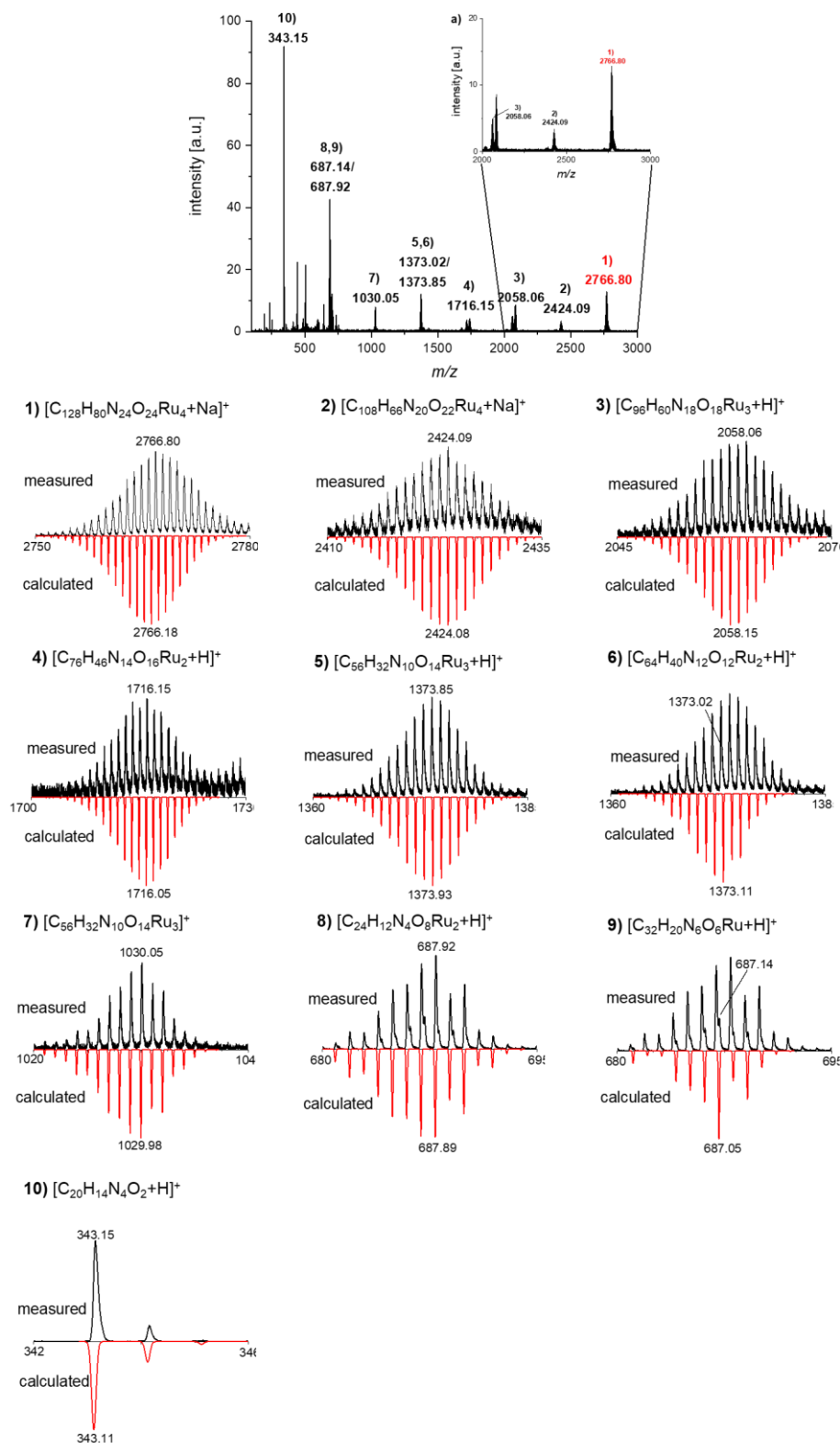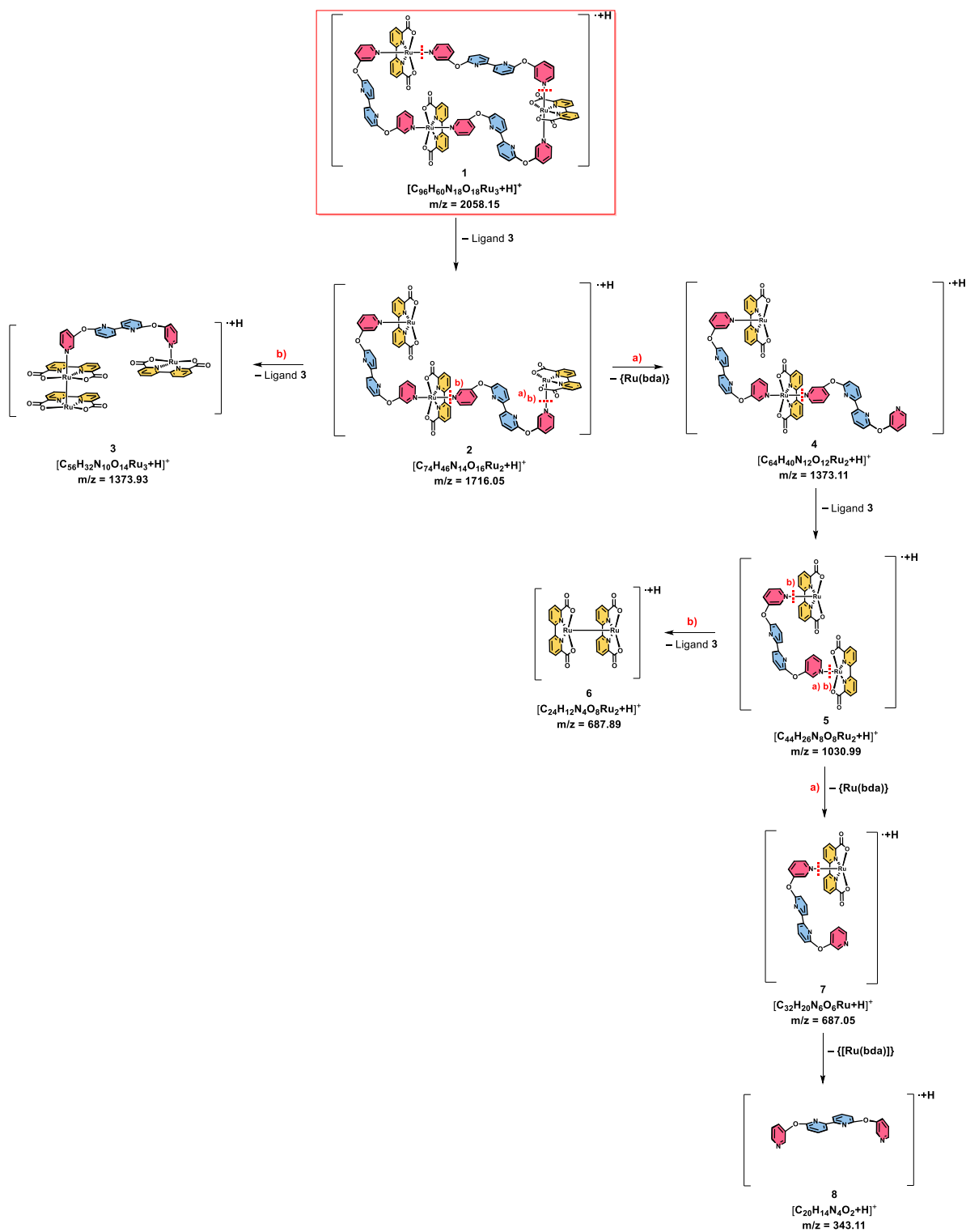
Figure A8.3.36. HR MALDI mass spectrum (CH₂Cl₂/CH₃OH 1:1, positive mode, DCTB) of **4C** before water oxidation catalysis The inset a) shows the amplified region between 2000−3000 m/z and insets 1−10) show the measured and calculated isotopic distribution of the most prominent fragmentation peaks.

Stability tests under conditions of chemical water oxidation

1) $[C_{64}H_{40}N_{12}O_{12}Ru_2+H]^+$

2) $[C_{44}H_{26}N_8O_{10}Ru_2+H]^+$

3) $[C_{24}H_{12}N_4O_8Ru_2+H]^+$

4) $[C_{32}H_{20}N_6O_6Ru+H]^+$

5) $[C_{20}H_{14}N_4O_2+H]^+$
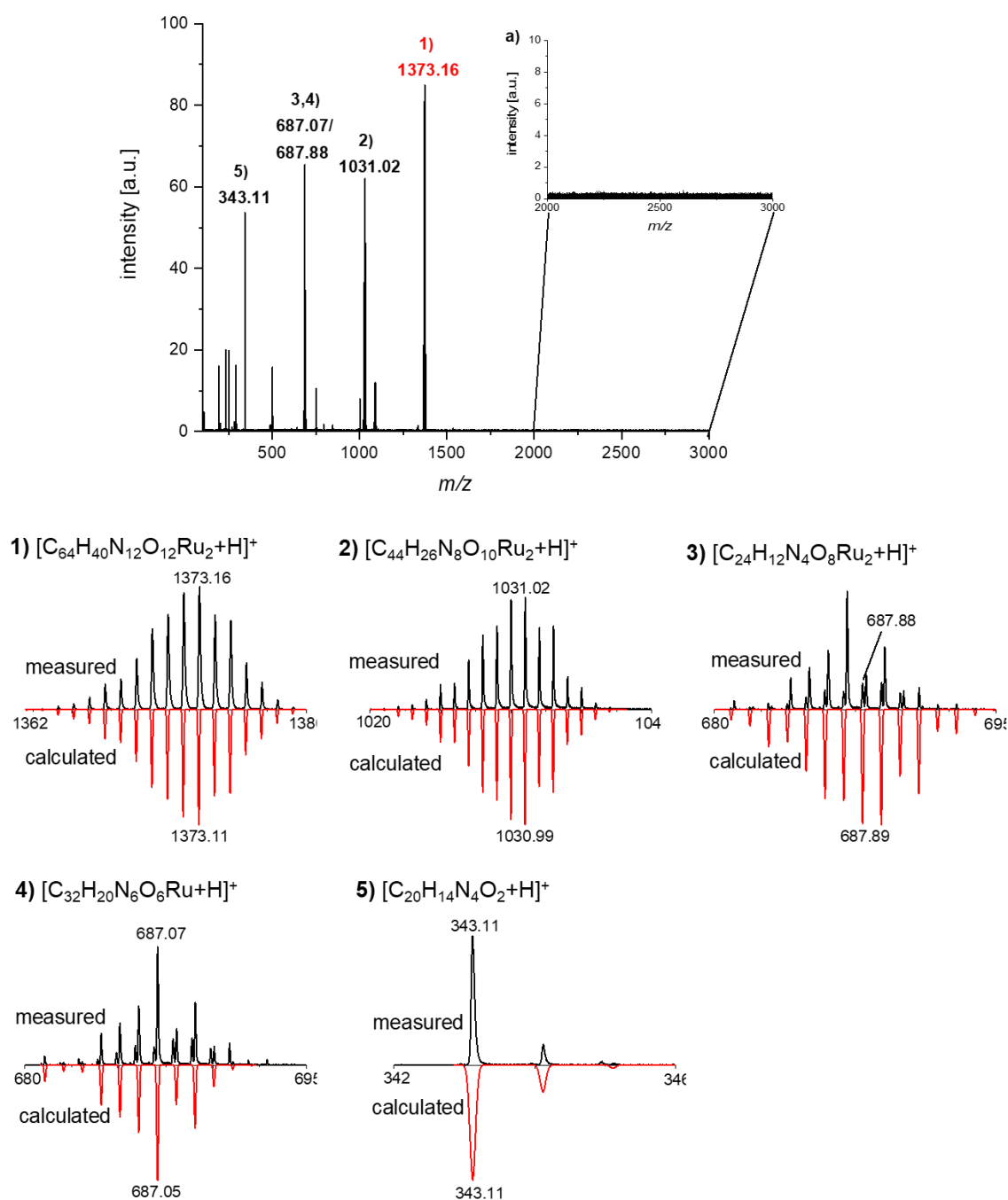
Figure A8.3.37. HR MALDI mass spectrum (CH₂Cl₂/CH₃OH 1:1, positive mode, DCTB) of **2C** after water oxidation catalysis (~40 catalytic cycles) with cerium ammonium nitrate (CAN) as oxidant in 4:6 CH₃CN/H₂O (pH 1, triflic acid). Before the measurement, the sample was reduced with ascorbic acid. The inset a) shows the amplified region between 2000−3000 m/z and insets 1−5) show the measured and calculated isotopic distribution of the most prominent fragmentation peaks.
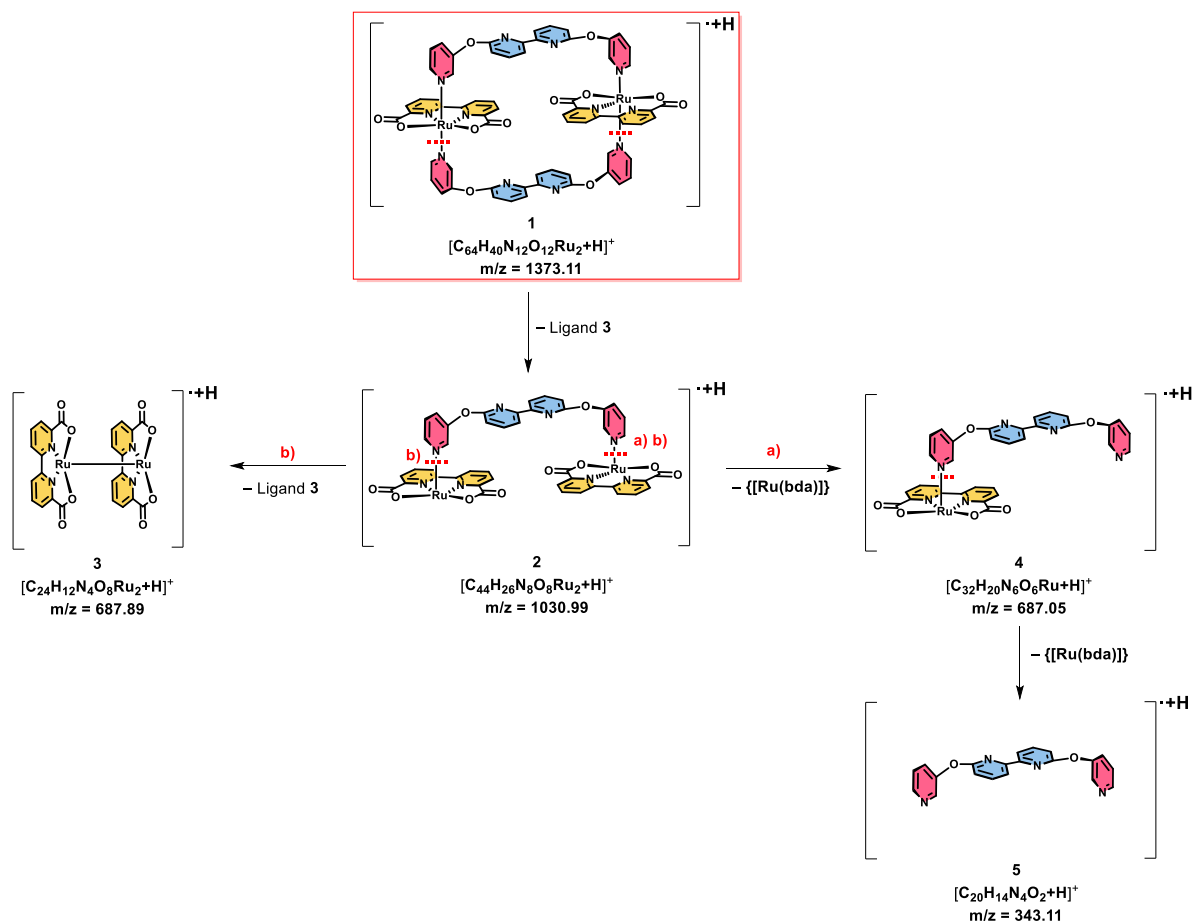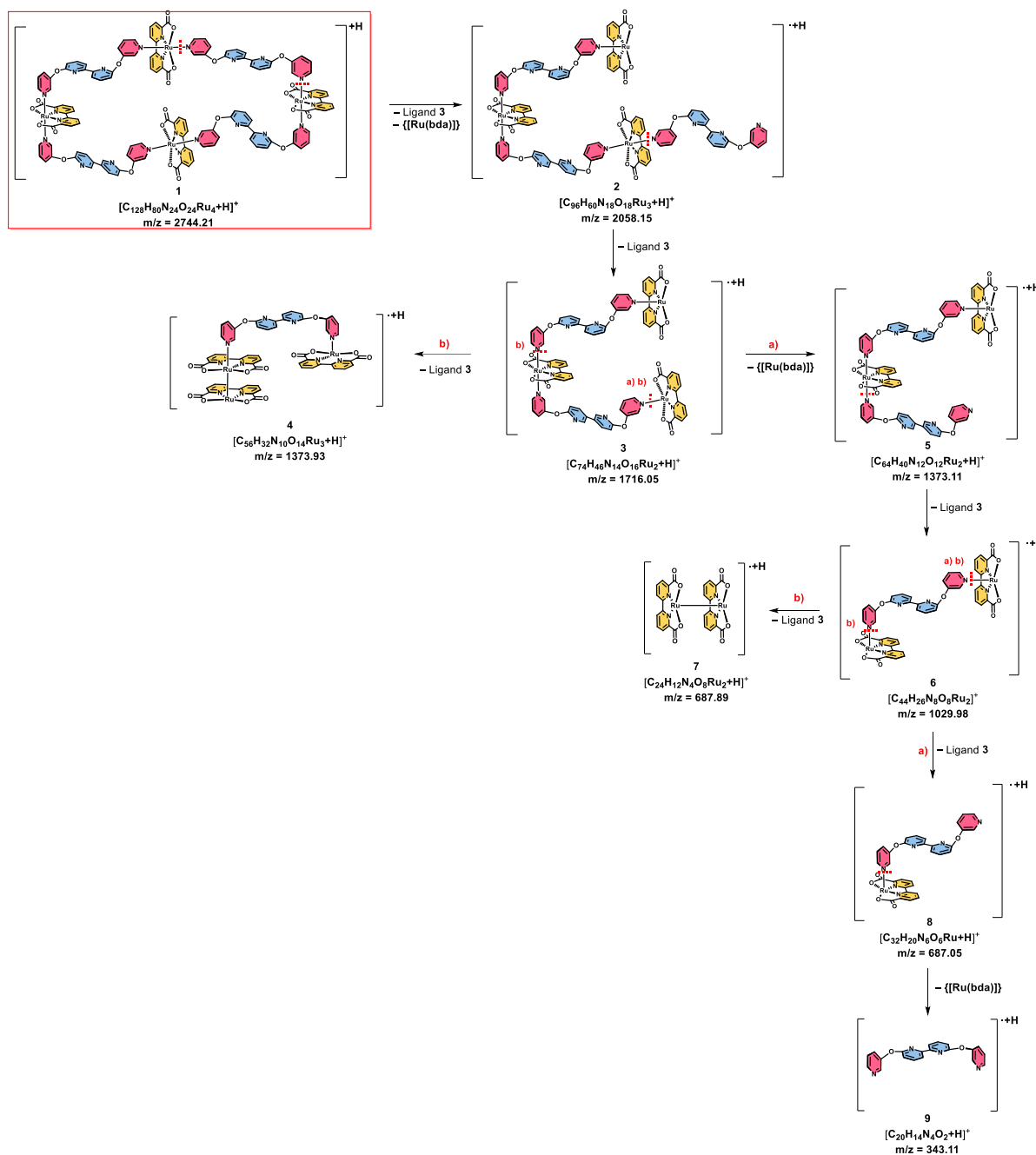
Figure A8.3.38. Proposed fragmentation pathway for dimer **2C** after chemical water oxidation catalysis.

Figure A8.3.39. HR MALDI mass spectrum (CH$_2$Cl$_2$/CH$_3$OH 1:1, positive mode, DCTB) of **3C** after water oxidation catalysis (~40 catalytic cycles) with cerium ammonium nitrate (CAN) as oxidant in 4:6 CH$_3$CN/H$_2$O (pH 1, triflic acid). Before the measurement, the sample was reduced with ascorbic acid. The inset a) shows the amplified region between 2000−3000 m/z and insets 1−8) show the measured and calculated isotopic distribution of the most prominent fragmentation peaks.

Figure A8.3.40. Proposed fragmentation pathway for trimer **3C** after chemical water oxidation catalysis.
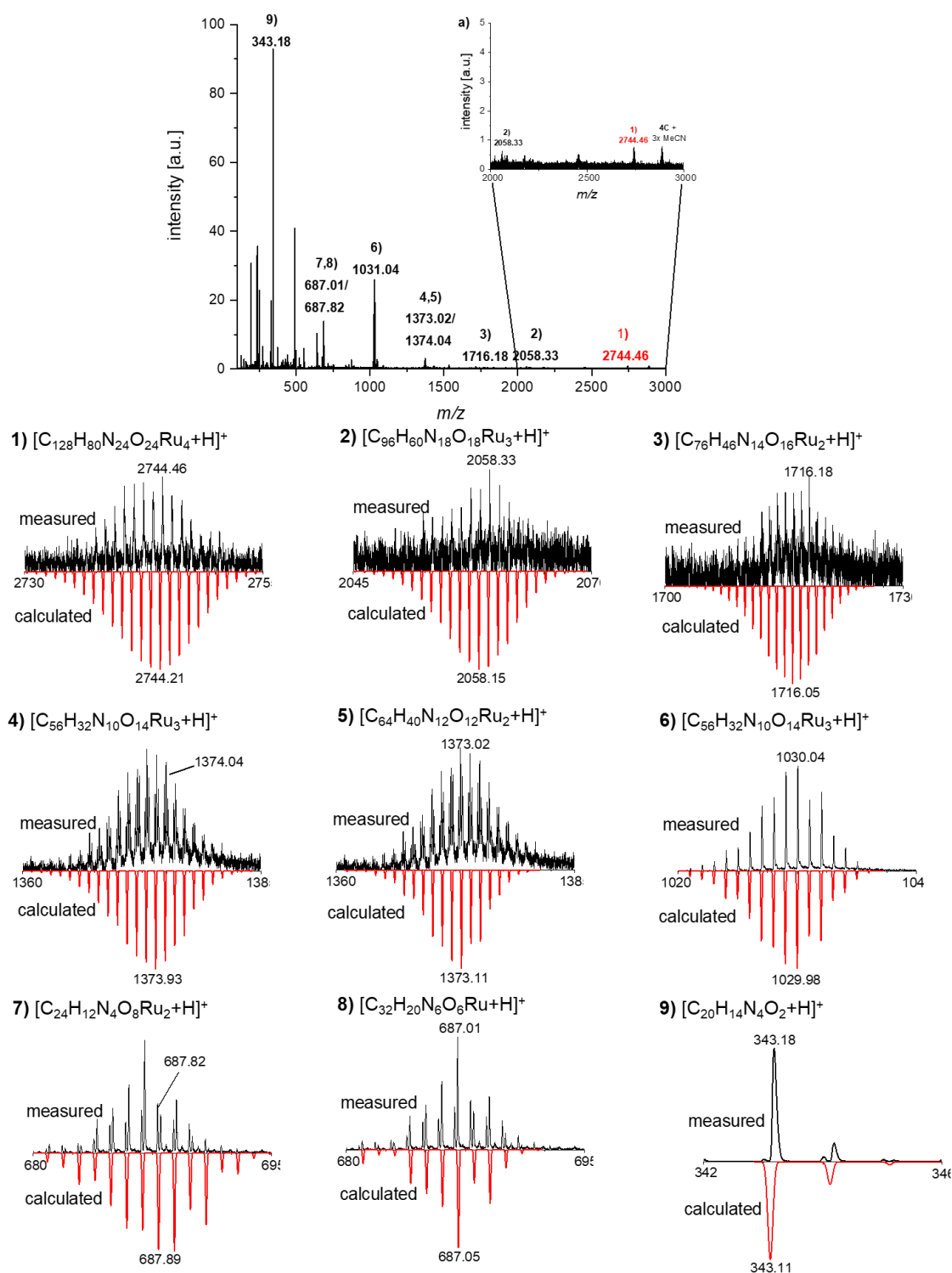
Figure A8.3.41. HR MALDI mass spectrum (CH_2Cl_2/CH_3OH 1:1, positive mode, DCTB) of **4C** after water oxidation catalysis (~40 catalytic cycles) with cerium ammonium nitrate (CAN) as oxidant in 4:6 CH_3CN/H_2O (pH 1, triflic acid). Before the measurement, the sample was reduced with ascorbic acid. The inset a) shows the amplified region between 2000−3000 m/z and insets 1−9) show the measured and calculated isotopic distribution of the most prominent fragmentation peaks.

Figure A8.3.42. Proposed fragmentation pathway for tetramer **4C** after chemical water oxidation catalysis.
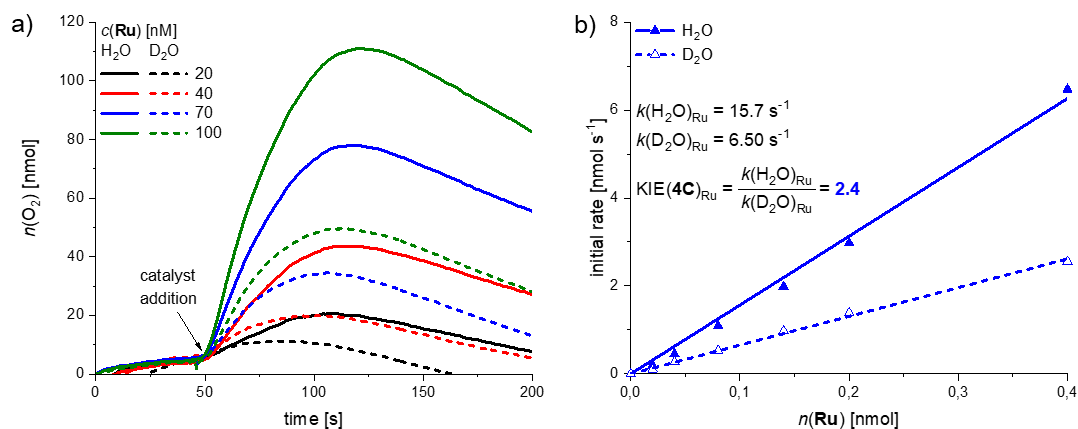
Kinetic Isotope Effect
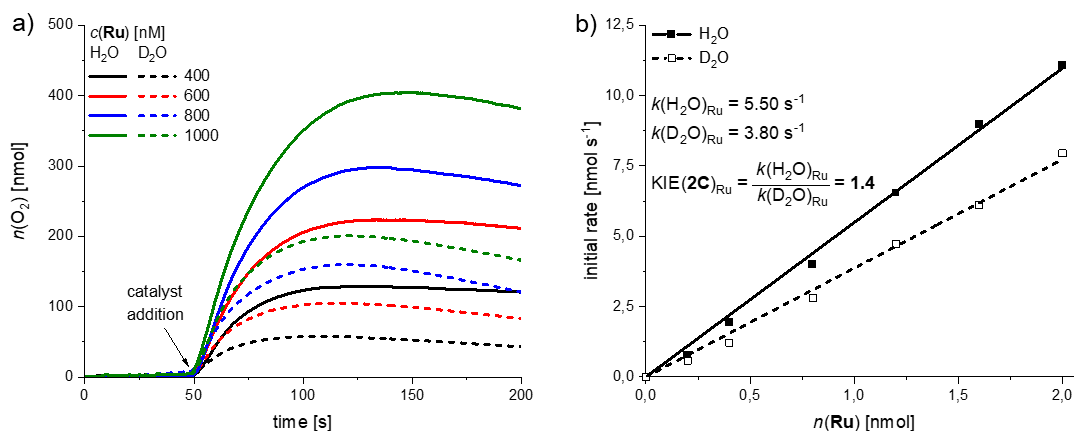
Figure A8.3.43. a) Concentration-dependent experiments for **2C per Ru unit** as WOC in CH_3CN/H_2O or D_2O 4:6 (pH 7, 50 mM phosphate buffer) c(PS) = 1.5 mM, c($Na_2S_2O_8$) = 37 mM. b) plot of the initial rates vs. the catalyst amount with linear regression for the determination of the individual reaction rates $k(H_2O)_{Ru}$ and $k(D_2O)_{Ru}$.
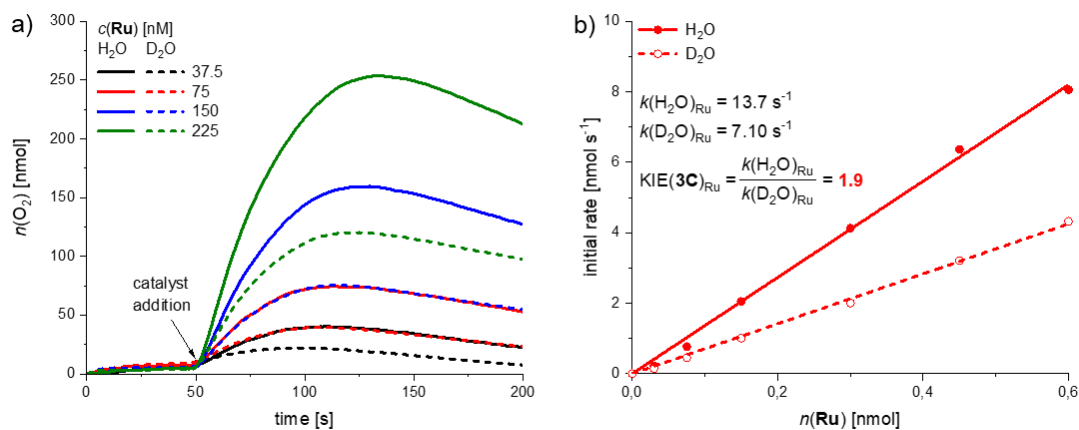
Figure A8.3.44. a) Concentration-dependent experiments for **3C per Ru unit** as WOC in CH_3CN/H_2O or D_2O 4:6 (pH 7, 50 mM phosphate buffer) c(PS) = 1.5 mM, c($Na_2S_2O_8$) = 37 mM. b) plot of the initial rates vs. the catalyst amount with linear regression for the determination of the individual reaction rates $k(H_2O)_{Ru}$ and $k(D_2O)_{Ru}$.

Figure A8.3.45. a) Concentration-dependent experiments for **4C per Ru unit** as WOC in CH_3CN/H_2O or D_2O 4:6 (pH 7, 50 mM phosphate buffer) $c(PS) = 1.5$ mM, $c(Na_2S_2O_8) = 37$ mM. b) plot of the initial rates vs. the catalyst amount with linear regression for the determination of the individual reaction rates $k(H_2O)_{Ru}$ and $k(D_2O)_{Ru}$.

Electrochemistry

Table A8.3.7. Redox properties of the multinuclear complexes **2C−4C** under neutral (pH 7) aqueous conditions with 40% 2,2,2-trifluorethanol (TFE) as organic co-solvent. The measurements were performed in 0.1 M ionic strength phosphate buffered aqueous mixtures at the respective pH.[a]

Conditions	4:6 MeCN/H$_2$O (**pH 7**)		
	E vs. NHE [V]		
Catalyst	Ru^{III}/Ru^{II}	Ru^{V}/Ru^{IV}	Ru^{V}/Ru^{IV}
dimer **2C**	+0.67	+0.86	+1.04
trimer **3C**	+0.68	+0.84	+1.01
tetramer **4C**	+0.68	+0.83	+1.00

[a] CV and DPV measurements neutral conditions were performed at *c* = 2.5 · 10^{-4} M.
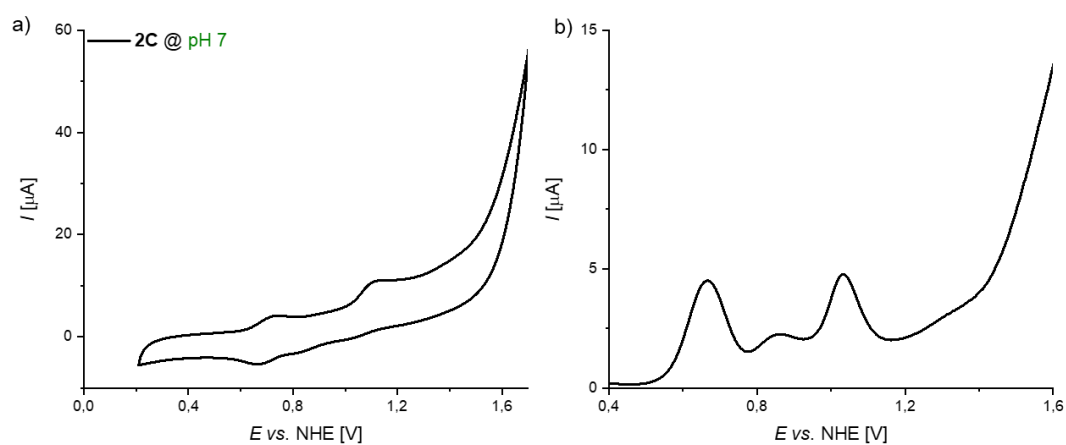
Figure A8.3.46. a) CV and b) DPV of **2C** in TFE/H$_2$O 4:6 (pH 7, phosphate buffer, *c* = 2.5·10^{-4} M).
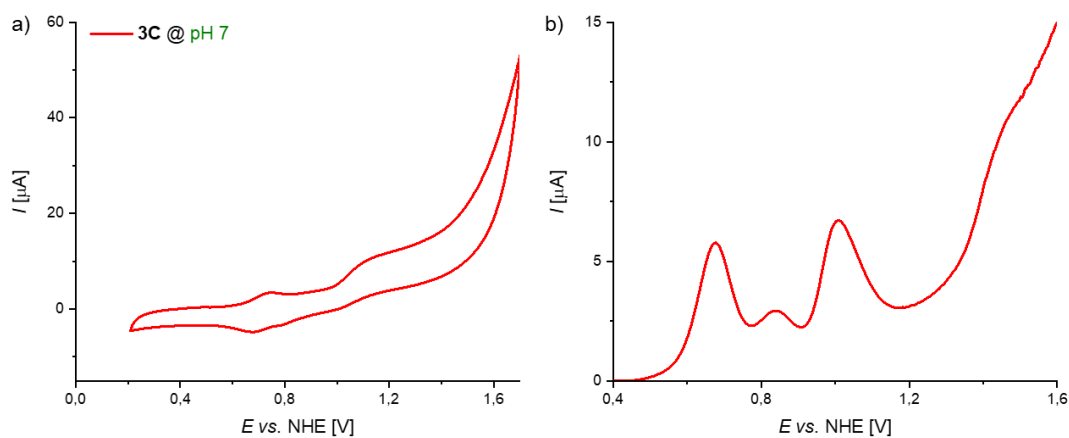

Figure A8.3.47. a) CV and b) DPV of **3C** in TFE/H$_2$O 4:6 (pH 7, phosphate buffer, *c* = 2.5·10^{-4} M).
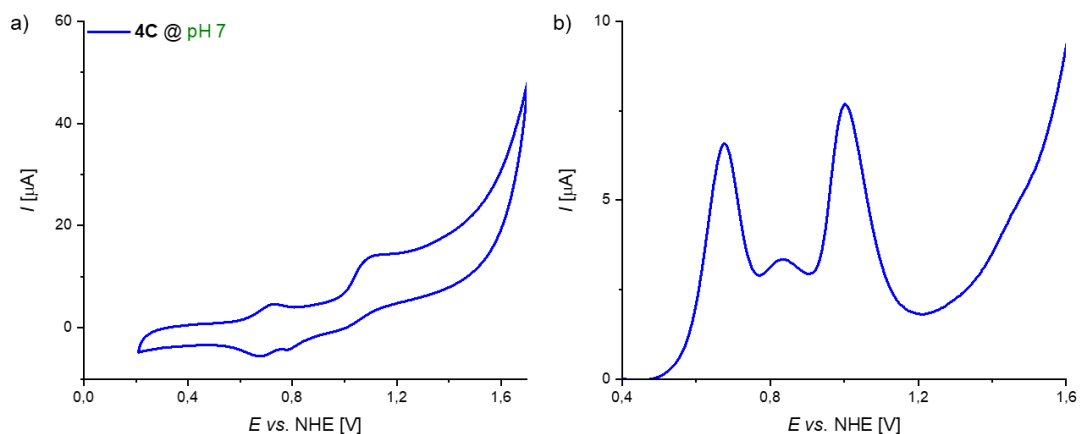
Figure A8.3.48. a) CV and b) DPV of **4C** in TFE/H$_2$O 4:6 (pH 7, phosphate buffer, c = 2.5·10^{-4} M).
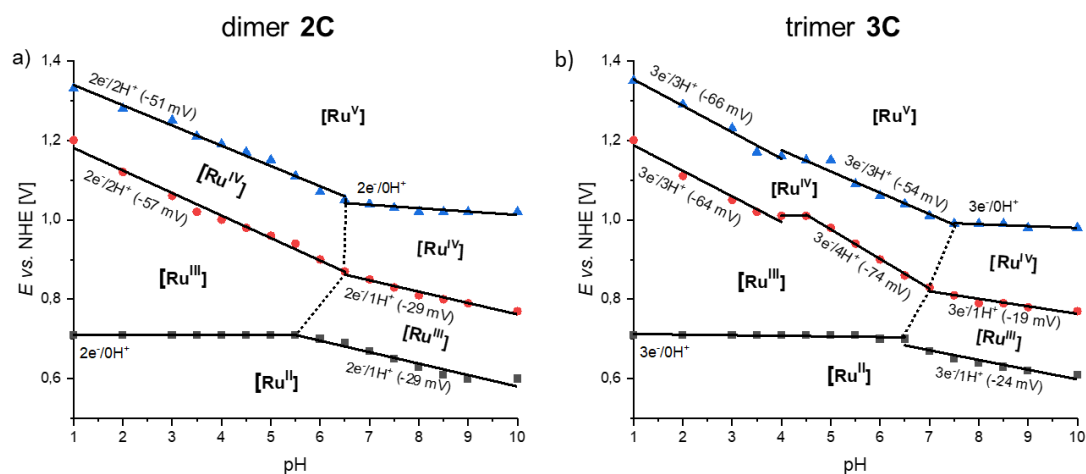

Figure A8.3.49. Pourbaix diagrams of a) dimer **2C** and b) trimer **3C**. Respective differential pulse voltammogram measurements were performed in TFE/H2O 4:6 (phosphate buffer at different pH values with I = 0.1 M, c(**WOC**) = 2.5·10^{-4} M).
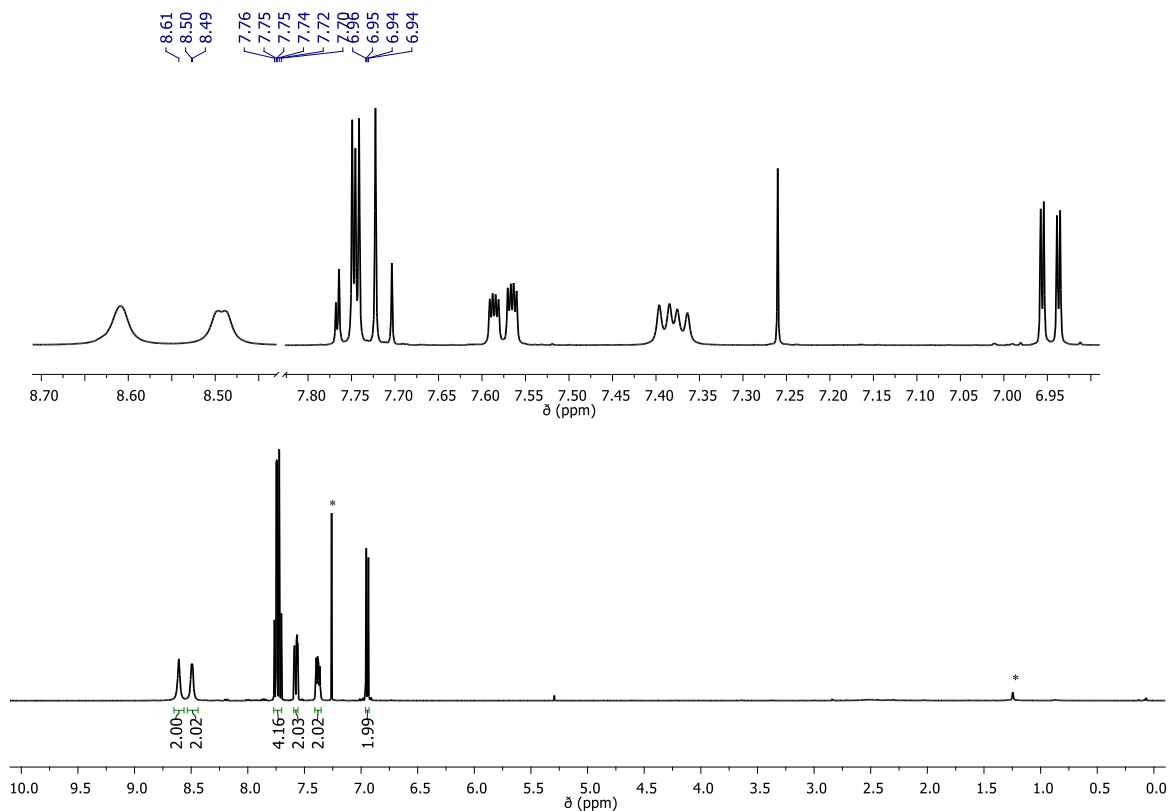
NMR spectra

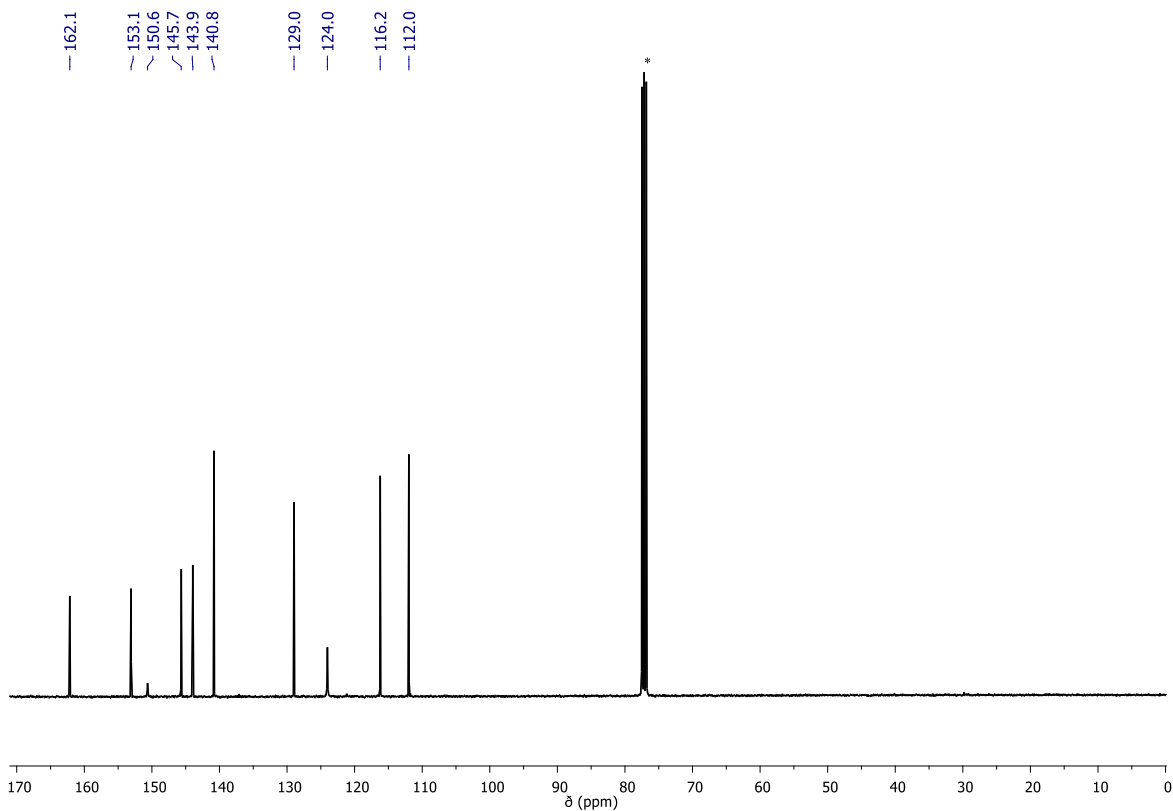**Figure A8.3.50.** ^{1}H NMR spectrum (400 MHz, CDCl$_3$) of ligand **46** (* residual solvent).

Figure A8.3.51. ^{13}C NMR spectrum (100 MHz, CDCl$_3$) of ligand **46** (* residual solvent).
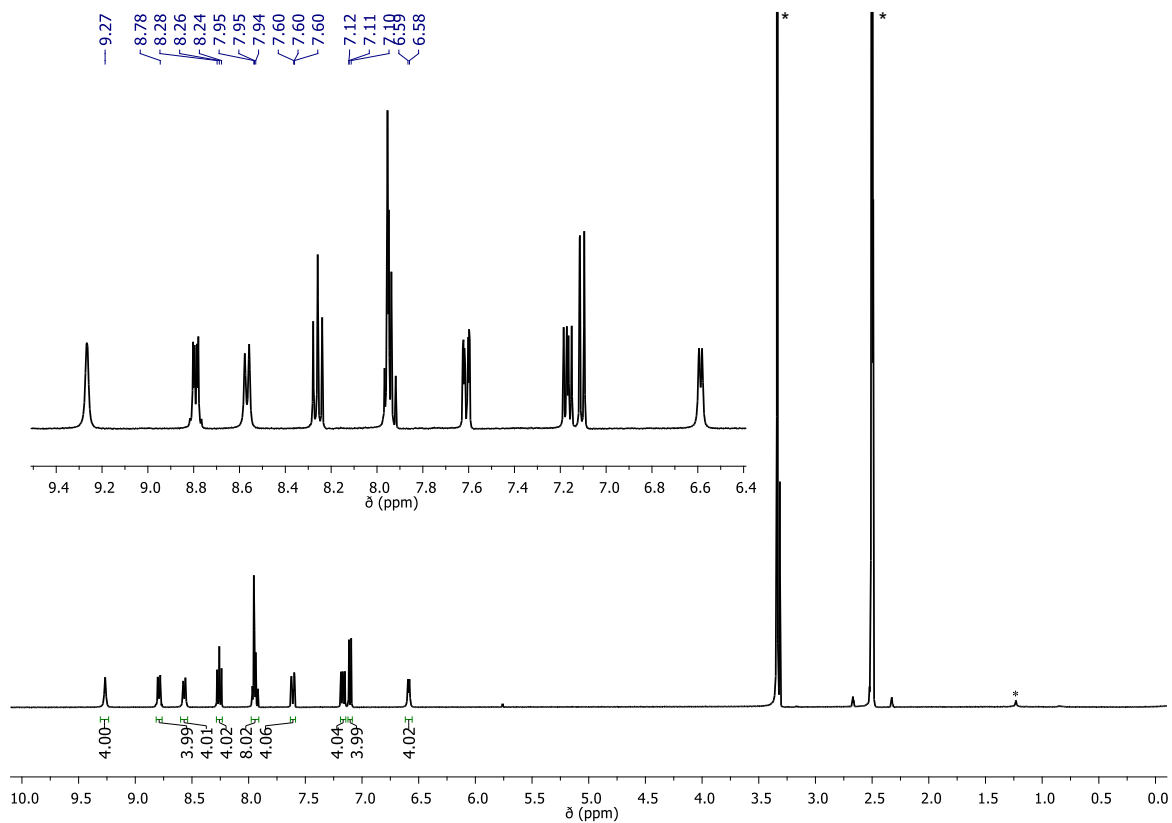
Figure A8.3.52. ^{1}H NMR spectrum (400 MHz, DMSO$-d_6$) of dimer **2C** (* residual solvent).
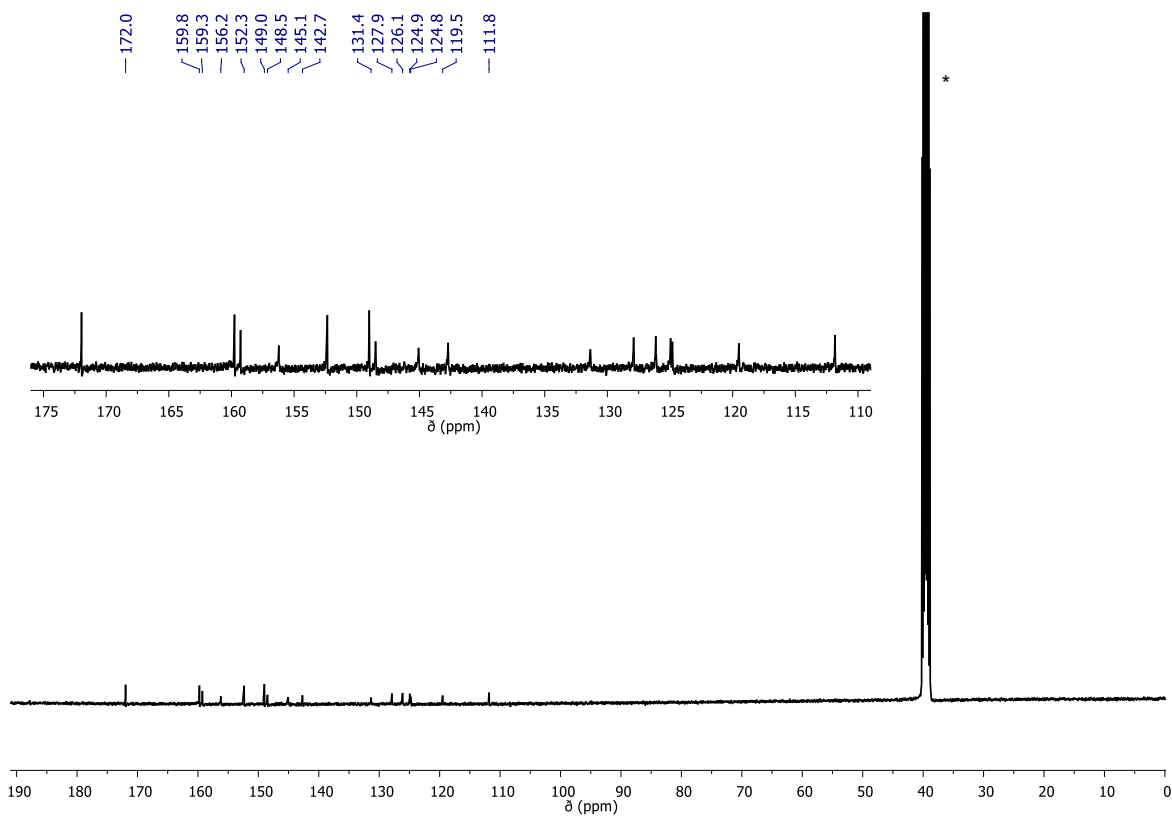

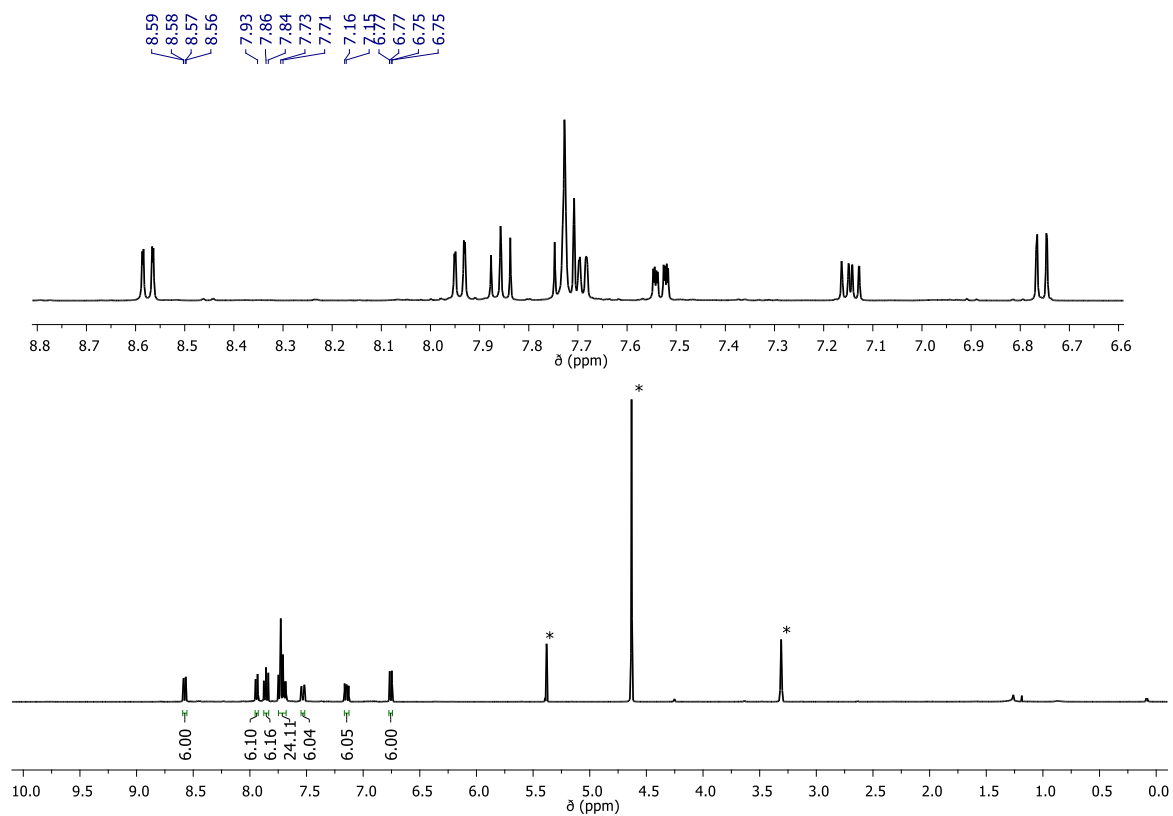**Figure A8.3.53.** ^{13}C NMR spectrum (100 MHz, DMSO$-d_6$) of dimer **2C** (* residual solvent).

Figure A8.3.54. ^1H NMR spectrum (400 MHz, CD_2Cl_2/CD_3OD (1:1)) of trimer **3C** (* residual solvent).
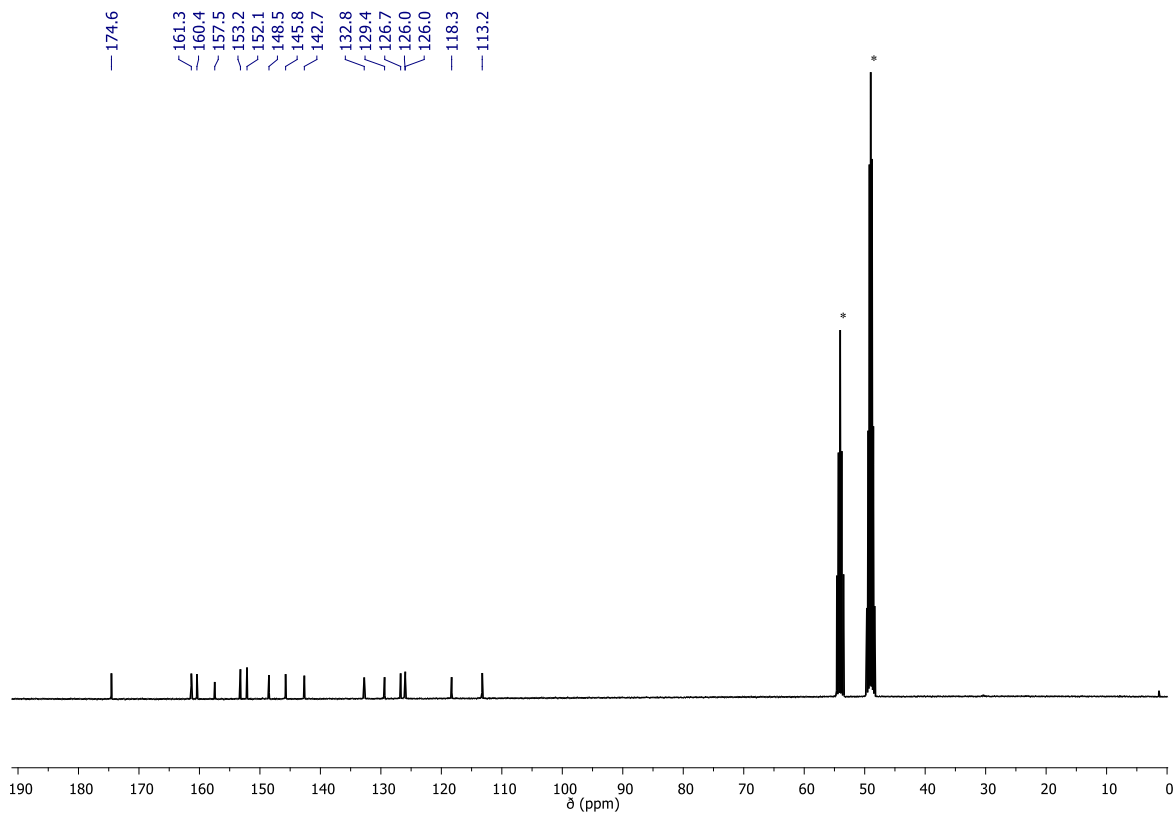

Figure A8.3.55. ^{13}C NMR spectrum (100 MHz, CD_2Cl_2/CD_3OD (1:1)) of trimer **3C** (* residual solvent).
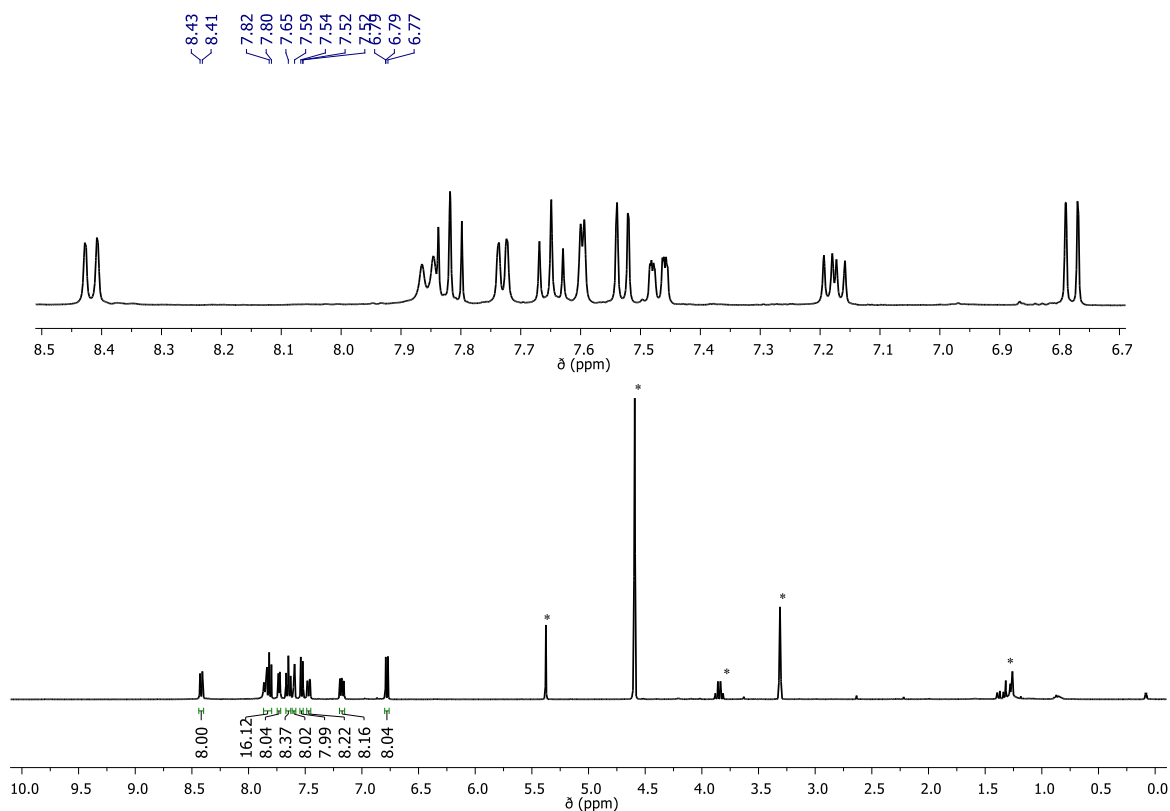
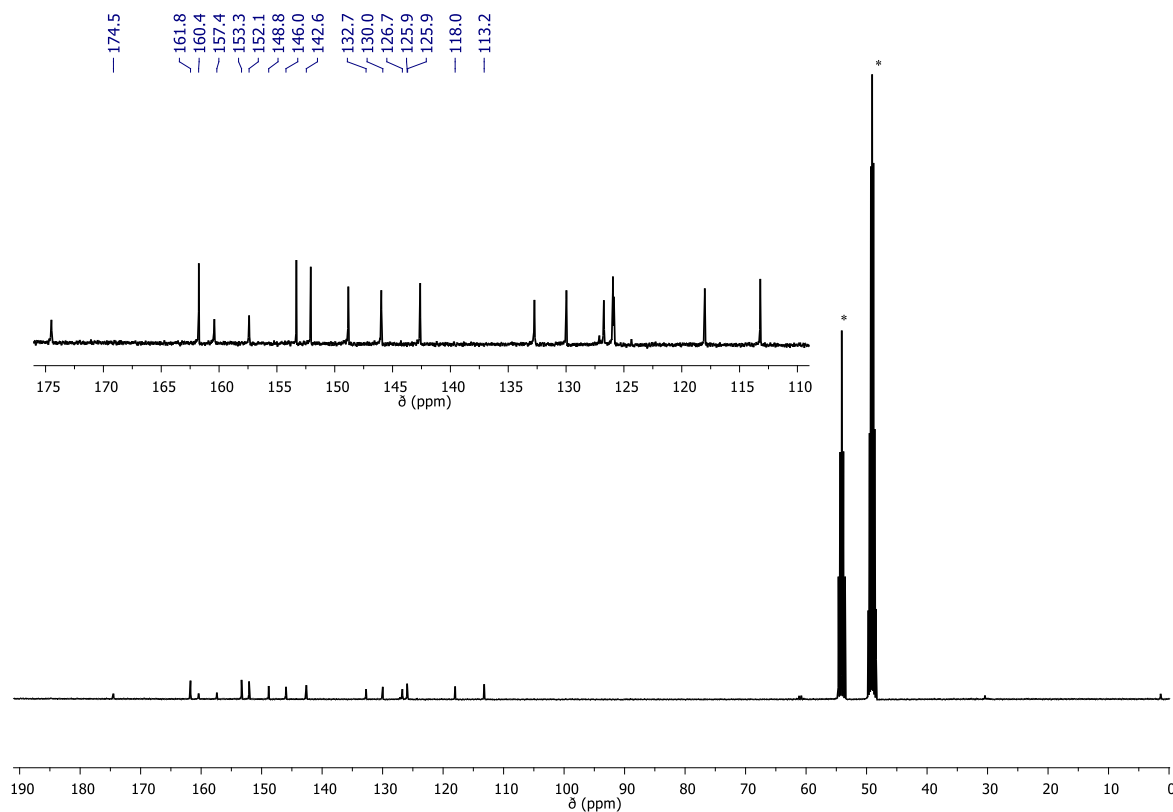**Figure A8.3.56.** ^{1}H NMR spectrum (400 MHz, CD$_2$Cl$_2$/CD$_3$OD (1:1)) of tetramer **4C** (* residual solvent).

Figure A8.3.57. ^{13}C NMR spectrum (100 MHz, CD$_2$Cl$_2$/CD$_3$OD (1:1)) of tetramer **4C** (* residual solvent).

HR mass spectra

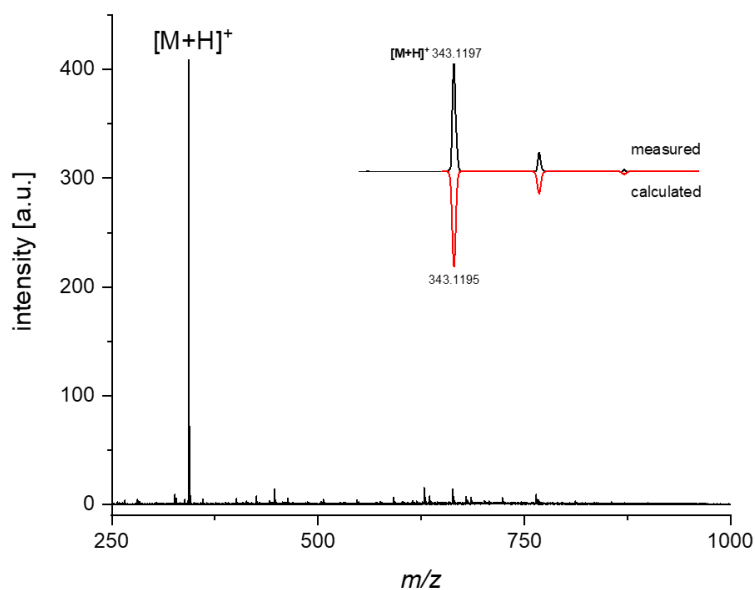**Figure A8.3.58.** HRMS (ESI-TOF, pos mode) mass spectrum (CH$_3$CN/CHCl$_3$ 1:1, positive mode) of ligand **46** with the inset showing the measured and calculated isotopic distribution of [M+H]$^+$.
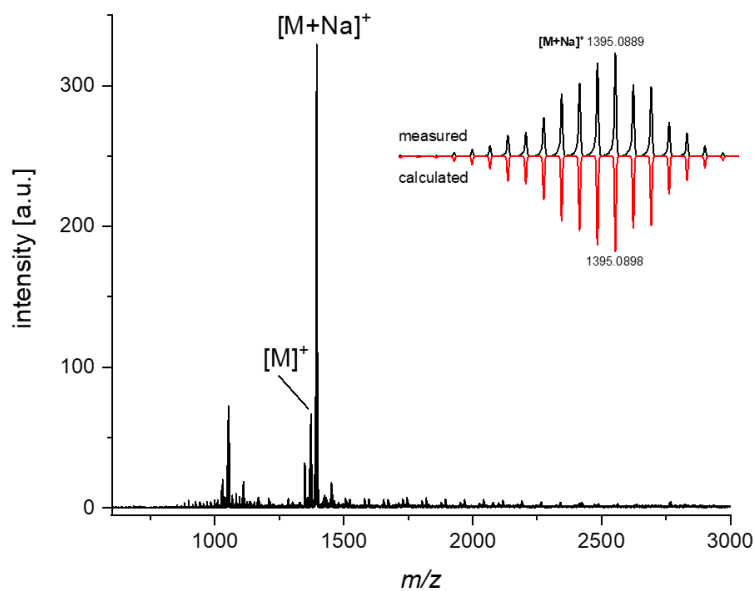
Figure A8.3.59. HRMS (ESI-TOF, pos mode) mass spectrum (CH$_3$CN/CHCl$_3$ 1:1, positive mode) of dimer **2C** with the inset showing the measured and calculated isotopic distribution of [M+Na]$^+$.

Figure A8.3.60. HRMS (ESI-TOF, pos mode) mass spectrum (CH$_3$OH/CH$_2$Cl$_2$ 1:1, positive mode) of trimer **3C** with the inset showing the measured and calculated isotopic distribution of [M+H]$^{2+}$.

Figure A8.3.61. HRMS (ESI-TOF, pos mode) mass spectrum (CH$_3$OH/CH$_2$Cl$_2$ 1:1, positive mode) of tetramer **4C** with the inset showing the measured and calculated isotopic distribution of [M]$^{2+}$.

References
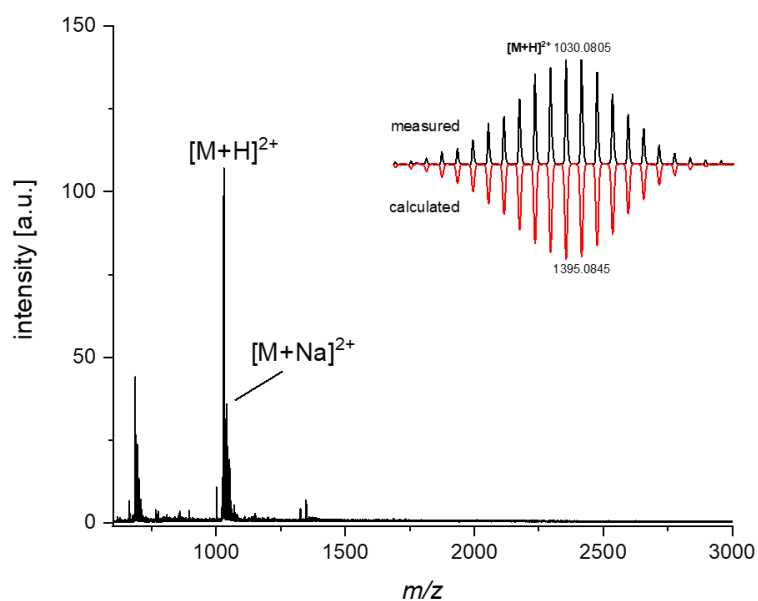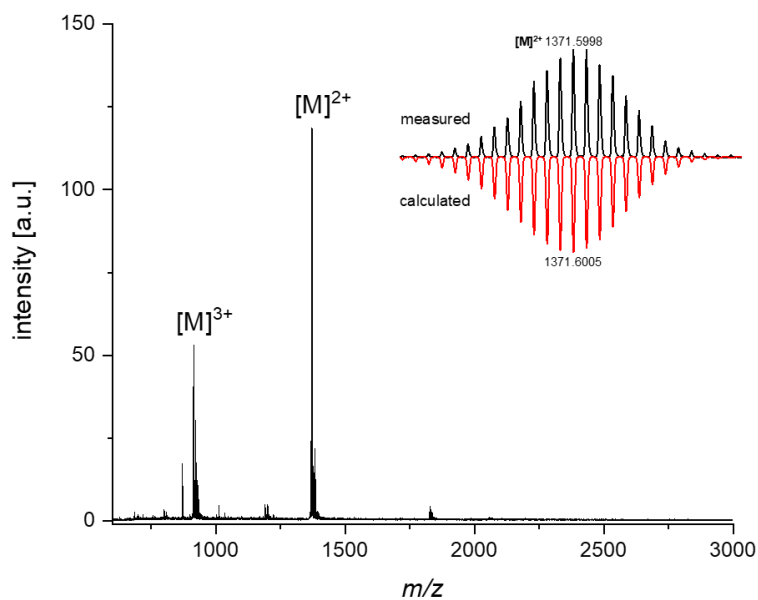
[1]   United Nations Framework Convention on Climate Change (UNFCCC), In *Adoption of the Paris Agreement.*, Report No. FCCC/CP/2015/L.9/Rev.1, http://unfccc.int/resource/docs/2015/cop21/eng/l09r01.pdf Paris, **2015**, 1−32.

[2]   Intergovernmental Panel on Climate Change (IPCC), In *Climate Change 2022: Impacts, Adaption and Vulnerability: Summary for Policymakers*, Cambridge University Press, Cambridge, UK and New York, NY, USA, **2022**, 3−33.

[3]   J. Tollefson, *Nature* **2020,** *580*, 443−445.

[4]   BP p.l.c., In *BP Statistical Review of World Energy 2022*, London, **2022**, 1−57.

[5]   International Energy Agency (IEA), In *World Energy Outlook 2022: Executive Summary 2022*, Paris, **2022**, 1−522.

[6]   N. S. Lewis, D. G. Nocera, *Proc. Natl. Acad. Sci. USA* **2006,** *103*, 15729−15735.

[7]   M. Roeb, H. Müller-Steinhagen, *Science* **2010,** *329*, 773−774.

[8]   N. S. Lewis, *Science* **2016,** *351*, aad1920.

[9]   N. Nitta, F. Wu, J. T. Lee, G. Yushin, *Mater. Today* **2015,** *18*, 252−264.

[10]   G. E. Blomgren, *J. Electrochem. Soc.* **2017,** *164*, A5019−A5027.

[11]   A. R. Dehghani-Sanij, E. Tharumalingam, M. B. Dusseault, R. Fraser, *Renew. Sustain. Energy Rev.* **2019,** *104*, 192−208.

[12]   J. Barber, *Chem. Soc. Rev.* **2009,** *38*, 185−196.

[13]   N. Nelson, A. Ben-Shem, *Nat. Rev. Mol. Cell Biol.* **2004,** *5*, 971−982.

[14]   J. R. Shen, *Annu. Rev. Plant. Biol.* **2015,** *66*, 23−48.

[15]   N. Armaroli, V. Balzani, *Chem. Eur. J.* **2016,** *22*, 32−57.

[16]   A. J. Bard, M. A. Fox, *Acc. Chem. Res.* **1995,** *28*, 141−5.

[17]   J. Barber, P. D. Tran, *J. R. Soc. Interface* **2013,** *10*, 20120984.

[18]   P. D. Frischmann, K. Mahata, F. Würthner, *Chem. Soc. Rev.* **2013,** *42*, 1847−1870.

[19]   H. Dau, E. Fujita, L. Sun, *ChemSusChem* **2017,** *10*, 4228−4235.

[20]   A. Züttel, A. Remhof, A. Borgschulte, O. Friedrichs, *Phil. Trans. R. Soc. A* **2010,** *368*, 3329−3342.

[21]   P. P. Edwards, V. L. Kuznetsov, W. I. F. David, N. P. Brandon, *Energy Policy* **2008,** *36*, 4356−4362.

[22]   N. Armaroli, V. Balzani, *ChemSusChem* **2011,** *4*, 21−36.

[23]   D. Gust, T. A. Moore, A. L. Moore, *Acc. Chem. Res.* **2009,** *42*, 1890−1898.

[24] V. Balzani, L. Moggi, M. F. Manfrin, F. Bolletta, M. Gleria, *Science* **1975,** *189*, 852−856.

[25] V. Balzani, A. Credi, M. Venturi, *Curr. Opin. Chem. Biol.* **1997,** *1*, 506−513.

[26] H. Dau, C. Limberg, T. Reier, M. Risch, S. Roggan, P. Strasser, *ChemCatChem* **2010,** *2*, 724−761.

[27] N. Cox, D. A. Pantazis, F. Neese, W. Lubitz, *Acc. Chem. Res.* **2013,** *46*, 1588−1596.

[28] D. J. Vinyard, G. M. Ananyev, G. C. Dismukes, *Annu. Rev. Biochem.* **2013,** *82*, 577−606.

[29] D. J. Vinyard, G. W. Brudvig, *Annu. Rev. Phys. Chem.* **2017,** *68*, 101−116.

[30] D. Ringe, G. A. Petsko, *Science* **2008,** *320*, 1428−1429.

[31] Y. Umena, K. Kawakami, J.-R. Shen, N. Kamiya, *Nature* **2011,** *473*, 55−60.

[32] J. S. Kanady, E. Y. Tsui, M. W. Day, T. Agapie, *Science* **2011,** *333*, 733−736.

[33] C. Zhang, C. Chen, H. Dong, J.-R. Shen, H. Dau, J. Zhao, *Science* **2015,** *348*, 690−693.

[34] V. Kunz, D. Schmidt, M. I. S. Röhr, R. Mitrić, F. Würthner, *Adv. Energy Mater.* **2017,** *7*, 1602939.

[35] R. Matheu, M. Z. Ertem, C. Gimbert-Suriñach, X. Sala, A. Llobet, *Chem. Rev.* **2019,** *119*, 3453−3471.

[36] T. Keijer, T. Bouwens, J. Hessels, J. N. H. Reek, *Chem. Sci.* **2021,** *12*, 50−70.

[37] M. Schulze, V. Kunz, P. D. Frischmann, F. Würthner, *Nat. Chem.* **2016,** *8*, 576−583.

[38] V. Kunz, J. O. Lindner, M. Schulze, M. I. S. Röhr, D. Schmidt, R. Mitrić, F. Würthner, *Energy Environ. Sci.* **2017,** *10*, 2137−2153.

[39] D. Schindler, A.-L. Meza-Chincha, M. Roth, F. Würthner, *Chem. Eur. J.* **2021,** *27*, 16938−16946.

[40] A.-L. Meza-Chincha, J. O. Lindner, D. Schindler, D. Schmidt, A.-M. Krause, M. I. S. Röhr, R. Mitrić, F. Würthner, *Chem. Sci.* **2020,** *11*, 7654−7664.

[41] S. W. Ragsdale, *Chem. Rev.* **2006,** *106*, 3317−3337.

[42] Y. Lu, N. Yeung, N. Sieracki, N. M. Marshall, *Nature* **2009,** *460*, 855−862.

[43] J. P. McEvoy, G. W. Brudvig, *Chem. Rev.* **2006,** *106*, 4455−4483.

[44] M. Wikström, K. Krab, V. Sharma, *Chem. Rev.* **2018,** *118*, 2469−2490.

[45] W. Lubitz, H. Ogata, O. Rüdiger, E. Reijerse, *Chem. Rev.* **2014,** *114*, 4081−4148.

[46] J. T. J. Lecomte, D. A. Vuletich, A. M. Lesk, *Curr. Opin. Struct. Biol.* **2005,** *15*, 290−301.

[47] C. A. Gersbach, T. Gaj, C. F. Barbas, *Acc. Chem. Res.* **2014,** *47*, 2309−2318.

[48] J. B. Stock, A. M. Stock, J. M. Mottonen, *Nature* **1990,** *344*, 395−400.

References

[49]   C. Van Stappen, Y. Deng, Y. Liu, H. Heidari, J.-X. Wang, Y. Zhou, A. P. Ledray, Y. Lu, *Chem. Rev.* **2022,** *122*, 11974−12045.

[50]   W. J. Shaw, *Catal. Rev. Sci. Eng.* **2012,** *54*, 489−550.

[51]   M. Zhao, H.-B. Wang, L.-N. Ji, Z.-W. Mao, *Chem. Soc. Rev.* **2013,** *42*, 8360−8375.

[52]   B. Ginovska-Pangovska, A. Dutta, M. L. Reback, J. C. Linehan, W. J. Shaw, *Acc. Chem. Res.* **2014,** *47*, 2621−2630.

[53]   A. Gora, J. Brezovsky, J. Damborsky, *Chem. Rev.* **2013,** *113*, 5871−5923.

[54]   M. Frey, *ChemBioChem* **2002,** *3*, 153−160.

[55]   J. W. Peters, G. J. Schut, E. S. Boyd, D. W. Mulder, E. M. Shepard, J. B. Broderick, P. W. King, M. W. W. Adams, *Biochim. Biophys. Acta* **2015,** *1853*, 1350−1369.

[56]   K. A. Vincent, A. Parkin, F. A. Armstrong, *Chem. Rev.* **2007,** *107*, 4366−4413.

[57]   O. Lampret, A. Adamska-Venkatesh, H. Konegger, F. Wittkamp, U.-P. Apfel, E. J. Reijerse, W. Lubitz, O. Rüdiger, T. Happe, M. Winkler, *J. Am. Chem. Soc.* **2017,** *139*, 18222−18230.

[58]   J. Duan, M. Senger, J. Esselborn, V. Engelbrecht, F. Wittkamp, U.-P. Apfel, E. Hofmann, S. T. Stripp, T. Happe, M. Winkler, *Nat. Commun.* **2018,** *9*, 4726.

[59]   S. T. Stripp, B. R. Duffus, V. Fourmond, C. Léger, S. Leimkühler, S. Hirota, Y. Hu, A. Jasniewski, H. Ogata, M. W. Ribbe, *Chem. Rev.* **2022,** *122*, 11900−11973.

[60]   N. D. M. Noor, H. Matsuura, K. Nishikawa, H. Tai, S. Hirota, J. Kim, J. Kang, M. Tateno, K.-S. Yoon, S. Ogo, S. Kubota, Y. Shomura, Y. Higuchi, *Chem. Commun.* **2018,** *54*, 12385−12388.

[61]   M. Senger, V. Eichmann, K. Laun, J. Duan, F. Wittkamp, G. Knör, U.-P. Apfel, T. Happe, M. Winkler, J. Heberle, S. T. Stripp, *J. Am. Chem. Soc.* **2019,** *141*, 17394−17403.

[62]   G. T. Babcock, M. Wikström, *Nature* **1992,** *356*, 301−309.

[63]   S. Iwata, C. Ostermeier, B. Ludwig, H. Michel, *Nature* **1995,** *376*, 660−669.

[64]   T. Tsukihara, H. Aoyama, E. Yamashita, T. Tomizaki, H. Yamaguchi, K. Shinzawa-Itoh, R. Nakashima, R. Yaono, S. Yoshikawa, *Science* **1996,** *272*, 1136−1144.

[65]   S. Yoshikawa, K. Muramoto, K. Shinzawa-Itoh, *Annu. Rev. Biophys.* **2011,** *40*, 205−23.

[66]   R. M. Nyquist, D. Heitbrink, C. Bolwien, R. B. Gennis, J. Heberle, *Proc. Nat. Acad. Sci. USA* **2003,** *100*, 8715−8720.

[67]   S. Supekar, A. P. Gamiz-Hernandez, V. R. I. Kaila, *Angew. Chem. Int. Ed.* **2016,** *55*, 11940−11944.

[68]   J. M. Berg, J. L. Tymoczko, G. J. Gatto, L. Stryer, In *Stryer Biochemie*, Springer Verlag GmbH Deutschland: **2018**, 31−122.

[69]   E.-M. Aro, I. Virgin, B. Andersson, *Biochim. Biophys. Acta* **1993,** *1143*, 113−134.

[70]   A. Zouni, H.-T. Witt, J. Kern, P. Fromme, N. Krauss, W. Saenger, P. Orth, *Nature* **2001,** *409*, 739−743.

[71]   K. N. Ferreira, T. M. Iverson, K. Maghlaoui, J. Barber, S. Iwata, *Science* **2004,** *303*, 1831−1838.

[72]   J. Yano, J. Kern, K. Sauer, M. J. Latimer, Y. Pushkar, J. Biesiadka, B. Loll, W. Saenger, J. Messinger, A. Zouni, V. K. Yachandra, *Science* **2006,** *314*, 821−825.

[73]   A. Llobet, In *Molecular Water Oxidation Catalysis: A Key Topic for New Sustainable Energy Conversion Schemes*, John Wiley & Sons, Ltd.: **2014**, 1−14.

[74]   F. A. Armstrong, *Phil. Trans. R. Soc. B* **2008,** *363*, 1263−1270.

[75]   V. K. Yachandra, J. Yano, *J. Photochem. Photobiol. B, Biol.* **2011,** *104*, 51−59.

[76]   F. H. M. Koua, Y. Umena, K. Kawakami, J.-R. Shen, *Proc. Nat. Acad. Sci. USA* **2013,** *110*, 3889−3894.

[77]   G. W. Brudvig, *Phil. Trans. R. Soc. B* **2008,** *363*, 1211−1219.

[78]   S. Bang, Y.-M. Lee, S. Hong, K.-B. Cho, Y. Nishida, M. S. Seo, R. Sarangi, S. Fukuzumi, W. Nam, *Nat. Chem.* **2014,** *6*, 934−940.

[79]   D. Lionetti, T. Agapie, *Nature* **2014,** *513*, 495−496.

[80]   T. Lohmiller, N. Cox, J.-H. Su, J. Messinger, W. Lubitz, *J. Biol. Chem.* **2012,** *287*, 24721−24733.

[81]   G. C. Dismukes, R. Brimblecombe, G. A. N. Felton, R. S. Pryadun, J. E. Sheats, L. Spiccia, G. F. Swiegers, *Acc. Chem. Res.* **2009,** *42*, 1935−1943.

[82]   S. Mukherjee, J. A. Stull, J. Yano, T. C. Stamatatos, K. Pringouri, T. A. Stich, K. A. Abboud, R. D. Britt, V. K. Yachandra, G. Christou, *Proc. Nat. Acad. Sci. USA* **2012,** *109*, 2257−2262.

[83]   J. S. Kanady, P.-H. Lin, K. M. Carsch, R. J. Nielsen, M. K. Takase, W. A. Goddard, T. Agapie, *J. Am. Chem. Soc.* **2014,** *136*, 14373−14376.

[84]   L. Sun, *Science* **2015,** *348*, 635−636.

[85]   C. Chen, Y. Li, G. Zhao, R. Yao, C. Zhang, *ChemSusChem* **2017,** *10*, 4403−4408.

[86]   L. Vogt, D. J. Vinyard, S. Khan, G. W. Brudvig, *Curr. Opin. Chem. Biol.* **2015,** *25*, 152−158.

[87]   J. Kern, R. Chatterjee, I. D. Young, F. D. Fuller, L. Lassalle, M. Ibrahim, S. Gul, T. Fransson, A. S. Brewster, R. Alonso-Mori, R. Hussein, M. Zhang, L. Douthit, C. de Lichtenberg, M. H. Cheah, D. Shevela, J. Wersig, I. Seuffert, D. Sokaras, E. Pastor, C. Weninger, T. Kroll, R. G. Sierra, P. Aller, A. Butryn, A. M. Orville, M. Liang, A. Batyuk, J. E. Koglin, S. Carbajo, S. Boutet, N. W. Moriarty, J. M. Holton, H. Dobbek,

P. D. Adams, U. Bergmann, N. K. Sauter, A. Zouni, J. Messinger, J. Yano, V. K. Yachandra, *Nature* **2018**, *563*, 421−425.

[88] R. Hussein, M. Ibrahim, A. Bhowmick, P. S. Simon, R. Chatterjee, L. Lassalle, M. Doyle, I. Bogacz, I.-S. Kim, M. H. Cheah, S. Gul, C. de Lichtenberg, P. Chernev, C. C. Pham, I. D. Young, S. Carbajo, F. D. Fuller, R. Alonso-Mori, A. Batyuk, K. D. Sutherlin, A. S. Brewster, R. Bolotovsky, D. Mendez, J. M. Holton, N. W. Moriarty, P. D. Adams, U. Bergmann, N. K. Sauter, H. Dobbek, J. Messinger, A. Zouni, J. Kern, V. K. Yachandra, J. Yano, *Nat. Commun.* **2021,** *12*, 6531.

[89] S. Nakamura, K. Ota, Y. Shibuya, T. Noguchi, *Biochemistry* **2016,** *55*, 597−607.

[90] P. Joliot, G. Barbieri, R. Chabaud, *Photochem. Photobiol.* **1969**, *10*, 309−329.

[91] B. Kok, B. Forbush, M. McGloin, *Photochem. Photobiol.* **1970,** *11*, 457−475.

[92] N. Cox, M. Retegan, F. Neese, D. A. Pantazis, A. Boussac, W. Lubitz, *Science* **2014,** *345*, 804−808.

[93] W. Lubitz, M. Chrysina, N. Cox, *Photosynth. Res.* **2019**, *142*, 105−125.

[94] L. Hammarström, S. Styring, *Energy Environ. Sci.* **2011,** *4*, 2379−2388.

[95] M. Suga, F. Akita, K. Yamashita, Y. Nakajima, G. Ueno, H. Li, T. Yamane, K. Hirata, Y. Umena, S. Yonekura, L.-J. Yu, H. Murakami, T. Nomura, T. Kimura, M. Kubo, S. Baba, T. Kumasaka, K. Tono, M. Yabashi, H. Isobe, K. Yamaguchi, M. Yamamoto, H. Ago, J.-R. Shen, *Science* **2019**, *366*, 334−338.

[96] N. Cox, D. A. Pantazis, W. Lubitz, *Annu. Rev. Biochem.* **2020,** *89*, 795−820.

[97] Y. Guo, J. Messinger, L. Kloo, L. Sun, *J. Am. Chem. Soc.* **2022,** *144*, 11736−11747.

[98] J. Barber, *Biochemistry* **2016,** *55*, 5901−5906.

[99] P. E. M. Siegbahn, *Chem. Eur. J.* **2006,** *12*, 9217−9227.

[100] P. E. M. Siegbahn, *Biochim. Biophys. Acta* **2013,** *1827*, 1003−1019.

[101] P. E. M. Siegbahn, *Proc. Natl. Acad. Sci. USA* **2017,** *114*, 4966−4968.

[102] V. L. Pecoraro, M. J. Baldwin, M. T. Caudle, W.-Y. Hsieh, N. A. Law, *Pure & Appl. Chem.* **1998,** *70*, 925−929.

[103] J. Barber, *Nat. Plants* **2017,** *3*, 17041.

[104] M. Shoji, H. Isobe, Y. Shigeta, T. Nakajima, K. Yamaguchi, *Chem. Phys. Lett.* **2018,** *698*, 138−146.

[105] Y. Pushkar, K. M. Davis, M. C. Palenik, *J. Phys. Chem. Lett.* **2018**, *9*, 3525−3531.

[106] B. Zhang, L. Sun, *Dalton Trans.* **2018,** *47*, 14381−14387.

[107] B. Zhang, L. Sun, *ChemSusChem* **2019,** *12*, 3401−3404.

[108] M. D. Kärkäs, O. Verho, E. V. Johnston, B. Åkermark, *Chem. Rev.* **2014**, *114*, 11863−12001.

[109] J. D. Blakemore, R. H. Crabtree, G. W. Brudvig, *Chem. Rev.* **2015,** *115*, 12974−13005.

[110] J. Hessels, R. J. Detz, M. T. M. Koper, J. N. H. Reek, *Chem. Eur. J.* **2017,** *23*, 16413−16418.

[111] C. Costentin, S. Drouet, M. Robert, J.-M. Savéant, *J. Am. Chem. Soc.* **2012,** *134*, 11235−11242.

[112] D. J. Wasylenko, R. D. Palmer, C. P. Berlinguette, *Chem. Commun.* **2013,** *49*, 218−227.

[113] T. A. Betley, Q. Wu, T. Van Voorhis, D. G. Nocera, *Inorg. Chem.* **2008,** *47*, 1849−1861.

[114] L. Tong, R. P. Thummel, *Chem. Sci.* **2016,** *7*, 6591−6603.

[115] J. G. Vos, J. M. Kelly, *Dalton Trans.* **2006**, 4869−4883.

[116] M. D. Kärkäs, B. Åkermark, *Dalton Trans.* **2016,** *45*, 14421−14461.

[117] J. Lloret-Fillol, M. Costas, *Adv. Organomet. Chem.* **2019,** *71*, 1−52.

[118] W. P. Griffith, The Chemistry of Ruthenium Oxidation Complexes. In *Ruthenium Oxidation Complexes: Their Uses as Homogenous Organic Catalysts*, Springer Dordrecht New York Heidelberg London: **2011**, 1−134.

[119] P. Garrido-Barros, C. Gimbert-Suriñach, R. Matheu, X. Sala, A. Llobet, *Chem. Soc. Rev.* **2017,** *46*, 6088−6098.

[120] I. Rapaport, L. Helm, A. E. Merbach, P. Bernhard, A. Ludi, *Inorg. Chem.* **1988,** *27*, 873−879.

[121] L. Helm, A. E. Merbach, *Chem. Rev.* **2005,** *105*, 1923−1960.

[122] B. Zhang, L. Sun, *Chem. Soc. Rev.* **2019,** *48*, 2216−2264.

[123] S. Fukuzumi, D. Hong, *Eur. J. Inorg. Chem.* **2014,** *2014*, 645−659.

[124] X. Sala, S. Maji, R. Bofill, J. García-Antón, L. Escriche, A. Llobet, *Acc. Chem. Res.* **2014,** *47*, 504−516.

[125] D. W. Shaffer, Y. Xie, J. J. Concepcion, *Chem. Soc. Rev.* **2017,** *46*, 6170−6193.

[126] D. R. Weinberg, C. J. Gagliardi, J. F. Hull, C. F. Murphy, C. A. Kent, B. C. Westlake, A. Paul, D. H. Ess, D. G. McCafferty, T. J. Meyer, *Chem. Rev.* **2012,** *112*, 4016−4093.

[127] R. Tyburski, T. Liu, S. D. Glover, L. Hammarström, *J. Am. Chem. Soc.* **2021,** *143*, 560−576.

[128] B. Zhang, L. Sun, *J. Am. Chem. Soc.* **2019,** *141*, 5565−5580.

[129] S. Romain, F. Bozoglian, X. Sala, A. Llobet, *J. Am. Chem. Soc.* **2009,** *131*, 2768−2769.

[130] L. Zhang, Y. Gao, X. Ding, Z. Yu, L. Sun, *ChemSusChem* **2014,** *7*, 2801−2804.

[131] F. Li, K. Fan, L. Wang, Q. Daniel, L. Duan, L. Sun, *ACS Catal.* **2015,** *5*, 3786−3790.

References

[132] L. Tong, L. Duan, Y. Xu, T. Privalov, L. Sun, *Angew. Chem. Int. Ed.* **2011,** *50*, 445−449.

[133] R. Staehle, L. Tong, L. Wang, L. Duan, A. Fischer, M. S. G. Ahlquist, L. Sun, S. Rau, *Inorg. Chem.* **2014,** *53*, 1307−1319.

[134] Z. Liu, Y. Gao, M. Zhang, J. Liu, *Inorg. Chem. Commun.* **2015,** *55*, 56−59.

[135] A. R. Parent, R. H. Crabtree, G. W. Brudvig, *Chem. Soc. Rev.* **2013,** *42*, 2247−2252.

[136] V. Nair, A. Deepthi, *Chem. Rev.* **2007,** *107*, 1862−1891.

[137] D. G. H. Hetterscheid, J. N. H. Reek, *Eur. J. Inorg. Chem.* **2014,** *2014*, 742−749.

[138] S. A. Hayes, P. Yu, T. J. O'Keefe, M. J. O'Keefe, J. O. Stoffer, *J. Electrochem. Soc.* **2002,** *149*, C623.

[139] J. J. Concepcion, J. W. Jurss, J. L. Templeton, T. J. Meyer, *J. Am. Chem. Soc.* **2008,** *130*, 16462−16463.

[140] D. B. Grotjahn, D. B. Brown, J. K. Martin, D. C. Marelius, M.-C. Abadjian, H. N. Tran, G. Kalyuzhny, K. S. Vecchio, Z. G. Specht, S. A. Cortes-Llamas, V. Miranda-Soto, C. van Niekerk, C. E. Moore, A. L. Rheingold, *J. Am. Chem. Soc.* **2011,** *133*, 19024−19027.

[141] M. M. Najafpour, A. N. Moghaddam, H. Dau, I. Zaharieva, *J. Am. Chem. Soc.* **2014,** *136*, 7245−7248.

[142] H. N. Kagalwala, L. Tong, R. Zong, L. Kohler, M. S. G. Ahlquist, T. Fan, K. J. Gagnon, R. P. Thummel, *ACS Catal.* **2017,** *7*, 2607−2615.

[143] Y. Xu, L. Duan, T. Åkermark, L. Tong, B.-L. Lee, R. Zhang, B. Åkermark, L. Sun, *Chem. Eur. J.* **2011,** *17*, 9520−9528.

[144] L. Duan, C. M. Araujo, M. S. G. Ahlquist, L. Sun, *Proc. Nat. Acad. Sci. USA* **2012,** *109*, 15584−15588.

[145] L. C. Clark, Jr., R. Wolf, D. Granger, Z. Taylor, *J. Appl. Physiol.* **1953,** *6*, 189−93.

[146] B. Limburg, E. Bouwman, S. Bonnet, *ACS Catal.* **2016,** *6*, 5273−5284.

[147] S. Fukuzumi, J. Jung, Y. Yamada, T. Kojima, W. Nam, *Chem. Asian J.* **2016,** *11*, 1138−1150.

[148] M. Natali, F. Nastasi, F. Puntoriero, A. Sartorel, *Eur. J. Inorg. Chem.* **2019**, 2027−2039.

[149] L. Duan, Y. Xu, P. Zhang, M. Wang, L. Sun, *Inorg. Chem.* **2010,** *49*, 209−215.

[150] A. Juris, V. Balzani, F. Barigelletti, S. Campagna, P. Belser, A. von Zelewsky, *Coord. Chem. Rev.* **1988,** *84*, 85−277.

[151] M. D. Kärkäs, B. Åkermark, *Chem. Rec.* **2016,** *16*, 940−963.

[152] A. Harriman, G. Porter, P. Walters, *J. Chem. Soc., Faraday Trans. 1* **1983,** *79*, 1335−1350.

[153] A.-L. Meza-Chincha, D. Schindler, M. Natali, F. Würthner, *ChemPhotoChem* **2021,** *5*, 173−183.

[154] U. S. Akhtar, E. L. Tae, Y. S. Chun, I. C. Hwang, K. B. Yoon, *ACS Catal.* **2016,** *6*, 8361−8369.

[155] R. Matheu, S. Neudeck, F. Meyer, X. Sala, A. Llobet, *ChemSusChem* **2016,** *9*, 3361−3369.

[156] R. M. Bullock, A. K. Das, A. M. Appel, *Chem. Eur. J.* **2017,** *23*, 7626−7641.

[157] K. L. Materna, R. H. Crabtree, G. W. Brudvig, *Chem. Soc. Rev.* **2017,** *46*, 6099−6110.

[158] M. A. Hoque, M. Gil-Sepulcre, A. de Aguirre, J. A. A. W. Elemans, D. Moonshiram, R. Matheu, Y. Shi, J. Benet-Buchholz, X. Sala, M. Malfois, E. Solano, J. Lim, A. Garzón-Manjón, C. Scheu, M. Lanza, F. Maseras, C. Gimbert-Suriñach, A. Llobet, *Nat. Chem.* **2020,** *12*, 1060−1066.

[159] D. Schindler, M. Gil-Sepulcre, J. O. Lindner, V. Stepanenko, D. Moonshiram, A. Llobet, F. Würthner, *Adv. Energy Mater.* **2020,** *10*, 2002329.

[160] E. M. Stuve, Overpotentials in Electrochemical Cells. In *Encyclopedia of Applied Electrochemistry*, Kreysa, G.; Ota, K.-i.; Savinell, R. F., Springer New York: New York, NY, **2014**, 1445−1453.

[161] A. J. Bard, L. R. Faulkner, In *Electrochemical Methods: Fundamentals and Applications, 2nd Edition*, John Wiley & Sons, Incorporated: **2000**, 1−856.

[162] E. S. Rountree, B. D. McCarthy, T. T. Eisenhart, J. L. Dempsey, *Inorg. Chem.* **2014,** *53*, 9983−10002.

[163] K. S. Joya, Y. F. Joya, K. Ocakoglu, R. van de Krol, *Angew. Chem. Int. Ed.* **2013,** *52*, 10426−10437.

[164] R. G. Ehl, A. J. Ihde, *J. Chem. Educ.* **1954,** *31*, 226.

[165] J. E. Jones, L. D. Hansen, S. E. Jones, D. S. Shelton, J. M. Thorne, *J. Phys. Chem.* **1995,** *99*, 6973−6979.

[166] S. W. Gersten, G. J. Samuels, T. J. Meyer, *J. Am. Chem. Soc.* **1982,** *104*, 4029−4030.

[167] J. A. Gilbert, D. S. Eggleston, W. R. Murphy, Jr., D. A. Geselowitz, S. W. Gersten, D. J. Hodgson, T. J. Meyer, *J. Am. Chem. Soc.* **1985,** *107*, 3855−3864.

[168] P. Doppelt, T. J. Meyer, *Inorg. Chem.* **1987,** *26*, 2027−2034.

[169] R. A. Binstead, C. W. Chronister, J. Ni, C. M. Hartshorn, T. J. Meyer, *J. Am. Chem. Soc.* **2000,** *122*, 8464−8473.

References

[170] F. Liu, J. J. Concepcion, J. W. Jurss, T. Cardolaccia, J. L. Templeton, T. J. Meyer, *Inorg. Chem.* **2008,** *47*, 1727−1752.

[171] D. Moonshiram, J. W. Jurss, J. J. Concepcion, T. Zakharova, I. Alperovich, T. J. Meyer, Y. Pushkar, *J. Am. Chem. Soc.* **2012,** *134*, 4625−4636.

[172] D. Moonshiram, V. Purohit, J. J. Concepcion, T. J. Meyer, Y. Pushkar, *Materials* **2013,** *6*, 392−409.

[173] D. Moonshiram, I. Alperovich, J. J. Concepcion, T. J. Meyer, Y. Pushkar, *Proc. Natl. Acad. Sci. USA* **2013,** *110*, 3765−3770.

[174] J. P. Collin, J. P. Sauvage, *Inorg. Chem.* **1986,** *25*, 135−141.

[175] K. Nagoshi, S. Yamashita, M. Yagi, M. Kaneko, *J. Mol. Cat. A* **1999,** *144*, 71−76.

[176] C. Sens, I. Romero, M. Rodríguez, A. Llobet, T. Parella, J. Benet-Buchholz, *J. Am. Chem. Soc.* **2004,** *126*, 7798−7799.

[177] F. Bozoglian, S. Romain, M. Z. Ertem, T. K. Todorova, C. Sens, J. Mola, M. Rodríguez, I. Romero, J. Benet-Buchholz, X. Fontrodona, C. J. Cramer, L. Gagliardi, A. Llobet, *J. Am. Chem. Soc.* **2009,** *131*, 15176−15187.

[178] S. Maji, L. Vigara, F. Cottone, F. Bozoglian, J. Benet-Buchholz, A. Llobet, *Angew. Chem Int. Ed.* **2012,** *51*, 5967−5970.

[179] S. Neudeck, S. Maji, I. López, S. Meyer, F. Meyer, A. Llobet, *J. Am. Chem. Soc.* **2014,** *136*, 24−27.

[180] R. Zong, R. P. Thummel, *J. Am. Chem. Soc.* **2005,** *127*, 12802−12803.

[181] D. Moonshiram, Y. Pineda-Galvan, D. Erdman, M. Palenik, R. Zong, R. Thummel, Y. Pushkar, *J. Am. Chem. Soc.* **2016,** *138*, 15605−15616.

[182] D. G. H. Hetterscheid, J. N. H. Reek, *Angew. Chem. Int. Ed.* **2012,** *51*, 9740−9747.

[183] J. J. Concepcion, M.-K. Tsai, J. T. Muckerman, T. J. Meyer, *J. Am. Chem. Soc.* **2010,** *132*, 1545−1557.

[184] M. Shigeyuki, S. Ken, *Chem. Lett.* **2009,** *38*, 182−183.

[185] A. Kimoto, K. Yamauchi, M. Yoshida, S. Masaoka, K. Sakai, *Chem. Commun.* **2012,** *48*, 239−241.

[186] D. J. Wasylenko, C. Ganesamoorthy, B. D. Koivisto, M. A. Henderson, C. P. Berlinguette, *Inorg. Chem.* **2010,** *49*, 2202−2209.

[187] D. J. Wasylenko, C. Ganesamoorthy, M. A. Henderson, B. D. Koivisto, H. D. Osthoff, C. P. Berlinguette, *J. Am. Chem. Soc.* **2010,** *132*, 16094−16106.

[188] R. Kang, K. Chen, J. Yao, S. Shaik, H. Chen, *Inorg. Chem.* **2014,** *53*, 7130−7136.

[189] T. Norrby, A. Börje, B. Åkermark, L. Hammarström, J. Alsins, K. Lashgari, R. Norrestam, J. Mårtensson, G. Stenhagen, *Inorg. Chem.* **1997,** *36*, 5850−5858.

[190] B. Das, A. Rahaman, A. Shatskiy, O. Verho, M. D. Kärkäs, B. Åkermark, *Acc. Chem. Res.* **2021,** *54*, 3326−3337.

[191] Y. Xu, T. Åkermark, V. Gyollai, D. Zou, L. Eriksson, L. Duan, R. Zhang, B. Åkermark, L. Sun, *Inorg. Chem.* **2009,** *48*, 2717−2719.

[192] Y. Xu, L. Duan, L. Tong, B. Åkermark, L. Sun, *Chem. Commun.* **2010,** *46*, 6506−6508.

[193] Y. Xu, A. Fischer, L. Duan, L. Tong, E. Gabrielsson, B. Åkermark, L. Sun, *Angew. Chem. Int. Ed.* **2010,** *49*, 8934−8937.

[194] L. Duan, A. Fischer, Y. Xu, L. Sun, *J. Am. Chem. Soc.* **2009,** *131*, 10397−10399.

[195] L. Wang, L. Duan, B. Stewart, M. Pu, J. Liu, T. Privalov, L. Sun, *J. Am. Chem. Soc.* **2012,** *134*, 18868−18880.

[196] Q. Daniel, P. Huang, T. Fan, Y. Wang, L. Duan, L. Wang, F. Li, Z. Rinkevicius, F. Mamedov, M. S. G. Ahlquist, S. Styring, L. Sun, *Coord. Chem. Rev.* **2017,** *346*, 206−215.

[197] J. J. Concepcion, D. K. Zhong, D. J. Szalda, J. T. Muckerman, E. Fujita, *Chem. Commun.* **2015,** *51*, 4105−4108.

[198] T. Liu, G. Li, N. Shen, L. Wang, B. J. J. Timmer, S. Zhou, B. Zhang, A. Kravchenko, B. Xu, M. S. G. Ahlquist, L. Sun, *CCS Chem.* **2022,** *4*, 2481−2490.

[199] D. Lebedev, Y. Pineda-Galvan, Y. Tokimaru, A. Fedorov, N. Kaeffer, C. Copéret, Y. Pushkar, *J. Am. Chem. Soc.* **2018,** *140*, 451−458.

[200] R. Matheu, A. Ghaderian, L. Francàs, P. Chernev, M. Z. Ertem, J. Benet-Buchholz, V. S. Batista, M. Haumann, C. Gimbert-Suriñach, X. Sala, A. Llobet, *Chem. Eur. J.* **2018,** *24*, 12838−12847.

[201] J. Nyhlén, L. Duan, B. Åkermark, L. Sun, T. Privalov, *Angew. Chem. Int. Ed.* **2010,** *49*, 1773−1777.

[202] S. Zhan, D. Mårtensson, M. Purg, S. C. L. Kamerlin, M. S. G. Ahlquist, *Angew. Chem. Int. Ed.* **2017,** *56*, 6962−6965.

[203] T. Fan, S. Zhan, M. S. G. Ahlquist, *ACS Catal.* **2016,** *6*, 8308−8312.

[204] R. Hoffmann, B. F. Beier, E. L. Muetterties, A. R. Rossi, *Inorg. Chem.* **1977,** *16*, 511−522.

[205] S. Zhan, B. Zhang, L. Sun, M. S. G. Ahlquist, *ACS Catal.* **2020,** *10*, 13364−13370.

[206] T. Fan, L. Duan, P. Huang, H. Chen, Q. Daniel, M. S. G. Ahlquist, L. Sun, *ACS Catal.* **2017,** *7*, 2956−2966.

[207] L. Duan, Y. Xu, M. Gorlov, L. Tong, S. Andersson, L. Sun, *Chem. Eur. J.* **2010,** *16*, 4659−4668.

[208] Y. Sato, S.-y. Takizawa, S. Murata, *Eur. J. Inorg. Chem.* **2015,** *2015*, 5495−5502.

References

[209] B. J. J. Timmer, O. Kravchenko, B. Zhang, T. Liu, L. Sun, *Inorg. Chem.* **2021,** *60*, 1202–1207.

[210] N. Vereshchuk, R. Matheu, J. Benet-Buchholz, M. Pipelier, J. Lebreton, D. Dubreuil, A. Tessier, C. Gimbert-Suriñach, M. Z. Ertem, A. Llobet, *J. Am. Chem. Soc.* **2020,** *142*, 5068–5077.

[211] A. Ghosh, S. Dasgupta, A. Kundu, S. Mandal, *Dalton Trans.* **2022,** *51*, 10320–10337.

[212] L. Duan, F. Bozoglian, S. Mandal, B. Stewart, T. Privalov, A. Llobet, L. Sun, *Nat. Chem.* **2012,** *4*, 418–423.

[213] S. Zhan, R. Zou, M. S. G. Ahlquist, *ACS Catal.* **2018,** *8*, 8642–8648.

[214] Y. Xie, D. W. Shaffer, J. J. Concepcion, *Inorg. Chem.* **2018,** *57*, 10533–10542.

[215] C. J. Richmond, R. Matheu, A. Poater, L. Falivene, J. Benet-Buchholz, X. Sala, L. Cavallo, A. Llobet, *Chem. Eur. J.* **2014,** *20*, 17282–17286.

[216] B. J. J. Timmer, O. Kravchenko, T. Liu, B. Zhang, L. Sun, *Angew. Chem. Int. Ed.* **2021,** *60*, 14504–14511.

[217] V. Kunz, V. Stepanenko, F. Würthner, *Chem. Commun.* **2015,** *51*, 290–293.

[218] B. Yang, X. Jiang, Q. Guo, T. Lei, L.-P. Zhang, B. Chen, C.-H. Tung, L.-Z. Wu, *Angew. Chem. Int. Ed.* **2016,** *55*, 6229–6234.

[219] T. Schlossarek, V. Stepanenko, F. Beuerle, F. Würthner, *Angew. Chem. Int. Ed.* **2022,** *61*, e202211445.

[220] J. Yi, S. Zhan, L. Chen, Q. Tian, N. Wang, J. Li, W. Xu, B. Zhang, M. S. G. Ahlquist, *J. Am. Chem. Soc.* **2021,** *143*, 2484–2490.

[221] L. Wang, L. Duan, Y. Wang, M. S. G. Ahlquist, L. Sun, *Chem. Commun.* **2014,** *50*, 12947–12950.

[222] Q. Daniel, L. Wang, L. Duan, F. Li, L. Sun, *Dalton Trans.* **2016,** *45*, 14689–14696.

[223] T. Zheng, L. Li, *New J. Chem.* **2018,** *42*, 2526–2536.

[224] J. Zhang, J. Du, J. Wang, Y. Wang, C. Wei, M. Li, *Angew. Chem. Int. Ed.* **2018,** *57*, 16698–16702.

[225] L. Duan, L. Wang, A. K. Inge, A. Fischer, X. Zou, L. Sun, *Inorg. Chem.* **2013,** *52*, 7844–7852.

[226] N. Song, J. J. Concepcion, R. A. Binstead, J. A. Rudd, A. K. Vannucci, C. J. Dares, M. K. Coggins, T. J. Meyer, *Proc. Natl. Acad. Sci. USA* **2015,** *112*, 4935–4940.

[227] R. Matheu, M. Z. Ertem, J. Benet-Buchholz, E. Coronado, V. S. Batista, X. Sala, A. Llobet, *J. Am. Chem. Soc.* **2015,** *137*, 10786–10795.

[228] S. Zhan, J. A. De Gracia Triviño, M. S. G. Ahlquist, *J. Am. Chem. Soc.* **2019,** *141*, 10247–10252.

[229] Y. Xie, D. W. Shaffer, A. Lewandowska-Andralojc, D. J. Szalda, J. J. Concepcion, *Angew. Chem. Int. Ed.* **2016,** *55*, 8067−8071.

[230] D. W. Shaffer, Y. Xie, D. J. Szalda, J. J. Concepcion, *J. Am. Chem. Soc.* **2017,** *139*, 15347−15355.

[231] N. Vereshchuk, J. Holub, M. Gil-Sepulcre, J. Benet-Buchholz, A. Llobet, *ACS Catal.* **2021**, 5240−5247.

[232] A. G. Nash, C. J. Breyer, B. D. Vincenzini, G. I. Elliott, J. Niklas, O. G. Poluektov, A. L. Rheingold, D. K. Smith, D. G. Musaev, D. B. Grotjahn, *Angew. Chem. Int. Ed.* **2021,** *60*, 1540−1545.

[233] J. L. Atwood, L. J. Barbour, S. Dalgarno, C. L. Raston, H. R. Webb, *J. Chem. Soc. Dalton Trans.* **2002**, 4351−4356.

[234] M. Yoshida, M. Kondo, S. Torii, K. Sakai, S. Masaoka, *Angew. Chem. Int. Ed.* **2015,** *54*, 7981−7984.

[235] Z. Liu, Y. Gao, J. Wang, Y. n. Yao, Y. Wei, X. Chen, *J. Energy Chem.* **2018,** *27*, 1402−1408.

[236] M. Gil-Sepulcre, M. Böhler, M. Schilling, F. Bozoglian, C. Bachmann, D. Scherrer, T. Fox, B. Spingler, C. Gimbert-Suriñach, R. Alberto, R. Bofill, X. Sala, S. Luber, C. J. Richmond, A. Llobet, *ChemSusChem* **2017,** *10*, 4517−4525.

[237] S. Zarra, D. M. Wood, D. A. Roberts, J. R. Nitschke, *Chem. Soc. Rev.* **2015,** *44*, 419−432.

[238] C. J. Brown, F. D. Toste, R. G. Bergman, K. N. Raymond, *Chem. Rev.* **2015,** *115,* 3012−3035.

[239] S. H. A. M. Leenders, R. Gramage-Doria, B. de Bruin, J. N. H. Reek, *Chem. Soc. Rev.* **2015,** *44*, 433−448.

[240] B. Li, F. Li, S. Bai, Z. Wang, L. Sun, Q. Yang, C. Li, *Energy Environ. Sci.* **2012,** *5*, 8229−8233.

[241] F. Yu, D. Poole III, S. Mathew, N. Yan, J. Hessels, N. Orth, I. Ivanović-Burmazović, J. N. H. Reek, *Angew. Chem. Int. Ed.* **2018,** *57*, 11247−11251.

[242] S. Karak, V. Stepanenko, M. A. Addicoat, P. Keßler, S. Moser, F. Beuerle, F. Würthner, *J. Am. Chem. Soc.* **2022,** *144*, 17661−17670.

[243] Y. Jiang, F. Li, B. Zhang, X. Li, X. Wang, F. Huang, L. Sun, *Angew. Chem. Int. Ed.* **2013,** *52*, 3398−3401.

[244] L. L. Zhang, Y. Gao, Z. Liu, X. Ding, Z. Yu, L. Sun, *Dalton Trans.* **2016,** *45*, 3814−3819.

[245] B. Weber, In *Koordinationschemie: Grundlagen und aktuelle Trends*, Springer Berlin Heidelberg: **2014**, 95−114.

[246] T. Liu, G. Li, N. Shen, L. Wang, B. J. J. Timmer, A. Kravchenko, S. Zhou, Y. Gao, Y. Yang, H. Yang, B. Xu, B. Zhang, M. S. G. Ahlquist, L. Sun, *Chem. Eur. J.* **2022,** *28*, e202104562.

[247] N. Noll, F. Würthner, *Chem. Eur. J.* **2021,** *27*, 444−450.

[248] A. K. Ringsmuth, M. J. Landsberg, B. Hankamer, *Renew. Sust. Energ. Rev.* **2016,** *62*, 134−163.

[249] International Energy Agency (IEA), In *World Energy Outlook 2017: Executive Summary 2017*, Paris, **2017**, 1−763.

[250] V. Balzani, A. Credi, M. Venturi, *ChemSusChem* **2008,** *1*, 26−58.

[251] G. W. Brudvig, S. Campagna, *Chem. Soc. Rev.* **2017,** *46*, 6085−6087.

[252] S. Berardi, S. Drouet, L. Francas, C. Gimbert-Suriñach, M. Guttentag, C. Richmond, T. Stoll, A. Llobet, *Chem. Soc. Rev.* **2014,** *43*, 7501−7519.

[253] L. Hammarström, *Acc. Chem. Res.* **2015,** *48*, 840−850.

[254] W. Rüttinger, G. C. Dismukes, *Chem. Rev.* **1997,** *97*, 1−24.

[255] V. Artero, M. Fontecave, *Chem. Soc. Rev.* **2013,** *42*, 2338−2356.

[256] R. Matheu, P. Garrido-Barros, M. Gil-Sepulcre, M. Z. Ertem, X. Sala, C. Gimbert-Suriñach, A. Llobet, *Nat. Chem. Rev.* **2019,** *3*, 331−341.

[257] L. Duan, L. Wang, F. Li, F. Li, L. Sun, *Acc. Chem. Res.* **2015,** *48*, 2084−2096.

[258] F. Li, C. Xu, X. Wang, Y. Wang, J. Du, L. Sun, *Chin. J. Catal.* **2018,** *39*, 446−452.

[259] V. Kunz, M. Schulze, D. Schmidt, F. Würthner, *ACS Energy Lett.* **2017,** *2*, 288−293.

[260] Y. Dong, J. Zhang, J. Ma Synthesis of dinuclear ruthenium supramolecular macrocyclic compound applied in photo-catalyzing water decomposition to release oxygen gas. CN104558050A, 2015.

[261] Z. Liu, S. K. M. Nalluri, J. F. Stoddart, *Chem. Soc. Rev.* **2017,** *46*, 2459−2478.

[262] C. D. Gutsche, In *Calixarenes*, Vol. 1, The Royal Society of Chemistry, Cambridge: **1989**, 105−124.

[263] D. M. Homden, C. Redshaw, *Chem. Rev.* **2008,** *108*, 5086−5130.

[264] L. Wu, B. Yang, L. Xing, J. Jian, Z. Tong Bipyridine ruthenium (II) complex containing system for catalytic oxygen production, bipyridine ruthenium (II) complex preparation method, and oxygen production method. CN104148112A, 2014.

[265] P. Sreedevi, J. B. Nair, P. Preethanuj, B. S. Jeeja, C. H. Suresh, K. K. Maiti, R. L. Varma, *Anal. Chem.* **2018,** *90*, 7148−7153.

[266] S. Chakraborty, S. G. Ramkumar, S. Ramakrishnan, *Macromolecules* **2017,** *50*, 5004−5013.

[267] Y. Liang, S. Liu, R. Wang, J. Liu, K. S. Chichak Preparation of organic compounds useful as electron-transporting material by Suzuki coupling reaction. WO2010151389A1, 2010.

[268] F. Li, B. Zhang, X. Li, Y. Jiang, L. Chen, Y. Li, L. Sun, *Angew. Chem. Int. Ed.* **2011,** *50*, 12276−12279.

[269] T. Arimura, H. Kawabata, T. Matsuda, T. Muramatsu, H. Satoh, K. Fujio, O. Manabe, S. Shinkai, *J. Org. Chem.* **1991,** *56*, 301−306.

[270] Y. Jiang, F. Li, F. Huang, B. Zhang, L. Sun, *Chin. J. Catal.* **2013,** *34*, 1489−1495.

[271] J. An, L. Duan, L. Sun, *Faraday Discuss.* **2012,** *155*, 267−275.

[272] M. V. Sheridan, B. D. Sherman, Z. Fang, K.-R. Wee, M. K. Coggins, T. J. Meyer, *ACS Catal.* **2015,** *5*, 4404-4409.

[273] L. Francàs, X. Sala, J. Benet-Buchholz, L. Escriche, A. Llobet, *ChemSusChem* **2009,** *2*, 321−329.

[274] B. Radaram, J. A. Ivie, W. M. Singh, R. M. Grudzien, J. H. Reibenspies, C. E. Webster, X. Zhao, *Inorg. Chem.* **2011,** *50*, 10564-10571.

[275] Z. Chen, J. J. Concepcion, X. Hu, W. Yang, P. G. Hoertz, T. J. Meyer, *Proc. Natl. Acad. Sci. USA* **2010,** *107*, 7225−7229.

[276] F. A. Carey, R. J. Sundberg, In *Advanced Organic Chemistry: Part A: Structure and Mechanisms*, Springer US: **2007**, 222−225.

[277] N. Iordanova, S. Hammes-Schiffer, *J. Am. Chem. Soc.* **2002,** *124*, 4848−4856.

[278] S. Hammes-Schiffer, A. A. Stuchebrukhov, *Chem. Rev.* **2010,** *110*, 6939−6960.

[279] S. Hammes-Schiffer, *J. Am. Chem. Soc.* **2015,** *137*, 8860−8871.

[280] J. S. Kretchmer, T. F. Miller, *Inorg. Chem.* **2016,** *55*, 1022−1031.

[281] P. K. Ghosh, B. S. Brunschwig, M. Chou, C. Creutz, N. Sutin, *J. Am. Chem. Soc.* **1984,** *106*, 4772−4783.

[282] L. Francàs, R. Matheu, E. Pastor, A. Reynal, S. Berardi, X. Sala, A. Llobet, J. R. Durrant, *ACS Catal.* **2017,** *7*, 5142−5150.

[283] M. Hara, C. C. Waraksa, J. T. Lean, B. A. Lewis, T. E. Mallouk, *J. Phys. Chem. A* **2000,** *104*, 5275−5280.

[284] H. S. White, W. G. Becker, A. J. Bard, *J. Phys. Chem.* **1984,** *88*, 1840−1846.

[285] N. Noll, A.-M. Krause, F. Beuerle, F. Würthner, *Nat. Catal.* **2022,** *5*, 867−877.

[286] J.-M. Lehn, *Science* **1993,** *260*, 1762−1763.

References

[287] M. Raynal, P. Ballester, A. Vidal-Ferran, P. W. N. M. van Leeuwen, *Chem. Soc. Rev.* **2014,** *43*, 1734−1787.

[288] E. Fischer, *Ber. Dtsch. Chem. Ges.* **1894,** *27*, 3479−3483.

[289] P. Dydio, J. N. H. Reek, *Chem. Sci.* **2014,** *5*, 2135−2145.

[290] D. W. Mulder, E. S. Boyd, R. Sarma, R. K. Lange, J. A. Endrizzi, J. B. Broderick, J. W. Peters, *Nature* **2010,** *465*, 248−251.

[291] M. L. Helm, M. P. Stewart, R. M. Bullock, M. R. DuBois, D. L. DuBois, *Science* **2011,** *333*, 863−866.

[292] R. Zaffaroni, N. Orth, I. Ivanović-Burmazović, J. N. H. Reek, *Angew. Chem. Int. Ed.* **2020,** *59*, 18485−18489.

[293] W. P. Brezinski, M. Karayilan, K. E. Clary, N. G. Pavlopoulos, S. Li, L. Fu, K. Matyjaszewski, D. H. Evans, R. S. Glass, D. L. Lichtenberger, J. Pyun, *Angew. Chem. Int. Ed.* **2018,** *57*, 11898−11902.

[294] J. Daubignard, R. J. Detz, A. C. H. Jans, B. de Bruin, J. N. H. Reek, *Angew. Chem. Int. Ed.* **2017,** *56*, 13056−13060.

[295] J. Wen, F. Wang, X. Zhang, *Chem. Soc. Rev.* **2021,** *50*, 3211−3237.

[296] W. Fang, B. Breit, *Angew. Chem. Int. Ed.* **2018,** *57*, 14817−14821.

[297] S. S. Nurttila, P. R. Linnebank, T. Krachko, J. N. H. Reek, *ACS Catal.* **2018,** *8*, 3469−3488.

[298] S. Das, C. D. Incarvito, R. H. Crabtree, G. W. Brudvig, *Science* **2006,** *312*, 1941−1943.

[299] Y. Kuninobu, H. Ida, M. Nishi, M. Kanai, *Nat. Chem.* **2015,** *7*, 712−717.

[300] A. Fanourakis, P. J. Docherty, P. Chuentragool, R. J. Phipps, *ACS Catal.* **2020,** *10*, 10672−10714.

[301] M. C. Schwarzer, A. Fujioka, T. Ishii, H. Ohmiya, S. Mori, M. Sawamura, *Chem. Sci.* **2018,** *9*, 3484−3493.

[302] J. R. Frost, S. M. Huber, S. Breitenlechner, C. Bannwarth, T. Bach, *Angew. Chem. Int. Ed.* **2015,** *54*, 691−695.

[303] L. Vicens, G. Olivo, M. Costas, *Angew. Chem. Int. Ed.* **2022,** *61*, e202114932.

[304] P. Dydio, R. J. Detz, J. N. H. Reek, *J. Am. Chem. Soc.* **2013,** *135*, 10817−10828.

[305] T. Steiner, *Angew. Chem. Int. Ed.* **2002,** *41*, 48−76.

[306] X. Li, B. Lv, X.-P. Zhang, X. Jin, K. Guo, D. Zhou, H. Bian, W. Zhang, U.-P. Apfel, R. Cao, *Angew. Chem. Int. Ed.* **2022,** *61*, e202114310.

[307] P. Pyykkö, *J. Organomet. Chem.* **2006,** *691*, 4336−4340.

[308] N. Noll, T. Groß, K. Shoyama, F. Beuerle, F. Würthner, *Angew. Chem. Int. Ed.* **2023,** *62*, e202217745.

[309] D. J. Selkoe, *Nature* **2003,** *426*, 900−904.

[310] E. S. Wiedner, A. M. Appel, S. Raugei, W. J. Shaw, R. M. Bullock, *Chem. Rev.* **2022,** *122*, 12427−12474.

[311] D. K. Bediako, B. H. Solis, D. K. Dogutan, M. M. Roubelakis, A. G. Maher, C. H. Lee, M. B. Chambers, S. Hammes-Schiffer, D. G. Nocera, *Proc. Natl. Acad. Sci. USA* **2014,** *111*, 15001−15006.

[312] M. Schilling, R. A. Cunha, S. Luber, *ACS Catal.* **2020,** *10*, 7657−7667.

[313] R. Scott Lokey, B. L. Iverson, *Nature* **1995,** *375*, 303−305.

[314] S. Hecht, I. Huc, In *Foldamers: Structure, Properties and Applications*, Wiley-VCH Verlag GmbH & Co, KGaA: **2007**, 1−435.

[315] C. M. Goodman, S. Choi, S. Shandler, W. F. DeGrado, *Nat. Chem. Biol.* **2007,** *3*, 252−262.

[316] A.-B. Bornhof, A. Bauzá, A. Aster, M. Pupier, A. Frontera, E. Vauthey, N. Sakai, S. Matile, *J. Am. Chem. Soc.* **2018,** *140*, 4884−4892.

[317] B. Legrand, J. Aguesseau-Kondrotas, M. Simon, L. Maillard, *Catalysts* **2020,** *10*, 700.

[318] Z. C. Girvin, S. H. Gellman, *J. Am. Chem. Soc.* **2020,** *142*, 17211−17223.

[319] S. S. Batsanov, *Inorg. Mater.* **2001,** *37*, 871−885.

[320] K. Nakamoto, *J. Phys. Chem.* **1960,** *64*, 1420−1425.

[321] A. Volpe, C. Tubaro, M. Natali, A. Sartorel, G. W. Brudvig, M. Bonchio, *Inorg. Chem.* **2019,** *58*, 16537−16545.

[322] M. Bonchio, Z. Syrgiannis, M. Burian, N. Marino, E. Pizzolato, K. Dirian, F. Rigodanza, G. A. Volpato, G. La Ganga, N. Demitri, S. Berardi, H. Amenitsch, D. M. Guldi, S. Caramori, C. A. Bignozzi, A. Sartorel, M. Prato, *Nat. Chem.* **2019,** *11*, 146−153.

[323] A. Volpe, M. Natali, C. Graiff, A. Sartorel, C. Tubaro, M. Bonchio, *Dalton Trans.* **2020,** *49*, 2696−2705.

[324] G. A. Volpato, M. Marasi, T. Gobbato, F. Valentini, F. Sabuzi, V. Gagliardi, A. Bonetto, A. Marcomini, S. Berardi, V. Conte, M. Bonchio, S. Caramori, P. Galloni, A. Sartorel, *Chem. Commun.* **2020,** *56*, 2248−2251.

[325] F. Puntoriero, G. La Ganga, A. M. Cancelliere, S. Campagna, *Curr. Opin. Green Sustainable Chem.* **2022,** *36*, 100636.

[326] J. Barber, *Q. Rev. Biophys.* **2003,** *36*, 71−89.

[327] U. Markel, D. F. Sauer, J. Schiffels, J. Okuda, U. Schwaneberg, *Angew. Chem. Int. Ed.* **2019,** *58*, 4454−4464.

References

[328] C. L. Donnici, D. H. Maximo Filho, L. L. C. Moreira, G. Teixeira dos Reis, E. Cordeiro, I. M. Ferreira de Oliveira, S. Carvalho, E. B. Paniago, *J. Braz. Chem. Soc.* **1998,** *9*, 455−460.

[329] I. P. Evans, A. Spencer, G. Wilkinson, *J. Chem. Soc. Dalton Trans.* **1973**, 204−9.

[330] E. Dulière, M. Devillers, J. Marchand-Brynaert, *Organometallics* **2003,** *22*, 804−811.

[331] G. R. Fulmer, A. J. M. Miller, N. H. Sherden, H. E. Gottlieb, A. Nudelman, B. M. Stoltz, J. E. Bercaw, K. I. Goldberg, *Organometallics* **2010,** *29*, 2176-2179.

[332] S. Gawęda, G. Stochel, K. Szaciłowski, *J. Phys. Chem. C* **2008,** *112*, 19131-19141.

[333] J. J. P. Stewart, *J. Mol. Model.* **2007,** *13*, 1173−1213.

[334] J. J. P. Stewart, MOPAC2016, Version: 17.279L, Stewart Computational Chemistry, web: http://OpenMopac.net.

[335] A. Klamt, G. Schüürmann, *J. Chem. Soc., Perkin Trans. 2* **1993**, 799−805.

[336] J. Vicens, V. Böhmer, In *Calixarenes: A Versatile Class of Macrocyclic Compounds*, Vol. 3, Springer Netherlands: **1991**, 3-4.

[337] R. Evans, Z. Deng, A. K. Rogerson, A. S. McLachlan, J. J. Richards, M. Nilsson, G. A. Morris, *Angew. Chem. Int. Ed.* **2013,** *52*, 3199−3202.

[338] L. Wang, D. W. Shaffer, G. F. Manbeck, D. E. Polyansky, J. J. Concepcion, *ACS Catal.* **2020,** *10*, 580−585.

[339] S. Berardi, L. Francàs, S. Neudeck, S. Maji, J. Benet-Buchholz, F. Meyer, A. Llobet, *ChemSusChem* **2015,** *8*, 3688−3696.

[340] J. M. Cid, G. Duvey, G. Tresadern, V. Nhem, R. Furnari, P. Cluzeau, J. A. Vega, A. I. de Lucas, E. Matesanz, J. M. Alonso, M. L. Linares, J. I. Andrés, S. M. Poli, R. Lutjens, H. Himogai, J.-P. Rocher, G. J. Macdonald, D. Oehlrich, H. Lavreysen, A. Ahnaou, W. Drinkenburg, C. Mackie, A. A. Trabanco, *J. Med. Chem.* **2012,** *55*, 2388−2405.

[341] G. Sheldrick, *Acta Crystallogr. A* **2008,** *64*, 112-122.

[342] A. Spek, *J. Appl. Crystallogr.* **2003,** *36*, 7-13.

[343] A. Spek, *Acta Crystallogr. C* **2015,** *71*, 9-18.

[344] Y. Gao, X. Ding, J. Liu, L. Wang, Z. Lu, L. Li, L. Sun, *J. Am. Chem. Soc.* **2013,** *135*, 4219−4222.

[345] F. Olivé, S. K. Chaudhari, K. R. Patil, A. Coronas, *Can. J. Chem. Eng.* **1996,** *74*, 163−169.

[346] W. Kabsch, *Acta Crystallogr. D* **2010,** *66*, 125-132.

[347] *Bruker*. XREP Version 2014/2, Bruker AXS Inc., Madison: 2014.

[348] G. Sheldrick, *Acta Crystallogr. A* **2015,** *71*, 3-8.

[349] G. Sheldrick, *Acta Crystallogr. C* **2015,** *71*, 3-8.

[350]   The PyMOL Molecular Graphics Systeme, Version 2.4.2 Schrödinger, LLC.

Individual Contributions

The coauthors of the publications included in this cumulative thesis are informed and agree with the reprint and the individual contributions as stated below.

A Calix[4]arene-Based Cyclic Dinuclear Ruthenium Complex for Light-Driven Catalytic Water Oxidation

N. Noll, F. Würthner, *Chem. Eur. J.* **2021**, *27*, 444−450.

Autoren/innen (ggf. Haupt-/ Ko-/ korrespondierende/r Autor/in) mit Vorname Nachname (Initialen): Niklas Noll (Hauptautor, N.N.), Frank Würthner (korrespondierender Autor, F.W.)

Detaillierte Darstellung der Anteile an der Veröffentlichung (in %)

Autor	N.N.	F.W.	∑ in Prozent
Research concepcion	2%	3%	5%
Synthesis and characterization	35%	-	35%
Characterization of optical and redox properties	5%	-	5%
Theoretical calculations	5%	-	5%
Investigation of catalytic properties	30%	-	30%
Publication writing	7%	3%	10%
Publication correction	-	5%	5%
Publication coordination	-	5%	5%
Summe	84%	16%	100%

Enzyme-like water preorganization in a synthetic molecular cleft for homogenous water oxidation catalysis

N. Noll, A.-M. Krause, F. Beuerle, F. Würthner, *Nat. Catal.* **2022**, *5*, 867–877.

Autoren/innen (ggf. Haupt-/ Ko-/ korrespondierende/r Autor/in) mit Vorname Nachname (Initialen): Niklas Noll (Hauptautor, N.N.), Ana-Maria Krause (Koautor, A.-M.K.), Florian Beuerle (Koautor, F.B.), Frank Würthner (korrespondierender Autor, F.W.)

Detaillierte Darstellung der Anteile an der Veröffentlichung (in %)

Autor	N.N.	A.-M.K.	F.B.	F.W.	∑ in Prozent
Research concepcion	2%			4%	6%
Synthesis and characterization	30%				30%
Investigation of catalytic properties	20%				20%
pH-dependent NMR measurements	10%				10%
Crystallographic analysis		3%	2%		5%
Characterization of solid-state structures	10%				10%
Publication writing	8%		1%	1%	10%
Publication correction			2%	2%	4%
Publication coordination	1%		2%	2%	5%
Summe	81%	3%	7%	9%	100%

Folding-Induced Promotion of Proton-Coupled Electron Transfers via Proximal Base for Light-Driven Water Oxidation

N. Noll, T. Groß, K. Shoyama, F. Beuerle, F. Würthner, *Angew. Chem. Int. Ed.* **2023**, *62*, e202217745.

Autoren/innen (ggf. Haupt-/ Ko-/ korrespondierende/r Autor/in) mit Vorname Nachname (Initialen): Niklas Noll (Hauptautor, N.N.), Tobias Groß (Koautor, T.G.), Kazutaka Shoyama (Koautor, K.S.), Florian Beuerle (Koautor, F.B.), Frank Würthner (korrespondierender Autor, F.W.)

Detaillierte Darstellung der Anteile an der Veröffentlichung (in %)

Autor	N.N.	T.G.	K.S.	F.B.	F.W.	∑ in Prozent
Research concepcion	2%				4%	6%
Synthesis and general compound characterization	25%	10%				35%
Investigation of electronic properties	5%					5%
Investigation of catalytic properties	20%					20%
pH-dependent NMR measurements	10%					10%
Crystallographic analysis			5%			5%
Publication writing	8%			2%		10%
Publication correction				2%	2%	4%
Publication coordination	1%			2%	2%	5%
Summe	71%	10%	5%	6%	8%	100%

Acknowledgement/Danksagung

List of Publications

Enhancing the Stability of Photogenerated Benzophenone Triplet Radical Pairs through Supramolecular Assembly

B. A. DeHaven, D. W. Goodlett, A. J. Sindt, <u>N. Noll</u>, M. De Vetta, M. D. Smith, C. R. Martin, L. González, L. S. Shimizu, *J. Am. Chem. Soc.* **2018**, *140*, 13064−13070.

A Calix[4]arene-Based Cyclic Dinuclear Ruthenium Complex for Light-Driven Catalytic Water Oxidation

<u>N. Noll</u>, F. Würthner, *Chem. Eur. J.* **2021**, *27*, 444−450.

Supramolecular p/n-heterojunction of C60-functionalized bis(merocyanine) quadruple stack: A model system for charge carrier separation and recombination in organic solar cells

D. Bialas, F. Fennel, <u>N. Noll</u>, M. Holzapfel, A. Schmiedel, C. Lambert, F. Würthner, *Nat. Sci.* **2022**, *2*, e210430.

Enzyme-like water preorganization in a synthetic molecular cleft for homogenous water oxidation catalysis

<u>N. Noll</u>, A.-M. Krause, F. Beuerle, F. Würthner, *Nat. Catal.* **2022**, *5*, 867−877.

Folding-Induced Promotion of Proton-Coupled Electron Transfers via Proximal Base for Light-Driven Water Oxidation

<u>N. Noll</u>, T. Groß, K. Shoyama, F. Beuerle, F. Würthner, *Angew. Chem. Int. Ed.* **2023**, *62*, e202217745.